Understanding the Optical and Photophysical Properties of Organic and Hybrid Macromolecules and Polymers for Solar Cell Application

by

Ifeanyi Kizito Madu

A dissertation submitted in partial fulfillment
of the requirements for the degree of
Doctor of Philosophy
(Chemical Engineering)
in the University of Michigan
2021

Doctoral Committee:

 Professor Lola Eniola-Adefeso, Co-Chair
 Professor Theodore G. Goodson III, Co-Chair
 Assistant Professor Andrej Lenert
 Professor Anne McNeil
 Professor Robert Ziff

Ifeanyi Kizito Madu

kizmadu@umich.edu

ORCID iD: 0000-0003-3576-1427

Dedication

This work is dedicated to my family and to all my teachers for raising me in the ways of God and science. It is also dedicated to the hard-working organic photovoltaic scientists and engineers, the efficiency we desire is closer than we know.

Acknowledgements

I will start from how it all began. My love for math and science started in my Primary (Elementary) School days and was honed and nurtured by my class teacher at the time who made me participate in several science events and competitions at the time. My parents also made sure that I was learning ahead of my peers by investing in after-school tutoring, specifically for math, physics and chemistry. In Secondary (High) School, I had several teachers who in their own way wanted me to succeed academically and believed in me even when I did not believe in myself. Prominent among them was my Advanced Math teacher at the time – Mr. Fatoki, who always had his door open to me whenever I had any question about 'anything' math-related even if it was not directly related to what he was teaching at the time. Mr Fatoki went the extra mile to make sure that we not only did well in what was taught in class, but that we also understood the basics and governing principles to tackling most math problems.

Before the completion of my Secondary School education, I knew specifically what I wanted to study in college – Chemical Engineering. My college education at the Federal University of Technology, Owerri (FUTO), was funded by Exxon-Mobil Producing Nigeria in collaboration with the Nigerian National Petroleum Corporation, and I am immensely grateful for the scholarship. The training and education I received at FUTO was really what got me prepared and ready for graduate school. The efforts by my lecturers and academic advisors – Dr. Ike, Dr. Ibe, Dr. Onyelucheya, among others was vital to my success, and I am grateful to all of them. Dr. Ibe, an MIT alumnus and visiting scholar to FUTO at the time, was my key motivator to embarking on the PhD route. The award I received from his fund and from that of Dr. Osanakpo for finishing as

the best graduating student from the department of Chemical Engineering, motivated and reaffirmed my zeal to continue to graduate school. For this I am also grateful. I will also acknowledge Dr. Nwakaudu, my mentor and departmental chair when I was retained as a graduate assistant in FUTO, who pushed me to do research and publish scientific articles which did help in getting me admitted into graduate school.

I want to express my gratitude to the faculty, staff and students of the department of Chemical Engineering and Chemistry for accepting me to study with them and training me to do phenomenal research. More specifically, I am thankful to Dr. Lola Eniola-Adefeso for trusting in me to succeed academically and connecting me to the Goodson Lab. I am also thankful to her and her husband – Mr. Adefeso, for welcoming me into their home and providing a strong support system. I sincerely appreciate the care and attention I received from the chair of Chemical Engineering department and role-model, Dr. Sharon Glotzer. I am grateful to Susan Hamlin, the Chemical Engineering Graduate program coordinator, for all the guidance, and assistance she provided through-out my program. I am thankful to Dr. Benedetta Carlotti and to Dr. Oleg Varnavski for helping me understand the key experimental laser setups that were vital for most of the projects in this thesis. I appreciate my graduate advisor Dr. Theodore Goodson III for providing me with the opportunity to do research with his group and for pushing me to be a better scientist. I am also grateful to my collaborators – Hanjie Jiang (Dr. Zimmerman), Jun Guan (Dr. Laine), Evan Muller (Dr. Malika), Dr. Zhengxu Cai (Dr. Luping), because without their help, this thesis would not be complete. I thank my dissertation committee members: Dr. Andrej Lenert, Dr. Robert Ziff, Dr. Anne McNeil and Dr. Eniola-Adefeso for all the suggestions and feedback they provided towards this thesis. Finally, I am appreciative of all my colleagues in the Goodson Lab, including those who already graduated, for sustaining a fun, engaging, and interactive learning environment.

Table of Contents

List of Tables

List of Figures

List of Schemes

Abstract

Organic solar cell materials represent a better sustainable alternative relative to inorganic materials in terms of lower cost, ease of large-scale processing, better absorptivity, ease of tunability, and unique flexibility so as to be used on different kinds of surfaces. With the knowledge of the fundamental molecular structure of an organic solar cell material, scientists and engineers can predict the electronic and optically-excited properties. Hence, understanding the structure-property-function relationships is paramount in optimizing the solar cell device performance. This thesis is structured into two sections. The first section focuses on electron acceptors in the active layer of bulk heterojunction (BHJ) device architectures, and the second section discuses organic and hybrid electron donors.

In the first section, the optical and photophysical properties of several structural variations of a special class of non-fullerene acceptor compound – perylene diimide (PDI), are described in substantive details with a number of studies. In the active layer, this material functions as the electron acceptor, and acts in tandem as an excellent light-harvester. The first study on intramolecular singlet exciton fission (iSEF) in PDI trimers – the generation of two triplet charges from one photogenerated singlet, seeks to elucidate the important structural features required to obtain high yield triplet formation as a result of multiexciton generation and subsequent separation in multichromophoric PDI systems. Time-resolved spectroscopic measurements were used to show how the flexibility of the π-bridge connections in these multichromophoric PDI systems, strongly affect the triplet yield and triplet formation rate. The results obtained showed that the weak electronic coupling observed in the twisted PDI trimer is necessary to activate iSEF in

multichromophoric systems. The next chapter is about the effect of ring-fusion on the optically-excited properties of N-annulated thiophene π-bridged PDI dimers. The results of this study show that ring-fusion favors ultrafast photoinduced intramolecular charge transfer (CT) and opens up the triplet excited state deactivation pathway that was absent in the unfused dimer. The triplets were formed via spin-orbit CT intersystem crossing pathway owing to the strong electronic coupling present in the fused-ring thiophene π-bridged dimer. The final chapter about PDIs involves two analogous positional isomers, exhibiting twisted vs planar geometries. The results confirm an efficient and faster intramolecular CT mechanism (symmetry-breaking) taking place in the planar PDI dimer, leading to better device performance despite strong aggregation effects.

The second section involves the electron-donating portion of the active layer of BHJ devices. For donor polymers, the influence of furan vs thiophene π-bridge heterocycles and linear vs bulky sidechains on the optical properties of donor–π-bridge–acceptor polymers, was investigated. The results showed that the furan π-bridge polymer displayed better solar absorptivity and showed a more planar polymeric backbone that correlated to better CT and longer excitonic lifetimes. Also, the linear sidechain polymers showed improved solution-processability leading to better photophysical properties, like longer fluorescence lifetime, relative to the bulky sidechain polymers in BHJs. The final chapter of this dissertation covers three structural variations (Cube, Half and Corner) of hybrid silsesquioxanes, functionalized with donor chromophore(s) at the edge(s) of the cage unit. Improved excitation energy transport and ultrafast CT was observed in the Cube compound relative to the Half and Corner systems attributed to strong electronic coupling. A detailed summary of this dissertation alongside a set of molecular geometry guidelines for structure-function relationships and future direction, was provided.

Chapter 1

Introduction and Background

1.1 The World Energy Landscape: Alternative and Renewable Sources

The need to combat climate change, the fluctuation of energy prices due to geo-political constraints, the limited reserves of fossil fuels, the rapid population growth, as well as a bid to reduce over-dependence on fossil fuel as the main source of energy, has led to the development of a more sustainable means of energy. Power generating capacity using renewable energy is on a continuous rise despite the decline in oil prices, and lots of investments are continuously made to further improve its efficiency and get it to compete reasonably with fossil fuel.[1–3] **Figure 1.1** shows that net additions of renewable power generation capacity clearly outpaced net installations of both fossil fuel and nuclear power capacity combined. Renewable energy had another record-breaking year in 2019, as the installed power capacity grew more than 200 gigawatts (GW) – its largest increase ever.[3] Actually, it was reported that producing electricity from renewables nearly anywhere in the world is more cost effective than producing it from new coal-fired power plants. In a growing number of regions, it has become cheaper to build new wind or solar PV plants than to operate existing coal-fired power plants.[4,5]

Although renewable energy capacity is rising as observed in **Figure 1.1**, fossil fuels still dominates the energy landscape, supplying about 73% of the global electricity production by the end of 2019.[3] This leaves fossil fuel as currently the world's primary energy source. Fossil energy sources including crude oil, coal and natural gas, are non-renewable resources that formed from

decayed prehistoric plants and animals buried by layers of rock. Fossil fuels are finite resources, and their extraction can cause significant and irreparable damage to the local environment.[6] The burning of fossil fuel leads to the release of gases that contribute to the greenhouse effect and could potentially lead to catastrophic changes in the Earth's climate. These major drawbacks have led to extensive investigation into more renewable energy sources, technologies, materials, methods, and policies. In particular, there has been significant attention given to alternative energy sources such as geothermal, hydropower, wind, and solar.
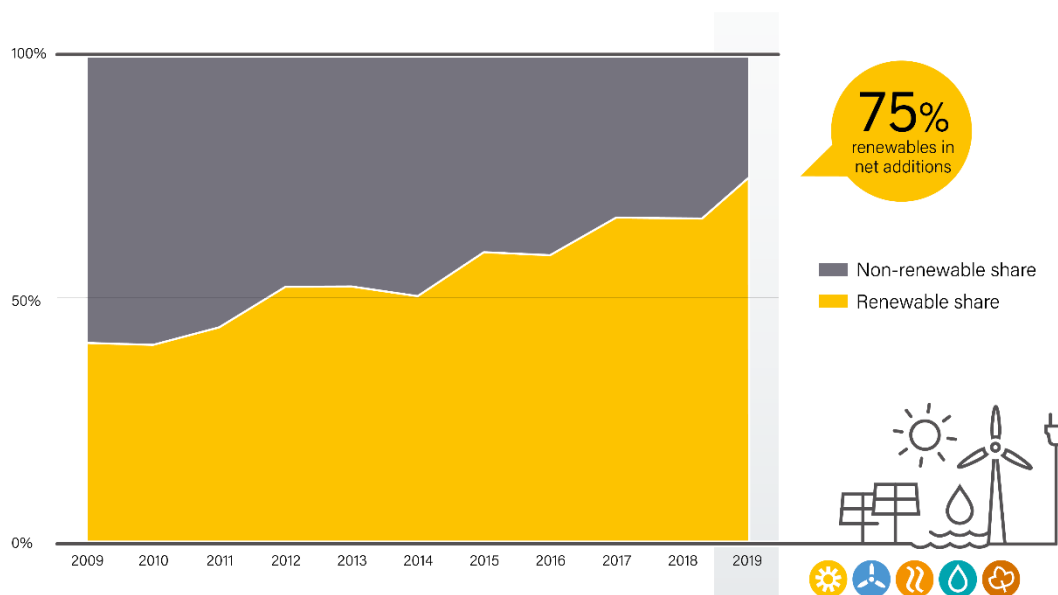
Figure 1.1 Renewable and non-renewable shares of net annual additions in power generating capacity (Source: REN21, 2020).[3]

Among the renewable sources, hydropower makes up the majority of the estimated generation share.[2,3,7] Hydropower is energy from water sources such as the ocean, rivers and waterfalls. Hydroelectric power generation uses either the flow of water or gravitational potential energy of water to drive turbines in order to generate electricity. Next after hydropower, wind energy takes up the highest energy share in the renewable energy space as the second most technologically advanced renewable energy source.[3] For power generation, the kinetic energy of wind is harvested using wind turbines. As wind travels in the pathway of the wind turbine, which

consists of electrical generator, shaft and rotor blades, the blades will experience forces that cause them to overcome the inertia and then start extracting power from the free stream.[8] Geothermal energy, another renewable source of energy, is the energy contained as heat in the Earth's interior. It is particularly attractive since it is the most concentrated form of so-called "zero-cost" energy and it is not subject to diurnal fluctuations or adverse weather changes like hydropower, wind or solar.[9–11] Bio-power obtained from biofuels (bioethanol, biodiesel), is another renewable source of energy.[12] These biofuel products, obtained from biomass, are chemically non-toxic in nature and biodegradable, in addition to insignificant contribution to CO_2 and other particulate matter emissions because atmospheric CO_2 is required to grow the biomass.[13,14]

The Sun is an enormous source of solar energy. It provides approximately 100,000 terawatts (TW) to the Earth which is about 10,000 times more than the present rate of the world's present energy consumption.[15] To put this into perspective, in 90 minutes, enough sunlight strikes the earth to provide the entire planet's energy needs for one year. The solar resource is enormous compared to our energy needs (see **Figure 1.2**). The annual amount of energy received from the Sun far surpasses the total estimated fossil resources, including uranium fission. It also dwarfs the yearly potential of renewable energy deriving from solar energy: photosynthesis (i.e., biomass), hydro power and wind power. It can be captured and transformed into heat or electricity. It varies in quantity and quality in places but also in time, in ways that are not entirely predictable.[16] The solar irradiance, i.e. amount of power that the Sun deposits per unit area that is directly exposed to sunlight and perpendicular to it, is 1,368 watts per square meter (W/m^2) at that distance. This measure is called the solar constant. However, sunlight on the surface of our planet is attenuated by the earth's atmosphere so less power arrives at the surface – about 1,000 W/m^2 in clear

conditions when the Sun is near the zenith.[16] Solar radiation from the Sun can also be viewed as a flux of electromagnetic particles or photons.
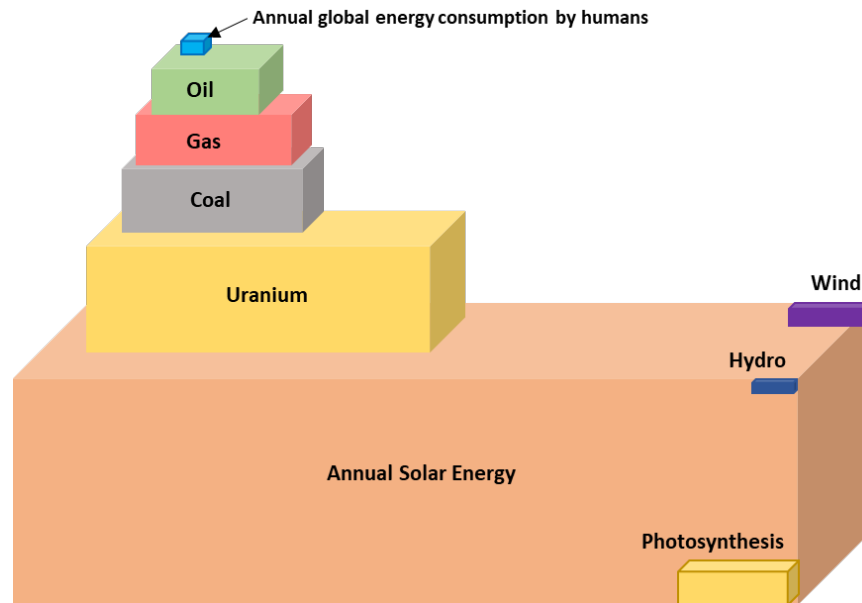
Figure 1.2 Total energy resources depicting solar energy as the largest resource on earth.

Solar irradiative energy is easily transformed into heat through absorption by gaseous, liquid or solid materials. This is referred to as a solar-thermal process.[17–19] This heat can then be used in space heating, in sanitary water heating or pool water heating, for evaporating water and drying things (notably crops and food). The heat can also be transformed into mechanical work or electricity via thermoelectric or thermoelectronic process.[20–22] Thermoelectric materials, which require no moving parts to convert thermal gradients directly into electricity, are an attractive possibility for reliable and inexpensive electricity production. Although, the thermoelectric effect has been known for nearly 200 years, materials that can potentially convert heat to electricity efficiently enough for widespread use have emerged only since the 1990s.[23] The most promising materials are nanostructured composites. Quantum-dot or nanowire substructures introduce spikes in the density of states to tune the thermopower, and interfaces between the composite materials block thermal transport but allow electrical transport.[24,25] Future ongoing challenges are to achieve

the same performance in nanostructured bulk materials that can handle large amounts of power and to use nanodot or nanowire inclusions to control the thermopower.[26–28] Finally, the heat can also facilitate chemical or physical transformations suitable for industrial processes or the manufacture of various energy vectors or fuels, notably hydrogen.[29–31]

Solar photons can also be directly transformed into chemical fuel. An estimated 100 TW of solar energy go into photosynthesis, the production of sugars and starches from water and carbon dioxide via various endothermic reactions.[32–34] In nature, there are many examples of metabolic systems that convert sunlight and chemicals into high-energy fuels (natural photosynthesis). Green plants use an elaborate complex of chlorophyll molecules coupled to a reaction center to split water into protons, electrons, and oxygen.[35–37] Artificial photosynthesis takes the ultimate step of using inanimate components to convert sunlight into chemical fuel.[38,39] Here, the antenna units harvest sunlight and the excitation energy is funneled to the reaction center where multistep electron-transfer reactions occur to generate potential that can drive chemical reactions to produce chemical energy that can be used and stored by the organism.[40–42]

Finally, solar photons can be captured to produce electricity. This is done with the use of solar cells or photovoltaic devices that capture photonic energy by exciting electrons across the bandgap of a semiconductor, creating electron-hole pairs that are then charge separated. Solar energy is one of the major sources of renewable power generation. Out of the 200 GW of new renewable power generating capacity installed in 2019 only, around 115 GW was from solar photovoltaics, cementing the technology's status as the leader in new electricity generation capacity.[3] This is depicted clearly in **Figure 1.3**. Photovoltaics is developing rapidly, and its costs are falling just as fast. Around the world, countries and companies are investing in solar generation capacity on an unprecedented scale, and, as a consequence, costs continue to fall, and technologies

improve. Solar cells can be used anywhere there is sunlight, on building rooftops, on building walls/windows, on roads, on cars. Solar energy holds a number of significant advantages over other alternative energy sources in that individuals can invest in their own power generation. Also, in solar cells, there are no moving parts, hence lower manufacturing cost and lower down time.
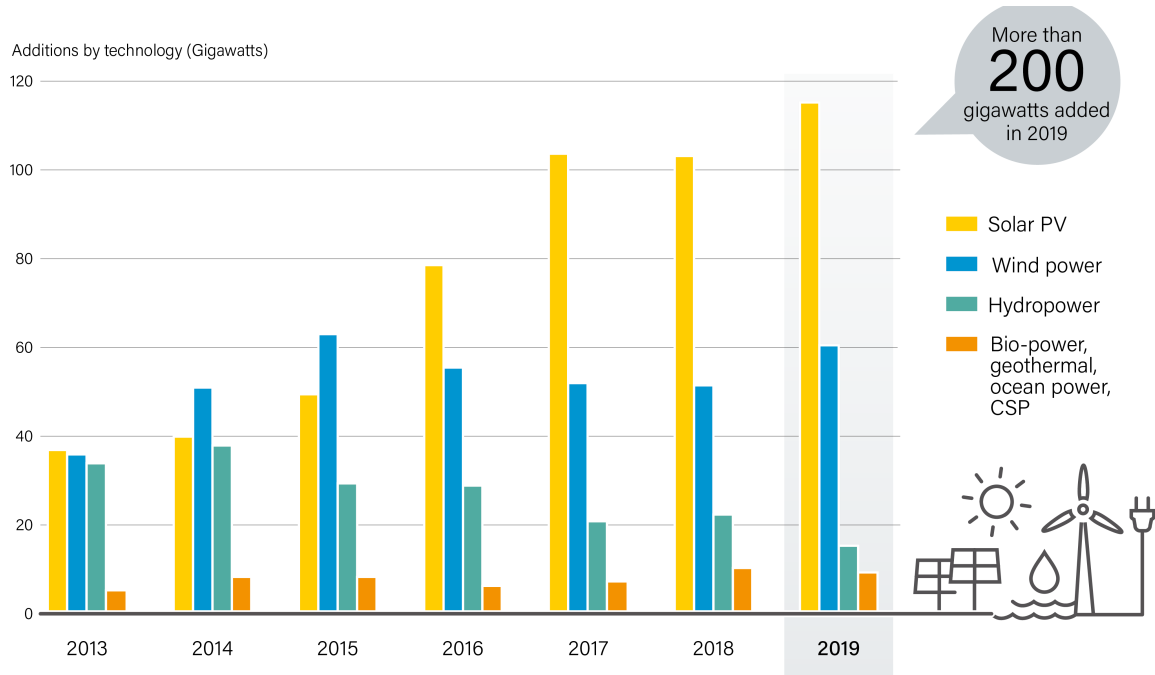
Figure 1.3 Annual additions of renewable power capacity, by technology and total (Source: REN21, 2020).[3]

1.2 Solar Cell History, Applications and Principles

Solar cell or photovoltaic devices comprises of semiconductors used to generate useful electrical energy from sunlight. The photovoltaic effect i.e., light induced voltage, was first observed in 1839 by a French physicist Edmund Becquerel. The experimental physicist confirmed the generation of electrical current when AgCl and platinum electrode in an electrolyte solution was exposed to light.[43] In 1873, Willoughby Smith discovered that conductivity of the selenium rods increased significantly when exposed to sunlight. This was process was later referred to as photoconductivity. Smith described the "Effect of light on selenium during the passage of an electric current" in an article published in the February 1873 issue of Nature.[44] This discovery

6

eventually led to the invention of photoelectric cells. The first working solar module was built in 1883 by Charles Edgar Fritts. The module was constructed by coating a wide plate of copper with selenium and then topped it with an extremely thin semi-transparent layer of gold leaf. In a semiconductor material like selenium, the photons from the light source carry enough energy to knock poorly held electrons from their atomic orbitals, and when wires are attached to the selenium bars, the liberated electrons flow through them in the form of electricity. His device yielded an efficiency of ~0.5 %.[45] Albert Einstein provided photoelectricity with a scientific framework it had previously lacked. In 1905, Einstein postulated that light contains packets of energy which he called light quanta (now called photons) and suggested that the amount of power that light quanta carry varies according to the wavelength of light.[46] This formed the basis of photoelectric effect, for which theory could now explain the phenomenon in terms understandable to science. The photoelectric effect (**Figure 1.4a**) describes the release of electrons, referred to as photoelectrons, from the surface of a substance in response to incident light, while the photovoltaic effect (**Figure 1.4b**) describes the process in which two dissimilar materials in close contact produce an electrical voltage and current (photocurrent) when exposed to light.
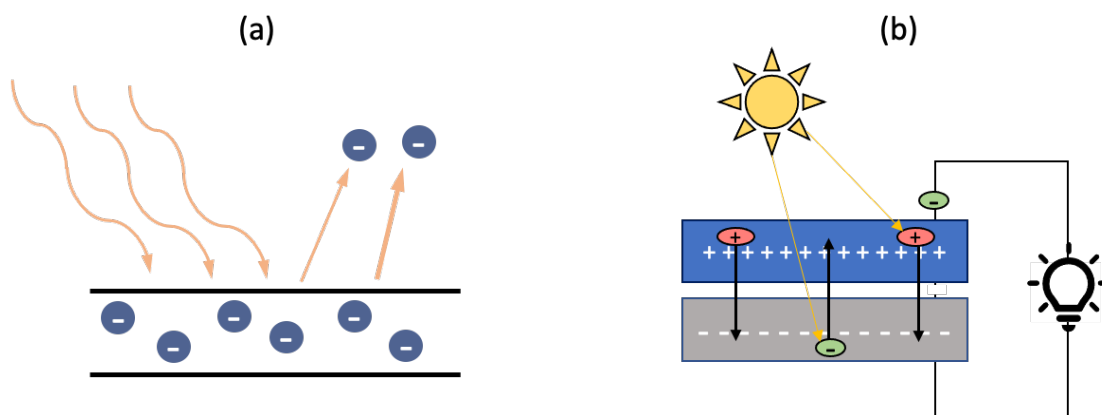
Figure 1.4 Schematic description of (a) photoelectric effect, (b) photovoltaic effect.

The first US patent for the conversion of sunlight to electricity was received by William Coblentz in 1913, and it was titled "Thermal Generator".[47] In 1946, modern silicon solar cells were

patented in by Ohl and demonstrated in 1954 by Chapin, Fuller, and Pearson at Bell Laboratories.[48] Their cell employed a single-crystal Si (sc-Si) wafer for light absorption and a p-n junction for charge separation, and gave an efficiency of about 6%.[49] Ever since, there has been a rise in the development of materials and the technology that absorb energy from the Sun and converts to electricity. The majority of today's commercial solar cells still resemble the Bell Laboratories cell,[49] i.e., they utilize a Si wafer in either single-crystal or polycrystalline form. As time progressed, solar technology started receiving the recognition as a possible replacement of fossil fuel for electricity generation, then the issue of cost started to factor into the development of an efficient solar cell. This will be discussed in a subsequent section of this thesis.

A solar device functions as a junction diode, although its construction is slightly different from conventional p-n junction diodes. Before describing the operating principles of a photovoltaic cell, it is critical to discuss the source of light, and the standard used in the solar community to describe the solar source. During the process of nuclear fusion, the Sun produces energy in the form of electromagnetic waves or electromagnetic radiation (EMR). This radiation is referred to as the solar flux. As this EMR passes through the earth's atmosphere, some is reflected, absorbed and scattered, resulting in a reduction in the amount that reaches the surface. Light from the Sun can be distinguished according to their wavelengths, which determine visible light, infrared and ultraviolet radiation. See **Figure 1.5** below. The visible light constitutes about 40% of the radiated energy, infrared (near infrared) 50% and ultraviolet the remaining 10%.[16] The Ozone absorbs radiation at wavelengths below 300 nm. Depletion of ozone from the atmosphere allows more ultraviolet radiation to reach the Earth, which has harmful effects on earth's biological systems. The intensity of the solar source is not constant. It varies considerably throughout the day, year and location. These fluctuations are based on the time of day, weather, latitude and the season,

resulting from the earth's geography and its astronomical movements (its rotation towards the East, and its orbiting the Sun).
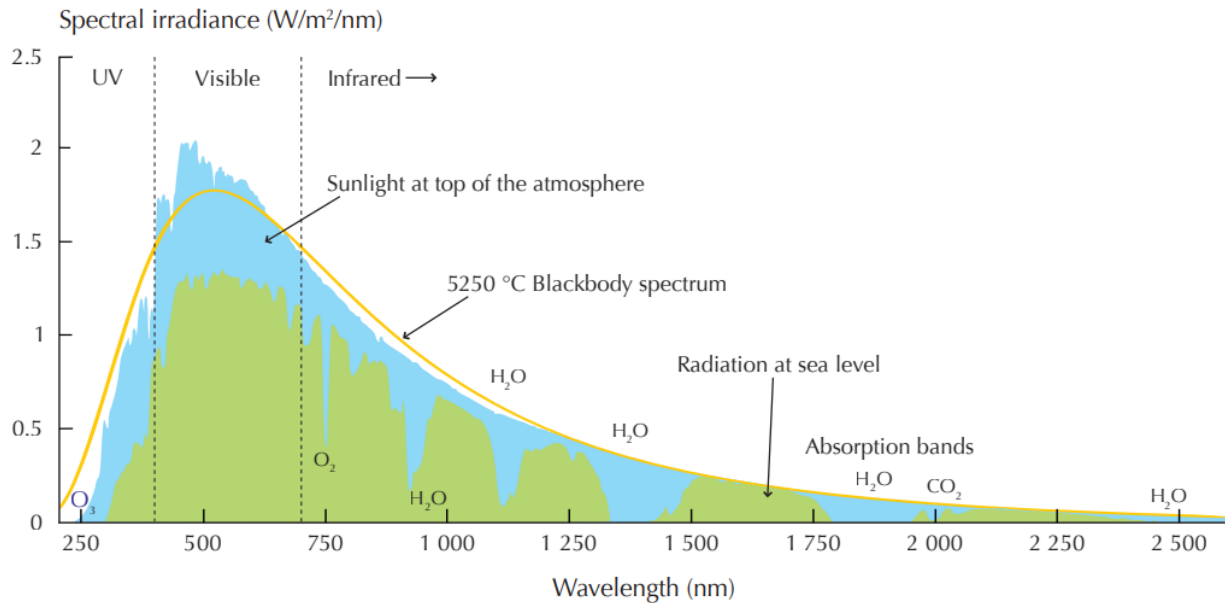
Figure 1.5 Solar spectrum at the top of the atmosphere and at sea level (Source: IEA, 2011).[16]

The sun (blackbody, BB) spectrum obtained at a temperature of 5250ºC is shown in **Figure 1.5**. It is called the AM0 spectrum because no atmosphere is traversed, and it matches with the "sunlight at top of the atmosphere" spectrum in the figure. The ratio of the actual path length of the sunlight to the minimal distance, which is obtained when the Sun is directly overhead (at its zenith), is known as the optical air mass. When the Sun is at its zenith, the optical air mass is unity and the spectrum is called the air mass 1 or AM1 spectrum.[50] When the Sun is set at an angle θ with the zenith, the air mass is given by

$$AM = \frac{1}{cos\theta}$$
Equation 1.1

For example, when the Sun is 60º from the zenith i.e., 30º above the horizon, the Earth receives an AM2 spectrum and when the Sun is ~48º from the zenith, the Earth receives an AM1.5 spectrum. Solar cells are produced by many different companies and laboratories; different solar cell

technologies are also investigated and sold. It is therefore paramount to the solar community to define conditions that allow a comparison of all the different solar cells and photovoltaic modules. These conditions are the standard test conditions (STC), characterized by an irradiance of 1,000 Wm^{-2}, an AM1.5 and a cell temperature of 25ºC.[50,51] The total irradiance of the AM1.5 spectrum is 1000 Wm^{-2} and is close to the maximum received at the surface of the maximum received at the surface of the Earth on a cloudless day.

The working principle of solar cells is based on the photovoltaic effect. The photovoltaic effect can be divided into three processes: (i) The absorption of photons that lead to the generation of charge carriers, (ii) The separation of the photo-generated charge carriers, and (iii) The collection of the photo-generated charge carriers at the terminals.[50] Solar cell device efficiency is used to characterize the performance of solar cells under illumination. The power conversion efficiency (PCE) is calculated as the ratio between the maximal generated power and the incident power and is limited by losses due to the material deficiencies, morphology deficiencies, and device deficiencies. Its main parameters are the *peak power* P_{max}, the *short circuit current density* J_{SC}, the *open circuit voltage* V_{OC} and the *fill factor* FF,[50] obtained from the current-voltage (J-V) characteristics (**Figure 1.6**), under standard test conditions (STC) i.e., $I_{in} = 1000 \, W/m^2$.

$$PCE = \frac{P_{max}}{I_{in}} = \frac{J_{MPP} \cdot V_{MPP}}{I_{in}} = \frac{J_{SC} \cdot V_{OC} \cdot FF}{I_{in}} \qquad \textbf{Equation 1.2}$$

The *short circuit current density* J_{SC} is the current that flows through the external circuit when the electrodes of the solar cell are short circuited. It depends on the photon flux incident on the solar cell, which is determined by the spectrum of the incident light. In an ideal case, J_{SC} is equal to the *photo-generated current density* J_{ph} flowing an external circuit upon illumination. Following a detailed derivation according to Arno Smets et al,[50] the *photo-generated current density* J_{ph} of the p-n junction under a uniform *photo-generation rate* G, is given by:

$$J_{ph} = q \cdot G \left(\sqrt{\frac{k_B T}{q} \mu_n \tau_n} + \sqrt{\frac{k_B T}{q} \mu_p \tau_p} + W \right) \qquad \textbf{Equation 1.3}$$

In **Equation 1.3**, q is the elementary charge (1.602×10^{-19} C); G represents the photo-generation rate; k_B is the Boltzmann's constant (1.38×10^{-23} J/K); T is the temperature; μ_n and μ_p represents the mobility of the electrons and holes, respectively; τ_n and τ_p represent the lifetime of the charge carriers; W is the width of the depletion/space-charge region. The width of the depletion region W is not uniformly distributed in the n- and p- regions. It is determined by the doping concentrations in the n-type and p-type material.[50]

The *open circuit voltage* V$_{OC}$ is the voltage at which no current flows through the external circuit. It is the maximum voltage that a solar cell can deliver when there is no net current through the device. It depends on the *photo-generated current density* J$_{ph}$ and can be calculated from:

$$V_{OC} = \frac{k_B T}{q} \ln \left(\frac{J_{ph}}{J_0} + 1 \right) \qquad \textbf{Equation 1.4}$$

In **Equation 1.4**, J_{ph} represents photo-generated current density; and J_0 represent saturation current density. J_0 depends on the recombination taking place in the solar cell.

Finally, the *fill factor* FF is the ratio between the maximum power $P_{max} = J_{MPP} \times V_{MPP}$ generated by the solar cell and the product of V_{OC} with J_{SC} (See **Figure 1.6**). J_{MPP} and V_{MPP} represent the current density and voltage at the "maximum power point", respectively, which is the point on the J-V characteristic of the solar cell, at which the solar cell has the maximal power output. Also, in practice, FF is often lower due to the presence of resistive losses – series and shunt resistances. The fill factor can be expressed as a function of open circuit voltage V_{OC} and an ideality factor n – a measure of the junction quality and the type of recombination in a solar cell.[52]

$$FF = \frac{V_{OC} \cdot \frac{q}{\mathbf{n}k_BT} - ln\left(V_{OC} \cdot \frac{q}{\mathbf{n}k_BT} + 0.72\right)}{V_{OC} \cdot \frac{q}{\mathbf{n}k_BT} + 1}$$

Equation 1.5
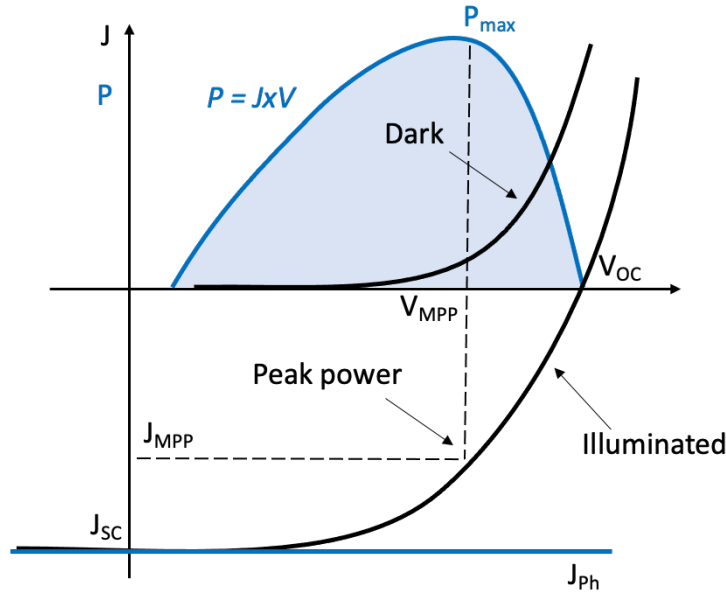
Figure 1.6 J-V characteristics of a p-n junction in the dark and under illumination.

1.3 Inorganic Solar Cells and their Operations

Inorganic photovoltaic cells, have dominated the photovoltaic solar energy converter space.[15] Materials used in inorganic solar cell devices include silicon (Si), group III-V compounds such as gallium arsenide (GaAs), gallium antimony (GaSb), indium phosphide (InP) and metal chalcogenides such as cadmium telluride (CdTe), copper indium selenide or CIS ($CuInSe_2$), copper indium gallium selenide or CIGS ($CuIn_xGa_{1-x}Se_2$), with silicon dominating over 90% of the market share.[15,45,53] All of these semiconductors have energy bandgaps within the range $1.1 - 1.7$ eV, that is, they are near to the optimum energy bandgap (1.5 eV) for solar energy conversion by a single-junction solar cell.[54] The inorganic photovoltaic technologies comprises of single-junction crystalline cells, multijunction cells, thin-film cells, and new emerging technologies such as carbon nanotubes, hybrid cells, with over 350 companies involved globally in manufacturing PV cells.[55]

The evolution of most of the principal photovoltaic cells, over the last four decades, is shown in **Figure 1.7**, and it suggests the materials and technology with the best solar cell efficiency.
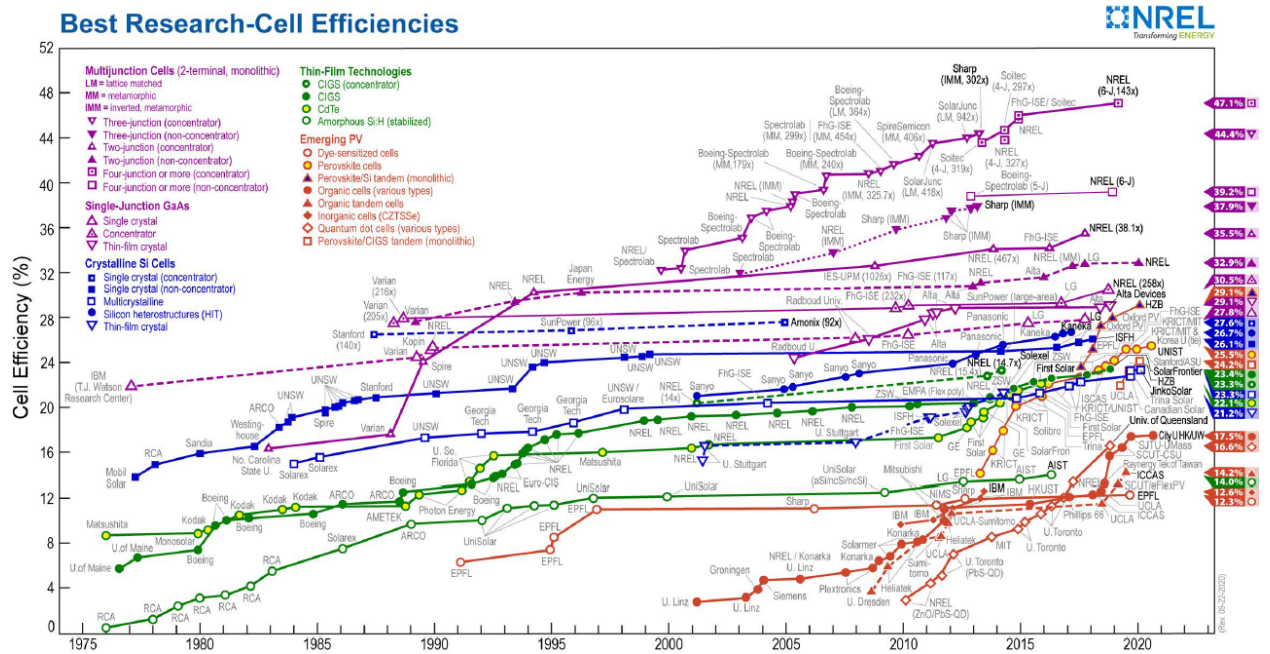
Figure 1.7 Evolution of the world-record lab solar cell efficiencies (Source: NREL, 2020).

An inorganic solar cell essentially functions as a p-n junction with a large surface area, for which electrons and holes are introduced into the junction following photoexcitation and are removed at the electrodes. The pure inorganic semiconductor material has to doped to introduce into its atomic unit, extra amounts of electrons or holes making it an n-type or p-type material, respectively. These two materials are then brought in contact with each other to form a p-n junction. See **Figure 1.8**. The electrical currents are generated in the PV device due to the transport of charge by electrons and holes. The two basic transport mechanisms are diffusion and drift.[50]

Silicon solar cells are considered as first-generation solar cells. There are several technical and economic factors leading to the dominance of Si in the inorganic solar cell industry. Among them is the technical know-how developed by the semiconductor industry by the 1970s. Also, silicon is an indirect band gap semiconductor and, therefore, requires a relatively thick active layer

of up to 1.5 mm to absorb the full solar spectrum. Direct band gap semiconductors like CdTe, CIS, require only 1 mm of material to be effective.[56]
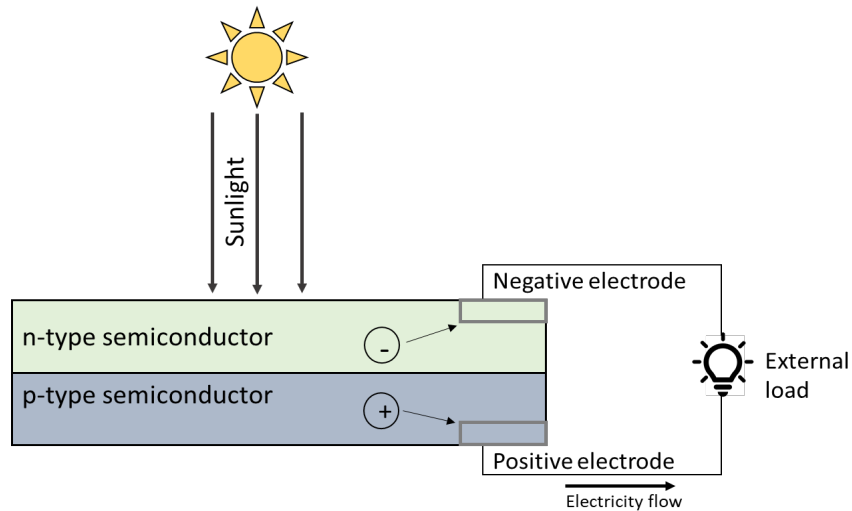
Figure 1.8 Basic architecture of an inorganic solar cell.

There are several variations of silicon that have been used in a silicon solar cell, and they include: single-crystal silicon (sc-Si), polycrystalline silicon (poly-Si), amorphous silicon (a-Si), microcrystalline silicon (μc-Si) and ribbon silicon (ribbon-Si).[45,55] The device efficiency varies based on the kind of silicon wafer used (see **Figure 1.7**). The schematics for the fabrication of sc-Si cell, given by Meng Tao[45] is shown in **Figure 1.9**.
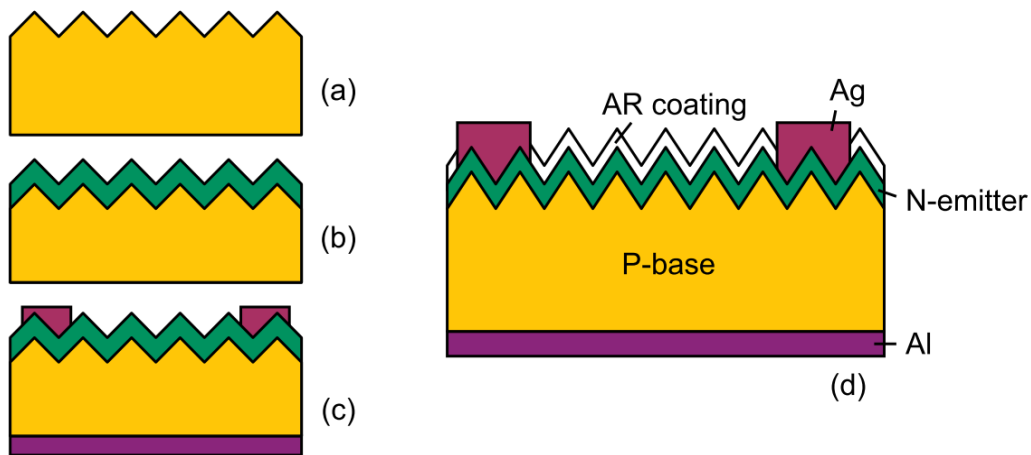
Figure 1.9 Schematics of the fabrication process of single-crystal Si solar cell: **(a)** surface texturing, **(b)** n-emitter diffusion, **(c)** metallization, and **(d)** antireflection coating.[45]
Reproduced with permission from ref 45. Copyright 2008 Electrochemical Society, Inc.

Gallium arsenide (GaAs) is the most commonly used cell among the single junction group III-V solar cells. It has a similar structure with silicon cells with an energy bandgap of 1.4 eV.[55,57] Advantages of GaAs are high optical absorption coefficients, high resistance to heat, and strong resistance to radiation damage. GaAs also has good values of minority carrier lifetimes and mobilities (in highly pure, single-crystalline material), making it an excellent material for high-efficiency solar cells.[58] Cadmium telluride (CdTe) is a polycrystalline semiconductor compound made of cadmium and tellurium. Its polycrystalline nature makes it show a high level of light absorptivity – only about a micrometer thick can absorb 90% of the solar spectrum.[57] Another advantage is that it is relatively easy and cheaper to manufacture relative to GaAs. A major drawback of CdTe for PV cell is the instability of cell and module performance. Another drawback is that cadmium is a highly toxic substance, and this has slowed the introduction of this CdTe based technology.[59,60] Other polycrystalline inorganic PVs are copper indium selenide (CIS) and the copper indium gallium selenide (CIGS). They are direct band gap semiconductors with a band gap of 1.04 eV at room temperature.[60] CIS is one of the most light-absorbent semiconductors – 0.5 micrometers can absorb 90% of the solar spectrum. One of the disadvantages of CIS is that it is a complex material. Its complexity makes it difficult to manufacture. Also, safety issues might be another concern in the manufacturing process as it involves hydrogen selenide, an extremely toxic gas.

1.4 Organic Solar Cells

1.4.1 History, advantages and disadvantages of organic solar cells

Organic semiconductors are a less expensive alternative to inorganic semiconductors like silicon, GaAs. Given the possibilities of tailoring the organic molecular structure to improve the

photocurrent and of producing low-cost photocells, researchers have been led to look afresh at solar cells based on organic semiconductors. Anthracene was the first organic compound in which photoconductivity was observed by Pochettino in 1906[61] and later confirmed by Volmer in 1913.[62] About 50 years later, photovoltaic effects were then observed in common dyes e.g. methylene blue, and biological molecules like carotene and chlorophylls. The first kind of organic solar cell device structure is the single layer OPV done using organic dyes – porphyrins and phthalocyanines. The single layer structure (**Figure 1.10a**) has an intrinsic limitation in achieving high efficiency because the organic layer, which is either p-type or n-type, between electrodes cannot properly generate individual charges (holes and electrons) owing to the extremely low charge separation yield originated from the nature of tightly-bound excitons in organic semiconductors.[63] In 1958, Kearns and Calvin worked with magnesium phthalocyanines (MgPC) sandwiched between two electrodes of glass, and obtained a voltage of 200 mV.[64,65] Polymers were first tested as an active layer by Karg et al in 1993,[66] and by Marks et al in 1994.[67] Poly(p-phenylene vinylene) was sandwiched between two electrodes – Indium Tin oxide (ITO) as anode and Al or Mg or Ca as cathode, power conversion efficiency (PCE) obtained was 0.1%. They discovered that in the presence of atmospheric oxygen, electron abstraction from the polymer increases conductance. This led to the inclusion of an electron acceptor component to aid electron separation, which became an important finding. Some years prior to this finding, C. W. Tang published a paper on the use of a bi-layer OPV cell, comprising of copper phthalocyanine functioning as a donor molecule and perylene tetracarboxylic derivative functioning as an acceptor, to obtain PCE of 1% under AM2 solar illumination condition (76 mWcm^{-2}).[68] This work had a strong impact on the field, and schematic is shown in **Figure 1.10b** below. These developments and more led to the discovery of the bulk heterojunction cell, the future of higher efficiency OPVs (**Figure 1.10c**).
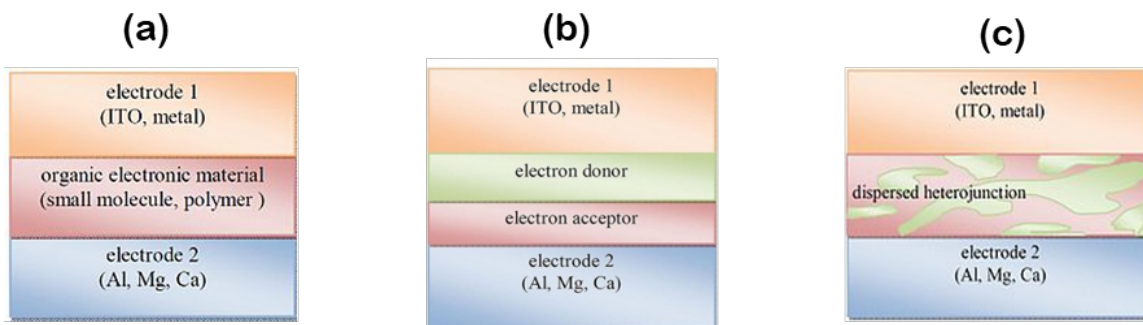
Figure 1.10 Basic schematic of **(a)** single layer, **(b)** bi-layer, **(c)** bulk heterojunction, OPV cell.

Successful largescale commercialization of solar energy depends on three criteria in particular: efficiency, lifetime and cost. Organic materials for photovoltaic applications are relatively cheap, as they can be manufactured and sold by the kiloton.[69] Organic molecules are relatively easier to handle than atoms of their inorganic counterpart. This makes the tunability of selective properties easier, as well as the need to come up with novel molecular designs to suit a particular application or market. Indeed, the number of molecules that could potentially be used in an organic solar cell is limited only by the imagination of the synthetic chemist. Organic materials (with thicknesses of $50 - 100$ nm) have the advantage of being able to absorb light across the entire solar spectrum due to the presence of π-bonded electrons which are able to move along the delocalized π-orbitals arising from sp2-hybridization states of carbon atoms.[70] Furthermore, because they are thin, these cells could be manufactured on a roll-to-roll process, transported easily and simply unrolled on the customer's roof, window and/or wall. Other advantages include: low weight, semitransparency, easy integration into other products, new market opportunities (e.g. wearable PVs), short energy payback times and low environmental impact during manufacturing and operations.[69]

Unlike in inorganic semiconductors with a 3D crystal lattice forming a CB (conduction band) and a VB (valence band) throughout the material, in organic semiconductors, the intermolecular forces are too weak to form 3D crystal lattices. This results in the formation of

HOMOs (highest occupied molecular orbitals) and LUMOs (lowest unoccupied molecular orbitals), instead. Thus charge transport proceeds by hopping between localized states, rather than transport within a band.[64] This means that charge carrier mobility in organic semiconductors are generally low compared to inorganic semiconductors. Also, charge separation is more difficult in organic semiconductors due to the low dielectric constant. At room temperature, in many inorganic semiconductors, photon absorption produces a free electron and a hole (sometimes called charge carriers), whereas in organic semiconductors, the excited electron is bound to the hole commonly referred to as an exciton. Another disadvantage of organic solar cells compared to inorganic cells is that the exciton diffusion length is relatively small, due to large exciton binding energies.[71–73] Strong electric fields are required to dissociate them into free charge carriers that can contribute to the photovoltaic response. These excitons are more likely to become stuck (trapped) due to the amorphous nature of organic molecules or recombine and disappear. All these contribute to the limitation of the efficiency of organic solar cells. Another concerning disadvantage of organic solar cell is its operational lifetime. Overtime, the molecules might react with atmospheric oxygen, water, and may also degrade as a result of constant illumination.

1.4.2 Operation of organic solar cells

Organic solar cells operate under similar principles as inorganic solar cell, with slight differences. A key feature of organic semiconductors that has impacted the design and geometry of organic photovoltaic devices is the excitonic character of their optical properties.[74,75] While optical absorption in a conventional inorganic semiconductor results in the immediate creation of free charge carriers, in an organic semiconductor it leads to the formation of a spatially localized electron-hole pair, i.e., a Frenkel-type exciton, which is electrically neutral. The key steps in the

optical-to-electrical conversion taking place in organic solar cells include optical light absorption (exciton formation), exciton diffusion, charge transfer (exciton dissociation) and charge collection.
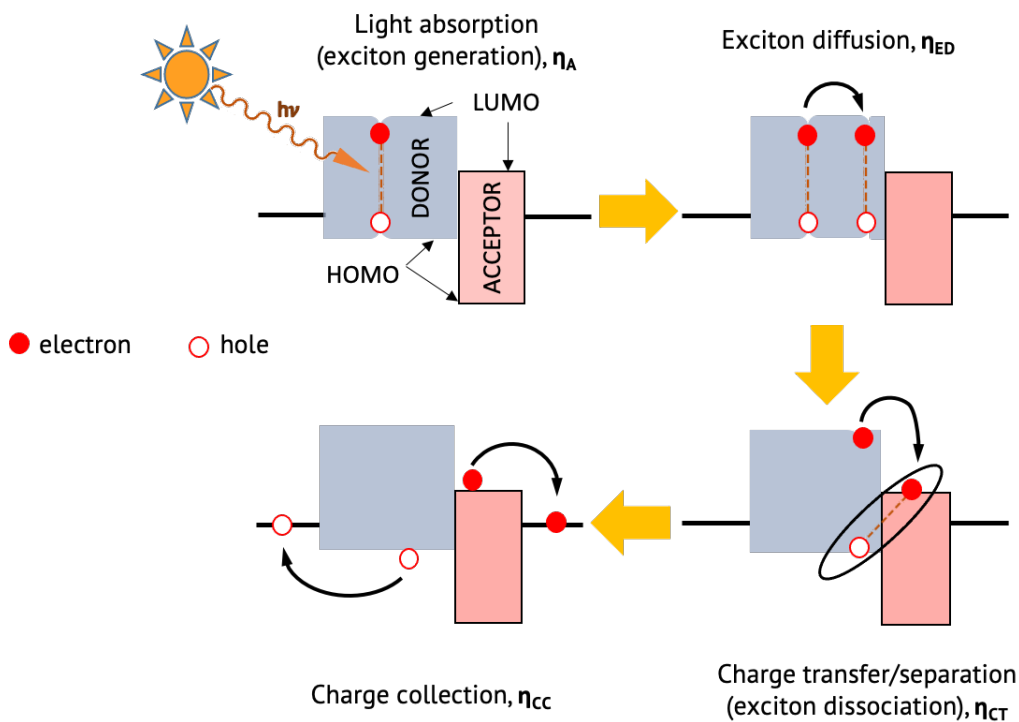
Figure 1.11 Steps in the photocurrent generation process of organic photovoltaics.

The first step in the optical-to-electrical conversion process is photon absorption, leading to the creation of excitons. An electron is excited from the highest occupied molecular orbital (HOMO) to the lowest unoccupied molecular orbital (LUMO). The large extinction coefficients of organic semiconductors over a wide wavelength range can lead to a good match with a sizable portion of the solar spectrum and efficient light harvesting in layers that are relatively thin. In contrast to inorganic semiconductors, the absorption of a photon at room temperature in conjugated materials does not lead to free charge carriers but to neutral, bound electron-hole pairs. This is the reason why two components, an electron donor and an electron acceptor, are required to promote the generation of charge carriers. Knowledge of the light distribution in the solar cell is important

to model the steady-state exciton distribution and consequently the photocurrent produced in the solar cell.[75]

The generated excitons need to diffuse to the donor-acceptor interface in order to generate separated negative and positive charges. This has to occur prior to their decay back to the ground state. Hence, the thickness of the organic layers (or phases) has to be comparable to the exciton diffusion length L, $L = (D\tau)^{1/2}$, where D is the diffusion coefficient and τ is the lifetime of the exciton. Electric fields do not influence the random motion of excitons, since excitons are neutral species. Singlet excitons have been said to move more quickly relative to triplet excitons. The migration of singlet excitons has often been described via a Forster resonant energy-transfer (FRET) mechanism, which involves the long-range electrostatic coupling between the excitation transition dipoles at the initial and final sites; while in the case of triplet excitons, motions are considered to be restricted to adjacent sites, because they depend upon a short-range exchange (Dexter-type) mechanism relying on orbital overlap.[74,75]

For the next step, at the donor/acceptor interface, the excitons can dissociate provided their energy is higher than that of charge-transfer or charge-separated states. The exciton binding energy is typically large, on the order of or larger than 0.4 eV.[76–78] This high value is a reflection not only of the rather low dielectric constant of π-conjugated organic materials, but also of the significant electron correlation and geometry relaxation effects present in these materials.[74,75] In most instances, the dissociation process is described as involving a transition from the exciton state down to the lowest CT state, which corresponds to the situation where the hole sits on the HOMO level of a donor molecule and the electron on the LUMO level of an adjacent acceptor molecule (see **Figure 1.11**). This step is the rate-limiting step in the OPV process.

Finally, following the separation of charges, they can diffuse and drift towards their respective electrodes with efficiency depending on their mobilities. The nature of the electrode/organic layer interfaces is complex. The efficiency of the charge collection process cannot be simply determined from the difference between the work-function of the isolated electrode and the donor ionization potential (IP) or acceptor electron affinity (EA). Surface modification of the electrodes via deposition of self-assembled monolayers is an efficient way to enhance the quality of the electrical contact as well as, in particular when dealing with conducting oxide electrodes.[79]

The external quantum efficiency η_{EQE} is defined as the number of electrons flowing in the external circuit per photon incident on the PV cell.[80,81] It is given as the product of the efficiencies of the four corresponding steps in the charge generation process:

$$\eta_{EQE} = \eta_A \cdot \eta_{ED} \cdot \eta_{CT} \cdot \eta_{CC} \qquad \textbf{Equation 1.6}$$

Where η_A is the efficiency of light absorption within the active region of the solar cell; η_{ED} is the exciton diffusion efficiency to a dissociation site; η_{CT} is the charge transfer efficiency, which is the efficiency for dissociation of an exciton into a free electron and hole pair at that site; and η_{CC} is the charge collection efficiency.

1.5 Bulk Heterojunction (BHJ) Organic Solar Cells

1.5.1 Description and architecture of a bulk heterojunction (BHJ)

For a two-component system – with a polymer as *donor* (D) and a macromolecule as *acceptor* (A) – bulk heterojunction (BHJ) is referred to as a network of internal donor-acceptor (D-A) composites. It involves controlling the nanomorphology of the phase separated D-A interpenetrating network composites.[82] Through control of the morphology of the phase separation, one can achieve a large interfacial area within a bulk material. Ideally, the microphase domains

should be no larger than the exciton diffusion length. Bilayers of semiconducting polymers with the acceptor compound (e.g. fullerene) show low power conversion efficiency,[83] consequently interpenetrating phase separated D-A network composites (**Figure 1.12**) will appear to be the ideal photovoltaic material.[84–86] This is because any point in the composite is within a few nanometers of a D-A interface (mimicking the bilayer in every few nm); such a composite is referred to as a BHJ.
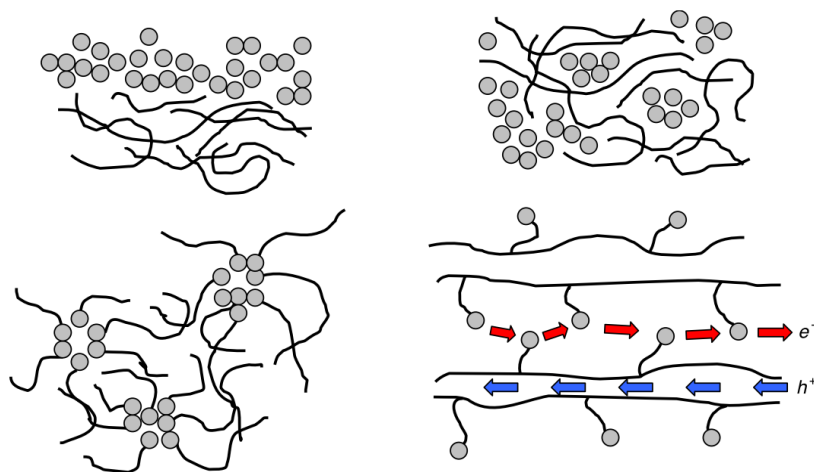
Figure 1.12 Different donor-acceptor morphologies of a bulk heterojunction.[64]
Reproduced with permission from ref 64. Copyright 2004 Elsevier.

The bulk heterojunction is the most successful device architecture for polymeric photovoltaics because exciton harvesting is made near-perfect by creating a highly folded architecture such that all excitons are formed near a heterojunction.[87] BHJs are formed by spin-casting the electron donor polymer and an electron acceptor from a common solvent. The key to making efficient BHJ cells, is to ensure that the two materials are intermixed at a length scale less than the exciton diffusion length, so that every exciton formed in the electron donor polymer can reach an interface with the electron acceptor to undergo charge transfer. Most successful organic BHJ cells use transparent metal oxides, such as TiO_2 or ZnO, as the electron transport layer, because of their high electron mobility, transparency and ease of processing.[87] Indium tin oxide

(ITO)-coated glass is often used to enable electron transport, and function as the anode of the device. The device cathode used for electron collection include Aluminum (Al), Gold (Au). Also, the mixture between a conductive polymer, poly(3,4-ethylenedioxythiophene) and anions of poly(styrene sulfonate) referred to as PEDOT-PSS, is often used as a hole-transport layer in the BHJ architecture.[70]
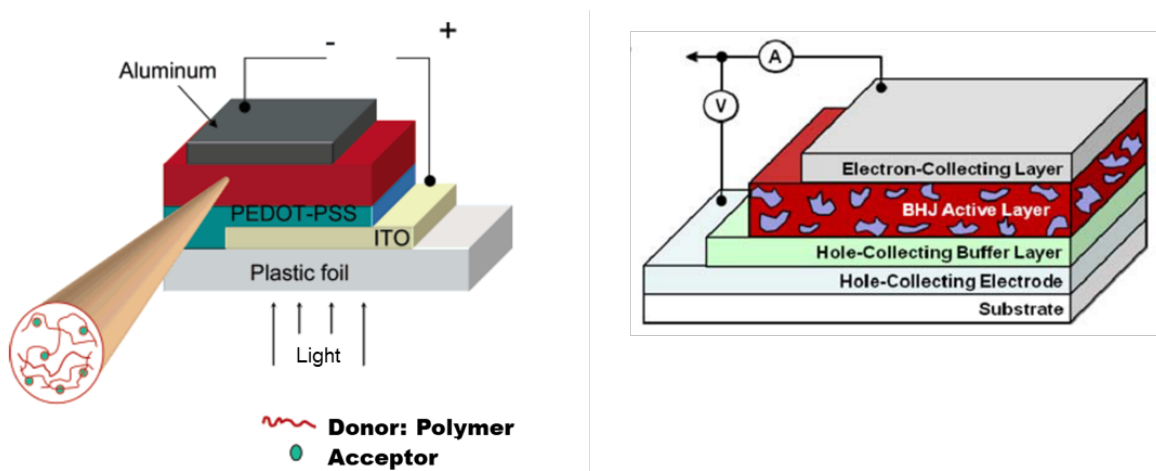
Figure 1.13 Device structures for a bulk heterojunction (BHJ) solar cell.[63,88]
Left figure reprinted with permission from ref 88. Copyright 2007 American Chemical Society, Inc. Right figure reprinted with permission from ref 63. Copyright 2014 Springer Nature.

In the active layer of BHJs, the pioneer examples of conjugated polymers that have been used include MEH-PPV,[82,89] MDMO-PPV,[90,91] P3HT,[92–94] with varying absorption spectrum width, HOMO energy level, altering the short-circuit current, open-circuit voltage and fill-factor. Common acceptors used in BHJs are fullerenes,[95–98] n-type inorganic nanoparticles,[99–102] polymers,[84,103–105] and n-type organic non-fullerene (e.g. perylene diimide, ITIC).[106–111] The most common kind of donor/acceptor BHJ solar cells are the polymer /fullerene BHJs. Since the early conceptual works on polymer/fullerene BHJs by Sariciftci et al,[89] and Yu et al,[82] significant progress and breakthrough have been made with these kind of architecture. The science of annealing – thermal annealing and room temperature annealing ("solvent-annealing"), that alters the size of the phase segregation to reach an optimum phase-segregated morphology, was

introduced sometime later. Also, the degree of phase separation and domain size was found to depend on solvent choice, speed of evaporation, solubility, miscibility of the donor and acceptor. Electron donors and acceptors will be discussed in more detail in subsequent sections.

1.5.2 Donor polymers and macromolecules in the bulk active layer of BHJs

Polymer is a high molecular weight substance usually organic, composed of long chains of repeating units, each relatively light and simple. The interesting electronic properties of organic molecules arise when they have a conjugated chemical structure. This means they are represented as having alternating double and single carbon-to-carbon bonds within their structure (see **Figure 1.14**). The actual structure is more symmetrical with each carbon atom having three of its valence electrons in sp^2 hybrid orbitals forming covalent bonds with its two carbon neighbors and with a hydrogen atom or other group. The fourth electron occupies a p_z orbital, which can interact with one of its neighbors to form the second bond of the double bond representation of a conjugated molecule. However, collectively, the p_z orbitals can overlap to form delocalized π-bonds which can extend the full length of the molecule.[60] This electronic delocalization provides the "highway" for charge mobility along the backbone of the polymer chain. Conducting polymers are the most recent generation of polymers. They opened the way to progress in understanding the fundamental chemistry and physics of π-bonded macromolecules. They also provided an opportunity to address questions that had been of fundamental interest to quantum chemistry for decades: Is there bond alternation in long chain polyenes? What is the relative importance of the electron-electron and the electron-lattice interactions in π-bonded macromolecules? More importantly, conducting polymers offered the promise of achieving a new generation of polymers: materials that exhibit the electrical and optical properties of metals or semiconductors and that retain the attractive mechanical properties and processing advantages of polymers.[112]
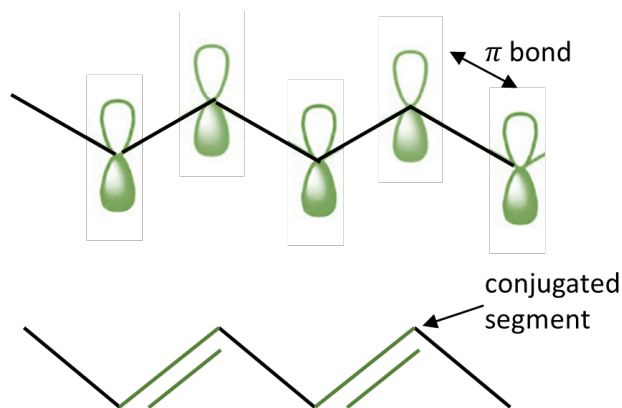
Figure 1.14 The π-conjugated system of conducting polymers.

Conducting polymers tend to be insoluble and infusible because their interchain electron-transfer interactions are relatively strong compared with the van der Waals and hydrogen bonding interchain interactions typical of saturated polymers.[112] Thus, there were serious doubts about the processing techniques of π-conjugated polymers. Side chain functionalization – principally used for processing semiconducting polymers from solution in organic solvents or from water – became a crucial field of study. The side chains decrease the interchain coupling and increase entropy, making the processing of these π-conjugated polymer derivatives from solution to be possible. Solution processing resulted in materials with improved homogeneity and crystallinity, and with correspondingly improved electrical conductivities.[112,113] Side-chain functionalization has also made it possible to fabricate optically viable thin films for electronic devices, by spin-casting from solution. An example is PEDOT-PSS, the important hole-transport layer in the architecture of BHJ solar cells, which can be prepared as a stable dispersion in water, and can be spin cast on a thin film.[114]

In the active layer of BHJ systems, semiconducting π-conjugated polymers function as electron donors upon photoexcitation. One of the most important properties of conjugated polymers for the design of BHJ solar cells is the bandgap, as it controls their electrical and optical characteristics. The bandgap refers to the energy difference between the highest occupied

molecular orbital (HOMO) and the lowest unoccupied molecular orbital (LUMO). The two most investigated polymers for photovoltaic cell application are poly[3-alkyl-thiophenes] (P3ATs), and poly[p-phenylene vinylene] (PPV). They have both been considered as low-bandgap polymers. Karg et al was the first to investigate PPV for light-emitting and photovoltaic application.[66,115] They investigated the optical and electrical properties of PPV-based OPV devices using the ITO/PPV/Al architecture, and obtained V_{OC} of 1 V and PCE of 0.1 %.[115] Other well studied derivatives of PPV include poly[2-methoxy-5-(2′-ethyl-hexyloxy)-1,4-phenylene vinylene] (MEH-PPV),[116] and poly[2,5-diheptyloxy-p-phenylene vinylene] (HO-PPV).[117] Upon the nanoscale mixing with acceptor compounds such as, fullerenes, efficiencies up to 2.5 % have been observed by employing ITO/PEDOT-PSS/MDMO-PPV:PCBM/LiF/Al device architecture.[91] Gebeyehu and Saricifti et al were the first to investigate P3ATs – specifically poly[3-octylthiophene] (P3OT) and fullerene – for photovoltaic application.[118] They achieved a PCE of 1.5 % under 10 mW/cm^2 monochromatic illumination. Following this, a myriad of studies on P3ATs – specifically poly[3-hexylthiophene] (P3HT), have been carried out. Between the year 2002 and 2010, a total of 579 publications reported the PCE of P3HT:PCBM solar cells, and PCE as high as 6.5 % have been observed.[81,119]
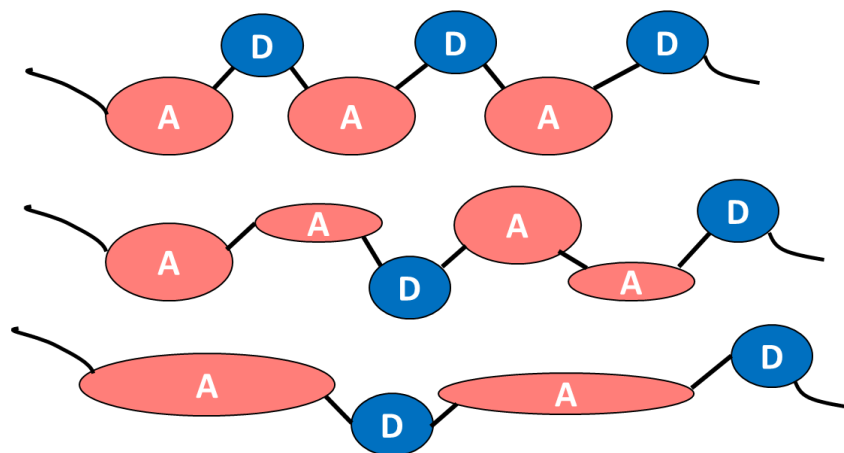
Figure 1.15 Schematics of π-conjugated polymers with D-A structural motif.

As the interest in P3HT:PCBM solar cells started to decline in 2015, the use of D-A polymers increased.[120] Donor-Acceptor (D-A) polymers, depicted in **Figure 1.15** are conjugated semiconducting polymers which contain a combination π-electron rich (donor) and π-electron deficient (acceptor) conjugated moieties arrayed along the polymer chain.[121] Unlike in the case of compound semiconductors for which the bandgap is tuned via elemental composition, for D-A polymers the bandgap tuning is achieved through the choice of donor and acceptor moieties. The donor moiety typically determines the energetic positions of the highest occupied molecular orbital (HOMO), and the acceptor moiety determines the lowest unoccupied molecular orbital (LUMO).[122–124] The electronic structure is manipulated because of the built-in intramolecular charge transfer (iCT). Using an ICT strategy, new polymers have been developed to better harvest the solar spectrum, especially in the $1.4 - 1.9$ eV region.[123] Among the myriad of electron-donating moieties, some common ones include thiophene, oligothiophenes (-TT-), benzodithiophene (BDT), benzodifuran (BDF), naphthodithiophene (NDT), naphthodifuran (NDF). Electron-accepting moieties include diketopyrrolopyrrole (DPP), isoindigo, quinoline, anthrazoline, quinoxaline, 2,1,3-benzothiadiazole (BT), thieno[3,4-b]pyrazine (TPZ), benzobisazoles.[121,125,126] Among the myriad of D-A polymers, some common and promising polymers include PTB7, PTB7-Th, PDBT-T1, PBDTT-F-TT, P3TEA. Some of the highest PCE achieved for OPV BHJ systems have been with these D-A polymers. The approach of forming copolymers of alternating electron-rich and electron-poor conjugated moieties has enabled breakthroughs in various fields of applications for organic semiconductors and continue to be explored till this day.

1.5.3 Acceptor macromolecules in the bulk active layer of BHJs

The basic underlying operational concept of a bulk heterojunction solar cell is that light is absorbed in either phase (donor and/or acceptor) of the active layer of the device by creating

excitons that diffuse to their interface. The acceptor is critical in a BHJ solar cell. A lot of focus has been on the photon absorbing materials that are responsible for donating an electron that is used in the generation of electricity, but the organic electron accepting material is equally important. The acceptor material accepts the excited electron from the LUMO of electron donor polymer, so the LUMO of the acceptor most be low-lying in order to successfully dissociate the electron from the exciton created. The acceptor material can also be directly photoexcited, as is the case for efficient BHJ solar cells, in order to generate excitons that can migrate to the donor-acceptor interface of the organic solar cell. This is represented as A-Ex (Acceptor-excitons) in the acceptor layer of the BHJ cell in **Figure 1.16** below. Many organic compounds exhibit potential properties as electron acceptor material, but only a very few electron acceptor materials can be used in highly efficient OPV devices.
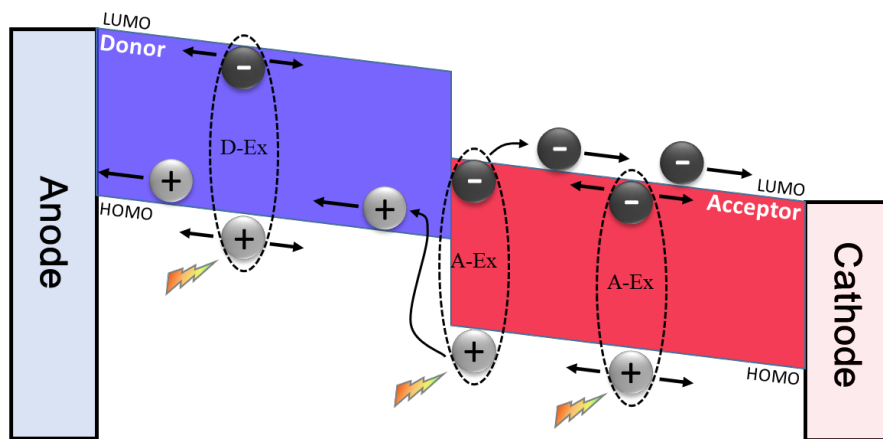
Figure 1.16 Processes taking place in a BHJ solar cell. Acceptor material also absorbs a photon to create an exciton.

Fullerene and its derivatives are the most successful electron acceptor materials. The most used acceptors in heterojunction cells are the derivatives of fullerene C_{60}, C_{70}, C_{76}, C_{78} and C_{84}. They possess high electron affinity, high photoconductivities, ultrafast photoinduced charge separation, slow charge recombination.[127–129] **Figure 1.17** shows the structure of selected fullerene derivatives. One of the most used fullerene derivatives in heterojunction cells is the C_{60}

molecule.[128,129] It is referred to as the Buckminsterfullerene by Sariciftci et al, and it opened a number of new opportunities for semiconducting polymers via the discovery of photo-induced electron transfer.[89,130] C_{60} is a redox-active chromophore. It behaves like an electronegative molecule which reversibly accepts up to six electrons in solution.[131–133] One of the most remarkable properties of C_{60} fullerene in electron-transfer processes is that it efficiently gives rise to a rapid photoinduced charge separation and a further slow charge recombination in the dark.[134] A problem that arises in the preparation of composite films of C_{60} with π-conjugated polymers is the intrinsic incompatibility of the two materials; at higher concentrations, C_{60} usually phase segregates from the conjugated polymer matrix due to a tendency to crystallize. To this regard, in BHJ solar cells, C_{60} derivatives with solubilizing side chains, $PC_{60}BM$, are often used.[135] Also, in order to tune some other properties such as absorption, dark conductivity, photoconductivity, higher fullerene C_{70}, C_{76}, C_{78}, C_{84},[129] and indene-fullerene have been used as electron acceptor materials in OPVs.[125]
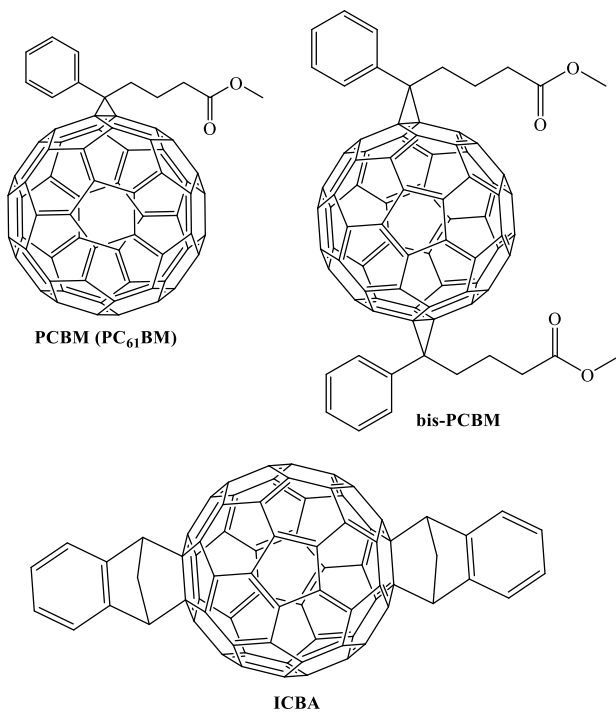
Figure 1.17 Molecular structures of selected fullerene derivative.

29

Although fullerene acceptors have been utilized in many of the highest performing BHJ organic solar cells, they have some significant drawbacks. They are expensive, thermally unstable and have limited absorption in the longer wavelength region of the solar spectrum.[136] Fullerenes also have limited energetics i.e. their energy levels are not tunable. A lot of research efforts have been made to develop new electron acceptors characterized by strong intramolecular electron push−pull effects to replace the fullerenes; they are generally categorized as non-fullerene acceptors (NFAs). Earlier on, due to the difficulties in morphological control, these NFAs showed low PCEs in BHJ solar cells. However, this situation have changed recently.[137] The PCEs of NFA BHJ solar cells have increased dramatically since 2015, now reaching a high value of 18%.[138–140] At present, such a high value is better than the efficiency obtained in the best fullerene-based OSCs. The two major classic examples are the rylene diimides (which includes perylene diimides, terylene diimides, naphthalene diimides), and fused-ring electron acceptors (which includes ITIC, ITCC, IT-M, IT-4F, IDT, IEIC, IEICO-4F).[137,141,142] The quick development of NFA BHJ solar cells during the past two years has benefited a lot from the synthetic methods, materials design strategies and device engineering protocols developed during the past two decades for fullerene-based OSCs. From the device point of view, the fact that excitons can separate efficiently upon negligible driving energies contributes to high PCEs in NFA BHJ solar cells.[143–145] As a result, they often show high photocurrent and low voltage losses at the same time. In contrast, charge separation in fullerene-based BHJ solar cells usually becomes problematic under low driving energies, presenting a trade-off between high photocurrent and high photovoltage.[146] One of the key challenges for NFAs is their anisotropic structures, which unlike for fullerene derivatives (isotropic, ball-like structure), makes it more challenging to ensure efficient π–π interactions.[147–149] Therefore, in NFA BHJ organic solar cells, it is critically important to pair the donor polymers

with acceptors that have the right chemical structure, which must ensure optimal molecular orientation as well as fine-tuned phase separation. The use of NFAs implies new working photophysical processes, which could be fundamentally different from those in fullerene-based OSCs. Therefore, a major portion of this thesis seeks to uncover and elucidate some of these critical processes for varying structural systems of perylene diimide (PDI) – an important NFA.

1.6 Perylene diimide (PDI) Macromolecules as a Non-Fullerene Acceptor (NFA)

In the class of rylene diimide non-fullerene acceptor, perylene diimide (PDI) or perylene bisimide (PBI) is the most widely studied NFA. PDIs exhibit electron affinities comparable with those of fullerenes, and in addition the show stronger absorption in the visible and NIR–region of the solar spectrum. They are cheaper and better chemical, thermal and photochemical stability in comparison to both fullerene and fused-ring non-fullerene acceptors.[150] Indeed, the first bilayer OSC developed by Tang used a perylene-based acceptor.[68] The solubility of PDIs in halogenated solvents (commonly used for the preparation of BHJ active layer), can be obtained by inserting long alkyl or aryl substituents at the N-positions or at the bay core positions.[151] These molecules and their derivatives have been used not only as building blocks for electronic and optoelectronic devices such as organic light-emitting diodes,[152] dye lasers,[153] optical switches,[92] and photodetectors,[154] but also as electron acceptors for studying photoinduced energy- and electron-transfer processes.

The parent PDI monomer exhibit flat π-systems as confirmed by X-ray diffraction of several single crystals, and in BHJ solar cells, they form 1D π stacks in their crystals. As much as electron transport is efficient within a stack, electron transport between stacks is greatly limited. This ultimately limits the electron-transport pathways from these domains to the electrodes in the organic solar cell device.[155,156] Furthermore, the optically generated excitons in some 1D π-stacked

PDI aggregates are rapidly deactivated by excimer formation, which act as possible exciton traps.[157] However, despite these problems, optimized BHJ solar cells consisting of certain polymeric donors in combination with the rather simple monomeric PDI have yielded PCEs ranging from 3% to 5%.[158] It was only recently that the idea of introducing a molecular "twist" into the backbone of PDI systems in order to prohibit aggregation, became of great interest. This was achieved by using a dimeric system of PDIs connected at their 'bay' positions, and sometimes including a π-bridge between the two PDI units.[159–161] These π-bridge compounds were either donor moieties like thiophenes or weak acceptor moieties like isoquinoline-dione, to form A-D-A or A-wA-A configurations, respectively. These all showed better BHJ device performance relative to monomeric systems. Rajaram et al[162] proposed that the disruption of the crystallinity without adversely impacting the charge-transfer properties is an important design principle. However, a strongly twisted π-conjugation is likely to undermine the charge transport and diminish their potential as effective electron acceptors. Later on in the field, there were comparisons between twisted PDI dimers and planar PDI monomers, and they all stated how excessive aggregation obtained in planar systems limit the device performance.[108,163] However, comparing a monomer to a dimer is not accurate in any regard. Thereafter, our group published a study that determines the critical balance between aggregation effect and charge transfer rate in PDI dimeric systems.[136] We studied two analogous PDI dimeric isomers that each preferentially assumed a planar or twisted (by the introduction of steric hindrance) geometry, in order to isolate and study the core effect of molecular geometry on aggregation and charge transfer. The two PDI isomers had the exact same molecular compositions (same chemical formula), and molecular weight. The results from this study are detailed in Chapter 5 of this dissertation.
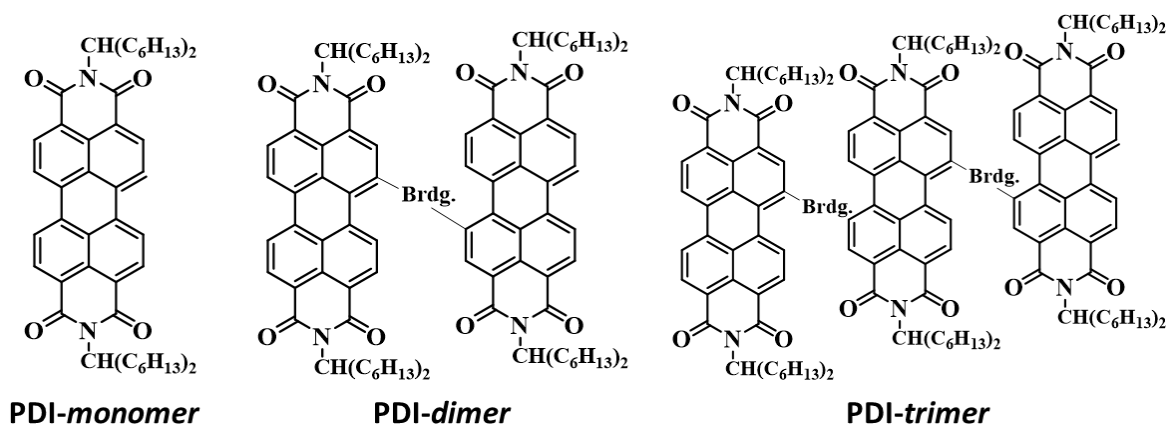
Figure 1.18 Molecular structures of PDI monomer, dimer and trimer with π-bridge connector.

Other impressive efforts to further improve the performance of PDIs in BHJ solar cells are by mimicking the 3D architecture of fullerene, which might enable isotropic charge transport. The PDI systems displayed 3D configurations, and indeed better device performance was obtained relative to 1D or in most cases 2D systems.[106,164–169] PDI linear trimers, tetramers and oligomers have also been studied, and they showed high PCEs.[170] There are also interests in annulated PDI dimers, which comprises of two polycyclic aromatic hydrocarbons tacked in the bay positions, at the extreme ends of the compound.[171] These polycyclic aromatic hydrocarbons include thiophene, selenophene, or pyrrole heterorings, forming S-annulated,[172] Se-annulated,[173] or N-annulated[174–176] PDI dimers, respectively. These annulated PDI dimers are a novel class of compounds that haven't received much attention, and the structure-function relationships of selected N-annulated dimers are clearly elucidated in Chapter 4 of this dissertation.

1.7 Photophysics of the Active Layer (AL) Compounds in Bulk Heterojunctions

1.7.1 Donor polymer photophysics

There have been a lot of interest in understanding the photophysics of conducting polymers. Illumination of a polymer sample with light past the absorption edge can result in excitation of a variety of entities or "particles", and an electron is raised to the LUMO and a hole is left behind in

the HOMO. The resulting fate of the electron-hole pair include the formation of polarons, bipolarons, singlet excitons, triplet excitons, excimers, aggregates, solitons.[177] The formation of singlet excitons is the most likely fate for an electron-hole pair generated by optical excitation. The electron-hole pair remain on the same chain bound to each other by their electrostatic attraction and to a lesser extent by the (relatively small) chain deformation or relaxation they cause.[177] These excitons are singlets because the electron and hole are created with opposite spin. The formation of a polaron requires that the electron and hole be separated sufficiently so that they do not interact to form an exciton; this happens if they reside on different polymeric chains in the ensemble. This have been studied in good details for poly[*p*-phenylene vinylene] (PPV) by Murata et al using light-induced ESR and theoretical modeling.[178] An excimer is a complex between an excited state of a molecule and a molecule of the same species in the ground state. It follows that the molecules must be close enough for sufficient interaction but not so close that the ground states form a new stable molecule.[179] Aggregates differ from excimers in that the electronic wave-function is delocalized over two or more chains in the ground state as well as in the excited state. Thus, an aggregate should provide additional absorption, which should be detectable by comparison with absorption in the dissolved polymer, as well as the additional emission.[177,180] Photoinduced absorption and fluorescence measurements are used to identify the relevant electron-hole pairs formed following photoexcitation by observing the photogeneration and recombination dynamics.

The photophysics of the active layer polymer is strongly affected by the degree of planarity of the polymeric backbone. In D-A conjugated polymers, the use of heterocyclic π-bridges (in connecting the D- moieties and the A- moieties) can greatly affect the polymeric backbone, in turn affecting the photophysical properties of the polymer. The polymeric sidechain on the polymer

backbone, to ensure good solubility and miscibility, is also crucial in predicting the optical and photopysical properties. The use of bulky or linear sidechains affects the fluorescence lifetime of polymers in solution relevant in predicting the excitonic lifetime.[181] Quantum chemical calculations are often used to complement the photophysical measurements, although many assumptions (such as reduced polymer chain, truncated sidechains) are made with the theory, altering the accuracy of the theoretical results.[177]

1.7.2 Donor-Acceptor photophysics and connection to device physics

The photophysical properties of the active layer comprising of both a donor and an acceptor in the right molecular ratio, garnered so much attention in the early 90s. Photophysical properties such as charge transfer (electron transfer), charge recombination, energy transfer, hot exciton dissociation, triplet production have been studied. Several optical techniques have been implemented. They include steady state absorption and photoluminescence measurements, transient absorption measurements, time-resolved fluorescence measurements, electron spin resonance (ESR) measurements. One of the pioneers photophysical approach to confirm the charge transfer (or 'doping') effect in a D-A active layer mixture, is the quenching or suppression of the photoluminescence. According to Morita et al,[130] increasing the concentration of C_{60} in a poly(3-alkylthiophene)-C_{60} mixture showed the suppression of the high energy peak in the absorption spectra (as a new absorption peak emerged in the infrared region) and the drastic quenching of the photoluminescence spectra (and a blue-shift). This was associated to electron transfer from the poly(3-alkylthiophene) chains to C_{60} molecule with the formation of P^+ polarons.

The transient absorption or pump-probe measurement is a powerful tool for studying the fundamental photophysics in these materials on a molecular temporal scale.[182] A lot of studies have been carried out to characterize the photoinduced charge transfer, culminating with a study

of the dynamics of electron transfer from semiconducting polymers to acceptors using time-resolved photoinduced absorption measurements with both IR and visible probes. Polymer–C_{60} studies demonstrated that the charge transfer occurs within 50 fs after photoexcitation. Since the charge-transfer rate is more than 1000 times faster than any competing process (the luminescence lifetime is greater than 300 ps), the quantum efficiency for charge separation approaches unity.[135,183,184] Charge recombination back to the ground state or to some triplet state can also be identified and probed using longer timescale transient absorption spectroscopy.[185]

Understanding the optical and photophysical properties of active layer materials plays a key role in predicting the device performance of said materials (see **Figure 1.11**). The photophysical measurement of the molar absorptivity determines the light absorptivity or exciton creation capability of the solar device. Obtaining the photophysics of exciton energy transfer, photoluminescence quenching helps in predicting the exciton diffusion length of a D-A system. Electron transfer, hot exciton dissociation, photophysical studies help in predicting the rate determining charge transfer step in the device operation. Finally, charge recombination and even triplet production photophysical studies can be used to predict the charge collection time of the photovoltaic device. The charge carrier lifetime (or recombination time) should be longer than the charge collection time. For these studies, the nanoscale morphology of the D-A mixture strongly influences the measured photophysical properties, and in turn the power conversion efficiency in the corresponding device, so a careful design of the morphology is required.

1.7.3 Perylene diimide (PDI) photophysics: Charge transfer and triplet production

With all the series of structural variations of PDIs, it evidently became important to seek to understand the structure–function relationship of these macromolecular systems and the critical mechanisms taking place following photoexcitation. One of the fundamental photophysical

process is intramolecular charge transfer (CT) and subsequent charge separation (CS). It is important to understand how the structure of multichromophoric PDI systems affect the intramolecular CT and CS process taking place, towards the effective conversion of solar light. In a donor-acceptor (D-A) system either covalently bound (intramolecular) or spatially separated (intermolecular), photoinduced electron- (or hole-) transfer process is described in the following steps,[112]

Step 1: $D + A \rightarrow D^* + A$ (donor excitation)

Step 2: $D^* + A \rightarrow (D--A)^*$ (excitation delocalized on D-A complex)

Step 3: $(D--A)^* \rightarrow (D^{\delta+}--A^{\delta-})^*$ (charge transfer initiated)

Step 4: $(D^{\delta+}--A^{\delta-})^* \rightarrow (D^{\bullet+}--A^{\bullet-})$ (ion radical pair formation)

Step 5: $(D^{\bullet+}--A^{\bullet-}) \rightarrow D^{\bullet+} + A^{\bullet-}$ (charge separation)
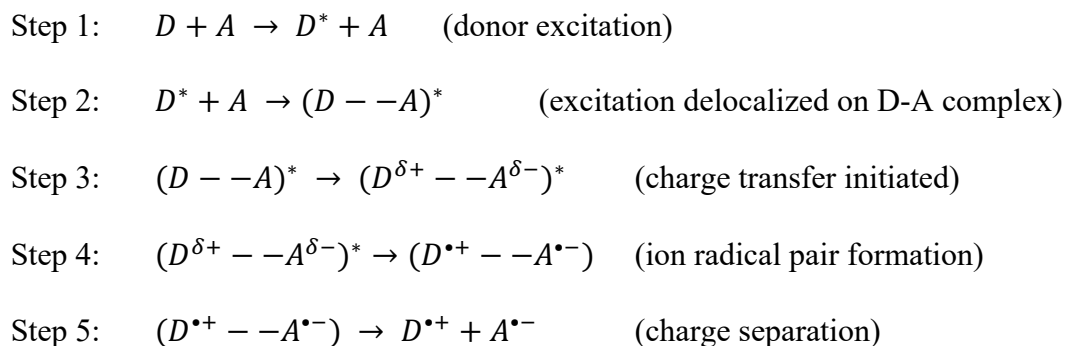
The loss mechanism, in which the oppositely charged species ($D^{\bullet+}$ and $A^{\bullet-}$) are brought together and annihilate each other, is known as charge recombination. One important function of an efficient organic solar cell material is to understand how the initially delocalized charge density ultimately localizes in order to facilitate the generation of full charges and to hinder recombination to the neutral species. A powerful technique for understanding these transient processes is pump-probe or transient absorption spectroscopy.[182,186] The ultrafast pump pulse triggers an excited state reaction *P-P whose dynamics is subsequently probed by a second ultrafast pulse. Since all the transitions occur in the electronic band, visible light sources are used in this type of spectroscopy. A lot of studies have investigated the CT, CS and subsequent charge recombination processes of several structural variations of PDIs.[187–191] The charge transfer species of a symmetric PDI monomer, P^+ and P^-, have been studied via electrochemistry, and their absorption spectra is shown in **Figure 1.19a** below. This helps in identifying these species as the form and decay when

employing transient absorption spectroscopy. **Figure 1.19b** also shows an easy kinetic scheme for photoinduced intramolecular electron transfer in PDIs resulting in the production of a CS state.
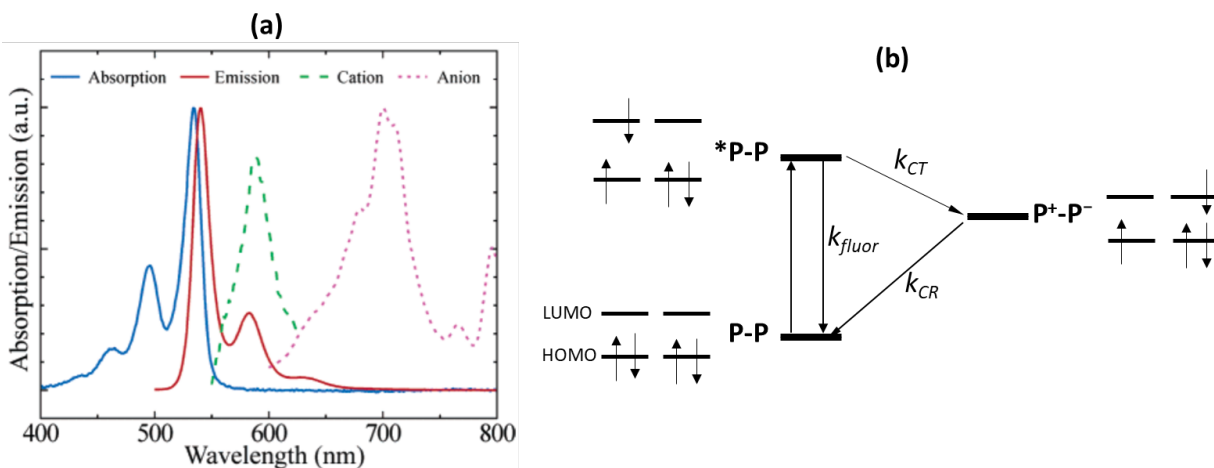
Figure 1.19 (a) Absorption, emission spectra of a PDI dimer and the absorption spectra of the electrochemically generated cation and anion of a PDI monomer, **(b)** kinetic scheme for a photoinduced intramolecular CS process taking place in a PDI dimer.[192]
Reprinted with permission from ref 192. Copyright 2005 American Chemical Society

Another fundamental photophysical process in PDI systems is triplet production. This could take place via conventional intersystem crossing (ISC) – spin orbit charge transfer ISC (SOCT-ISC) and radical pair ISC (RPISC),[193] or via an unconventional process known as singlet exciton fission (SEF) – intermolecular or intramolecular.[194] Triplets for PDIs are important for understanding fundamental photophysics related to photovoltaic applications. There are conflicting reports as to the importance of triplets in photovoltaic devices. Zhenyi Yu et al reported that the access to the PDI triplet state clearly represents an attractive interest for solar energy conversion due to the prolonged exciton diffusion length.[195] However, Veldman et al reported that triplet formation in PDIs reduces the lifetime of the charge transfer state that serves as a precursor for free charge carriers.[196] A common fact in both viewpoints is that for PDI systems, the triplet formation mechanism occurs from the charge transfer state. Triplet formation via singlet exciton fission (SEF) is commonly accepted to be highly beneficial for organic photovoltaic devices. In

fact, it believed to allow photovoltaics obtain efficiencies beyond the Shockley–Queisser limit. SEF is the process that splits a singlet exciton into two triplet excitons, to be collected as independent electrons. A more detailed description of this important process is given in the next section, and more specifically, as they occur in PDIs.

1.8 Singlet Exciton Fission

1.8.1 Background of singlet exciton fission in OPV materials

Singlet exciton fission (SEF) is the generation of two triplet excitons from one excited singlet exciton. It is a multiexciton generation process to increase the yield of excitations per absorbed photon (see **Figure 1.20a**). In this process, a singlet excitation S_1 of a molecular chromophore is converted into triplet excitations T_1 on two molecular chromophores, both of which can then in principle generate electron-hole pairs. Singlet fission can therefore be viewed as a special case of internal conversion (radiationless transition between two electronic states of equal multiplicity). Like many other internal conversion processes, it can be very fast, particularly in molecular crystals. The SF process is the inverse of the long known and much studied triplet-triplet annihilation.[197] Singlet fission was first observed by Siebrand, Schneider et al in crystalline anthracene.[198] It was subsequently invoked to account for the thermally induced fluorescence quenching in crystalline tetracene,[199] and confirmed beyond doubt by several studies of tetracene and pentacene crystals in rapid succession. A quantitative analysis of the possible contribution of SEF to excitonic solar cell efficiency was carried out by Hanna and Nozik.[200] For single gap photovoltaic devices, the maximum efficiency increases from 33.7 % to 44.4 %.
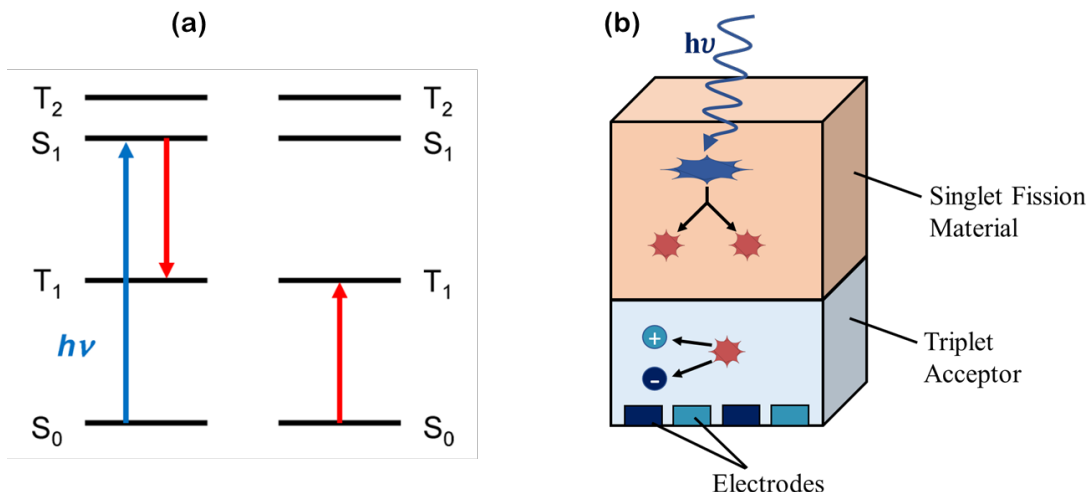
Figure 1.20 (a) Energy level diagram for SEF, **(b)** extraction of triplet charges in SEF sensitized solar cells.

In the early 2000s, when SEF was applied to photovoltaics, SEF sensitizers were used (**Figure 1.20b**). A suitable sensitizer, based on the energetics of the system, has to be chosen. For the efficient operation of a SEF sensitizer, one has to make sure that electron injection from the originally excited singlet state S_1 is slower than the rate of SEF, while electron injection from the triplet state T_1 is faster than the decay of the T_1 into the ground state S_0. This appears feasible, given the huge difference between the usual lifetimes of the S_1 and T_1 states.[197] Also limiting triplet-triplet annihilation is very important. Annihilation could be a very serious problem in dimers and oligomers, in which the triplet excitons cannot diffuse apart as they can in crystals. One of the initial design criteria proposed by Paci et al[201] for SEF organic materials is the availability of two or more chromophoric subunits weakly interacting in the ground state (i.e. weak interchromophore coupling). To this regard, two fundamental molecular physics questions that may then arise are what are the desirable properties of the individual subunit chromophores? And what is the optimal structure for their coupling? Another initial design criterion is the satisfaction of the energetics for SEF, $E(S_1) \geq 2E(T_1)$. This requirement, meant to ensure a high yield of SEF, is not easy to meet, since in most common chromophores the $E(S_1) - E(T_1)$ gap is considerably

smaller than the $E(T_1) - E(S_0)$ gap. Finally, it need not be easy to detect singlet fission even when it does take place. Unless the yield of the triplets exceeds 100%, it is natural to assume first that they were formed by ordinary spin-orbit induced intersystem crossing.[202] This is another important criteria for SEF materials. Two mechanistic pathways have been proposed for the formation of triplet-pairs, (i) direct two-electron transfer, and (ii) mediated charge transfer (CT). These are represented in **Figure 1.21**.
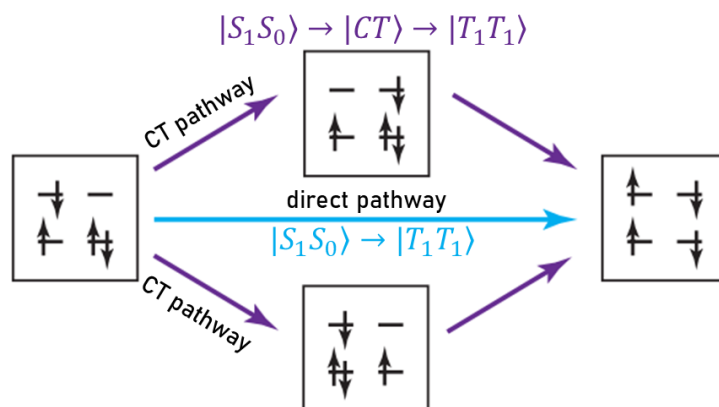
Figure 1.21 Two pathways from the photoexcitated S1, to the formation of triplet pairs.

1.8.2   Intermolecular and intramolecular singlet exciton fission

Majority of the published SEF studies have been about intermolecular SEF i.e., solid state (single crystals, polycrystalline thin films) aggregates, wherein the absorption of one photon leads to the formation of two triplet excitons on adjacent molecules. Given the nature of this process, strong electronic coupling between nearest neighbors is required. In crystalline solids, the correlated triplet pairs (TT) rapidly dissociate at room temperature and diffuse apart, making it difficult to study their multiexciton states. A bulk of these intermolecular SEF studies involve tetracene and pentacene derivatives, and there have also been intermolecular studies in units of diketopyrrolopyrrole,[203] diphenylisobenzofuran,[204,205] polythiophenes,[206] carotenoids.[207]

In crystalline and solid-state media, the crystal packing and morphology has significant effect on SEF rates, and the packing and morphology is often difficult to control. Hence, for OPV

devices made with intermolecular SEF chromophores, where solid-state packing interactions are crucial, slight perturbations can have a drastic effect on the rate and yield of SEF. To this regards, a more suitable approach would be implementation of intramolecular SEF.[194,208–210] Another benefit of intramolecular SEF is that it provides little insight into the short-range molecular interactions that govern singlet fission, which cannot be otherwise obtained from intermolecular SEF studies. The first intramolecular SEF study that was carried out was done by Walker et al,[211] and they used very concentrated solutions of TIPS pentacene (~10^{-2} M). Although excimer intermediates were produced, they were able to achieve a singlet-to-triplet yield of ~200%. The molecular design strategy for intramolecular SEF were founded on the CT-mediated pathway to the formation of triplet-pairs.[209,212] However, another strategy involves the covalent coupling of two intermolecular SEF chromophores, and carefully tuning the conjugation and spatial dynamics within these chromophores.[213–215] Some have used a combination of both strategies in the design of intramolecular SEF molecules.[194,216]
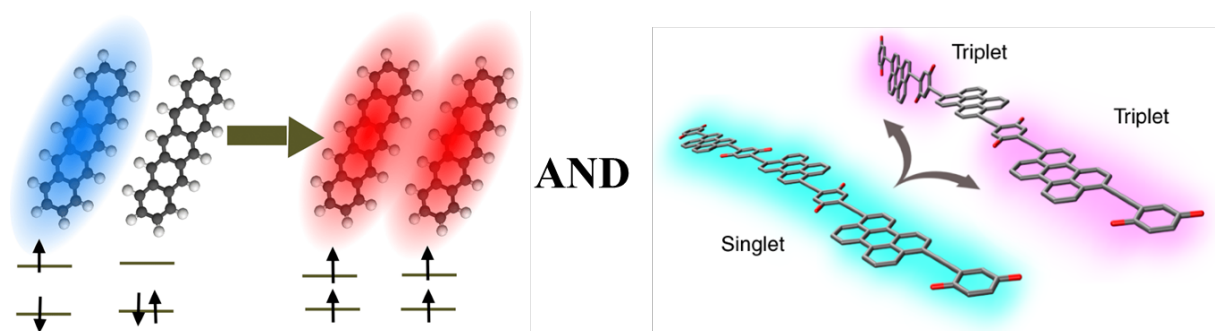
Figure 1.22 Representation of intermolecular[217] and intramolecular[218] singlet exciton fission. Left figure reprinted with permission from ref 217. Copyright 2018 Royal Society of Chemistry. Right figure reprinted with permission from ref 218. Copyright 2020 Springer Nature.

1.8.3 Singlet exciton fission in perylene diimides (PDIs)

Acene derivatives (anthracene, tetracene, pentacene) have been the focus of many experimental and theoretical studies as the primary chromophore that undergoes SEF with a high triplet quantum yield (up to 200%). There are ranging disadvantages that have hindered their

practical applications in actual OPV devices. These include poor solubility in common solvents, instability in the presence of oxygen and photo-instability. A few techniques have been tried to improve their solubility such as the arylation of tetracene,[219] and to improve their stability by substitution with cyano groups.[220] However, stability is improved for only a couple of months whereas for rubrene (phenyl-substituted), it decomposes after a few days on solution. Perylene diimide (PDI) and its derivatives have attracted great interest as visible chromophores for energy and charge transport studies, especially with regard to potential applications as visible light-absorbing electron acceptors in organic photovoltaics. Not only are PDIs more thermally and photochemically stable than the acene derivatives been explored for SEF, they also exhibit a strong propensity to self-organize into ordered assemblies, both in solution and in the solid state via $\pi-\pi$ stacking interactions, often aided by hydrogen-bonding and nano/microsegregation.[221–223] Another distinct advantage that PDI derivatives have over SEF acene derivatives that absorb only at shorter wavelengths is that PDIs absorb light strongly in the middle of the visible spectrum, so the triplet energy is sufficiently high such that hole injection from the triplet manifold into semiconductor electrodes should be facile.

The energetics for SEF $E(S_1) \geq 2E(T_1)$ is satisfied with PDIs. Ford and Kamat reported that the lowest triplet-state energy $E(T_1)$ and singlet-state energy $E(S_1)$ of PDI are approximately 1.19 eV and 2.34 eV, respectively.[224] This makes PDIs a potential SEF material. The first SEF study on perylene crystals was reported by Albrecht et al in 1979.[225] For the first time, SEF behavior was investigated in the excimer-forming crystals in trying to obtain information on the dynamics of excimer formation from fission experiments. A very detailed study about SEF in vapor-deposited polycrystalline thin films of PDI was carried out by Eaton et al in 2013. They were able to obtain the crystal structure of the film by X-ray diffraction, which revealed segregated,

slip-stacked columns that are π−π stacked at a 3.5 Å interplanar distance.[226] More importantly, they were able to demonstrate the formation of triplet species via SEF pathway by employing femtosecond transient absorption and emission spectroscopy. They obtained a triplet yield of 140% and an ultrafast triplet formation time of 180 ps. Subsequently, SEF has also been observed in α-perylene single crystals,[227] and in thin films of terrylenes (a rylene dye) with similar rapid triplet formation time and ~200% triplet yield.[228,229] These were all done in solid state – intermolecular SEF.

Prior to the study published by our group (Chapter 3), unlike with the intermolecular SEF studies, intramolecular SEF investigations of rylene-based compounds was carried out for just terrylene diimide (TDI) dimers.[216,230] A triptycene or xanthene spacer is used to hold the two TDI molecules in a series of π-stacked geometries. The use of this spacer greatly minimizes any through-bond coupling between the TDI molecules, and thus mimics the coupling observed in non-covalent solids. For the TDI compounds, Margulies et al[216] discovered that in polar solvents, ultrafast CT states are formed that could compete with intramolecular SEF, but in non-polar solvents, rapid, high-yield singlet fission occurs. Intramolecular SEF in multichromophoric PDI systems, and the suitable molecular structure and coupling strength required to activate SEF, will be discussed in more detail in Chapter 3 of this dissertation.

1.9 Big Picture of the Dissertation and Outline

In the ongoing discussion about solar energy technologies for electricity generation, organic solar cells play a vital role in achieving a cost-effective alternative relative to their inorganic counterpart. With the intensive research efforts, single-junction devices containing an electron donor polymer and an electron acceptor macromolecule in its active layer have been able to reach record power conversion efficiencies (PCE) of 18.2%.[140] The efficiency-to-cost ratio for

organic solar cells has certainly improved and their commercialization are currently underway following lifetime (device stability) and scalability analyses.[231] The clear pathway to arriving at these record efficiencies through organic material research and development, have been explained in detail throughout this chapter. There have been extensive improvements in organic synthetic procedures, improvement in active-layer nano-/microstructures, improvement in device architecture, and most importantly the open communication among material scientists, physical scientists, device physicists and synthetic chemists to direct a more targeted design. For the continuous improvement of the conversion efficiency of organic solar devices, a clear understanding of the fundamental molecular, optical and photophysical properties of the active layer materials, is required.

This thesis work seeks to elucidate the optical and photophysical properties of organic and hybrid materials for organic solar cell application. The structure-property–performance correlation of selected materials are investigated by employing state-of-the-art ultrafast laser spectroscopic techniques such as steady state absorption and fluorescence, time-resolved fluorescence, two-photon absorption, pump-probe/transient absorption, to point out the underpinning optical processes that make these materials excellent solar cell alternatives. The steady state measurements provide molecular structural information and ground-state absorptivity of the materials. Time-resolved fluorescence measurement is used to obtain information about the photogenerated exciton dynamics, used to quantify the exciton lifetime and estimate the mobility of the charge carriers. It functions by tracking the emissive species of the excited state after photoexcitation. The two-photon absorption cross-section, a non-linear optical property, is related to the change in the static dipole moment and the transition dipole moment of the molecule. It provides information about the intramolecular charge transfer rate and character of the material. The transient absorption

technique is able to track the dynamics of both the emissive and non-emissive species formed after photoexcitation. These species include singlets, triplets, charge transfer species, excimers, all pertinent to organic solar cell processes. The pump-probe techniques (both femtosecond and nanosecond) are highly versatile and are used to measure the formation time, the decay time and the yield of these photogenerated species.

In Chapter 2, more details about all the experimental techniques used will be provided. The setup schematics, theory and practical application(s) will be discussed in detail.

Chapter 3 presents a study on the physical science of intramolecular singlet exciton fission (SEF) in a perylene diimide (PDI) trimer electron acceptor system. The chapter discusses the distinct advantages of intramolecular SEF process taking place in A–D-π-bridge–A PDI systems, resulting in increased charge density and improved solar device efficiency. The compounds were synthesized by the Luping Yu group at the University of Chicago. The project in this chapter sought to identify the unique structural and optical properties of A–D-π-bridge–A PDI systems that suggest intramolecular SEF is taking place upon photoexcitation, by employing advanced laser spectroscopic measurements. This work was published in the Royal Society of Chemistry journal – *Chemical Science*.

In Chapter 4, the impact of ring-fusion on the photophysical properties and excited state decay pathways in N-annulated thiophene π-bridged PDI dimer systems, is investigated. The study was able to show that ring fusion led to an increased electronic coupling between the PDI units of the dimer, which in turn led to an increased charge transfer rate and in addition opened up the triplet excited-state deactivation pathway that was not present in the unfused dimer. The compounds used in this study was synthesized by the Welch group at the University of Calgary, and the manuscript for this work is ready to be submitted.

In Chapter 5, two analogous positional isomers exhibiting twisted vs planar geometries were optically characterized in order to elucidate the core effects of intramolecular charge transfer (iCT) on molecular geometry alone, and the dominance of iCT over aggregation effects in thin film. The positional isomers, having the exact same molecular weight and composition, were synthesized by the Luping Yu group at the University of Chicago. The optical and electronic property characterization was done by employing steady-state and non-linear ultrafast laser spectroscopic measurements. This work was published in the journal of *Chemistry of Materials*.

In Chapter 6, the effect of using two different heterocyclic π-bridge compounds (furan vs thiophene) on the optical properties of donor–π-bridge–acceptor polymers for organic photovoltaic application, was investigated. The effect of linear vs bulky sidechains on the solution processability of these polymers, and hence the optical properties were also investigated. These polymers were synthesized by the Malika Jeffries-EL group at Boston University. This study was published in the *Journal of Physical Chemistry C*.

Chapter 7 encompasses three projects on several variations of silisesquioxane, a 3D-caged hybrid semiconductor molecule. These caged compounds were synthesized by the Laine group here at the University of Michigan. The ability of these cage compounds to function as electronic materials is probed by two-photon absorption measurements, time-resolved measurements and pump-probe absorption measurements. The results of this study have been published in the *Journal of Physical Chemistry C* and *Macromolecules*.

Chapter 8 briefly provides an overall summary of the research presented in this dissertation, set of guidelines for molecular geometry and future directions on the use of the ultrafast spectroscopic techniques as well as on the investigated organic macromolecules.

References

1   REN21. 2015, *Renewables 2015 Global Status Report (Paris: REN21 Secretariat)*, .

2   REN21. 2017, *Renewables Global Futures Report: Great debates towards 100% renewable energy (Paris: REN21 Secretariat)*, .

3   REN21. 2020, *Renewables 2020 Global Status Report (Paris: REN21 Secretariat)*, .

4   J. Yan, Y. Yang, P. Elia Campana and J. He, *Nat. Energy*, 2019, **4**, 709–717.

5   SolarPower Europe (2020), *EU Market Outlook for Solar Power 2020-2024*, .

6   N. Butt, H. L. Beyer, J. R. Bennett, D. Biggs, R. Maggini, M. Mills, A. R. Renwick, L. M. Seabrook and H. P. Possingham, *Science (80-.).*, 2013, **342**, 425–426.

7   E. F. Moran, M. C. Lopez, N. Moore, N. Müller and D. W. Hyndman, *Proc. Natl. Acad. Sci. U. S. A.*, 2018, **115**, 11891–11898.

8   A. Khalid and C. D. Roper, in *ASEE Annual Conference and Exposition, Conference Proceedings*, 2016.

9   L. Awerbuch, T. E. Lindemuth, S. C. May and A. N. Rogers, *Desalination*, 1976, **19**, 325–336.

10   D. D. Putra and I. Lelawati, *Energy Procedia*, 2014, **47**, 71–75.

11   P. L. Younger, *Nat. Geosci.*, 2014, **7**, 479–480.

12   K. Chomvong, V. Kordić, X. Li, S. Bauer, A. E. Gillespie, S. J. Ha, E. J. Oh, J. M. Galazka, Y. S. Jin and J. H. D. Cate, *Biotechnol. Biofuels*, 2014, **7**, 1–11.

13   A. Galadima and O. Muraza, *Energy*, 2014, **78**, 72–83.

14   J. L. Faeth, P. J. Valdez and P. E. Savage, *Energy and Fuels*, 2013, **27**, 1391–1398.

15   M. Grätzel, *Philos. Trans. R. Soc. A Math. Phys. Eng. Sci.*, 2007, **365**, 993–1005.

16   International Energy Agency (IEA), *Sol. Energy Perspect.*, 2011, **9789264124**, 1–228.

17   C. Dennis, *Nature*, 2006, **443**, 23–24.

18   O. Behar, D. Sbarbaro and L. Morán, *Sustain.*, 2020, **12**, 1–16.

19   M. Á. Reyes-Belmonte, *Sustain.*, , DOI:10.3390/su12198217.

20   D. Mills, *Sol. Energy*, 2004, **76**, 19–31.

21   W. G. Le Roux, T. Bello-Ochende and J. P. Meyer, *Energy Convers. Manag.*, 2014, **84**, 457–470.

22   J. Sarkar and S. Bhattacharyya, *Arch. Thermodyn.*, 2012, **33**, 23–40.

23   R. F. Service, *Science (80-.).*, 2004, **306**, 806–807.

24   R. Venkatasubramanian, E. Siivola, T. Colpitts and B. O'Quinn, *Nature*, 2001, **413**, 597–602.

25   L. D. Hicks and M. S. Dresselhaus, *Phys. Rev. B*, 1993, **47**, 12727–12731.

26   J. Gainza, F. Serrano-Sánchez, N. Biskup, N. M. Nemes, J. L. Martínez, M. T. Fernández-Díaz and J. A. Alonso, *Materials (Basel).*, , DOI:10.3390/ma12223783.

27   K. F. Hsu, S. Loo, F. Guo, W. Chen, J. S. Dyck, C. Uher, T. Hogan, E. K. Polychroniadis and M. G. Kanatzidis, *Science (80-.).*, 2004, **303**, 818–821.

28   E. Quarez, K. F. Hsu, R. Pcionek, N. Frangis, E. K. Polychroniadis and M. G. Kanatzidis, *J. Am. Chem. Soc.*, 2005, **127**, 9177–9190.

29   A. Steinfeld and R. Palumbo, *Encycl. Phys. Sci. Technol.*, 2003, **15**, 237–256.

30   A. Steinfeld, *Sol. Energy*, 2005, **78**, 603–615.

31   E. A. Fletcher, *J. Sol. Energy Eng. Trans. ASME*, 2001, **123**, 63–74.

32   D. R. Ort, X. Zhu and A. Melis, *Plant Physiol.*, 2011, **155**, 79–85.

33   M. E. El-Khouly, E. El-Mohsnawy and S. Fukuzumi, *J. Photochem. Photobiol. C Photochem. Rev.*, 2017, **31**, 36–83.

34   J. Barber, *Chem. Soc. Rev.*, 2009, **38**, 185–196.

35   W. Lubitz, E. J. Reijerse and J. Messinger, *Energy Environ. Sci.*, 2008, **1**, 15–31.

36   A. Badura, D. Guschin, T. Kothe, M. J. Kopczak, W. Schuhmann and M. Rögner, *Energy Environ. Sci.*, 2011, **4**, 2435–2440.

37   M. Hambourger, G. F. Moore, D. M. Kramer, D. Gust, A. L. Moore and T. A. Moore, *Chem. Soc. Rev.*, 2009, **38**, 25–35.

38   D. Gust and T. A. Moore, *Science (80-.).*, 1989, **244**, 35–41.

39   T. J. Meyer, *Acc. Chem. Res.*, 1989, **22**, 163–170.

40   M. R. Wasielewski, *Chem. Rev.*, 1992, **92**, 435–461.

41   G. R. Fleming and R. van Grondelle, *Curr. Opin. Struct. Biol.*, 1997, **7**, 738–748.

42   M. R. Wasielewski, *J. Org. Chem.*, 2006, **71**, 5051–5066.

43   E. Becquerel, *C. R. Hebd. Seances Acad. Sci.*

44   *Nature*, 1873, **7**, 303–303.

45   M. Tao, *Electrochem. Soc. Interface*, 2008, **17**, 30–35.

46   A. Einstein, *Ann. Phys.*, 1905, 4, 132–148.

47   U.S. Patent 1,077,219, 1913, 3.

48   U. S. Patent, U.S. Patent 2,402,662, 1946, 14.

49   D. M. Chapin, C. S. Fuller and G. L. Pearson, *J. Appl. Phys.*, 1954, **25**, 676–677.

50   A. Smets, J. Klaus, O. Isabella, V. S. Rne and Z. Miro, *Solar Energy*, England, UIT Cambridge, 2015.

51   W. Shockley and H. J. Queisser, *J. Appl. Phys.*, 1961, **32**, 510–519.

52   M. A. Green, *Solar Cells: Operating Principles, Technology, and System Applications*, Prentice Hall, 1981.

53   A. A. D. T. Adikaari, D. M. N. M. Dissanayake and S. R. P. Silva, *IEEE J. Sel. Top. Quantum Electron.*, 2010, **16**, 1595–1606.

54   L. Fraas and L. Partain, *Solar Cells and Their Applications*, Wiley, 2nd edn., 2010.

55   M. Gul, Y. Kotak and T. Muneer, *Review on recent trend of solar photovoltaic technology*, 2016, vol. 34.

56   T. M. Bruton, *Sol. Energy Mater. Sol. Cells*, 2002, **72**, 3–10.

57   O. Mah, *Natl. Sol. Power Res. Inst. Rep.*, 1998, 1–10.

58   R. W. Miles, G. Zoppi and I. Forbes, *Mater. Today*, 2007, **10**, 20–27.

59   P. Meyers and R. Birkmire, *Prog. Photovilatics Res. Appl.*, 1995, **3**, 393–402.

60   M. A. Green, in *Materials for energy conversion devices*, 2005, pp. 3–34.

61   A. Pochettino, *Acad. Lincei Rend.*, 1906, **15**, 355–363.

62   M. Volmer, *Ann. Phys.*, 1913, **40**, 775.

63   H. Kim, S. Nam, J. Jeong, S. Lee, J. Seo, H. Han and Y. Kim, *Korean J. Chem. Eng.*, 2014, **31**, 1095–1104.

64   H. Spanggaard and F. C. Krebs, *Sol. Energy Mater. Sol. Cells*, 2004, **83**, 125–146.

65   G. A. Chamberlain, *Sol. Cells*, 1983, **8**, 47–83.

66   S. Karg, W. Riess, M. Meier and M. Schwoerer, *Mol. Cryst. Liq. Cryst. Sci. Technol. Sect. A. Mol. Cryst. Liq. Cryst.*, 1993, **236**, 79–86.

67   R. N. Marks, J. J. M. Halls, D. D. C. Bradley, R. H. Friend and A. B. Holmes, *J. Phys. Condens. Matter*, 1994, **6**, 1379–1394.

68   C. W. Tang, *Appl. Phys. Lett.*, 1986, **48**, 183–185.

69   A. Mohammad Bagher, *Int. J. Renew. Sustain. Energy*, 2014, **3**, 53.

70   S. Antohe, S. Iftimie, L. Hrostea, V. A. Antohe and M. Girtan, *Thin Solid Films*, 2017, **642**, 219–231.

71   N. S. Sariciftci, *Primary Photoexcitations In Conjugated Polymers: Molecular Exciton Versus Semiconductor Band Model*, World Scientific Publishing Co. Plc. Ltd., Singapore, 1997.

72   A. K. Ghosh and T. Feng, *Appl. Phys. Lett.*, 1978, **49**, 5982.

73   B. A. Gregg and M. C. Hanna, *J. Appl. Phys.*, 2003, **93**, 3605–3614.

74   J.-C. Brédas, J. E. Norton, J. Cornil and V. Coropceanu, *Acc. Chem. Res.*, 2009, **42**, 1691–1699.

75   B. Kippelen and J. L. Brédas, *Energy Environ. Sci.*, 2009, **2**, 251–261.

76   S. F. Alvarado, P. F. Seidler, D. G. Lidzey and D. D. C. Bradley, *Phys. Rev. Lett.*, 1998, **81**, 1082–1085.

77   R. Kersting, U. Lemmer, M. Deussen, H. J. Bakker, R. F. Mahrt, H. Kurz, V. I. Arkhipov, H. Bässler and E. O. Göbel, *Phys. Rev. Lett.*, 1994, **73**, 1440–1443.

78   I. G. Hill, A. Kahn, Z. G. Soos and R. A. Pascal, *Chem. Phys. Lett.*, 2000, **327**, 181–188.

79   S. Khodabakhsh, B. M. Sanderson, J. Nelson and T. S. Jones, *Adv. Funct. Mater.*, 2006, **16**, 95–100.

80   P. Peumans, A. Yakimov and S. R. Forrest, *J. Appl. Phys.*, 2003, **93**, 3693–3723.

81   J. Yan and B. R. Saunders, *RSC Adv.*, 2014, **4**, 43286–43314.

82   G. Yu, J. Gao, J. C. Hummelen, F. Wudl and A. J. Heeger, *Science (80-.).*, 1995, **270**, 1789–1791.

83   N. S. Sariciftci, D. Braun, C. Zhang, V. I. Srdanov, A. J. Heeger, G. Stucky and F. Wudl, *Appl. Phys. Lett.*, 1993, **62**, 585–587.

84   J. J. M. Halls, C. A. Walsh, N. C. Greenham, E. A. Marseglia, R. H. Friend, S. C. Moratti and A. B. Holmes, *Nature*, 1995, **376**, 498–500.

85   G. Yu and A. J. Heeger, *J. Appl. Phys.*, 1995, **78**, 4510–4515.

86   U.S. Patent 5,454,880, 1995.

87   A. D'Amore, V. Mottaghitalab and A. K. Haghi, *Biosci. Methodol. Phys. Chem. An Eng. Mol. Approach*, 2013, **10**, 79–110.

88   S. Günes, H. Neugebauer and N. S. Sariciftci, *Chem. Rev.*, 2007, **107**, 1324–1338.

89   N. S. Sariciftci, L. Smilowitz, A. J. Heeger and F. Wudl, *Science (80-.).*, 1992, **258**,

1474–1476.

90   H. Hoppe, T. Glatzel, M. Niggemann, W. Schwinger, F. Schaeffler, A. Hinsch, M. C. Lux-Steiner and N. S. Sariciftci, *Thin Solid Films*, 2006, **511**–**512**, 587–592.

91   S. E. Shaheen, C. J. Brabec, N. S. Sariciftci, F. Padinger, T. Fromherz and J. C. Hummelen, *Appl. Phys. Lett.*, 2001, **78**, 841–843.

92   Y. Kim, S. A. Choulis, J. Nelson, D. D. C. Bradley, S. Cook and J. R. Durrant, *Appl. Phys. Lett.*, 2005, **86**, 1–3.

93   Y. Kim, S. Cook, S. M. Tuladhar, S. A. Choulis, J. Nelson, J. R. Durrant, D. D. C. Bradley, M. Giles, I. McCulloch, C. S. Ha and M. Ree, *Nat. Mater.*, 2006, **5**, 197–203.

94   F. Padinger, R. S. Rittberger and N. S. Sariciftci, *Adv. Funct. Mater.*, 2003, **13**, 85–88.

95   W. Ma, C. Yang, X. Gong, K. Lee and A. J. Heeger, *Adv. Funct. Mater.*, 2005, **15**, 1617–1622.

96   M. Reyes-Reyes, K. Kim, J. Dewald, R. López-Sandoval, A. Avadhanula, S. Curran and D. L. Carroll, *Org. Lett.*, 2005, **7**, 5749–5752.

97   J. Peet, J. Y. Kim, N. E. Coates, W. L. Ma, D. Moses, A. J. Heeger and G. C. Bazan, *Nat. Mater.*, 2007, **6**, 497–500.

98   J. Y. Kim, S. H. Kim, H. H. Lee, K. Lee, W. Ma, X. Gong and A. J. Heeger, *Adv. Mater.*, 2006, **18**, 572–576.

99   W. U. Huynh, J. J. Dittmer and P. A. Alivisatos, *Science (80-.)*., 2002, **295**, 2425–2427.

100   W. J. E. Beek, M. M. Wienk and R. A. J. Janssen, *Adv. Mater.*, 2004, **16**, 1009–1013.

101   B. Sun, H. J. Snaith, A. S. Dhoot, S. Westenhoff and N. C. Greenham, *J. Appl. Phys.*, , DOI:10.1063/1.1804613.

102   N. C. Greenham, X. Peng and A. P. Alivisatos, *Synth. Met.*, 1997, **84**, 545–546.

103   S. C. Veenstra, W. J. H. Verhees, J. M. Kroon, M. M. Koetse, J. Sweelssen, J. J. A. M. Bastiaansen, H. F. M. Schoo, X. Yang, A. Alexeev, J. Loos, U. S. Schubert and M. M. Wienk, *Chem. Mater.*, 2004, **16**, 2503–2508.

104   M. M. Koetse, J. Sweelssen, K. T. Hoekerd, H. F. M. Schoo, S. C. Veenstra, J. M. Kroon, X. Yang and J. Loos, *Appl. Phys. Lett.*, 2006, **88**, 88–91.

105   C. R. McNeill, S. Westenhoff, C. Groves, R. H. Friend and N. C. Greenham, *J. Phys. Chem. C*, 2007, **111**, 19153–19160.

106   Q. Wu, D. Zhao, A. M. Schneider, W. Chen and L. Yu, *J. Am. Chem. Soc.*, 2016, **138**, 7248–7251.

107   X. Jiang, Y. Xu, X. Wang, F. Yang, A. Zhang, C. Li, W. Ma and W. Li, *Polym. Chem.*,

2017, **8**, 3300–3306.

108   X. Zhang, Z. Lu, L. Ye, C. Zhan, J. Hou, S. Zhang, B. Jiang, Y. Zhao, J. Huang, S. Zhang, Y. Liu, Q. Shi, Y. Liu and J. Yao, *Adv. Mater.*, 2013, **25**, 5791–5797.

109   D. Zhao, Q. Wu, Z. Cai, T. Zheng, W. Chen, J. Lu and L. Yu, *Chem. Mater.*, 2016, **28**, 1139–1146.

110   Y. Lin, J. Wang, S. Dai, Y. Li, D. Zhu and X. Zhan, *Adv. Energy Mater.*, 2014, **4**, 2–6.

111   Y. Xiong, B. Wu, X. Zheng, Z. Zhao, P. Deng, M. Lin, B. Tang and B. S. Ong, *Adv. Sci.*, 2017, **4**, 1–6.

112   A. J. Heeger, *J. Phys. Chem. B*, 2001, **105**, 8475–8491.

113   R. Menon, C. O. Yoon, D. Moses and A. J. Heeger, *Handb. Conduct. Polym.*, 1998, 27–84.

114   U.S. Patent 5,300,575, 1994.

115   S. Karg, W. Riess, V. Dyakonov and M. Schwoerer, *Synth. Met.*, 1993, **54**, 427–433.

116   G. Yu, C. Zhang and A. J. Heeger, *Appl. Phys. Lett.*, 1994, **64**, 1540–1542.

117   E. Frankevich, A. Zakhidov and K. Yoshino, *Phys. Rev. B - Condens. Matter Mater. Phys.*, 1996, **53**, 4498–4508.

118   D. Gebeyehu, C. J. Brabec, F. Padinger, T. Fromherz, J. C. Hummelen, D. Badt, H. Schindler and N. S. Sariciftci, *Synth. Met.*, 2001, **118**, 1–9.

119   M. T. Dang, L. Hirsch and G. Wantz, *Adv. Mater.*, 2011, **23**, 3597–3602.

120   A. T. Kleinschmidt, S. E. Root and D. J. Lipomi, *J. Mater. Chem. A*, 2017, **5**, 11396–11400.

121   J. D. Yuen and F. Wudl, *Energy Environ. Sci.*, 2013, **6**, 392–406.

122   S. A. Jenekhe, L. Lu and M. M. Alam, *Macromolecules*, 2001, **34**, 7315–7324.

123   N. Blouin, A. Michaud, D. Gendron, S. Wakim, E. Blair, R. Neagu-Plesu, M. Belletête, G. Durocher, Y. Tao and M. Leclerc, *J. Am. Chem. Soc.*, 2008, **130**, 732–742.

124   L. Dou, J. Gao, E. Richard, J. You, C. C. Chen, K. C. Cha, Y. He, G. Li and Y. Yang, *J. Am. Chem. Soc.*, 2012, **134**, 10071–10079.

125   J. Hou and X. Guo, in *Organic Solar Cells, Green Energy and Technology*, ed. W. C. H. Choy, Springer-Verlag London Limited, 2013, pp. 17–42.

126   M. Jeffries-El, B. M. Kobilka and B. J. Hale, *Macromolecules*, , DOI:10.1021/ma501236v.

127   A. Hamed, Y. Y. Sun, Y. K. Tao, R. L. Meng and P. H. Hor, *Phys. Rev. B*, 1993, **47**,

10873–10880.

128   N. Martín, L. Sánchez, B. Illescas and I. Pérez, *Chem. Rev.*, 1998, **98**, 2527–2547.

129   M. K. Hassan Bhuiyan and T. Mieno, *Thin Solid Films*, 2003, **441**, 187–191.

130   S. Morita, A. A. Zakhidov and K. Yoshino, *Solid State Commun.*, 1992, **82**, 249–252.

131   R. E. Haufler, J. Conceicao, L. P. F. Chibante, Y. Chai, N. E. Byrne, S. Flanagan, M. M. Haley, S. C. O'Brien, C. Pan, Z. Xiao, W. E. Billups, M. A. Ciufolini, R. H. Hauge, J. L. Margrave, L. J. Wilson, R. F. Curl and R. E. Smalley, *J. Phys. Chem.*, 1990, **94**, 8634–8636.

132   P. M. Allemand, A. Koch, F. Wudl, Y. Rubin, F. Diederich, M. M. Alvarez, S. J. Anz and R. L. Whetten, *J. Am. Chem. Soc.*, 1991, **113**, 1050–1051.

133   F. Arias, Q. Xie, L. Echegoyen, Y. Wu, Q. Lu and S. R. Wilson, *J. Am. Chem. Soc.*, 1994, **116**, 6388–6394.

134   P. A. Liddell, J. P. Sumida, A. N. Macpherson, L. Noss, G. R. Seely, K. N. Clark, A. L. Moore, T. A. Moore and D. Gust, *Photochem. Photobiol.*, 1994, **60**, 537–541.

135   R. A. J. Janssen, J. C. Hummelen, K. Lee, K. Pakbaz, N. Serdar Sariciftci, A. J. Heeger and F. Wudl, *J. Chem. Phys.*, 1995, **103**, 788–793.

136   B. Carlotti, Z. Cai, H. Kim, V. Sharapov, I. K. Madu, D. Zhao, W. Chen, P. M. Zimmerman, L. Yu and T. Goodson, *Chem. Mater.*, 2018, **30**, 4263–4276.

137   J. Hou, O. Inganäs, R. H. Friend and F. Gao, *Nat. Mater.*, 2018, **17**, 119–128.

138   Y. Cui, H. Yao, J. Zhang, K. Xian, T. Zhang, L. Hong, Y. Wang, Y. Xu, K. Ma, C. An, C. He, Z. Wei, F. Gao and J. Hou, *Adv. Mater.*, 2020, **32**, 1–7.

139   Z. Wang, Z. Peng, Z. Xiao, D. Seyitliyev, K. Gundogdu, L. Ding and H. Ade, *Adv. Mater.*, 2020, **2005386**, 2005386.

140   Q. Liu, Y. Jiang, K. Jin, J. Qin, J. Xu, W. Li, J. Xiong, J. Liu, Z. Xiao, K. Sun, S. Yang, X. Zhang and L. Ding, *Sci. Bull.*, 2020, **65**, 272–275.

141   C. Yan, S. Barlow, Z. Wang, H. Yan, A. K. Y. Jen, S. R. Marder and X. Zhan, *Nat. Rev. Mater.*, 2018, **3**, 1–19.

142   Y. Lin and X. Zhan, *Adv. Energy Mater.*, 2015, **5**, 1–9.

143   P. Cheng, M. Zhang, T.-K. Lau, Y. Wu, B. Jia, J. Wang, C. Yan, M. Qin, X. Lu and X. Zhan, *Adv. Mater.*, 2017, **29**, 1605216.

144   J. Liu, S. Chen, D. Qian, B. Gautam, G. Yang, J. Zhao, J. Bergqvist, F. Zhang, W. Ma, H. Ade, O. Inganäs, K. Gundogdu, F. Gao and H. Yan, *Nat. Energy*, 2016, **1**, 1–7.

145   S. Chen, Y. Liu, L. Zhang, P. C. Y. Chow, Z. Wang, G. Zhang, W. Ma and H. Yan, *J. Am.*

Chem. Soc., 2017, **139**, 6298–6301.

146   K. Vandewal, Z. Ma, J. Bergqvist, Z. Tang, E. Wang, P. Henriksson, K. Tvingstedt, M. R. Andersson and F. Zhang, *Adv. Funct. Mater.*, 2012, **22**, 3480–3490.

147   L. Ye, X. Jiao, M. Zhou, S. Zhang, H. Yao, W. Zhao, A. Xia, H. Ade and J. Hou, *Adv. Mater.*, 2015, **27**, 6046–6054.

148   J. Lee, R. Singh, D. H. Sin, H. G. Kim, K. C. Song and K. Cho, *Adv. Mater.*, 2016, **28**, 69–76.

149   J. W. Jung, J. W. Jo, C. C. Chueh, F. Liu, W. H. Jo, T. P. Russell and A. K. Y. Jen, *Adv. Mater.*, 2015, **27**, 3310–3317.

150   X. Zhan, A. Facchetti, S. Barlow, T. J. Marks, M. A. Ratner, M. R. Wasielewski and S. R. Marder, *Adv. Mater.*, 2011, **23**, 268–284.

151   E. Kozma and M. Catellani, *Dye. Pigment.*, 2013, **98**, 160–179.

152   C. Ego, D. Marsitzky, S. Becker, J. Zhang, A. C. Grimsdale, K. Müllen, J. D. MacKenzie, C. Silva and R. H. Friend, *J. Am. Chem. Soc.*, 2003, **125**, 437–443.

153   M. Sadrai, L. Hadel, R. R. Sauers, S. Husain, K. Krogh-Jespersen, J. D. Westbrook and G. R. Bird, *J. Phys. Chem.*, 1992, **96**, 7988–7996.

154   K. Y. Law, *Chem. Rev.*, 1993, **93**, 449–486.

155   W. S. Shin, H. H. Jeong, M. K. Kim, S. H. Jin, M. R. Kim, J. K. Lee, J. W. Lee and Y. S. Gal, *J. Mater. Chem.*, 2006, **16**, 384–390.

156   S. Shoaee, T. M. Clarke, C. Huang, S. Barlow, S. R. Marder, M. Heeney, I. McCulloch and J. R. Durrant, *J. Am. Chem. Soc.*, 2010, **132**, 12919–12926.

157   A. Schubert, V. Settels, W. Liu, F. Würthner, C. Meier, R. F. Fink, S. Schindlbeck, S. Lochbrunner, B. Engels and V. Engel, *J. Phys. Chem. Lett.*, 2013, **4**, 792–796.

158   A. Sharenko, C. M. Proctor, T. S. Van Der Poll, Z. B. Henson, T. Q. Nguyen and G. C. Bazan, *Adv. Mater.*, 2013, **25**, 4403–4406.

159   W. Jiang, L. Ye, X. Li, C. Xiao, F. Tan, W. Zhao, J. Hou and Z. Wang, *Chem. Commun.*, 2014, **50**, 1024–1026.

160   Q. Yan, Y. Zhou, Y. Q. Zheng, J. Pei and D. Zhao, *Chem. Sci.*, 2013, **4**, 4389–4394.

161   Y. Zhong, M. T. Trinh, R. Chen, W. Wang, P. P. Khlyabich, B. Kumar, Q. Xu, C. Y. Nam, M. Y. Sfeir, C. Black, M. L. Steigerwald, Y. L. Loo, S. Xiao, F. Ng, X. Y. Zhu and C. Nuckolls, *J. Am. Chem. Soc.*, 2014, **136**, 15215–15221.

162   S. Rajaram, R. Shivanna, S. K. Kandappa and K. S. Narayan, *J. Phys. Chem. Lett.*, 2012, **3**, 2405–2408.

163   R. Singh, J. Lee, M. Kim, P. E. Keivanidis and K. Cho, *J. Mater. Chem. A*, 2017, **5**, 210–220.

164   J. Zhang, Y. Li, J. Huang, H. Hu, G. Zhang, T. Ma, P. C. Y. Chow, H. Ade, D. Pan and H. Yan, *J. Am. Chem. Soc.*, 2017, **139**, 16092–16095.

165   W. Chen, X. Yang, G. Long, X. Wan, Y. Chen and Q. Zhang, *J. Mater. Chem. C*, 2015, **3**, 4698–4705.

166   Y. Lin, Y. Wang, J. Wang, J. Hou, Y. Li, D. Zhu and X. Zhan, *Adv. Mater.*, 2014, **26**, 5137–5142.

167   H. Lin, S. Chen, H. Hu, L. Zhang, T. Ma, J. Y. L. Lai, Z. Li, A. Qin, X. Huang, B. Tang and H. Yan, *Adv. Mater.*, 2016, 8546–8551.

168   Y. Liu, C. Mu, K. Jiang, J. Zhao, Y. Li, L. Zhang, Z. Li, J. Y. L. Lai, H. Hu, T. Ma, R. Hu, D. Yu, X. Huang, B. Z. Tang and H. Yan, *Adv. Mater.*, 2015, **27**, 1015–1020.

169   Q. Wu, D. Zhao, J. Yang, V. Sharapov, Z. Cai, L. Li, N. Zhang, A. Neshchadin, W. Chen and L. Yu, *Chem. Mater.*, 2017, **29**, 1127–1133.

170   Y. Zhong, M. T. Trinh, R. Chen, G. E. Purdum, P. P. Khlyabich, M. Sezen, S. Oh, H. Zhu, B. Fowler, B. Zhang, W. Wang, C. Y. Nam, M. Y. Sfeir, C. T. Black, M. L. Steigerwald, Y. L. Loo, F. Ng, X. Y. Zhu and C. Nuckolls, *Nat. Commun.*, 2015, **6**, 1–8.

171   H. Qian, W. Yue, Y. Zhen, S. Di Motta, E. Di Donato, F. Negri, J. Qu, W. Xu, D. Zhu and Z. Wang, *J. Org. Chem.*, 2009, **74**, 6275–6282.

172   D. Sun, D. Meng, Y. Cai, B. Fan, Y. Li, W. Jiang, L. Huo, Y. Sun and Z. Wang, *J. Am. Chem. Soc.*, 2015, **137**, 11156–11162.

173   D. Meng, D. Sun, C. Zhong, T. Liu, B. Fan, L. Huo, Y. Li, W. Jiang, H. Choi, T. Kim, J. Y. Kim, Y. Sun, Z. Wang and A. J. Heeger, *J. Am. Chem. Soc.*, 2016, **138**, 375–380.

174   A. D. Hendsbee, S. V. Dayneko, J. A. Pells, J. R. Cann and G. C. Welch, *Sustain. Energy Fuels*, 2017, **1**, 1137–1147.

175   A. D. Hendsbee, J.-P. Sun, W. K. Law, H. Yan, I. G. Hill, D. M. Spasyuk and G. C. Welch, *Chem. Mater.*, 2016, **28**, 7098–7109.

176   A. Laventure, S. Stanzel, A. J. Payne, B. H. Lessard and G. C. Welch, *Synth. Met.*, 2019, **250**, 55–62.

177   R. Farchioni and G. Grosso, *Organic Electronic Materials: Conjugated Polymers and Low Molecular Weight Electronic Solids.*, 2001.

178   K. Murata, Y. Shimoi, S. Abe, S. Kuroda, T. Noguchi and T. Ohnishi, *Chem. Phys.*, 1998, **227**, 191–201.

179   J. Grüner, P. J. Hamer, R. H. Friend, H. Huber, U. Scherf and A. B. Holmes, *Adv. Mater.*, 1994, **6**, 748–752.

180   J. Huber, K. Müllen, J. Salbeck, H. Schenk, U. Scherf, T. Stehlin and R. Stern, *Acta Polym.*, 1994, **45**, 244–247.

181   I. K. Madu, E. W. Muller, H. Kim, J. Shaw, A. A. Burney-Allen, P. Zimmerman, M. Jeffries-El and T. Goodson, *J. Phys. Chem. C*, 2018, **122**, 17049–17066.

182   H. Ohkita, Y. Tamai, H. Benten and S. Ito, *IEEE J. Sel. Top. Quantum Electron.*, 2016, **22**, 100–111.

183   B. Kraabel, J. C. Hummelen, D. Vacar, D. Moses, N. S. Sariciftci, A. J. Heeger and F. Wudl, *J. Chem. Phys.*, 1996, **104**, 4267–4273.

184   G. Lanzani, C. Zenz, G. Cerullo, W. Graupner, G. Leising, U. Scherf and S. De Silvestri, *Synth. Met.*, 2000, **111**, 493–496.

185   R. M. Williams, H.-C. Chen, D. Di Nuzzo, S. C. J. Meskers and R. A. J. Janssen, *J. Spectrosc.*, 2017, **2017**, 1–16.

186   M. Koch, M. Myahkostupov, D. G. Oblinsky, S. Wang, S. Garakyaraghi, F. N. Castellano and G. D. Scholes, *J. Am. Chem. Soc.*, 2017, **139**, 5530–5537.

187   R. E. Cook, B. T. Phelan, R. J. Kamire, M. B. Majewski, R. M. Young and M. R. Wasielewski, *J. Phys. Chem. A*, 2017, **121**, 1607–1615.

188   P. Spenst, R. M. Young, B. T. Phelan, M. Keller, J. Dostal, T. Brixner, M. R. Wasielewski and F. Wurthner, *J. Am. Chem. Soc.*, 2017, **139**, 2014–2021.

189   J. M. Giaimo, A. V. Gusev and M. R. Wasielewski, *J. Am. Chem. Soc.*, 2002, **124**, 8530–8531.

190   Y. Wu, R. M. Young, M. Frasconi, S. T. Schneebeli, P. Spenst, D. M. Gardner, K. E. Brown, F. Würthner, J. F. Stoddart and M. R. Wasielewski, *J. Am. Chem. Soc.*, 2015, **137**, 13236–13239.

191   O. F. Mohammed, *J. Phys. Chem. A*, 2010, **114**, 11576–82.

192   M. W. Holman, P. Yan, D. M. Adams, S. Westenhoff and C. Silva, *J. Phys. Chem. A*, 2005, **109**, 8548–8552.

193   P. Spenst, R. M. Young, M. R. Wasielewski and F. Würthner, *Chem. Sci.*, 2016, **7**, 5428–5434.

194   B. Carlotti, I. K. Madu, H. Kim, Z. Cai, H. Jiang, A. K. Muthike, L. Yu, P. M. Zimmerman and T. Goodson, *Chem. Sci.*, 2020, **11**, 8757–8770.

195   Z. Yu, Y. Wu, Q. Peng, C. Sun, J. Chen, J. Yao and H. Fu, *Chem. - A Eur. J.*, 2016, **22**, 4717–4722.

196   D. Veldman, S. M. A. Chopin, S. C. J. Meskers, M. M. Groeneveld, R. M. Williams and R. A. J. Janssen, *J. Phys. Chem. A*, 2008, **112**, 5846–5857.

197   J. Michl, A. J. Nozik, X. Chen, J. C. Johnson, G. Rana, A. Akdag and A. F. Schwerin, in *Organic Photovoltaics VIII*, 2007, vol. 6656, p. 66560E.

198   S. Singh, W. J. Jones, W. Siebrand, B. P. Stoicheff and W. G. Schneider, *J. Chem. Phys.*, 1965, **42**, 330–342.

199   C. E. Swenberg and W. T. Stacy, *Chem. Phys. Lett.*, 1968, **2**, 327–328.

200   M. C. Hanna and A. J. Nozik, *J. Appl. Phys.*, , DOI:10.1063/1.2356795.

201   I. Paci, J. C. Johnson, X. Chen, G. Rana, D. Popović, D. E. David, A. J. Nozik, M. A. Ratner and J. Michl, *J. Am. Chem. Soc.*, 2006, **128**, 16546–16553.

202   M. B. Smith and J. Michl, *Chem. Rev.*, 2010, **110**, 6891–6936.

203   C. M. Mauck, P. E. Hartnett, E. A. Margulies, L. Ma, C. E. Miller, G. C. Schatz, T. J. Marks and M. R. Wasielewski, *J. Am. Chem. Soc.*, 2016, **138**, 11749–11761.

204   J. N. Schrauben, J. L. Ryerson, J. Michl and J. C. Johnson, *J. Am. Chem. Soc.*, 2014, **136**, 7363–7373.

205   J. L. Ryerson, J. N. Schrauben, A. J. Ferguson, S. C. Sahoo, P. Naumov, Z. Havlas, J. Michl, A. J. Nozik and J. C. Johnson, *J. Phys. Chem. C*, 2014, **118**, 12121–12132.

206   A. J. Musser, M. Al-Hashimi, M. Maiuri, D. Brida, M. Heeney, G. Cerullo, R. H. Friend and J. Clark, *J. Am. Chem. Soc.*, 2013, **135**, 12747–12754.

207   C. Wang and M. J. Tauber, *J. Am. Chem. Soc.*, 2010, **132**, 13988–13991.

208   S. N. Sanders, E. Kumarasamy, A. B. Pun, M. T. Trinh, B. Choi, J. Xia, E. J. Taffet, J. Z. Low, J. R. Miller, X. Roy, X. Y. Zhu, M. L. Steigerwald, M. Y. Sfeir and L. M. Campos, *J. Am. Chem. Soc.*, 2015, **137**, 8965–8972.

209   E. Busby, J. Xia, Q. Wu, J. Z. Low, R. Song, J. R. Miller, X. Y. Zhu, L. M. Campos and M. Y. Sfeir, *Nat. Mater.*, 2015, **14**, 426–433.

210   X. Feng, D. Casanova and A. I. Krylov, *J. Phys. Chem. C*, 2016, **120**, 19070–19077.

211   B. J. Walker, A. J. Musser, D. Beljonne and R. H. Friend, *Nat. Chem.*, 2013, **5**, 1019–1024.

212   O. Varnavski, N. Abeyasinghe, J. Aragó, J. J. Serrano-Pérez, E. Ortí, J. T. López Navarrete, K. Takimiya, D. Casanova, J. Casado and T. Goodson, *J. Phys. Chem. Lett.*, 2015, **6**, 1375–1384.

213   S. Lukman, A. J. Musser, K. Chen, S. Athanasopoulos, C. K. Yong, Z. Zeng, Q. Ye, C. Chi, J. M. Hodgkiss, J. Wu, R. H. Friend and N. C. Greenham, *Adv. Funct. Mater.*, 2015, **25**, 5452–5461.

214   S. N. Sanders, E. Kumarasamy, A. B. Pun, K. Appavoo, M. L. Steigerwald, L. M. Campos and M. Y. Sfeir, *J. Am. Chem. Soc.*, 2016, **138**, 7289–7297.

215   N. V. Korovina, S. Das, Z. Nett, X. Feng, J. Joy, R. Haiges, A. I. Krylov, S. E. Bradforth and M. E. Thompson, *J. Am. Chem. Soc.*, 2016, **138**, 617–627.

216   E. A. Margulies, C. E. Miller, Y. Wu, L. Ma, G. C. Schatz, R. M. Young and M. R. Wasielewski, *Nat. Chem.*, 2016, **8**, 1120–1125.

217   R. F. Ribeiro, L. A. Martínez-Martínez, M. Du, J. Campos-Gonzalez-Angulo and J. Yuen-Zhou, *Chem. Sci.*, 2018, **9**, 6325–6339.

218   N. V. Korovina, C. H. Chang and J. C. Johnson, *Nat. Chem.*, 2020, **12**, 391–398.

219   M. Kytka, A. Gerlach, F. Schreiber and J. Ková č, *Appl. Phys. Lett.*, , DOI:10.1063/1.2717561.

220   Y. F. Chang, Z. Y. Lu, L. J. An and J. P. Zhang, *J. Phys. Chem. C*, 2012, **116**, 1195–1199.

221   M. J. Ahrens, L. E. Sinks, B. Rybtchinski, W. Liu, B. A. Jones, J. M. Giaimo, A. V. Gusev, A. J. Goshe, D. M. Tiede and M. R. Wasielewski, *J. Am. Chem. Soc.*, 2004, **126**, 8284–8294.

222   F. Würthner, C. Thalacker and A. Sautter, *Adv. Mater.*, 1999, **11**, 754–758.

223   A. P. H. J. Schenning, J. V. Herrikhuyzen, P. Jonkheijm, Z. Chen, F. Würthner and E. W. Meijer, *J. Am. Chem. Soc.*, 2002, **124**, 10252–10253.

224   W. E. Ford and P. V. Kamat, *J. Phys. Chem.*, 1987, **91**, 6373–6380.

225   W. G. Albrecht, M. E. Michel-Beyerle and V. Yakhot, *J. Lumin.*, 1979, **20**, 147–149.

226   S. W. Eaton, L. E. Shoer, S. D. Karlen, S. M. Dyar, E. A. Margulies, B. S. Veldkamp, C. Ramanan, D. A. Hartzler, S. Savikhin, T. J. Marks and M. R. Wasielewski, *J. Am. Chem. Soc.*, 2013, **135**, 14701–14712.

227   L. Ma, K. J. Tan, H. Jiang, C. Kloc, M. E. Michel-Beyerle and G. G. Gurzadyan, *J. Phys. Chem. A*, 2014, **118**, 838–843.

228   S. W. Eaton, S. A. Miller, E. A. Margulies, L. E. Shoer, R. D. Schaller and M. R. Wasielewski, *J. Phys. Chem. A*, 2015, **119**, 4151–4161.

229   E. A. Margulies, J. L. Logsdon, C. E. Miller, L. Ma, E. Simonoff, R. M. Young, G. C. Schatz and M. R. Wasielewski, *J. Am. Chem. Soc.*, 2017, **139**, 663–671.

230   M. Chen, Y. J. Bae, C. M. Mauck, A. Mandal, R. M. Young and M. R. Wasielewski, *J. Am. Chem. Soc.*, 2018, **140**, 9184–9192.

231   M. Riede, D. Spoltore and K. Leo, *Adv. Energy Mater.*, 2020, **2002653**, 1–10.

<center>**Chapter 2**</center>

<center>**Experimental Techniques**</center>

2.1 Overview

This chapter provides the theoretical background of the various experimental techniques and instrumentations used carry out the steady-state, non-linear and time-resolved measurements. All the relevant details of the respective techniques used throughout this thesis are provided here. Excerpts of these techniques are used in the publications presented in subsequent chapters.

2.2 Steady-State Absorption and Emission Spectroscopy

The steady-state absorption technique is primarily used to provide background information about the ground-state (GS) absorptivity of the molecule. It investigates the linear response of the light-matter interactions taking place in a material. The measurement is done using a UV-Vis spectrophotometer, meaning that the spectroscopic properties are investigated using a UV (ultra-violet) and visible light. Measurements are often carried out in solution phase using a cuvette.

In UV-Vis absorption spectroscopy, as the sample interacts and absorbs energy in the form of packets of light known as photons, there is a transition from the ground state to the excited state.[1] This transition is what is reflected in what is known as the absorption spectrum, which is a measure of absorbed intensity of light as a function of the wavelength (or energy) of the light. The absorption process is based on two principal laws: Lambert's law and Beer's law, often combined as the Beer-Lambert law. Lambert's law applies for only solvent in a cuvette for which concentration is zero.[2] It relates the intensity of transmitting light to the path length the light travels.

<center>60</center>

$$-\frac{dI(z,0)}{dz} = a' \cdot I(z,0)$$

Equation 2.1

In **Equation 2.1**, $I(z,0)$ represents the light intensity at path length z and concentration of 0, and a' is the absorptivity of the pure medium at a certain wavelength. Beer's law accounts for the inclusion of an absorbing solute in the solvent with concentration c mol/lit, where $c \ll 1$. For the situation where both Beer and Lambert law apply, the governing equations are,

Lambert's law:
$$-\frac{\partial I(z,c)}{\partial z} = I(z,c)[a' + g(c)]$$

Equation 2.2

Beer's law:
$$-\frac{\partial I(z,c)}{\partial z} = k(z) \cdot I(z,c)$$

Equation 2.3

Where $g(c)$ is a function of concentration only and $k(z)$ is a function of path length only. Solving these two partial differential equations, accounting for the reflectivity at the boundary conditions results in the well-known Beer-Lambert equation, given as:

$$A = -log\left(\frac{I}{I_0}\right) = \varepsilon \cdot l \cdot c$$

Equation 2.4

In **Equation 2.4**, A is the absorbance or optical density of the sample; I_0 and I represent the intensity of the light before and after passing through the sample, respectively (see **Figure 2.1**); ε is the molar extinction coefficient or absorptivity with unit in $M^{-1}cm^{-1}$; l is the path length of the light through the sample or often represented as the cuvette length (cm); c is the molar concentration of the sample, with unit in mol/l or M.
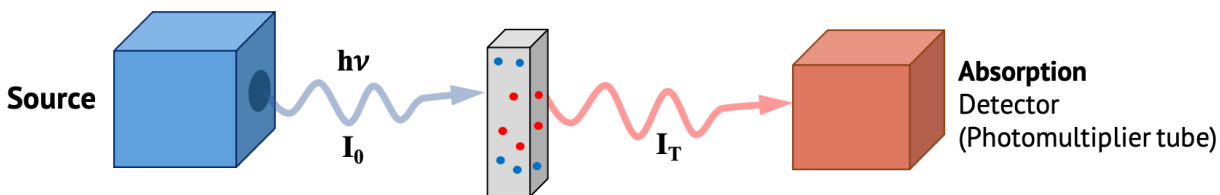
Figure 2.1 Schematics of the absorption process.

The strength of light absorption is reported in the form of molar extinction coefficient (ε), and in the literature this ranges from 10^3 to 10^6 M^{-1}cm^{-1} for organic molecules. The molar extinction coefficient increases with the increasing strength of the organic molecules to absorb solar photons and hence could be used to provide an idea of the efficiency of light absorption η_{Abs} (see **Figure 1.12**). For the projects in this dissertation, absorption measurements were carried out with an *Agilent* 8432 UV-Vis absorption spectrophotometer, and the absorption data was collected with the Agilent Chemstation software connected to the device. In the spectrophotometer, the light source is a combination of a deuterium-discharge lamp and a tungsten lamp, spanning the ultraviolet to the near-infrared range of the electromagnetic, 190 nm – 1100 nm. Optical lenses collect the light from the sources and collimate it to pass through the shutter or stray light filter into the sample. *Starna Cells* cuvettes (1 cm x 0.4 cm path length) made with quartz are used because unlike glass, quartz have minimum scattering and little to no absorption in the UV.[3] Transmitted light from the cuvette is then dispersed onto a photodetector. Prior to any measurement, the spectrophotometer is always blanked with air or the solvent to correct variation of the refractive index.

The steady-state emission technique is used to investigate the fluorescence emission of a molecule following photoexcitation. Emission is one of the pathways a photoexcited compound can dissipate its excitation energy. Therefore, emission usually occurs at lower energy (higher wavelength) than the excitation, producing less photons than what is initially absorbed. Combining the fluorescence and absorption spectra can provide information about the molecular structure of the compound by quantifying what is known as the Stokes shift. This is the spectral shift to lower energy between the absorption light and emitted light after interaction with a sample.[1,4] Also, the efficiency of photoemission or the amount of radiative species produced following light absorption

can estimated by what is referred to as the fluorescence quantum yield ϕ_F. Quantum yield is the number of emitted photons relative to the number of absorbed photons. The quantum yield of a *sample* is measured by a comparative method, which involves the use of *reference* compound with known quantum yield value.[5] It is expressed mathematically as

$$\phi_{F,samp} = \phi_{F,ref} \cdot \left(\frac{A_{ref}}{A_{samp}}\right)\left(\frac{\int I_{F,samp}}{\int I_{F,ref}}\right)\left(\frac{\eta_{samp}}{\eta_{ref}}\right)^2 \qquad \textbf{Equation 2.5}$$

In **Equation 2.5**, the subscripts $samp$ and ref denote *sample* and *reference*, respectively; A is the absorbance or optical density at the chosen excitation wavelength (excitation wavelength should be same for both *sample* and *reference*); $\int I_F$ represents the integrated fluorescence intensity cross the entire spectrum; η is the refractive index. The *reference* compound is chosen such that it has some absorbance at the excitation wavelength of the *sample*, and its emission spectrum closely matches that of the *sample*. Also, to minimize re-absorption effects, the optical densities of the *sample* and the *reference* should not exceed 0.1.[5]

Fluorescence measurements were carried out with a Spex FluoroMax-2 and a PTI QuantaMaster™ 8000 Series spectrofluorometer, both from HORIBA. The light source in the spectrophotometer for excitation is a xenon arc lamp that is mounted vertically. The light beam from the arc lamp is focused on the adjustable entrance slit of an excitation monochromator. The excitation monochromator (coma-aberration corrected) contains diffraction gratings responsible for enabling single wavelength excitation of samples placed in the sample chamber. Standard 1 cm quartz *Starna Cells* cuvettes are used. Fluorescence is collected at 90º relative to the excitation source to eliminate background signal and minimize noise due to stray light, using a photomultiplier tube (PMT) detector. The emission monochromater also contains gratings placed in front of the detector in order to ensure efficient collection at each emission wavelength. Owing

to the quantum efficiency of the detector, the computer-controlled spectrofluorometer is sensitive in the 185 nm to 900 nm spectral range.

2.3 Transient Absorption Spectroscopy

2.3.1 The science of pump-probe spectroscopy

Pump-probe or transient absorption spectroscopy is a very versatile and powerful technique for probing and characterizing photochemical and/or photophysical transient (fleeting/short-lived) species of molecules.[6] Generally, transient absorption (or emission) provide information on the electronic properties of transient states, and high-quality kinetic profiles of formation and decay can be extracted through various stages of a photochemical or photophysical pathway. Historically, Norrish and Porter developed the flash photolysis technique around 1950 before the invention of the laser.[7,8] Their pioneering study opened a new world of research in a microsecond time domain, which enables the detection of short-lived transient species directly. Subsequently, this technique has been further improved in temporal resolution with the emergence of short-pulsed lasers (femtosecond, picosecond). The combination of a pulsed laser and high-performance multichannel spectrometer or photomultiplier tube detector allows for the effective formation and detection of transient species respectively. This time-resolved technique can be assembled in various optical configurations and span a wide range of timescales from femtosecond to hundreds of nanoseconds.
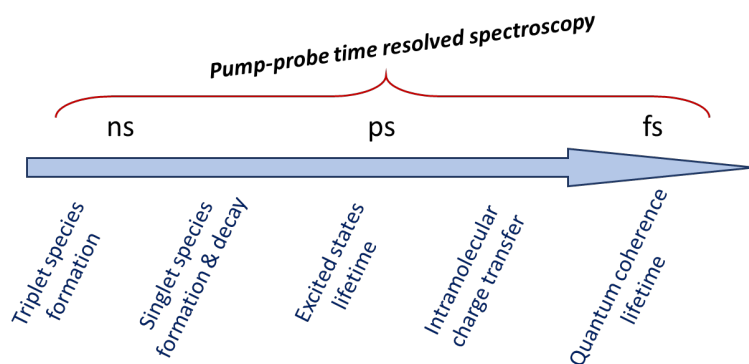
Figure 2.2 Relevant timescales of pump-probe time-resolved spectroscopy.

In photovoltaics, pump-probe is one of the most useful and powerful methods for observing transient species such as excitons, charge carriers (cations and anions), triplets, excimers generated upon photoexcitation.[9] It tracks both the bright and dark state species created upon excitation, unlike time-resolved fluorescence measurements. In transient absorption spectroscopy, a fraction of the molecules is promoted to an electronically excited state by means of an excitation (or pump) pulse. A weak probe pulse (i.e., a pulse that has low intensity, to avoid multiphoton/multistep processes) is sent through the sample with a delay, t with respect to the pump pulse. A difference absorption spectrum is then calculated, i.e., the absorption spectrum of the excited sample minus the absorption spectrum of the sample in the ground state (ΔA).[6] The ΔA spectrum contains contribution from the ground-state bleach (GSB), stimulated emission (SE) and excited-state absorption (ESA). See **Figure 2.3** below. *GSB* is observed because after the pump pulse has promoted some fraction of molecules to the excited state, the white light probe pulse comes in to further excite molecules from the ground-state or bleach the ground-state, resulting in a negative ΔA signal that matches the steady-state absorption spectrum. *SE* occurs when spontaneous emission, resulting from the pump pulse action, is stimulated by the probe pulse (same direction and phase). This results in an increase of light intensity on the detector, corresponding to a negative ΔA signal that matches the fluorescence spectrum. *ESA* is observed when higher excited states are populated with the probe beam following the initial excitation with the pump beam, resulting in a positive ΔA signal. $\Delta A(\lambda, t)$ contains information on the dynamic processes that occur in the photovoltaic system under study, such as vibrational or structural relaxation, excited-state energy transfer, electron/charge transfer processes, triplet production via intersystem crossing or singlet fission. In order to extract this information, single wavelength analysis in addition to global and/or target analysis procedures may be applied.[10–12]
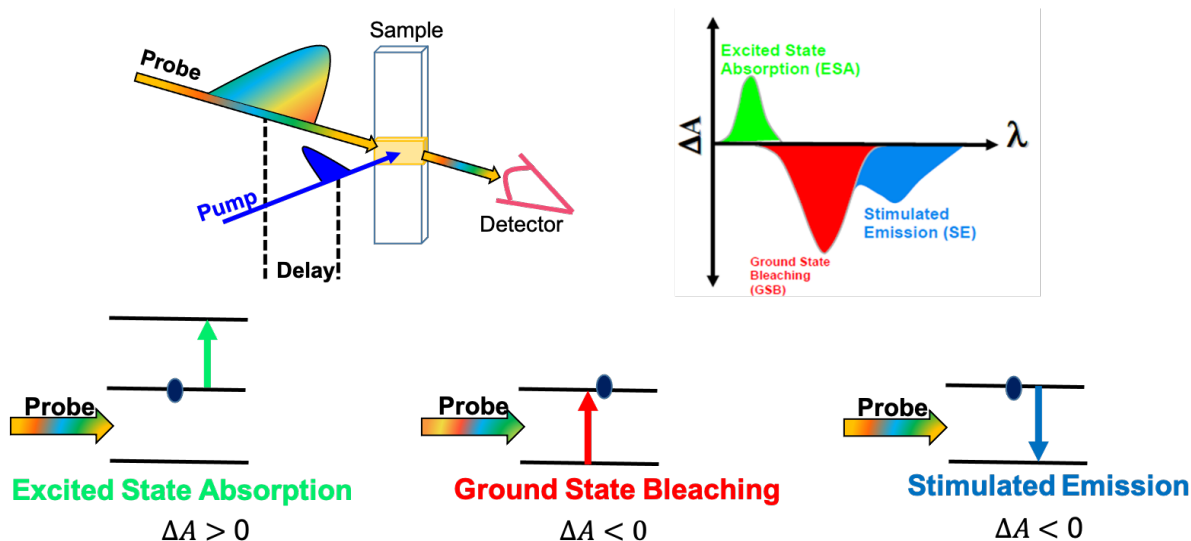
Figure 2.3 Schematics of pump-probe spectroscopy and the ΔA spectrum contribution.

2.3.2 Transient species analysis – single-wavelength, global and target analysis

Transient species are generated upon photoexcitation and can be probed using laser pulses with widths much smaller than its lifetime. The species appear as GSB, SE and ESA signals. These species include singlet species ($S_1 \rightarrow S_n$; $S_0 \rightarrow S_1$ and $S_1 \rightarrow S_0$), charge transfer species (D^+ and A^-), triplet species ($T_1 \rightarrow T_n$ and $T_1 \rightarrow T_0$), etc. A confirmation of the exact nature of the species is required prior to any kind of analysis with exponential models. This is done by obtaining photophysical information (e.g., steady-state spectral information) about the compound of interest. $S_0 \rightarrow S_1$ and $S_1 \rightarrow S_0$ species can be confirmed by matching the GSB and SE signals with the steady-state absorption and fluorescence spectra, respectively. In cases where the Stokes shift (i.e., the energy difference between the absorption and fluorescence) is small, the GSB and SE might appear overlapped. The steady-state absorption and emission can be modeled with two Gaussians and convoluted to try to match the obtained overlapped GSB and SE signal. The charge transfer species (D^+ and A^-) can be confirmed by matching the ESA signal with the absorption spectra of electrochemically generated cation and anion, obtained via spectroelectrochemical measurements.

$T_1 \rightarrow T_n$ species can be confirmed by matching the ESA signal with previously reported signals or by carrying out oxygen purging measurements, because oxygen is known to quench triplet species.

Single wavelength analysis provides photophysical information about the photovoltaic compound at the selected wavelength of interest. It involves carrying out exponential fittings at selected wavelengths to obtain dynamic and lifetime information about the prior-identified photogenerated species. The photogenerated species (appearing as band signals) can be identified by its absorption wavelength peak, and exponential fits carried out at the wavelength. The instrument response function (IRF) is usually accounted for in the exponential fitting. For example, carrying out single wavelength analysis at the ESA wavelength peak identified as the absorption of cationic species provides information regarding both the formation time (charge separation) and the decay time (charge recombination) of the charged species.

Global analysis is the simultaneous analysis of all the transient species present upon photoexcitation. It extracts the relevant species (singlets, triplets, and charge transfer species), the evolution spectra and concentration/kinetic profiles. It is a well-known technique for complex data analysis to obtain quantitative values for physical constants of interest.[10,11] In global analysis, $\Delta A(\lambda, t)$ is viewed and operated upon as a matrix with vector components in λ and t. In this thesis, global analysis was carried out via singular value decomposition (SVD) and simultaneous data fitting using Glotaran® – a Java-based graphical user interface to the R package TIMP (a problem-solving environment for fitting superposition models to multi-dimensional data). The program was built to support time-resolved spectroscopy data. The model underlying the data matrix is a superposition of $n_{compts.}$ components given by the equation

$$\Delta A(\lambda, t) = \sum_{i=1}^{n_{compts.}} \varepsilon_i(\lambda)\, c_i(t) \qquad \textbf{Equation 2.6}$$

Where ε_i and c_i are the unknown spectrum and concentration dynamics of component i respectively. SVD is a matrix factorization technique used to explore the number of spectrally and temporally independent components in the data matrix, which is an important aspect of defining an initial model.[12] The singular values give an indication of the number of independent components in the data. The SVD of the data-matrix is

$$\Delta A(\lambda, t)_{SVD} = \sum_{n=1}^{n_{max.}} [u_n(\lambda) \cdot w_n(t)] SV_n \qquad \textbf{Equation 2.7}$$

Where $n_{max.}$ represent the maximum number of rows and columns; SV_n represent the significant values; u_n and w_n are the singular independent vector components of λ and t respectively. The singular independent vector components are then modeled **_sequentially_** and fitted via an iterative modeling technique detailed by Stokkum and Bal.[13] The quality of the fit is determined by computing the sum of square of errors (SSE). The obtained results include the kinetic parameters, the decay associated spectra (DAS), the evolution associated spectra (EAS) (because a sequential or unbranched unidirectional model is used), and the concentration profiles. In Target analysis, a branched/compartmental model is used. Target analysis involves the combination of global analysis SVD approach with the testing of a specific compartmental photophysical model, where the ratios of branching are chosen by the user based on prior knowledge about the system under study. Similar results are obtained with the Target analysis, only that the EAS spectra is replaced with a species associated spectra (SAS).

2.3.3 Femtosecond transient absorption (fsTA)

It is an ultrafast measurement technique used for monitoring and tracking the ultrafast formation (~150 fs) and excited state dynamics of various transient species upon photoexcitation. The time-resolution, determined by the temporal overlap or cross-correlation of the pump and

probe pulses, is limited by the pulse width of the laser source used to generate the pump and probe light. Here, a tunable optical delay line is used to control the arrival time of the probe beam relative to the pump beam. Previously in the fsTA measurement, for each delay position, the probe light intensity before (I_0) and after (I) passing through the sample under constant photoexcitation with the pump pulse, has to be known. From the intensity ratio, the change in absorbance is given as $\Delta A = -log(I/I_0)$.[9] However, measuring I_0 at every delay position is a difficult task. The invention and use of optical choppers remedy this problem as I_0 doesn't need to be known to obtain ΔA. All that is needed is the intensity of the probe light when the pump light is blocked ($I_{pumpOFF}$) and unblocked (I_{pumpON}) by the chopper, whose frequency is synchronized with that of the excitation source. This is derived as,

$$\Delta A = A_{pumpON} - A_{pumpOFF} \qquad \textbf{Equation 2.8}$$

$$\Delta A = -log\left(\frac{I_{pumpON}}{I_{0,pumpON}}\right) - -log\left(\frac{I_{pumpOFF}}{I_{0,pumpOFF}}\right) \qquad \textbf{Equation 2.9}$$

Knowing that for the same laser source, the intensity of the white light before hitting the sample, whether the pump light is blocked or unblocked, is the same, i.e. $I_{0,pumpON} = I_{0,pumpOFF}$, this results to

$$\Delta A = -log\left(\frac{I_{pumpON}}{I_{pumpOFF}}\right) \qquad \textbf{Equation 2.10}$$

The fsTA setup used for all the projects in this dissertation measures the above parameter at every delay position. The setup comprises of three key parts, all synchronized with each other: (a) The 800 nm light source, (b) the optical parametric amplifier (for pump wavelength selection), and (c) the Helios® fsTA spectrometer (optical delay line + white-light generator + spectrometer). Single wavelength analysis is carried out using the Surface Xplorer® program developed by *Ultrafast Systems*. Global and Target analyses was carried out using
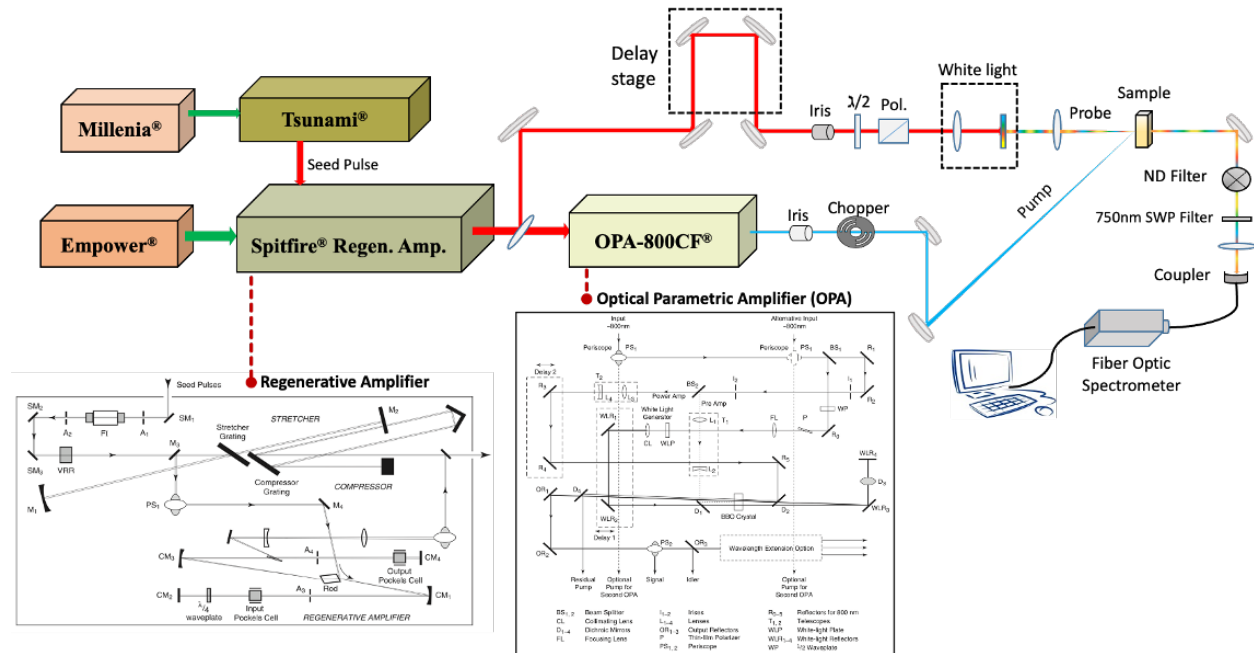
Figure 2.4 Schematics of the femtosecond transient absorption (fsTA) setup.

The 800 nm light source can be split into two parts, (i) low energy, high repetition rate, and (ii) high energy (amplified), low repetition rate. The first part comprises of a *Spectra Physics* Millenia Pro® diode-pumped Nd:YVO$_4$ CW laser (532 nm, 4.2 W), pumping a *Spectra Physics* Tsunami® Ti:sapphire oscillator, generating the low energy (3 nJ), high repetition rate (80 MHz), ~100 fs seed pulses. These seed pulses gets amplified in the second part that comprises of a *Spectra Physics* Empower® Nd:YLF laser (527 nm, 7 W), pumping a *Spectra Physics* Spitfire® Ti:sapphire regenerative amplifier, generating the high energy (1 mJ), low repetition rate (1 kHz), ~130 fs seed pulses. In the regenerative amplifier, amplification takes place in three (3) stages. This idea won the 2018 Nobel Prize for physics (Gërard Mourou and Donna Strickland). The seed pulses are first of all stretched using a multi-pass grating and mirror combination. Then the stretched pulses are selected by polarization using voltage-controlled pockel cells and amplified by passing the stretched pulses multiple times (> 20 passes) through the Ti:sapphire amplifier stage (pumped by the Empower®). A time-delay generator (TDG) is used to provide accurate timing needed to

synchronize the pockel cells to the passage of pulses into and out of the amplification stage. Finally, the amplified pulses are recompressed to their original duration using a second multi-pass grating and mirror combination. The pulse compression stage can be adjusted for temperature or environmental variations using a motion-controlled mirror combination on a translational track to set the compressor length for optimum compression. The resulting output pulse is 800 nm, ~130 fs, 1 mJ, 1 kHz, 1 W (average power) and 7 mm beam diameter. A beam splitter splits the resulting output from the Spitfire®, with 15% of the pulse directed into the Helios box (for white probe beam generation), while 85% of the pulse is directed into the optical parametric amplifier (OPA) for pump wavelength generation.

The OPA used in this study produces high energy fs pulses that are tunable over a broad wavelength (λ) region, 300 nm to 10 μm. An OPA derives gain from a non-linear frequency conversion process. In the parametric amplification process, a high intensity *pump beam* is used to amplify a low energy *seed beam* (white light or signal/idler beam). The Spectra Physics OPA-800CF used comprises of three stages: (i) white light generation, (ii) pre-amplification (and delay-stage 1), and (iii) power-amplification (and delay-stage 2). White light is generated by focusing a few μJ of the input pulse (~4%) onto a sapphire plate. This produces a 400 – 4400 nm light (limited by the optics range) that functions as a *seed beam* for the generation of a wider-tuning-range and more stable output. In the pre-amplification stage, 15% of the remaining input pulse acts as the *pump beam* and the white light as *seed beam*. The *pump beam* and *seed beam* are temporally overlapped (using the delay-stage 1) on a type II β-barium borate (BBO) crystal leading to the 1st stage amplification, producing a signal + idler beam based on the crystal tuning angle. In the power-amplification stage, the other 85% of the remaining input pulse acts as the *pump beam* and the signal + idler output beam acts as the *seed beam*. These two beams are temporally overlapped

(using the delay-stage 2) at the back of the BBO crystal while the signal + idler beam is returning after its generation. The resultant beam is a higher energy signal (1100 nm – 1600 nm) + idler (1600 – 3100 nm), and a residual 800 nm pump. To obtain further coverage in the visible and mid-IR spectral region, the following are integrated in the OPA-800CF: (i) second and fourth harmonic generation (SHG and FHG) of the signal and idler. SHG = 580 – 1200 nm; FHG = 300 – 600 nm (ii) sum-frequency mixing (SFM) of the signal and idler with the residual 800 nm pump. SFM = 480 – 600 nm (iii) difference frequency mixing (DFM) of the signal and idler with the residual 800 nm pump. DFM (with an AgGaS$_2$ crystal) = 480 – 600 nm. The selected pump wavelength for pump-probe measurement is then sent through an optical chopper that is synchronized with the Empower® light source and focused onto the 2 mm quartz cuvette containing the sample that is constantly stirred by a rotating magnetic stirrer to minimize sample degradation.
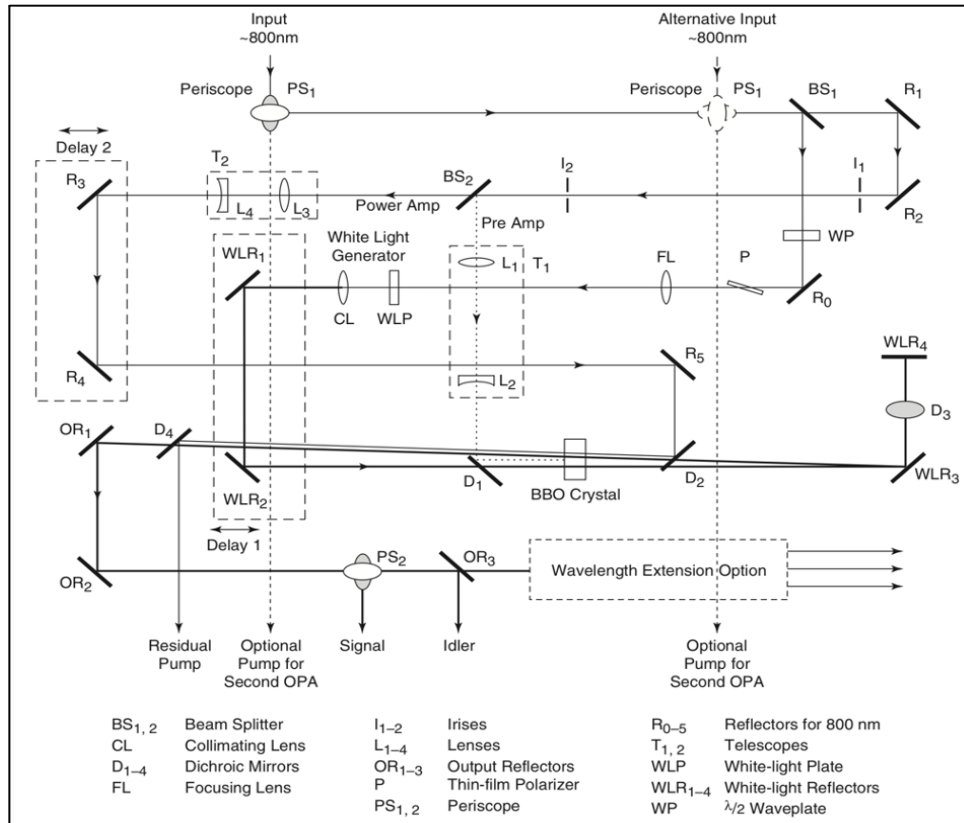
Figure 2.5 Schematics of the femtosecond optical parametric amplifier.
(Source: *Spectra Physics* OPA-800C user manual).

The Helios® fsTA spectrometer by *Ultrafast Systems* comprises of an optical delay line (time-window = 1.5 ns; minimum step size = 7 fs), another sapphire plate white light generator and a fiber-coupled Ocean Optics® 2000 spectrometer. See **Figure 2.4**. The 15% of the Spitfire® pulse directed into the Helios box passes through the optical delay line, where it is delayed relative to the pump beam. The beam then passes through an iris (for controlling intensity), a half-wave plate and a polarizer (to set its polarization to magic angle, 54.7º). It is then focused onto a sapphire plate to generate white light. The white light is then overlapped with the excitation beam in the cuvette containing the sample. The white light from the sample is then filtered using a 750 nm short wave pass filter to remove the residual 800 nm following the white light generation process, and its intensity decreased using a neutral density filter. The filtered light is focused into a fiber-coupled UV-Vis spectrometer, whose spectral range spans 500 nm (i.e., 350 – 850 nm). Data acquisition is controlled by the software from *Ultrafast Systems* – Helios.

2.3.4 Nanosecond transient absorption (nsTA)

Transient absorption with nanosecond time resolution is used to measure transient absorption at longer timescales. The fsTA uses laser pulses derived from a single femtosecond laser source (see **Section 2.3.3**) and delayed relative to each other by varying the optical paths, but this technique reaches the time scale directly following the absorption of the excitation photon from a few nanoseconds up to milliseconds. It functions exactly like the laser flash photolysis technique that was birthed from the flash photolysis process in the 1950s.[7,8] In laser flash photolysis, investigated molecules are excited by a short light flash, typically a laser pulse (pump), to populate an electronically excited state which then develops – possibly via several intermediate states – to the final state of the system. The dynamics of these states is probed by a second light source that records the photoinduced transmission changes.[14,15] Nowadays, the excitation flash is

typically an excimer laser or the second or third harmonic of a Nd:YAG (yttrium aluminum garnet) laser, or an Nd:YAG – pumped optical parametric oscillator (OPO) for pump wavelength tunability.[15–18]

The nsTA setup (**Figure 2.6**) used for some projects in this dissertation comprises of three key parts: (a) the Nd:YAG laser light source, (b) the optical parametric oscillator, and (c) the spectrometer system. The laser head comprises of a Spectra Physics QuantaRay® flash lamp-pumped Nd:YAG Q-switched laser (producing 1064 nm), and a two-stage harmonic generator for producing high energy 532 nm and 355 nm pulsed light. High energy (~220 mJ) 355 nm light, produced by frequency mixing 1064 nm and 532 nm in one stage of the harmonic generator, is used to pump the *GWU* optical parametric oscillator (OPO). The OPO contains a β-barium borate (BBO) crystal in its resonator and is able to produce signal + idler tunable from 410 nm – 2600 nm, and a sum frequency mixing crystal to combine the signal and idler to produce UV light in the range 206 nm – 410 nm. For the studies in this thesis, excitation/pump wavelengths were used from only the signal range, i.e., 410 – 709 nm. The selected pump was sent into the *Edinburgh* LP980 spectrometer system that comprises of a probe source, an electronics chamber, a monochromator and a photomultiplier tube (PMT). The probe source is a 150 W ozone-free xenon arc lamp that produces 6 ms pulses and span the 190 – 2600 nm spectral range. It creates the background for the time-dependent absorption measurements. The probe pulse excites the sample perpendicular to the pump pulse which maximizes the change in absorbance (ΔA), while minimizing scattering and fluorescence. After passing through the sample at a right angle to the pump pulse, the light is directed to a monochromator for wavelength selection. The transient signal of the selected wavelength is then detected using a *Hamamatsu* R928 PMT with sensitivity between the spectral range 185 – 870 nm. The probe light transmission signal from the sample

before, during, and after the arrival of the pump pulse is converted into electrical signals in the electronics chamber. The electric signals are detected by a TDS3052B Model oscilloscope and the *Edinburgh* supplied software converts the electric signal into change in absorbance. Most of the kinetic and spectral analysis were carried out using the Origin 8® software.
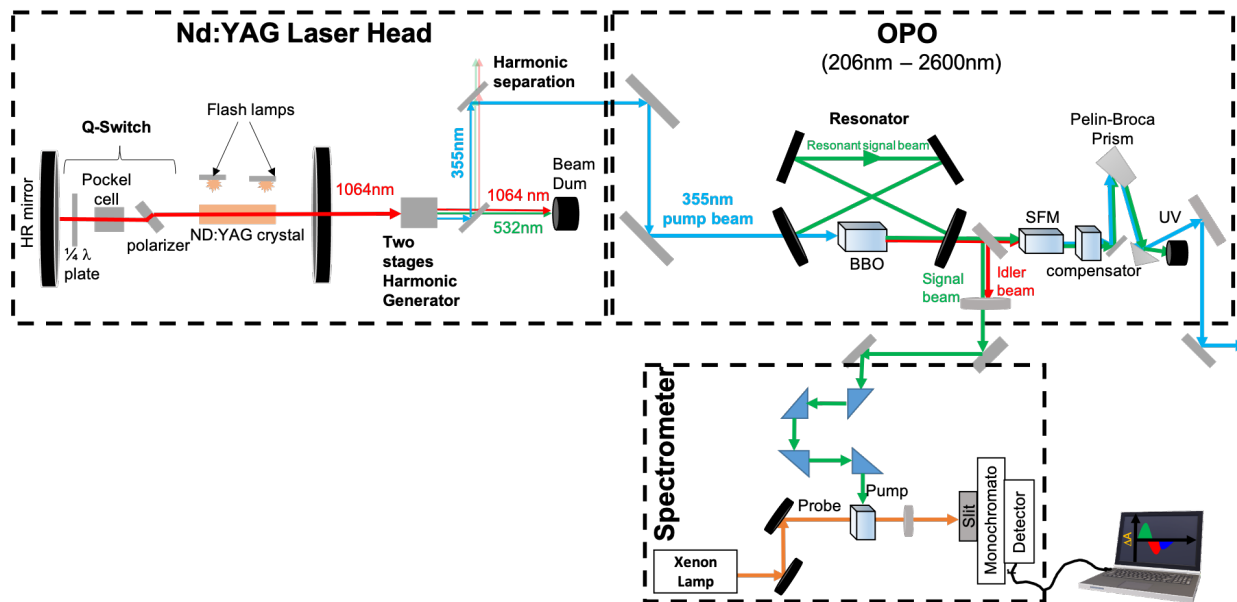
Figure 2.6 Schematics of the nanosecond transient absorption (nsTA) setup.

2.4 Two-photon Absorption Spectroscopy

Two-photon absorption (TPA) is a non-linear optical process that involves the simultaneous absorption of two photons by the same molecule. The two photons can have the same or different energies (or frequencies), but the sum of the energy of the two photons need to match the ground-to-excited state transition energy. TPA was first analyzed theoretically in the 1930s by Göppert-Mayer,[19] and was first demonstrated experimentally in 1961.[20] TPA became easier to investigate as the sub-picosecond lasers became more readily available in 1990s, particularly the solid-state Ti:sapphire laser.
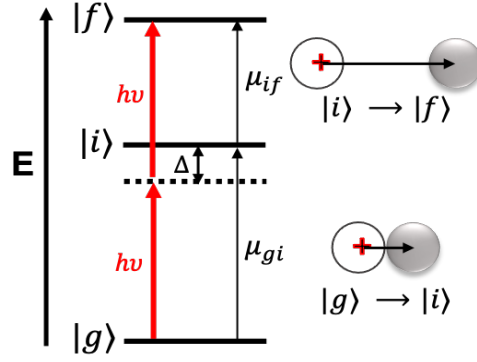
Figure 2.7 Energy level diagram for the two-photon absorption (TPA) process.

The main difference between one-photon absorption (1PA) and two-photon absorption (TPA) is that TPA involves the simultaneous interaction of two photons, and so it increases with the square of the light intensity, whereas 1PA depends linearly on the intensity.[21] Similar to Lambert law of the 1PA process (**Equation 2.2**), the attenuation of a beam light from TPA is given as,

$$-\frac{dI}{dz} = \delta_{TPA} \cdot I^2$$ **Equation 2.11**

Just as in the 1PA process (characterized by the absorptivity), TPA materials are characterized by the TPA cross-section (δ_{TPA}). It is reported in Göppert-Mayer units (GM = 10^{-50} cm^4 s photons^{-1} molecule^{-1}), following her amazing discovery of this process. Theoretically, for a plane-polarized light, the δ_{TPA} at the maximum TPA band with a Lorentzian line shape is given as,[22–24]

$$\delta_{TPA} = \frac{2\pi h\nu^2 [(\eta^2 + 2)/3]^4}{\varepsilon_0^2 \eta^2 c^2} \left(\frac{1}{\Gamma}\right) \frac{1}{5} \left[\left(\frac{\Delta\mu_{gf}\mu_{gf}}{h\nu}\right)^2 + \sum_{i \neq f,g} \left(\frac{\mu_{gi}^2 \mu_{if}^2}{\Delta^2}\right) \right]$$ **Equation 2.12**

In **Equation 2.12**, the subscripts g, f and i represent the ground, final and intermediate state, respectively (see **Figure 2.7**); $h\nu$ is photon energy; η is the refractive index; ε_0 is the vacuum permittivity; c is the speed of light; Γ is the half-width at half-maximum of the 2PA band; $\Delta\mu_{gf}$ is the change in the static dipole moment from ground state (g) to the final state (f); μ_{ab} represent

the transition dipole moment from state a to b. The δ_{TPA} of a molecule is directly correlated to the molecular electronic delocalization, the degree of molecular planarity and the intramolecular charge transfer character of the molecule. Direct measurement of the δ_{TPA} is usually difficult because only a small fraction of photons is absorbed in the two-photon process.[25] A very sensitive technique referred to as two photon excited fluorescence (TPEF) is often used to obtain the δ_{TPA}, provided that the material is fluorescent and its fluorescence quantum yield (ϕ_F) is known.

The TPEF technique was explored in this thesis work. In this technique, a laser beam of ultrashort pulses (far from one-photon resonances) is focused on the sample while the upconverted fluorescence signal (excited by two-photon) is monitored using an efficient photons collection system. The first setup consist of a Kapteyn-Murnane Lab. Inc® mode-locked Ti:sapphire laser pumped by a Millennia® diode-pumped Nd:YVO4 laser delivering ~110 fs output pulses at a repetition rate of 80 MHz. In this laser setup, only 780 – 820 nm excitation beam are obtainable. A second laser setup is available for obtaining 750 – 890 nm excitation using a MaiTai® laser delivering 100fs pulses at a repetition rate of 80MHz, and 1100 – 2250 nm excitation using a MaiTai®-pumped (with 775 nm) OPAL optical parametric oscillator (OPO). The beam parameters such as bandwidth, beam divergence, beam diameter, polarization come as specified by the laser supplier – *Spectra Physics* now *MKS*. Other wavelengths can also be obtained through frequency doubling of the OPAL output using BBO crystals. The mode-lock quality and laser beam wavelength selection is monitored a fiber optic spectrometer from *Ocean Optics*. The excitation beam is then directed to the TPEF set up (schematics in **Figure 2.8**). The excitation beam power is varied from 40 mW to 110 mW (increments of 10 mW), using a variable neutral density (ND) wheel and a power sensor & meter. Following the ND filter, a beam splitter divides the incident beam into two unequal portions. The less intense beam (~10%) is directed into a high-speed silicon

photodiode connected to a multimeter which gives feedback to the computer interface so that the varying intensity can be recorded as a function of voltage (which can be calibrated to power in mW). The more intense incident beam is directed and focused unto the sample cell (1 cm, quartz cuvette) using a lens of 11.5 cm focal length. The resulting fluorescence was collected perpendicular to the excitation beam, to avoid the excitation beam finding its way into the photomultiplier tube (PMT). Another lens (plano-convex) with focal length of 2.54 cm was used to direct the fluorescence into a monochromator whose output is coupled to the PMT.
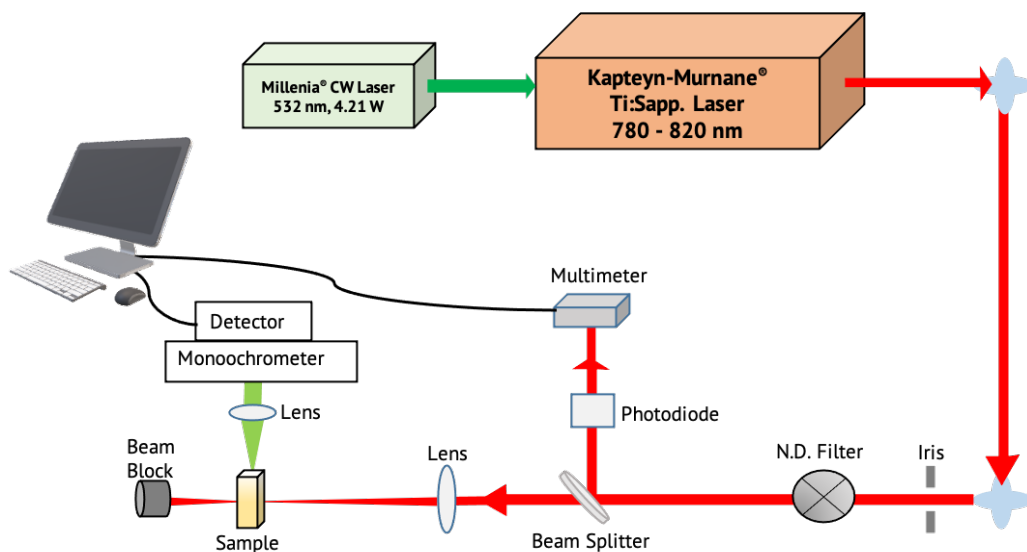
Figure 2.8 Optical set-up for the two-photon excited fluorescence (TPEF) technique.

Experimentally, the δ_{TPA} of a *sample* is determined using the comparative technique, derived from first principles from **Equation 2.11**. The comparative technique uses a *reference* compound (commercial dyes e.g. Rhodamine B or 6G, Coumarin 153 or 485, Styryl 9M) of known δ_{TPA} at a selected excitation wavelength.[25,26] The technique assumes that the same excitation wavelength, laser condition (pulse width, shape factor), and detection system (quantum collection efficiency) are used for both *sample* and *reference* measurements. During each excitation power scan, for both the *sample* and *reference* compounds, the monochromator is set to the maximum emission wavelength (where max. photons are generated), and the photons are

converted into counts by a photon-counting unit. A logarithmic plot of the fluorescence count signal versus the excitation power intensity was performed to confirm if the signal to power intensity relationship is indeed quadratic. The equation used is given as,

$$\delta_{TPA,samp} \cdot \phi_{F,samp} = \delta_{TPA,ref} \cdot \phi_{F,ref} \cdot \frac{[c]_{ref} \cdot \eta_{ref} \cdot 10^{b_{samp}}}{[c]_{samp} \cdot \eta_{samp} \cdot 10^{b_{ref}}} \qquad \textbf{Equation 2.13}$$

Where the subscripts $samp$ and ref denote *sample* and *reference*, respectively; δ is the TPA cross-section; ϕ_F is the fluorescence quantum yield (see **Equation 2.5**); $[c]$ is the molar concentration; η is the refractive index; b is the intercept of the log-log plot of the fluorescence count signal versus the excitation power intensity, the plot for which its slope is 2.

2.5 Time-Resolved Fluorescence Spectroscopy

2.5.1 Background

Time-resolved fluorescence measurements provide more information about the excited state of a compound in comparison to just the steady-state fluorescence measurement. The photons are emitted randomly (spontaneous emission) with no specific phase or direction. For an exponentially-fitted decay profile, the fluorescence lifetime is the time it takes for 63% $(1 - 1/e)$ of the population of the excited electrons to return to the ground state.[1] Analysis of lifetime measurements can provide better insights into the energy transfer, charge transfer, triplet production processes taking place in organic molecules. The lifetime of a fluorophore in the absence of non-radiative processes is called the intrinsic or natural lifetime, and is given by,

$$\tau_n = \frac{1}{k_r} \qquad \textbf{Equation 2.14}$$

Where k_r is the emissive rate of the fluorescent compound. In principle, the intrinsic fluorescence lifetime can be obtained by only steady state measurements – absorption spectra, emission spectra and the extinction coefficient. The radiative decay rate k_r can be calculated using,[27]

$$k_r = 2.88 \times 10^9 \eta^2 < \bar{v}^{-3} >^{-1} \int \frac{\varepsilon(\bar{v})d\bar{v}}{\bar{v}} \qquad \textbf{Equation 2.15}$$

In **Equation 2.15**, $\varepsilon(\bar{v})$ is the absorption spectrum; η is the refractive index of the medium; $\bar{v}$ is the wavenumber. The integrals are calculated over the $S_0 \leftrightarrow S_1$ absorption and emission spectra. In very few cases (with fluorescence quantum yield, $\phi_F \approx 1$), this expression works rather well. However, in majority of organic compounds, especially those used for organic photovoltaic applications, this equation doesn't apply and thus their fluorescence lifetime has to be obtained via time-resolved fluorescence measurements.

Depending on the desired time resolution for the lifetime measurement, two different techniques were used during this research study: time-correlated single photon counting (TCSPC) and fluorescence upconversion (FUC). TCSPC is generally used for measurements in the nanosecond to microsecond time scales, while the FUC is suitable for lifetime measurements in the femtosecond to picosecond timescales. For any lifetime measurement to be significant, it has to be outside the instrument response function (IRF) of the experimental setup. The IRF is the response of the instrumentation to scattered excitation pulse. The IRF was measured by using a dilute scattering sample such as water and detecting the response with the emission monochromator set at the excitation wavelength. For lifetime measurements in the scale of the IRF, the instrument response should be measured and subtracted from the experimental data. This is done through a process known as deconvolution. If the measured instrument response function is I(t) and the sample response to a pulse excitation is f(t), then the experimentally measured signal is given by the convolution integral:

$$F(t) = \int_0^t I(t) \cdot f(t - \tau)d\tau \qquad \textbf{Equation 2.16}$$

A MATLAB-based deconvolution program developed in the Goodson's laboratory was used to obtain the sample response that corresponds to the experimentally measured signal shown the equation above.

2.5.2 Time correlated single photon counting (TCSPC)

Time correlated single photon counting (TCSPC) is a time-resolved fluorescence technique that measures the excited state fluorescence lifetime of a fluorophore following photoexcitation in the timescale of nanoseconds to microseconds. The resolution of this technique is around 350 ps. The TCSPC set-up (**Figure 2.9**) consists of a home-built mode-locked Ti:sapphire laser with cavity dumper, pumped by a Spectra Physics Millenia® CW laser. The repetition rate of the laser can be set as 765 kHz or 383 kHz. The 30fs, 800 nm output beam is frequency-doubled to 400 nm by employing a β-barium borate (BBO) crystal. For polarization studies, the beam is passed through a polarizer in order to set its polarization before hitting the sample. In studies where the polarization effects are not desired, the polarizer can be set at the magic angle of 54.7⁰. At this angle, the total fluorescence detected is measured without reference to the polarization. The 400 nm beam is then split using a beam splitter. The first part is focused onto a silicon-based fast trigger photodiode connected to the TimeHarp 200 processor chipset in the computer CPU, and the second part is focused onto the sample cell (quartz cuvette, 1 cm path length) using a lens of focal length 11.5 cm. This portion of the 400 nm beam photoexcites the samples leading to fluorescence emission. The fluorescence of the sample is collected at a direction perpendicular to the excitation beam and is passed through a monochromator which is used to spectrally resolve the fluorescence beam, letting only one wavelength through. The photomultiplier tube detects the fluorescence, and the result is transmitted to the computer through the TimeHarp 200 interface card.
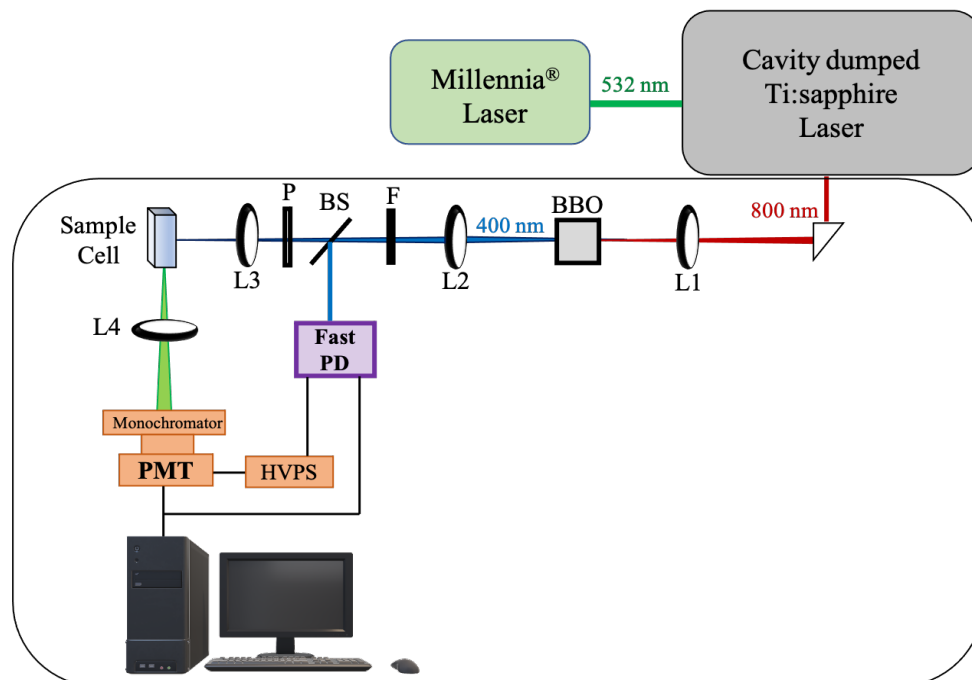
Figure 2.9 Set-up of the time correlated single photon counting (TCSPC) technique. Lenses are indicated as 'L'; non-linear BBO crystal, 'BBO'; focusing elements, 'F'; beam splitter, 'BS'; polarizer, 'P'; photodiode, 'PD'; photomultiplier tube, 'PMT'.

The time-resolved fluorescence measurement using the TCSPC setup is unique because of its method of collecting the fluorescence – by single photons. It creates a histogram by detecting and resolving the arrival time of single photons with respect to a trigger signal, which is the excitation source hitting the fast photodiode. Therefore, the TCSPC setup requires a high repetitive light source to accumulate enough photonic events for the creation of a high precision histogram. The fluorescence signal is passed through a constant function discriminator (CFD), which accurately correlate the arrival time of the fluorescence signal with that of the trigger signal. Then, the fluorescence signal is passed to a time-to-amplitude converter (TAC) which converts the signal to a voltage ramp. The voltage ramp continues to increase until the emission pulse arrives at the detector and stops the ramp-up process. Therefore, this technique is considered an electrical technique. The voltage signal is amplified by a programmable gain amplifier and converted to a numerical value by an analog-to-digital converter (ADC). The computer displays the histogram of

the different time bins using a specialized software, PicoQuant. The IRF is measured via the Rayleigh scattering technique. PicoQuant Fluofit software and Origin 8® are used to analyze the result and fit the lifetime distribution models into exponential decay function, also accounting for the IRF. Sample degradation is checked by noting the absorbance before and after each measurement.

2.5.3 Time-resolved fluorescence upconversion (FUC)

The fluorescence upconversion (FUC) technique is used to measure the fluorescence lifetime in the ultrafast timescale – femtosecond to a few picoseconds. Some electronic processes such as excitation delocalization, energy transfer occur in these very fast timescales, hence this technique is the most suitable for tracking their dynamics. The FUC set-up (in **Figure 2.10**) consists of a *Spectra Physics* Tsunami® mode-locked Ti:sapphire laser pumped by a Millennia V® diode-pumped Nd:YVO$_4$ laser, delivering ~100 fs, 800 nm output pulses at a repetition rate of 82 MHz. The 800 nm beam is passed through a series of focusing elements on to a β–barium borate (BBO) crystal to generate 400 nm beam by second harmonic generation. The output from the BBO is sent to a dichroic mirror that reflects the 400 nm light and transmits the residual 800 nm light. The residual 800 nm is sent to an optical delay line (step-size = 6.25 fs) and will later function as the fundamental gate pulse. The 400 nm beam (for sample excitation) is sent to a berek compensator, which is used to control the polarization of the beam so that the beam entering the sample is plane-polarized. This is then focused onto the 1 mm rotating cell. The cell is constantly rotating to eliminate the effect of localized excitation of the sample which can result photo-degradation and damage of the sample. The excitation beam used for the study is kept between 20 – 30 mW.
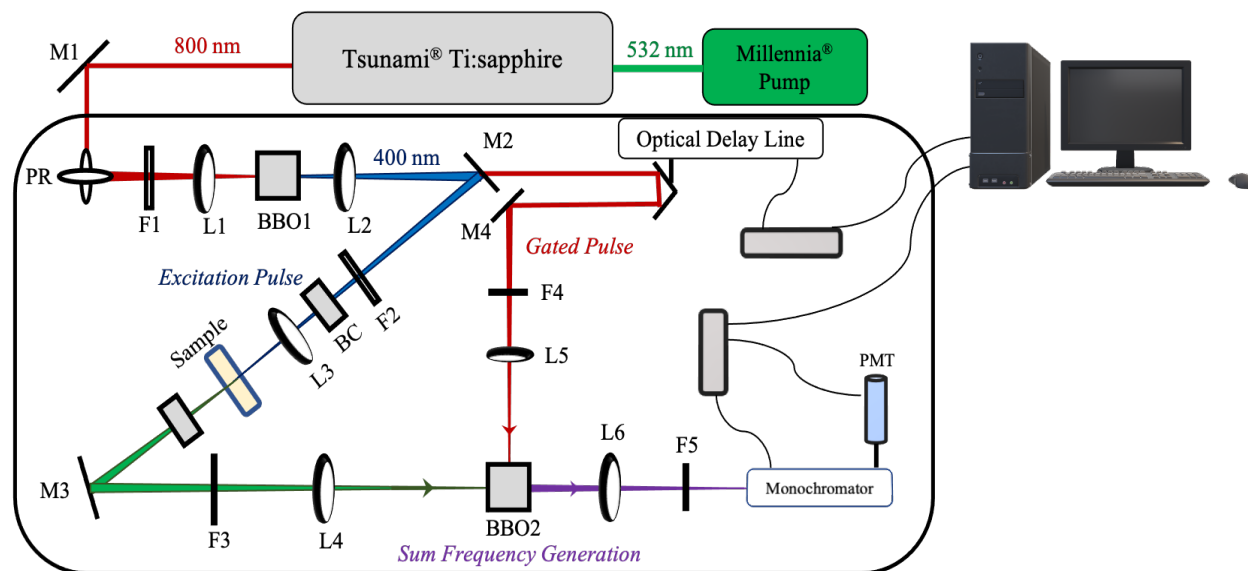
Figure 2.10 Optical set-up of the fluorescence upconversion (FUC) technique. Lenses are indicated as 'L'; BBO crystals, 'BBO'; focusing elements, 'F'; berek compensator, 'BC'; mirror, 'M'; two mirror polarization rotator, 'PR'; photomultiplier tube, 'PMT.

Fluorescence from the sample is collected by an achromatic lens and directed through several focusing elements and mirrors into a nonlinear sum-frequency generator crystal made of β–barium borate, where it is recombined with the fundamental gate pulse. The fluorescence and the gate pulse must be spatially and temporally overlapped for efficient sum-frequency generation. For most of the studied organic photovoltaic samples, the sum-frequency generated or upconverted beam is usually in the wavelength range of 300 – 400 nm. The sum-frequency generated or upconverted beam is passed through a focusing lens and into the monochromator which picks out the desired detection wavelength and send it into the *Hamamatsu* R152P photomultiplier tube, for detection. Standard dyes such as coumarin 30 and coumarin 153 were used in the alignment of the FUC system. The choice of which standard dye to use for alignment depends on the fluorescence wavelength to be detected. Sample degradation is checked by noting the absorbance before and after each measurement, especially for long experimental scans. The instrument response function (IRF) has been determined from the Raman signal of water to have a width of 110 fs.

References

1   J. R. Lakowicz, *Principles of Fluorescence Spectroscopy*, Springer Science, Singapore, Third ed., 2006.

2   F. H. Lohman, *J. Chem. Educ.*, 1955, **32**, 155.

3   S. Schröeder, M. Kamprath, A. Duparré, A. Tünnermann, B. Kühn and U. Klett, *Opt. Express*, 2006, **14**, 10537.

4   G. G. Stokes, *Philos. Trans. R. Soc. London*, 1852, **142**, 463–562.

5   Jobin Yvon, *A Guide to Recording Fluorescence Quantum Yields Introduction:*, 2014, vol. 15.

6   R. Berera, R. van Grondelle and J. T. M. Kennis, *Photosynth. Res.*, 2009, **101**, 105–118.

7   G. Porter, *Proc. R. Soc. London. Ser. A. Math. Phys. Sci.*, 1950, **200**, 284–300.

8   R. G. W. Norrish and G. Porter, *Nature*, 1949, **164**, 658–658.

9   H. Ohkita, Y. Tamai, H. Benten and S. Ito, *IEEE J. Sel. Top. Quantum Electron.*, 2016, **22**, 100–111.

10   J. M. Beechen and M. Ameloot, *Instrum. Sci. Technol.*, 1985, **14**, 379–402.

11   I. H. M. Van Stokkum, D. S. Larsen and R. Van Grondelle, *Biochim. Biophys. Acta - Bioenerg.*, 2004, **1657**, 82–104.

12   J. J. Snellenburg, S. P. Laptenok, R. Seger, K. M. Mullen and I. H. M. van Stokkum, *J. Stat. Softw.*, 2012, **49**, 1–2.

13   I. H. M. Van Stokkum and H. E. Bal, *Concurr. Comput. Pract. Exp.*, 2006, **18**, 263–269.

14   J. Schneider, K. Nikitin, R. Dillert and D. W. Bahnemann, *Faraday Discuss.*, 2017, **197**, 505–516.

15   U. Schmidhammer, S. Roth, E. Riedle, A. A. Tishkov and H. Mayr, *Rev. Sci. Instrum.*, , DOI:10.1063/1.2047828.

16   M. Wakasa and H. Hayashi, *Chem. Phys. Lett.*, 2000, **327**, 343–350.

17   F. S. Davis, G. A. Nemeth, D. M. Anjo, L. R. Makings, D. Gust and T. A. Moore, *Rev. Sci. Instrum.*, 1987, **58**, 1629–1631.

18   B. Carlotti, I. K. Madu, H. Kim, Z. Cai, H. Jiang, A. K. Muthike, L. Yu, P. M. Zimmerman and T. Goodson, *Chem. Sci.*, 2020, **11**, 8757–8770.

19   M. Goppert-Mayer, *Ann. Phys.*, 1931, **401**, 273–294.

20   W. Kaiser and C. G. B. Garrett, *Phys. Rev. Lett.*, 1961, **7**, 229–231.

21   M. Pawlicki, H. A. Collins, R. G. Denning and H. L. Anderson, *Angew. Chemie - Int. Ed.*, 2009, **48**, 3244–3266.

22   P. N. Butcher, *The Elements of Non-Linear Optics*, Cambridge University Press, Cambridge, 1990.

23   R. Loudon, *The Quantum Theory of Light*, Oxford University Press, Oxford, 1973.

24   R. W. Boyd, *Non-Linear Optics*, Elsevier, London, 2nd ed., 2003.

25   C. Xu and W. W. Webb, *J. Opt. Soc. Am. B*, 1996, **13**, 481.

26   N. S. Makarov, M. Drobizhev and A. Rebane, *Opt. Express*, 2008, **16**, 4029–4047.

27   S. J. Strickler and R. A. Berg, *J. Chem. Phys.*, 1962, **37**, 814–822.

Chapter 3

Activating Intramolecular Singlet Exciton Fission by Altering π−Bridge Flexibility in Perylene Diimide Trimers for Organic Solar Cells

3.1 Original Publication Information

The work in this chapter was published in the journal of *Chemical Science* as:

Ifeanyi Madu and Benedetta Carlotti contributed equally to this work as first authors. Synthesis of the compounds was carried out by the Luping group at the University of Chicago and quantum calculations by the Zimmerman group at the University of Michigan. Modifications were made to the original publication to adapt it to the style of the content of this dissertation. References and supporting information of the original manuscript are included in this chapter.

3.2 Abstract

In this study, two analogous perylene diimide (PDI) trimers, whose structures show rotatable single bond π−bridge connection (twisted) vs. rigid/fused π−bridge connection (planar), were synthesized and investigated. We show via time resolved spectroscopic measurements how the π−bridge connections in A−π−D−π−A−π−D−π−A multichromophoric PDI systems strongly affect the triplet yield and triplet formation rate. In the planar compound, with stronger intramolecular charge transfer (ICT) character, triplet formation occurs via conventional intersystem crossing. However, clear evidence of efficient and fast intramolecular singlet exciton fission (iSEF) is observed in the twisted trimer compound with weaker ICT character. Multiexciton triplet generation and separation occur in the twisted (flexible−bridged) PDI trimer, where weak coupling among the units is observed as a result of the degenerate double triplet and quintet states, obtained by quantum chemical calculations. The high triplet yield and fast iSEF observed in the twisted compound are due not only to enthalpic viability but also to the significant entropic gain allowed by its trimeric structure. Our results represent a significant step forward in structure−property understanding and may direct the design of new efficient iSEF materials.

3.3 Introduction

The scientific benefits and applications of understanding the dynamics of multiexciton triplet generation in organic chromophores cannot be overemphasized. One benefit is evaluating the actual potential impact singlet exciton fission (SEF) has on improving the power conversion efficiency (PCE) of organic solar cells.[1] The effect of SEF on the device photocurrent has been demonstrated by means of magnetic field dependent measurements in literature reports.[2–4] Another benefit is to account for the excess absorption energy used to generate singlet electron−hole pairs often lost as heat.[5] Finally, understanding the dynamics of multiexciton generation aids in the careful design and synthesis of selective organic chromophores with high SEF yields, to be used in photovoltaic devices or photocatalytic cells, for the generation of more photocurrent.[6–8] The ability to advance our insight is limited by the number of materials capable of undergoing SEF.[9,10] A lot of focus has been placed on acenes (mostly tetracene, pentacene) since the discovery of SEF in anthracene crystals.[7,11–17] There are relatively fewer SEF studies on perylene diimides (PDIs),[18,19] which are mostly used as electron acceptors in non−fullerene photovoltaic devices, in comparison to acenes. Understanding the science and mechanism by which PDI acceptors themselves exhibit SEF can be beneficial in avoiding the extra layer to be taken up by a "SEF sensitizer" in an actual photovoltaic device, reducing the complexity, cell thickness, and greatly improving the absorption of solar photons.

Intermolecular SEF (xSEF) has been observed in solid state aggregates of PDI derivatives.[18–22] High rate of xSEF has often been associated to highly–ordered crystalline systems in comparison to their amorphous counterpart. This has been associated with a SEF assisted process – crystal lattice vibration.[23] The ordered chromophores have to be in close proximity and achieve a slip–stacked or herringbone dimeric structure. This leads to them having weaker

interchromophore (excitonic) interactions.[24] In these solid state films, triplet formation is significantly influenced by the morphology and crystal packing, which are usually difficult to control. Hence, for devices made with xSEF chromophores where solid–state packing interactions are crucial, slight perturbations can have a drastic effect on the rate and yield of xSEF. This limits the understanding of the underlying key factors affecting the rate and efficiency of singlet fission in xSEF materials. To this regards, a more suitable approach would be intramolecular singlet exciton fission (iSEF).[13,25–29] Materials capable of iSEF can overcome these challenges because each molecule undergoes SEF via through–bond interactions in multichromophoric systems – that is, not depending on intermolecular orientation, intermolecular coupling, or through–space interactions.

Donor–Acceptor configuration, which induces an intramolecular charge transfer character, is a molecular design strategy for iSEF molecules.[10] Another strategy involves the covalent coupling of two xSEF chromophores where the triplet yield has been reported to be affected by the conjugation between the two chromophores.[14,15,30–32] There are also reports about the effects of through–bond proximity between the chromophores on the triplet production. Campos et al[13] gave a very detailed account for pentacene dimers where the proximity of the pentacene moieties and the extent of conjugation was varied using (oligo) phenylene spacers. It was suggested that the rate of singlet fission (rate of triplet production) and the rate of recombination of the two triplets could be controlled by using spacers of varying length. In another study, Thompson et al[17] looked at how connecting two SEF chromophores to a bridge moiety at its *ortho*, *meta* or *para* position influences the through–bond and through–space contributions to the coupling of the compound. Intramolecular SEF was observed only in the *ortho* and *para* systems, not in the *meta*; and this was associated to the lack of effective conjugation, hence very weak coupling, causing

predominantly radiative decay of the excited state. However, all these studies were reported for acene dimers for the end purpose of sandwiching them with organic photovoltaic (OPV) active layer materials. There are little to no studies about the effects of the π−bridge in multichromophoric OPV active layer materials themselves, e.g. PDIs, in tuning the iSEF rate or in activating/deactivating iSEF.

The aim of this study is to investigate the unique role of the π−bridge in allowing or inhibiting triplet production (rate and yield) in oligomeric multichromophoric PDI systems. In few recent literature reports,[15–17] structural flexibility of the covalently linked units has been proposed to be crucial in activating SEF. However, these studies lack a direct comparison with rigidly bridged units of the same chromophore in order to isolate the effects of π−bridge flexibility. This is what our current investigation seeks to illuminate − the impact of the π−bridge rotation vs. rigidity on the dynamics of triplet exciton formation, and the triplet production efficiency. Most literature studies involve dimers. Investigations about oligomeric structures, with more than two chromophores attached linearly, are very few. In the development of iSEF−OPV materials using a strong Acceptor−strong Donor configuration,[10] the role of the flexibility/rigidity of the π−bridge in influencing the triplet production rate and efficiency, has not been investigated.

In this work, two PDI trimers with push−pull character were synthetized (see **Scheme 3.1**). For each molecule, the unit PDI electron acceptor moieties are bridged at the beta (β) position(s) with benzodithiophene (BDT) electron donor moieties, forming an A−D−A−D−A assembly. The connections between the donor and the acceptor moieties were realized via single bonds in the **β** compound, and through ring cyclization in the **βC** compound (color coded in the structures in **Scheme 3.1**). This results in the single−bond−bridged **β** compound having a twisted PDI−BDT−PDI structure (dihedral angles ∼ 55°), and the cyclized **βC** compound achieving a

planar PDI−BDT−PDI structure (dihedral angles ∼ 0°). These two compounds show different triplet production dynamics owing to their respective degree of electronic coupling. The photoinduced dynamics of triplet production – via iSEF or regular intersystem crossing (ISC) – was thoroughly investigated with a variety of time resolved spectroscopic techniques, employing both femtosecond and nanosecond time resolution while probing both excited state absorption and emission. The experimental spectroscopic study was carried out in a joint effort with theoretical calculations to further elucidate the excited state deactivation mechanism of the two compounds.

βC
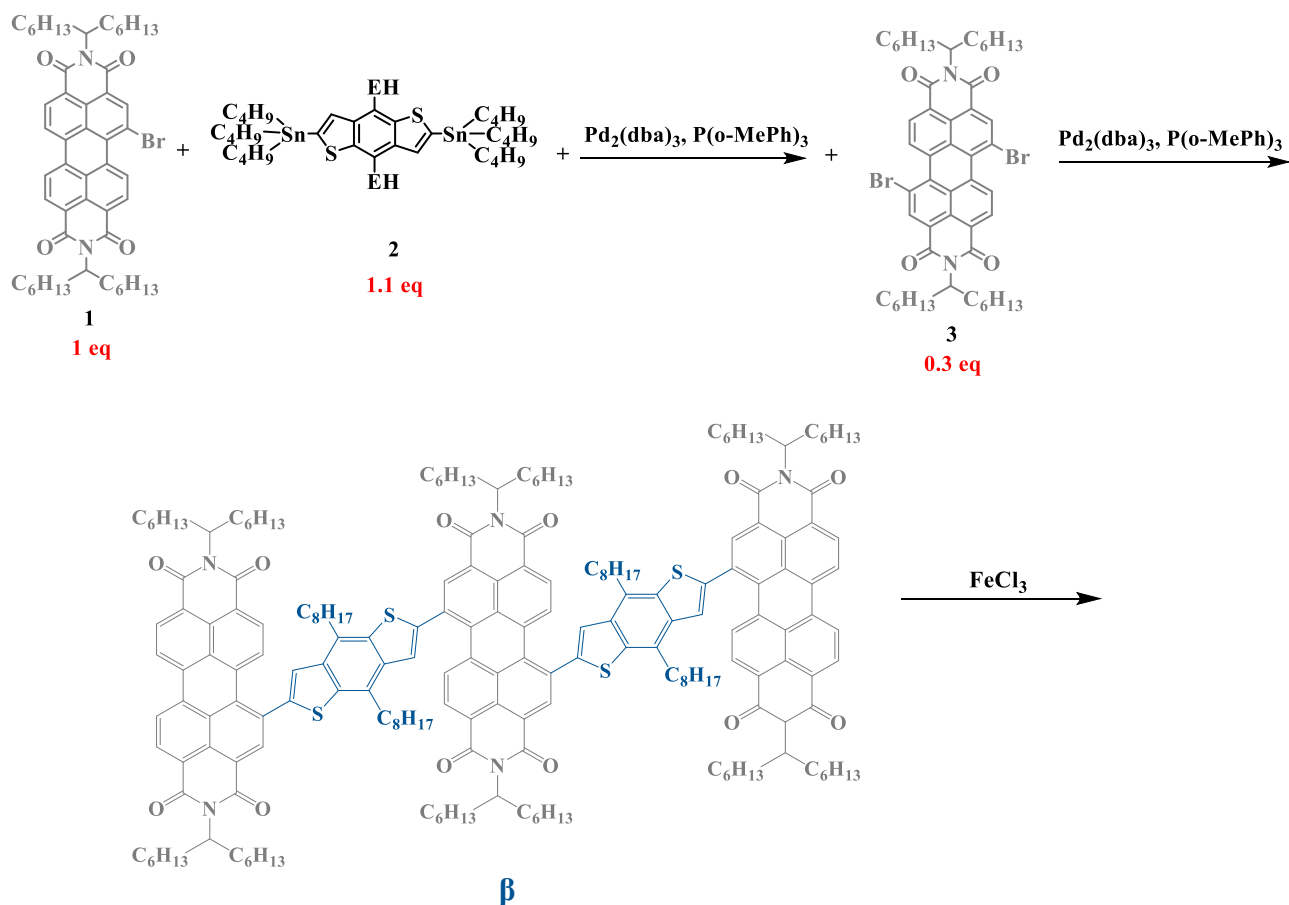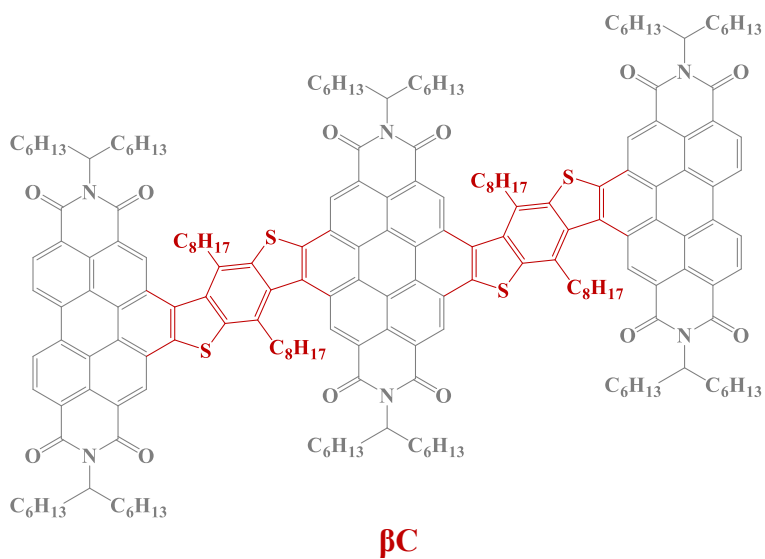
Scheme 3.1 Molecular structures of the investigated trimers.

3.4 Results

3.4.1 Steady–State and Two–Photon Absorption Measurements

The steady-state absorption and emission spectra of the investigated trimers are shown in **Figure 3.1**. These electron acceptor compounds are excellent light absorbers with sizable molar extinction coefficients, ca. $60000-70000$ M^{-1} cm^{-1} (**Table 3.1**). Their broad absorption spectra extend in a region complementary to that of electron donors employed in OPV devices. Both the absorption and emission spectra of **β** appear to be less structured in comparison to those of **βC**. The structured spectra and small Stokes shift (**Figure 3.1**/**Table 3.1**) of the **βC** compound reflect its molecular rigidity. The emission spectrum of **β** is extremely broad and its peak is significantly red shifted in comparison to the emission peak of **βC**. The extremely broad emission spectrum and the large Stokes shift suggest a drastic rearrangement of this flexible molecule in the excited state.[33,34] The theoretical calculations indeed reveal that the **β** compound has a twisted PDI−BDT−PDI structure (dihedral angles $\sim 55°$), and the **βC** compound has a planar PDI−BDT−PDI structure (dihedral angles $\sim 0°$). In both cases, the hole transition orbitals are localized on the electron-rich BDT units, and electron transition orbitals show more localization

on the PDI acceptor unit(s) (**Figure 3.2**). Also, the theoretical calculations reveal electron localization on only one PDI unit for the twisted **β** compound, but complete delocalization across all trimer units for the planar **βC** compound. This indicates minimal ground state interaction or excitonic coupling among the chromophores[35] in **β** – hence its similar absorption peak (λ^{max}) to that of the parent PDI monomer (**Figure 3.1**). However, the spectral behavior of **βC** is indicative of a much stronger coupling among the PDIs, and with the BDT core.
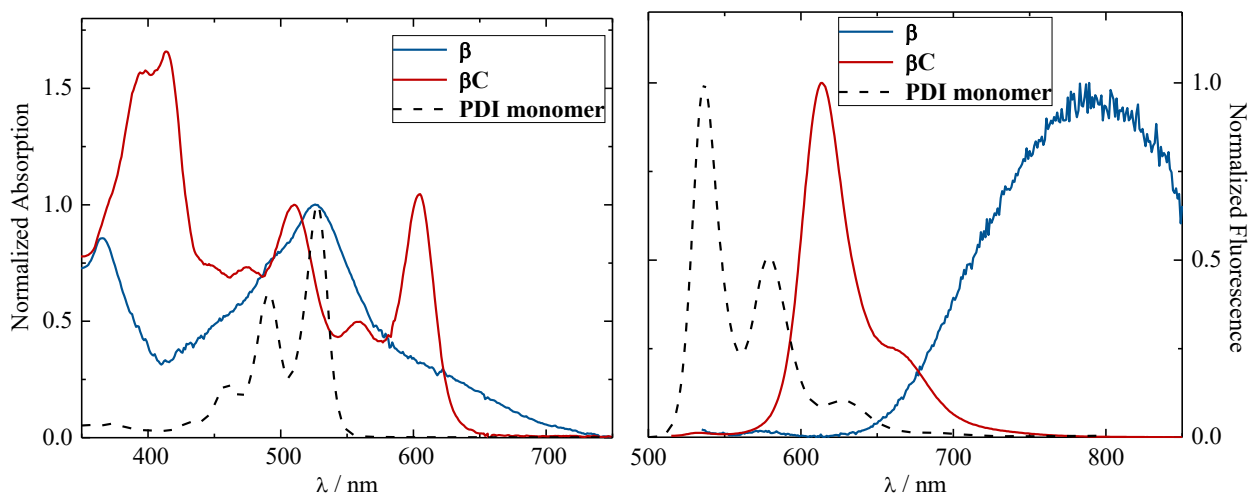
Figure 3.1 Normalized absorption and emission spectra of the trimers in chloroform.
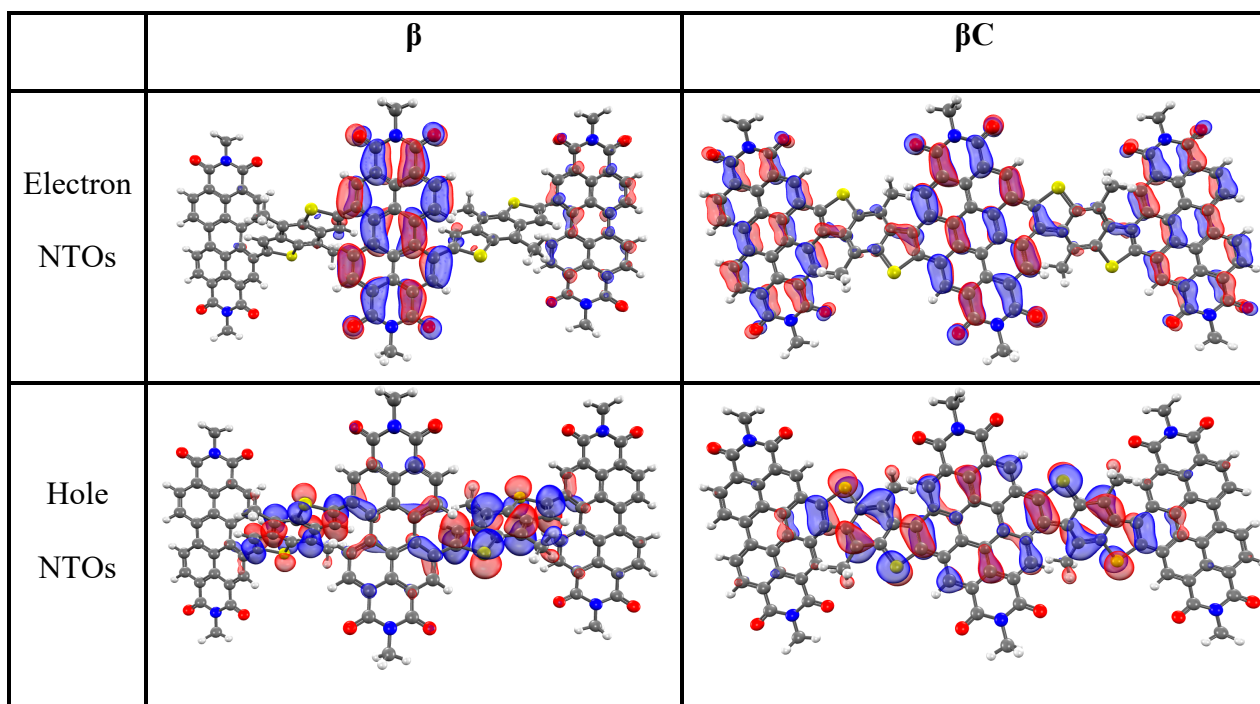
Figure 3.2 Natural transition orbitals for the S_0 geometry ($S_0 \rightarrow S_1$ transition) of the trimers. (isodensity = 0.05. Color scheme; Hydrogen–white, carbon–black, nitrogen–blue, oxygen–red, sulfur–yellow).

No concentration effect on the absorption spectral shape was observed in the range of concentrations employed in this investigation (see **Figure 3.11**), which are similar to, or lower than the 'low concentration'/dilute limit employed in other literature studies about xSEF compounds in solution.[27] Therefore, it is possible to rule out the occurrence of any intermolecular interactions due to aggregation which may affect our experimental results. Hence, the optical properties exhibited by the compounds investigated here are due to isolated molecules in solution.

The fluorescence quantum yield of the investigated compounds is low (0.3% and 9%, see **Table 3.1**) in comparison to that of the parent PDI monomer (88%).[36] The fluorescence efficiency is 30 times lower in the case of compound **β** relative to **βC**. This behavior parallels the observed trend of the Stokes shift in the two trimers and agrees with the increased molecular rigidity of **βC** relative to **β**. More rigid molecular structures are indeed known to exhibit enhanced fluorescence capability.[33,37] This result suggests that the excited state deactivation of these trimer compounds takes place mainly through non−radiative pathways − possibly triplet production/decay, in competition with the fluorescence decay pathway. This non−radiative deactivation is more efficient for the twisted **β** compound, whose fluorescence quantum yield is almost negligible.

Previous studies have observed the relationship between molecular planarity and two−photon absorption.[34,38,39] Here, the two−photon absorption cross section (δ_{TPA}) is enhanced by over one order of magnitude for the planar **βC** (ca. 300 GM) relative to the twisted **β** compound (ca. 10 GM). The increased two−photon absorption cross section of the planar, rigid, fused ring connected molecule, as expected, indicate its higher intramolecular charge transfer character in the excited state relative to the twisted, flexible, single bond bridged analogue. The degree of charge

transfer for the **β** and **βC** excited state was further analyzed in detail with the help of quantum chemical simulations. These compounds were divided into 5 subunits/moieties, considering their acceptor(1)−donor(2)−acceptor(3)−donor(4)−acceptor(5) structure where the acceptors and the donors are the PDI the BDT fragments, respectively. The amount of charge transferred during emission is reported in **Table 3.3**. The charge transfer degree for the excited state of **βC** (0.80 e⁻) is indeed higher than that of **β** (0.74 e⁻).

Table 3.1 Absorption and fluorescence properties, and two–photon absorption cross sections for the Trimers in chloroform.

Comp.nd	λ_{abs} / nm	λ_{em} / nm	$\Delta\upsilon^a$ /cm^{-1}	ε^b / M^{-1}cm^{-1}	ϕ_F / %	δ_{TPA} / GM λ_{exc}=875 nm
β	526, 630$^{(sh)}$	790	3215	71100	0.3	11.5
βC	510, 605	613, 665$^{(sh)}$	215	58500	9	318

$^a\Delta\upsilon$ is the Stokes shift; ^{b}at the underlined wavelength

3.4.2 Femtosecond Transient Absorption

The excited state dynamics was investigated by femtosecond transient absorption. The time resolved spectra (**Figures 3.3** & **3.13**) show positive excited state absorption (ESA) and negative Ground State Bleaching (GSB) signals. The ESA at 740 nm has been previously associated with the PDI anion, whereas signals between 550 and 600 nm have been assigned to the PDI cation.[40–46] The transient spectra of the investigated trimers at short delays following photoexcitation suggest the occurrence of intramolecular charge transfer (ICT), and no significant spectral shift was observed. It is possible that a singlet excited state with ICT character is formed very fast (within solvation).[46] At longer delays this signal decays, resulting in the simultaneous formation of an ESA at 514 nm and 543 nm for **β** and **βC**, respectively. The kinetics at these wavelengths exhibit a rise (**Figure 3.3**). This rise occurs very fast for the twisted **β** compound (344 ps), but clearly slower for the rigid−bridged **βC** compound (1800 ps). Global analysis, via singular value

96

decomposition (SVD), of the transient absorption data revealed the presence of four exponential components (**Figure 3.13B** & **Table 3.4**). The first two fast components can be associated to solvation and vibrational cooling/structural relaxation. The third component, assigned to the relaxed S_1, shows a lifetime of 320 ps for the **β** compound and 1300 ps for the **βC** compound. The fourth component represents the Rest species formed upon S_1 decay and peaked around 510−550 nm. This long−lived species are triplets, as demonstrated by their spectral similarity to the species detected by nanosecond transient absorption (see next section). Therefore, the ultrafast absorption measurements allow us to follow the triplet formation dynamics in these molecules. The triplet formation occurs fast for **β** (~340 ps) and much slower for **βC** pointing to a different mechanisms for triplet production in the two molecules−SEF for **β** and ISC for **βC**, respectively. Additionally, triplet fomation takes place slower in a less polar solvent relative to chloroform (e. g. for **β** in toluene triplet rise occurs in ca. 690 ps).

Triplet quantum yields were also computed following the SVD analysis of the femtosecond transient absorption results.[47–50] Quantitatively related singlet and triplet ESA spectra were obtained by matching their GSB and then the temporal population dynamics of these states were determined. The population data (**Figures 3.18** & **3.23**) indicate a triplet quantum yield of 189 % for **β** and higher than 46 % for **βC**. Although this analysis contains some approximations, our result thus show that triplet production takes place via iSEF for the twisted **β** compound (φ_T close to 200 %) and via conventional ISC for the planar/rigid−bridged **βC** system ($\varphi_T \ll 100$ %).
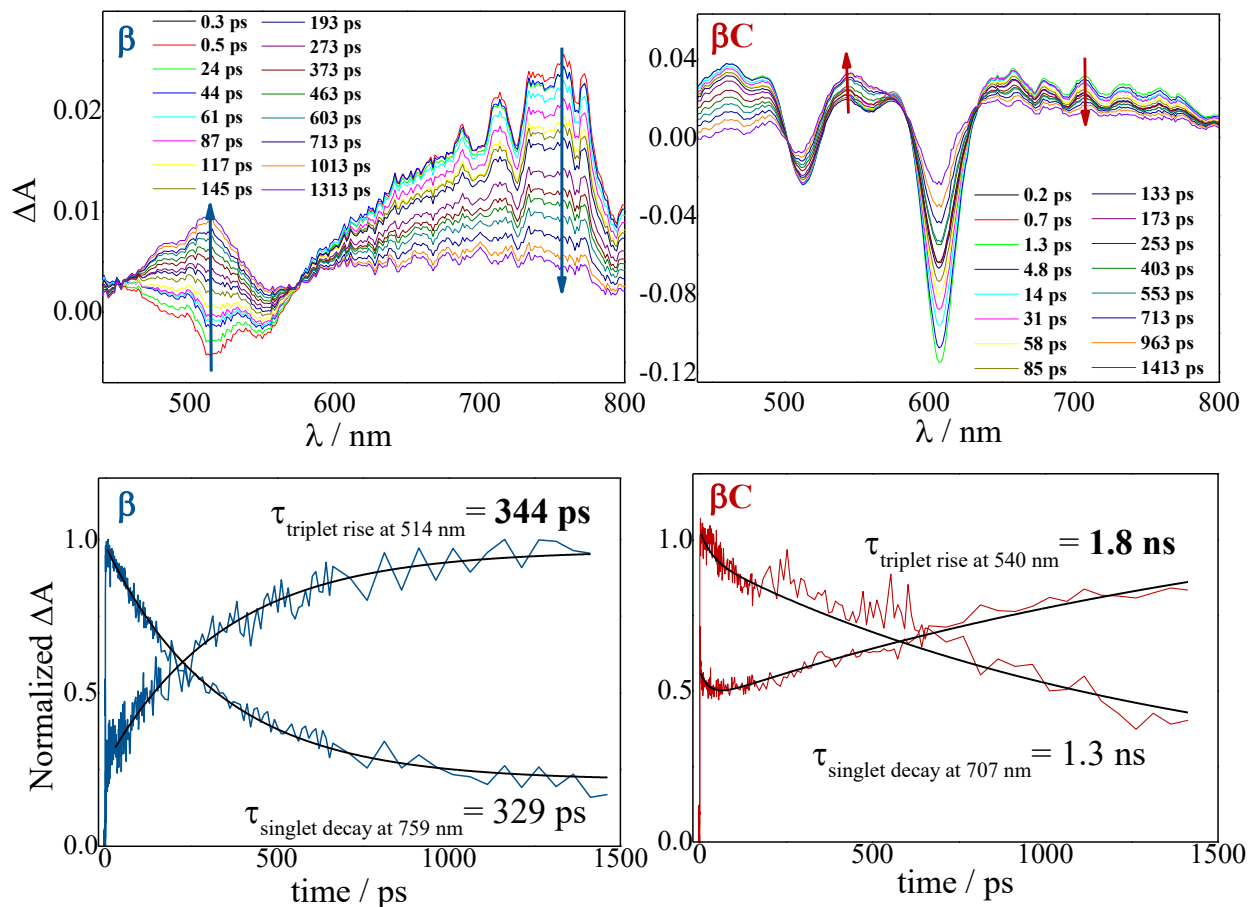
Figure 3.3 Time−resolved spectra obtained by femtosecond TA for the trimers in chloroform. Singlet decay and triplet rise kinetics for the trimers in chloroform.

3.4.3 Nanosecond Transient Absorption

To investigate the long−lived excited state dynamics, nanosecond transient absorption measurements were carried out (**Figure 3.4**). No pump wavelength dependence was observed. The transient spectra show negative signals due to GSB, and a positive ESA peak centered at 490 nm and 540 nm for **β** and **βC**, respectively. It is worthy to note that signals of triplet absorption have been reported for other PDI derivatives between 500 and 600 nm.[18,36,51,52] This signal can be quenched by oxygen (either via energy transfer or electron transfer).[53] The transient lifetimes change from hundreds of nanoseconds in air equilibrated solution to tens of microseconds in deaerated/nitrogen purged solution (**Figure 3.25** & **Table 3.2**). Quenching by molecular oxygen

thus occurs at an almost diffusional rate (1.2×10^{10} M^{-1}s^{-1} in chloroform). Also, these transient species can be sensitized by higher−triplet energy donors, or are able to sensitize lower−triplet energy acceptors, such as tetracene as shown in **Figure 3.5**. These results allow us to undoubtedly assign these long−lived transients revealed by nanosecond transient absorption experiments to the $T_n \leftarrow T_1$ transition of the trimers. As shown in **Table 3.2**, for **β**, the triplets produced upon photoexcitation decay much faster i.e. shorter lifetimes (6.0 µs), in comparison to the triplets produced in **βC** (40 µs). This is an evidence leaning to a SEF−induced mechanism of triplet production in the twisted **β**. It has indeed been observed in many SEF literature studies[17,54–56] that a molecule hosting two triplet excitons usually exhibits a much faster triplet decay than one hosting a single triplet, due to the increased probability of triplet−triplet annihilation.
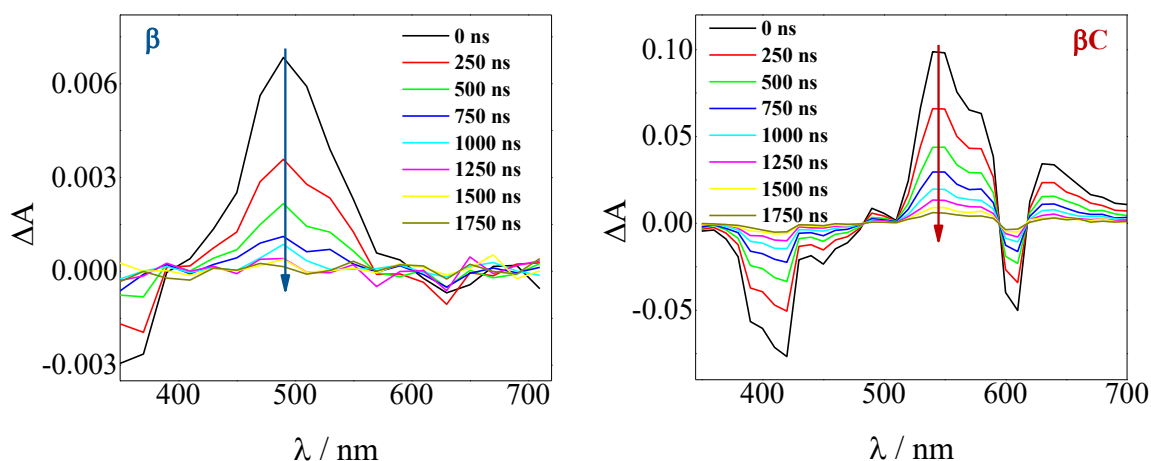
Figure 3.4 Time−resolved spectra obtained by nanosecond TA measurements for the Trimers in air-equilibrated chloroform upon 415 nm laser excitation.

Table 3.2 Triplet properties for the trimers in chloroform from nanosecond transient experiments.

Comp.	λ_T / nm	$\tau_{T,air}$ / µs [a]	$\tau_{T,N2}$ / µs [b]	$\phi_T \cdot \varepsilon_T$ / M^{-1} cm^{-1}	ε_T / M^{-1} cm^{-1}[c]	ϕ_T
β	490	0.39	6.0[d]	2785	1637	1.70
βC	540	0.50	40	7460	52800	0.16

[a]in air-saturated chloroform; [b]in N$_2$-saturated chloroform; [c]in cyclohexane; [d] ~7µs lifetime was obtained by triplet sensitization in cyclohexane, see **Figure 3.29**.

Sensitization experiments were performed via nanosecond transient absorption measurements. These experiments give important information about the triplet energy of the compounds (see **Figure 3.5**). Tetracene (E_T = 1.27 eV) was successfully employed as an energy donor to sensitize the triplet of **β**, but relatively acted as a triplet energy acceptor to **βC**. This result proves that the triplet energy of the twisted **β** trimer is significantly lower than the triplet energy of the planar **βC** trimer. Our experimental results thus support the feasibility of SEF in the **β** compound which requires a low triplet energy for the SEF energetic condition to be fulfilled (E_T = 0.55 eV; obtained from theoretical calculations). The sensitization experiments also allowed for the accurate evaluation of triplet extinction coefficients (see **Table 3.2**), useful for evaluating the singlet → triplet quantum yield. A very detailed step-by-step triplet extinction calculation for the two compounds is given in the Supporting Information. A lower extinction coefficient was observed for the twisted relative to the planar, rigid system. These experiments, together with the relative actinometry measurements described in the Supporting Information, allowed for the accurate computation of the singlet → triplet quantum yields. A triplet quantum yield of 16 % was obtained for the planar **βC** compound, suggesting that conventional intersystem crossing occurs in this chromophore. Triplet yield significantly higher than 100 % was obtained in the case of the twisted **β** compound (ϕ_T =170 %), thus suggesting that iSEF indeed takes place in this molecule.
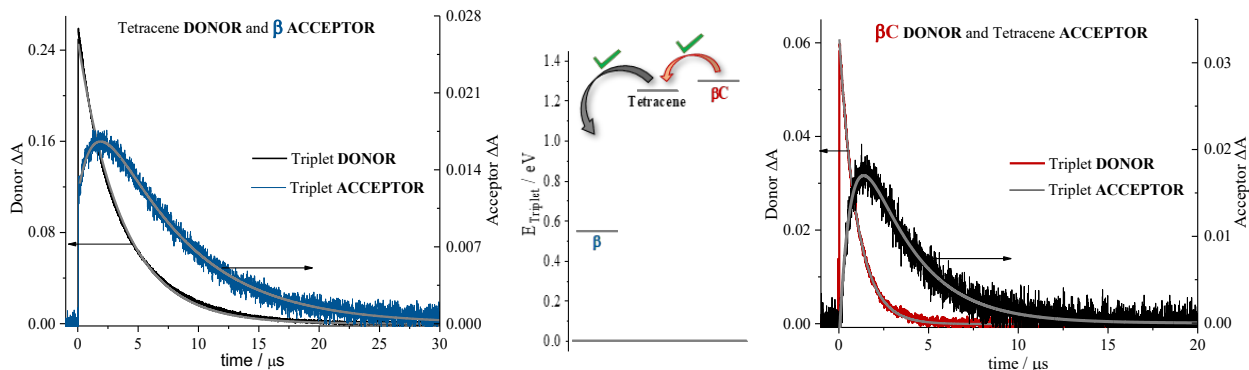
Figure 3.5 Decay and rise dynamics of trimers (extreme left for **β**; and extreme right for **βC**) in cyclohexane obtained by nanosecond TA for triplet sensitization measurements. Middle graph shows the triplet energy for samples and sensitizers.

3.4.4 Two–Color Transmission Measurements of Triplet Yield

To selectively probe the ESA without contribution from the GSB, the trimer compounds were investigated using two-color transmission spectroscopy.[28] This was performed by probing the samples at 850 nm, where linear absorption is negligible, under excitation with femtosecond pulses at 425 nm. Attenuation of the probe beam was observed for both samples: 29.7 % attenuation for **β** at OD = 0.116 and 34.6 % attenuation for **βC** at OD = 0.885, both under an average pump power of 4.25 mW (**Figure 3.6**). This demonstrates the accumulation of triplets upon irradiation of the trimers, observed to be more in the case of **β**. Indeed, the theoretical calculations predicted significant absorption by T_1 species around 850 nm: transition $T_1 \rightarrow T_8$ at 898 nm and $T_1 \rightarrow T_{10}$ at 826 nm for **β**; transition $T_1 \rightarrow T_{16}$ at 849 nm for **βC**.
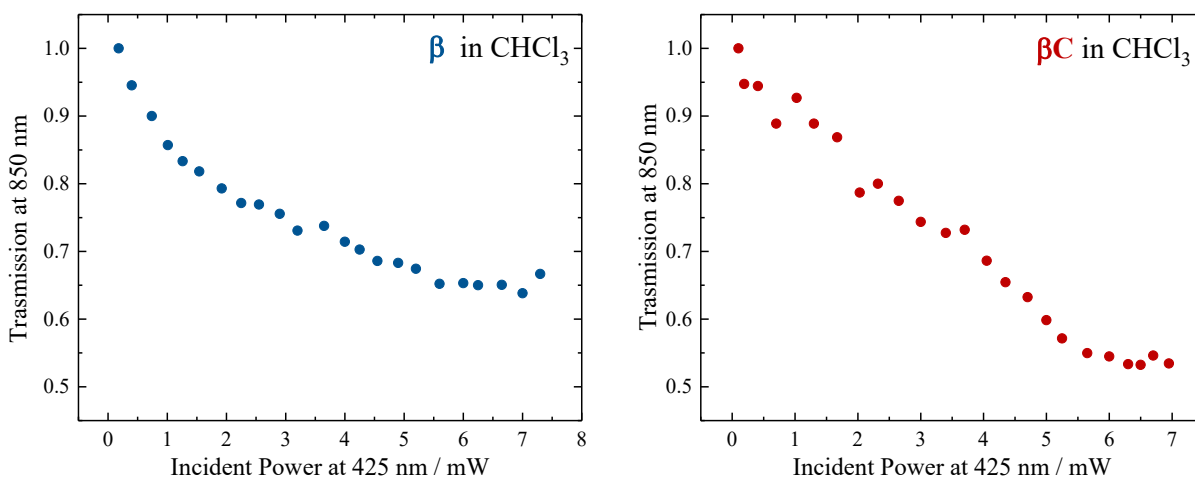
Figure 3.6 Transmission of **β** (left) and **βC** (right) in CHCl₃ for the probe light at 850 nm as a function of the pump power at 425 nm.

Analysis of the obtained results was carried out in order to obtain an estimation of the triplet quantum yield for the two compounds. See the Supporting Information for the detailed calculation performed according to a procedure described in ref. 25. It entails computing the triplet number

density using the 850 nm probe beam attenuation (as shown in **Figure 3.6**) and the singlet excitation number density from the ground state OD and 425 nm pump beam parameters. The triplet extinction coefficients at 850 nm used for this calculation were obtained via nanosecond transient absorption measurements, by taking the ratio of the ΔA signal at 850 nm with that at the triplet peak for which the extinction coefficient is known (see **Table 3.2**). This was accurately done for **β** which had a distinct triplet ESA signal ~850 nm . However, for **βC** the triplet ESA signal was convoluted with the phosphorescence around 850 nm. Therefore, the same ratio of the ΔA signal between the triplet peak and that at 850 nm for **β** was assumed for the **βC** molecule. From the calculation, the triplet number density was evaluated to be 2.32×10^{10} cm^{-3} for **β** and 8.61×10^{8} cm^{-3} for **βC**; the singlet number density 1.24×10^{10} cm^{-3} for **β** and 3.14×10^{11} cm^{-3} for **βC**. Therefore, a much higher triplet quantum yield was indeed obtained for the twisted **β** trimer (~187 %) relative to the planar **βC** (~0.3 %). It has to be noted that for the case of the **βC** compound, the estimated triplet yield value is not accurate because of the observed phosphorescence interference at 850 nm. This analysis contains some approximations, however the result obtained for the **β** trimer is consistent with the triplet quantum yield accurately measured by the nanosecond transient absorption sensitization experiments. This once again confirms that the **β** compound thus undergo singlet exciton fission in solution, owing to its triplet yield also obtained by two–color transmission measurements to be >> 100%.

3.4.5 Time Resolved Fluorescence

Time resolved fluorescence measurements, both with femtosecond and nanosecond time resolution, have been extremely valuable in providing information about the rate constants of the ultrafast intramolecular charge transfer process and about the decay of the double triplet species, respectively. Fluorescence kinetics were acquired by femtosecond fluorescence up conversion

(FUC). Their fitting revealed the presence of exponential components (**Table 3.7**), whose lifetimes agree with those obtained via femtosecond transient absorption measurements. The much smaller time window of the FUC allows for a more accurate evaluation of the lifetime of the ultrafast components, as 1.0 ps for **β** and 0.2 ps for **βC**. Our FUC results show that the ICT is indeed faster in the rigid relative to the twisted trimer. Also, that SEF could be a CT−mediated process in the twisted trimer.[10,22] However, when ICT is extremely fast it becomes competitive with SEF, as observed in the planar trimer.[49]
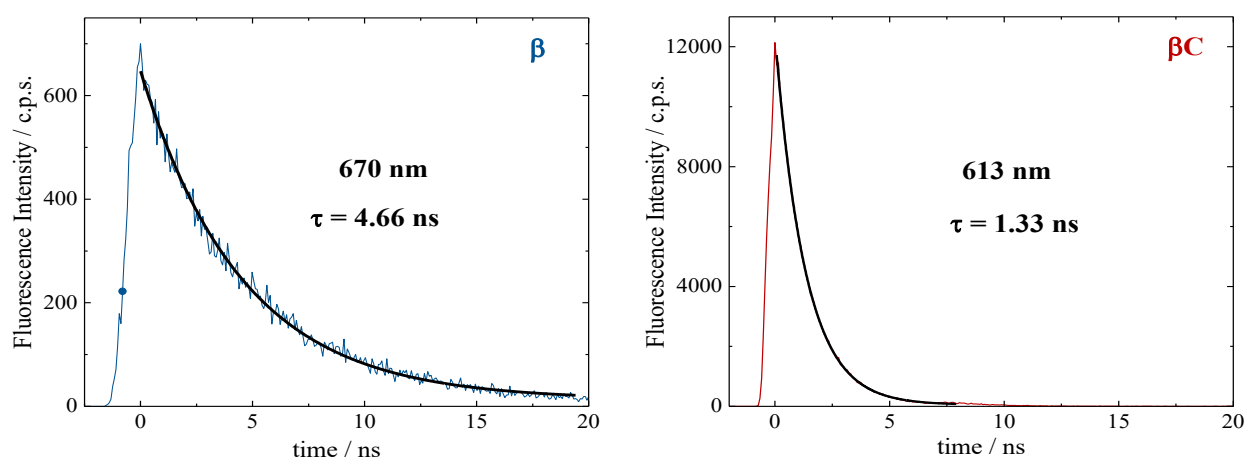
Figure 3.7 Fluorescence kinetics obtained by nanosecond TCSPC in air equilibrated chloroform.

Fluorescence kinetics were also acquired by single photon counting (SPC) with nanosecond resolution (**Figure 3.7**). For the rigid **βC**, these experiments revealed a lifetime of 1.33 ns, in agreement with the femtosecond TA measurement – 1.3 ns (**Figure 3.6** & **Table 3.6**). For **β**, the SPC fluorescence decay is surprisingly slower, and the fitting revealed a lifetime of 4.66 ns. This fluorescent component exhibits a lifetime quite different from that estimated by the femtosecond transient absorption for S_1 – 320 ps, and by the high resolution FUC. Therefore, the 4.66 ns component may be due to a precursor of T_1, possibly a double triplet excited state $^1(TT)^*$. This component could be either a result of direct $^1(TT)^*$ emission,[57–59] or delayed S_1 fluorescence from the $^1(TT)^*$ state.[1,19,23,52] Time resolved emission and/or temperature-dependent spectra

obtained by photoluminescence measurements with broadband detection would be required to identify the specific mechanism of the double triplet emission. A 4.66 ns lifetime is not unusual for double triplet states as observed in the literature for perylene diimide chromophores. Wasielewski et al[18] reported a lifetime of 2.8 ns for polycrystalline thin films of slip stacked PDI, attributed to a small amount of delayed fluorescence resulting from triplet-triplet annihilation. Sean Roberts et al[52] also reported lifetime of ~10 ns associated to the non-radiative decay of the triplet (or double triplet) excitons to the ground state.

3.4.6 Quantum Chemical Simulations: Intersystem Crossing and Singlet Fission

Quantum chemical simulations were performed to give an insight into triplet formation mechanisms. Triplet formation via ISC was predicted to be much faster for the planar βC than for its twisted analogue due to large cancellation between ΔE_{ST} and reorganization energies for β (i.e. 8.44×10^5 s^{-1}/1185 ns for β and 1.35×10^7 s^{-1}/74.1 ns for βC). However, experimentally, the long−lived triplet species appear much faster (340 ps) for the twisted β. This implies the existence of another pathway of triplet generation: iSEF. Similar timescales of triplet formation via SEF in other PDI derivatives have been reported.[18,52] TD−DFT was used to illustrate the SEF relevant energetics and to check if the energetic requirement or ***thermodynamic feasibility***, $E(S_1) \geq 2 \times E(T_1)$ is met. Energies of the relaxed S_1 state were predicted to be 1.30 eV and 1.89 eV for β and βC, respectively. T_1 state energies at its minimum structures were 0.55 eV and 1.24 eV for β and βC, respectively. This energetics indicates that SEF in the twisted β is thermodynamically favorable by 0.20 eV ($2 \times 0.55 - 1.30 = -0.20$), but not in the planar βC for which it is energetically uphill by 0.59 eV ($2 \times 1.24 - 1.89 = 0.59$).

A recent perspective pointed out that the accessibility of double triplet state of singlet character (^1TT), that is the ***kinetic feasibility***, is more instrumental to judge the potentiality of SEF

taking place than just the simple singlet–triplet energy gap.[60] Though TD–DFT calculations were conducted to obtain the energetics of singly excited states, it is clearly stated by theorists that TD–DFT is not an ideal method for calculation of the multi–excitonic (ME) states, i.e., double-triplet states. The RAS–SF method, on the other hand, has shown to be capable of correctly describing the characters of multi–excitonic states and providing a more in–depth picture of the interactions between the locally excited singlet and multi–exciton states. Importantly for trimers like **β** and **βC**, RAS–SF is also able to compute all possible multi–exciton states, obtaining their spatial as well as their spin components (**Figures 3.8**, **3.9** and **3.10**). RAS–SF can provide the relative energies of all the double–triplet states, and identify behavior discrimination between these states in each trimer. However, RAS-SF overestimates the excitation energies because of an incomplete account of dynamic correlation.[21,61] Even though the absolute energies are not accurate (and this explains the poor agreement with the DFT energies), the trends and the relative energy values can still be discussed. The TT states from the RAS–SF trimer models are qualitatively described in **Figure 3.8**.
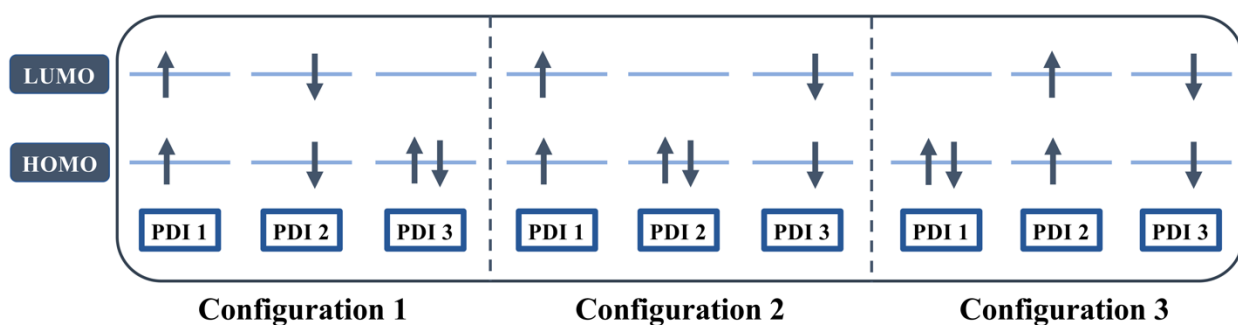
Figure 3.8 Possible electronic configurations of active space orbitals for both **β** and **βC** compounds.

Krylov has shown that it is not uncommon for perylene diimide compounds to have their lowest ^{1}TT state above their lowest excited singlet exciton state.[21] In **β** and **βC**, the lowest ^{1}TT state is placed 0.49 eV and 1.10 eV above their respective S_1 stat. This ^{1}TT state becomes nearly

inaccessible in the **βC** compound due to an additional energy of more than twice that of the **β** compound (0.61 eV), required to reach the multiexcitonic state from the S_1 state. As shown in **Figure 3.9**, the multi-excitonic state with lowest excitation energy for the **β** compound is Configuration 3. More specifically, the RAS–SF calculation shows that excitons in the lowest multi–exciton state are localized on *adjacent* PDI units. The two higher energy configurations (Configuration 1 and 2) are within 0.02 eV of Configuration 3, indicating that all TT states of **β** compound are easily energetically accessible. In the case of the **βC** compound, the lowest multi– exciton state is Configuration 2 of **Figure 3.8**, where the triplet excitons reside on the left−most and right−most PDI units. The energy of this state is about 0.2 eV under that of the two other configurations (one order of magnitude higher in comparison to **β**), suggesting a nontrivial difference in energy to access Configurations 1 and 3.

A photo–excited singlet state S_1 can evolve into a triplet–paired state $^1(TT)$ in singlet fission chromophores via state crossings when the S_1 and TT states are close in energy.[62] Throughout this non–adiabatic transition, it is true in some cases that the singlet exciton of S_1 state resides over several adjacent chromophores. This phenomenon promotes the $^1(TT)$ formation and thus increases the SF efficiency.[60] Only the couplings of the singly excited state S_1 with the ME state on adjacent chromophores will be playing significant roles throughout this non– adiabatic transition. In this particular case of **β** compound, as suggested by the electronic configuration of its lowest TT state (**Figure 3.9**), the S_1 exciton is located on two adjacent units, PDI2 and 3. This spatial characteristic explains why the TT formation is promoted in this **β** compound. Nevertheless, this S_1 exciton is spread out on the two isolated units in **βC**. As discussed above, since the S_1 excitons are less likely to reside across PDI1 and PDI3, it is therefore not surprising to conclude that forming the TT state is more difficult in **βC** than it is in **β** compound.

Additionally, performing analysis on energy differences between ^{1}TT state and quintet state energies allows us to judge the ***feasibility of separation of the double triplet into two independent triplets***. This energy difference, sometimes called inter–triplet interaction energy, is also known as the energy penalty for separating two triplets. This inter–triplet interaction energy accounts for the unmixing of charge transfer contributions in the singlet TT state by comparing the ^{1}TT state to the corresponding quintet state, which always is a pure diabatic TT state.[21] For the twisted **β** compound, the ^{1}TT states are nearly degenerate with their corresponding quintet states, giving inter–triplet interaction energies of 0.006 eV for the two lower multi–exciton states (**Figure 3.9**). This result suggests that the interaction between two triplets in **β** is quite small, and two entangled triplets can thus easily be separated into two independent triplets. In **βC** compound, however, the inter–triplet interaction energies increase by an order of magnitude, up to 0.066 eV, for the two higher multi–exciton states (**Figure 3.10**). This result entails that the formation of double triplets and the subsequent separation of entangled triplets require much less energy for **β** than for **βC**. Another notable fact is that the lowest ME state in the planar **βC** compound, which is the same case as the highest ME state in the twisted **β** compound, has no other but only the pure ME contributions toward the states. This fact also makes sense since the two triplet excitons are located on the two isolated chromophores so that it is apparently harder for charge transfer contribution to play a role in this particular situation.

Overall, quantum chemical simulations support that iSEF is the dominant pathway to generate *independent* triplets only in **β** but not in **βC**, based on the thermodynamic viability ($\Delta E_{S-2\times T}$), kinetic accessibility, and feasibility of separation of the double triplets.
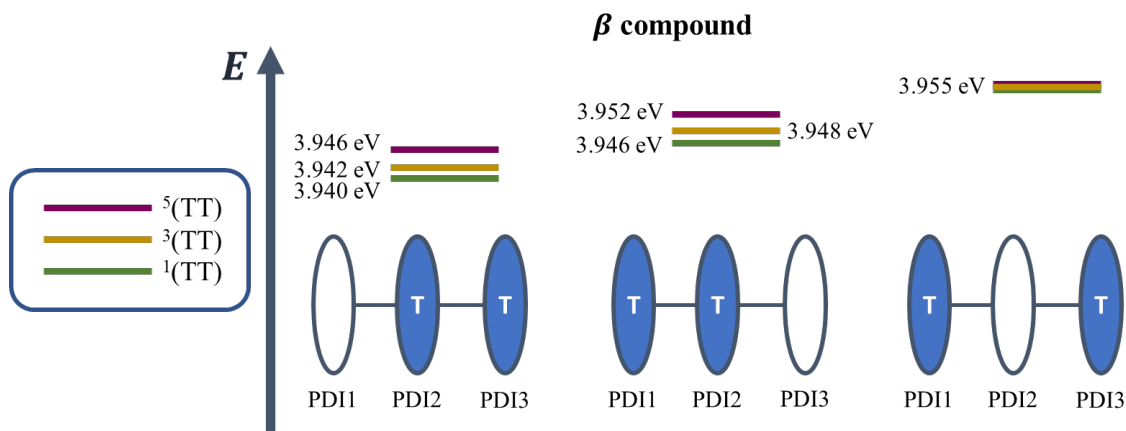
Figure 3.9 Energy level diagram illustrating the relative energies of all the double–triplet states found in **β** compound, with the colored PDI chromophores indicating where the triplet excitons are located.
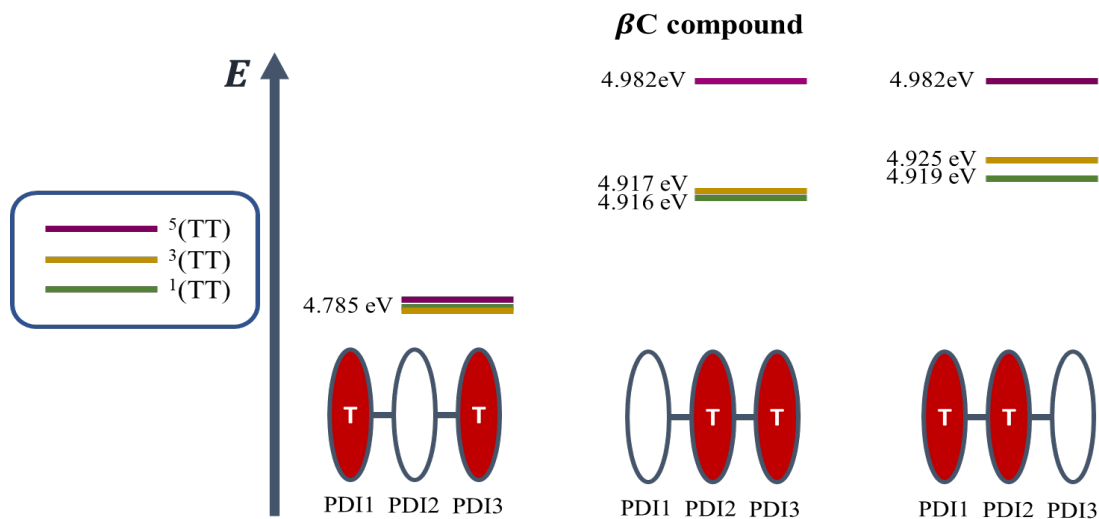
Figure 3.10 Energy level diagram illustrating the relative energies of all the double–triplet states found in **βC** compound, with the colored PDI chromophores indicating where the triplet excitons are located.

3.5 Discussion

In the literature, it has been proposed for multichromophoric systems that using a rotatable linker is crucial in obtaining iSEF.[15–17] Those studies, however, do not report the direct comparison between rigid−bridged and flexible−bridged units of the same chromophore in order to isolate the effect of the π−bridge. In this work, we point out the key differences between planar

(rigid−bridged) and twisted (flexible−bridged) systems as they relate to the efficiency and rate of triplet production upon singlet photoexcitation. The systems investigated are newly synthesized oligomeric PDI trimers. Typically, the fluorescence quantum yield of PDI monomers is around 90 %, indicating that the radiative decay pathway is the most preferred. However, for these PDI trimers, especially for the flexible−bridged **β** trimer, the fluorescence efficiency is found to be very low suggesting a prevalent non−radiative deactivation − triplet production.

For the planar **βC** trimer, we obtain a triplet yield of 16 % via triplet sensitization experiments employing a nanosecond transient absorption technique. The femtosecond transient absorption results show ultrafast intramolecular charge transfer and slow triplet formation occurring in few nanoseconds for this molecule. This rate agrees with the intersystem crossing rate predicted by quantum chemical simulations. Our experimental and computational results thus conclude that triplet production for the rigid **βC** trimer proceeds via regular intersystem crossing. Conversely, in the case of the flexible−bridged **β** trimer we clearly show that the mechanism of triplet production is different and involves iSEF, based on the following evidence. (i) Triplet yield >> 100%, obtained via triplet sensitization as well as two–color transmission experiments. (ii) A fast triplet formation ($\sim 340\ ps$) observed via femtosecond transient absorption measurements. (iii) Distinct triplet species detected via transient absorption experiments – the correlated triplet pair and the independent triplets with lifetime of 6 μs.[63–65] (iv) A decay lifetime different from that of the S_1 species (4.7 ns), attributed to the double triplet species. (v) Thermodynamic viability − $E(S_1) \geq 2 \times E(T_1)$. (vi) Kinetic feasibility allowed by the energetic accessibility of the double triplet state from the S_1 state − the rate is given as: $r \approx e^{-const.(ES_1 - E^1TT)}$.[21] Our findings thus suggest that iSEF takes place in the flexible−bridged **β** trimer. *As an important result of our study, we demonstrate that the rotational flexibility of the linker, as in the β trimer compound, is*

necessary to activate multiexciton triplet generation in multichromophoric PDIs. Our findings constitute a significant progress in structure−property relationships and may drive future design of extremely efficient iSEF materials.
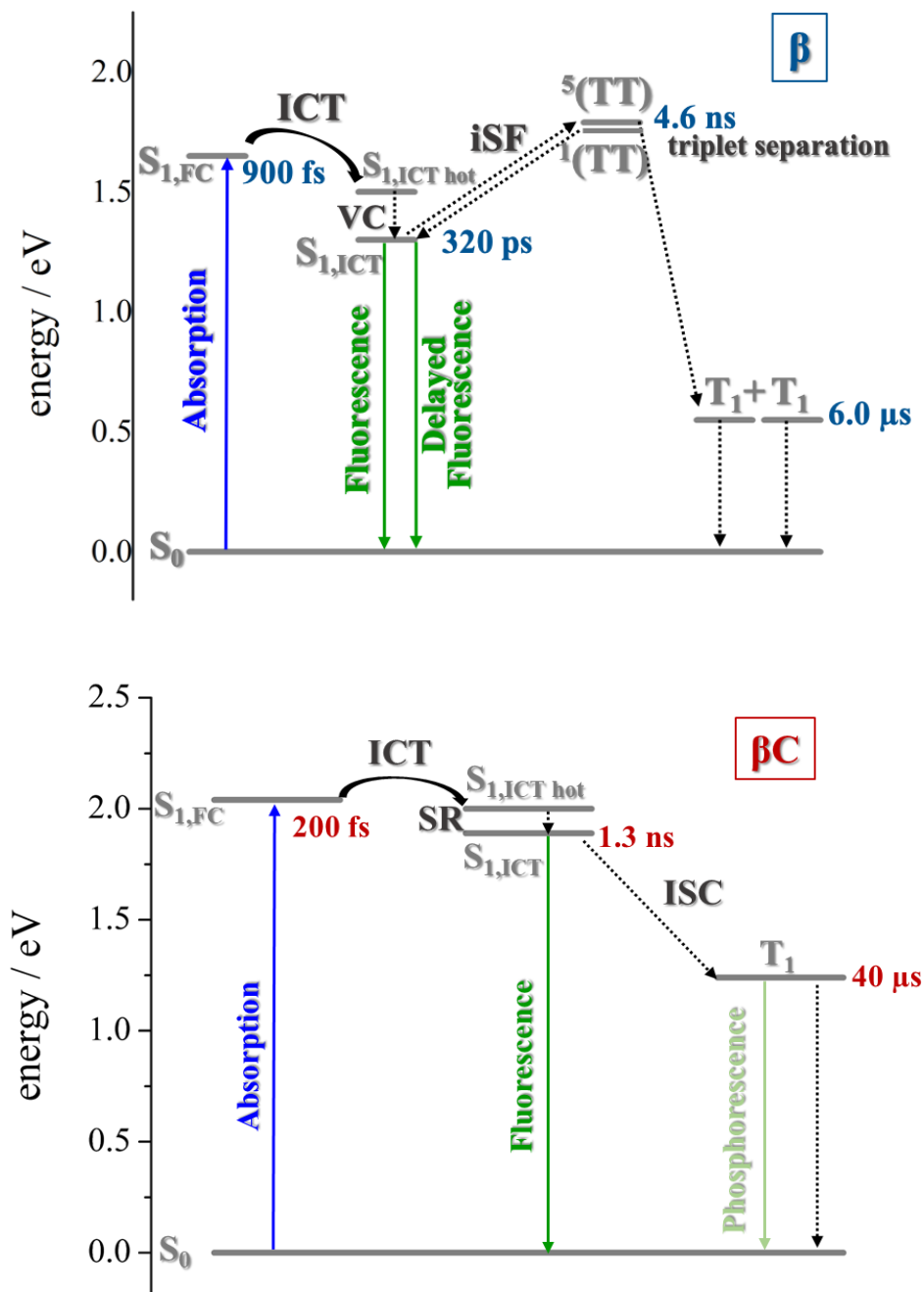
Scheme 3.2 Sketch of the proposed excited state deactivations based on the excited state energies predicted via quantum simulations and the excited state dynamics observed via time resolved spectroscopic experiments.

To gain a deeper insight into the thermodynamics of multiexciton generation, we obtained all the relevant enthalpic and entropic quantities for the trimers following an approach proposed by Krylov et al.[21,66] Multiexciton generation was considered to occur in two steps: a first step proceeding from the excited singlet to the double triplet state (from S_1 to ^1TT) and a second step leading to triplet separation (from ^1TT to T_1). The total enthalpy and entropy change were evaluated as the sum of the changes observed in the two steps. Detailed results are reported in **Table 3.11**. The SEF process is indeed exothermic for the **β** twisted compound ($\Delta H_{TOT} = -0.20 eV$) and endothermic for the **βC** planar trimer($\Delta H_{TOT} = +0.59 eV$). In the literature about iSEF in covalently linked dimers, only enthalpy has been considered in describing their thermodynamics. This is because covalently linked dimers can accommodate just one correlated triplet pair, hence no entropic contribution. However, for trimeric structures the role of entropy should be considered. In a covalently linked trimer, like those investigated here, the double triplet has three possible accommodations on two of its three PDIs; and in particular two equivalent accommodations on each pair of adjacent PDIs owing to molecular symmetry. In principle, the trimeric structure allows entropic gain to play a significant role in the SEF thermodynamics, as literature studies have reported for solid state films[8,66] and very recently for oligomers.[55] The quantum chemical simulations indeed showed the presence of three multiexcitonic states. For **β**, the two ^1TT accommodated on adjacent PDIs of the structure, as well as that on the left−most and right−most PDI units, are energetically accessible from S_1. The *high triplet yield and fast iSEF rate observed in β is not only due to the enthalpic viability but also to the entropic gain ($T\Delta S_{TOT} = +0.028 eV$) allowed by its trimeric structure.* This leads to a negative total change in Gibbs energy for **β** ($\Delta G_{TOT} = -0.228 eV$), confirming the iSEF thermodynamic feasibility. On the other hand, for **βC**, the lowest energy ^1TT state is the one for which the triplet excitons reside on the left−most

and right−most PDI units whereas the two ^{1}TT states allowing for an entropic gain are enthalpically inaccessible from S_1. This leads to no entropic contribution, and since the total change in Gibbs energy is positive ($\Delta G_{TOT} = +0.59 eV$), iSEF is not thermodynamically feasible for the planar **βC** trimer.

While strong coupling among the PDI chromophores can be inferred for the planar **βC** trimer, for the twisted **β** compound, weak coupling is observed because the singlet electron NTOs are localized on a single PDI unit. *We suggest that the poor electronic communication among the PDI chromophores caused by the rotatable linker is crucial in permitting efficient iSEF. Our results demonstrate that the single−bond connections capable of weakening the coupling between the chromophores favor high iSEF yield.* The fused ring connections induce strong coupling among the PDI units, as the singlet electron NTOs are delocalized over the planar trimer structure, and inhibit SEF completely. This is due to competition with other ultrafast processes in the planar system, such as intramolecular charge transfer.[26] The two−photon absorption (TPA) cross section − a measure of intramolecular charge transfer character − is indeed enhanced by over one order of magnitude for the planar **βC** (ca. 300 GM) with respect to the twisted **β** compound (ca. 10 GM). Quantum chemical simulations confirm the higher degree of charge transfer in the excited state for **βC** (0.80 e$^-$) relative to **β** (0.74 e$^-$) by dividing their structure into 5 subunits of PDI acceptor and BDT donor fragments. Weak coupling among the PDI units is crucial not only for multiexciton generation but also for triplet separation. The rate of triplet separation is indeed given as: $r \approx e^{-const.(E^5TT-E^1TT)}$ by Krylov et al.[21] For the twisted **β** compound, the ^{1}TT states are nearly degenerate with their corresponding ^{5}TT states, giving inter–triplet interaction energies (E^5TT$-E^1$TT) as 0.006 eV. This result suggests that the interaction between two triplets in **β** is indeed small, and two entangled triplets can thus easily be separated into two independent triplets.

However, in **βC**, the inter–triplet interaction energies increase by one order of magnitude, up to 0.066 eV. For the **β** trimer, the long−lived independent triplets are experimentally observed following their separation, and each of them is localized on a single PDI unit, as shown by the theoretical calculations. Compared to other SEF rylene derivatives reported in the literature,[19,49,52] the **β** trimer shows a much longer triplet lifetime. This is highly beneficial for its use in solar energy conversion devices, allowing efficient extraction of multiple charge carriers per incident photon.[67]

3.6 Conclusions

Here, we report a comparative study between rigid−bridged (planar) and flexible−bridged (twisted) perylene diimide trimer systems to highlight the role of the π−bridge linker in activating intramolecular singlet exciton fission. We show via time resolved spectroscopic measurements how a slight structural variation of the π−bridge of multichromophoric perylene diimide (PDI) systems strongly affects the triplet yield and triplet formation rate. Triplet formation proceeds via conventional intersystem crossing for the planar trimer as evidenced by its triplet yield of 16 % and triplet production in the nanosecond timescale. On the other hand, we find clear evidence of highly efficient (170 %) and fast (few hundred picoseconds) intramolecular singlet exciton fission taking place in the twisted trimer. A fused ring connection induces strong coupling among the PDI units as in the planar system and this inhibits singlet exciton fission completely due to a strong competition with other ultrafast processes, such as intramolecular charge transfer. Our results demonstrate that a rotatable π−bridge, capable of lowering the coupling between the chromophores, is necessary to activate intramolecular singlet exciton fission in multichromophoric systems. The quantum chemical simulations prove that the entropic gain allowed by multiple possibilities of accommodating the correlated triplet pair on adjacent PDIs in the twisted trimer is a crucial determinant for multiexciton triplet generation. Successive multiexciton triplet separation

occurs in the flexible−bridged PDI due to weak coupling among the units, and degenerate double triplet and quintet states.

3.7 Supporting Information

3.7.1 Experimental Section

Materials, Synthesis and Characterization. The trimer structures were synthesized according to the synthetic route described in Chart 1. All of the chemicals were purchased from Aldrich. All reagents purchased commercially were used without further purification except for toluene and tetrahydrofuran (THF), which were dried over sodium/benzophenone. ^{1}H NMR and ^{13}C NMR spectra were recorded on a Bruker DRX–500 spectrometer with tetramethylsilane as an internal reference. High Resolution MALDI–TOF spectra were recorded on Bruker Solarix 9.4T. Compounds **β** and **βC** were synthesized according to the procedures developed in our lab.[68]

Synthesis of Compound β. To a round–bottom flask equipped with a condenser, **1** (311 mg, 0.37 mmol), **2** (170 mg, 0.41 mmol), **Pd₂(dba)₃** (34 mg, 0.04 mmol), and **P(o-MePh)₃** (45 mg, 0.14 mmol) were added. The system was evacuated and refilled with N_2 three times, then charged with toluene (50 mL). The reaction mixture was refluxed under N_2 for 8 h. Then, compound **3** (102 mg, 0.11 mmol), **Pd₂(dba)₃** (8.5 mg, 0.01 mmol), and **P(o-MePh)₃** (12 mg, 0.04 mmol) were added. The reaction mixture was refluxed under N_2 for another 8 h. After cooling to room temperature, the reaction mixture was concentrated under reduced pressure. The residue was purified by column chromatography with hexane and CH_2Cl_2 (1:1, v/v) as the eluent. Compound **β** was obtained as a red solid (292 mg, 25.4% yield). ^{1}H NMR (CDCl₃): δ 8.87 (m, 4H), 8.70-8.65 (m, 8H), 8.35 (s, 4H), 8.23 (m, 4H), 7.77 (s, 2H), 7.68 (s. 2H) 5.19 (m, 6H), 3.14 (s, 4H), 3.02 (s, 4H), 2.25 (m, 12H), 1.84 (m, 16H), 1.23 (m, 130H), 0.83 (m, 48H), 0.74 (m, 12H). ^{13}C NMR (CDCl₃): δ 144.4, 144.1, 139.6, 139.5, 137.9, 137.6, 134.2, 133.9, 133.9, 133.6, 130.1, 130.0, 129.9, 129.2, 129.1,

128.4, 128.1, 127.5, 123.7, 123.0, 122.6, 122.0, 54.7, 40.3, 38.4, 32.4, 31.8, 31.7, 29.3, 29.2, 28.9, 28.8, 27.0, 26.9, 23.0, 22.6, 22.6, 14.1, 14.1, 14.1, 14.0, 11.2, 11.1. MALDI-TOF: calcd. for $[C_{202}H_{256}N_6O_{12}S_3]$, 3085.9, found, 3085.018.

Synthesis of Compound βC. A solution of $FeCl_3$ (800 mg, 4.9 mmol) in 2 mL nitromethane was added dropwise to a stirred solution of compound **β** (170 mg, 0.55 mmol) in 10 mL CH_2Cl_2. The reaction was stirred with Ar. After stirring for 10 h at room temperature, 1 mL methanol was added to the solution. The solvent was evaporated under reduced pressure, and the crude product was filtered with silica gel with a large amount of $CHCl_3$ to yield the solid product (158 mg, 93%). ^{1}H NMR ($C_2D_2Cl_4$, ppm, 353 K): δ 10.54 (d, 2H), 10.39 (d, 2H), 9.99 (s, 2H), 9.93 (s, 2H), 9.35 (m, 4H), 9.08 (m, 4H), 5.48-5.21 (m, 6H), 4.13 (Br, 8H), 2.31-1.98 (br, 28H), 1.37-1.20 (m, 130H), 0.85-0.79 (m, 60H). ^{13}C NMR cannot be measured due to the aggregation issue. MALDI-TOF: calcd. for $[C_{202}H_{248}N_6O_{12}S_3]$, 3077.8, found, 3077.9.

Steady−State Measurements. All of the measurements were performed at room temperature. Concentrations ranging from 1.6×10^{-6} to 1.6×10^{-4} M were used for the spectroscopic investigations. Absorption spectra were measured using an Agilent 8432 UV−visible absorption spectrophotometer. The emission spectrum measurements were performed with a Fluoromax−2 spectrofluorimeter. The fluorescence quantum yields of the samples were calculated using a known procedure[69,70] and Rhodamine B in ethanol (ϕ_F = 0.68)[71] was used as the standard.

Two−Photon Excited Fluorescence Measurements. Two−photon excited fluorescence measurements were performed using a Kapteyn Murnane (KM) mode−locked Ti:Sapphire laser tunable from 700 to 900 nm, and delivering 110 fs output pulses at a repetition rate of 80 MHz as described previously.[68,72,73] Emission scans were performed either at 820 or 875 nm excitation

while scanning the emission in the 400−850 nm range, but the exact emission detection wavelength during the power dependence scan was selected by the emission wavelength that produced the highest number of counts. Input power from the laser was varied using a variable neutral density filter. Two−photon power−dependent fluorescence intensity was utilized to determine the two−photon absorption cross section using the comparative method. Rhodamine B in ethanol was used as the standard (cross section 120 GM at 820 nm and 30 GM at 875 nm).[74]

Femtosecond Transient Absorption. An amplified laser (Spectra Physics Spitfire) with pulse duration of ~100 fs, repetition rate of 1 kHz, and power of 1 W was directed at a beam splitter to generate the pump (85%) and the probe beams (15%). The pump beam (~66 mJ per pulse) was generated from the second harmonic of the amplifier's output (~405 nm) using a BBO crystal in an optical parametric amplifier (Spectra Physics OPA-800CF) and was focused onto the sample cell (l = 2 mm) preceded by an optical chopper. The probe beam was passed through a computer−controlled delay line and focused onto a 2 mm sapphire plate to generate the white light continuum (Ultrafast Systems Inc.).[33,34] The white light was focused onto the sample and overlapped with the pump beam. The absorption difference (ΔA) of the signal was collected by a CCD detector (Ocean Optics). Data acquisition was performed with the software Helios by Ultrafast Systems Inc. The IRF was measured by the Raman scattering of water at 466 nm and is found to be 110 fs. Data analysis was performed with Surface Xplorer Pro and Glotaran softwares. All the experiments were performed in dilute solutions, at concentrations below 1×10^{-4} M.

Nanosecond Transient Absorption. The spectral properties and the lifetimes of long lived transient species were probed by transient absorption with nanosecond time resolution measurements.[75] These experiments were performed in dilute deaerated solutions, where

photodegradation was checked by recording UV−vis absorption spectra before and after each experiment. All the experiments were performed in dilute solutions, at concentrations below 7×10^{-5} M. An LP980 (Edinburgh) spectrometer system, with a monochromator and PMT for signal detection (PMT−LP), was coupled with a Spectra Physics QuantaRay Nd:YAG nanosecond pulsed laser and a GWU Optical Parametric Oscillator (OPO) tunable for the excitation source. Flash lamps excite the ND:YAG rod in the laser head containing a polarizer, pockel cell, and ¼ wave plate, producing Q-switched 1064 nm light. Two-stage harmonic generation then produces high energy 355 nm light used to pump the OPO. The OPO produces excitation source from 206 nm to 2600 nm employing second harmonic generation and sum-frequency mixing nonlinear processes. For this investigation, 415 nm, 441 nm and 510 nm excitation wavelengths were used to pump the samples and a pulsed xenon lamp white light continuum was used to probe the absorption properties of the produced excited states. Relative actinometry measurement,[76,77] using an optically matched solution of Tetracene ($\varphi_T = 0.62$ and $\varepsilon_T = 31200$ M^{-1} cm^{-1} at λ_T of 465 nm)[78] in chlorobenzene as reference, was used to compute the product of the triplet yield and triplet−triplet extinction coefficient ($\varphi_T \cdot \varepsilon_T$) of the samples. The same OD was maintained at 441 nm excitation λ for both reference and sample, hence generating equal concentration of singlets in both solutions. Then knowing that: $[singlet] = [triplet]/\phi_T$ and using Beer-Lambert's law: $[triplet] = \Delta A/l \cdot \varepsilon_T$ for both the sample and the reference, the product: $\varphi_T \cdot \varepsilon_T$ of the sample can be computed. To compute the triplet yield (φ_T), triplet–triplet absorption coefficients (ε_T) were determined by triplet energy transfer measurements[79–81] to and from Tetracene in cyclohexane. Tetracene ($E_T = 1.27$ eV) was employed as a triplet energy donor for β, but as an acceptor for **βC**, giving a qualitative hint about their triplet energies i.e. $E_T < 1.27$ eV for **β**, but $E_T > 1.27$ eV for **βC**. For computing ε_T successfully, in the donor + acceptor mixture, at the donor λ_T there has to be a

decrease in the triplet lifetime (i.e. higher decay rate) in comparison to its lifetime with only the donor in solution. Also, at the acceptor λ_T, a triplet concentration rise has to be observed. These observations thus confirm triplet energy transfer from a donor to an acceptor. Using the decay rate of the donor only (k_D) and the acceptor (k_A) alongside the rate of energy transfer (k_{ET}), the ΔA_A and ΔA_D, the ε_T of donor or acceptor can be evaluated knowing the ε_T of the other.

Two–Color Transmission Measurements of Triplet Yield. Femtosecond two-color transmission measurements were carried out using a tunable Mai Tai laser system (Spectra Physics) giving 130 fs pulses with a repetition rate of 80 MHz, tunable from 700 – 900 nm.[28] The light with wavelength of 850 nm plays the role of probe beam, and second harmonic generated (425 nm) light using a BBO crystal was used as the pump beam. To obtain the transmission profile, the excited state absorption at 850 nm was investigated with pump irradiation at 425 nm. The selected wavelength region is reasonable since there is negligible steady-state absorption at 850 nm for the investigated samples. A variable neutral density filter is placed to modulate the excitation power. The position of focusing lens is adjusted to place the focusing point on the sample. Blank chloroform solvent gives a reference line. A calibrated photodiode was used to measure the pump power. The transmitted power has been measured with a wide aperture power meter which is free of any thermal lensing effect.

Time−Resolved Fluorescence Measurements. Time−correlated single photon counting (TCSPC) technique, which has been described previously,[33] was used to study the long decay component of the investigated samples. The laser used for the TCSPC measurements was a home-built mode−locked Ti−sapphire laser with cavity dumper with repetition rate below 700 kHz. The output beam from the KM laser was at 800 nm wavelength, with a pulse duration of ca. 30 fs. The

output beam was frequency−doubled using a nonlinear barium borate crystal to obtain a 400 nm beam. A polarizer was used to vary the power of the 400 nm beam that excites the sample. Focus on the sample cell (quartz cuvette, 0.4 cm path length) was ensured using a lens of focal length 11.5 cm. Collection of fluorescence was carried out in a direction perpendicular to the incident beam into a monochromator, and the output from the monochromator was coupled to a photomultiplier tube, which converted the photons into counts.

The femtosecond−resolved fluorescence experiments were performed using an ultrafast fluorescence Up−Conversion setup that had previously been described.[34,82−84] Mode−locked Ti−Sapphire femtosecond laser (Spectra Physics Tsunami) was used to generate 80 fs pulses at 800 nm wavelength with a repetition rate of 82 MHz. This mode−locked laser was pumped by a 532 nm continuous light output from another laser (Spectra Physics Millennia), which has a gain medium of neodymium−doped yttrium vanadate ($Nd:YVO_4$). A 400 nm excitation pulse was generated by a second harmonic β−barium borate crystal, and the residual 800 nm beam was made to pass through a computer−controlled motorized optical delay line. The polarization of the excitation beam was controlled by a Berek compensator. The power of the excitation beam varied between 33 to 36 mW. The fluorescence emitted by the sample was up−converted by a nonlinear crystal of β−barium borate by using the residual 800 nm beam, which had been delayed by the optical delay line with a gate step of 6.25 fs. By this procedure, the fluorescence can be measured temporally. The monochromator is used to select the wavelength of the up−converted beam of interest, and the selected beam is detected by a photomultiplier tube (R152P, Hamamatsu, Hamamatsu City, Japan). The photomultiplier tube converts the detected beam into photon counts, which can be read from a computer. Coumarin 30 was used for calibrating the set up. The instrument response function (IRF) has been determined from the Raman signal of water to have

a width of 110 fs. Lifetimes of fluorescence decay were obtained by fitting the fluorescence decay profile to the most accurate fit. Mono and multi−exponential decay functions convoluted with IRF in MATLAB and Origin 8 were necessary for the data analysis.

Quantum Chemical Simulations. Theoretical investigation has been performed on molecular structures where the long alkyl chains are replaced by short chains (octyl and hexyl groups [C_6H_{13}, C_8H_{17}] attached to the PDI moieties and the BDT linker are replaced by hydrogen atoms and methyl groups, respectively) to save computational time without significant effect on the electronic properties. The ground state geometry of each compound was obtained by density functional theory (DFT). The B3LYP functional and the 6−31G* basis sets have been employed. Excited state simulations using time−dependent DFT (TD-DFT) were performed. The same functional and basis sets used in the ground state calculations, were employed for the geometry optimization of the first singlet excited state (S_1) and the first triplet excited state (T_1) in the gas phase. The geometries of S_1 were obtained with TD-DFT simulations. T_1 geometries could be obtained via two approaches: an unrestricted triplet calculation, and TD-DFT targeting a triplet state. In this study, TD-DFT triplet geometry optimization was conducted for consistency with the S_1 geometries. Single−point energy calculations to evaluate the electronic property were performed using the system−dependent, nonempirically tuned version of long−range corrected functional ωB97X−D[85,86] which is known to significantly improve the charge delocalization problem in conventional DFT functionals and 6−31G* basis sets. The ω value is tuned to minimize the square sum of the difference between HOMO energy (ε_{HOMO}) and ionization potential (*IP*), and LUMO energy (ε_{LUMO}) and electron affinity (*EA*), $(\varepsilon_{HOMO}+IP)^2+(\varepsilon_{LUMO}+EA)^2$. The ω value is significantly affected by the environment,[87] and inclusion of the solvent (chloroform) dielectric field induces a reduced ω value. The optimal ω values of **β** and **βC** are 0.004 and 0.003,

respectively. The medium effect was included using polarizable continuum model with the dielectric constant of 4.31 for chloroform. Characters of excitations were described with natural transition orbitals (NTOs). The driving force of singlet fission – the energy difference between $E(S_1)$ and $2\times E(T_1)$, $\Delta E_{S-2\times T}$ – was estimated with the same computational details mentioned above. S_1 and T_1 energies should be calculated at the optimized states since the vibrational relaxation is much faster than SF process. Recently, Krylov et al. pointed out the importance of ^{1}(TT) energy in predicting feasibility of SF and relevant kinetics.[21] Restricted active space with double spin-flip (RAS-2SF) has successfully provided the energetics of SF-relevant states in a number of studies.[12,61,66,88–92] While the RAS-2SF approach works well for dichromophoric systems, **β** and **βC** trimeric compounds require one additional spin-flip to locate all available multiexcitonic states distributed over three chromophores. In this study, we employed a high spin restricted open Hartree-Fock septet reference state. The orbital space of interest was divided into three parts: RAS1, RAS2 and RAS3. Two subspaces, RAS1 and RAS3, correspond to fully occupied, and virtual spaces, respectively. Six singly occupied orbitals were considered in the RAS2 active space. Core inactive occupied orbitals and 1200 virtual orbitals were kept frozen to enable RAS-3SF calculation for such large chromophores. The localized frontier orbitals were obtained using RAS-3SF method via Pipek-Mezey localization scheme with Q-Chem 4.0.[93] Energies of multiexciton state were estimated at the S_1 geometries obtained by the TD-DFT calculation described above. Details on the procedure of intersystem crossing calculations are provided in Supporting Information. All the quantum chemical simulations were conducted using Q−Chem 5.0.

Device fabrication and characterization. Polymer PTB7−Th was obtained from *1−Material*. Chlorobenzene and 1,8−diiodooctane for active layer solution preparation were obtained from Sigma-Aldrich. For ZnO preparation using sol−gel approach, we used $Zn(CH_3COO)_2 \cdot 2H_2O$, 2-

methoxyethanol and 2-aminoethanol, all purchased from Sigma−Aldrich. Chloroform and cyclohexane from Sigma−Aldrich were used as solvents for the spectral and photophysical characterization. All chemicals were used as obtained from the manufacturer without further purification. Devices were fabricated in inverted configuration consisting of ITO/ZnO/active layer/MoO$_3$/Ag. ITO substrates, obtained from Thin Film Devices Inc., were ultrasonicated in chloroform, acetone and isopropanol for 15 min and then treated with UV−ozone for 30 min. Sol−gel solution of ZnO precursor, prepared following procedures described elsewhere, was added dropwise onto ITO substrates through PTFE syringe filter and spin coated at 4000 rpm for 40 seconds. Immediately after spin coating, substrates were annealed at 200^{0}C for 30 minutes in air. Active layer components were dissolved in chlorobenzene overnight at 70^{0}C and solution at room temperature was spin coated onto the substrates in a glovebox. Films were immediately transferred to a vacuum chamber and MoO$_3$ (8 nm) and Ag (80 nm) were thermally evaporated under the pressure lower than $2 \cdot 10^{-6}$ Torr.

J−V curves of the devices were measured with Keithley 2420 source meter unit. Devices were tested under 1 sun conditions (AM1.5G, 100 mW/cm^2) using xenon lamp (Oriel 69920) intensity of which was calibrated with a standard NREL certified Si cell (Newport, 91150V). Masks with a well−defined area of 3.14 mm^2 were used to define an active area of the device.

3.7.2 Steady–State and Two–Photon Absorption Measurements [S.I.]
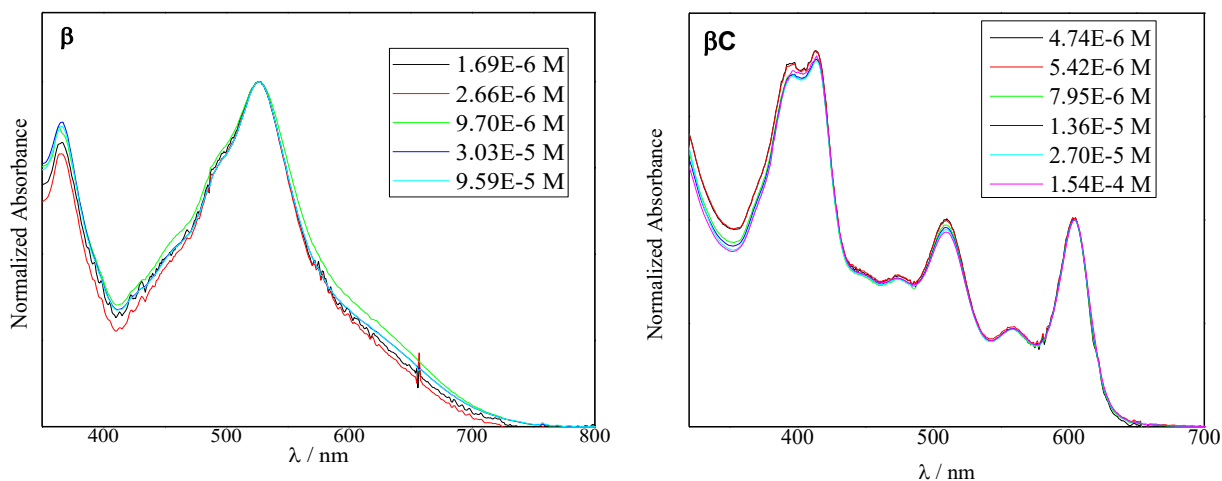
Figure 3.11 Concentration effect on the absorption spectra of the Trimers in chloroform.
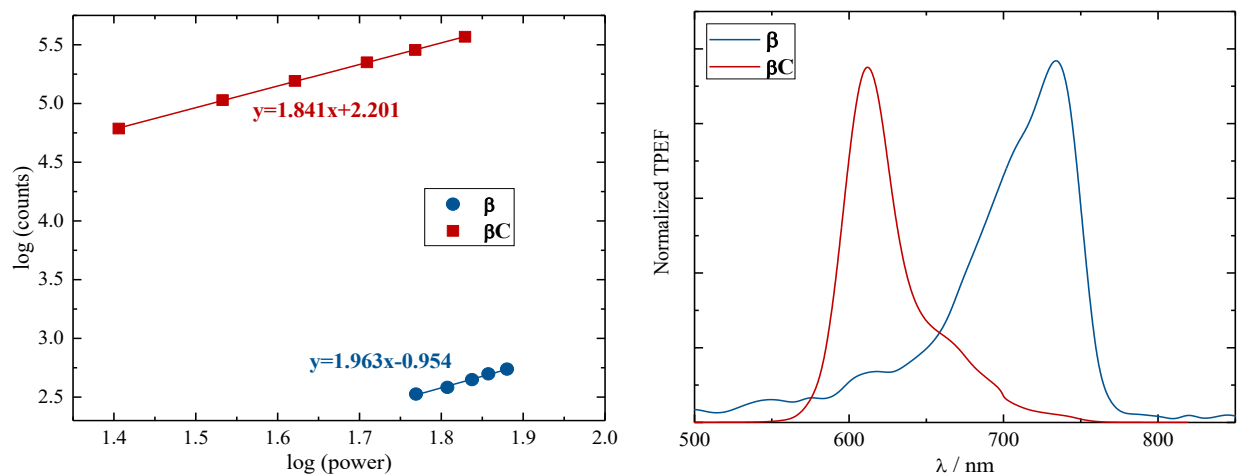
Figure 3.12 Power dependence of the two–photon excited emission (left) and two–photon emission spectra (right) for the Trimers in chloroform upon 820 nm excitation.

Table 3.3 Change in atomic charge from S_0 to S_1 on the subunits of compound **β** and **βC**.[a]

	β					βC				
	A	D	A	D	A	A	D	A	D	A
Absorption[b]	−0.07	+0.50	−0.66	+0.27	−0.03	−0.19	+0.32	−0.25	+0.32	−0.19
Emission[c]	+0.07	+0.64	**−0.74**	+0.03	0.00	**−0.79**	+0.61	+0.10	+0.08	**−0.01**

[a] Mulliken charge is given in e^-; [b]Calculated at S_0 geometry; [c]Calculated at S_1 geometry

3.7.3 Femtosecond Transient Absorption (fsTA) [S.I.]

Table 3.4 Lifetimes (τ) obtained by global fitting of the femtosecond Transient Absorption data in chloroform.

Compound	τ_1 / ps	τ_2 / ps	τ_3 / ps	τ_4 / ps
β	0.18	7.4	320	Rest
βC	0.14	33	1300	Rest
assignment	*Solv. / ICT*	*VC/SR*	*S_1*	*T*
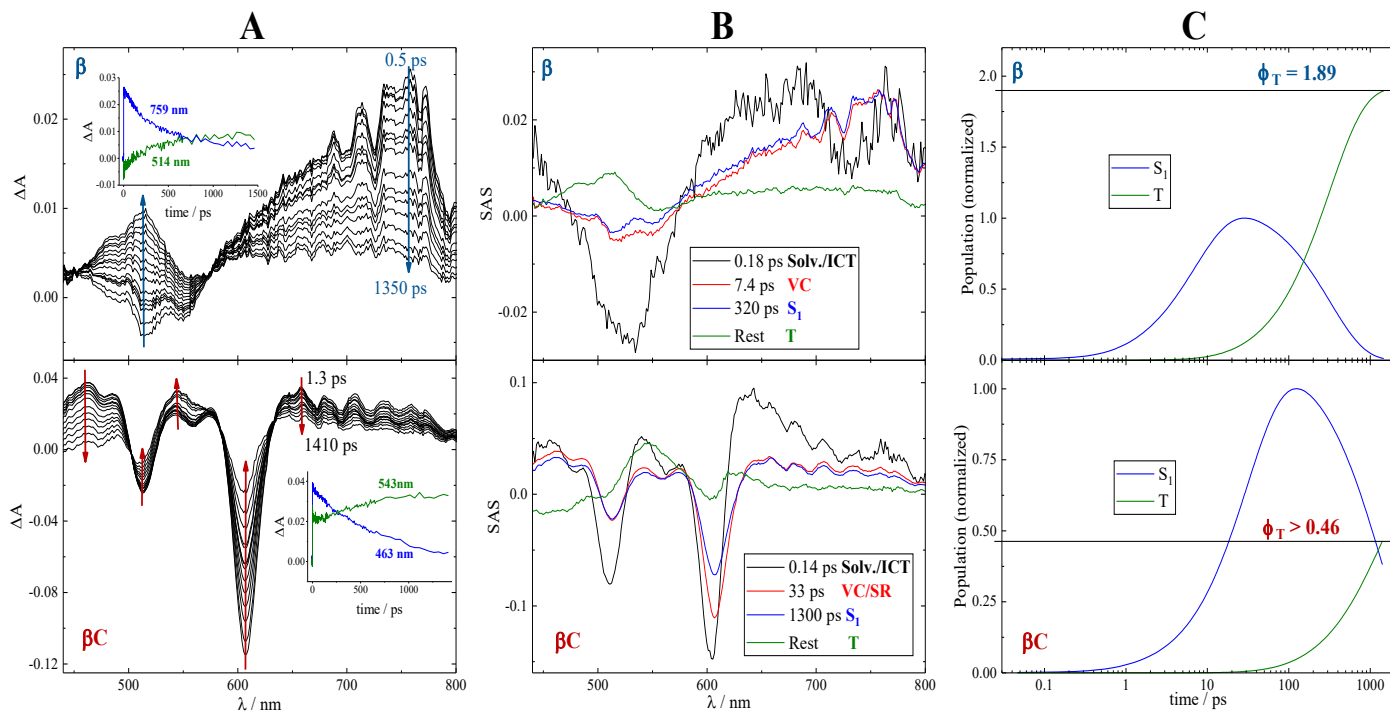
Figure 3.13 A) Time−resolved spectra and kinetics (inset) obtained by femtosecond TA for the Trimers in chloroform. B) Species Associated Spectra and lifetimes obtained by global fitting the TA data. C) Population dynamics of the excited singlet and triplet states.

3.7.4 Triplet Yield Calculation from fsTA [S.I.]

Triplet yield was evaluated from the temporal dynamics of the lowest excited singlet and triplet state populations, as obtained through analysis of the femtosecond transient absorption data, according to a procedure already described in the literature, and here detailed for the trimer samples.[25,49]

Global Fitting of the femtosecond transient absorption data was carried out using the Glotaran software which provided us with the Species Associated Spectra of the four exponential components (assignments and lifetimes described in **Table 3.4**) and their temporal composition (**Figure 3.14**).
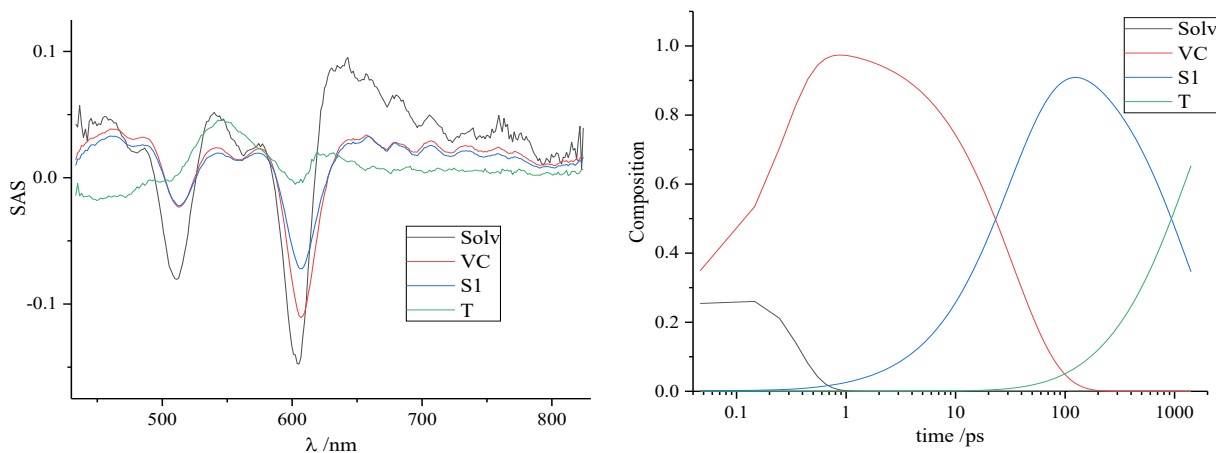
Figure 3.14 Species Associated Spectra (left) and composition in time (right) of the four exponential components resulting from global fitting of the femtosecond transient absorption data of **βC** in chloroform.

To obtain the spectral shapes of the excited singlet and triplet states, the transient spectra at time delays of 129 and 1413 ps were selected, respectively (**Figure 3.15**). At these time delays, the singlet and triplet species were at the maximum in the fsTA data (**Figure 3.14**).
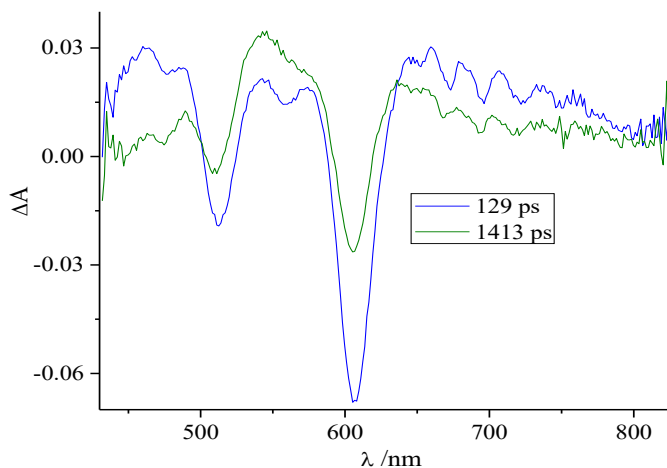
Figure 3.15 Transient absorption spectra at 129 and 1413 ps delay recorded for **βC** in chloroform.

The spectra of the lowest singlet and triplet excited states must be related through the GSB they share in common. The ground state absorption spectrum was scaled and subtracted from the 129/1413 ps transient spectra in order to remove the GSB contribution. The ground state absorption spectrum was normalized to the transient absorption spectrum at the peak of the ground state bleaching, and then subtracted. The resulting spectra only show the S1/T1 ESA relative to a known amount of GSB (**Figure 3.16**).
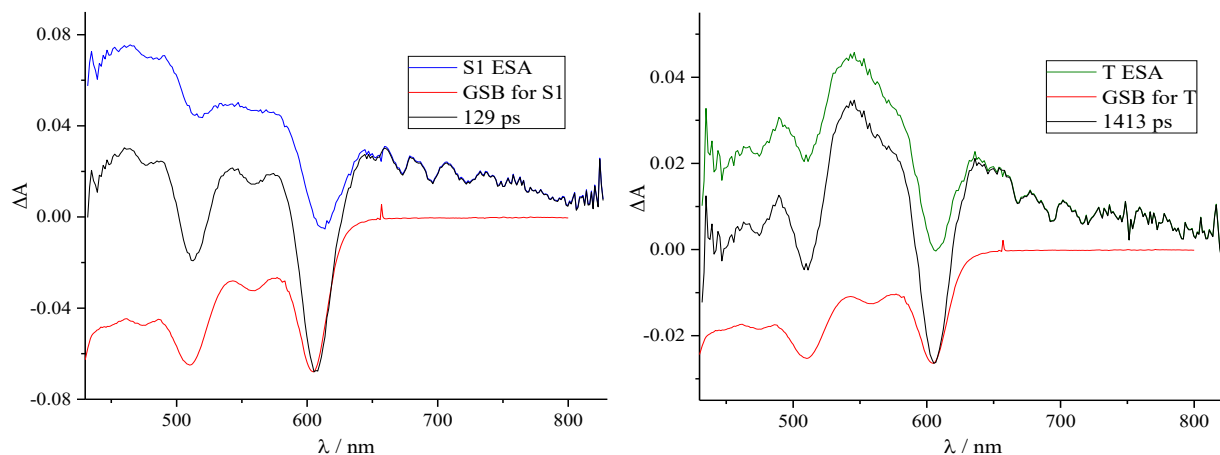
Figure 3.16 Transient (black) and steady state (red) absorption spectra used to reconstruct the absorption spectra of the excited singlet (blue, left) and triplet (green, right) states.

The S1 and T spectra are then normalized to the GSB they share, resulting in two spectra that are quantitatively related (**Figure 3.17**).
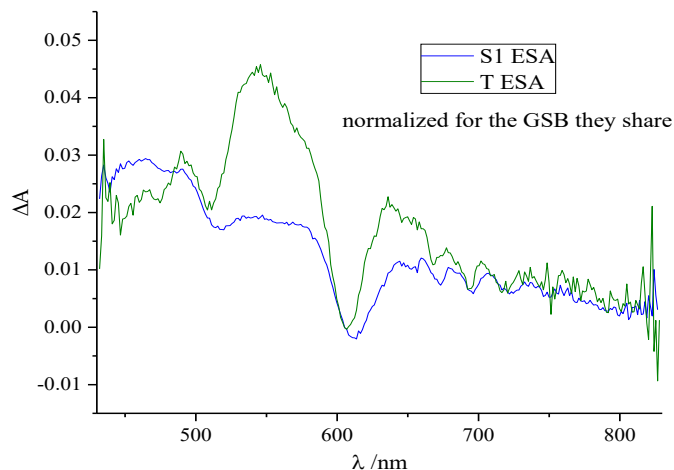
Figure 3.17 Excited state absorption spectra, normalized to GSB, used to correct composition profile in **Figure 3.14** and to obtain population dynamics in **Figure 3.18**.

The quantitatively related spectra of S1 and T were used to correct the composition profiles previously shown. The temporal composition of the components resulting from the global fitting reported in **Figure 3.14** is indeed related to the differential absorbance measured during the ultrafast absorption experiments. Therefore, according to the Lambert−Beer law, it is dependent on both the absorption ability and the concentration of S1 and T. From the quantitatively related S1 and T spectra reported in **Figure 3.17**, it is clear that the ratio between the triplet excited state absorption at its peak (0.0454 at 540 nm) and the singlet excited state absorption at its peak (0.0292 at 460 nm) is $\frac{\varepsilon_T}{\varepsilon_S} = 1.55$. By scaling the S1 and T temporal compositions in **Figure 3.21** for this factor (multiplying the singlet profile by 1.55), the correct concentration profiles were obtained: $\frac{c_S}{c_T} = \frac{\Delta A_S}{\Delta A_T} \times \frac{\varepsilon_T}{\varepsilon_S}$. From the population profiles normalized at the singlet population peak (**Figure 3.18**), a triplet quantum yield **higher than 46%** was estimated for **βC**.
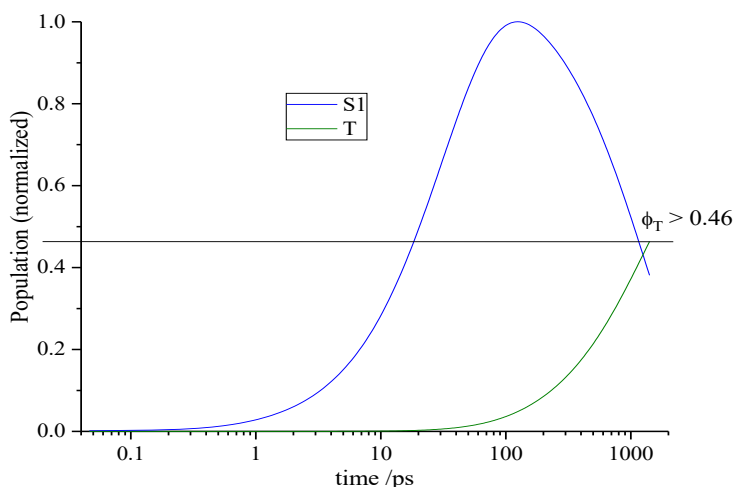
Figure 3.18 Population dynamics of the excited singlet and triplet states for **βC** in chloroform.

*Note: For **βC**, from the fs transient data we estimate a triplet yield somehow higher than that accurately measured by the ns sensitization experiments. However, all the methods agree in giving a triplet yield lower than 100 % for the **βC** compound, clearly suggesting a triplet production via conventional ISC.*

A similar procedure was employed to evaluate the triplet yield for **β**. Global Fitting revealed the presence of four exponential components whose Species Associated Spectra and composition in time are shown below in **Figure 3.19**.
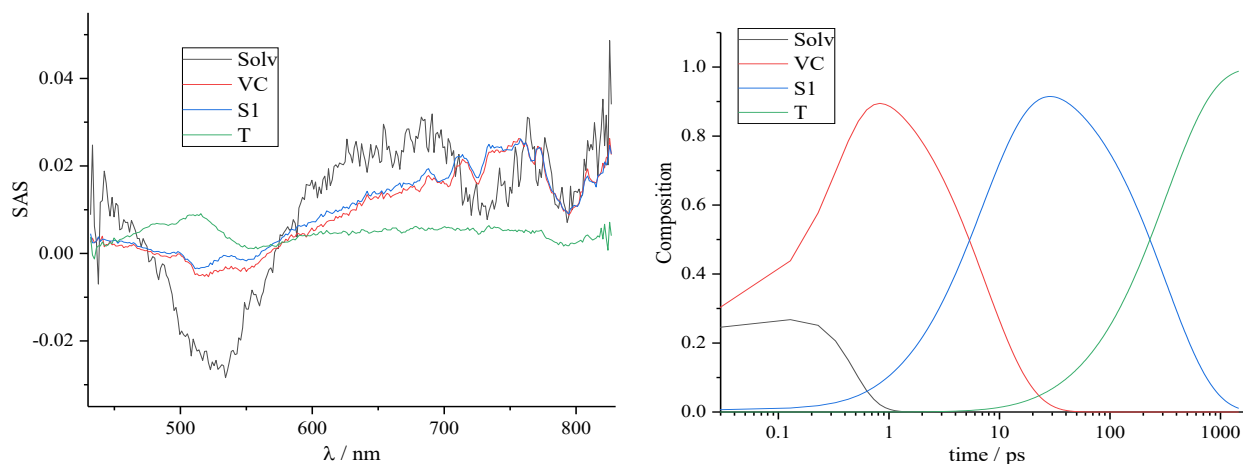
Figure 3.19 Species Associated Spectra (left) and composition in time (right) of the four exponential components resulting from global fitting of the femtosecond transient absorption data of β in chloroform.

Looking at the singlet and triplet composition profiles, transient spectra at time delays of 29 and 1165 ps were selected to obtain spectral shapes associated to the excited singlet and triplet state, respectively (**Figure 3.20**).
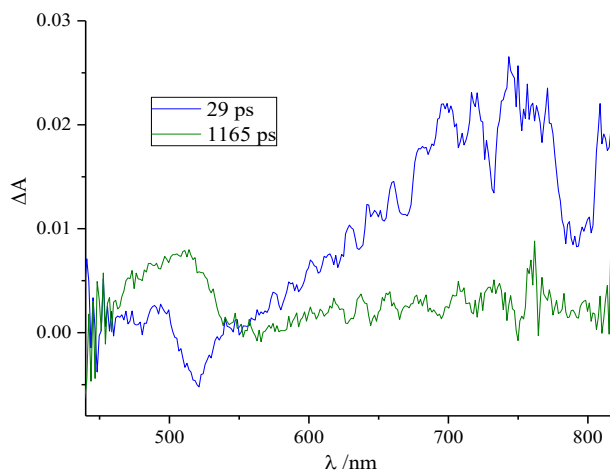
Figure 3.20 Transient absorption spectra at 29 and 1165 ps delay from excitation recorded for **β** in chloroform.

The ground state absorption spectrum was scaled and subtracted from the 29/1165 ps transient spectra in order to remove the GSB contribution (**Figure 3.21**). In this case the same amount of GSB was subtracted from both spectra because no clear negative band is exhibited by the transient spectrum at long delays. This is due to spectral overlap between the ground state and the triplet excited state absorption.
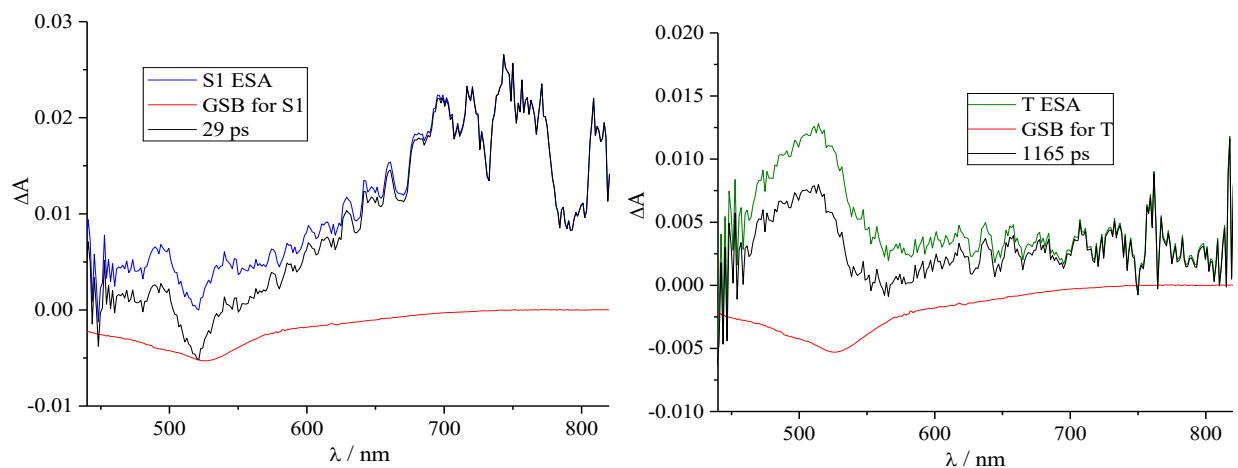
Figure 3.21 Transient (black) and steady state (red) absorption spectra used to reconstruct the absorption spectra of the excited singlet (blue, left) and triplet (green, right) states.
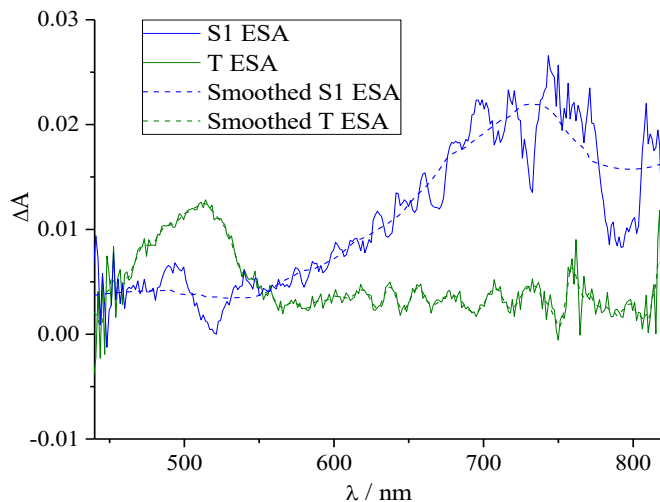
Figure 3.22 Excited state absorption spectra used to correct composition profile in **Figure 3.19** and to obtain population dynamics in **Figure 3.23**.

These spectra were used to correct the composition profiles shown in **Figure 3.19**. The ratio between the triplet excited state absorption at its peak (0.0125 at 510 nm) and the singlet excited

state absorption at its peak (0.0219 at 740 nm) is 0.571. The temporal population profiles for these excited states were thus obtained, by scaling the composition profiles in **Figure 3.19** using this factor (multiplying the singlet profile by 0.571). Population dynamics normalized at the singlet peak (**Figure 3.19**) demonstrates the formation of 1.89 triplets per initially excited singlet. A triplet quantum yield of **189%** was estimated for **β**.
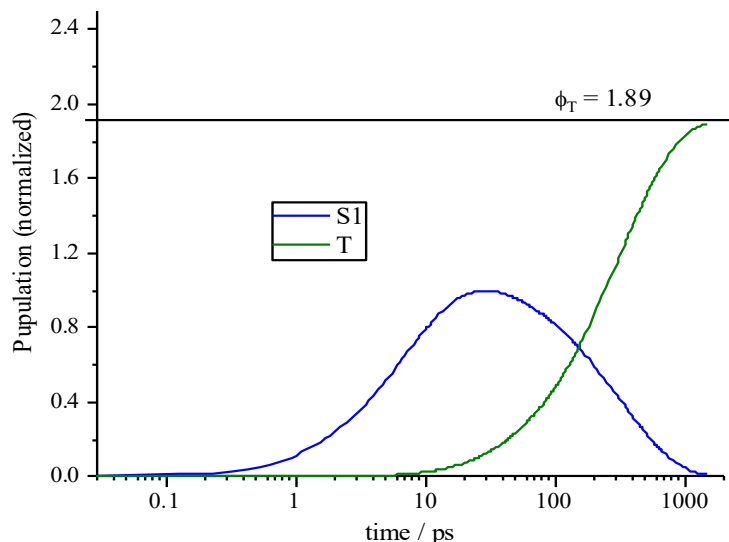
Figure 3.23 Population dynamics of the excited singlet and triplet states for **β** in chloroform.

3.7.5 Nanosecond Transient Absorption (nsTA) [S.I.]
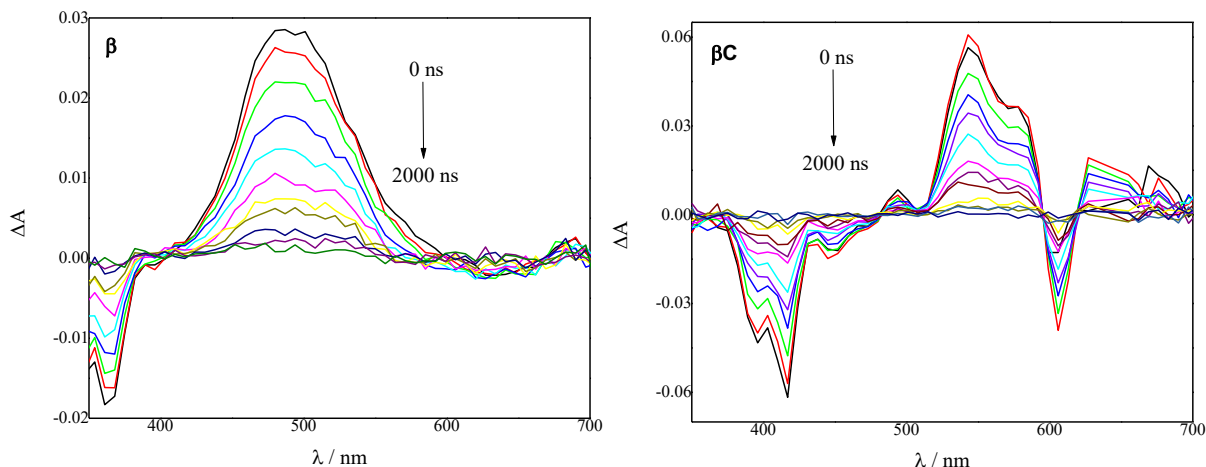
Figure 3.24 Time−resolved spectra obtained by nanosecond TA measurements for the Trimers in air-equilibrated chloroform upon 500 nm (for **β**) and 600 nm (for **βC**) laser excitations.
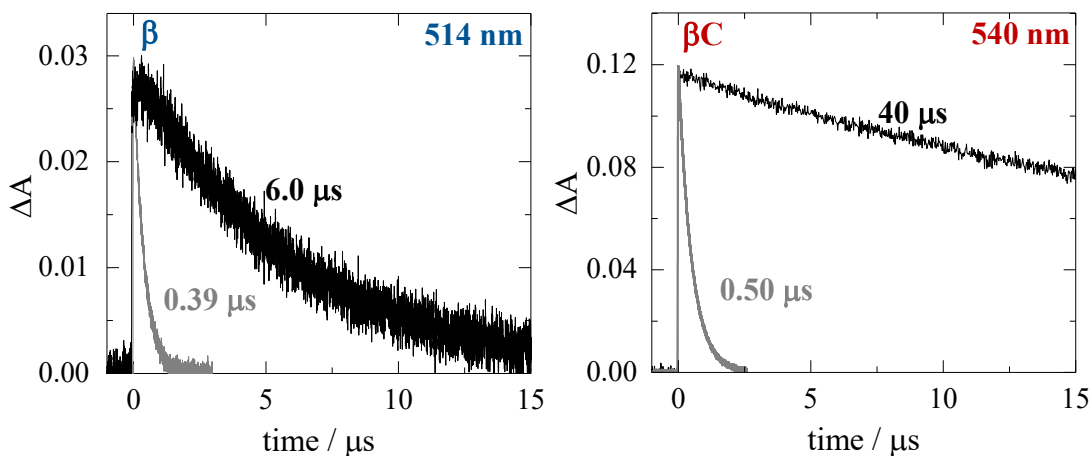
Figure 3.25 Kinetics of triplet species in air-equilibrated (gray) vs. deaerated (black) chloroform.

3.7.6 Triplet Sensitization Experiments by nsTA [S.I.]
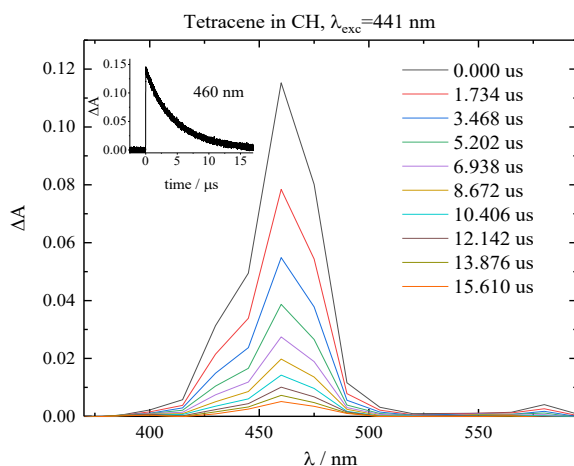
Figure 3.26 Transient absorption spectra of Tetracene in cyclohexane upon excitation at 441 nm.
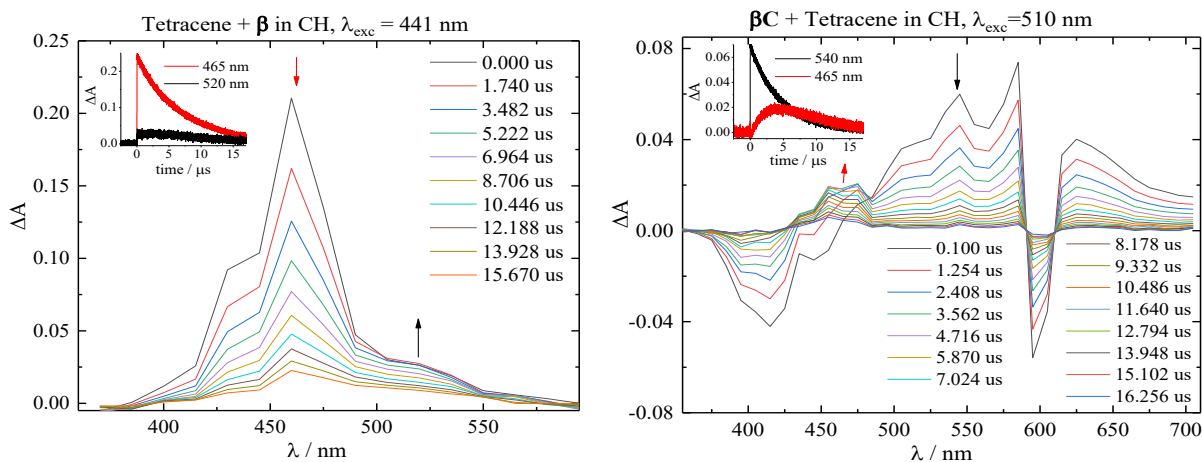
Figure 3.27 Transient absorption sensitization spectra of the Trimer compounds and Tetracene in cyclohexane, showing the triplet species decay of the donor and the rise of the acceptor (inset).

Triplet extinction coefficient of **β** was obtained by triplet energy transfer from Tetracene donor (E_T = 1.27 eV) to the **β** triplet energy acceptor (E_T << 1.27 eV). For **βC**, its triplet extinction coefficient was obtained by energy transfer to the Tetracene acceptor from **βC** acting as a triplet energy donor (E_T > 1.27 eV). Here, the employed procedures for the two trimer compounds are reported.

1) **Determination of the triplet extinction coefficient of β in cyclohexane (CH) at 520 nm by energy transfer from Tetracene (λ_{exc} = 441 nm)**[77,79–81]
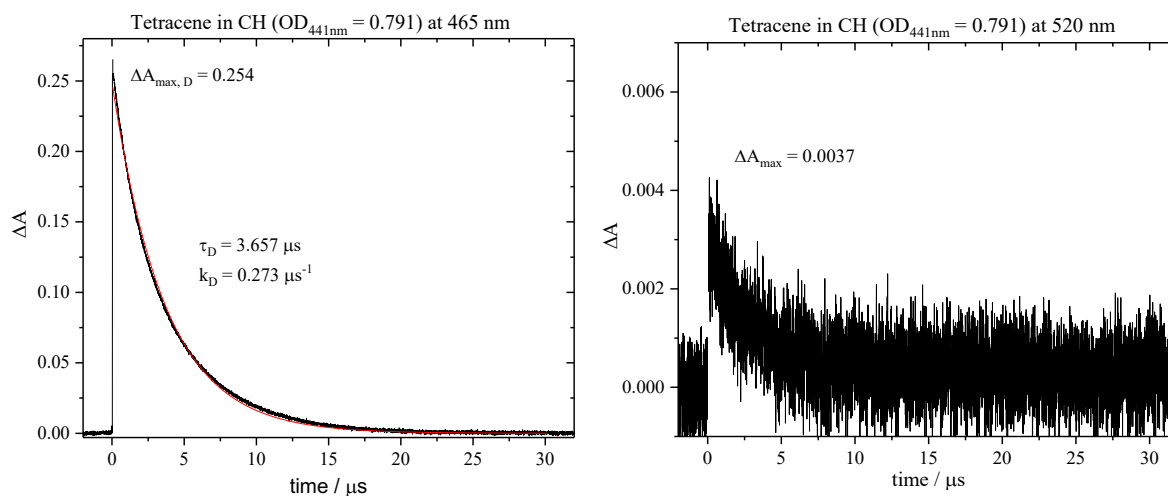
Figure 3.28 Kinetics recorded during nanosecond transient absorption measurements of Tetracene (donor) in cyclohexane upon laser excitation at 441 nm.
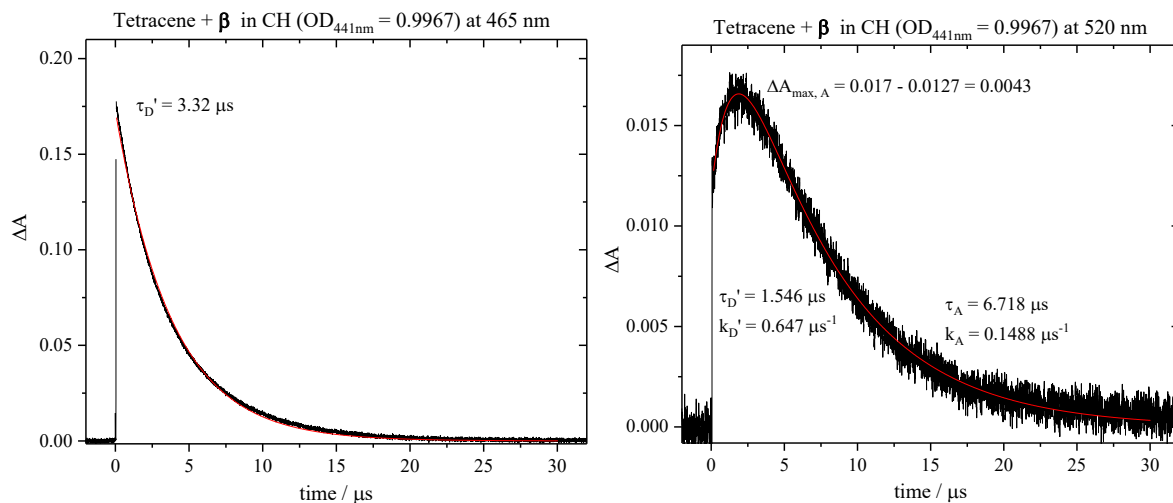
Figure 3.29 Kinetics recorded during nanosecond transient absorption measurements of **β** sensitized by Tetracene (quenched donor at 465 nm and sensitized acceptor at 520 nm) in cyclohexane upon laser excitation at 441 nm.

$$\varepsilon_A = \varepsilon_D \times \frac{\Delta A_{max,A}}{\Delta A_{max,D}} \times \frac{1}{f_D \times p_{ET} \times w}$$ **Equation 3.1**

$$\varepsilon_A = 31200 \; M^{-1}cm^{-1} \times \frac{0.0043}{0.254} \times \frac{1}{0.8514 \times 0.5773 \times 0.6446} = 1667 \; M^{-1}cm^{-1}$$

Where:

$f_D = \frac{A_D}{A_{D+A}} \times \left(\frac{1-10^{-A_{D+A}}}{1-10^{-A_D}} \right) = 0.8514$ is the fraction of light absorbed by the donor

$p_{ET} = \frac{k_D'-k_D}{k_D'} = 0.5773$ is the energy transfer probability

$w = exp\left[-\frac{\ln\left(\frac{k_D'}{k_A}\right)}{\frac{k_D'}{k_A}-1} \right] = 0.6446$ factor accounting for the quenched donor and acceptor lifetimes

where,

ε_A = triplet-triplet extinction coefficient of the acceptor (UNKNOWN)

ε_D = triplet-triplet extinction coefficient of the donor/sensitizer (KNOWN)

$\Delta A_{max,A}$ = maximum absorbance change of the Acceptor in the "Donor + Acceptor" mixture

$\Delta A_{max,D}$ = maximum absorbance change of the Donor/sensitizer **alone**

f_D = fraction of light absorbed by the Donor/sensitizer in the "Donor + Acceptor" mixture w.r.t. the Donor alone

k_D' = rise rate constant of the Acceptor in the "Sensitizer + Acceptor" mixture (should be similar to the quenched Sensitizer decay rate constant)

k_D = decay rate constant of the Donor ONLY

k_A = decay rate constant of the Acceptor in the "Donor + Acceptor" mixture

*Note: In estimating k_D', ideally (in the absence of any spectral overlap) the decay rate constant of the quenched Donor (at 465 nm) should match the rise rate constant of the Acceptor (at 520 nm).[80] This was not the case here for the **β** compound as there is an overlap of its triplet spectrum and that of the tetracene Donor such that at 465 nm both the Donor and the Acceptor contribute to the decay rate constant (see **Figures 3.4** and **3.26**). For this reason, we decided to set k_D' as the rise rate constant of the Acceptor because at 520 nm only the **β** compound triplet shows an absorption.*

To Calculate the Triplet Quantum Yield.

Relative Actinometry approach was used.[76] This was done using the computed triplet extinction coefficient from the energy transfer measurement. Tetracene, with its known ε_T and ϕ_T,

was used as a reference compound (ref.). In order to obtain the ΔA of both sample and reference, the ground state absorption (i.e. OD) of both sample and reference has to be the same at the excitation wavelength (441 nm).

$$\frac{[\phi_T \varepsilon_T]_{sample\ (\beta)}}{[\phi_T \varepsilon_T]_{ref.}} = \frac{[\Delta A]_{sample\ (\beta)}}{[\Delta A]_{ref.}} \qquad \textbf{Equation 3.2}$$

$$[\phi_T \varepsilon_T]_{sample\ (\beta)} = [\phi_T \varepsilon_T]_{ref.} \times \frac{[\Delta A]_{sample\ (\beta)}}{[\Delta A]_{ref.}} = (0.62 \cdot 31200 M^{-1}cm^{-1}) \times \frac{0.0527}{0.366}$$

$$= 2785\ M^{-1}cm^{-1}$$

where,

$\varepsilon_{T\ sample\ (\beta)}$ = triplet-triplet extinction coefficient of the **β** sample (computed using *energy transfer measurements*)

$\phi_{T\ sample\ (\beta)}$ = triplet quantum yield of the sample **β**

$[\Delta A]_{sample\ (\beta)}$ = change in absorption of the sample **β** (whose OD is similar to that of the reference at $\lambda_{\text{excitation}}$)

$[\Delta A]_{ref}$ = change in absorption of the reference compd. (whose OD is similar to that of the sample at $\lambda_{\text{excitation}}$)

Table 3.5 Summary of the parameters recorded for the two triplet energy transfer measurements performed for **β** in CH to ensure reproducibility. Tetracene used as a triplet energy donor.

Parameters	Measurement 1	Measurement 2
$\varepsilon_D(\textbf{\textit{Donor}})$	31200 $M^{-1}cm^{-1}$ (Tetracene)	31200 $M^{-1}cm^{-1}$ (Tetracene)
ΔA_A	0.0043	0.005
ΔA_D	0.254	0.170
f_D	0.8514	0.746
k_D	0.273 µs⁻¹	0.175 µs⁻¹
$k'_D = k_D + k_{ET}[A]$	0.647 µs⁻¹	1.919 µs⁻¹
k_A	0.149 µs⁻¹	0.109 µs⁻¹
$\varepsilon_A = \varepsilon_{T\ sample\ (\beta)}$	1667 $M^{-1}cm^{-1}$	1607 $M^{-1}cm^{-1}$
$[\varepsilon_T \cdot \phi_T]_{sample\ (\beta)}$ (Rel. Actinom. meas.)	2785 $M^{-1}cm^{-1}$	2785 $M^{-1}cm^{-1}$
$\phi_{T\ sample\ (\beta)}$	**1.67**	**1.73**

Taking an **average** of these two measurements, the triplet yield was evaluated to be: ~ **1.70**

2) **Determination of the triplet extinction coefficient of βC in cyclohexane (CH) at 540 nm by energy transfer to Tetracene (λ_{exc}=510 nm)**

$$\varepsilon_D = \varepsilon_A \times \frac{\Delta A_{max,D}}{\Delta A_{max,A}} \times f_D \times p_{ET} \times w \qquad \textbf{Equation 3.3}$$

$$\varepsilon_D = 31200 \, M^{-1}cm^{-1} \times \frac{0.0814}{0.0183} \times 0.9985 \times 0.5594 \times 0.4652 = 36061 \, M^{-1}cm^{-1}$$

where:

$f_D = \frac{A_D}{A_{D+A}} \times \left(\frac{1-10^{-A_{D+A}}}{1-10^{-A_D}}\right) = 0.9985$ is the fraction of light absorbed by the donor

$p_{ET} = \frac{k'_D - k_D}{k'_D} = 0.5594$ is the energy transfer probability

$w = exp\left[-\frac{\ln\left(\frac{k'_D}{k_A}\right)}{\frac{k'_D}{k_A}-1}\right] = 0.4652$ accounts for the quenched donor and acceptor lifetimes
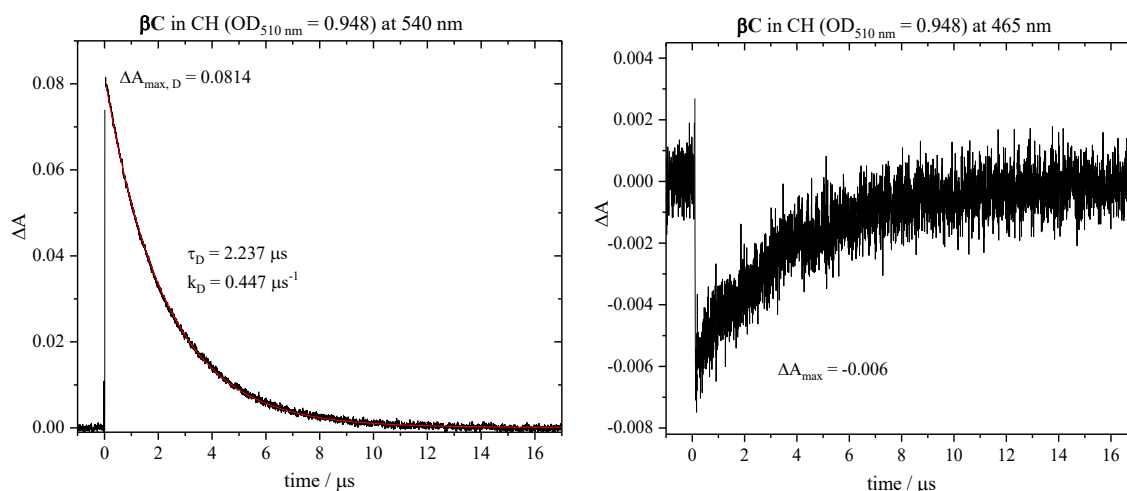
Figure 3.30 Kinetics recorded during nanosecond transient absorption measurements of **βC** (donor) in cyclohexane upon laser excitation at 510 nm.
It should be noted that the difference in the lifetime of **βC** *in comparison to that reported in* **Table 3.2** *is due to the different solvent employed here and to the different nitrogen purging conditions (time, flow rate, etc).*
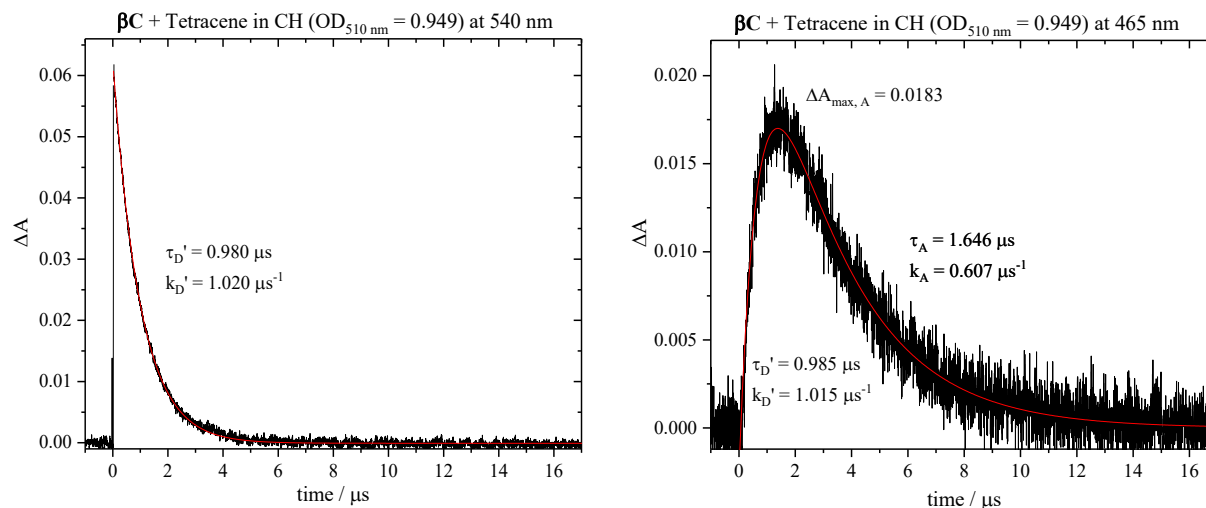
Figure 3.31 Kinetics recorded during nanosecond transient absorption measurements of Tetracene sensitized by **βC** (quenched donor at 540 nm and sensitized acceptor at 465 nm) in cyclohexane upon laser excitation at 510 nm.

The difference in the lifetime of Tetracene *in comparison to that reported in **Figure 3.26** is due to the non-consistent nitrogen purging conditions (time, flow rate, etc.).*

<u>Note</u>: *Here, in estimating k'_D, the decay rate constant of the quenched Donor (at 540 nm) matches the rise rate constant of the Acceptor (at 465 nm). This is because there is no overlap of the triplet absorption spectrum of the **βC** compound and that of the tetracene Acceptor (see **Figures 3.4**, **3.24** and **3.26**), unlike in the case of the **β** compound.*

$$\frac{[\phi_T \varepsilon_T]_{sample\,(\beta C)}}{[\phi_T \varepsilon_T]_{ref.}} = \frac{[\Delta A]_{sample(\beta C)}}{[\Delta A]_{ref.}}$$

$$[\phi_T \varepsilon_T]_{sample\,(\beta C)} = [\phi_T \varepsilon_T]_{ref.} \times \frac{[\Delta A]_{sample\,(\beta C)}}{[\Delta A]_{ref.}} = (0.62 \cdot 31200 M^{-1} cm^{-1}) \times \frac{0.125}{0.324}$$

$$= 7460 M^{-1} cm^{-1}$$

Table 3.6 Summary of the parameters recorded for the two triplet energy transfer measurements performed for **βC** in CH to ensure reproducibility. Tetracene is the triplet energy acceptor.

Parameters	Measurement 1	Measurement 2
ε_A (*Acceptor*)	$31200\,M^{-1}cm^{-1}$ (Tetracene)	$31200\,M^{-1}cm^{-1}$ (Tetracene)
ΔA_D	0.0814	0.086
ΔA_A	0.0183	0.012
f_D	0.9985	1
k_D	0.4470 μs^{-1}	0.2476 μs^{-1}

136

$k'_D = k_D + k_{ET}[A]$	1.0145 µs⁻¹	0.7158 µs⁻¹
k_A	0.6074 µs⁻¹	0.4063 µs⁻¹
$\varepsilon_D = \varepsilon_{T\ sample\ (\beta C)}$	36061 $M^{-1}cm^{-1}$	69545 $M^{-1}cm^{-1}$
$[\varepsilon_T \cdot \phi_T]_{sample\ (\beta C)}$ (Rel. Actinom. Meas.)	7460 $M^{-1}cm^{-1}$	7460 $M^{-1}cm^{-1}$
$\phi_{T\ sample\ (\beta C)}$	**0.21**	**0.11**

Taking an **average** of these two measurements, the triplet yield was evaluated to be: ~ **0.16**

3.7.7 Fluorescence Upconversion [S.I.]
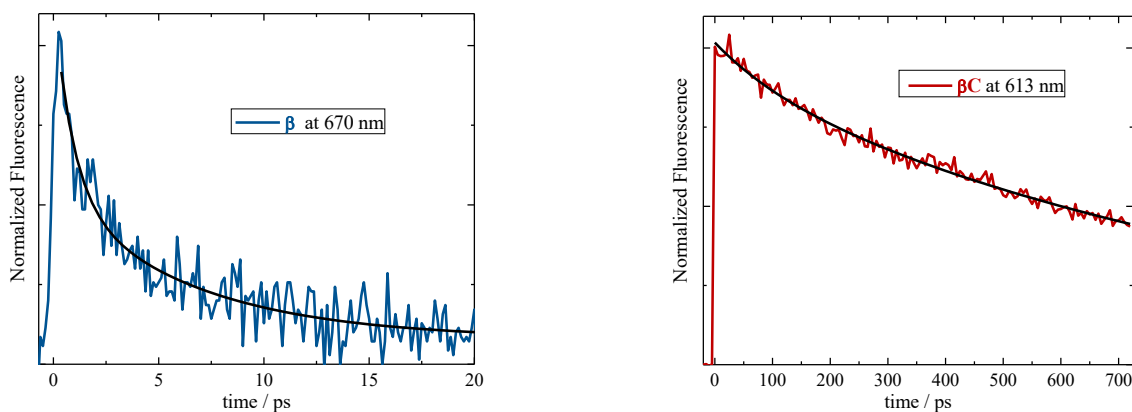
Figure 3.32 Fluorescence decay kinetics recorded for compounds **β** and **βC** in chloroform by femtosecond resolved FUC, together with their poly-exponential fittings (black).

Table 3.7 Lifetimes (τ) and pre-exponential factors (A) obtained by fitting the FUC kinetics.

Compound	$A_{FUC,1}$	$\tau_{FUC,1}$ / ps	$A_{FUC,2}$	$\tau_{FUC,2}$ / ps	$A_{FUC,3}$	$\tau_{FUC,3}$ / ps
β	0.60	1.0	0.46	6.0	–	–[b]
βC	−0.20[a]	0.20[a]	0.11	110	0.90	1000[c]
assignment		*Solv. / ICT*		*VC / SR*		*S₁*

[a]Rise time obtained from fitting of the fluorescence kinetics acquired on a 3 ps time window (see **Figure 3.33** left). [b]The fact that the third component (τ_3 in **Table 3.7**) is not revealed is likely due to acquisition at 670 nm, in the blue part of the emission spectrum, where time resolved red shift of the emission spectra accompanying relaxation is primarily detected. Acquisition at the emission maximum was indeed prevented by the extremely red shifted fluorescence of **β**. [c]Corresponds to the lifetime obtained with the single photon counting measurements (1.33 ns) with the latter being a better evaluation for the decay time of this long living component.
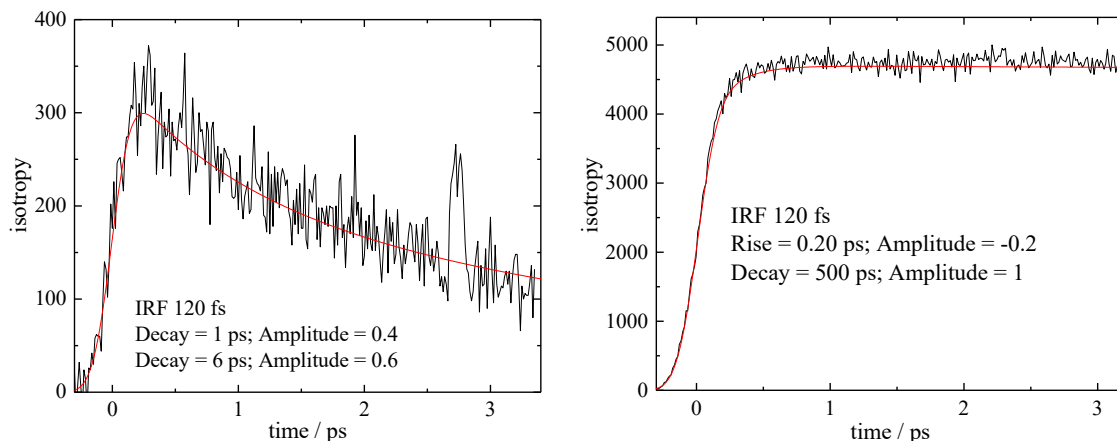
Figure 3.33 Fluorescence kinetics for **β** at 670 nm (left) and **βC** at 613 nm (right) in chloroform; best fit to a bi−exponential function is also shown.

3.7.8 Quantum Chemical Simulations

Details about intersystem crossing rate calculations. The first excited triplet state (T_1) geometry of the compound **β** and **βC** was obtained with time−dependent density functional theory (TDDFT). The same functional and basis sets (B3LYP and 6−31G*) used to locate the ground state geometry were employed for the geometry optimization. Single−point energy was refined using the system−dependent, nonempirically tuned version of long−range corrected functional ωB97X−D with the optimal ω values. (You can find the optimal ω values in the main text.) The medium effect was included using polarizable continuum model with the dielectric constant of 4.31 for chloroform. The first excited singlet (S_1) geometry was used to calculate the spin–orbit coupling. All the quantum chemical simulations were conducted using Q–Chem 5.0.

The rate constant of intersystem crossing (ISC) was estimated via Fermi's Golden rule.[94,95]

$$k_{\text{ISC}} = \frac{2\pi}{\hbar} \rho_{\text{FC}} |\langle S_1 | H_{SO} | T_1 \rangle|^2 \qquad \textbf{Equation 3.4}$$

Where, $\langle S_1 | H_{SO} | T_1 \rangle$ is the spin−orbit coupling element between S_1 and T_1, ρ_{FC} denotes the Franck−Condon−weighted density of states, and $\hbar$ is the reduced Planck constant of 6.582×10^{-16} eVs. ρ_{FC} is evaluated with Marcus−Levich−Jortner theory.[96,97]

$$\rho_{FC} = \frac{1}{\sqrt{4\pi\lambda_M k_B T}} \sum_{n=0}^{\infty} \exp(-S)\frac{S^n}{n!} \exp\left[-\frac{(\Delta E_{ST} + n\hbar\omega_{eff} + \lambda_M)^2}{4\pi\lambda_M k_B T}\right] \qquad \textbf{Equation 3.5}$$

Where, λ_M is the Marcus reorganization energy associated with the intermolecular and intramolecular low−frequency vibrations, k_B is for Boltzmann constant of 8.6173×10^{-5} eV/K, T is the temperature (in this study, 298.15 K), $\hbar\omega_{eff}$ represents the effective energy of a mode representing the nonclassical high−frequency intramolecular vibrations, and ΔE_{ST} is the adiabatic energy difference between S_1 and T_1. Huang−Rhys factor associated with these modes are given as S.

One recent computational study on thermally activated delayed fluorescence (TADF) mechanism discussed the rate of reverse ISC within the same framework used in this work.[98] The researchers from the same group computed the contribution of nonclassical intramolecular vibrations, and estimated the Marcus reorganization energy due to low−frequency intramolecular vibrations and the medium−induced relaxation effects. In addition, they assumed the Huang−Rhys factors can be neglected without significant changes to the results for large molecules.[97,99] The numerical values of each property to predict the rate of ISC are given in the table below.

Table 3.8 Properties used to predict the rate of ISC in the trimers.

	β	βC
λ (eV)	0.244	0.424
Spin–orbit coupling (cm^{-1})	2.704	0.257
ΔE_{ST} (eV)	−0.704	−0.595
Rate of ISC (s^{-1})	8.44×10^5	1.35×10^7
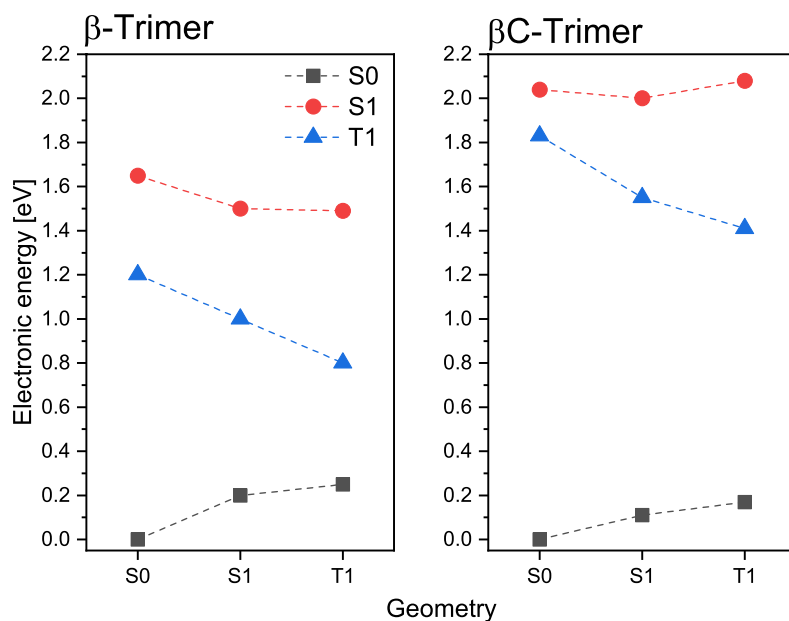
Figure 3.34 Singlet fission energetics for **β** (left) and **βC** (right); energies are given in eV.

Table 3.9 Calculated singlet and triplet energy values (in eV) from **Figure 3.34**.

eV	β			βC		
Electronic state	S_0	S_1	T_1	S_0	S_1	T_1
S_0	0.00	0.20	0.25	0.00	0.11	0.17
S_1	1.65	1.50	1.49	2.04	2.00	2.08
T_1	1.20	1.00	0.80	1.83	1.55	1.41
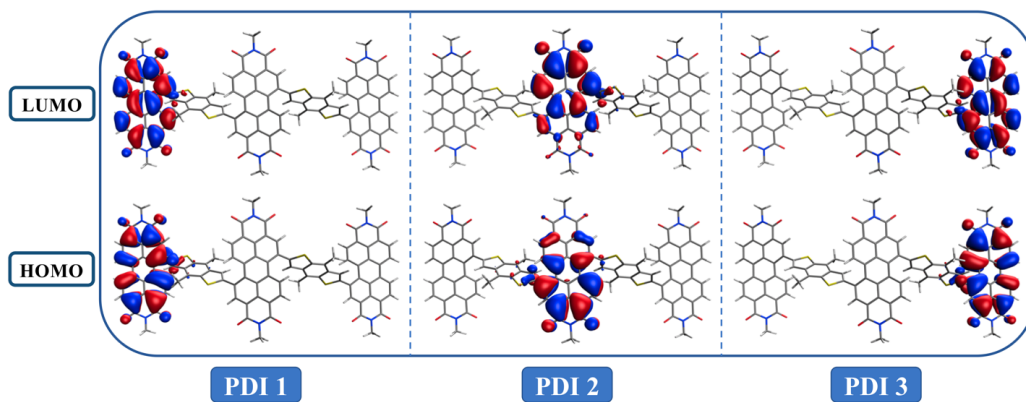
Figure 3.35 Frontier orbitals considered in RAS-SF calculations for **β** compound.
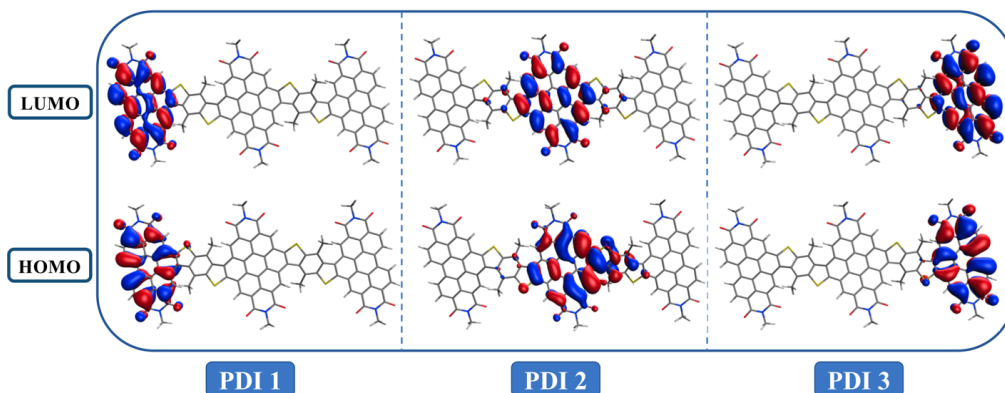
Figure 3.36 Frontier orbitals considered in RAS-SF calculations for **βC** compound.

Table 3.10 Energy levels estimated by 3SF-RAS based on the S_1 geometries of each chromophore (S: Singlet, T: Triplet, Q: Quintet, ME: Multiexciton. Energies are given in eV).

β		βC	
State	Energy	State	Energy
S_0	0.000	S_0	0.000
T_1	1.960	T_1	2.371
T_2	1.962	T_2	2.371
T_3	1.967	T_3	2.591
S_1	3.452	S_1	3.683
S_2	3.568	S_2	4.100
S_3	3.586	S_3	4.106
S_4, ME (^{1}TT)	3.940	T_4	4.187
T_4	3.942	T_5	4.335
S_5, ME (^{1}TT)	3.946	T_6	4.340
Q_1	3.946	S_4	4.596
T_5	3.948	S_5	4.604
Q_2	3.952	T_7	4.721
S_6, ME (^{1}TT)	3.955	T_8	4.732
T_6	3.955	T_9	4.785
Q_3	3.955	Q_1	4.785
		S_6, ME (^{1}TT)	4.785
		S_7	4.812
		S_8, ME (^{1}TT)	4.916
		T_{10}	4.917
		S_9, ME (^{1}TT)	4.919
		T_{11}	4.925
		S_{10}	4.962
		Q_2	4.982
		Q_3	4.982
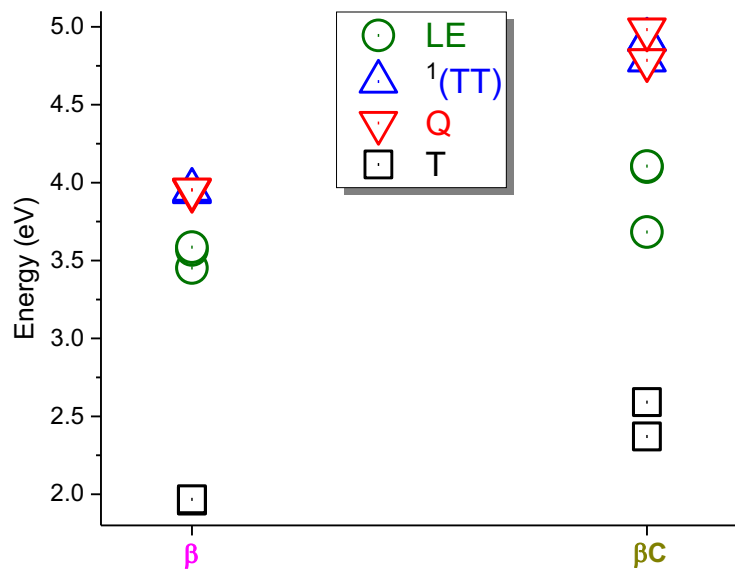
Figure 3.37 SF relevant energetics for **β** and **βC** Trimers showing interaction energies. *It should be noted that the LE (S_1) and T_1 energies are overestimated in SF-RAS calculations relative to TD-DFT calculations.*

ME₁, S₄

1.09 1.03 0.97 0.91

ME₂, S₅

1.09 1.02 0.97 0.91

ME₃, S₆

1.01 1.00 1.00 0.99
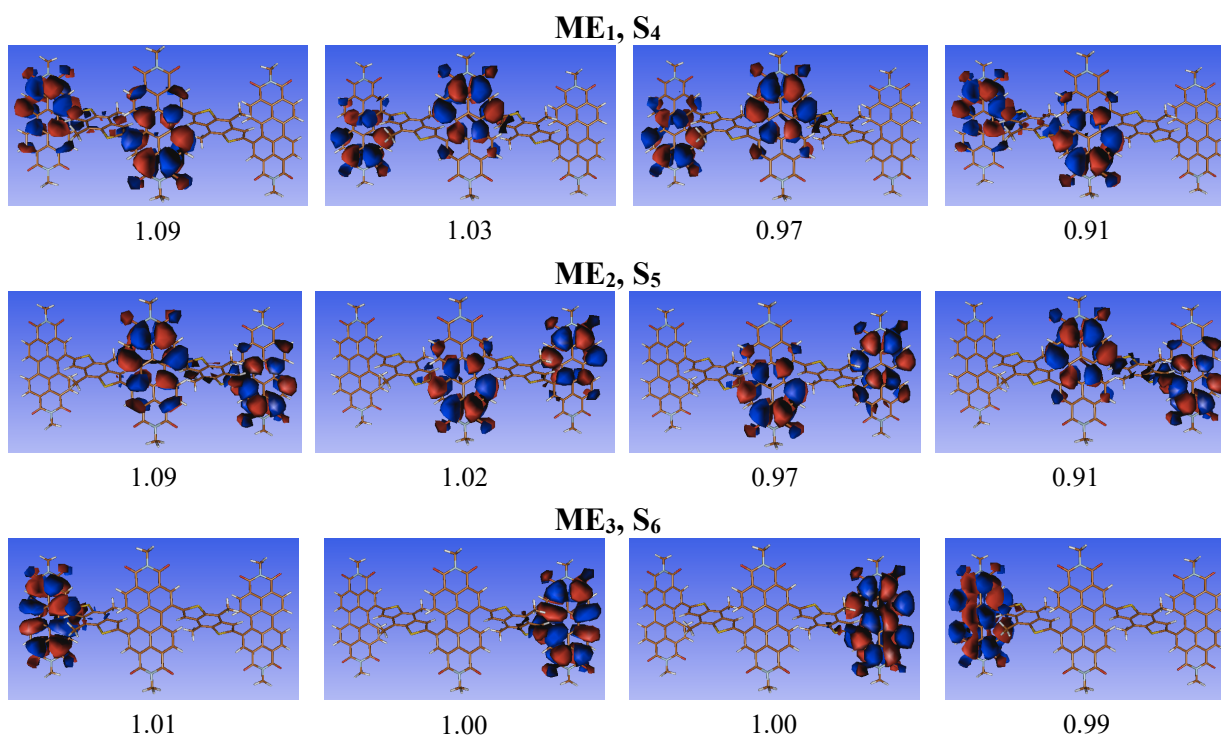
Figure 3.38 Natural Orbitals for the Multiexcitonic States of **β** with their occupation numbers.

142

ME$_1$, S$_6$

| 1.01 | 1.00 | 1.00 | 0.99 |

ME$_2$, S$_8$

| 1.76 | 1.45 | 1.28 | 0.84 | 0.51 | 0.25 |

ME$_3$, S$_9$

| 1.75 | 1.49 | 1.25 | 0.73 | 0.58 | 0.28 |
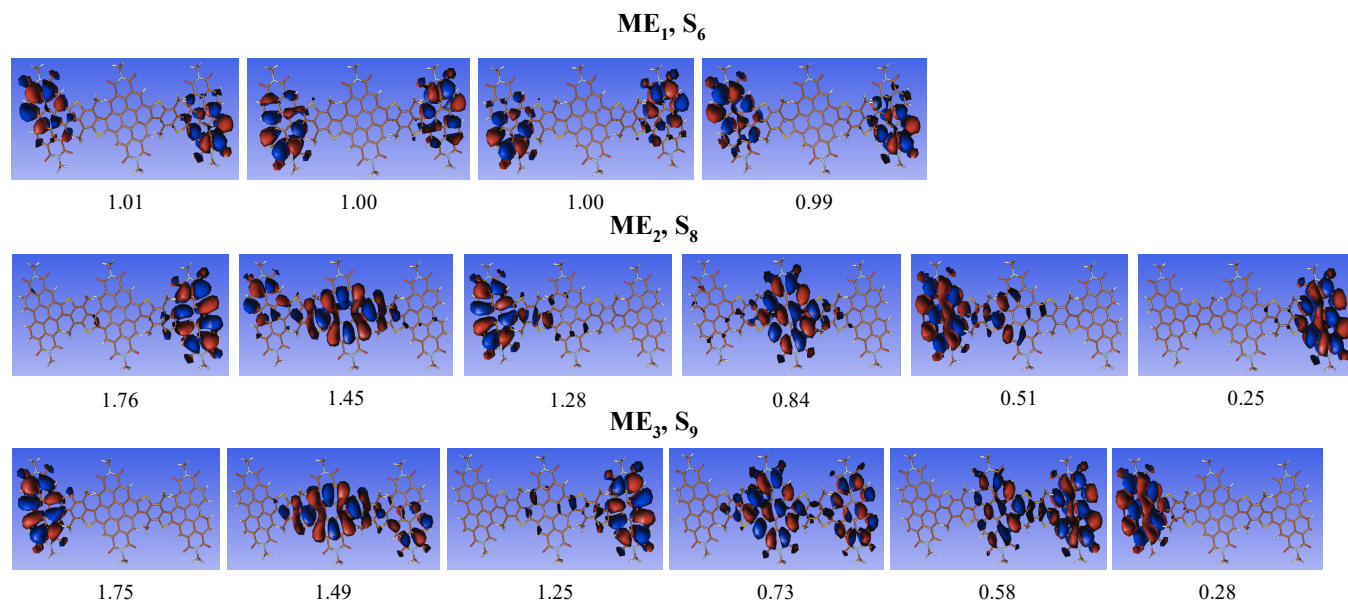
Figure 3.39 Natural Orbitals for the Multiexcitonic States of **βC** with their occupation numbers.

Table 3.11 Relevant thermodynamic quantities (eV) for **β** and **βC** at 298 K computed following Krylov et al.

	β	**βC**
$E_{stt} = 2 \times E(T_1) - E(S_1)$	−0.20	+0.59
$E_b = E(^5TT) - E(^1TT)$	+0.006	+0.066
$H_1 = E_{stt} - E_b$	−0.206	+0.524
$H_2 = E_{stt}$	−0.20	+0.59
$TS_1 = k_B T \ln \Omega_1$	+0.028	0
$TS_2 = k_B T \ln \Omega_2$	+0.028	0
$G_1 = E_{stt} - E_b - TS_1$	−0.234	+0.524
$G_2 = E_{stt} - TS_2$	−0.228	+0.59
$\Delta H_{TOT} = \Delta H_1 + \Delta H_2 = E_{stt}$	**−0.20**	**+0.59**
$T\Delta S_{TOT} = T\Delta S_1 + T\Delta S_2$	**+0.028**	**0**
$\Delta G_{TOT} = \Delta G_1 + \Delta G_2$	**−0.228**	**+0.59**

1 is the first step of singlet fission (from state 0, S$_1$, to state 1, ^{1}TT); 2 is the second step of triplet separation (from state 1, ^{1}TT, to state 2, T$_1$); for **β**, $\Omega_1=\Omega_2=3$, all the three double triplets are energetically close and accessible; for **βC**, $\Omega_1=\Omega_2=1$, only one double triplet state is energetically accessible; $\Delta\chi_1=\chi_1-\chi_0$ and $\Delta\chi_2=\chi_2-\chi_1$ where χ is H, S or G; k$_B$T=0.026 eV at 298 K.

References

(1)   Müller, A. M.; Avlasevich, Y. S.; Schoeller, W. W.; Müllen, K.; Bardeen, C. J. Exciton Fission and Fusion in Bis(Tetracene) Molecules with Different Covalent Linker Structures. *J. Am. Chem. Soc.* **2007**, *129* (46), 14240–14250.

(2)   Pun, A. B.; Sanders, S. N.; Kumarasamy, E.; Sfeir, M. Y.; Congreve, D. N.; Campos, L. M. Triplet Harvesting from Intramolecular Singlet Fission in Polytetracene. *Adv. Mater.* **2017**, *29* (41), 1–9.

(3)   Lee, J.; Jadhav, P.; Reusswig, P. D.; Yost, S. R.; Thompson, N. J.; Congreve, D. N.; Hontz, E.; Van Voorhis, T.; Baldo, M. A. Singlet Exciton Fission Photovoltaics. *Acc. Chem. Res.* **2013**, *46* (6), 1300–1311.

(4)   Kawata, S.; Pu, Y. J.; Saito, A.; Kurashige, Y.; Beppu, T.; Katagiri, H.; Hada, M.; Kido, J. Singlet Fission of Non-Polycyclic Aromatic Molecules in Organic Photovoltaics. *Adv. Mater.* **2016**, *28* (8), 1585–1590.

(5)   Chan, W.-L.; Ligges, M.; Jailaubekov, A.; Kaake, L.; Miaja-Avila, L.; Zhu, X.-Y. Observing the Multiexciton State in Singlet Fission and Ensuing Ultrafast Multielectron Transfer. *Science (80-.).* **2011**, *334* (6062), 1541–1545.

(6)   Paci, I.; Johnson, J. C.; Chen, X.; Rana, G.; Popović, D.; David, D. E.; Nozik, A. J.; Ratner, M. A.; Michl, J. Singlet Fission for Dye-Sensitized Solar Cells: Can a Suitable Sensitizer Be Found? *J. Am. Chem. Soc.* **2006**, *128* (51), 16546–16553.

(7)   Burdett, J. J.; Müller, A. M.; Gosztola, D.; Bardeen, C. J. Excited State Dynamics in Solid and Monomeric Tetracene: The Roles of Superradiance and Exciton Fission. *J. Chem. Phys.* **2010**, *133* (14).

(8)   Chan, W. L.; Ligges, M.; Zhu, X. Y. The Energy Barrier in Singlet Fission Can Be Overcome through Coherent Coupling and Entropic Gain. *Nat. Chem.* **2012**, *4* (10), 840–845.

(9)   Smith, M. B.; Michl, J. Recent Advances in Singlet Fission. *Annu. Rev. Phys. Chem.* **2013**, *64* (1), 361–386.

(10)   Busby, E.; Xia, J.; Wu, Q.; Low, J. Z.; Song, R.; Miller, J. R.; Zhu, X. Y.; Campos, L. M.; Sfeir, M. Y. A Design Strategy for Intramolecular Singlet Fission Mediated by Charge-Transfer States in Donor-Acceptor Organic Materials. *Nat. Mater.* **2015**, *14* (4), 426–433.

(11)   Singh, S.; Jones, W. J.; Siebrand, W.; Stoicheff, B. P.; Schneider, W. G. Laser Generation of Excitons and Fluorescence in Anthracene Crystals. *J. Chem. Phys.* **1965**, *42* (1), 330–342.

(12)   Zimmerman, P. M.; Bell, F.; Casanova, D.; Head-Gordon, M. Mechanism for Singlet Fission in Pentacene and Tetracene: From Single Exciton to Two Triplets. *J. Am. Chem. Soc.* **2011**, *133* (49), 19944–19952.

(13)   Sanders, S. N.; Kumarasamy, E.; Pun, A. B.; Trinh, M. T.; Choi, B.; Xia, J.; Taffet, E. J.;

Low, J. Z.; Miller, J. R.; Roy, X.; et al. Quantitative Intramolecular Singlet Fission in Bipentacenes. *J. Am. Chem. Soc.* **2015**, *137* (28), 8965–8972.

(14) Sakai, H.; Inaya, R.; Nagashima, H.; Nakamura, S.; Kobori, Y.; Tkachenko, N. V.; Hasobe, T. Multiexciton Dynamics Depending on Intramolecular Orientations in Pentacene Dimers: Recombination and Dissociation of Correlated Triplet Pairs. *J. Phys. Chem. Lett.* **2018**, *9* (12), 3354–3360.

(15) Yamakado, T.; Takahashi, S.; Watanabe, K.; Matsumoto, Y.; Osuka, A.; Saito, S. Conformational Planarization versus Singlet Fission: Distinct Excited-State Dynamics of Cyclooctatetraene-Fused Acene Dimers. *Angew. Chemie - Int. Ed.* **2018**, *57* (19), 5438–5443.

(16) Kumarasamy, E.; Sanders, S. N.; Tayebjee, M. J. Y.; Asadpoordarvish, A.; Hele, T. J. H.; Fuemmeler, E. G.; Pun, A. B.; Yablon, L. M.; Low, J. Z.; Paley, D. W.; et al. Tuning Singlet Fission in π-Bridge-π Chromophores. *J. Am. Chem. Soc.* **2017**, *139* (36), 12488–12494.

(17) Korovina, N. V.; Joy, J.; Feng, X.; Feltenberger, C.; Krylov, A. I.; Bradforth, S. E.; Thompson, M. E. Linker-Dependent Singlet Fission in Tetracene Dimers. *J. Am. Chem. Soc.* **2018**, *140* (32), 10179–10190.

(18) Eaton, S. W.; Shoer, L. E.; Karlen, S. D.; Dyar, S. M.; Margulies, E. A.; Veldkamp, B. S.; Ramanan, C.; Hartzler, D. A.; Savikhin, S.; Marks, T. J.; et al. Singlet Exciton Fission in Polycrystalline Thin Films of a Slip-Stacked Perylenediimide. *J. Am. Chem. Soc.* **2013**, *135* (39), 14701–14712.

(19) Le, A. K.; Bender, J. A.; Roberts, S. T. Slow Singlet Fission Observed in a Polycrystalline Perylenediimide Thin Film. *J. Phys. Chem. Lett.* **2016**, *7* (23), 4922–4928.

(20) Sanders, S. N.; Sfeir, M. Y.; Le, A. K.; Bender, J. A.; Arias, D. H.; Cotton, D. E.; Johnson, J. C.; Roberts, S. T. Singlet Fission Involves an Interplay between Energetic Driving Force and Electronic Coupling in Perylenediimide Films. *J. Am. Chem. Soc.* **2018**, *4* (2), 814–826.

(21) Farag, M. H.; Krylov, A. I. Singlet Fission in Perylenediimide Dimers. *J. Phys. Chem. C* **2018**, *122* (45), 25753–25763.

(22) Margulies, E. A.; Logsdon, J. L.; Miller, C. E.; Ma, L.; Simonoff, E.; Young, R. M.; Schatz, G. C.; Wasielewski, M. R. Direct Observation of a Charge-Transfer State Preceding High-Yield Singlet Fission in Terrylenediimide Thin Films. *J. Am. Chem. Soc.* **2017**, *139* (2), 663–671.

(23) Roberts, S. T.; McAnally, R. E.; Mastron, J. N.; Webber, D. H.; Whited, M. T.; Brutchey, R. L.; Thompson, M. E.; Bradforth, S. E. Efficient Singlet Fission Discovered in a Disordered Acene Film. *J. Am. Chem. Soc.* **2012**, *134* (14), 6388–6400.

(24) Michl, J.; Nozik, A. J.; Chen, X.; Johnson, J. C.; Rana, G.; Akdag, A.; Schwerin, A. F. Toward Singlet Fission for Excitonic Solar Cells. In *Organic Photovoltaics VIII*; 2007; Vol. 6656, p 66560E.

(25)   Ramanan, C.; Smeigh, A. L.; Anthony, J. E.; Marks, T. J.; Wasielewski, M. R. Competition between Singlet Fission and Charge Separation in Solution-Processed Blend Films of 6,13-Bis(Triisopropylsilylethynyl)Pentacene with Sterically-Encumbered Perylene-3,4:9,10-Bis(Dicarboximide)S. *J. Am. Chem. Soc.* **2012**, *134* (1), 386–397.

(26)   Margulies, E. A.; Miller, C. E.; Wu, Y.; Ma, L.; Schatz, G. C.; Young, R. M.; Wasielewski, M. R. Enabling Singlet Fission by Controlling Intramolecular Charge Transfer in π-Stacked Covalent Terrylenediimide Dimers. *Nat. Chem.* **2016**, *8* (12), 1120–1125.

(27)   Walker, B. J.; Musser, A. J.; Beljonne, D.; Friend, R. H. Singlet Exciton Fission in Solution. *Nat. Chem.* **2013**, *5* (12), 1019–1024.

(28)   Varnavski, O.; Abeyasinghe, N.; Aragó, J.; Serrano-Pérez, J. J.; Ortí, E.; López Navarrete, J. T.; Takimiya, K.; Casanova, D.; Casado, J.; Goodson, T. High Yield Ultrafast Intramolecular Singlet Exciton Fission in a Quinoidal Bithiophene. *J. Phys. Chem. Lett.* **2015**, *6* (8), 1375–1384.

(29)   Chien, A. D.; Molina, A. R.; Abeyasinghe, N.; Varnavski, O. P.; Goodson, T.; Zimmerman, P. M. Structure and Dynamics of the 1(TT) State in a Quinoidal Bithiophene: Characterizing a Promising Intramolecular Singlet Fission Candidate. *J. Phys. Chem. C* **2015**, *119* (51), 28258–28268.

(30)   Greyson, E. C.; Stepp, B. R.; Chen, X.; Schwerin, A. F.; Paci, I.; Smith, M. B.; Akdag, A.; Johnson, J. C.; Nozik, A. J.; Michl, J.; et al. Singlet Exciton Fission for Solar Cell Applications: Energy Aspects of Interchromophore Coupling. *J. Phys. Chem. B* **2010**, *114* (45), 14223–14232.

(31)   Lukman, S.; Chen, K.; Hodgkiss, J. M.; Turban, D. H. P.; Hine, N. D. M.; Dong, S.; Wu, J.; Greenham, N. C.; Musser, A. J. Tuning the Role of Charge-Transfer States in Intramolecular Singlet Exciton Fission through Side-Group Engineering. *Nat. Commun.* **2016**, *7*, 1–13.

(32)   Lukman, S.; Musser, A. J.; Chen, K.; Athanasopoulos, S.; Yong, C. K.; Zeng, Z.; Ye, Q.; Chi, C.; Hodgkiss, J. M.; Wu, J.; et al. Tuneable Singlet Exciton Fission and Triplet-Triplet Annihilation in an Orthogonal Pentacene Dimer. *Adv. Funct. Mater.* **2015**, *25* (34), 5452–5461.

(33)   Carlotti, B.; Cai, Z.; Kim, H.; Sharapov, V.; Madu, I. K.; Zhao, D.; Chen, W.; Zimmerman, P. M.; Yu, L.; Goodson, T. Charge Transfer and Aggregation E Ff Ects on the Performance of Planar vs Twisted Nonfullerene Acceptor Isomers for Organic Solar Cells. *Chem. Mater.* **2018**, *30*, 4263–4276.

(34)   Madu, I. K.; Muller, E. W.; Kim, H.; Shaw, J.; Burney-Allen, A.; Zimmerman, P. M.; Jeffries-EL, M.; Goodson III, T. Heteroatom and Side Chain Effects on the Optical and Photo-Physical Properties: Ultrafast and Nonlinear Spectroscopy of New Naphtho[1,2-B:5,6-B′]Difuran Donor Polymers. *J. Phys. Chem. C* **2018**, acs.jpcc.8b03914.

(35)   Whited, M. T.; Patel, N. M.; Roberts, S. T.; Allen, K.; Djurovich, P. I.; Bradforth, S. E.; Thompson, M. E. Symmetry-Breaking Intramolecular Charge Transfer in the Excited State

of Meso-Linked BODIPY Dyads. *Chem. Commun.* **2012**, *48* (2), 284–286.

(36)   Yu, Z.; Wu, Y.; Peng, Q.; Sun, C.; Chen, J.; Yao, J.; Fu, H. Accessing the Triplet State in Heavy-Atom-Free Perylene Diimides. *Chem. - A Eur. J.* **2016**, *22* (14), 4717–4722.

(37)   Zheng, T.; Cai, Z.; Ho-Wu, R.; Yau, S. H.; Shaparov, V.; Goodson, T.; Yu, L. Synthesis of Ladder-Type Thienoacenes and Their Electronic and Optical Properties. *J. Am. Chem. Soc.* **2016**, *138* (3), 868–875.

(38)   Pond, S. J. K.; Rumi, M.; Levin, M. D.; Parker, T. C.; Beljonne, D.; Day, M. W.; Brédas, J. L.; Marder, S. R.; Perry, J. W. One- and Two-Photon Spectroscopy of Donor-Acceptor-Donor Distyrylbenzene Derivatives: Effect of Cyano Substitution and Distortion from Planarity. *J. Phys. Chem. A* **2002**, *106* (47), 11470–11480.

(39)   Vázquez, R. J.; Kim, H.; Kobilka, B. M.; Hale, B. J.; Jeffries-EL, M.; Zimmerman, P.; Goodson, T. Evaluating the Effect of Heteroatoms on the Photophysical Properties of Donor–Acceptor Conjugated Polymers Based on 2,6-Di(Thiophen-2-Yl)Benzo[1,2-b:4,5-B′]Difuran: Two-Photon Cross-Section and Ultrafast Time-Resolved Spectroscopy. *J. Phys. Chem. C* **2017**, *121* (27), 14382–14392.

(40)   Wu, Y.; Young, R. M.; Frasconi, M.; Schneebeli, S. T.; Spenst, P.; Gardner, D. M.; Brown, K. E.; Würthner, F.; Stoddart, J. F.; Wasielewski, M. R. Ultrafast Photoinduced Symmetry-Breaking Charge Separation and Electron Sharing in Perylenediimide Molecular Triangles. *J. Am. Chem. Soc.* **2015**, *137* (41), 13236–13239.

(41)   Spenst, P.; Young, R. M.; Wasielewski, M. R.; Würthner, F. Guest and Solvent Modulated Photo-Driven Charge Separation and Triplet Generation in a Perylene Bisimide Cyclophane. *Chem. Sci.* **2016**, *7* (8), 5428–5434.

(42)   Brown, K. E.; Veldkamp, B. S.; Co, D. T.; Wasielewski, M. R. Vibrational Dynamics of a Perylene-Perylenediimide Donor-Acceptor Dyad Probed with Femtosecond Stimulated Raman Spectroscopy. *Journal of Physical Chemistry Letters*. 2012, pp 2362–2366.

(43)   Giaimo, J. M.; Gusev, A. V.; Wasielewski, M. R. Excited-State Symmetry Breaking in Cofacial and Linear Dimers of a Green Perylenediimide Chlorophyll Analogue Leading to Ultrafast Charge Separation. *J. Am. Chem. Soc.* **2002**, *124* (29), 8530–8531.

(44)   Van der Boom, T.; Hayes, R. T.; Zhao, Y.; Bushard, P. J.; Weiss, E. A.; Wasielewski, M. R. Charge Transport in Photofunctional Nanoparticles Self-Assembled from Zinc 5,10,15,20-Tetrakis(Perylenediimide)Porphyrin Building Blocks. *J. Am. Chem. Soc.* **2002**, *124* (32), 9582–9590.

(45)   Lukas, A. S.; Zhao, Y.; Miller, S. E.; Wasielewski, M. R. Biomimetic Electron Transfer Using Low Energy Excited States: A Green Perylene-Based Analogue of Chlorophyll A. *J. Phys. Chem. B* **2002**, *106* (6), 1299–1306.

(46)   Guo, Y.; Ma, Z.; Niu, X.; Zhang, W.; Tao, M.; Guo, Q.; Wang, Z.; Xia, A. Bridge-Mediated Charge Separation in Isomeric N-Annulated Perylene Diimide Dimers. *J. Am. Chem. Soc.* **2019**, *141* (32), 12789–12796.

(47) Van Stokkum, I. H. M.; Larsen, D. S.; Van Grondelle, R. Global and Target Analysis of Time-Resolved Spectra. *Biochim. Biophys. Acta - Bioenerg.* **2004**, *1657* (2–3), 82–104.

(48) Snellenburg, J. J.; Laptenok, S. P.; Seger, R.; Mullen, K. M.; van Stokkum, I. H. M. Glotaran : A Java-Based Graphical User Interface for the R Package TIMP. *J. Stat. Softw.* **2012**, *49* (3), 1–2.

(49) Margulies, E. A.; Miller, C. E.; Wu, Y.; Ma, L.; Schatz, G. C.; Young, R. M.; Wasielewski, M. R. Enabling Singlet Fission by Controlling Intramolecular Charge Transfer in π-Stacked Covalent Terrylenediimide Dimers. *Nat. Chem.* **2016**, *8* (12), 1120–1125.

(50) Margulies, E. A.; Wu, Y. L.; Gawel, P.; Miller, S. A.; Shoer, L. E.; Schaller, R. D.; Diederich, F.; Wasielewski, M. R. Sub-Picosecond Singlet Exciton Fission in Cyano-Substituted Diaryltetracenes. *Angew. Chemie - Int. Ed.* **2015**, *54* (30), 8679–8683.

(51) Ford, W. E.; Kamat, P. V. Photochemistry of 3,4,9,10-Perylenetetracarboxylic Dianhydride Dyes. 3. Singlet and Triplet Excited-State Properties of the Bis(2,5-Di-Tert-Butylphenyl)Imide Derivative. *J. Phys. Chem.* **1987**, *91* (25), 6373–6380.

(52) Le, A. K.; Bender, J. A.; Arias, D. H.; Cotton, D. E.; Johnson, J. C.; Roberts, S. T. Singlet Fission Involves an Interplay between Energetic Driving Force and Electronic Coupling in Perylenediimide Films. *J. Am. Chem. Soc.* **2018**, *140* (2), 814–826.

(53) Schweitzer, C.; Schmidt, R. Physical Mechanisms of Generation and Deactivation of Singlet Oxygen. *Chem. Rev.* **2003**, *103* (5), 1685–1757.

(54) Eaton, S. W.; Miller, S. A.; Margulies, E. A.; Shoer, L. E.; Schaller, R. D.; Wasielewski, M. R. Singlet Exciton Fission in Thin Films of Tert -Butyl-Substituted Terrylenes. *J. Phys. Chem. A* **2015**, *119* (18), 4151–4161.

(55) Korovina, N. V.; Chang, C. H.; Johnson, J. C. Spatial Separation of Triplet Excitons Drives Endothermic Singlet Fission. *Nat. Chem.* **2020**, *12* (4), 391–398.

(56) Sanders, S. N.; Kumarasamy, E.; Pun, A. B.; Appavoo, K.; Steigerwald, M. L.; Campos, L. M.; Sfeir, M. Y. Exciton Correlations in Intramolecular Singlet Fission. *J. Am. Chem. Soc.* **2016**, *138* (23), 7289–7297.

(57) Yong, C. K.; Musser, A. J.; Bayliss, S. L.; Lukman, S.; Tamura, H.; Bubnova, O.; Hallani, R. K.; Meneau, A.; Resel, R.; Maruyama, M.; et al. The Entangled Triplet Pair State in Acene and Heteroacene Materials. *Nat. Commun.* **2017**, *8* (May).

(58) Stern, H. L.; Cheminal, A.; Yost, S. R.; Broch, K.; Bayliss, S. L.; Chen, K.; Tabachnyk, M.; Thorley, K.; Greenham, N.; Hodgkiss, J. M.; et al. Vibronically Coherent Ultrafast Triplet-Pair Formation and Subsequent Thermally Activated Dissociation Control Efficient Endothermic Singlet Fission. *Nat. Chem.* **2017**, *9* (12), 1205–1212.

(59) Lukman, S.; Richter, J. M.; Yang, L.; Hu, P.; Wu, J.; Greenham, N. C.; Musser, A. J. Efficient Singlet Fission and Triplet-Pair Emission in a Family of Zethrene Diradicaloids. *J. Am. Chem. Soc.* **2017**, *139* (50), 18376–18385.

(60)   Kim, H.; Zimmerman, P. M. Coupled Double Triplet State in Singlet Fission. *Phys. Chem. Chem. Phys.* **2018**, *20* (48), 30083–30094.

(61)   Feng, X.; Casanova, D.; Krylov, A. I. Intra- and Intermolecular Singlet Fission in Covalently Linked Dimers. *J. Phys. Chem. C* **2016**, *120* (34), 19070–19077.

(62)   Felter, K. M.; Grozema, F. C. Singlet Fission in Crystalline Organic Materials: Recent Insights and Future Directions. *J. Phys. Chem. Lett.* **2019**, *10* (22), 7208–7214.

(63)   Pensack, R. D.; Ostroumov, E. E.; Tilley, A. J.; Mazza, S.; Grieco, C.; Thorley, K. J.; Asbury, J. B.; Seferos, D. S.; Anthony, J. E.; Scholes, G. D. Observation of Two Triplet-Pair Intermediates in Singlet Exciton Fission. *J. Phys. Chem. Lett.* **2016**, *7* (13), 2370–2375.

(64)   Lee, T. S.; Lin, Y. L.; Kim, H.; Pensack, R. D.; Rand, B. P.; Scholes, G. D. Triplet Energy Transfer Governs the Dissociation of the Correlated Triplet Pair in Exothermic Singlet Fission. *J. Phys. Chem. Lett.* **2018**, *9* (14), 4087–4095.

(65)   Grieco, C.; Kennehan, E. R.; Kim, H.; Pensack, R. D.; Brigeman, A. N.; Rimshaw, A.; Payne, M. M.; Anthony, J. E.; Giebink, N. C.; Scholes, G. D.; et al. Direct Observation of Correlated Triplet Pair Dynamics during Singlet Fission Using Ultrafast Mid-IR Spectroscopy. *J. Phys. Chem. C* **2018**, *122* (4), 2012–2022.

(66)   Kolomeisky, A. B.; Feng, X.; Krylov, A. I. A Simple Kinetic Model for Singlet Fission: A Role of Electronic and Entropic Contributions to Macroscopic Rates. *J. Phys. Chem. C* **2014**, *118* (10), 5188–5195.

(67)   Wu, Q.; Zhao, D.; Schneider, A. M.; Chen, W.; Yu, L. Covalently Bound Clusters of Alpha-Substituted PDI-Rival Electron Acceptors to Fullerene for Organic Solar Cells. *J. Am. Chem. Soc.* **2016**, *138* (23), 7248–7251.

(68)   Cai, Z.; Vázquez, R. J.; Zhao, D.; Li, L.; Lo, W. Y.; Zhang, N.; Wu, Q.; Keller, B.; Eshun, A.; Abeyasinghe, N.; et al. Two Photon Absorption Study of Low-Bandgap, Fully Conjugated Perylene Diimide-Thienoacene-Perylene Diimide Ladder-Type Molecules. *Chem. Mater.* **2017**, *29* (16), 6726–6732.

(69)   Guan, J.; Tomobe, K.; Madu, I.; Goodson, T.; Makhal, K.; Trinh, M. T.; Rand, S. C.; Yodsin, N.; Jungsuttiwong, S.; Laine, R. M. Photophysical Properties of Partially Functionalized Phenylsilsesquioxane: [RSiO1.5]7[Me/NPrSiO1.5] and [RSiO1.5]7[O0.5SiMe3]3 (R = 4-Me/4-CN-Stilbene). Cage-Centered Magnetic Fields Form under Intense Laser Light. *Macromolecules* **2019**, *52*, 4008–4019.

(70)   Jobin Yvon. *A Guide to Recording Fluorescence Quantum Yields Introduction:*; 2014; Vol. 15.

(71)   Kubin, R. F.; Fletcher, A. N. Fluorescence Quantum Yields of Some Rhodamine Dyes. *J. Lumin.* **1982**, *27* (4), 455–462.

(72)   Keller, B.; McLean, A.; Kim, B. G.; Chung, K.; Kim, J.; Goodson, T. Ultrafast Spectroscopic Study of Donor-Acceptor Benzodithiophene Light Harvesting Organic

Conjugated Polymers. *J. Phys. Chem. C* **2016**, *120* (17), 9088–9096.

(73) Villabona-Monsalve, J. P.; Varnavski, O.; Palfey, B. A.; Goodson, T. Two-Photon Excitation of Flavins and Flavoproteins with Classical and Quantum Light. *J. Am. Chem. Soc.* **2018**, *140* (44), 14562–14566.

(74) Xu, C.; Webb, W. W. Measurement of Two-Photon Excitation Cross Sections of Molecular Fluorophores with Data from 690 to 1050 Nm. *J. Opt. Soc. Am. B* **1996**, *13* (3), 481.

(75) Vázquez, R. J.; Kim, H.; Zimmerman, P. M.; Goodson, T. Using Ultra-Fast Spectroscopy to Probe the Excited State Dynamics of a Reported Highly Efficient Thermally Activated Delayed Fluorescence Chromophore. *J. Mater. Chem. C* **2019**, *7* (14), 4210–4221.

(76) Carmichael, I.; Hug, G. L. Triplet-Triplet Absorption Spectra of Organic Molecules in Condensed Phases. *J. Phys. Chem. Ref. Data* **1986**, *15* (1), 1–250.

(77) Bensasson, R.; Dawe, E. A.; Long, D. A.; Land, E. J. Singlet → Triplet Intersystem Crossing Quantum Yields of Photosynthetic and Related Polyenes. *J. Chem. Soc. Faraday Trans. 1 Phys. Chem. Condens. Phases* **1977**, *73*, 1319.

(78) Murov, S.; Carmichael, I.; Hug, G. L. *Handbook of Photochemistry*, second.; MARCEL DEKKER, INC.: New York, 1993.

(79) Cogdell, R. J.; Land, E. J.; Truscott, T. G. The Triplet Extinction Coefficients of Some Bacterial Carotenoids. *Photochem. Photobiol.* **1983**, *38* (6), 723–725.

(80) Amouyal, E.; Bensasson, R.; Land, E. J. Triplet States of Ubiquinone Analogs Studied By Ultraviolet and Electron Nanosecond Irradiation. *Photochem. Photobiol.* **1974**, *20* (5), 415–422.

(81) Nielsen, B. R.; Jørgensen, K.; Skibsted, L. H. Triplet-Triplet Extinction Coefficients, Rate Constants of Triplet Decay and Rate Constants of Anthracene Triplet Sensitization by Laser Flash Photolysis of Astaxanthin, β-Carotene, Canthaxanthin and Zeaxanthin in Deaerated Toluene at 298 K. *J. Photochem. Photobiol. A Chem.* **1998**, *112* (2–3), 127–133.

(82) Zhang, J.; Sulaiman, S.; Madu, I. K.; Laine, R. M.; Goodson, T. Ultrafast Excited-State Dynamics of Partially and Fully Functionalized Silsesquioxanes. *J. Phys. Chem. C* **2019**, *123* (8), 5048–5060.

(83) Taylor, E. L.; Metcalf, K. J.; Carlotti, B.; Lai, C. T.; Modica, J. A.; Schatz, G. C.; Mrksich, M.; Goodson, T. Long-Range Energy Transfer in Protein Megamolecules. *J. Am. Chem. Soc.* **2018**, *140* (46), 15731–15743.

(84) Adegoke, O. O.; Jung, I. H.; Orr, M.; Yu, L.; Goodson, T. Effect of Acceptor Strength on Optical and Electronic Properties in Conjugated Polymers for Solar Applications. *J. Am. Chem. Soc.* **2015**, *137* (17), 5759–5769.

(85) Chai, J.-D.; Head-Gordon, M. Long-Range Corrected Hybrid Density Functionals with Damped Atom–Atom Dispersion Corrections. *Phys. Chem. Chem. Phys.* **2008**, *10* (44), 6615.

(86) Chai, J. Da; Head-Gordon, M. Systematic Optimization of Long-Range Corrected Hybrid Density Functionals. *J. Chem. Phys.* **2008**, *128* (8).

(87) Zheng, Z.; Brédas, J.-L.; Coropceanu, V. Description of the Charge Transfer States at the Pentacene/C $_{60}$ Interface: Combining Range-Separated Hybrid Functionals with the Polarizable Continuum Model. *J. Phys. Chem. Lett.* **2016**, *7* (13), 2616–2621.

(88) Korovina, N. V.; Das, S.; Nett, Z.; Feng, X.; Joy, J.; Haiges, R.; Krylov, A. I.; Bradforth, S. E.; Thompson, M. E. Singlet Fission in a Covalently Linked Cofacial Alkynyltetracene Dimer. *J. Am. Chem. Soc.* **2016**, *138* (2), 617–627.

(89) Casanova, D. Electronic Structure Study of Singlet Fission in Tetracene Derivatives. *J. Chem. Theory Comput.* **2014**, *10* (1), 324–334.

(90) Zimmerman, P. M.; Musgrave, C. B.; Head-Gordon, M. A Correlated Electron View of Singlet Fission. *Acc. Chem. Res.* **2013**, *46* (6), 1339–1347.

(91) Piland, G. B.; Burdett, J. J.; Dillon, R. J.; Bardeen, C. J. Singlet Fission: From Coherences to Kinetics. *J. Phys. Chem. Lett.* **2014**, *5* (13), 2312–2319.

(92) Chien, A. D.; Zimmerman, P. M. Recovering Dynamic Correlation in Spin Flip Configuration Interaction through a Difference Dedicated Approach. *J. Chem. Phys.* **2017**, *146* (1).

(93) Shao, Y.; Gan, Z.; Epifanovsky, E.; Gilbert, A. T. B.; Wormit, M.; Kussmann, J.; Lange, A. W.; Behn, A.; Deng, J.; Feng, X.; et al. Advances in Molecular Quantum Chemistry Contained in the Q-Chem 4 Program Package. *Mol. Phys.* **2015**, *113* (2), 184–215.

(94) Robinson, G. W.; Frosch, R. P. Electronic Excitation Transfer and Relaxation. *J. Chem. Phys.* **1963**, *38* (5), 1187–1203.

(95) Lawetz, V.; Orlandi, G.; Siebrand, W. Theory of Intersystem Crossing in Aromatic Hydrocarbons. *J. Chem. Phys.* **1972**, *56* (8), 4058–4072.

(96) Brédas, J.-L.; Beljonne, D.; Coropceanu, V.; Cornil, J. Charge-Transfer and Energy-Transfer Processes in π-Conjugated Oligomers and Polymers: A Molecular Picture. *Chem. Rev.* **2004**, *104* (11), 4971–5004.

(97) Schmidt, K.; Brovelli, S.; Coropceanu, V.; Beljonne, D.; Cornil, J.; Bazzini, C.; Caronna, T.; Tubino, R.; Meinardi, F.; Shuai, Z.; et al. Intersystem Crossing Processes in Nonplanar Aromatic Heterocyclic Molecules. *J. Phys. Chem. A* **2007**, *111* (42), 10490–10499.

(98) Samanta, P. K.; Kim, D.; Coropceanu, V.; Brédas, J. L. Up-Conversion Intersystem Crossing Rates in Organic Emitters for Thermally Activated Delayed Fluorescence: Impact of the Nature of Singlet vs Triplet Excited States. *J. Am. Chem. Soc.* **2017**, *139* (11), 4042–4051.

(99) Beljonne, D.; Shuai, Z.; Pourtois, G.; Bredas, J. L. Spin-Orbit Coupling and Intersystem Crossing in Conjugated Polymers: A Configuration Interaction Description. *J. Phys. Chem. A* **2001**, *105* (15), 3899–3907.

Chapter 4

Impact of Ring-fusion on the Excited State Decay Pathways of N-annulated Perylene Diimides

4.1 Original Publication Information

The work in this chapter is ready to be submitted for publication as:

"Impact of Ring-fusion on the Excited State Decay Pathways of N-annulated Perylene Diimides" Ifeanyi K. Madu, Hanjie Jiang, Audrey Laventure, Paul M. Zimmerman, Gregory C. Welch, and Theodore Goodson III.

Synthesis of the compounds was carried out by the Welch group at the University of Calgary and quantum calculations by the Zimmerman group at the University of Michigan. Modifications were made to the original publication to adapt it to the style of the content of this dissertation. References and supporting information of the original manuscript are included in this chapter.

4.2 Abstract

N-annulated perylene dimide (PDI) dimers offer added advantages over conventional (non-annulated) dimers or S/Se-annulated dimers due to the two extra positions of functionalization they provide, which can be used to improve the solution-processability, impact the packing and self-assembly of the molecules in thin film, and tune energetics. In this work about N-annulated thiophene π-bridged PDI dimers, we present a new strategy to use ring-fusion to highlight the different excited state decay pathways taking place in these bowed-shaped systems. Two analogous N-annulated PDI dimers were investigated, whose structures show a rotatable single-bond thiophene π-bridge connection (**M1**) relative to a rigid fused π-bridge connection (**M1F**). We show that ring-fusion of this dimeric system yields ultrafast intramolecular charge transfer and charge separation, relative to the unfused dimer. For **M1F** – the fused N-annulated thiophene π-bridged PDI dimer, charge separation rate increased by over one-order of magnitude compared to the charge separation rate of **M1**. Also, ring-fusion opened up the triplet excited state deactivation pathway that was not present in the unfused dimer. The rate of triplet production was shown to be dependent on the polarity of the solvent environment for the fused **M1F** dimer. Time-resolved spectroscopic measurements were used to carry out the detailed analysis of the excited state dynamics to elucidate the decay pathways of the unfused and fused N-annulated thiophene π-bridged PDI dimers. We were able to track the respective excited state species (PDI*, PDI$^{\bullet+}$, PDI$^{\bullet-}$, PDI^{3*}) generated upon photoexcitation, using both femtosecond and nanosecond time resolution to obtain a complete description of the entire activation and deactivation pathways. Non-linear two-photon absorption measurement was used to provide insights into the excited state charge transfer properties of the compounds. The results were able to show that ring fusion leads to increased electronic coupling between the PDI units of the dimer, which in turn leads to increased

charge separation rate and dictates the production mechanism of the long-lived triplet species. Also, this detailed study points out that ring fusion in N-annulated PDIs, with a slightly twisted backbone, can provide the bulk advantages of excellent π-conjugation, increased electronic delocalization, as well as the advantage of limiting the aggregation effects.

4.3 Introduction

Among the reported electron-deficient n-type materials, perylene diimide (PDI) or perylene bisimide based compounds are one of the most studied, and have found utility in electron-transporting technologies.[1–4] Such applications include organic field-effect transistors (OFETs),[5–7] imaging fluorescent probes,[8,9] photosensitizers for photodynamic therapy,[10,11] molecular switches and wires,[12] organic solar cells (OSCs).[13–19] For bulk heterojunction (BHJ) organic OSCs, non-fullerene acceptors still remain a critical component, and PDI acceptors are leading the pack in terms of usage for studies because of their outstanding chemical and physical properties. Specifically, the advantages of low cost, strong absorptivity, excellent electron mobility, remarkable thermal, chemical and photo stability, has made PDI excellent non-fullerene acceptor candidates for BHJ devices.[13,20]

Several PDI oligomeric systems have been synthesized and studied, including trimers,[21,22] tetramers,[15,23–26] and their structure-property-function relationships have been clearly elucidated. For PDI dimers, a novel class of compounds that have not received much attention are the annulated dimers. Sun et al[27] reported efficient device properties (PCE ~7.1 %) using S-annulated PDI dimers which comprised of two thiophene heterorings tacked in the bay positions, at the extreme ends of the compound. This was the highest PCE value reported in the literature at the time for non-fullerene acceptors. Meng et al[28] replaced the thiophene heterorings with selenophene heterorings given that selenium has a bigger and looser outmost electron cloud than that of sulfur,

which improves orbital overlap and increases charge carrier mobility. In addition, it was expected that this Se-annulated PDI dimer will show increased intramolecular interactions because the selenium atom is more easily polarized relative to the sulfur atom. An efficiency of ~8.4 %, also one of the highest reported at the time, was achieved. Their works highlighted the important fact that annulated PDI dimers show immense promise for application in OSCs. Inspired by this idea, the Welch research group synthesized pyrrole-ring (or "N-annulated") PDI dimers in a bid to overcome the limitation in structural diversity of the S- and Se-annulated derivatives, stemming from their set molecular geometry (at ~80⁰) and from the fact that the bay position cannot be further functionalized.[29–31] N-annulated PDI dimers show a higher device open-circuit voltages (V_{OC}) relative to conventional (no annulation) and S-/Se-annulated PDI dimers, owing to higher LUMO energy.[29]

Annulation, in the bay region, should impose some kind of curved bowl-shaped or bowed molecular geometry that have been said to significantly alter intermolecular interactions, chemical and physical properties of the PDI system.[32] The bowed geometry is achieved by incorporating thiophene, selenophene or pyrrole heterorings into the bay regions of the PDI systems, inducing ring strain in the molecular backbone. However, as was previously reported by Qian et al,[32] crystal structure study revealed that the S-annulated compound showed a rather planar perylene core probably because of the long length of the C–S bonds (~1.78 Å), which led to a weak ring strain. In similar view, given that the C–Se bond length is even longer (~1.98 Å),[33] it should be expected that the Se-annulated ring strain will be weaker, also leading to a planar perylene core. In contrast, a deeply bowl-shaped configuration was observed by Qian et al[32] and Hendsbee et al[29] for the N-annulated compound due to the stronger strain resulting from the short length of the C–N bonds (~1.41 Å). Another unique characteristic of the N-annulated PDI structure over the conventional

(non-annulated) and S-/Se-annulated PDI dimers is its ability to be functionalized in two more positions by alkyl groups. This greatly impacts the degree of solubility of these materials further increasing its flexibility for solution-based applications. Also, and more importantly, this opens up the opportunity for the reduction in the density of the alkyl sidechains attached to the imide position (only iso-C_5H_{11} for N-annulated), which conventional and S/Se-annulated PDIs (contain iso-$C_{13}H_{27}$ or -$C_{11}H_{23}$) do not have, greatly impacting the packing and self-assembly of these molecules in thin films. This also opens up the space, creating a potential avenue, for sidechain engineering and thin film studies.

The introduction of a thiophene heterocyclic block into the molecular backbone as a π-bridge, increases the electron density present in the molecule, leading to even higher lying LUMO level,[30,31] and increased V_{OC}.[34–36] From a photophysical standpoint, there is also the increased probability of a non-radiative decay pathway which often denotes improved charge transfer (CT)/charge separation (CT). This is as a result of the improved donor-acceptor strength by the introduction of an electron-rich thiophene block into the molecular structure. Fusing the thiophene π-bridge alters the photopysical and optical properties, by inducing higher rigidity in the molecular geometry and increasing the coupling to the electron rich linker.[37] It is important to note that ring fusion does not necessarily lead to the formation of a planar geometry, as is the case in this study where a molecular twist from sterics was observed following ring fusion. Ring fusion in π-bridged PDI systems is an effective approach that have been successfully employed to increase π-conjugation, increase electronic delocalization, increase electron mobility and improve molecular packing. While some studies have reported ring fusion to limit PCE due to loss in structural flexibilty,[38] most studies agree that fusion benefits the overall optical, electronic and device properties.[24,36,37,39] For the N-annulated thiophene π-bridged dimers investigated in this study,

similar V_{OC} were obtained for the fused and unfused structures, but the PCE was greater for the fused dimer by ~37 %.[30,31] The reason for these differences is linked to the varying optical and electronic properties, imposed by their fused and unfused molecular geometry.

Many OSC studies have explored the interfacial charge transfer between a donor polymer and an acceptor molecule, to study the conversion of singlet excitation into charge transfer species.[40–44] Charge transfer (CT) and subsequent charge separation (CS) can be enhanced in a BHJ if the charge separation barrier can be reduced within one of the material (donor or acceptor), by increasing the charge transfer rate and degree of charge separation within that material. A popular way of doing this is by adapting the material to have a D-A configuration. Here, we explore two N-annulated thiophene π-bridged PDI dimers with A-D-A configuration – **M1** and **M1F** (**Figure 4.1**), for which **M1** has a thiophene π-bridge linking two bowl-shaped N-annulated PDIs[30] and **M1F** has the thiophene π-bridge fused with the two bowl-shaped N-annulated PDIs.[31] **M1F** fused structure shows a slight molecular twist as a result of the steric repulsion imposed by two carbonyl oxygen atoms, each from the two PDI units. It also possesses a bowed shape geometry induced from ring deformation, following N-annulation. The motivation for this study stems from the fact that unlike conventional (non-annulated) PDI dimers, the optical and photophysical properties of N-annulated thiophene π-bridged systems have not been explored. In this study, the effects of ring fusion on the optical and electronic properties of N-annulated thiophene π-bridged dimers are investigated via steady-state, non-linear, and time-resolved spectroscopic measurements. We hypothesize that fusing the backbone of the N-annulated thiophene π-bridged dimer would induce ultrafast CT and charge separation CS, possibly leading to CT/CS-induced triplet production. Increased triplet production has been observed in PDIs with enhanced intramolecular CT character.[45–48] This work seeks to confirm an important finding by Hartnett et

al[37] and Jiang et al,[18] where they demonstrate that ring fusion is a promising design principle for dimeric PDI acceptors so long as π-stacking is sufficiently disrupted to avoid excessive aggregation. We plan to confirm this finding specifically for N-annulated thiophene π-bridged PDI dimers, by spectroscopically probing the excited state dynamics of the fused and unfused compounds. The results of this study show that ring fusion induces strong intramolecular CT interactions that in turn leads to the formation of long-lived triplet species. This work is a productive route in the design of efficient solution-processable N-annulated acceptors, towards better performing non-fullerene solar cells.

(a)

(b)
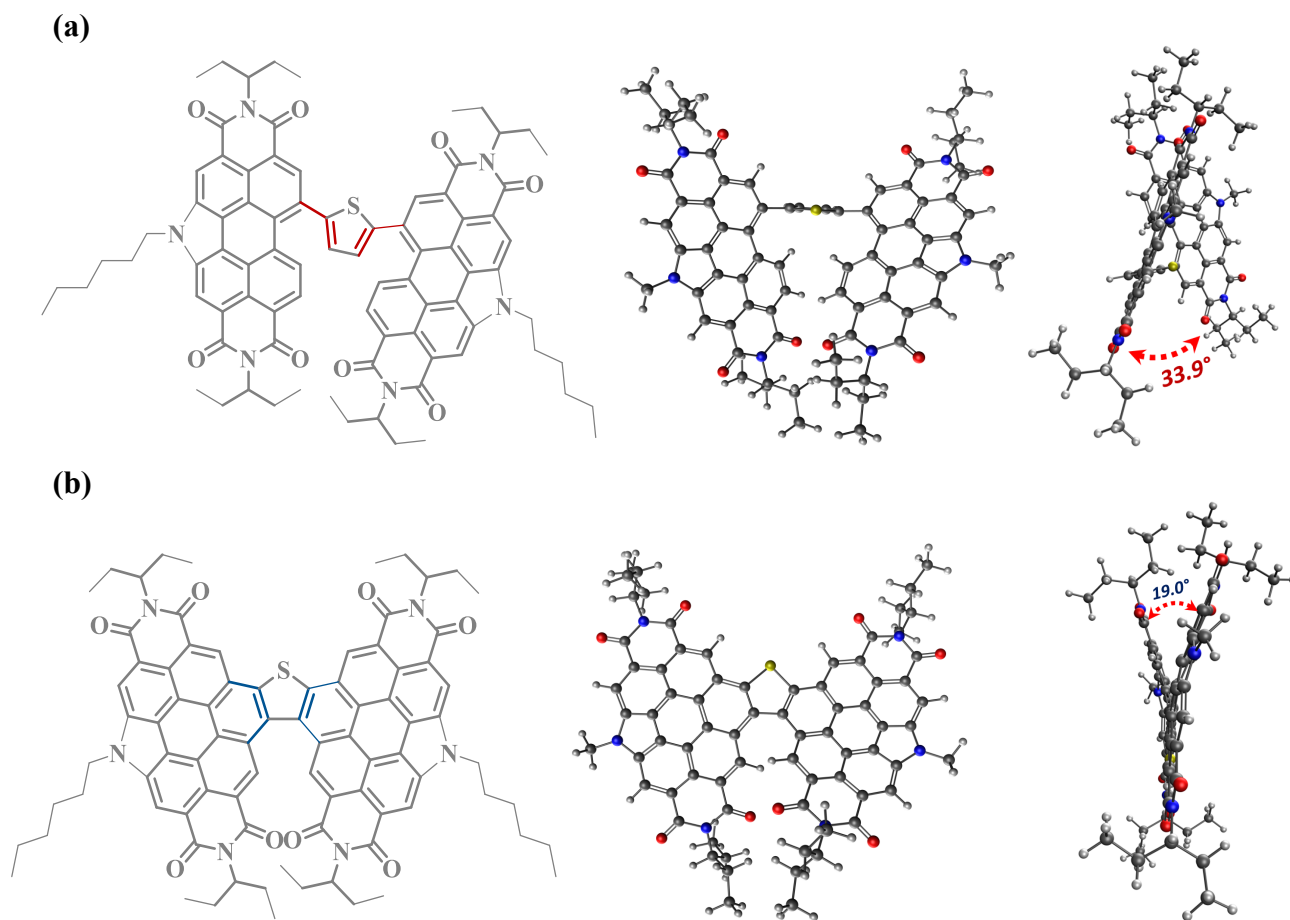
Figure 4.1 Chemical structures and optimized ground-state molecular geometry of (a) **M1** and (b) **M1F**.

4.4 Experimental Section

4.4.1 Steady State Measurements

All of the measurements were performed at room temperature. Concentrations ranging from 3×10^{-7} to 1×10^{-6} M were used for the spectroscopic investigations. Absorption spectra were measured using an Agilent 8432 UV−visible absorption spectrophotometer. The molar extinction coefficient was obtained by varying the concentrations of a sample and noting the absorbance for each concentration. Then a linear plot of absorbance vs concentration is obtained whose slope is the product of the cuvette length (0.4 cm) and the molar extinction coefficient according to Beer and Lambert's law. The emission measurements were performed with a PTI QuantaMaster™ 8000 Series spectrofluorometer from HORIBA. The fluorescence quantum yields of the samples were calculated using a known procedure[49,50] and Rhodamine B in ethanol ($\phi_F \approx 0.7$),[51,52] excited at 510 nm was used as the standard.

4.4.2 Two−Photon Excited Fluorescence Measurements

Two−photon excited fluorescence measurements were performed using a Kapteyn Murnane (KM) mode−locked Ti:Sapphire laser, pumped by a Millennia diode laser, tunable from 700 to 900 nm, and delivering 110 fs output pulses at a repetition rate of 80 MHz as described previously.[53–55] Two photon emission scans were performed under 800 nm excitation, scanning the emission in the 400−850 nm range. For the power dependence measurement, the emission wavelength that produced the highest number of counts was selected as the emission detection wavelength. Input power from the laser was varied using a variable neutral density filter and focused unto the sample cell (1 cm path, quartz cuvette) using a lens of 11.5 cm focal length and the resultant fluorescence was collected perpendicular to the excitation beam. Another lens (plano-convex) with focal length of 2.54 cm was used to direct the fluorescence into a monochromator whose output was coupled to a photomultiplier tube. Two−photon power−dependent fluorescence

intensity was utilized to determine the two−photon absorption cross section using the comparative method. Rhodamine B in methanol (cross section 120 GM at 800 nm)[56,57] was used as the standard. To confirm the experimental accuracy of this approach, another set of experiments were performed using a different reference compound – Rhodamine 6G in methanol (cross section 65 GM at 800 nm).[56]

4.4.3 Femtosecond Transient Absorption

High repetition rate, seed pulses were generated from a Millenia Pro diode-pumped Spectra Physics Tsunami Ti:sapphire oscillator. The seed pulses were fed to an Nd:YLF (Empower®) – pumped Spectra Physics Spitfire® Ti:sapphire regenerative amplifier which generated low repetition rate (1kHz), high power (1 mJ), 800 nm pulses with pulse width of ~100 fs. The amplified light was directed a beam splitter to generate the pump (85%) and the probe beams (15%).[13,21,58] The pump beam for excitation was generated in an optical parametric amplifier (Spectra Physics OPA−800CF®) producing a signal and idler using a β−barium borate (BBO) type II crystal. Excitation light of 528 nm and 540 nm were obtained via sum frequency mixing (SFM) of the 800 nm pump with the signal and idler beams respectively. The excitation light was then focused onto the sample cell (l = 2 mm) preceded by an optical chopper. The probe beam was passed through a computer−controlled delay line and focused onto a 2 mm sapphire plate to generate the white light continuum (Ultrafast Systems Inc.). The white light is then overlapped with the excitation beam in the 2 mm quartz cuvette containing the sample that is constantly stirred by a rotating magnetic stirrer to minimize sample degradation. The pump−on pump−off absorption difference (ΔA) of the signal was collected by a CCD detector (Ocean Optics). Data acquisition was carried out using the Helios software by Ultrafast Systems Inc. The IRF was measured by the Raman scattering of water at 466 nm and is found to be 110 fs. Data analysis was then performed

with Surface Xplorer and Glotaran softwares. All the experiments were performed in dilute solutions, at concentrations below 2×10^{-5} M.

4.4.4 Nanosecond Transient Absorption

The spectral properties and dynamics of long lived transient species were probed by transient absorption measurements with nanosecond time resolution. These experiments were performed in dilute aerated and deaerated solutions (below 1×10^{-5} M), where photodegradation was checked by recording UV−vis absorption spectra before and after each experiment. An Edinburgh LP980 spectrometer system, with a monochromator and PMT for signal detection (PMT−LP), was coupled with a Spectra Physics QuantaRay Nd:YAG nanosecond pulsed laser and a GWU Optical Parametric Oscillator (OPO) tunable for the excitation source. Flash lamps excite the ND:YAG rod in the laser head containing a polarizer, pockel cell, and ¼ wave plate, producing Q-switched 1064 nm light. Two-stage harmonic generation then produces high energy 355 nm light used to pump the OPO. The OPO produces excitation source from 206 nm to 2600 nm employing second harmonic generation and sum-frequency mixing nonlinear processes.[21,59] For this investigation, 531 nm and 544 nm excitation wavelengths were used to pump the samples and a pulsed xenon lamp white light continuum was used to probe the absorption properties of the produced excited states.

4.4.5 Time−Resolved Fluorescence Measurements

Time−correlated single photon counting (TCSPC) technique, which has been described previously,[13] was used to study the fluorescence decay dynamics of the investigated samples. A home-built mode−locked Ti−sapphire laser with cavity dumper was used in this measurement. The repetition rate was set at 765 kHz. The output beam from the KM laser was at 800 nm wavelength,

with a pulse duration of ca. 30 fs. The output beam was frequency−doubled using a nonlinear β−barium borate crystal to obtain a 400 nm beam. Some portion of the 400 nm beam was focused on the sample cell (quartz cuvette, 1 cm path length) using a lens of focal length 11.5 cm. To set the polarization and reduce the intensity of the 400 nm excitation beam, a polarizer was used right before the lens. The other portion of the 400 nm beam was focused onto a silicon-based fast trigger photodiode connected to the TimeHarp 200 processor chipset. Collection of fluorescence was carried out in a direction perpendicular to the excitation beam into a monochromator set at the maximum emission wavelength of the sample. The output from the monochromator was coupled to a photomultiplier tube, which converted the photons into counts. The TimeHarp software created time histograms by converting timing information from both the fast trigger photodiode and the photomultiplier. Data analysis was carried by fitting mono−exponential decay functions in Origin.

4.4.6 Quantum Chemical Simulations

Theoretical investigation has been performed on molecular structures where the long alkyl chains are replaced by short chains alkyl groups [C_3H_7, C_6H_{13}] attached to the PDI to save computational time without significant effect on the electronic properties. The ground state geometry of each compound was obtained by density functional theory (DFT), using the long−range corrected ωB97X-D,[60,61] and B3LYP functional, together with the 6−31G** basis set. Optimization of the lowest energy triplet state (T_1) was performed using unrestricted DFT and the ground state (S_0), first excited singlet state (S_1) was performed using the restricted DFT. Excited state simulations were performed using time dependent DFT (TD-DFT). Single-point energy calculations were conducted using ωB97X-D,[60,61] and B3LYP functional with the 6−31G** basis set. Polarizable continuum model (PCM)[62] was used for solvation effect corrections, using the

dielectric constant of 4.81 for chloroform, 12.4 for pyridine and 2.38 for toluene. Characters of excitations were described with natural transition orbitals (NTOs). Spin-orbit coupling (SOC)[63,64] constants were also calculated with TD-DFT. The first excited singlet (S_1) geometry was used to calculate these SOC constants. All the calculations were performed using Q-Chem 5.0 software package.[65] Natural transition orbitals (NTOs) of TD-DFT calculations were visualized using IQMOL and Gabedit.[66]

4.5 Results

4.5.1 Steady State Absorption and Emission

The UV-Vis absorption spectra for the N-annulated thiophene π-bridged dimers in dilute chloroform solution are shown in **Figure 4.2**. The spectra for monomeric parent PDI is also included. Just like the parent PDI monomer, the absorption spectra of these dimers are strongly structured and are influenced, only to some extent, by solvent effects (see **Figure 4.10**). However, the absorption spectra of the dimer compounds are red-shifted relative to that of the parent PDI monomer, indicating some form of electron delocalization. The absorption spectrum of the unfused **M1** dimer is similar in structure to that of the parent PDI monomer, indicating that excitation is localized on one PDI unit. It displays a strong 0-0 vibronic transition (λ_{0-0}) at 534 nm, and a weaker peak for the 0-1 transition (λ_{0-1}) at 498 nm. The 0-2 transition (λ_{0-2}) appears less resolved, as a small shoulder, for the dimer compound at ~465 nm. These vibronic peaks correspond to transitions from the vibrationless electronic ground state (S_0) to the first electronic excited state (S_1) with *0*, *1* and *2* vibrational quanta, represented by λ_{0-0}, λ_{0-1} and λ_{0-2} respectively.[67] Also, in comparing the absorption spectrum of unfused **M1** dimer with that of the parent PDI monomer, there is a slight difference in their vibronic progression (i.e. between the peak positions of λ_{0-0} and λ_{0-1}), 46 nm/1354 cm^{-1} and 38 nm/1469 cm^{-1} for **M1** and parent PDI monomer, respectively

The absorption spectrum of the fused **M1F** dimer is not structurally similar to that of the unfused **M1** dimer and the parent PDI monomer. In addition to being more red-shifted, the respective vibronic transitions $(\lambda_{0-0}, \lambda_{0-1})$ are varying in intensity, relative to those of **M1**. This indicates pronounced excitonic coupling between adjacent PDI chromophores due to stronger intramolecular interactions.[46,68–71] It originates from a complex interplay of excitonic and vibronic couplings (intermediate coupling regime).[68,72] No spectral broadening in the 400 – 600 nm region is observed for the fused **M1F** relative to the unfused **M1** dimer consistent with the rigid architecture of **M1F** due to ring fusion. There is a broad band at the lower wavelength spectral region (< 400 nm) that could be associated with the absorption of thiophene heterocycle.[73,74] This band is more pronounced and red-shifted for the fused **M1F** dimer, which complies also with its rigid structure.[68] The fused **M1F** dimer has a larger solvatochromic shift relative to the unfused **M1** dimer, indicating a greater effect of solvent polarity on its photophysical properties (**Figure 4.10**).

Unlike in the case of the parent PDI monomer, for the thiophene π-bridged dimers, the emission spectra are not mirror images of the absorption spectra. This indicates that some form of PDI-PDI interactions do exist in these dimers.[71] The emission spectrum of the unfused **M1** dimer was more red-shifted relative to that of the fused **M1F** dimer. This resulted in a larger Stokes-shift for **M1**, by over one order of magnitude. This was expected given that **M1** has a larger dihedral angle in comparison to **M1F**, and the unfused thiophene unit in **M1** causes the N-annulated PDI units to become more spatially separated and less sterically encumbered. Hence the two PDI units can rotate more freely with respect to each other. Also, unlike the fluorescence spectra of the unfused **M1** dimer, the striking resemblance of the spectrum of **M1F** with that of the parent monomeric PDI, is quite interesting. Its shows that emission is most likely taking place from one

PDI unit of the dimer compound. This has been observed for compounds for which the LUMO is largely localized on a single PDI, and said to be exhibiting intramolecular symmetry breaking charge separation upon photoexcitation.[13,75]

The fluorescence quantum yields obtained (see **Table 4.1**) indicate that these dimers are good emitters. Fluorescence quantum yield was found to be 35 – 60% lower for these thiophene π-bridged dimers relative to the dimer not having any thiophene π-bridge – **T-PDI₂** (see **Table 4.6**).[29] In comparing the fluorescence quantum yield of the two N-annulated thiophene π-bridged dimers, the fused **M1F** showed a higher quantum yield relative to the unfused **M1**. As reported in the literature, increased molecular planarity is indeed associated with a higher fluorescence quantum yield.[13,21] In a less polar solvent, their fluorescence quantum yield value increased; **M1** was 0.30 and **M1F** was 0.55. The increase in the quantum yield in going from a polar solvent (chloroform, relative polarity $\varepsilon_r = 0.259$) to a less polar solvent (toluene, $\varepsilon_r = 0.099$) was greater in the case of the fused **M1F** dimer. This is characteristic of an improved charge separation rate in this compound owing to ring fusion.
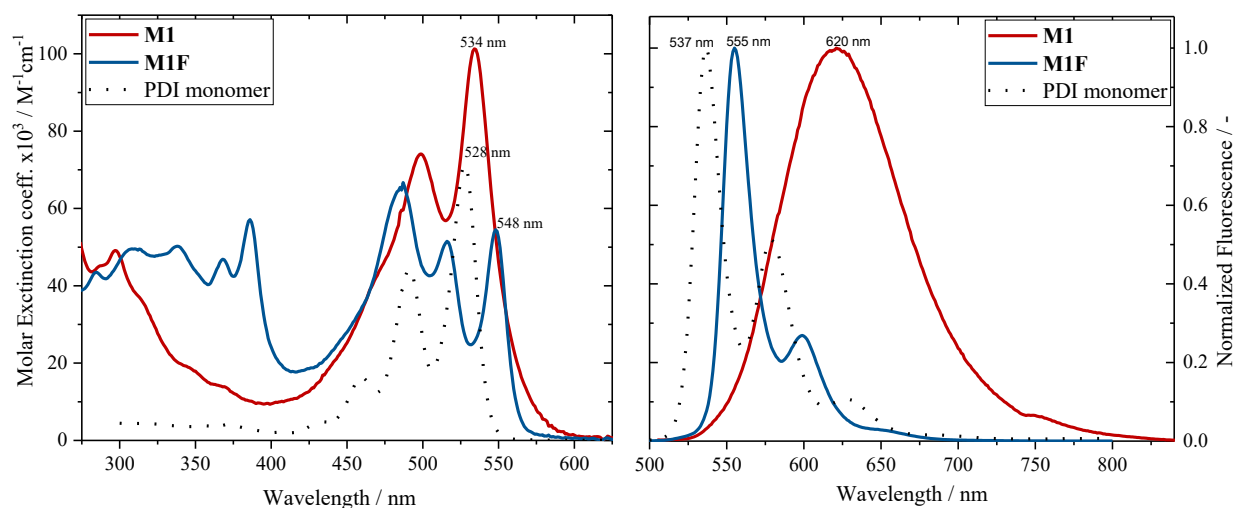
Figure 4.2 Molar extinction spectra (left) and normalized photoluminescence spectra (right) of the N-annulated thiophene π-bridged PDI dimers and PDI monomer in chloroform (CHCl₃) of ~3 x 10⁻⁵ M, at room temperature.

Table 4.1 Optical steady state properties for the N-annulated thiophene π-bridged dimers in CHCl₃.
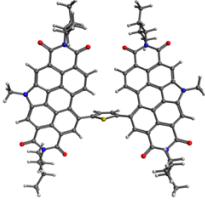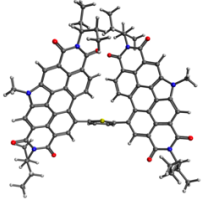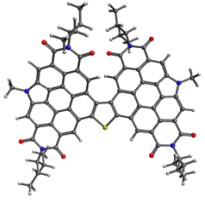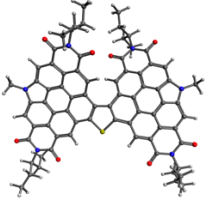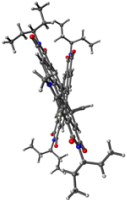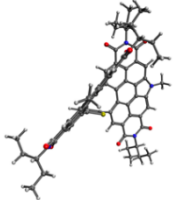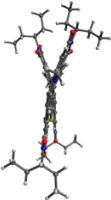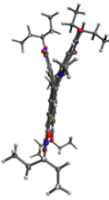
Comp.nd	λ_{abs} [a] / nm	λ_{em} / nm	$\Delta\upsilon$ [b] /cm⁻¹	ε [c] / M⁻¹cm⁻¹	ϕ_F
M1	<u>534</u>, 499	620	2598	101300	0.28
M1F	548, 516, <u>487</u>	555, 600	230	66700	0.47

[a] peak position of λ_{0-0}, λ_{0-1}, and λ_{0-2} in this order; [b] using λ_{0-0} and λ_{em}; [c] at the underlined wavelength (λ_{abs}^{max})

4.5.2 Quantum Chemical Simulations

As expected, the excitation energies predicted by TD-DFT calculations, both using B3LYP and ωB97X-D functional, are blue-shifted when compared to the actual experimental data. Based on Farina et al,[76] the discrepancies between the experimental data and simulation results could be due to the optimized geometry used and, in particular, to the dihedral angle between the perylene groups. Hence, a more systematic analysis on dihedral angles of the optimized structures should be conducted.

Table 4.2 Ground state optimized geometry (top and lateral views) computed for **M1** and **M1F**.

	M1		M1F	
	B3LYP	ωB97X-D	B3LYP	ωB97X-D
Top structure				
Lateral structure				
Dihedral angle (PDI-PDI)	32.21°	33.91°	21.10°	19.14°
Dihedral angle (PDI-thiophene)	86.55°, 58.25°	60.01°, 80.55°	1.82°, 1.82°	0.03°, 0.04°

A desired structural analysis is shown in **Table 4.2**. The optimized geometries obtained from using B3LYP and ωB97X-D functional are quite similar. Both of the functionals predict that

M1F will have a smaller dihedral angle between the two PDI chromophores. This fact could be explained by the more constrained structure of **M1F** when comparing to **M1**. However, since the propyl chains attached at the end of chromophores are included in the calculations, the bent structure of **M1F** could be due to the repulsion force between the long chains.

4.5.3 Two-Photon Absorption

Two-photon excited fluorescence (TPEF) measurements were carried out in chloroform to obtain the two-photon absorption cross-section (TPA-δ) of the N-annulated thiophene π-bridged dimers using Rhodamine B in methanol as the reference. The quadratic dependence of the fluorescence signal on the laser excitation power was verified for the dimers upon 800 nm excitation. This is evident by the slope of 2 obtained from the fitted log(fluorescence) vs. log(excitation power) plot shown in **Figure 4.3a**. Using the intercept of the linear fit and some other parameters, the TPA-δ was computed and is presented in **Table 4.3**. Similar TPA-δ was obtained using a different reference compound (Rhodamine 6G in methanol) thus validating the accuracy of this measurement. The two-photon excited emission spectra of the dimers given in **Figure 4.3b** is very similar to the one-photon/steady state emission spectra (**Figure 4.2, right**); this suggests that the achieved singlet S_1 state responsible for the fluorescence is the similar for one-photon and two-photon excitation. The peak emission of **M1F** (555 nm) matches perfectly with that of its steady state spectra, but the 600 nm peak is a little less resolved. For **M1**, its peak emission is slightly blue-shifted relative to its steady state spectra. This could just be due to the poor sensitivity of the photomultiplier in this wavelength region.
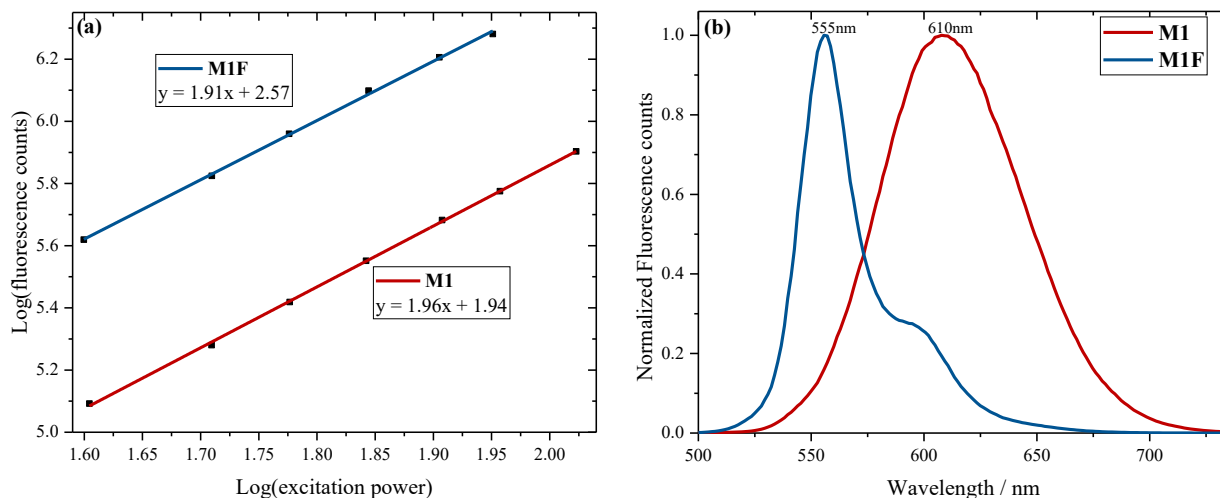
Figure 4.3 (a) Fluorescence signal intensity dependence on average excitation power, (b) Two-photon excited fluorescence spectra, for the N-annulated thiophene π-bridged dimers in CHCl₃ upon 800 nm pulsed excitation.

Two-photon cross-section is strongly dependent on the π-conjugation length, the degree of conformational planarity (obtained from the dihedral angle, **Table 4.3**); and it directly correlates to the intramolecular charge transfer property of the molecule.[13;21;77] The TPA-δ of the fused **M1F** dimer (18.4 GM) is three times larger than that of the unfused **M1** dimer (6.0 GM). As stated, this observed trend directly correlates to the dihedral angle of the dimers, with the fused compound **M1F**, showing the highest TPA-δ. The TPA response and cross-section observed for the investigated dimers is in agreement with the rate of photoinduced intramolecular charge transfer revealed to take place in these structures evident by the femtosecond absorption study. It is also key to note that these dimers with a thiophene π-bridge separator show higher two-photon cross-sections relative to the dimer with no thiophene π-bridge - **T-PDI₂** (see **Table 4.6**). This is due to the presence of the electron rich heterocycle at the center of the molecule, inducing a stronger donor-acceptor character, which enhances its static and transition dipole moments.[77]

Table 4.3 Two-photon absorption cross-section (TPA-δ) and dihedral angle of the N-annulated thiophene π-bridged dimers.

Comp.nd	TPA-δ / GM [a]	PDI-thiophene dihedral angle (avg.)[b]	PDI-PDI dihedral angle[b]

M1	6.0	70⁰	34⁰
M1-F	18.4	0⁰	19⁰

[a] at 800 nm excitation; [b] angles obtained from using ωB97X-D

4.5.4 Femtosecond Transient Absorption

To provide further insights into the intramolecular charge transfer mechanisms which highlights the effect of ring fusion on charge transfer/charge separation and excited state dynamics in the N-annulated thiophene π-bridged dimers, femtosecond transient absorption (fsTA) measurements were carried out. Pulsed laser excitations of 540 nm and 528 nm were employed for the dimers in different solvents of varying polarity. Toluene (relative polarity, $\varepsilon_r = 0.099$), chlroform ($\varepsilon_r = 0.259$) and pyridine ($\varepsilon_r = 0.302$) were used. **Figure 4.4** shows the fsTA spectra of the N-annulated thiophene π-bridged dimers in chloroform. The steady state absorption spectra were added for identifying the ground state bleach (GSB) signal. The fsTA spectra, at *later times*, show the maximum GSB signal at 536 nm/498 nm and 550 nm/516 nm for **M1** and **M1F** respectively corresponding with their respective $\lambda_{0-0}/\lambda_{0-1}$ steady state transitions.

For the unfused **M1** dimer, the λ_{0-0} transition of the GSB signal show a blue-shift in time, following photoexcitation. However, the fused **M1F** dimer showed a slight red-shift instead. The blue-shift of the GSB signal in time of the unfused **M1** dimer, confirms the high degree of structural changes taking place in solution following photoexcitation. This induces a slight perturbation from its lowest energy equilibrium state, causing its $S_0{\rightarrow}S_1$ transition energy to change. Despite the quantifiable fluorescence quantum yield of the dimers in chloroform, stimulated emission band for all three compounds was not observed in the fsTA spectra; it was overshadowed by excited state absorption (ESA) species with peaks around 576 nm and 650 nm/622 nm. The 576 nm transient species, to be discussed later in more detail, is the PDI cationic (PDI$^{\bullet+}$) charge transfer species.[75,78–82] The ESA band associated with the excited singlet species,

$S_n \leftarrow S_1$ (PDI*), was observed between 622 nm and 650 nm for both compounds.[75] At ~700 nm, PDI anionic (PDI$^{\bullet-}$) charge transfer species,[75,78–83] was observed in the spectra of both dimers following photoexcitation (see broken line in **Figure 4.4**). This anionic band, PDI$^{\bullet-}$ of the fused **M1F** is relatively more intense and slightly more broadened relative to that of the unfused **M1** dimer. These features have been observed and elucidated by Hartnett et al, by carrying out electron paramagnetic resonance (EPR) and optical spectroscopic studies on chemically reduced PDI dimer species.[37] The blue-shifted and more broadened anionic band of the fused **M1F** dimer is indicative of increased anionic delocalization due to stronger electronic coupling.

For the unfused **M1** dimer, the rapid decay of the excited state singlet species (PDI*) band at 650 nm led to the concomitant formation of the 576 nm species, attributed to the PDI$^{\bullet+}$ charge separated species (**Figure 4.4**). This is an indication that the decay of the PDI* species in **M1**, led to the formation of the PDI$^{\bullet+}$ charge separated species. The formation time of this PDI$^{\bullet+}$ species is ~23.4 ps in chloroform (ε_r = 0.259). It formed at a slightly slower rate of 25 ps in toluene (ε_r = 0.099) and relatively faster, 11 ps in pyridine (ε_r = 0.302), indeed confirming its charged nature. However, for the fused **M1F** dimer, the formation of the PDI$^{\bullet+}$ species, at ~576 nm, was as fast as the IRF (<120 fs) of the setup regardless of the solvent polarity and can be said to be of the same timescale as the formation of the PDI* species. This confirms that an ultrafast charge separation process is taking place in the fused **M1F** dimer, as hinted by its high TPA-δ. The early coexistence of both the PDI$^{\bullet+}$ (~576 nm) and PDI$^{\bullet-}$ (~700 nm) species in the fused **M1F** dimer, almost immediately following photoexcitation and of similar amplitudes, is a clear and distinctive confirmation of ultrafast charge formation and subsequent separation, which is most likely driven by symmetry breaking.[13,81]
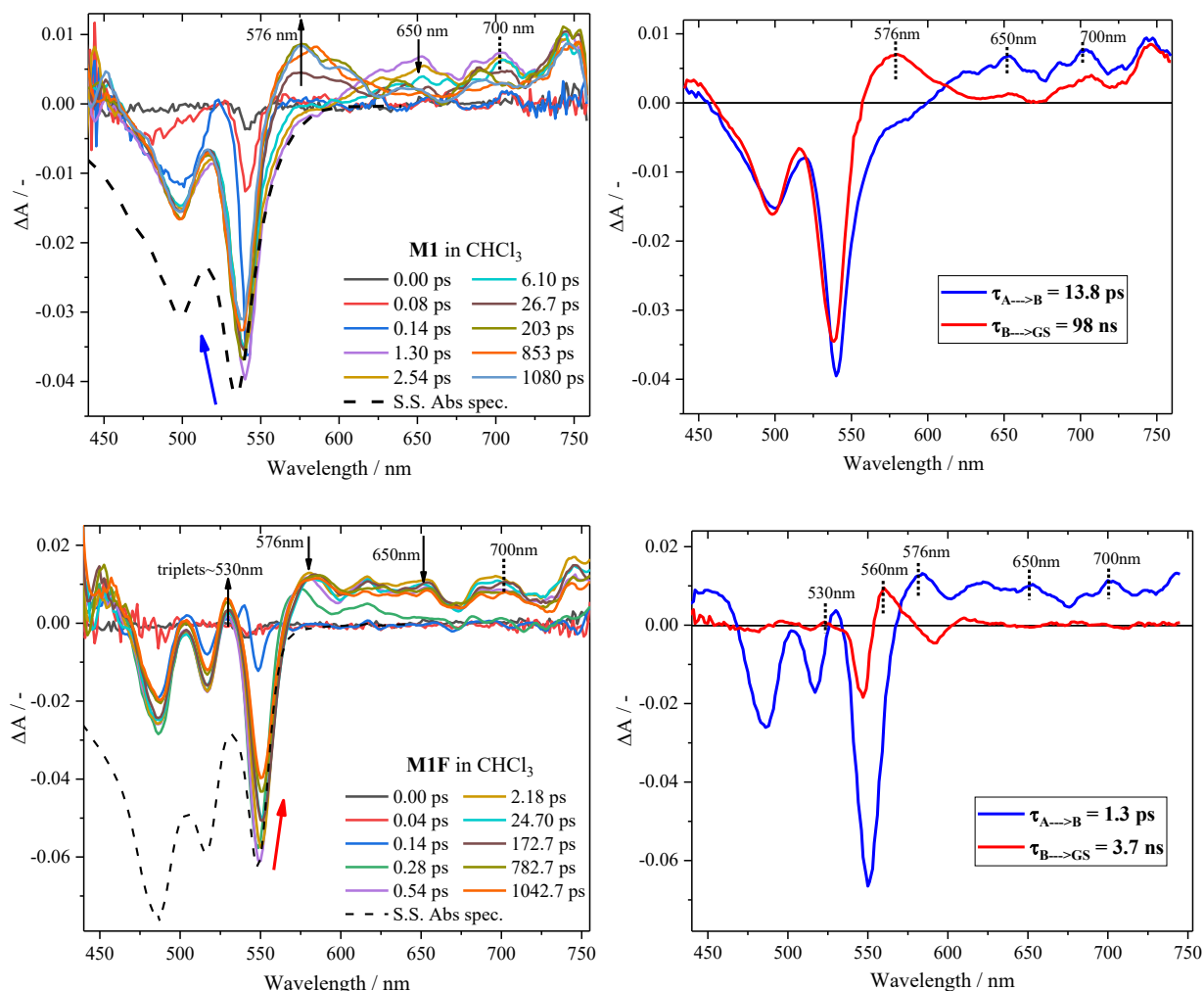
Figure 4.4 Femtosecond transient absorption spectra (left) and their corresponding evolution-associated spectra (right) of **M1** and **M1F** in chloroform following excitation at 540 nm. Steady state absorption spectra (broken line) is included to identify the ground-state bleaching signals.

To gain a clearer understanding of the excited state relaxation mechanism and obtain more information about the charge separation mechanism taking place in both the unfused and fused dimers, global analysis of the fsTA data via a sequential scheme was carried out. Global analysis, revealed the presence of the principal components, their evolution-associated spectra (EAS) and their kinetics.[84,85] Two components were obtained for the N-annulated thiophene π-bridged dimers in chloroform (see **Figure 4.4**, right). For **M1**, the first relaxation component yielded a time constant of 13.8 ps, and for the fused **M1F** dimer, the first component time constant was 1.3 ps. This first relaxation component is associated to intramolecular charge separation taking pace in

the dimers, given the similarity of these time constants to the formation time of the PDI[•+] species observed at ~576 nm. Similar ultrafast charge separation lifetimes, as obtained for **M1F**, have been obtained by Lefler et al for π-π stacked PDI molecules attached to a Xanthene scaffold,[47] and Margulies et al for a set of terrylene diimide dimers in chloroform.[86] This component also includes in it, the sub-picosecond structural relaxation effect. It is again evident that the fused **M1F** dimer show a faster charge separation relative to the twisted dimers, by one order of magnitude. The result of the unfused **M1** dimer is consistent with the result obtained by Guo et al,[75] where the formation of the charge separation state for the *para*-substituted N-annulated PDI dimer was obtained to be 12.4 ps. It is also consistent with the charge separation lifetime obtained by Wasielewski et al for a cyclic perylene diimide trimer (12 ps),[69] and for a donor-bridge-acceptor compound with a *trans*-stilbene bridge (14 ps).[87] The second relaxation component appear to be much greater than the limited time measurement window of the femtosecond TA (1.7 ns), especially for the unfused **M1** dimer and is assigned to charge recombination as given in **Table 4.4**. A better resolution of this slowly decaying component is provided by the nanosecond transient absorption (see **Figure 4.7** and **Table 4.5**). For **M1F**, the time constant for the second component was 3.7 ns, which is exactly the fluorescence lifetime obtained via time-resolved fluorescence measurement (3.63 ns) in **Figure 4.8**. This led to assigning this component as the convolution of the charge recombination process and the decay of the excited state singlet species PDI*, which are known to occur in similar timescales for PDI-containing compounds.[46,69,75,80,83]

Table 4.4 GSB wavelength-shifts and lifetimes (τ) obtained using the fsTA technique for the N-annulated thiophene π-bridged dimers in CHCl$_3$.

Comp.nd	GSB λ-shift / nm	τ_{CS} [a] / ps	τ_{CR} [a] / ns	PDI[•+] formation τ [b] / ps
M1	541 → 536	13.8	98	23.40
M1-F	548 → 550	1.3	3.7	< 0.12

[a] obtained from global analysis; [b] obtained by mono-exponential fit at 576 nm (PDI[•+])

Another interesting and important feature observed in the fsTA spectra of the fused **M1F** dimer is the formation of long-lived species ~528 nm. This long-lived species have been designated as PDI triplets (PDI^3*), that have been reported to appear in this spectral region.[21,46,47,79] The rate of formation of the triplet species is also observed to be solvent dependent as given in **Figure 4.5** and **4.6**, regardless of the accelerated charge separation witnessed in both polar and nonpolar environment. It is faster in a less polar solvent like toluene (0.4 ns), but a lot slower in a more polar solvent like pyridine (~7 ns). The decrease in the rate of triplet formation in more polar environments is a consequence of a stabilization or lowering of the charge transfer (CT) transition state by polar solvents, which may serve as an experimentally observable trap state.[86] The generation of triplet states from CT excited state, have been reported to be affected by CT interactions, even in the absence of heavy atom or paramagnetic species. To this regard, the mechanism of triplet formation in this fused **M1F** dimer is taking place either via spin-orbit charge transfer intersystem crossing (SOCT-ISC) and/or radical pair intersystem crossing (RP-ISC).[46–48,88,89] According to Veldman et al, RP-ISC [$S_1 \rightarrow {}^1CT \rightarrow {}^3CT \rightarrow T_1$] is favored by weak electronic coupling between the donor and acceptor unit to allow a spin-flip in the CT state, while SOCT-ISC [$S_1 \rightarrow {}^1CT \rightarrow T_1$] is favored by strong electronic coupling.[48] The exact mechanism of triplet production in the fused **M1F** dimer is not apparent from this measurement, but it points more to SOCT-ISC given the strong electronic coupling present in **M1F** as a result of ring fusion. More detailed studies such as magnetic field effect (MFE) measurements and time-resolved electron paramagnetic resonance (TREPR) spectroscopic measurements are required. These measurements are able to obtain the exchange coupling (2J) between donor and acceptor charge species, which is related to the required energy difference (if any) between the ${}^1CT$ and the ${}^3CT$ states, to be able to point out the specific triplet formation mechanism.[89–92]
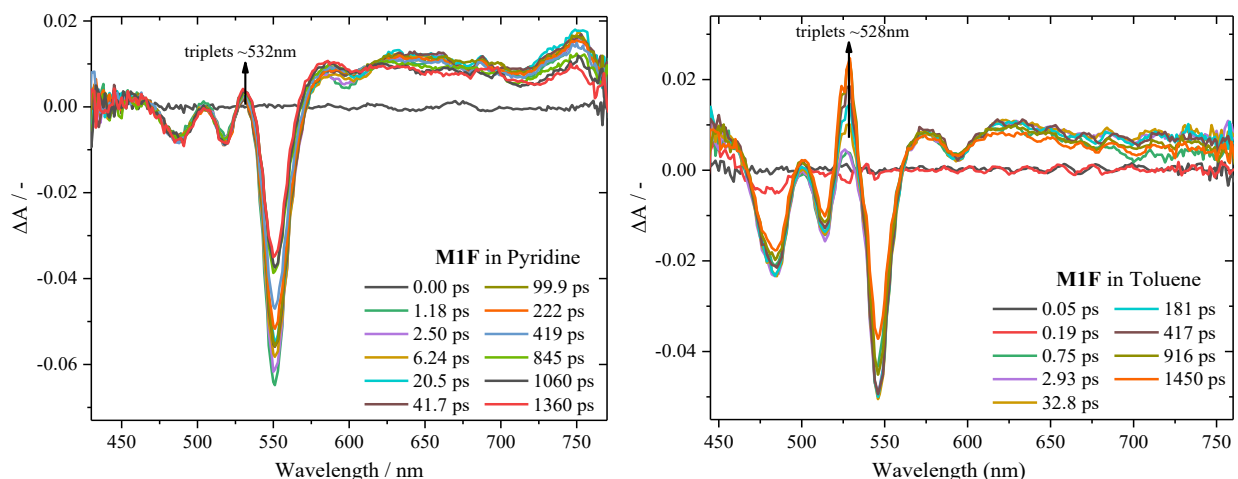
Figure 4.5 Femtosecond transient absorption spectra of **M1F** in pyridine (left) and toluene (right) following excitation at 540 nm and 530 nm, respectively.
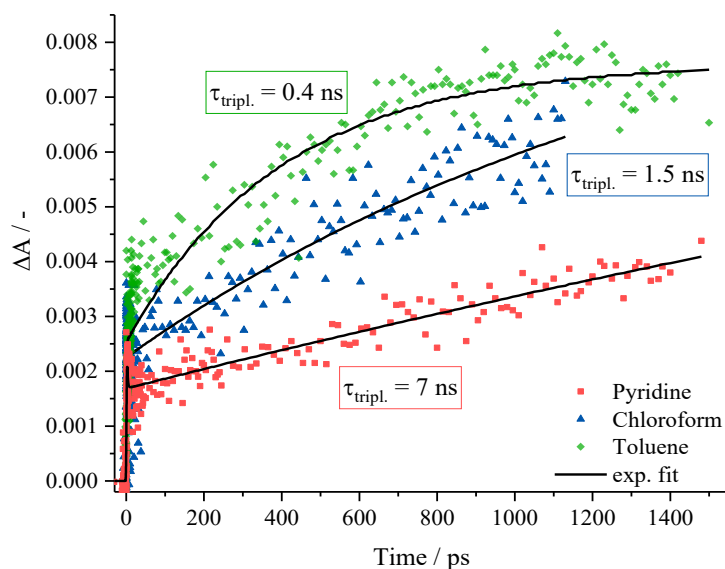
Figure 4.6 Triplet kinetics and bi-exponential fits for the fused M1F dimer in toluene, chloroform and pyridine.

4.5.5 Nanosecond Transient Absorption

To accurately measure the long charge recombination lifetime observed for the unfused **M1** dimer, and the triplet-state lifetime of the fused **M1F** dimer, nanosecond transient absorption (nsTA) measurements were carried out in toluene solution. Excitations at 531 nm and 544 nm were employed for **M1** and **M1F**, respectively, based on their λ_{0-0} absorption maxima. Unfused **M1** and fused **M1F** dimers showed GSB features at 530 nm/494 nm and 546 nm/ 513 nm, respectively,

similar to the GSB features obtained with the fsTA technique at later times. For **M1F**, these GSB features had a smaller width for both transitions, relative to the features of the fsTA. This is as a result of the persistent ESA species convoluted with the GSB features at 546 nm and 513 nm. These ESA species, to be confirmed later as triplets, show features at 501 nm, 524 nm and 556 nm. In addition, for **M1F**, the broad band at the lower spectral region (300 – 400 nm) in the steady state absorption spectra was observed as a GSB signal, while in this region for **M1**, an ESA centered ~ 415 nm was observed.
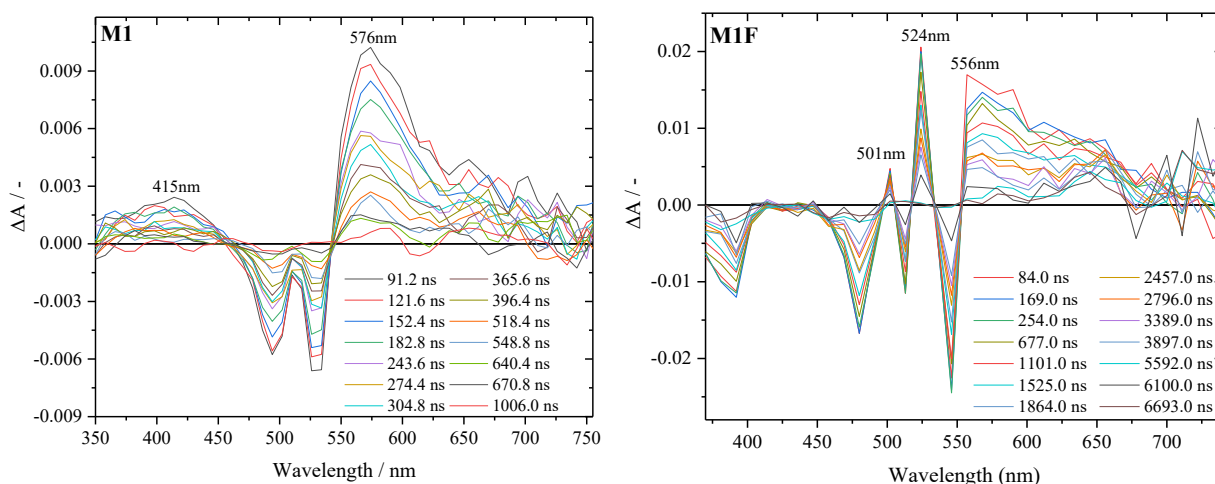
Figure 4.7 Nanosecond transient absorption spectra of **M1** and **M1F** in toluene following excitation at 531 nm and 544 nm, respectively.

For the charge transfer species of the unfused **M1** dimer, while the PDI$^{\bullet-}$ species observed at ~700 nm in the fsTA decayed completely, the PDI$^{\bullet+}$ species observed at ~576 nm persisted well into the nanoseconds timescales to be captured by nsTA. The charge recombination lifetime, solely determined by the lifetime of the PDI$^{\bullet+}$ species, following global analysis of the fsTA data of the unfused **M1** dimer was derived to be ~98 ns (see **Table 4.4**). Given the limited temporal measurement window of the fsTA setup, this mathematically derived lifetime needed to be verified with the nsTA technique. The lifetime of this PDI$^{\bullet+}$ species at 576 nm was determined to be 320 ns by carrying out a mono-exponential fit (**Figure 4.14**). For the fused **M1F** dimer, the decay of

both the PDI$^{\bullet+}$ and PDI$^{\bullet-}$ species was able to be captured within the time window of the fsTA. None of the CT species was observed with the nsTA, as they decayed well beyond the IRF (~7 ns), agreeing with the 3.7 ns lifetime observed with the fsTA technique (see **Table 4.4**). The only visible ESA feature is the long-lived broad band species, spanning 500 – 700 nm and peaked at 524 nm. This species is observed in the same spectral region as the long-lived species that formed in the fsTA ~528 nm (**Figure 4.4** and **4.5**), indicating that it is the triplet excited state of PDI (i.e., PDI^{3*}). This signal can be quenched by oxygen. The triplet lifetime changes from hundreds of nanoseconds in air equilibrated solution to a few microseconds in de-aerated/nitrogen-purged solution. These results allow us to undoubtedly assign these long−lived transients, revealed by the nanosecond transient absorption experiment, to the $T_n \leftarrow T_1$ transition of the fused **M1F** dimer. Once again, the fact that triplets, derived from the CT/CS state, were observed only in the fused **M1F** dimer speaks to the effect of ring fusion on the photophysical properties of N-annulated thiophene π-bridged dimers.

Table 4.5 Nanosecond transient absorption species and their lifetimes (τ) for the N-annulated thiophene π-bridged dimers in toluene.

Comp.nd	Detecting species	Peak λ / nm	τ_{CR} [a] / ns	$\tau_{triplet}$ [b] decay/ μs
M1	PDI$^{\bullet+}$	576	320	--
M1-F	PDI^{3*}	524	< 7	3.3

[a] only **M1** showed this persisting 576 nm species; [b] only **M1F** showed triplets at 524 nm

4.5.6 Time-Resolved Fluorescence Measurement

Fluorescence kinetic measurements were acquired by employing the time correlated single photon counting (TCSPC) technique with nanosecond time-resolution. The fluorescence kinetics in chloroform and toluene were acquired at the peak emission wavelength (λ_{em}) of the N-annulated dimers. Performing mono-exponential fits, as shown in **Figure 4.8**, yielded the fluorescence decay lifetime of the emitting component of the excited state. The lifetime for the unfused **M1** and fused

M1F thiophene π-bridged dimers in chloroform are 4.75 ns and 3.63 ns, respectively. The thiophene π-bridged dimers, **M1** and **M1F**, showed a much shorter fluorescence dynamics relative to the dimer with no thiophene π-bridge - **T-PDI₂** (see **Figure 4.16**). This result mirrors the smaller quantum yields obtained for the dimers containing thiophene in their molecular makeup, indicating once again their preference for a non-radiative relaxation pathway.

The fluorescence lifetime of the unfused **M1** dimer is slightly longer than that of the fused **M1F** dimer. This speaks to their relative degree of molecular rigidity, for which the more rigid compound showed a shorter-lived fluorescence component. The fluorescence lifetime of the fused **M1F** dimer (3.63 ns) is exactly similar to the second global fit component of the fsTA (3.7 ns) that was assigned to charge recombination. This shows that the charge transfer state is an emissive state. This was not the case for the unfused **M1** dimer that showed a long charge recombination lifetime of 321 ns. Despite its strong electronic coupling due to ring fusion, the fluorescence lifetime of the fused **M1F** dimer (3.63 ns) is very similar to that of the PDI monomer in chloroform, reported as 3.7 ns.[93] This is an interesting finding as it goes on to confirm that emission is indeed taking place from just one PDI unit of the dimeric structure. It supports the similar emission spectra observed for the fused **M1F** dimer and the parent PDI monomer in **Figure 4.2**.
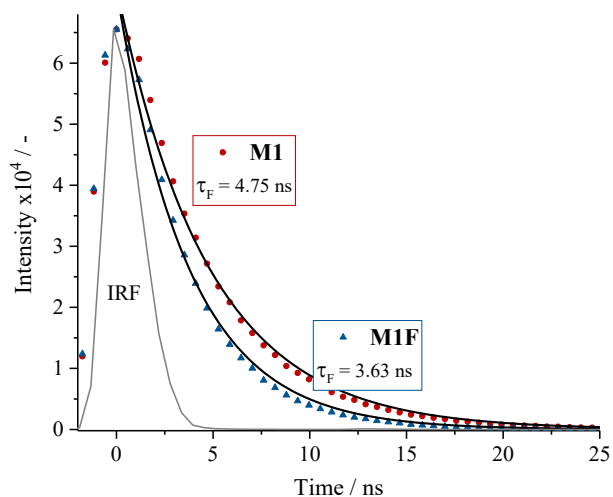
Figure 4.8 Fluorescence kinetics obtained by nanosecond TCSPC in air equilibrated chloroform.

4.6 Discussion

Ring-fusion have been said to increase electronic delocalization, extend effective π-conjugation, increase electron mobility, reduce the reorganization energy and improve molecular packing. Most ring-fusion studies on PDI systems in the literature only discuss the implications or benefits of ring-fusion on the photovoltaic device properties.[18,24,36–39] The device properties and device efficiency information is crucial, but it does not provide adequate structure-function information necessary to advise the synthesis of a more targeted PDI system for a specific electronic application. There are not a lot of discussions about the optical and photophysical properties that may arise as a result of ring-fusion, specifically for annulated π-bridged PDI systems, this work seeks to initiate the discussion. In this study, we point out the key differences between unfused and fused N-annulated thiophene π-bridged dimer systems, as they relate to the degree of electronic coupling, the rate of charge separation and triplet production upon photoexcitation. The charge separation and triplet formation studies were carried out in solvents of varying polarity, with relative polarity (ε_r) values ranging between: $0.099 \leq \varepsilon_r \leq 0.302$. Two analogous N-annulated thiophene π-bridged PDI dimers with A-D-A configuration were investigated, whose structures show a rotatable single-bond thiophene π-bridge connection (**M1**) relative to a rigid fused π-bridge connection (**M1F**). N-annulation of PDI dimers offer added advantages over conventional (no annulation) dimers or S/Se-annulated dimers owing to its ability to be functionalized in two more positions by alkyl groups. This could be used to improve solubility and guide in the use of shorter alkyl side chains (as used in present study) relative to those used in conventional or S/Se-annulated dimers, greatly impacting the packing and self-assembly in thin films.

In addition to the computational results detailing the optimized ground and excited state molecular geometry, the steady-state absorption and emission experimental results provide some information about the molecular rigidity of the N-annulated thiophene π-bridged dimers. The absorption spectra of the unfused **M1** dimer showed some structural similarity with that of the parent PDI monomer, indicating that excitation is localized on one PDI unit. This further indicates minimal ground state interaction or excitonic coupling among the PDI units.[21,94] However, the absorption spectra for the fused **M1F** dimer showed more structure, and this have been associated to molecular rigidity indicating stronger electronic coupling. Surprisingly, despite the strong electronic coupling imposed due to ring-fusion, the emission spectra of the fused **M1F** was more similar to that of the parent PDI monomer. In the literature, this have been associated to excited state symmetry breaking, causing the LUMO to be largely localized on a single PDI unit.[13] The Stokes-shift for the unfused **M1** dimer is larger that of the fused **M1F** dimer by over one order of magnitude, indeed confirming the molecular rigidity of **M1F** due to ring-fusion.

The femtosecond and nanosecond spectroscopic measurements provided valuable information about the excited state dynamics such as photoinduced intramolecular charge separation and triplet formation, taking place in the investigated N-annulated thiophene π-bridged dimers. The ground state bleach (GSB) signal showed a spectral blue-shift in time following photoexcitation for the unfused **M1** dimer but showed only a slight red-shift for the fused **M1F** dimer. This shift towards higher energy for the unfused **M1** dimer speaks to the higher degree of structural changes taking place upon photoexcitation. Spectral signatures of the PDI singlet (PDI*), radical anion (PDI$^{•-}$) and cation (PDI$^{•+}$) species were observed for both dimers. The PDI anionic species in the fused **M1F** dimer were blue-shifted and more broadened relative to that of the unfused **M1** dimer, and this have been attributed to increased anionic delocalization due to

stronger electronic coupling.[37] For the unfused **M1** dimer, PDI singlets were formed almost immediately following photoexcitation, and the early decay of the PDI* led to the concomitant formation of the PDI$^{\bullet+}$ species. This process is solvent dependent and faster charge separation lifetime was observed in the more polar solvent (e.g. pyridine). However, for the fused **M1F** dimer, the PDI$^{\bullet+}$ species formed as fast as the IRF, which is over one order of magnitude faster charge separation relative to the unfused **M1** dimer. The nonlinear two-photon absorption cross sections (TPA-δ) measured are in line with the charge separation observed upon light excitation, for which the fused **M1F** dimer show an order of magnitude larger TPA-δ relative to the unfused **M1** dimer. This ultrafast charge separation owing to strong electronic coupling was followed by the formation of triplet species via spin-orbit coupling charge transfer intersystem crossing (SOCT-ISC), for which the rate of triplet formation is dependent on the polarity of the environment. In the least polar environment (toluene, $\varepsilon_r = 0.099$), the rate was the fastest. This could be due to the lowering or stabilization of the charge transfer state using a polar solvent, which may then serve as experimentally observable trap state. Ring-fusion can be said to have opened up an excited state deactivation pathway (triplets) that was not present in the unfused dimer.

Time-resolved spectroscopic measurements were used to carry out the detailed analysis of the excited state dynamics in order to elucidate the varying decay pathways of the unfused and fused N-annulated thiophene π-bridged PDI dimers. The results obtained were able to show that ring-fusion leads to increased electronic coupling in these dimeric bowed-structure systems, leading to ultrafast intramolecular charge transfer and charge separation, also resulting in the formation of triplet species. These were not observed for the unfused **M1** dimer. The results of this study can be used advice the design of efficient PDI dimers with an electron-rich π-bridge unit by seeking for a fused-ring A-D-A configuration with a slight twist in the molecular backbone. This

provides the all the advantages of ring-fusion as elucidated in this study such as excellent π-conjugation, increased electronic delocalization, in addition to the advantage of limiting the aggregation effects by optimizing the micro-phase separation in bulk heterojunction systems.
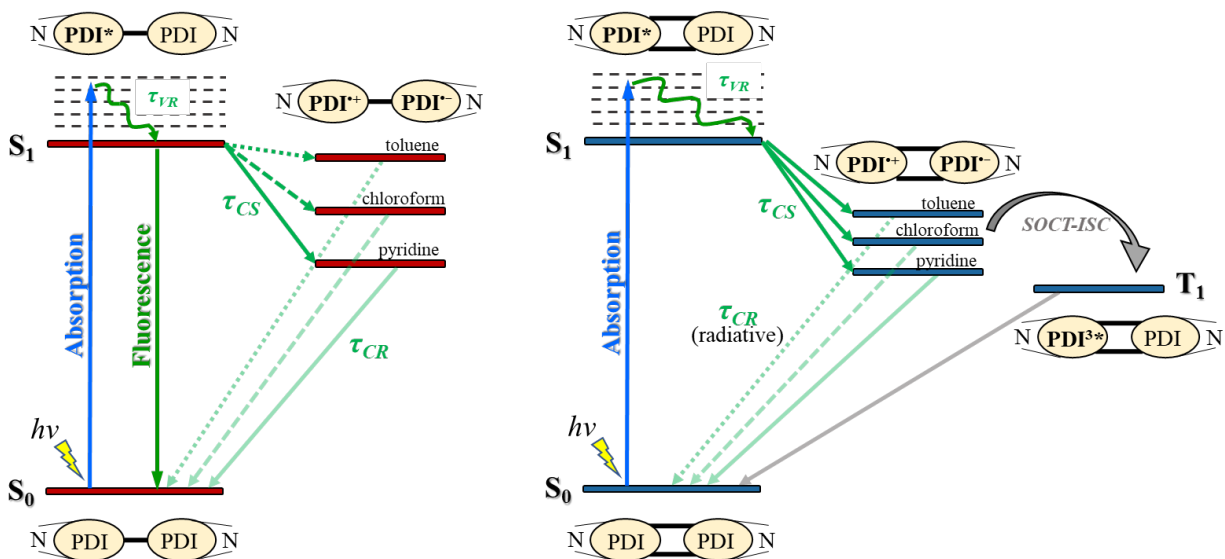
Figure 4.9 Sketch of the proposed excited state deactivations of **M1** (left) and **M1F** (right) observed via time-resolved spectroscopic measurements.

4.7 Conclusions

In summary, we have experimentally observed the effect of ring-fusion on charge transfer and charge separation in N-annulated thiophene π-bridged dimers. The charge separation rate of the fused **M1F** dimer is more than two orders of magnitude faster than that of the unfused **M1** dimer, which means that ring-fusion is a suitable strategy for obtaining better π-conjugation and effective charge communication in N-annulated π-bridged dimers with an A-D-A configuration. We have also experimentally shown that upon ring-fusion in these dimeric systems, triplet excited state decay pathway opens up as a potential deactivation of the photo-generated singlet species. We verified that this triplet excited state pathway is highly dependent on the polarity of the environment or microenvironment (for the case of films) and was able to associate spin-orbit charge transfer intersystem crossing (SOCT-ISC) as the potential triplet generation mechanism

taking place owing to the strong electronic coupling induced by ring-fusion. For PDI dimers, this places the ring-fusion approach in a preferentially suitable position for applications requiring S_1 →T_1 transitions and long-lived triplets. Introducing a slight molecular twist in the backbone of the fused PDI π-bridged dimer either via steric repulsion (as is the case in this study), varying the chalcogen atom (O < S < Se) of the electron-rich π-bridge,[39] or using a cis- vs trans- electron-rich π-bridge,[18] can provide the cumulative benefits of both ring-fusion and optimized morphology in bulk heterojunction devices. Following the detailed spectroscopic analysis carried out in this work, the results therein can be used to provide more clarity to the idea of ring-fusion enabling a novel class of efficient PDI non-fullerene acceptors for better performing organic solar cell devices.

4.8 Supporting Information

4.8.1 Steady-State and Two-photon Absorption Measurements [S.I.]
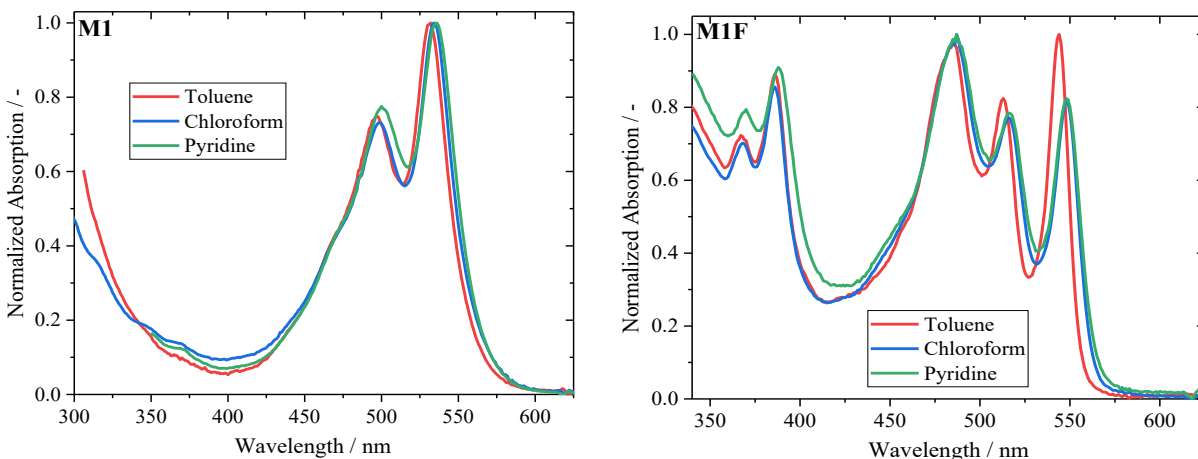
Figure 4.10 Absorption spectra of **M1** (left) and **M1F** (right) in solvents of varying polarity.
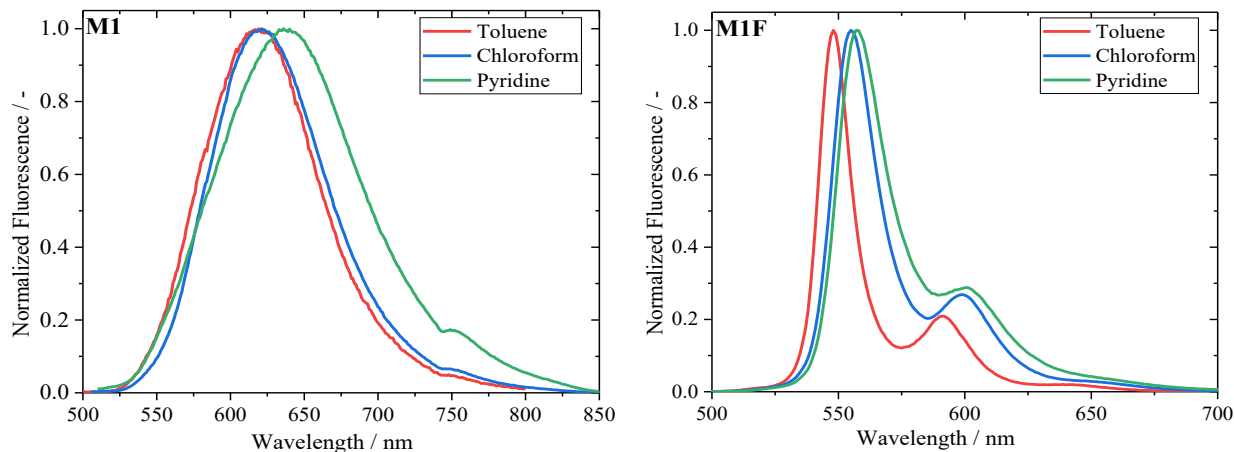
Figure 4.11 Emission spectra of **M1** (left) and **M1F** (right) in solvents of varying polarity.
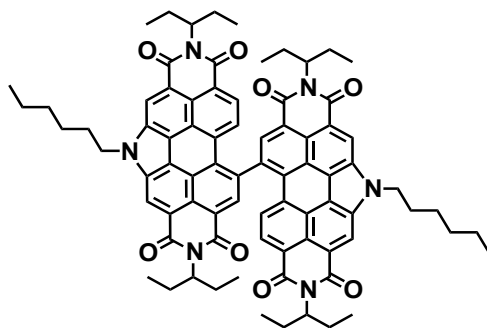
Figure 4.12 Chemical structure of the N-annulated **T-PDI₂** dimer (no thiophene π-bridge).[29]

Table 4.6 Linear and non-linear optical properties of the N-annulated **T-PDI₂** dimer (no thiophene π-bridge) in chloroform.

Comp.nd	λ_{abs} [a] / nm	λ_{em} / nm	$\Delta\upsilon$ [b] /cm^{-1}	ε [c] / M^{-1}cm^{-1}	ϕ_F	TPA-δ / GM [d]
T-PDI₂	<u>534</u>, 498	600	2060	114500	0.71	3.4

[a] peak positions of λ_{0-0}, λ_{0-1}, and λ_{0-2} in this order; [b] using λ_{0-0} and λ_{em}; [c] at the underlined wavelength (λ_{abs}^{max}); [d] at 800 nm excitation

4.8.2 Steady-State Femtosecond transient Absorption (fsTA) [S.I.]
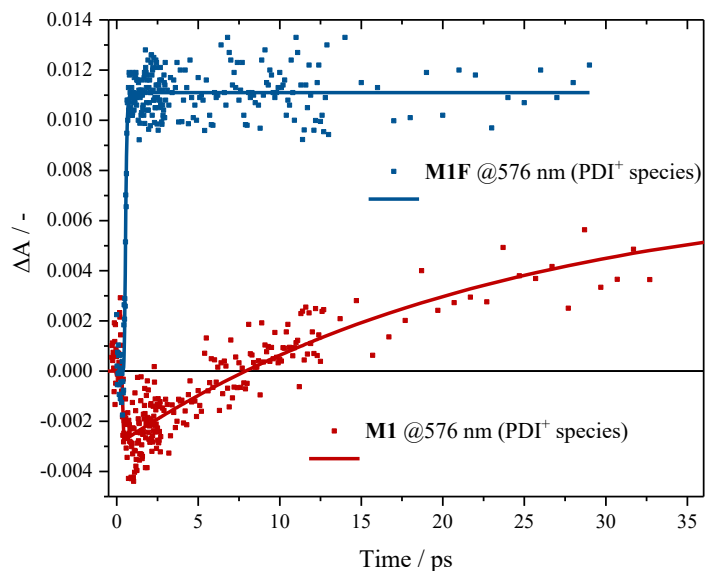
Figure 4.13 Early rise kinetics of the PDI•+species of **M1** and **M1F** in chloroform following excitation at 540 nm.

4.8.3 Nanosecond transient Absorption (nsTA) [S.I.]
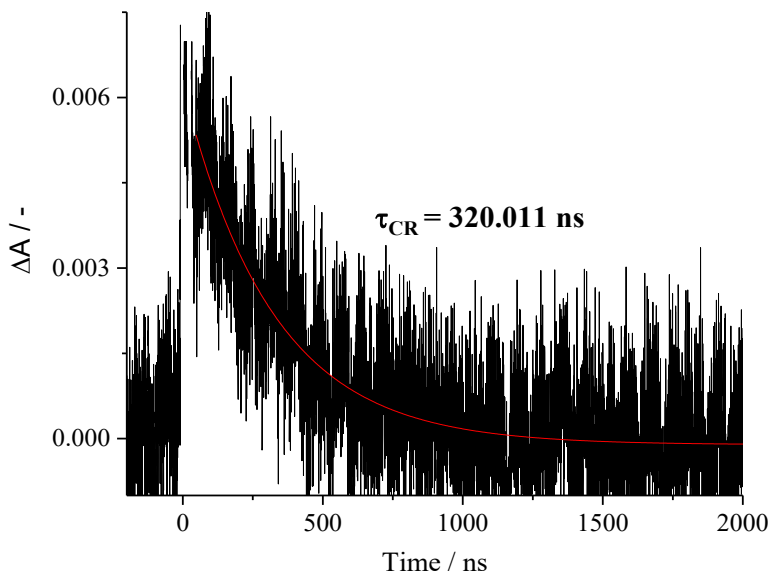
Figure 4.14 Charge recombination at 576 nm obtained by nanosecond TA measurements for **M1** in toluene upon 531 nm laser excitation.

$\tau_{triplet} = 3.2\mu s$
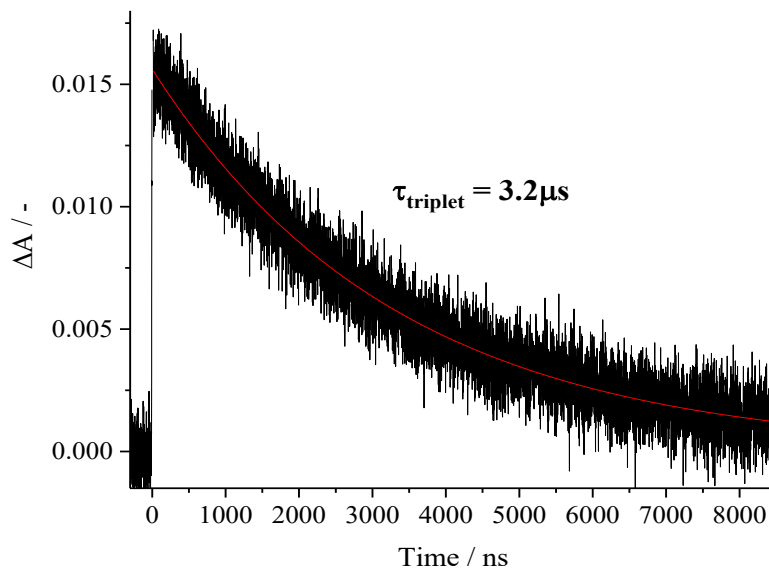
Figure 4.15 Triplet at 528 nm obtained by nanosecond TA measurements for **M1F** in purged toluene upon 544 nm laser excitation.

4.8.4 Nanosecond Time-Resolved Fluorescence Measurement [S.I.]

$\tau_F = 10.50$ ns
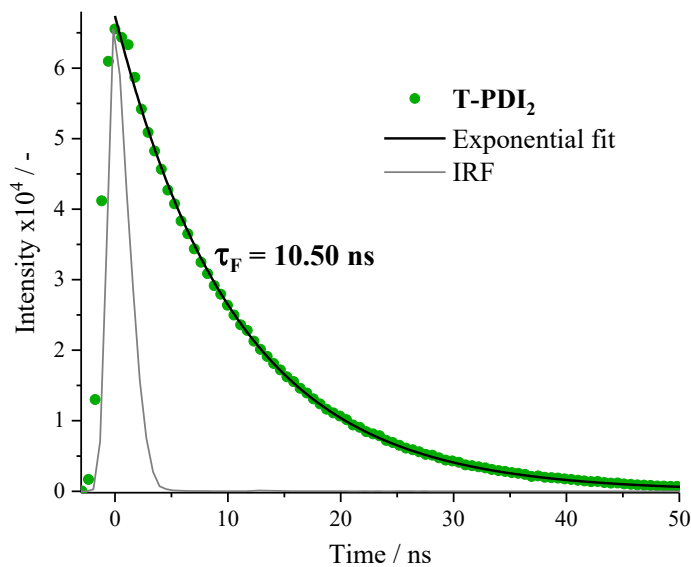
Figure 4.16 Fluorescence decay kinetics recorded for **T-PDI₂** in chloroform by the time correlated single photon counting TCSPC, together with its mono-exponential fit (black).

4.8.5 Quantum Chemical Simulations [S.I.]

Table 4.7 Excitation energies required for $S_0 \rightarrow S_1$ transitions. Calculations performed with 6-31G** basis sets and B3LYP functional for comparison with experimental and literature data.

Units in eV	Experiment	Literature[*] (B3LYP)	TD-DFT (B3LYP)	TD-DFT (B3LYP)
Phase	Chloroform	Gas	Gas	Chloroform
M1	**2.32** / 2.49	**2.51** / 2.79	**2.73** / 2.84	**2.59** / 2.71
M1F	2.26 / 2.40 / 2.55	N/A	2.50 / 2.65 / 2.79	2.41 / 2.48 / 2.60
T-PDI2	**2.32** / 2.49	**2.52** / 2.54	—[**]	—[**]

*Values from Reference[30]; **The T-PDI2 structure obtained is highly twisted and does not lead to reasonable excited state energetics.

Table 4.8 Excitation energies required for $S_0 \rightarrow S_1$ transitions. Calculations performed with 6-31G** basis sets and ωB97X-D functional.

Units in eV	Experiment	TD-DFT (ωB97X-D)	TD-DFT (ωB97X-D) $\omega = 0.003 - 0.005$
Phase	Chloroform	Gas	Chloroform
M1	**2.32** / 2.49	**3.16** / 3.39	**2.69** / 2.81[**]
M1F	2.26 / 2.40 / 2.55	3.12 / 3.25 / 3.34	2.48 / 2.55 / 2.67[***]
T-PDI2	**2.32** / 2.49	—[*]	—[*]

*The T-PDI2 structure obtained is highly twisted and does not lead to reasonable excited state energetics;
**Calculations were conducted with ω = 0.005; ***Calculations were conducted with ω = 0.003.

Table 4.9 Excitation energies required for $S_1 \rightarrow S_0$ transitions. Calculations performed with 6-31G** basis sets and ωB97X-D functional.

Units in eV	Experiment	TD-DFT (B3LYP)	TD-DFT (B3LYP)	TD-DFT (ωB97X-D)	TD-DFT (ωB97X-D)
Phase	Chloroform	Gas	Chloroform	Gas	Chloroform
M1	**2.00**	1.75	1.74	2.10	2.01
M1F	2.07, 2.23	2.15	2.08	2.87	-
T-PDI2	**2.07**	—[*]	—[*]	—[*]	—[*]

*The T-PDI2 structure obtained is highly twisted and does not lead to reasonable excited state energetics.

References

(1)   Guo, X.; Facchetti, A.; Marks, T. J. Imide- and Amide-Functionalized Polymer Semiconductors. *Chem. Rev.* **2014**, *114* (18), 8943–9012.

(2)   Jiang, W.; Li, Y.; Wang, Z. Heteroarenes as High Performance Organic Semiconductors. *Chem. Soc. Rev.* **2013**, *42* (14), 6113–6127.

(3)   Zhan, X.; Facchetti, A.; Barlow, S.; Marks, T. J.; Ratner, M. A.; Wasielewski, M. R.; Marder, S. R. Rylene and Related Diimides for Organic Electronics. *Adv. Mater.* **2011**, *23* (2), 268–284.

(4)   Würthner, F. Perylene Bisimide Dyes as Versatile Building Blocks for Functional Supramolecular Architectures. *Chem. Commun.* **2004**, *4* (14), 1564–1579.

(5)   Jiang, W.; Li, Y.; Wang, Z. Tailor-Made Rylene Arrays for High Performance n-Channel Semiconductors. *Acc. Chem. Res.* **2014**, *47* (10), 3135–3147.

(6)   Hüttner, S.; Sommer, M.; Thelakkat, M. N-Type Organic Field Effect Transistors from Perylene Bisimide Block Copolymers and Homopolymers. *Appl. Phys. Lett.* **2008**, *92* (9), 2006–2009.

(7)   Centore, R.; Ricciotti, L.; Carella, A.; Roviello, A.; Causà, M.; Barra, M.; Ciccullo, F.; Cassinese, A. Perylene Diimides Functionalized with N-Thiadiazole Substituents: Synthesis and Electronic Properties in OFET Devices. *Org. Electron.* **2012**, *13* (10), 2083–2093.

(8)   Naveenraj, S.; Raj, M. R.; Anandan, S. Binding Interaction between Serum Albumins and Perylene-3,4,9,10- Tetracarboxylate - A Spectroscopic Investigation. *Dye. Pigment.* **2012**, *94* (2), 330–337.

(9)   Doval, D. A.; Fin, A.; Takahashi-Umebayashi, M.; Riezman, H.; Roux, A.; Sakai, N.; Matile, S. Amphiphilic Dynamic NDI and PDI Probes: Imaging Microdomains in Giant Unilamellar Vesicles. *Org. Biomol. Chem.* **2012**, *10* (30), 6087–6093.

(10)   Dinçalp, H.; Kizilok, Ş.; Birel, Ö. H.; Içli, S. Synthesis and G-Quadruplex Binding Study of a Novel Full Visible Absorbing Perylene Diimide Dye. *J. Photochem. Photobiol. A Chem.* **2012**, *235*, 40–48.

(11)   Yukruk, F.; Dogan, A. L.; Canpinar, H.; Guc, D.; Akkaya, E. U. Water-Soluble Green Perylenediimide (PDI) Dyes as Potential Sensitizers for Photodynamic Therapy. *Org. Lett.* **2005**, *7* (14), 2885–2887.

(12)   Zhang, Y.; Xu, Z.; Cai, L.; Lai, G.; Qiu, H.; Shen, Y. Highly Soluble Perylene Tetracarboxylic Diimides and Tetrathiafulvalene-Perylene Tetracarboxylic Diimide-Tetrathiafulvalene Triads. *J. Photochem. Photobiol. A Chem.* **2008**, *200* (2–3), 334–345.

(13)   Carlotti, B.; Cai, Z.; Kim, H.; Sharapov, V.; Madu, I. K.; Zhao, D.; Chen, W.; Zimmerman, P. M.; Yu, L.; Goodson, T. Charge Transfer and Aggregation E Ff Ects on the Performance of Planar vs Twisted Nonfullerene Acceptor Isomers for Organic Solar Cells. *Chem. Mater.* **2018**, *30*, 4263–4276.

(14) Xiong, Y.; Wu, B.; Zheng, X.; Zhao, Z.; Deng, P.; Lin, M.; Tang, B.; Ong, B. S. Novel Dimethylmethylene-Bridged Triphenylamine-PDI Acceptor for Bulk-Heterojunction Organic Solar Cells. *Adv. Sci.* **2017**, *4* (10), 1–6.

(15) Lin, H.; Chen, S.; Hu, H.; Zhang, L.; Ma, T.; Lai, J. Y. L.; Li, Z.; Qin, A.; Huang, X.; Tang, B.; et al. Reduced Intramolecular Twisting Improves the Performance of 3D Molecular Acceptors in Non-Fullerene Organic Solar Cells. *Adv. Mater.* **2016**, 8546–8551.

(16) Lin, Y.; Wang, J.; Dai, S.; Li, Y.; Zhu, D.; Zhan, X. A Twisted Dimeric Perylene Diimide Electron Acceptor for Efficient Organic Solar Cells. *Adv. Energy Mater.* **2014**, *4* (13), 2–6.

(17) Zhang, X.; Lu, Z.; Ye, L.; Zhan, C.; Hou, J.; Zhang, S.; Jiang, B.; Zhao, Y.; Huang, J.; Zhang, S.; et al. A Potential Perylene Diimide Dimer-Based Acceptor Material for Highly Efficient Solution-Processed Non-Fullerene Organic Solar Cells with 4.03% Efficiency. *Adv. Mater.* **2013**, *25* (40), 5791–5797.

(18) Jiang, X.; Xu, Y.; Wang, X.; Yang, F.; Zhang, A.; Li, C.; Ma, W.; Li, W. Conjugated Polymer Acceptors Based on Fused Perylene Bisimides with a Twisted Backbone for Non-Fullerene Solar Cells. *Polym. Chem.* **2017**, *8* (21), 3300–3306.

(19) Zhao, D.; Wu, Q.; Cai, Z.; Zheng, T.; Chen, W.; Lu, J.; Yu, L. Electron Acceptors Based on α-Substituted Perylene Diimide (PDI) for Organic Solar Cells. *Chem. Mater.* **2016**, *28* (4), 1139–1146.

(20) Kozma, E.; Catellani, M. Perylene Diimides Based Materials for Organic Solar Cells. *Dye. Pigment.* **2013**, *98* (1), 160–179.

(21) Carlotti, B.; Madu, I. K.; Kim, H.; Cai, Z.; Jiang, H.; Muthike, A. K.; Yu, L.; Zimmerman, P. M.; Goodson, T. Activating Intramolecular Singlet Exciton Fission by Altering π-Bridge Flexibility in Perylene Diimide Trimers for Organic Solar Cells. *Chem. Sci.* **2020**, *11* (33), 8757–8770.

(22) Lin, Y.; Wang, Y.; Wang, J.; Hou, J.; Li, Y.; Zhu, D.; Zhan, X. A Star-Shaped Perylene Diimide Electron Acceptor for High-Performance Organic Solar Cells. *Adv. Mater.* **2014**, *26* (30), 5137–5142.

(23) Wu, Q.; Zhao, D.; Schneider, A. M.; Chen, W.; Yu, L. Covalently Bound Clusters of Alpha-Substituted PDI-Rival Electron Acceptors to Fullerene for Organic Solar Cells. *J. Am. Chem. Soc.* **2016**, *138* (23), 7248–7251.

(24) Wu, Q.; Zhao, D.; Yang, J.; Sharapov, V.; Cai, Z.; Li, L.; Zhang, N.; Neshchadin, A.; Chen, W.; Yu, L. Propeller-Shaped Acceptors for High-Performance Non-Fullerene Solar Cells: Importance of the Rigidity of Molecular Geometry. *Chem. Mater.* **2017**, *29* (3), 1127–1133.

(25) Chen, W.; Yang, X.; Long, G.; Wan, X.; Chen, Y.; Zhang, Q. A Perylene Diimide (PDI)-Based Small Molecule with Tetrahedral Configuration as a Non-Fullerene Acceptor for Organic Solar Cells. *J. Mater. Chem. C* **2015**, *3* (18), 4698–4705.

(26) Liu, Y.; Mu, C.; Jiang, K.; Zhao, J.; Li, Y.; Zhang, L.; Li, Z.; Lai, J. Y. L.; Hu, H.; Ma, T.; et al. A Tetraphenylethylene Core-Based 3d Structure Small Molecular Acceptor Enabling

Efficient Non-Fullerene Organic Solar Cells. *Adv. Mater.* **2015**, *27* (6), 1015–1020.

(27)   Sun, D.; Meng, D.; Cai, Y.; Fan, B.; Li, Y.; Jiang, W.; Huo, L.; Sun, Y.; Wang, Z. Non-Fullerene-Acceptor-Based Bulk-Heterojunction Organic Solar Cells with Efficiency over 7%. *J. Am. Chem. Soc.* **2015**, *137* (34), 11156–11162.

(28)   Meng, D.; Sun, D.; Zhong, C.; Liu, T.; Fan, B.; Huo, L.; Li, Y.; Jiang, W.; Choi, H.; Kim, T.; et al. High-Performance Solution-Processed Non-Fullerene Organic Solar Cells Based on Selenophene-Containing Perylene Bisimide Acceptor. *J. Am. Chem. Soc.* **2016**, *138* (1), 375–380.

(29)   Hendsbee, A. D.; Sun, J.-P.; Law, W. K.; Yan, H.; Hill, I. G.; Spasyuk, D. M.; Welch, G. C. Synthesis, Self-Assembly, and Solar Cell Performance of N-Annulated Perylene Diimide Non-Fullerene Acceptors. *Chem. Mater.* **2016**, *28* (19), 7098–7109.

(30)   Hendsbee, A. D.; Dayneko, S. V.; Pells, J. A.; Cann, J. R.; Welch, G. C. N-Annulated Perylene Diimide Dimers: The Effect of Thiophene Bridges on Physical, Electronic, Optical, and Photovoltaic Properties. *Sustain. Energy Fuels* **2017**, *1* (5), 1137–1147.

(31)   Laventure, A.; Stanzel, S.; Payne, A. J.; Lessard, B. H.; Welch, G. C. A Ring Fused N-Annulated PDI Non-Fullerene Acceptor for High Open Circuit Voltage Solar Cells Processed from Non-Halogenated Solvents. *Synth. Met.* **2019**, *250* (December 2018), 55–62.

(32)   Qian, H.; Yue, W.; Zhen, Y.; Di Motta, S.; Di Donato, E.; Negri, F.; Qu, J.; Xu, W.; Zhu, D.; Wang, Z. Heterocyclic Annelated Di(Perylene Bisimide): Constructing Bowl-Shaped Perylene Bisimides by the Combination of Steric Congestion and Ring Strain. *J. Org. Chem.* **2009**, *74* (16), 6275–6282.

(33)   Lide, D. *Handbook of Chemistry & Physics (65th Ed.)*, 65th editi.; CRC Press, 1984.

(34)   Zhang, X.; Zhang, J.; Lu, H.; Wu, J.; Li, G.; Li, C.; Li, S.; Bo, Z. A 1,8-Naphthalimide Based Small Molecular Acceptor for Polymer Solar Cells with High Open Circuit Voltage. *J. Mater. Chem. C* **2015**, *3* (27), 6979–6985.

(35)   Zhang, J.; Zhang, X.; Xiao, H.; Li, G.; Liu, Y.; Li, C.; Huang, H.; Chen, X.; Bo, Z. 1,8-Naphthalimide-Based Planar Small Molecular Acceptor for Organic Solar Cells. *ACS Appl. Mater. Interfaces* **2016**, *8* (8), 5475–5483.

(36)   Zhang, J.; Li, Y.; Huang, J.; Hu, H.; Zhang, G.; Ma, T.; Chow, P. C. Y.; Ade, H.; Pan, D.; Yan, H. Ring-Fusion of Perylene Diimide Acceptor Enabling Efficient Nonfullerene Organic Solar Cells with a Small Voltage Loss. *J. Am. Chem. Soc.* **2017**, *139* (45), 16092–16095.

(37)   Hartnett, P. E.; Ramakrishna Matte, H. S. S.; Eastham, N. D.; Jackson, N. E.; Wu, Y.; Chen, L. X.; Ratner, M. A.; Chang, R. P. H.; Hersam, M. C.; Wasielewski, M. R.; et al. Ring-Fusion as a Perylenediimide Dimer Design Concept for High-Performance Non-Fullerene Organic Photovoltaic Acceptors. *Chem. Sci.* **2016**, *7* (6), 3543–3555.

(38)   Jiang, W.; Ye, L.; Li, X.; Xiao, C.; Tan, F.; Zhao, W.; Hou, J.; Wang, Z. Bay-Linked

Perylene Bisimides as Promising Non-Fullerene Acceptors for Organic Solar Cells. *Chem. Commun.* **2014**, *50* (8), 1024–1026.

(39) Zhong, H.; Wu, C. H.; Li, C. Z.; Carpenter, J.; Chueh, C. C.; Chen, J. Y.; Ade, H.; Jen, A. K. Y. Rigidifying Nonplanar Perylene Diimides by Ring Fusion Toward Geometry-Tunable Acceptors for High-Performance Fullerene-Free Solar Cells. *Adv. Mater.* **2016**, *28* (5), 951–958.

(40) Lee, J.; Vandewal, K.; Yost, S. R.; Bahlke, M. E.; Goris, L.; Baldo, M. A.; Manca, J. V.; Voorhis, T. Van. Charge Transfer State versus Hot Exciton Dissociation in Polymer-Fullerene Blended Solar Cells. *J. Am. Chem. Soc.* **2010**, *132* (34), 11878–11880.

(41) Tamura, H.; Burghardt, I. Ultrafast Charge Separation in Organic Photovoltaics Enhanced by Charge Delocalization and Vibronically Hot Exciton Dissociation. *J. Am. Chem. Soc.* **2013**, *135* (44), 16364–16367.

(42) Jailaubekov, A. E.; Willard, A. P.; Tritsch, J. R.; Chan, W. L.; Sai, N.; Gearba, R.; Kaake, L. G.; Williams, K. J.; Leung, K.; Rossky, P. J.; et al. Hot Charge-Transfer Excitons Set the Time Limit for Charge Separation at Donor/Acceptor Interfaces in Organic Photovoltaics. *Nat. Mater.* **2013**, *12* (1), 66–73.

(43) Guo, J.; Ohkita, H.; Benten, H.; Ito, S. Charge Generation and Recombination Dynamics in Poly(3-Hexylthiophene)/ Fullerene Blend Films with Different Regioregularities and Morphologies. *J. Am. Chem. Soc.* **2010**, *132* (17), 6154–6164.

(44) Ohkita, H.; Tamai, Y.; Benten, H.; Ito, S. Transient Absorption Spectroscopy for Polymer Solar Cells. *IEEE J. Sel. Top. Quantum Electron.* **2016**, *22* (1), 100–111.

(45) Yu, Z.; Wu, Y.; Peng, Q.; Sun, C.; Chen, J.; Yao, J.; Fu, H. Accessing the Triplet State in Heavy-Atom-Free Perylene Diimides. *Chem. - A Eur. J.* **2016**, *22* (14), 4717–4722.

(46) Spenst, P.; Young, R. M.; Wasielewski, M. R.; Würthner, F. Guest and Solvent Modulated Photo-Driven Charge Separation and Triplet Generation in a Perylene Bisimide Cyclophane. *Chem. Sci.* **2016**, *7* (8), 5428–5434.

(47) Lefler, K. M.; Brown, K. E.; Salamant, W. A.; Dyar, S. M.; Knowles, K. E.; Wasielewski, M. R. Triplet State Formation in Photoexcited Slip-Stacked Perylene-3,4:9,10-Bis(Dicarboximide) Dimers on a Xanthene Scaffold. *J. Phys. Chem. A* **2013**, *117* (40), 10333–10345.

(48) Veldman, D.; Chopin, S. M. A.; Meskers, S. C. J.; Groeneveld, M. M.; Williams, R. M.; Janssen, R. A. J. Triplet Formation Involving a Polar Transition State in a Well-Defined Intramolecular Perylenediimide Dimeric Aggregate. *J. Phys. Chem. A* **2008**, *112* (26), 5846–5857.

(49) Jobin Yvon. *A Guide to Recording Fluorescence Quantum Yields Introduction:*; 2014; Vol. 15.

(50) Guan, J.; Tomobe, K.; Madu, I.; Goodson, T.; Makhal, K.; Trinh, M. T.; Rand, S. C.; Yodsin, N.; Jungsuttiwong, S.; Laine, R. M. Photophysical Properties of Partially

Functionalized Phenylsilsesquioxane: [RSiO1.5]7[Me/NPrSiO1.5] and [RSiO1.5]7[O0.5SiMe3]3 (R = 4-Me/4-CN-Stilbene). Cage-Centered Magnetic Fields Form under Intense Laser Light. *Macromolecules* **2019**, *52*, 4008–4019.

(51) Kubin, R. F.; Fletcher, A. N. Fluorescence Quantum Yields of Some Rhodamine Dyes. *J. Lumin.* **1982**, *27* (4), 455–462.

(52) Arbeloa, F. L.; Ojeda, P. R.; Arbeloa, I. L. Flourescence Self-Quenching of the Molecular Forms of Rhodamine B in Aqueous and Ethanolic Solutions. *J. Lumin.* **1989**, *44* (1–2), 105–112.

(53) Cai, Z.; Vázquez, R. J.; Zhao, D.; Li, L.; Lo, W. Y.; Zhang, N.; Wu, Q.; Keller, B.; Eshun, A.; Abeyasinghe, N.; et al. Two Photon Absorption Study of Low-Bandgap, Fully Conjugated Perylene Diimide-Thienoacene-Perylene Diimide Ladder-Type Molecules. *Chem. Mater.* **2017**, *29* (16), 6726–6732.

(54) Keller, B.; McLean, A.; Kim, B. G.; Chung, K.; Kim, J.; Goodson, T. Ultrafast Spectroscopic Study of Donor-Acceptor Benzodithiophene Light Harvesting Organic Conjugated Polymers. *J. Phys. Chem. C* **2016**, *120* (17), 9088–9096.

(55) Villabona-Monsalve, J. P.; Varnavski, O.; Palfey, B. A.; Goodson, T. Two-Photon Excitation of Flavins and Flavoproteins with Classical and Quantum Light. *J. Am. Chem. Soc.* **2018**, *140* (44), 14562–14566.

(56) Makarov, N. S.; Drobizhev, M.; Rebane, A. Two-Photon Absorption Standards in the 550-1600 Nm Excitation Wavelength Range. *Opt. Express* **2008**, *16* (6), 4029–4047.

(57) Xu, C.; Webb, W. W. Measurement of Two-Photon Excitation Cross Sections of Molecular Fluorophores with Data from 690 to 1050 Nm. *J. Opt. Soc. Am. B* **1996**, *13* (3), 481.

(58) Madu, I. K.; Muller, E. W.; Kim, H.; Shaw, J.; Burney-Allen, A. A.; Zimmerman, P.; Jeffries-El, M.; Goodson, T. Heteroatom and Side Chain Effects on the Optical and Photophysical Properties: Ultrafast and Nonlinear Spectroscopy of New Naphtho[1,2-b:5,6- B′]Difuran Donor Polymers. *J. Phys. Chem. C* **2018**, *122* (30), 17049–17066.

(59) Vázquez, R. J.; Kim, H.; Zimmerman, P. M.; Goodson, T. Using Ultra-Fast Spectroscopy to Probe the Excited State Dynamics of a Reported Highly Efficient Thermally Activated Delayed Fluorescence Chromophore. *J. Mater. Chem. C* **2019**, *7* (14), 4210–4221.

(60) Chai, J. Da; Head-Gordon, M. Long-Range Corrected Hybrid Density Functionals with Damped Atom-Atom Dispersion Corrections. *Phys. Chem. Chem. Phys.* **2008**, *10* (44), 6615–6620.

(61) Chai, J. Da; Head-Gordon, M. Systematic Optimization of Long-Range Corrected Hybrid Density Functionals. *J. Chem. Phys.* **2008**, *128* (8).

(62) Mewes, J. M.; Herbert, J. M.; Dreuw, A. On the Accuracy of the General, State-Specific Polarizable-Continuum Model for the Description of Correlated Ground- and Excited States in Solution. *Phys. Chem. Chem. Phys.* **2017**, *19* (2), 1644–1654.

(63) Samanta, P. K.; Kim, D.; Coropceanu, V.; Brédas, J. L. Up-Conversion Intersystem Crossing Rates in Organic Emitters for Thermally Activated Delayed Fluorescence: Impact of the Nature of Singlet vs Triplet Excited States. *J. Am. Chem. Soc.* **2017**, *139* (11), 4042–4051.

(64) Beljonne, D.; Shuai, Z.; Pourtois, G.; Bredas, J. L. Spin-Orbit Coupling and Intersystem Crossing in Conjugated Polymers: A Configuration Interaction Description. *J. Phys. Chem. A* **2001**, *105* (15), 3899–3907.

(65) Shao, Y.; Gan, Z.; Epifanovsky, E.; Gilbert, A. T. B.; Wormit, M.; Kussmann, J.; Lange, A. W.; Behn, A.; Deng, J.; Feng, X.; et al. Advances in Molecular Quantum Chemistry Contained in the Q-Chem 4 Program Package. *Mol. Phys.* **2015**, *113* (2), 184–215.

(66) Allouche, A. Software News and Updates Gabedit — A Graphical User Interface for Computational Chemistry Softwares. *J. Comput. Chem.* **2012**, *32*, 174–182.

(67) Pochas, C. M.; Kistler, K. A.; Yamagata, H.; Matsika, S.; Spano, F. C. Contrasting Photophysical Properties of Star-Shaped vs Linear Perylene Diimide Complexes. *J. Am. Chem. Soc.* **2013**, *135* (8), 3056–3066.

(68) Schlosser, F.; Moos, M.; Lambert, C.; Würthner, F. Redox-Switchable Intramolecular π-π-Stacking of Perylene Bisimide Dyes in a Cyclophane. *Adv. Mater.* **2013**, *25* (3), 410–414.

(69) Wu, Y.; Young, R. M.; Frasconi, M.; Schneebeli, S. T.; Spenst, P.; Gardner, D. M.; Brown, K. E.; Würthner, F.; Stoddart, J. F.; Wasielewski, M. R. Ultrafast Photoinduced Symmetry-Breaking Charge Separation and Electron Sharing in Perylenediimide Molecular Triangles. *J. Am. Chem. Soc.* **2015**, *137* (41), 13236–13239.

(70) Langhals, H. Control of the Interactions in Multichromophores: Novel Concepts. Perylene Bis-Imides as Components for Larger Functional Units. *Helv. Chim. Acta* **2005**, *88* (6), 1309–1343.

(71) Spenst, P.; Young, R. M.; Phelan, B. T.; Keller, M.; Dostal, J.; Brixner, T.; Wasielewski, M. R.; Wurthner, F. Solvent-Templated Folding of Perylene Bisimide Macrocycles into Coiled Double-String Ropes with Solvent-Sensitive Optical Signatures. *J. Am. Chem. Soc.* **2017**, *139* (5), 2014–2021.

(72) Kasha, M.; Rawls, H. R.; El-Bayoumi, M. A. The Exciton Model In Molecular Spectroscopy. *Pure Appl. Chem.* **1965**, *11* (3–4), 371–392.

(73) Campaigne, E.; Diedrich, J. L. Catalytic Reduction of 2-Acylthiophenes. *J. Am. Chem. Soc.* **1951**, *73* (11), 5240–5243.

(74) Fawcett, F. S.; Rasmussen, H. E. *Physical Properties of Thiophene*; 1945; Vol. 67.

(75) Guo, Y.; Ma, Z.; Niu, X.; Zhang, W.; Tao, M.; Guo, Q.; Wang, Z.; Xia, A. Bridge-Mediated Charge Separation in Isomeric N-Annulated Perylene Diimide Dimers. *J. Am. Chem. Soc.* **2019**, *141* (32), 12789–12796.

(76) Farina, A.; Paternò, G. M.; Scotognella, F. Optical Properties of Recent Non-Fullerene

Molecular Acceptors for Bulk Heterojunction Solar Cells. *Results Phys.* **2020**, *19* (August), 3–6.

(77)   Pawlicki, M.; Collins, H. A.; Denning, R. G.; Anderson, H. L. Two-Photon Absorption and the Design of Two-Photon Dyes. *Angew. Chemie - Int. Ed.* **2009**, *48* (18), 3244–3266.

(78)   W.E., F.; H., H.; Kamat, P. Photochemistry of 3,4.9.10-Perylenetetracarboxyllc Dianhydride Dyes. 4. Spectroscopic and Redox Properties of Oxidized and Reduced Forms of the Bis(2,5-Di-Tert-Butylphenyl)Imide Derivative. *J. Phys. Chem.* **1989**, *93* (18), 6692–6696.

(79)   Kircher, T.; Löhmannsröben, H. G. Photoinduced Charge Recombination Reactions of a Perylene Dye in Acetonitrile. *Phys. Chem. Chem. Phys.* **1999**, *1* (17), 3987–3992.

(80)   Holman, M. W.; Yan, P.; Adams, D. M.; Westenhoff, S.; Silva, C. Ultrafast Spectroscopy of the Solvent Dependence of Electron Transfer in a Perylenebisimide Dimer. *J. Phys. Chem. A* **2005**, *109* (38), 8548–8552.

(81)   Giaimo, J. M.; Gusev, A. V.; Wasielewski, M. R. Excited-State Symmetry Breaking in Cofacial and Linear Dimers of a Green Perylenediimide Chlorophyll Analogue Leading to Ultrafast Charge Separation. *J. Am. Chem. Soc.* **2002**, *124* (29), 8530–8531.

(82)   Gosztola, D.; Niemczyk, M. P.; Svec, W.; Lukas, A. S.; Wasielewski, M. R. Excited Doublet States of Electrochemically Generated Aromatic Imide and Diimide Radical Anions. *J. Phys. Chem. A* **2000**, *104* (28), 6545–6551.

(83)   Logsdon, J. L.; Hartnett, P. E.; Nelson, J. N.; Harris, M. A.; Marks, T. J.; Wasielewski, M. R. Charge Separation Mechanisms in Ordered Films of Self-Assembled Donor-Acceptor Dyad Ribbons. *ACS Appl. Mater. Interfaces* **2017**, *9* (39), 33493–33503.

(84)   Van Stokkum, I. H. M.; Larsen, D. S.; Van Grondelle, R. Global and Target Analysis of Time-Resolved Spectra. *Biochim. Biophys. Acta - Bioenerg.* **2004**, *1657* (2–3), 82–104.

(85)   Snellenburg, J. J.; Laptenok, S. P.; Seger, R.; Mullen, K. M.; van Stokkum, I. H. M. Glotaran : A Java-Based Graphical User Interface for the R Package TIMP. *J. Stat. Softw.* **2012**, *49* (3), 1–2.

(86)   Margulies, E. A.; Miller, C. E.; Wu, Y.; Ma, L.; Schatz, G. C.; Young, R. M.; Wasielewski, M. R. Enabling Singlet Fission by Controlling Intramolecular Charge Transfer in π-Stacked Covalent Terrylenediimide Dimers. *Nat. Chem.* **2016**, *8* (12), 1120–1125.

(87)   Ricks, A. B.; Solomon, G. C.; Colvin, M. T.; Scott, A. M.; Chen, K.; Ratner, M. A.; Wasielewski, M. R. Controlling Electron Transfer in Donor-Bridge-Acceptor Molecules Using Cross-Conjugated Bridges. *J. Am. Chem. Soc.* **2010**, *132* (43), 15427–15434.

(88)   Okada, T.; Karaki, I.; Matsuzawa, E.; Mataga, N.; Sakata, Y.; Misumi, S. Ultrafast Intersystem Crossing in Some Intramolecular Heteroexcimers. *J. Phys. Chem.* **1981**, *85* (26), 3957–3960.

(89)   Colvin, M. T.; Ricks, A. B.; Scott, A. M.; Co, D. T.; Wasielewski, M. R. Intersystem

Crossing Involving Strongly Spin Exchange-Coupled Radical Ion Pairs in Donor-Bridge-Acceptor Molecules. *J. Phys. Chem. A* **2012**, *116* (8), 1923–1930.

(90)   Colvin, M. T.; Ricks, A. B.; Scott, A. M.; Smeigh, A. L.; Carmieli, R.; Miura, T.; Wasielewski, M. R. Magnetic Field-Induced Switching of the Radical-Pair Intersystem Crossing Mechanism in a Donor-Bridge-Acceptor Molecule for Artificial Photosynthesis. *J. Am. Chem. Soc.* **2011**, *133* (5), 1240–1243.

(91)   Kandrashkin, Y. E.; Wang, Z.; Sukhanov, A. A.; Hou, Y.; Zhang, X.; Liu, Y.; Voronkova, V. K.; Zhao, J. Balance between Triplet States in Photoexcited Orthogonal BODIPY Dimers. *J. Phys. Chem. Lett.* **2019**, *10* (15), 4157–4163.

(92)   Miura, T.; Carmieli, R.; Wasielewski, M. R. Time-Resolved EPR Studies of Charge Recombination and Triplet-State Formation within Donor-Bridge-Acceptor Molecules Having Wire-like Oligofluorene Bridges. *J. Phys. Chem. A* **2010**, *114* (18), 5769–5778.

(93)   Ford, W. E.; Kamat, P. V. Photochemistry of 3,4,9,10-Perylenetetracarboxylic Dianhydride Dyes. 3. Singlet and Triplet Excited-State Properties of the Bis(2,5-Di-Tert-Butylphenyl)Imide Derivative. *J. Phys. Chem.* **1987**, *91* (25), 6373–6380.

(94)   Whited, M. T.; Patel, N. M.; Roberts, S. T.; Allen, K.; Djurovich, P. I.; Bradforth, S. E.; Thompson, M. E. Symmetry-Breaking Intramolecular Charge Transfer in the Excited State of Meso-Linked BODIPY Dyads. *Chem. Commun.* **2012**, *48* (2), 284–286.

Chapter 5

Charge Transfer and Aggregation Effects on the Performance of Planar vs. Twisted Non-Fullerene Acceptor Isomers for Organic Solar Cells

5.1 Original Publication Information

The work in this chapter was published in the journal of *Chemistry of Materials* as: "Charge Transfer and Aggregation Effects on the Performance of Planar vs. Twisted Non-Fullerene Acceptor Isomers for Organic Solar Cells" Benedetta Carlotti, Zhengxu Cai, Hyungjun Kim, Valerii Sharapov, Ifeanyi K. Madu, Donglin Zhao, Wei Chen, Paul M. Zimmerman, Luping Yu, and Theodore Goodson III. *Chem. Mater.*, 2018, 30, 4263–4276

Ifeanyi Madu worked with Benedetta Carlotti (a visiting Research scholar) in carrying out the spectroscopic characterization studies – specifically femtosecond transient absorption, two-photon absorption and time corelated single photon counting measurements, and the drafting of the manuscript. Synthesis of the compounds was carried out by the Zhengxu Cai and Valerii Sharapov in the Luping group at the University of Chicago. Density functional theory calculations were done by Hyungjun Kim in the Zimmerman group at the University of Michigan. Device fabrication, characterization and morphology studies was done by the Luping group as well. Modifications were made to the original publication to adapt it to the style of the content of this dissertation. References of the original manuscript are included in this chapter.

5.2 Abstract

Newly synthetized perylene diimide (PDI) dimers were investigated as non−fullerene electron acceptors for organic solar cells. In particular, two analogous positional isomers exhibiting twisted vs. planar geometries were prepared to make a direct comparison of their optical and electronic properties. These properties were investigated in order to provide information regarding the impact of the non−fullerene acceptor geometry on the ultimate photovoltaic performance. The two isomers exhibited strikingly different optical and photophysical properties in solution as well as in film. The ultrafast spectroscopic investigation in solution revealed the occurrence of charge transfer upon photoexcitation, which takes place more efficiently in the planar isomer. This is also supported by theoretical simulations. The planar conformation exhibits higher aggregation in the neat film as well as in the blend. However, our results suggest that the dominance of intra−molecular charge transfer in the planar isomer is the crucial factor in determining the improved power conversion efficiency (PCE) of organic solar cells.

5.3 Introduction

The growing demand for renewable energy sources has caused a rapid development in photovoltaic technologies. Despite a large number of photovoltaic technologies exist, organic solar cells offer unique advantages.[1–3] Organic solar cells are lightweight, semitransparent and flexible. They can be produced through low cost and easy preparation procedures, which employ environmentally friendly materials. Organic solar cells have demonstrated a short energy payback time, which is the time necessary to recover the energy used for fabrication of the device. Recently, owing to the introduction of bulk heterojunction structures, the development of organic solar cells has seen a significant rise in power−conversion efficiency (PCE) from less than 1% in the first reports to 14% in the latest publications.[4,5] Record efficiencies generally resulted from the employment of new electron−donor materials that showed improved properties.[6–8] Compared to the rapid design and synthesis of novel electron−donors, the development of new electron−acceptors has lagged far behind. Fullerenes and their derivatives have been the most widely employed electron acceptor materials in organic solar cells because of their high electron mobility, large electron affinity, low reorganization energy, isotropy of charge transport and ability to form favorable nanoscale blend films with donor materials.[9,10] However, these fullerenes are expensive and exhibit limited absorption in the longer wavelength region of the solar spectrum, as well as thermal instability. Lately, research efforts have been addressed to develop new electron acceptors characterized by strong intramolecular electron push−pull effects to replace the fullerenes.[11–14]

PDI is a very promising motif to be included in non−fullerene electron acceptors for organic solar cells.[15,16] It shows several appealing features including low−cost synthesis; easy functionalization; significant thermal, chemical and light stability; good electron accepting ability;

excellent electron mobility. Differently from fullerenes, PDIs show a strong absorption in the visible spectral region, which in some cases has proved to be complementary to that of the most effective electron donor materials. PDIs have been successfully employed as strongly electron−withdrawing monomers in new conjugated electron accepting polymers for All−Polymer solar cells.[17−19] Although the parent PDI has proved to be a good building block for designing small molecular electron acceptor systems, it possesses high planarity and thus shows strong intermolecular interactions and tendency towards aggregation. Large scale phase separation observed in monomeric PDI films is discussed in the literature as the cause for reduced exciton dissociation efficiencies, and consequently PCEs decreased by one order of magnitude.[20,21] Dimeric PDIs have been good non−fullerene electron acceptors that have shown improved performances compared to monomeric PDI molecules.[22,23] The strategy largely adopted to reduce aggregation between the PDI units is to break up the intermolecular $\pi-\pi$ interactions by introducing twisting in the backbone of dimeric or oligomeric structures. The loss of planarity and tridimensional structure of the resulting molecular acceptors has been discussed in the literature to be crucial in developing efficient photovoltaic cells.[22−24, 25−35] However, the many studies about twisted PDI derivatives do not report a direct comparison with the performance and behavior of an analogous planar derivative. This is what this work seeks to illuminate. We aim to investigate the effect of molecular structure (twisted vs. planar) on the photobehavior and photovoltaic performance of two isomeric PDI dimers.

Most reported PDI dimers utilize electron donating bridges for the lateral PDI electron deficient domains (Acceptor−Donor−Acceptor structures). There have been just few reports of PDI dimers connected by electron deficient cores (Acceptor−weak Acceptor−Acceptor) which have recently shown pronounced positive effects on the performance of the corresponding organic

solar cells.[36−38] Also, PDI derivatives characterized by fused rings as connection have proven to be highly performing electron acceptors.[39−41] We intend to carry out a study about newly synthetized dimeric PDI derivatives (PDI− core− PDI) characterized by the Acceptor−weak Acceptor−Acceptor structure with the central thieno−pyrido−thieno−isoquinoline−dione rigidly connected through cyclization to the lateral PDIs (compounds **2** and **3** in **Scheme 5.1**). These compounds are two positional isomers and thus analogous in structure. However, switching the relative position of the alkyl amino and keto groups in the central core should induce steric hindrance and thus introduce torsion in the conjugated backbone of isomer **2** (twisted) which should be absent in the case of isomer **3** (planar). The twisted and planar isomers (**2** and **3**) have been studied in comparison with the simpler bis−thienyl analogue (compound **1** in **Scheme 5.1**), where the PDI−core−PDI is an Acceptor−Donor−Acceptor structure. The work has been carried out by employing state−of−the−art femtosecond time resolved spectroscopies and quantum−mechanical TD−DFT computations as well as electrochemical, photovoltaic and x−ray scattering techniques.
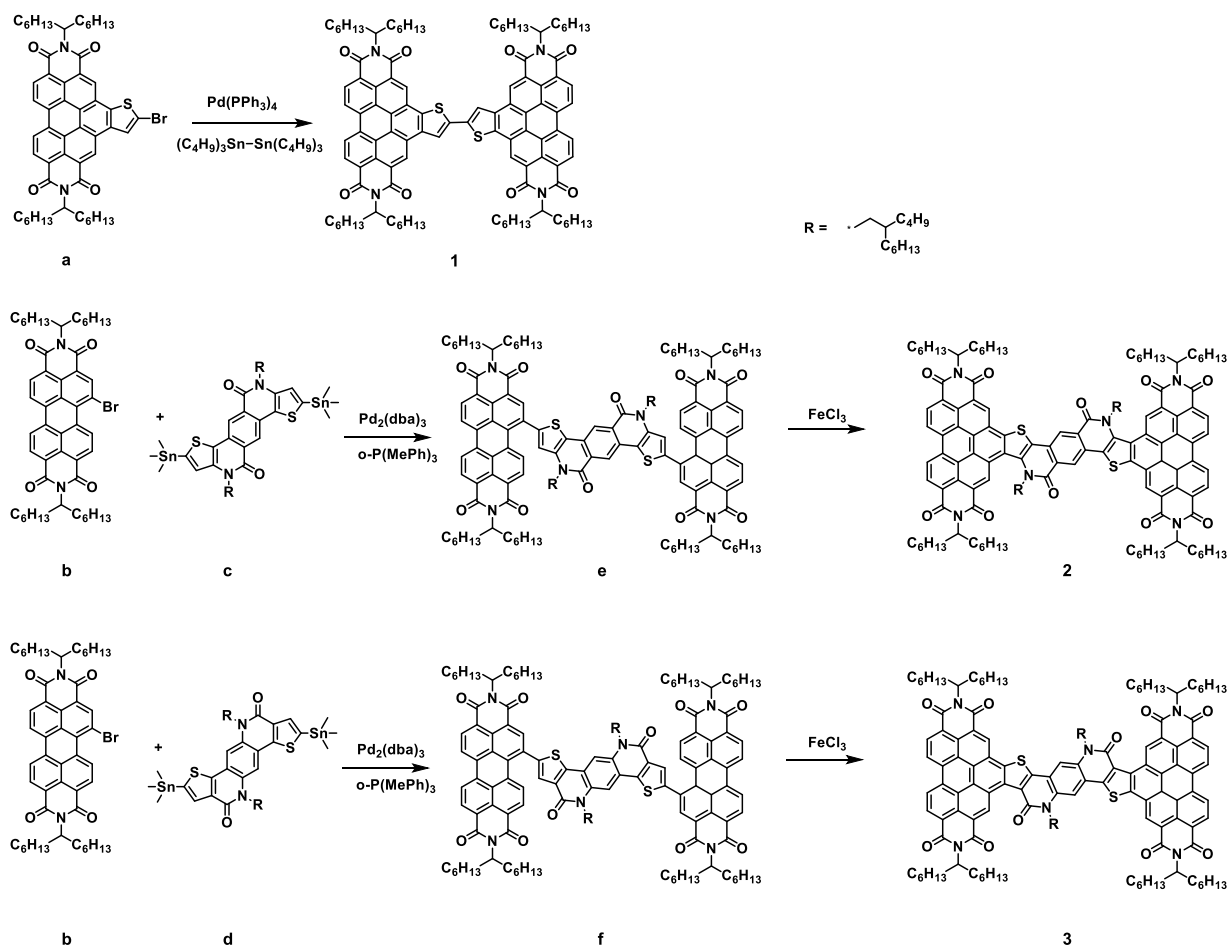
Scheme 5.1 Synthetic route for investigated structures.

5.4 Experimental Section

5.4.1 Materials

Polymer PTB7−Th was obtained from 1−Material. The structures 1, 2 and 3 were synthesized according to the synthetic route described in Scheme 1 and detailed in the publication manuscript. Chlorobenzene and 1,8−diiodooctane for active layer solution preparation were obtained from Sigma−Aldrich. For ZnO preparation using sol−gel approach we used $Zn(CH_3COO)_2 \cdot 2H_2O$, 2−methoxyethanol and 2−aminoethanol all purchased from Sigma−Aldrich. Chloroform from Sigma−Aldrich was used as the solvent for the spectral and photophysical characterization. All chemicals were used as obtained from the manufacturer without further purification.

5.4.2 Steady−State Measurements

All of the measurements were performed at room temperature. Concentrations ranging from 5×10^{-4} to 1×10^{-6} M were used for the spectroscopic investigation. Absorption spectra were measured using an Agilent 8432 UV−visible absorption spectrophotometer. The emission spectrum measurements were performed with a Fluoromax−2 spectrofluorometer. Absorption spectra were taken before and after each measurement to ensure that there was no appreciable photodegradation due to laser irradiation. The fluorescence quantum yields of the samples were calculated using a known procedure[40,41] and Rhodamine B in ethanol ($\phi_F = 0.68$) was used as the standard.[42]

5.4.3 Density Functional Theory Simulations

Molecular models of **1**−**3** were constructed with truncated alkyl chains (such as octyl, hexyl and butyl groups replaced by methyl groups) to save computational time without significant effect on the electronic properties. The ground state geometry of each compound was optimized by density functional theory (DFT), using the B3LYP functional and the 6−31G* basis set. Generally, time−dependent DFT (TD−DFT) gives more accurate excited state energetics than configuration interaction singles (CIS) since the latter lacks electronic correlation. Due to a close manifold of low−lying states, however, excited−state geometry optimization of compound **3** using TD−DFT did not easily lead to a symmetry broken state. On the other hand, this state was easily targeted using CIS geometry optimization. Therefore, the excited state geometries for the three compounds were optimized using CIS, and the excited energy levels refined using TD−DFT. These single−point energies were performed with a system−dependent, non−empirically tuned long−range corrected functional, ωB97X−D,[43,44] which is known to significantly improve the

charge delocalization problem in conventional DFT functionals. The ω value is tuned to minimize the square sum of the difference between HOMO and ionization potential (*IP*), and LUMO and electron affinity (*EA*), $(\varepsilon_{HOMO}+IP)^2+(\varepsilon_{LUMO}+EA)^2$. The ω value is significantly affected by the environment, and inclusion of the solvent dielectric field induces a reduced ω value.[45] The optimal ω values of each compound were found to be 0.004, 0.004, and 0.005 for compounds **1**, **2**, and **3**, respectively, when solvent (chloroform, dielectric constant of 4.31) is included using a polarizable continuum model.[46,47] Characters of excitations are described with natural transition orbitals (NTOs). All the ground and excited state calculations were conducted using Q−Chem 4.0.[48]

5.4.4 Time−Resolved Fluorescence Measurements

Time correlated single photon counting (TCSPC) technique, which has been described previously,[49] was used to study the long decay component of the investigated samples. The laser used for the TCSPC measurement was a Kapteyn Murnane (KM) mode-locked Ti:sapphire laser. The output beam from the KM laser was at 800 nm wavelength, with pulse duration of ca. 30 fs. The output beam was frequency−doubled using a nonlinear barium borate crystal to obtain a 400 nm beam. A polarizer was used to vary the power of the 400 nm beam that excites the sample. Focus on the sample cell (quartz cuvette, 0.4 cm path length) was ensured using a lens of focal length 11.5 cm. Collection of fluorescence was carried out in a direction perpendicular to the incident beam into a monochromator, and the output from the monochromator was coupled to a photomultiplier tube, which converted the photons into counts.

The femtosecond−resolved fluorescence experiments were performed using an ultrafast fluorescence Upconversion setup that had previously been described.[50] Mode-locked Ti:sapphire femtosecond laser (Spectra Physics Tsunami) was used to generate 80 fs pulses at 800 nm wavelength with a repetition rate of 82 MHz. This mode−locked laser was pumped by a 532 nm

continuous light output from another laser (Spectra Physics Millennia), which has a gain medium of neodymium−doped yttrium vanadate (Nd:YVO$_4$). A 400 nm excitation pulse was generated by a second harmonic β−barium borate crystal, and the residual 800 nm beam was made to pass through a computer−controlled motorized optical delay line. The polarization of the excitation beam was controlled by a Berek compensator. The power of the excitation beam varied between 33 to 36 mW. The fluorescence emitted by the sample was up−converted by a nonlinear crystal of β−barium borate by using the residual 800 nm beam, which had been delayed by the optical delay line with a gate step of 6.25 fs. By this procedure, the fluorescence can be measured temporally. The monochromator is used to select the wavelength of the up−converted beam of interest, and the selected beam is detected by a photomultiplier tube (R152P, Hamamatsu, Hamamatsu City, Japan). The photomultiplier tube converts the detected beam into photon counts, which can be read from a computer. Coumarin 30 was used for calibrating the laser. The instrument response function (IRF) has been determined from the Raman signal of water to have a width of 110 fs. Lifetimes of fluorescence decay were obtained by fitting the fluorescence decay profile to the most accurate fit. Mono and multi−exponential decay functions convoluted with IRF in MATLAB and Origin 8 were necessary for the data analysis.

5.4.5 Femtosecond Transient Absorption

An amplified laser (Spectra Physics Spitfire) with pulse duration of ~100 fs, repetition rate of 1 kHz, and pulse energy of 1 mJ was directed at a beam splitter to generate the pump (85%) and the probe beams (15%). The pump beam (~0.66 mJ per pulse) was generated from the second harmonic of the amplifier's output (~800 nm) using a β−barium borate crystal and was focused onto the sample cell ($l = 1$ mm). The probe beam was passed through a computer−controlled delay line and focused onto a 2 mm quartz plate to generate the white light continuum (Helios by

Ultrafast Systems Inc.). The white light was focused onto the sample and the pump beam was overlapped with it. The absorption difference (ΔA) of the signal was collected by a CCD detector (Ocean Optics). Data acquisition was performed with the software Helios by Ultrafast Systems Inc. The IRF was measured by the Raman scattering of water at 466 nm and is found to be 110 fs. Data analysis was performed with the Surface Xplorer Pro software.

5.4.6 Two−Photon Excited Fluorescence Measurements

Two−photon excited fluorescence measurements were performed using a mode−locked Ti:Sapphire laser which is tunable from 700 to 900 nm delivering 110 fs output pulses at a repetition rate of 80 MHz. Emission scans were performed both at 820 nm and 870 nm excitation while scanning the emission in the 400−800 nm range, but the exact emission detection wavelength during the power dependence scan was selected by the emission wavelength that produced the highest number of counts. Input power from the laser was varied using a variable neutral density filter. Two−photon power−dependent fluorescence intensity was utilized to determine the two−photon absorption cross section through the comparative method. Rhodamine B in ethanol was used as the standard (cross section 120 GM at 820 nm and 50 GM at 870 nm).[51]

5.4.7 Device fabrication and characterization

Devices were fabricated in inverted configuration consisting of ITO/ZnO/active layer/MoO$_3$/Ag. ITO substrates, obtained from Thin Film Devices Inc. were ultrasonicated in chloroform, acetone and isopropanol for 15 min and then treated with UV−ozone for 30 min. Sol−gel solution of ZnO precursor, prepared following procedures described elsewhere, was added dropwise onto ITO substrates through PTFE syringe filter and spin coated at 4000 rpm for 40 seconds. Immediately after spin coating, substrates were annealed at 200^{0}C for 30 minutes in air.

Active layer components were dissolved in chlorobenzene overnight at 70^0 C and solution at room temperature was spin coated onto the substrates in a glovebox. Films were immediately transferred to a vacuum chamber and MoO_3 (8 nm) and Ag (80 nm) were thermally evaporated under the pressure lower than $2 \cdot 10^{-6}$ Torr. J–V curves of the devices were measured with Keithley 2420 source meter unit. Devices were tested under 1 sun conditions (AM1.5G, 100 mW/cm^2) using xenon lamp (Oriel 69920) intensity of which was calibrated with a standard NREL certified Si cell (Newport, 91150V). Masks with a well−defined area of 3.14 mm^2 were used to define an active area of the device. EQE was measured with a Newport QE measurement system (IQE−200) with a tungsten halogen lamp as a light source.

5.4.8 Morphology studies

AFM studies were made with Asylum Cyfer microscope at the University of Chicago MRSEC MPML facilities. The GIWAXS measurements were performed at 8ID−E beamline of Advanced Photon Source, Argonne National Laboratory with a radiation wavelength 1.1364 Å. Samples for GIWAXS were prepared on polished Si wafer, covered with ZnO and coated with an active layer film being studied.

5.5 Results

5.5.1 Steady State Absorption and Fluorescence

The absorption spectra of compounds **1−3** in chloroform are shown in **Figure 5.1** (upper left graph). They appear to be extremely broad, covering most of the visible spectral range (onset wavelength around 550−650 nm depending on the considered molecule). Absorption molar coefficients for **1−3** are significantly high (between 80000 and 125000 M^{-1}cm^{-1} at the absorption maximum, see **Table 5.1**) ensuring that these molecular systems actually act as efficient light

absorbers. These features are indeed really promising in view of the use of these chromophores in solar cells; the most commonly employed fullerene acceptors show extremely low extinction coefficients in the visible (900 $M^{-1}cm^{-1}$ at 541 nm for C_{60} in methylcyclohexane).[52]

The absorption spectral shapes of **1−3** resemble the structured absorption observed for perylene diimide (PDI) dimers reported in the literature.[53,54] The relative intensities of the peaks are different from those reported for monomeric parent PDI because of the intramolecular feature of these compounds which consist of two joint units. It is very intriguing that the spectra of two positional isomers (such as **2** and **3**) appear to be so different (see blue and green trace in **Figure 5.1**, upper left graph). The first long wavelength absorption peak is in all cases associated to the $S_0 \rightarrow S_1$ transition (see section B of the Results about Density Functional Theory Simulations). This peak is very narrow (FWHM= 1125 cm^{-1}) and blue shifted (placed at 529 nm) in the case of compound **3**; it is extremely broader (FWHM = 4095 cm^{-1}) and red shifted (at 586 nm) for its isomer, compound **2**. The absorption coefficient measured in the case of **3** is significantly higher than that of **2** (see **Table 5.1**). The integrated oscillator strengths for the $S_0 \rightarrow S_1$ transition are quite similar for the two isomers (f = 0.263 for **2** and f = 0.328 for **3**), and consequently their ability to harvest solar radiation, even though their spectral shapes are significantly diverse. The emission spectra of **1−3** in chloroform are shown in the upper right graph of **Figure 5.1**. The emission of compounds **1** and **3** look structured and peaked at 575 and 547 nm, respectively. In contrast to this, the fluorescence band of compound **2** is significantly red shifted (maximum at 650 nm) and characterized by a bell−like shape. It has to be noted that no excitation wavelength effect is observed for the emission of the three investigated fluorophores. Also, no significant concentration effect is observed for the absorption and emission spectra of the investigated molecules in chloroform solution. **Figure 5.1** also reports the absorption and emission spectra recorded for

compounds **1**−**3** in spin coated thin films (lower graphs). Absorption spectra in film exhibit similar spectral shapes with respect to those recorded in solution, with the main peaks undergoing a certain red shift in the solid state. An additional low intensity broad peak above 600 nm, not revealed during the investigation in solution, is observed for compounds **1** and **3** in film. This feature may be due to the presence of aggregates of these molecules in the solid state. Very interestingly, all the dyes exhibit complementary absorption spectra with respect to those characteristics of the polymers often employed as electron donors for organic solar cells (such as PTB7−Th), which are placed in the 550−800 nm region. The use of these chromophores as electron acceptors for organic photovoltaics together with electron donor polymers thus allows a very efficient harvesting of the solar radiation in the entire visible spectral range (see **Figure 5.7a**). A bathochromic shift is observed also for the emission bands of **1**−**3** upon passing from solution to solid state. The computed Stokes−shift for the three molecules in chloroform solution are reported in **Table 5.1**. The Stokes−shift value is found to be rather small (620 cm^{-1}) for compound **3**. This feature is undoubtedly promising in view of use of this molecule in organic photovoltaics. In fact, a negligible Stokes−shift and thus very low reorganization energy is considered one extremely positive factor for fullerene being a remarkable acceptor. In electron transfer theory, systems with smaller reorganization energy should give faster electron transfer (Marcus inverted region). The observed Stokes−shift is relatively higher for the positional isomer **2** (1600 cm^{-1}) and intermediate in the case of the simpler compound **1** (1100 cm^{-1}) with respect to **3**. These findings point out a reduced molecular rigidity for **1** and **2**.

Fluorescence quantum yield values are found to be remarkable for the investigated systems (see **Table 5.1**), which therefore are intense yellow (**3**), orange (**1**), red (**2**) emitters. The highest fluorescence efficiency (0.52) is observed for compound **3**; the quantum yield appear to be halved

in the case of compound **1** (0.21) whereas the lowest value is retrieved for compound **2** (0.047). The quantum yield trend closely resembles the trend observed for the Stokes−shift of the three molecules. As repeatedly observed in the literature, the increased molecular rigidity is indeed associated to a higher fluorescence quantum yield.[55]

The fluorescence rate constant values for **1**−**3** have been computed from the experimental fluorescence quantum yields and lifetimes ($k_F = \phi_F/\tau_F$; for τ_F see section reporting the results for Time Resolved Fluorescence. The radiative rate constants have also been obtained with the Strickler−Berg equation[56] ($k_{F,SB}$) using the integrated first absorption band and the fluorescence band. The k_F and $k_{F,SB}$ values retrieved for compounds **1** and **3** are in very good mutual agreement (8.4×10^7 and 7.2×10^7 s^{-1} for **1** and 1.5×10^8 and 1.3×10^8 s^{-1} for **3**). This result suggests that the state reached by absorption at long wavelengths for these molecules is allowed as well as that responsible for their emission. Very interestingly, the two values are significantly different in the case of compound **2** ($k_F = 2.6\times10^7$ s^{-1} and $k_{F,SB} = 7.2\times10^7$ s^{-1}) and this finding might indicate that the fluorescent state is partially forbidden in this case.

Table 5.1 Absorption and emission properties of compounds **1**−**3** in chloroform solution and in film.

Comp.nd		λ_{abs} / nm	λ_{em} / nm	$\Delta\upsilon$ / cm^{-1}	ε / M^{-1}cm^{-1}	ϕ_F	τ_F / ns (SPC)
1	chloroform	461, 490, 541	575, 620(sh)	1100	88000	0.21	2.5
2	chloroform	450, 498, 586	647	1600	80500	0.047	1.8
3	chloroform	461, 493, 529	547, 590(sh)	620	125800	0.52	3.5
1	film	468, 494, 555	605				
2	film	457, 498, 600	670				
3	film	463, 499, 535	570				
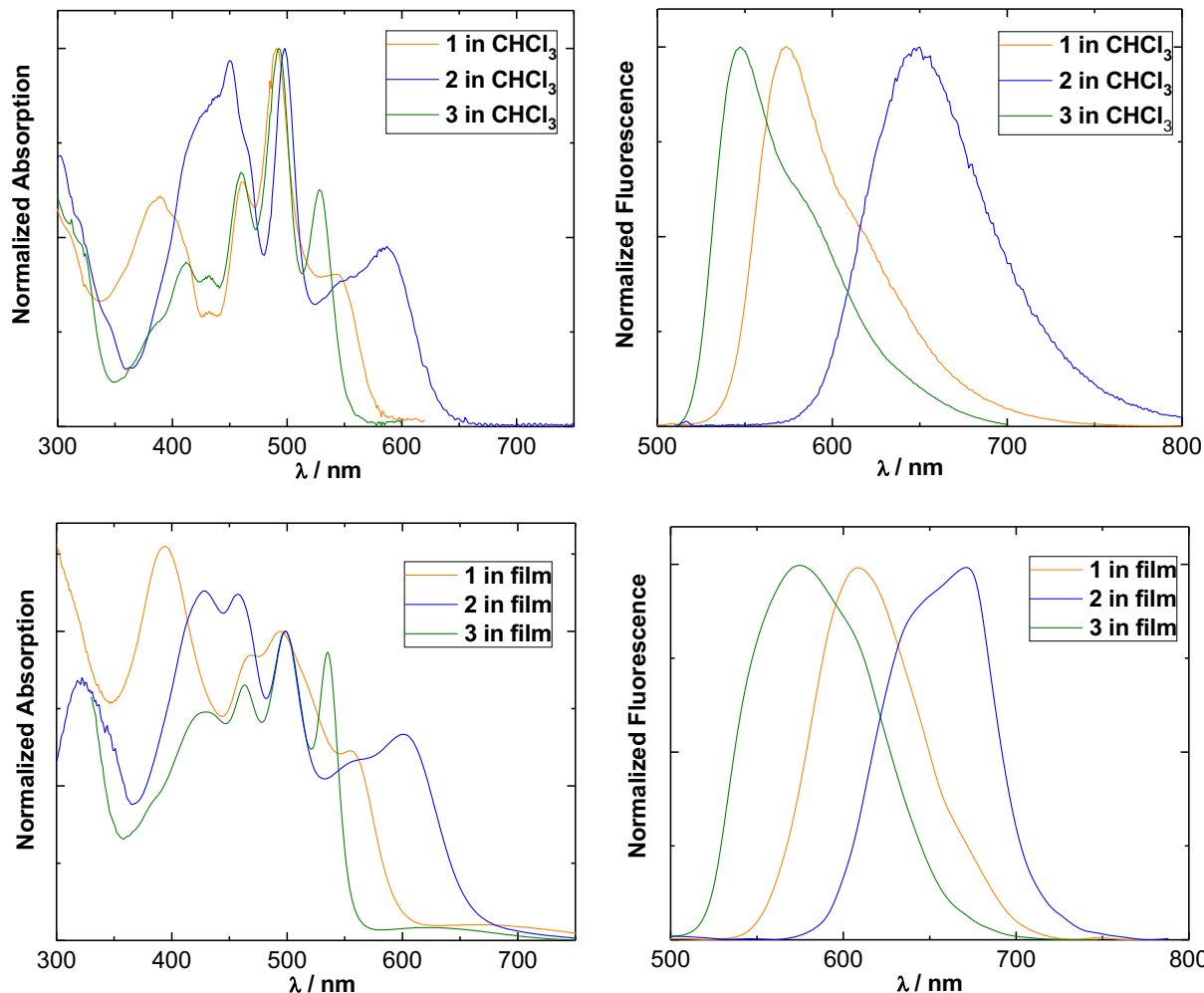
Figure 5.1 Normalized absorption and emission spectra of compounds **1−3** in chloroform solution (upper graphs) and in thin film (lower graphs).

5.5.2 Density Functional Theory Simulations

A comprehensive computational investigation was carried out to examine the structural and electronic properties of the three compounds in vacuum and in chloroform solution. In the ground state optimized geometries of **1−3**, in the case of **1** and **3** the ground state conformation is nearly planar, with a small distortion from planarity in the two lateral perylene diimides. For compound **2**, however, a significant deviation from planarity is caused by the steric hindrance between the dialkylamino groups of the central core and the hydrogens of the lateral perylene diimides. This steric hindrance is not present in isomer **3**. Similarly, the excited state optimized

geometry (**Figure 5.2**) appears perfectly planar in the case of compounds **1** and **3** but is twisted for **2**. The S_1 optimized geometry shows a small conformational rearrangement with respect to the ground state structure.
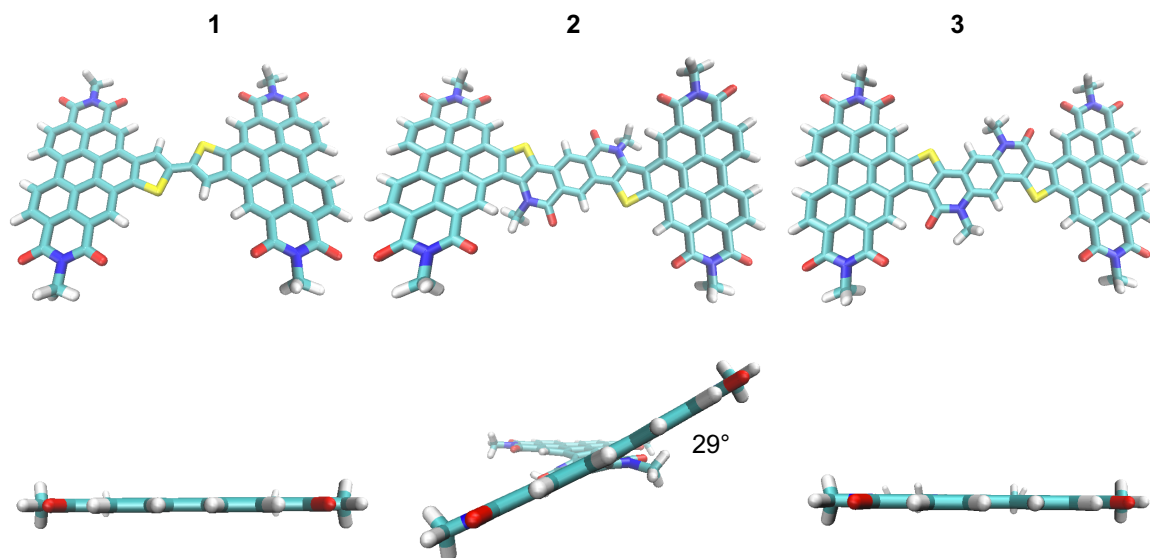
Figure 5.2 Excited state optimized geometry (top and lateral views) for compounds **1−3**.

In the frontier molecular orbitals (MOs) calculated for the S_0 optimized geometry of 1−3, the transition into the lowest excited singlet state S_1 is mainly described by the HOMO–LUMO configuration in all cases. The HOMO→LUMO transition entails a charge displacement from the central portion of the molecule (electron donor bithyenyl or weak electron acceptor thieno−pyrido−isoquinolinedione) toward the lateral strongly electron accepting perylene diimides. Also the other molecular orbitals involved in the experimentally recorded absorption spectra allow us to rationalize the observed multiple intense absorption peaks. Random phase approximation was used for theoretical prediction of the spectra because in this way the computed oscillator strengths resulted in better agreement with the experimental ones.

For the optimized S_1 state geometries of **1** and **2**, the HOMO and LUMO orbitals are similar to those of the ground state geometries. The charge transfer excitation for S_1 appears to break symmetry in compound **3**, where the LUMO is largely localized on a single PDI. Being the lowest

energy excited state, this geometrically relaxed, localized state represents the one from which emission will occur. Since much of the HOMO is also localized on one half of the molecule, the fluorescence from this state will bear resemblance to the emission of monomeric PDI. These findings emerging from quantum mechanical calculations provide a possible explanation for the blue−shifted intense emission spectrum of **3** (peaked at 547 nm), which closely resembles the emission of the single PDI (peaked at 533 nm and exhibiting a fluorescence quantum yield of 0.40).[53] The computed transition energy remarkably agrees with the experimental emission maximum position for the three investigated fluorophores. In the case of compound **2,** the calculations predict a forbidden S_2 excited state close in energy to S_1, where the latter is a fully allowed transition and thus strongly fluorescent. Vibronic coupling between these two close states may occur (as proposed by Lim for the proximity effect),[57] leading to internal conversion to the ground state as a principal excited state deactivation pathway. For compound **3**, S_2 is predicted to be much higher in energy than the allowed S_1 and shows significant oscillator strength for emission.

The HOMO and LUMO energies for the three molecules were computed. The LUMO orbitals have higher energies than fullerene, with **3** having the highest LUMO energy of the three examined compounds. This factor is expected to increase the open−circuit voltage of the photovoltaic cells realized with these acceptors, which indeed were found to be significantly higher than in the fullerene−containing solar cell employing the same donor polymer (see **Table 5.6**).

To analyze compounds **1**−**3** in greater detail, these compounds were divided into three subunits, Acceptor−Donor(weak Acceptor)−Acceptor for **1** (**2** and **3**). **Figure 5.3** shows the NTOs for compounds **1**−**3**; these orbitals represent the electron−hole pair of each excited state (which account for more than 95% of each transition's wave function). The amount of charge transfer

(CT) is quantified as the change in atomic charge of each fragment (**Table 5.2**) upon excitation, where $0.48e^-$, $0.70e^-$, and $0.66e^-$ migrated from the central fragment to the lateral groups in compounds **1**, **2**, and **3**, respectively. In compounds **2** and **3**, simulations show that the CT states have lower excitation energies than the local excitations within each PDI or the core linker. For the two vertical excitation S_1 states, compound **2** involves more CT character ($0.70e^-$) than compound **3** ($0.66e^-$), which is consistent with the lower excitation energy of **2**.

Table 5.2 Change in atomic charge from S_0 to S_1 on the subunits of compound **1−3**.[a]

	1			2			3		
	A	D	A	A	wA	A	A	wA	A
Absorption[b]	−0.24	+0.48	−0.24	−0.35	+0.70	−0.35	−0.33	+0.66	−0.33
Emission[c]	−0.22	+0.45	−0.22	−0.33	+0.65	−0.33	+0.03	+0.70	−0.73

[a]Mulliken charge is given in e; [b]Calculated at S_0 geometry; [c]Calculated at S_1 geometry

	1	2	3
Electron NTOs			
Hole NTOs			
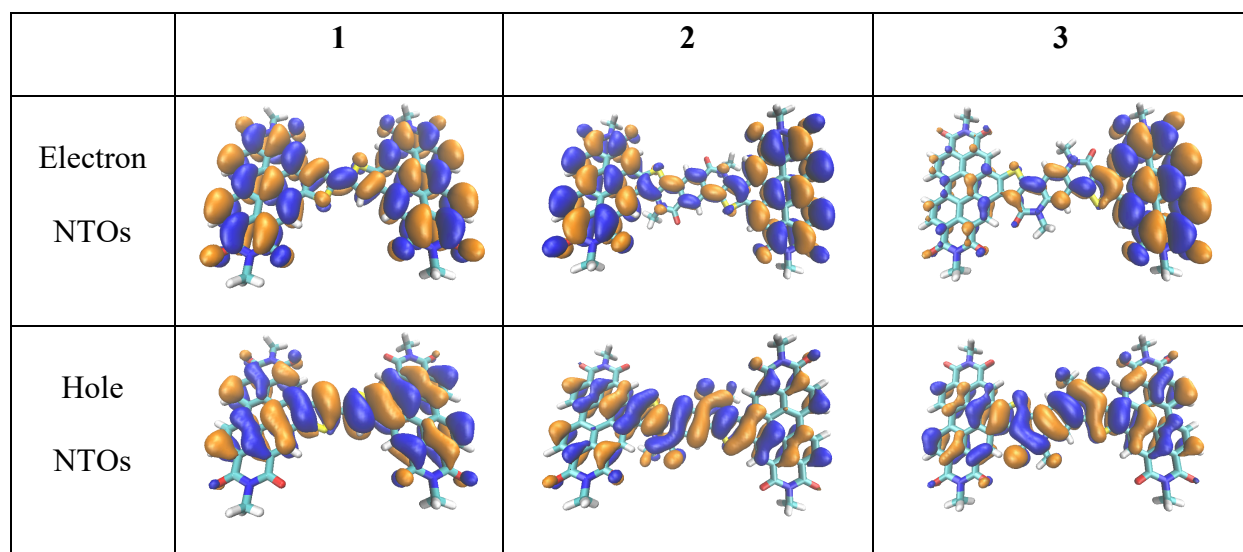
Figure 5.3 Natural transition orbitals for the S1 geometry of compounds **1−3** (Isovalue=0.01).

The number of transferred electrons was calculated at the relaxed S_1 geometry, in order to quantify the degree of CT for the emissive state. Since charge transfer occurs in a few hundreds of femtosecond after light absorption, the degree of CT at this state will likely correlate with cell efficiency. CT state is considered as an intermediate before complete charge separation. It is

expected that charge separation occurs easily from a state with high CT character, due to the fact that the electron−hole pair is already partly broken up within the molecule. Compounds **1** and **2** distribute the excited charge evenly between the two acceptor units. The CT state in compound **3**, however, becomes clearly unidirectional with accumulation of $0.73e^-$ on a single acceptor and negligible charge on the second acceptor. Interestingly, the more planar compound, **3** shows larger degree of CT than its isomer, **2**, by $0.08e^-$ (0.73 vs. 0.65) at the S_1 geometry.

5.5.3 Time Resolved Fluorescence

The fluorescence properties of the three samples in chloroform were investigated using a single photon counting technique with a nanosecond time resolution. Lifetimes of few nanoseconds resulted from the fitting and their values for **1**−**3** in chloroform are reported in **Table 5.1**. The lifetime trend among the three fluorophores ($\tau_{F,3}$ (3.5 ns)> $\tau_{F,1}$ (2.5 ns)> $\tau_{F,2}$ (1.8 ns)) parallels the trend already discussed for the fluorescence quantum yields of these dyes. The obtained results – few nanoseconds for the emitting state (similar to fullerene whose S_1 lifetime is 1.2 ns[52])−are interesting because in solar cells devices, the exciton diffusion length is proportional to the excited state lifetime. Long fluorescence decays for the electron acceptors might be beneficial for hole transfer from the PDI derivatives to the electron donor polymer in the photovoltaic device.[58,59]

The ultrafast dynamics of the fluorescence was studied by employing a femtosecond time−resolved fluorescence up−conversion set up and exciting the samples solutions with 400 nm ultrashort laser pulses. The kinetics recorded at wavelengths close to the emission peak of the investigated fluorophores are shown in **Figure 5.4** together with the bi−exponential fitting functions for the experimental decay (red trace in the figure). The lifetimes resulting from the fitting are reported in **Table 5.3**. The long living component in the nanosecond temporal range (τ_2

in **Table 5.3**) reflects the lifetime resulting from the TC−SPC investigation, which is the lifetime of the fully relaxed S_1 fluorescent state (τ_F in **Table 5.1**). The accuracy of the fluorescence up conversion for evaluation of the long living decay components is not good, due to the limited temporal window of investigation (720 ps). For this reason, the lifetime obtained with the single photon counting is considered a more accurate evaluation of the relaxed S_1 decay time. As for the short living component (τ_1 in **Table 5.3**), it shows values of ca. 10 ps for compounds **2/3** and of ca. 100 ps for compound **1**. This component is probably related to structural relaxation following photoexcitation of **1**−**3**. This result is in agreement with the small molecular rearrangement predicted by the calculations to take place on passing from the ground to the excited state optimized geometry.
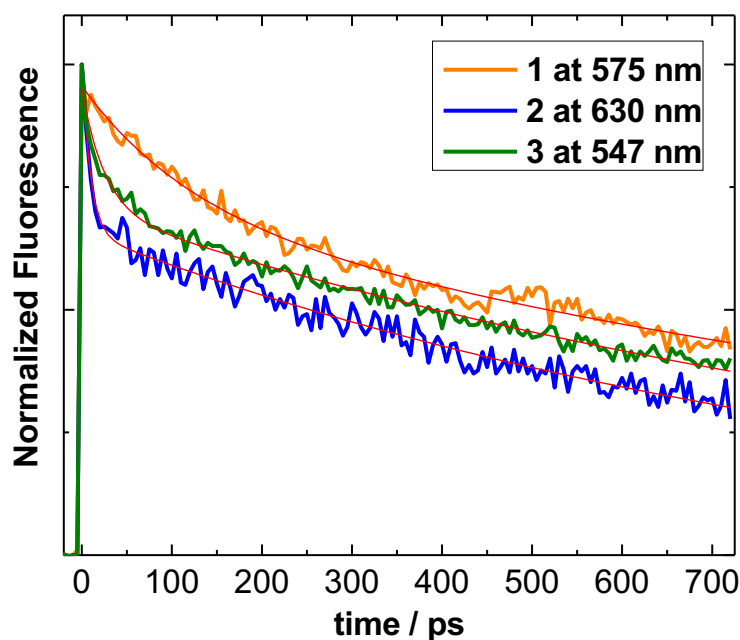
Figure 5.4 Fluorescence decay kinetics recorded for compounds **1**−**3** in chloroform at the peak wavelength by femtosecond resolved Fluorescence Upconversion.

The fluorescence kinetics recorded on a smaller time window, down to few picoseconds, exhibits a fast rise of a few hundred femtoseconds (ca. 250 fs, see **Table 5.3**) from the fit accounting for the instrumental response function (120 fs) by deconvolution. The 250 fs rise time

observed for the investigated samples can be assigned to solvation dynamics in chloroform. Fluorescence kinetics were acquired also employing both parallel and perpendicular relative polarization configuration for the excitation and gate beams. **Figure 5.5** (right graph) show the anisotropy decay results, r(t), for the three molecules in chloroform in a short time scale. The fluorescence anisotropy of all three samples decayed to a residual value (r_∞ ca. 0.07 for **1**, 0.13 for **2**, 0.25 for **3**) within the Instrumental Response Function of our apparatus (ca. 110 fs). This fast decay of anisotropy indicates fast energy/charge redistribution via a coherent excitonic mechanism between dipoles that are oriented in different directions. The residual anisotropy value is related to the angle between the absorption and emission transition dipole moments after this fast relaxation. It is feasible that different depolarization due to diverse energy/charge redistribution takes place in compounds **1** and **2** (residual anisotropy ca. 0.1) with respect to compound **3** (residual anisotropy ca. 0.25). On a long time scale the anisotropy decay was found to reflect the re-orientation dynamics, which for these large molecular systems is quite slow and takes hundreds of picoseconds.

Table 5.3 Lifetimes (τ) and pre−exponential factors (A) obtained by fitting the Fluorescence Upconversion kinetics for compounds **1−3** in chloroform.

Compound	λ_{em}/ nm	A_1	τ_1 / ps	A_2	τ_2 / ps*	Rise Time / fs
1	575	0.25	120	0.71	1500	250
2	630	0.35	10	0.63	920	250
3	547	0.25	10	0.70	1140	−

$^*\tau_2$ corresponds to the lifetime obtained with the single photon counting measurements (see **Table 5.1**) with the latter being a better evaluation for the decay time of this long living component.
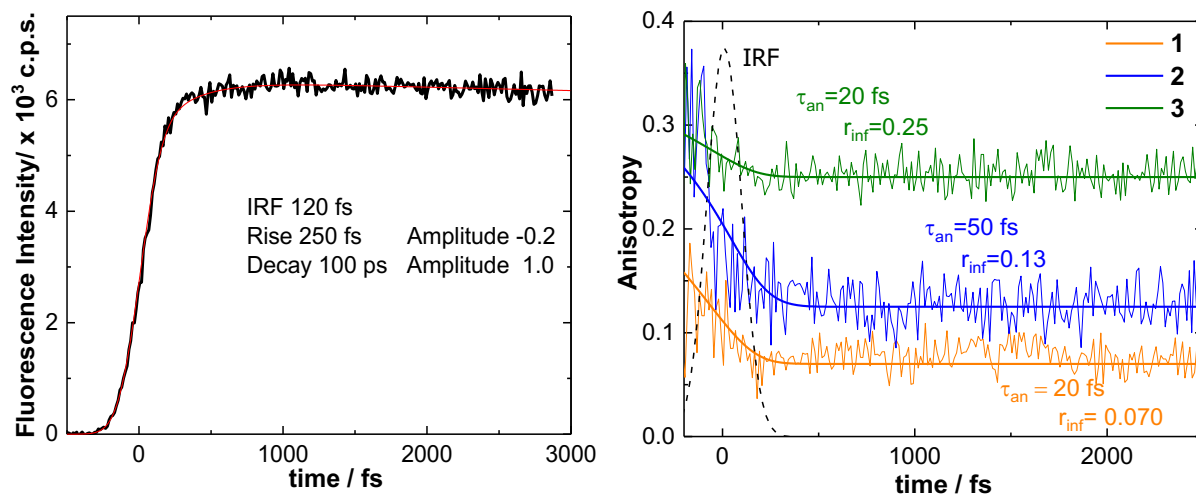
Figure 5.5 Left: magic angle fluorescence dynamics for compound **1** in chloroform at 575 nm, best fit to a bi−exponential function is also shown. Right: fluorescence anisotropy decay on a short time scale for **1−3** samples, the thick line is the result of a best fit.

5.5.4 Femtosecond Transient Absorption

Femtosecond transient absorption measurements were carried out upon a 400 nm laser excitation on solutions of compounds **1−3** in chloroform. The results obtained in term of spectra and kinetics data are shown in **Figure 5.6**. The time resolved absorption spectra (left graphs in the figure) exhibit below 540 nm some negative bands ascribable to ground state bleaching because they match the ground state absorption spectra of the three chromophores. The transient absorption spectra also present broad positive bands due to excited state absorption in the region between 550 and 700 nm. It is possible that in this longer wavelength spectral region the intense positive excited state absorption prevails over negative stimulated emission signals. Decay kinetics were recorded in the spectral region corresponding to positive differential absorbance signals, growth kinetics were recorded at wavelengths where negative ΔA is detected (right graphs of **Figure 5.6**). All three samples exhibited a clear broad excited state absorption peak at 740 nm. This spectral feature has been repeatedly associated in the literature to the radical anion of perylene diimide.[60–66] In the case of compound **3**, this band in the transient spectra appears together with the most intense excited state absorption peak around 580 nm which is absent in the case of **1** and **2**. Very interestingly,

absorption due to the perylene diimide radical cation has been reported to take place in this spectral region according to several ultrafast spectroscopic studies.[62,64,65,67] These findings point to the occurrence of charge transfer during the excited state relaxation of isomer **3**, taking place upon breaking the symmetry of the system between the two lateral perylene diimides. Charge transfer is occurring also upon photoexcitation of compounds **1** and **2** owing to the observed transient absorption at 740 nm due to the perylene diimide anion. However, it probably happens via a different mechanism determining a certain positive charge localized in the central core of these molecules, possibly responsible for the absorption signal observed around 650 nm. The proposed mechanisms of charge transfer are actually in agreement with the charge distribution predicted by the calculations for the HOMO/LUMO molecular orbitals describing the excited states of **1**−**3**, where the symmetry of the molecular structure is maintained for **1/2** and broken in the case of isomer **3**.

Global analysis of the data collected for samples **1**−**3** in chloroform (see results **Table 5.4**) revealed in all cases the presence of two exponential components characterized by lifetimes of tens of picoseconds (τ_1) and few nanoseconds (τ_2). The lifetimes here obtained for the shorter component (τ_1 in **Table 5.4**) are probably more accurate than those obtained using the fluorescence up conversion investigation (τ_1 in **Table 5.3**) as they are computed via a global fit analysis instead of a single wavelength fit. Lifetime τ_2 corresponds to the lifetime obtained with the single photon counting measurements with it being a better evaluation for the decay time of this long living component. As discussed before, the two components are assigned to small structural rearrangement and to the decay of the relaxed S_1 state, respectively. The S_1 state exhibits a certain charge transfer character as evidenced by its spectral features in the different samples. No significant spectral evolution is observed in time after light excitation (see **Figure 5.6**). It is

therefore likely that the charge transfer is extremely fast, occurs within the solvation time and that its dynamics is described by the rise time of hundreds of femtoseconds revealed during the fluorescence up−conversion investigation (see **Table 5.3**).
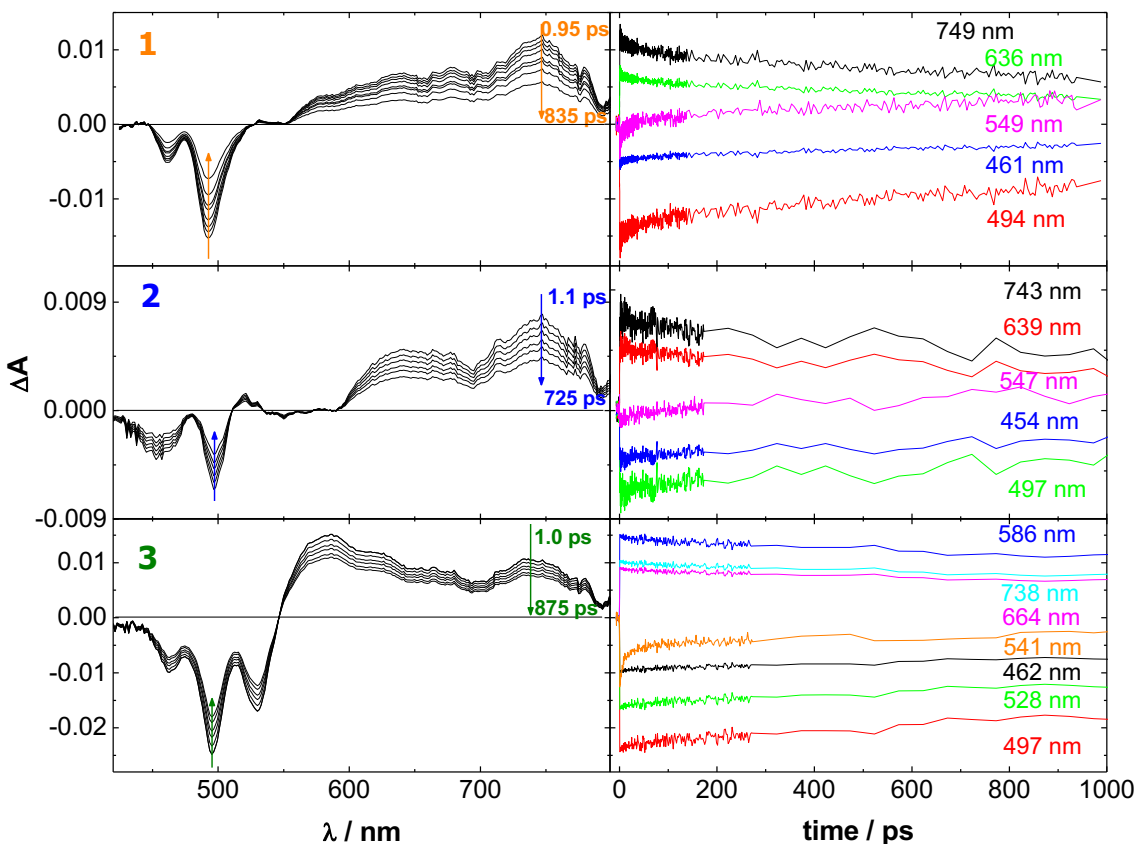
Figure 5.6 Time−resolved absorption spectra (left) and decay kinetics (right) obtained by femtosecond resolved Transient Absorption measurements of compounds **1−3** in chloroform.

Table 5.4 Lifetimes (τ) obtained by global fitting of the femtosecond Transient Absorption data.

Compound	τ_1 / ps	τ_2 / ps
1	48	2100
2	57	1800
3	39	3900

5.5.5 Two Photon Absorption

Two−Photon Excited Fluorescence measurements were carried out for the three compounds in chloroform solution upon both 820 and 870 nm excitation and collecting the emitted counts at the peak fluorescence wavelength of each sample. The quadratic dependence of the

fluorescence counts upon the excitation laser power was verified for all samples both under 820 nm and 870 nm excitations. In fact, the log(counts) versus log(power) plots was successfully fitted with a linear function exhibiting a slope of two in all cases. The emission spectra recorded for the three samples under infrared two−photon excitation are similar to the steady state emission profiles (see **Figure 5.1**). This suggests that the excited state responsible for the emission is the same for the mono−photonic and bi−photonic experiments. Two−Photon Absorption (TPA) cross-sections (δ) were obtained through the comparative method and the results are reported in **Table 5.5**. Compounds **1**−**3** show remarkable TPA cross-sections, of tens or hundreds of GM depending on the molecular structure and the excitation wavelength. All the investigated dimers exhibit enhanced TPA cross-sections with respect to the monomeric PDI ($\delta_{820 nm}$= 1 GM).[53] In fact, it has been repeatedly reported in the literature[68,69] that a common design strategy for optimizing δ is the use of centrosymmetric quadrupolar architectures. The excitation wavelength dependence of the cross section of **1**−**3** is certainly due to the shape of the TPA spectrum, which is not accurately known for the investigated systems. However, considering their mono−photonic spectrum (shown in **Figure 5.1**) it is feasible that the cross-sections of the three compounds are somehow similar when employing an 820 nm excitation (extinction coefficient in the steady state spectrum is not very different for the three chromophores at 410 nm). On the contrary, the response of compound **2** is significantly larger than that of the other molecules when an 870 nm excitation is employed. This is probably due to the diverse and more intense absorbance exhibited by this dye in the corresponding one-photon absorption spectral region (around 435 nm). In general, the two positional isomers **2** and **3** show enhanced TPA response in comparison to the simpler compound **1**, in a trend which parallels that of the computed transition dipole moments for the corresponding transitions. The significant TPA response observed for the compounds is in agreement with the

photoinduced charge transfer revealed to take place in these structures during the femtosecond absorption study. In particular, when employing an 820 nm excitation the TPA cross section measured for the planar isomer **3** is the highest among those of the three molecules. This result could reflect more efficient charge transfer for this planar molecule with respect to its twisted isomer, **2** and the simpler compound, **1**.

Table 5.5 Two-Photon Absorption cross sections (δ) obtained by Two−Photon Excited Fluorescence measurements upon 820 nm or 870 nm laser excitation using the comparative method.

Comp.nd	δ / GM λ_{exc}=820 nm	δ / GM λ_{exc}=870 nm
1	212	17
2	217	343
3	337	59

5.5.6 OPV Properties and Active Layer Characterization

We prepared the solar cells in inverted configuration with ITO/ZnO/active layer/MoO$_3$/Ag to evaluate the photovoltaic properties of these small molecules as acceptors together with PTB7−Th as the donor. A donor/acceptor ratio of 1:2 was spin casted from chlorobenzene solution at room temperature and an active layer with a thickness of about 100 nm was formed. The device fabrication conditions were optimized to maximize the OPV performance. As shown in **Figure 5.7a** blends of PTB7−Th and acceptor absorb in wide range of wavelengths from 350 to 800 nm. All major absorption peaks of acceptors **2** and **3** are present in the blend absorption, as well as two complementary polymer peaks at 640 and 720 nm. The J−V characteristics of these OPV cells are shown in **Table 5.6** and the J−V curves are plotted in **Figure 5.7b**. Similar open circuit voltages (V$_{OC}$), short circuit currents (J$_{SC}$) and fill factors (FF) were observed for blend films made from both PDI isomers. These results give an explanation to the analogous photovoltaic performances exhibited by the devices (4.79 % and 4.97 % for isomers **2** and **3** respectively). Both the isomers,

2 and **3**, show good power conversion efficiency (around 5 %). The external quantum efficiencies (EQE) of the optimal devices were measured and are shown in **Figure 5.7c**. It can be seen that all devices show broad EQE spectra from 350 to 800 nm, consistent with their absorption spectra. The quantum efficiency for isomer **3** based blends is higher relatively to isomer **2** both in the spectral region where acceptor absorption takes place (in agreement with the higher extinction coefficients measured for **3** in solution) and in the wavelength range where the donor absorption occurs. The EQE is relatively enhanced for **2** only between 550 and 620 nm, due to its broader absorption spectrum extending in this area differently from **3** (see **Figure 5.1**). After integration of EQE curves over AM1.5G spectrum, calculated J_{SC} values were 11.09 and 11.80 mA cm^{-2} for compounds **2** and **3**, respectively, which are in good agreement with the values measured from (J−V) curves.
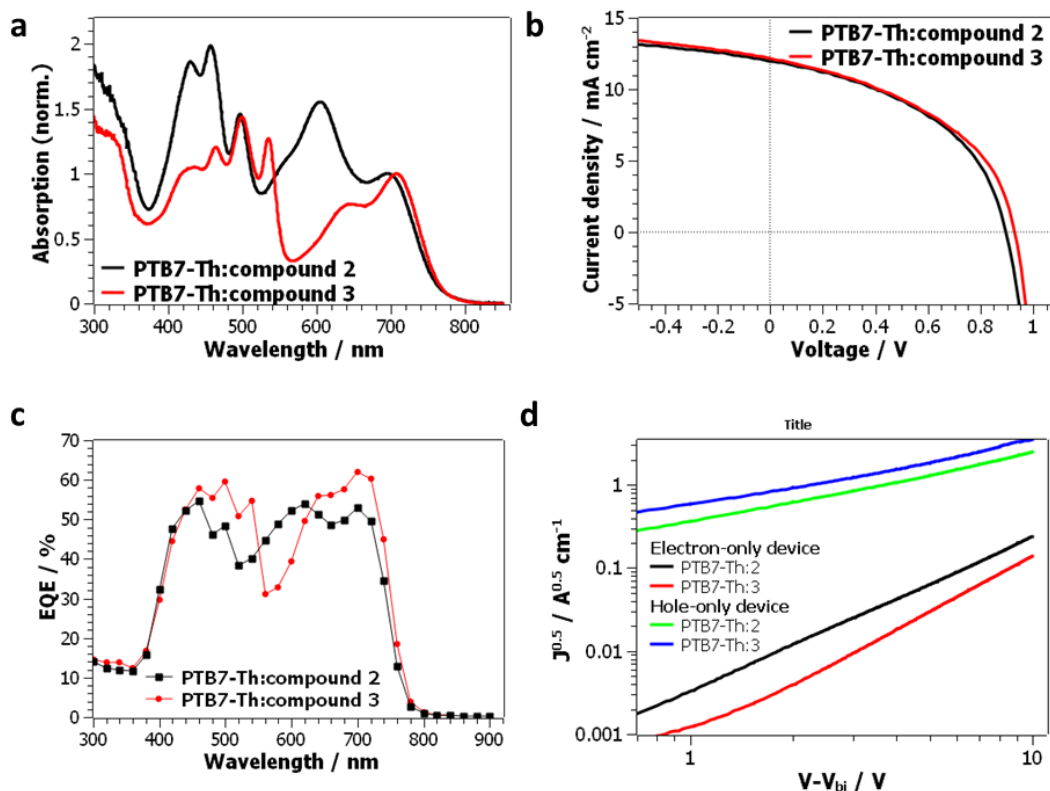
Figure 5.7 a) Normalized film absorption spectra of blends; b) J−V curves of solar cell devices using **2−3** as acceptors and PTB7−Th as the donor; c) External quantum efficiency (EQE) spectra; d) Hole and electron mobility J−V curves of PTB7−Th:acceptor blends.

In addition to photovoltaic data we have also measured SCLC hole and electron mobilities for blends of polymer PTB7−Th and acceptors. Hole−only devices had architecture ITO/PEDOT/PTB7−Th:acceptor/MoO$_3$/Ag, while electron−only devices were assembled in a configuration ITO/ZnO/PTB7−Th:acceptor/Ca/Al. Both types of device had active layer thicknesses larger than 115 nm to ensure SCL current. J−V curves were measured for these devices from 0 to 10V and current densities in SCLC region (with a slope equal to 2) were fitted with Mott-Gurney equation (**Figure 5.7d**). Interestingly, for hole mobilities we observed an increase when acceptor **2** was replaced with acceptor **3**, from $2.0 \cdot 10^{-4}$ cm^{2}V^{-1}s^{-1} to $8.5 \cdot 10^{-4}$ cm^{2}V^{1}s^{-1}, respectively, while for electron mobilities the opposite trend was observed – mobility decreased from $7.2 \cdot 10^{-6}$ cm^{2}V^{1}s^{-1} for compound **2** to $3.9 \cdot 10^{-6}$ cm^{2}V^{1}s^{-1} for compound **3**. To determine crystallinity and details of packing for neat materials and blends, we conducted GIWAXS experiments. The neat films of compounds **2** and **3** exhibit very similar scattering pattern with two broad peaks present, π−π stacking peak near 1.5 Å^{-1} and the peak near 0.35 Å^{-1}. The peaks are present in− and out−of plane direction, which indicates lack of preferential orientation on the surface of a substrate. On the contrary, for blend films the π−π stacking peak is well resolved only in q$_z$ direction, which indicates preferential face−on orientation for the polymer and acceptor molecules. The ratio of scattering intensities of q$_z$ to q$_y$ peaks at 1.65 Å^{-1} is 2.1 for blend PTB7−Th:compound **2** and 1.75 for a blend with compound **3**, thus indicating slightly more face−on component for blend with compound **2**. We have also studied the surface of the blends using AFM. At the micrometer scale both blends have shown similar surface morphology and calculated roughness is similar for both films as well − 0.79 RMS for a blend with compound **2** and 0.71 RMS for a blend with compound **3**.

Table 5.6 Parameters summary of solar cells devices and charge carrier mobilities with **2−3** as acceptors and PTB7−Th as the donor (results are averaged over 5 devices).

Acceptor	V_{OC}/ V	J_{SC}/ mA cm^{-2}	FF	PCE^{av} (PCE^{max})/ %	μ_h/ cm^{2}V^{-1}s^{-1}	μ_e/ cm^{2}V^{-1}s^{-1}
2	0.89±0.01	11.78±0.22	0.45±0.01	4.79±0.09 (4.91)	$2.0 \cdot 10^{-4}$	$7.2 \cdot 10^{-6}$
3	0.93±0.01	11.85±0.27	0.45±0.01	4.97±0.05 (5.03)	$8.5 \cdot 10^{-4}$	$3.9 \cdot 10^{-6}$

5.6 Discussion

We reported here the study of two newly synthetized perylene diimide (PDI) dimers, of interest as non−fullerene electron acceptors for organic solar cells, characterized by a ring fused Acceptor−weak Acceptor−Acceptor structure, which are positional isomers. They are analogous but the steric hindrance determined by the positional substitution induces a twisted conformation in one of the isomers (**2**) whereas the other (**3**) is substantially planar. Much recent literature has pointed out that employing twisted PDI derivatives is an effective strategy to avoid their aggregation; with the aggregation being considered the limiting factor for the efficiency of relative organic photovoltaic devices. In this study, we investigated the effect of twisting through a direct comparison of the light induced behavior and photovoltaic performance of twisted vs. planar PDI based isomers. These molecules have been investigated in comparison with the simpler basic compound **1**, characterized by a bi−thienyl core (donor) connected to the lateral PDI acceptors.

Despite their structural similarity, the two isomers show strikingly different spectral and photophysical behavior in solution, determined by their different conformations. The absorption spectra exhibited by the isomers can be interpreted considering the occurrence of excited state exciton splitting in composite molecules such as dimers.[70] For such molecules the energy of the exciton splitting between the two excited states that play a role, and their oscillator strengths depend on the relative angle between the transition dipole moments of the monomer portions. Different optimized geometries were predicted by the quantum−mechanical calculations for the two isomers (twisted for **2** and close to planarity for **3** in the ground state), which thus give an

explanation for their completely different absorption spectral shapes. Excited state geometries are theoretically predicted to be perfectly planar for compounds **1/3** and twisted for compound **2**. Indeed, the structured emission spectra and the high fluorescence quantum yields observed for both **1** and **3** are typical of fluorophores exhibiting perfectly planar S_1 geometries. The much lower fluorescence efficiency observed for **2** can be rationalized considering that twisted conformations are known to prefer non−radiative decay pathways to the ground state such as internal conversion. However, the fact that the fluorescence lifetime is only halved when comparing compounds **3** and **2**, whereas the fluorescence quantum yield is decreased by one order of magnitude suggests that some additional effect may play a role in determining the reduced emission of the twisted isomer. The presence of an energetically close forbidden state (S_2) and its mixing with the fluorescent state (S_1) was inferred by the results of the theoretical calculations in the case of isomer **2**. This proximity effect might give an explanation to the low fluorescence rate constant (k_F) experimentally obtained for this molecule. This effect, not observed in the case of the planar derivatives, is the reason for their remarkable k_F values.

The ultrafast spectroscopic investigation in solution gave valuable information about the photoinduced intramolecular charge transfer taking place in the investigated PDI derivatives. Spectral signatures of the formation of the PDI radical anion upon laser irradiation were retrieved for all the three samples in their transient absorption spectra. The remarkable Two Photon Absorption cross sections measured for the investigated compounds (hundreds of GM) are in line with the charge transfer observed upon light excitation. Charge transfer takes place upon maintaining the excited state symmetry in the case of **1** and **2** through charge displacement from the central core to the lateral PDIs. This is also confirmed by calculations of the molecular orbitals for the excited state of **1** and **2**. A completely different charge transfer mechanism was evidenced

in the case of the planar isomer **3**, for which hints of the presence of the PDI radical cation were observed in the transient spectra. For this derivative, a more efficient charge transfer between the two lateral PDIs occurs upon breaking the excited state symmetry. This result is in agreement with the localized HOMO and LUMO distributions predicted for the excited state of **3** by the calculations. It is apparent that the different conformations of the two isomers drive a diverse mechanism for photoinduced charge transfer in their molecular structures. The significant dihedral angle formed between the central core and each of the lateral PDIs in isomer **2** interrupts conjugation and favors charge transfer between vicinal portions of the molecule: positive charge on the core, negative charge on both lateral PDIs. On the contrary, the perfectly planar excited state geometry of isomer **3** allows electronic communication and charge transfer to take place between the two lateral PDIs (positive charge on one PDI, negative charge on the other) with formation of a highly dipolar excited state.

These results give an explanation to the photovoltaic efficiency exhibited by the solar cell devices using the PDI derivatives as electron acceptors and the PTB7−Th as electron donor. A significant efficiency of ca. 5 % was shown by solar cells containing both isomers **2** and **3**. In our investigation we had no evidence for excimer formation in the case of the planar derivative or for increased charge recombination in the latter with respect to the twisted system. These were mentioned in a recent paper[27] to be responsible for the low photovoltaic response of planar PDI acceptors. Our AFM study revealed similar morphology of the blends between the donor polymer and the two PDI isomer acceptors. This result argues that the donor polymer breaks up the bigger intra−acceptor aggregates formed by the planar isomer and consequently generates smooth films at the micrometer scale as recently reported in the literature.[71] This may be advantageous for solar cell performances. However, smaller aggregates of the planar PDI acceptor in the blend with the

donor polymer may be present at the nanometer scale in line with what was observed by Trasmission Electron Microscopy measurements in a recent paper.[71] The GIWAXS measurements revealed preferential face−on orientation for the polymer and the acceptors in the blend films, enhanced face−on component was observed for blends with the twisted isomer **2**. Despite this, similar power conversion efficiencies were measured for the two isomers used as electron acceptors in the solar cell. These findings suggest that there is a factor, not related to the morphology of the donor/acceptor blend, leading to enhancement of the photovoltaic performance of the planar isomer **3**. We suggest that this factor is its ability to undergo photoinduced intra−molecular charge transfer. The photoinduced formation of a symmetry−broken, dipolar excited state in the planar isomer implies several outstanding advantages in the device performance.[72] This is a result of improved interaction with the donor polymer: lower driving force for charge separation with the donor, increased directionality ensuring that electrons and holes are placed toward the appropriate electrode, as well as slower recombination.

5.7 Conclusions

New perylene diimide (PDI) dimers were investigated in this study as non−fullerene electron acceptors for organic solar cells. Two positional isomers were synthetized, exhibiting analogous structures with a weakly electron deficient core connected through ring fusion to the lateral strongly electron accepting PDIs. The two isomers showed planar and twisted geometries which induced strikingly diverse spectral and photophysical properties. Both isomers show charge transfer following light excitation as the femtosecond time−resolved investigation revealed and the theoretical calculations confirmed. However, a structure dependent charge transfer mechanism was observed: the twist between the central core and each of the lateral PDIs favors charge transfer between these vicinal parts and formation of a symmetrical charge transfer species ($A^{\delta-}-wA^+-A^{\delta-}$

). In contrast to this, the planar structure allows communication between the two furthest lateral ends of the molecule and charge transfer between the PDIs with the photoinduced production of a highly dipolar transient species (A^+−wA−A^-). Thus, charge transfer was found to occur maintaining the excited state symmetry in the case of the twisted isomer and breaking the excited state symmetry in the case of the planar isomer. The likely interaction of these two photoexcited PDI based acceptors with the donor polymer (PTB7−Th) in the active layer of the photovoltaic device may be sketched as follows: $\mathbf{D|A^{\delta-}{-}wA^+{-}A^{\delta-} \rightarrow D^+|A^{\delta-}{-}wA{-}A^{\delta-}}$ (twisted acceptor) with respect to $\mathbf{D|A^+{-}wA{-}A^- \rightarrow D^+|A{-}wA{-}A^-}$ (planar acceptor). The symmetry breaking charge transfer occurring in the planar isomer is clearly an attractive strategy to achieve charge separation with the donor polymer with a lower driving force, enhanced directionality and retarded recombination rate. Remarkable efficiencies were indeed achieved in the organic photovoltaic devices employing the two PDI acceptors (ca. 5%). The planar conformation exhibits higher aggregation in the pure acceptor film, as often speculated in the literature, as well as in the blend. Despite higher aggregation of the planar isomer, similar power conversion efficiencies were measured for the two isomers. This is interesting because, according to literature reports, the PCE for a planar acceptor is expected to be one order of magnitude lower than for a twisted acceptor due to aggregation.[21] Our OPV results indicate that there is a factor, unrelated to the morphology of the donor-acceptor blend, which leads to enhancement of the photovoltaic performance of the planar acceptor. We suggest here that the dominance of intra−molecular charge transfer in the planar PDI isomer is the crucial factor in determining the improved power conversion efficiency in organic solar cells.

References

(1)   Lin, Y. Z.; Li, Y. F.; Zhan, X. W. Small molecule semiconductors for high−efficiency organic photovoltaics. *Chem. Soc. Rev.* **2012**, 41, 4245−4272.

(2)   Cheng, Y. J.; Hang, S. H.; Hsu, C. S. Synthesis of Conjugated Polymers for Organic Solar Cell Applications. *Chem. Rev.* **2009**, 109, 5868−5923.

(3)   Lu, L.; Zheng, T.; Wu, Q.; Schneider, A. M.; Zhao, D.; Yu, L. Recent Advances in Bulk Heterojunction Polymer Solar Cells. *Chem. Rev.* **2015**, 115, 12666−12731.

(4)   Zhao, W.; Li, S.; Yao, H.; Zhang, S.; Zhang, Y; Yang, B.; Hou, J. Molecular Optimization Enables over 13% Efficiency in Organic Solar Cells. *J. Am. Chem. Soc.* **2017**, 139, 7148−7151.

(5)   Li, S.; Ye, L.; Zhao, W. Yan, H., Yang, B.; Liu, D.; Li, W.; Ade, H.; Hou, J. A Wide Band Gap Polymer with a Deep Highest Occupied Molecular Orbital Level Enables 14.2% Efficiency in Polymer Solar Cells. *J. Am. Chem. Soc.* **DOI:** 10.1021/jacs.8b02695.

(6)   Carsten, B.; Szarko, J. M.; Son, H. J.; Wang, W.; Lu, L.; He, F.; Rolczynski, B. S.; Lou, S. J.; Chen, L. X.; Yu, L. Examining the effect of the dipole moment on charge separation in donor−acceptor polymers for organic photovoltaic applications. *J. Am. Chem. Soc.* **2011**, 133, 20468−20475.

(7)   Liang, Y.; Luping, Y. A New Class of Semiconducting Polymers for Bulk Heterojunction Solar Cells with Exceptionally High Performance. *Acc. Chem. Res.* **2010**, 43, 1227−1236.

(8)   Keller, B.; McLean, A.; Kim, B. G.; Chung, K.; Kim, J.; Goodson, T. III Ultrafast Spectroscopic Study of Donor−Acceptor Benzodithiophene Light Harvesting Organic Conjugated Polymers. *J. Phys. Chem. C* **2016**, 120, 9088−9096.

(9)   Guo, X. G.; Zhou, N. J.; Lou, S. J.; Smith, J.; Tice, D. B.; Hennek, J. W.; Ortiz, R. P.; Navarrete, J. T. L.; Li, S. Y.; Strzalka, J.; Chen, L. X.; Chang, R. P. H.; Facchetti, A.; Marks, T. J. Polymer solar cells with enhanced fill factors. *Nat. Photonics* **2013**, 7, 825−833.

(10)   Li, C. Z.; Chang, C. Y.; Zang, Y.; Ju, H. X.; Chueh, C. C.; Liang, P. W.; Cho, N.; Ginger, D. S.; Jen, A. K. Y. Suppressed Charge Recombination in Inverted Organic Photovoltaics via Enhanced Charge Extraction by Using a Conductive Fullerene Electron Transport Layer. *Adv. Mater.* **2014**, 26, 6262−6267.

(11)   Facchetti, A. Polymer donor–polymer acceptor (all−polymer) solar cells. *Mater. Today* **2013**, 16, 123−132.

(12)   Kwon, O. K.; Park, J. H.; Kim, D. W.; Park, S. K.; Park, S. Y. An All−Small−Molecule Organic Solar Cell with High Efficiency Nonfullerene Acceptor. *Adv. Mater.* **2015**, 27, 1951−1956.

(13) Holliday, S.; Ashraf, R. S.; Wadsworth, A.; Baran, D.; Yousaf, A. A.; Nielsen, C. B.; Tan, C.; Dimitrov, S. D.; Shang, Z.; Gasparini, N.; Alamoudi, M.; Laquai, F.; Brabec, C. J.; Salleo, A.; Durrant, J. R.; McCulloch, I. High Efficiency and air-stable P3HT-based polymer solar cells with a new non-fullerene acceptor. *Nat. Commun.* **2016**, 7:11585, 1−11.

(14) Hou, J.; Inganas, O.; Friend, R. H.; Gao, F. Organic Solar Cells Based on Non-Fullerene Acceptors. *Nat. Mater.* **2018**, 17, 119–128.

(15) Li, C.; Wonneberg, H. Perylene Imides for Organic Photovoltaics: Yesterday, Today and Tomorrow. *Adv. Mater.* **2012**, 24, 613−636.

(16) Kozma, E.; Catellani, M. Perylene Diimides Based Materials for Organic Solar Cells. *Dyes and Pigments.* **2013**, 98, 160−179.

(17) Huo, L.; Zhou, Y., Li, Y. Synthesis and Absorption Spectra of n−Type Conjugated Polymers Based on Perylene Diimide. Macromol. *Rapid Commun.* **2008**, 29, 1444−1448.

(18) Jung, I. H.; Lo, W. Y.; Jang, J.; Chen, W.; Zhao, D.; Landry, E. S.; Lu, L.; Talapin, D. V.; Yu, L. Synthesis and Search for Design Principles of New Electron Accepting Polymers for All−Polymer Solar Cells. *Chem. Mater.* **2014**, 26, 3450−3459.

(19) Adegoke, O. O.; Jung, I. H.; Orr, M.; Yu, L.; Goodson, T. III Effect of Acceptor Strength on Optical and Electronic Properties in Conjugated Polymers for Solar Applications. *J. Am. Chem. Soc.* **2015**, 137, 5759−5769.

(20) Li, M.; Wang, L; Liu, J.; Zhou, K.; Yu, X.; Xing, R.; Geng, Y., Han, Y. Cooperative Effects Of Solvent And Polymer Acceptor Co-Additives in P3HT:PDI Solar Cells: Simultaneous Optimization in Lateral and Vertical Phase Separation. *Phys. Chem. Chem. Phys.* **2014**, 16, 4528−4537.

(21) Rajaram, S.; Shivanna, R.; Kandappa, S. K.; Narayan, K. S. Nonplanar Perylene Diimides as Potential Alternatives to Fullerenes in Organic Solar Cells. *J. Phys. Chem. Lett.* **2012**, 3, 2405−2408.

(22) Zhang, X.; Lu, Z.; Ye, L.; Zhan, C.; Hou, J.; Zhang, S.; Jiang, B.; Zhao, Y; Huang, J.; Zhang, S.; Liu, Y.; Shi, Q.; Liu, Y.; Yao, J. A Potential Perylene Diimide Dimer Based Acceptor Material for Highly Efficient Solution Processed Non Fullerene Organic Solar Cells with 4.03% Efficiency. *Adv. Mater.* **2013**, 25, 5791−5797.

(23) Zhong, Y; Trinh, T.; Chen, R.; Wang, W.; Khlyabich, P. P.; Kumar, B.; Xu, Q.; Nam, C. Y.; Sfeir, M. Y.; Black, C.; Steigerwald, M. L.; Loo, Y. L.; Xiao, S.; Ng; F. Zhu, X. Y.; Nuckolls, C. Efficient Organic Solar Cells with Helical Perylene Diimide Electron Acceptors. *J. Am. Chem. Soc.* **2014**, 136, 15215−15221.

(24) Zhan, C.; Yao, J. More than Conformational "Twisting" or "Coplanarity": Molecular Strategies for Designing High−Efficiency Nonfullerene Organic Solar Cells. *Chem. Mater.* **2016**, 28, 1948−1964.

(25)   Lin, Y.; Wang, Y.; Wang, J.; Li, Y.; Zhu, D.; Zhan, X. A Star−Shaped Perylene Diimide Electron Acceptor for High Performance Organic Solar Cells. *Adv. Mater.* **2014**, 26, 5137−5142.

(26)   Lin, Y.; Wang, J.; Dai, S.; Li, Y.; Zhu, D.; Zhan, X. A Twisted Dimeric Perylene Diimides Electron Acceptor for Efficient Organic Solar Cells. *Adv. Energy Mater.* **2014**, 4, 1400420, 1−5.

(27)   Chen, W.; Yang, X.; Long, G.; Wan, X.; Chen, Y.; Zhang, Q. A Perylene Diimide Based Small Molecule with Tetrahedral Configuration as a Non−Fullerene Acceptor for Organic Solar Cells. *J. Mater. Chem. C* **2015**, 3, 4698−4705.

(28)   Hwang, Y.; Li, H.; Courtright, B. A.; Subramaniyan, S.; Jenekhe, S. A. Nonfullerene Polymer Solar Cells with 8.5 % Efficiency Enabled by a New Highly Twisted Electron Acceptor Dimer. *Adv. Mater.* **2016**, 28, 124−131.

(29)   Li, S.; Liu, W.; Li, C.; Liu, F.; Zhang, Y.; Shi, M.; Chen, H.; Russell, T. P. A Simple Perylene Diimide Derivative with a Highly Twisted Geometry as an Electron Acceptor for Efficient Organic Solar Cells. *J. Mater. Chem. A* **2016**, 4, 10659−10665.

(30)   Lin, H.; Chen, S.; Hu, H.; Zhang, L.; Ma, T.; Lin Lai, J. Y.; Li, Z.; Qin, A.; Huang, X.; Tang, B.; Yan, H. Reduced Intramolecular Twisting Improves the Performance of 3D Molecular Acceptors in Non−Fullerene Organic Solar Cells. *Adv. Mater.* **2016**, 28, 8546−8551.

(31)   Sun, H.; Song, X.; Xie, J.; Sun, P.; Gu, P.; Liu, C.; Chen, F.; Zhang, Q.; Chen, Z.; Huang, W. PDI Derivative through Fine−Tuning the Molecular Structure for Fullerene−Free Organic Solar Cells. *ACS Appl. Mater. Interfaces* **2017**, 9, 29924−29931.

(32)   Xiong, Y.; Wu, B.; Zheng, X.; Zhao, Z.; Deng P.; Lin, M.; Tang, B.; Ong, B.S. Novel Dimethylmethylene-Bridged Triphenylamine-PDI Acceptor for Bulk-Heterojunction Organic Solar Cells. *Adv Sci.* **2017**, 4 (10), 1−6.

(33)   Jiang, X.; Xu, Y.; Wang, X; Yang, X.; Zhang, A; Li, C.; Ma, W.; Li, W. Conjugated polymer acceptors based on fused perylene bisimides with a twisted backbone for non-fullerene solar cells. *Polym Chem.* **2017**, 8(21), 3300−3306.

(34)   Zhao, D.; Wu, Q.; Cai, Z.; Zheng, T.; Chen, W.; Lu, J.; Yu, L. Electron Acceptors Based on α−Substituted Perylene Diimide (PDI) for Organic Solar Cells. *Chem. Mater.* **2016**, 28, 1139−1146.

(35)   Wu, Q.; Zhao, D.; Schneider, A. M.; Chen, W.; Yu, L. Covalently Bound Clusters for Alpha−Substituted PDI−Rival Electron Acceptors to Fullerene for Organic Solar Cell s. *J. Am. Chem. Soc.* **2016**, 138, 7248−7251.

(36)   Duan, Y.; Xu, X.; Yan, H.; Wu, W.; Li, Z.; Peng, Q. Pronounced Effects of a Triazine Core on Photovoltaic Performance Efficient Organic Solar Cells Enabled by a PDI Trimer Based Small Molecular Acceptor. *Adv. Mater.* **2017**, 29, 1605115, 1−6.

(37)   Zhong, Y.; Kumar, B.; Oh, S.; Trinh, M. T.; Wu, Y.; Elbert, K.; Li, P.; Zhu, X.; Xiao, S.; Ng, F.; Steigerwald, M. L.; Nuckolls, C. Helical Ribbons for Molecular Electronics. *J. Am. Chem. Soc.* **2014**, 136, 8122−8130.

(38)   Wu, Q.; Zhao, D. Yang, J.; Sharapov, V.; Cai, Z.; Li, L.; Zhang, N.; Neshchadin, A.; Chen, W.; Yu, L. Propeller Shaped Acceptors for High Performance Non−Fullerene Solar Cells: Importance of the Rigidity of Molecular geometry. *Chem Mater.* **2017**, 29, 1127−1133.

(39)   Hartnett, P. E.; Matte, R. H. S. S.; Eastham, N. D.; Jackson, N. E.; Wu, Y.; Chen, L. X.; Ratner, M. A.; Chang, R. P. H.; Hersam, M. C.; Wasielewski, M. R.; Marks, T. J. Ring−Fusion as a Perylenediimide Dimer Design Concept for High−Performance Non−Fullerene Organic Photovoltaic Acceptors. *Chem. Sci.* **2016**, 7, 3543−3555.

(40)   Furgal, J. C.; Jung, J. H.; Goodson, T.; Laine, R. M. Analyzing Structure−Photophysical Property Relationships for Isolated T8, T10, and T12 Stilbenevinylsilsesquioxanes. *J. Am. Chem. Soc.* **2013**, 135, 12259−12269.

(41)   Maciejewski, A.; Steer, R. P. Spectral and Photophysical Properties of 9, 10−Diphenylanthracene in Perfluoro−n−Hexane: the Influence of Solute−Solvent Interactions. *J. Photochem.* **1986**, 35, 59−69.

(42)   Kubin, R. F.; Fletcher, A. N. Fluorescence Quantum Yields of Some Rhodamine Dyes. *J. Luminescence* **1982**, 27, 455−462.

(43)   Chai, J. D.; Head−Gordon, M. Long−Range Corrected Hybrid Density Functionals with Damped Atom−Atom Dispersion Corrections. *Phys. Chem. Chem. Phys.* **2008**, 10, 6615−6620.

(44)   Chai, J. D.; Head−Gordon, M. Systematic Optimization of Long Range Corrected Hybrid Density Functionals. *J. Chem. Phys.* **2008**, 128, 084106, 1−15.

(45)   Zheng, Z; Bredas, J. L.; Coropceanu, V. Description of the Charge Transfer States at the Pentacene/C_{60} Interface: Combining Range−Separated Hybrid Functionals with the Polarizable Continuum Model. *J. Phys. Chem. Lett.* **2016**, 7, 2616−2621.

(46)   Lange, A. W.; Herbert, J. M. A smooth, nonsingular, and faithful discretization scheme for polarizable continuum models: The switching/Gaussian approach. *J. Chem. Phys.* **2010**, 133, 244111, 1−18.

(47)   Lange, A. W.; Herbert, J. M. Symmetric versus asymmetric discretization of the integral equations in polarizable continuum solvation models. *Chem. Phys. Lett.* **2011**, 509, 77−87.

(48)   Shao, Y.; et al. Advances in Molecular Quantum Chemistry Contained in the Q−Chem 4 Program Package. *Mol. Phys.* **2015**, 113, 184−215.

(49)   Ramakrishna, G.; Bhaskar, A.; Goodson, T. Ultrafast Excited State Relaxation Dynamics of Branched Donor−π−Acceptor Chromophore: Evidence of a Charge−Delocalized State. *J. Phys. Chem. B* **2006**, 110, 20872−20878.

(50)   Varnavski, O.; Samuel, I. D. W.; Palsson, L. O.; Beavington, R.; ˚Burn, P. L.; Goodson, T. Investigations of Excitation Energy Transfer and Intramolecular Interactions in a Nitrogen Corded Distrylbenzene Dendrimer System. *J. Chem. Phys.* **2002**, 116, 8893−8903.

(51)   Xu, C.; Webb, W. W. Measurement of two−photon excitation cross sections of molecular fluorophores with data from 690 to 1050 nm. *J. Opt. Soc. Am. B* **1996**, 13, 481−491.

(52)   Lin, S.; Shiu, L.; Chien, K; Luh, T.; Lin, T. Fluorescence of Fullerene Derivatives at Room Temperature. *J. Phys. Chem.* **1995**, 99, 105−111.

(53)   Cai, Z.; Vazquez, R. J.; Zhao, D.; Li, L.; Lo, W.; Zhang, N. Wu, Q.; Keller, B.; Eshun, A.; Abeyasinghe, N.; Banaszaket−Holl, H.; Goodson III, T.; Yu, L. Two Photon Absorption Study of Low Bandgap, Fully Conjugated Perylene Diimide−Thienoacene−Perylene Diimide Ladder−Type Molecules. *Chem. Mater.* **2017**, 29, 6726–6732.

(54)   Spenst, P.; Wurthner, F. Photo− and redoxfunctional cyclophanes, macrocycles, and catenanes based on aromatic bisimides. *J. Photochem. Photobiol. C* **2017**, 31, 114–138.

(55)   Zheng, T.; Cai, Z.; Ho−Wu, R.; Yau, S. H.; Shaparov, V.; Goodson III, T.; Yu, L. Synthesis of Ladder Type Thienoacenes and Their Electronic and Optical Properties. *J. Am. Chem. Soc.* **2016**, 138, 868−875.

(56)   Strickler, S. J.; Berg, R. A. Relationship between Absorption Intensity and Fluorescence Lifetime of Molecules. *J. Chem. Phys.* **1962**, 37, 814−822.

(57)   Lim, E. C. Proximity effect in molecular photophysics: dynamical consequences of pseudo−Jahn−Teller interaction. *J. Phys. Chem.* **1986**, 90, 6770−6777.

(58)   Vazquez, R. J.; Kim, H.; Kobilka, B. M.; Hale, B. J.; Jeffries−EL, M.; Zimmerman, P.; Goodson, T. III Evaluating the Effect of Heteroatoms on the Photophysical Properties of Donor−Acceptor Conjugated Polymers Based on 2,6−Di(thiophen−2−yl)benzo[1,2−b:4,5−b']difuran:Two−Photon Cross−Section and Ultrafast Time Resolved Spectroscopy. *J. Phys. Chem. C* **2017**, 121, 14382−14392.

(59)   Gunes, S.; Neugebauer, H.; Sariciftci, N. S. Conjugated Polymer Based Organic Solar Cells. *Chem. Rev.* **2007**, 107, 1324−1338.

(60)   Brown, K. E.; Veldkamp, B. S.; Co, D. T.; Wasielewski, M. R. Vibrational Dynamics of a Perylene−Perylenediimide Donor−Acceptor Dyad Probed with Femtosecond Stimulated Raman Spectroscopy. *J. Phys. Chem. Lett.* **2012**, 3, 2362−2365.

(61)   Fron, E.; Pilot, R.; Schweitzer, G. Qu, J.; Herrman, A. Mullen, K.; Hofkens, J.; Van der Auweraer, M.; De Schryver, F. C. Photoinduced Electron Transfer in Perylenediimide Triphenylamine−Based Dendrimers: Single Photon Timing and Femtosecond Transient Absorption Spectroscopy. *Photochem. Photobiol. Sci.* **2008**, 7, 597−604.

(62)   Giaimo, J. M.; Gusev, A. V.; Wasielewski, M. R. Excited State Symmetry Breaking in Cofacial and Linear Dimers of a Green Perylenediimide Chlorophyll Analogue Leading to Ultrafast Charge Separation. *J. Am. Chem. Soc.* **2002**, 124, 8530−8531.

(63)   Van der Boom, T.; Hayes, R. T.; Zhao, Y.; Bushard, P. J.; Weiss, E. A.; Wasielewski, M. R. Charge Transport in Photofunctional Nanoparticles Self−Assembled from Zinc 5,10,15,20−Tetrakis(perylenediimide)porphyrin Building Blocks. *J. Am. Chem. Soc.* **2002**, 124, 9582−9590.

(64)   Lukas, A. S.; Zhao, Y.; Miller, S. E.; Wasielewski, M. R. Biomimetic Electron Transfer Using Low Energy Excited States: A Green Perylene Based Analogues of Chlorophyll a. *J. Phys. Chem. B* **2002**, 106, 1299−1306.

(65)   Sung, J.; Nowak Krol, A.; Schlosser, F.; Fimmel, B.; Kim, W.; Kim, D.; Wurthner, F. Direct Observation of Excimer Mediated Intramolecular Electron Transfer in a Cofacially Stacked Perylene Bisimide Pair. *J. Am. Chem. Soc.* **2016**, 138, 9029−9032.

(66)   Vagnini, M. T.; Smeigh, A. L.; Blakemore, J. D.; Eaton, S. W.; Schley, N. D.; D'Souza, F.; Crabtree, R. H.; Brudvig, G. W.; Co, D. T.; Wasielewski, M. R. Ultrafast Photodriven Intramolecular Electron Transfer from an Iridium Based Water Oxidation Catalyst to Perylene Diimide Derivatives. *PNAS* **2012**, 109, 15651−15656.

(67)   Berberich, M.; Krause, A. M.; Orlandi, M.; Scandola, F.; Wurthner, F. Toward Fluorescent Memories with Nondestructive Readout: Photoswitching of Fluorescence by Intramolecular Electron Transfer in a Diaryl Ethene Perylene Bisimide Photochromic System. *Angew. Chem.* **2008**, 120, 6718−6721.

(68)   Drobizhev, M.; Stepanenko, Y.; Dzenis, Y.; Karotki, A.; Rebane, A.; Taylor, P. N.; Anderson, H. L. Understanding Strong Two Photon Absorption in π−Conjugated Porphyrin Dimers via Double Resonance Enhancement in a Three Level Model. *J. Am. Chem. Soc.* **2004**, 126, 15352−15353.

(69)   Wilkinson, J. D.; Wicks, G.; Nowak Krol, A.; Lukasiewicz, L. G.; Wilson, C. J.; Drobizhev, M.; Rebane, A.; Gryko, D. T.; Anderson, H. L. Two Photon Absorption in Butadiyne Linked Porphyrin Dimers: Torsional and Substituent Effects. *J. Mater. Chem. C* **2014**, 2, 6802−6809.

(70)   Kasha, M.; Rawls, H. R.; Ashraf El−Bayoumi, M. The Exciton Model in Molecular Spectroscopy. *Pure Appl. Chem.* **1965**, 11, 371−392.

(71)   Hartnett, P. E.; Timalsina, A.; Ramakrishna Matte, H. S.; Zhou, N.; Guo, X.; Zhao, W.; Facchetti, A.; Chang, R. P. H.; Hersam, M. C.; Wasielewski, M. R.; Marks, T. J. Slip−Stacked Perylenediimides as an Alternative Strategy for High Efficiency Nonfullerene Acceptors in Organic Photovoltaics. *J. Am. Chem. Soc.* **2014**, 136, 16345−16356.

(72)   Carsten, B.; Szarko, J. M.; Son, H. J.; Wang, W.; Lu, L.; He, F.; Rolczynski, B. S.; Luo, S. J.; Chen, L. X.; Yu, L. Examining the Effect of the Dipole Moment on Charge Separation in Donor−Acceptor Polymers for Organic Photovoltaic Applications. *J. Am. Chem. Soc.* **2011**, 133, 20468−20475.

Chapter 6

Heteroatom and Side Chain Effects on the Optical and Photo-physical Properties: Ultrafast and Nonlinear Spectroscopy of New Naphtho[1,2-b:5,6-b′]difuran Donor Polymers

6.1 Original Publication Information

The work in this chapter was published in the *Journal of Physical Chemistry C* as:

"Heteroatom and Side Chain Effects on the Optical and Photo-physical Properties: Ultrafast and Nonlinear Spectroscopy of New Naphtho[1,2-b:5,6-b′]difuran Donor Polymers" Ifeanyi K. Madu, Evan W. Muller, Hyungjun Kim, Jessica Shaw, Alfred A. Burney-Allen, Paul M. Zimmerman, Malika Jeffries-EL, and Theodore Goodson III. *J. Phys. Chem. C*, 2018, 122, 30, 17049–17066

Synthesis of the polymers was done by the Jeffries-EL team at Boston University. Quantum chemical calculations were done by Hyungjun Kim in the Zimmerman group at the University of Michigan. Device fabrication and characterization was also done by the Jeffries-EL team. Modifications were made to the original publication to adapt it to the style of the content of this dissertation. References of the original manuscript are included in this chapter.

6.2 Abstract

The photophysical and electronic properties of four novel conjugated donor polymers were investigated to understand the influence of heteroatoms (based on the first two member chalcogens) in the polymer backbone. The sidechains were varied as well to evaluate the effect of polymer solubility on the photophysical properties. The donor-acceptor polymer structure is based on naptho [1,2-b:5,6-b′] difuran (NDF) as the donor moiety, and either 3,6-di (furan-2-yl) - 1,4 diketopyrrolo [3,4-c] pyrrole (F-DPP) or 3,6-di (thiophen-2-yl) - 1,4 diketopyrrolo [3,4-c] pyrrole (T-DPP) as the acceptor moiety. Steady state absorption studies showed that the polymers with furan moiety in the backbone displayed a favorable tendency of capturing more solar photons when used in a photovoltaic device. This is observed experimentally by the higher extinction coefficient in the visible and near-infrared region of these polymers relative to their thiophene counterparts. The excitonic lifetimes were monitored using ultrafast dynamics, and the results obtained show that the type of heteroatom π-linker used in the backbone affects the decay dynamics. Furthermore, the side chain also plays a role in determining the fluorescence decay time. Quantum chemical simulations were performed to describe the absorption energies and transition characters. Two-photon absorption cross-sections (TPA-δ) were analyzed with the simulations, illustrating the planarity of the backbone in relation to its torsional angles. Due to the planarity in the molecular backbone, the polymer with the furan π-linker showed a higher TPA-δ relative to its thiophene counterpart. This suggest that the furan compound will display higher charge transfer (CT) tendencies in comparison to their thiophene analogues. Pump-probe transient absorption technique was employed to probe the non-emissive states (including the CT state) of the polymers, and unique activities were captured at 500nm and 750nm for all the studied compounds. Single wavelength and global analyses were performed to understand the dynamics of each peak, and

deduce the number of components responsible for the transient behavior observed, respectively. The results obtained suggest that furan π-linker component of a donor and acceptor moiety in a conjugated polymer might be a more suitable candidate compared to its more popular chalcogenic counterpart – thiophene for use as donor materials in bulk heterojunction photovoltaic devices.

6.3 Introduction

Conjugated polymers (CPs) have been shown to be useful materials for efficient solar cell (photovoltaic) applications.[1,2,11–13,3–10] In recent years, there have been many efforts not only to provide important device parameters regarding the use of organic polymers but to also probe the many structure-function relationships in the entire organic photovoltaic system. As a result of the many lessons learned by the field of organic electronics regarding the optical and electronic properties of these materials there have been a few CPs that have stood out in terms of their efficiency. There have been several structure-function studies of organic devices in terms of the structure of the polymer and fundamental parameters of the working device such as the fill factor (FF), turn on voltage and mobility in addition to the power conversion efficiency (PCE) of the solar cell.[7,9,14–16] Other structure-function relationships look more inward and probe the molecular attributes of the polymers in order to provide insight in to the physical-chemical properties which ultimately dictate their device behavior.[17,18] While the early investigations of the molecular approach seemed to focus on discovering new molecular building blocks or polymer topologies, in more recent reports the effect of altering similar structures chemically but remaining with a basic structural framework has been investigated.

The PTB7[19–21] and PTB7-Th donor polymers have been widely studied and as a result there is detailed information regarding structure-function relationships within these polymers and efficiencies as high as >10% have been reported.[1,22] However, there remains some particular

questions regarding the mechanism (electronic, charge related, photon or energy transfer) of the photovoltaic effect in this system. Other derivatives of PTB7 have been created and the suitable functionality has enabled the critical structure-function analysis of the system both at the molecular level as well as in terms of the device properties.[2,3,7–9,12,17,23] For example, adding electronegative fluorine substituents to the backbone of the donor-conjugated polymer has become a popular and effective strategy for improving the PCE of polymer solar cells. Concurrently, there has been interest in probing the heteroatom effect on the PCE as well as electronic (molecular) properties of the system. One of the heteroatom effects investigated in recent years is the comparison between thiophenes and furans within the backbone of conjugated polymers. In review of the literature, it can be seen that the majority of conjugated polymers are based on thiophene derivatives relative to furan due to its relative instability in oxidative conditions[14,23,24]. However, furan's intrinsic chemical properties (reduced aromaticity, smaller size, increased electron richness) have motivated researchers to begin exploring its use in conjugated electronic materials. It is now well accepted that furan derivatives are very promising alternatives due to their smaller heteroatom size, more stable HOMO level, and larger dipole moment. It has also been reported that conjugated polymers with furan units show a higher degree of conjugation with reduced twisting between adjacent units, smaller π-stacking distance, and improved solubility.[7,12,14] Indeed, these are important structural parameters.

To date, there have been only a few detailed reports comparing the structure-function relationships of thiophene- and furan-based CPs using laser spectroscopic techniques.[21,25,26] In one report, the photophysical properties of four polymers based on benzo[1,2-b:4,5-b′]difuran (BDF) donor moiety and diketopyrrolopyrrole (DPP) acceptor moiety (flanked by either furan or thiophene spacers) was investigated.[26] It was found that while the absorption spectra of these

polymers generally look similar and span the 300-900nm region, the thiophene system has a slightly red-shifted shoulder peak. Additionally, the fluorescence lifetime decay profile shows that the furan-containing polymers have a longer fluorescence lifetime decay profile for the contribution from the donor in comparison to the thiophene systems, but there is no difference in the fluorescence lifetime decay profile of the acceptor. Furthermore, the two-photon absorption cross-section (a measure of charge transfer) of the furan polymers is an order of magnitude than the thiophene polymers, and it was also suggested that the π- π stacking properties of the furan polymers are much better than that formed for the thiophene polymers. It is known that the furan polymers have greater solubility relative to the thiophene polymers, but the solubility of these polymers is also affected by the sidechains. A comparison of the bulky (2-ethylhexyl) sidechains vs the linear (tetradecyl) sidechain, showed that the polymers with the 2-ethylhexyl sidechains have better solubility than the polymers with the linear tetradecyl carbons sidechains, and those with the 2-ethylhexyl side chain had a longer fluorescence lifetime decay profile in comparison with the linear tetradecyl carbon sidechain polymers analog. In addition to these conclusions, it was also found that π-π stacking properties of the linear tetradecyl sidechain polymers are much better than those for the 2-ethylhexyl sidechain polymers under the context of the heteroatom comparison of thiophenes vs furans. There have also been reports regarding the change in carrier mobility of conjugated polymer films when one considers the heteroatom effect of substituting a furan for a thiophene.[18,27] In these reports, X-ray diffraction measurements revealed that when a dithiophene core was replaced by a difuran, the molecular packing was largely maintained, while the resulting difference in charge transport was substantial; substituting dithiophene with difuran results in more than one order of magnitude increase in hole mobility with a loss in electron mobility. This was surprising as it suggested that a molecular structure-function relationship (not

a macroscopic or packing discussion) had a major impact on macroscopic properties of electron and hole mobility. Interestingly, electronic structure calculations found that the reorganization energies of dithiophene are noticeably higher than those of difuran due to the non-planarity of dithiophene. Molecular dynamic simulations have shown that the disordered hole mobility predictions are in good agreement with the experimental measurements, for which the thiophene to furan substitution results in an increase in hole mobility. These previous results mentioned above suggest a great deal of interest in the furan-thiophene approach for heteroatom affect as well as substitution, and that further detailed structure-function relationships are necessary in order to fully characterize these interesting systems.

In this paper we investigate the effect of conjugation length on the heteroatom effect in photovoltaic polymers with thiophene and furan units serving as a linker between naptho [1,2-b:5,6-b′] difuran (NDF) moiety and a diketopyrrolopyrrole (DPP) moiety. Two different side chains, ethylhexyl (EH) and dodecyl were also investigated. The novel synthesis and characterization of the four polymers is provided. Optical measurements of both steady state absorption and emission as well time-resolved fluorescence and absorption were carried to probe the variation in electronic and energy dynamics in these novel polymers. Electronic structure calculations as well as measurements of the efficiencies of cells done with these polymers are also provided in order to correlate with the optical measurements and to focus the discussion regarding conjugation, solubility, stability as well as charge transfer within the polymers investigated.

6.4 Experimental Section

6.4.1 Synthesis and Characterization

All reactions were carried out under ambient temperature (18-25°C) and pressure unless otherwise specified. Solvents for Pd-catalyzed reactions were deoxygenated prior to reaction by

bubbling Ar through the solvent for 30 minutes. 2-dodecanone was purchased from Alfa Aesar; trans-Bis(acetato)bis[o-(di-o-tolylphosphino)benzyl]dipalladium(II) was purchased from Strem Chemicals. All other chemicals were purchased from Sigma-Aldrich and were used without further purification unless otherwise specified. Bromododecan-2-one,[2] 3,6-bisfuryl-2,5-bis(2-ethylhexyl)pyrrolo[3,4-c]pyrrole-1,4(2H,5H)-dione[28], 3,6-bisfuryl-2,5-bis(dodecyl)pyrrolo[3,4-c]pyrrole-1,4(2H,5H)-dione,[29] 3,6-bisthienyl-2,5-bis(2-ethylhexyl)pyrrolo[3,4-c]pyrrole-1,4(2H,5H)-dione,[28] and 3,6-bisthienyl-2,5-bis(dodecyl)pyrrolo[3,4-c]pyrrole-1,4(2H,5H)-dione[29] were synthesized according to previously published procedures. Nuclear magnetic resonance (NMR) spectra were obtained in CDCl$_3$ and recorded at 400MHz (^{1}H) using an Agilent 400 MHz VNMRS. ^{1}H NMR were internally referenced to the residual protonated solvent peak, and the ^{13}C NMR were referenced to the central carbon peak of the solvent. In all spectra, chemical shifts are given in δ relative to the solvent. Gel permeation chromatography (GPC) measurements were performed on a Shimadzu LC-20A system with a UV-Vis detector. Analyses were conducted at 35°C using chloroform as the eluent at a flow rate of 1.0 mL/min. Calibration was based on polystyrene standards.

General procedure for the synthesis of copolymers. To a 15mL round bottomed flask was added naphthodifuran –**1** (1.0 equiv.), diketopyrrolopyrrole **2** (1.0 equiv.) and dry, deoxygenated N,N-dimethylacetamide (DMAC, 3 mL). The reaction vessel was allowed to build an atmosphere of Ar, after which pivalic acid (1.0 equiv), Tri-tert-butylphosphonium tetrafluoroborate (0.1 equiv.), cesium carbonate (2.5 equiv.), and Herrmann-Beller catalyst (0.05 equiv.) were added in one portion and the reaction was heated to 160°C for 3-4 days. The reaction mixture was cooled to ambient temperature and precipitated into cold methanol followed by filtration through a cellulose thimble. The polymers were purified via Soxhlet extraction by rinsing with acetone, hexanes, and

chloroform. The final product was obtained by removal of solvent from the chloroform fraction and drying under vacuum.

Synthesis of NDF-F-C₁₂DPP (P1). Following the general polymerization conditions using 2,7 dibromo 1,6 didecylnaphtho [1,2 b:5,6 b′] difuran (171 mg, 0.25 mmol) and F-C₁₂DPP (154 mg, 0.25 mmol) using a reaction time of 3 days yielded a dark blue-black solid (97 mg, 63%).^{1}H NMR; CDCl₃ 0.87 (12H, b), 1.25 (72H, b), 3.02 (4H, b), 7.75 (4H, b), 8.20 (4H, b) GPC (CHCl₃, 35°C): M_n = 38.4 kDa. M_w = 45.7 kDa. PDI = 1.19.

Synthesis of NDF-F-EHDPP (P2). Following the general polymerization conditions using 2,7 dibromo 1,6 didecylnaphtho [1,2 b:5,6 b′] difuran (269 mg, 0.41 mmol) and F-EHDPP (196 mg, 0.40 mmol) using a reaction time of 3 days yielded a dark blue-black solid (172 mg, 59%). ^{1}H NMR; CDCl₃ 0.87 (18H, b), 1.25 (50H, b), 2.75 (4H, b), 4.08 (4H, b) 6.82 (2H, b) 7.71 (2H, b), 8.14 (2H, b), 8.61 (2H, b) GPC (CHCl₃, 35°C): M_n = 38.6 kDa. M_w = 47.9 kDa. PDI = 1.23.

Synthesis of NDF-T-C₁₂DPP (P3). Following the general polymerization conditions using 2,7 dibromo 1,6 didecylnaphtho [1,2 b:5,6 b′] difuran (171 mg, 0.26 mmol) and T- C₁₂DPP (145 mg, 0.26 mmol) using a reaction time of 3 days yielded a dark blue-black solid (114mg, 68%). ^{1}H NMR; CDCl₃ 0.87 (12H, b), 1.25 (68H, b), 3.02 (4H, b), 4.00 (4H, b),7.32 – 7.71 (4H, b), 7.85 (2H, b), 9.01 – 9.21 (4H, b) GPC (CHCl₃, 35°C): M_n = 39.7 kDa. M_w = 52.4 kDa. PDI = 1.32.

Synthesis of NDF-T-EHDPP (P4). Following the general polymerization conditions using 2,7 dibromo 1,6 didecylnaphtho [1,2 b:5,6 b′] difuran (160 mg, 0.24 mmol) and T-EHDPP (130 mg, 0.26 mmol) using a reaction time of 3 days yielded a dark blue-black solid (102 mg, 65%). ^{1}H NMR; CDCl₃ 0.87 (18H, b), 1.25 (50H, b), 2.80 (4H, b), 4.04 (4H, b), 7.39 – 8.28 (8H, b) GPC (CHCl₃, 35°C): M_n = 44.6 kDa. M_w = 57.7 kDa. PDI = 1.29.

6.4.2 Electrochemistry

Cyclic voltammetry was performed using a potentiostat with a scanning rate of 100 mV/s. The polymer solutions were drop-cast on a glassy carbon electrode from chloroform and Ag/Ag$^+$ was used as the reference electrode. The reported values are referenced to Fc/Fc$^+$ (-5.1 vs vacuum). All electrochemistry experiments were performed in degassed CH$_3$CN under an Ar atmosphere using 0.1 M tetrabutylammonium hexafluorophosphate as the electrolyte.

6.4.3 Steady-state Measurements

The absorption spectra were obtained using an Agilent 8432 UV-Visible absorption spectrophotometer at room temperature. The device was referenced with a spectrophotometric-grade chloroform (CHCl$_3$), and 1cm quartz cuvettes were used with a concentration range between 3.08E-7 M and 3.26E-6 M for the samples. The molar absorptivity was obtained by varying the concentrations of a sample and noting the absorbance at each concentration, after which a linear plot is obtained whose slope is the product of the cuvette length and the molar extinction coefficient according to Beer and Lambert's law. The emission spectra for all four polymers were obtained using a Horiba Fluoromax-2 spectrofluorometer with slits set at 3.5 nm, also operated at room temperature with the help of a chiller. Spectra correction owing to the decrease in the PMT's quantum efficiency in the 630 – 900 nm region wasn't accounted for; however the same spectra is expected, only slightly higher in intensity around that region. The fluorescence quantum yield (Φ_F) of the samples was determined by a comparison method[30–32] using two standards – zinc phthalocyanine (ZnPc) in pyridine and CCl$_4$ ($\Phi_F = 0.3$), and rhodamine-b in ethanol ($\Phi_F = 0.7$) - cross-referenced with each other, and using 400nm excitation wavelength. The Φ_F calculation was performed using the second band of the fluorescence spectra, which overlapped with the ZnPc standard emission spectra. In the determination of the Φ_F, owing to the fast rate of photo-

degradation of the samples, the absorption spectra were taken right before and after the fluorescence measurements.

6.4.4 Two-Photon Excited Fluorescence (TPEF) Measurements

In order to determine the two-photon absorption cross-section (TPA-δ), the two-photon excited fluorescence (TPEF) method as reported in the literature[33,34] was performed in this study. Here, the two-photon excited fluorescence excitation spectra of the samples were compared to that of a reference compound, zinc phthalocyanine dissolved in pyridine and CCl_4, under identical conditions, whose TPA-δ is well known and have been reported in the literature[35]. To confirm the experimental accuracy of this approach, another set of experiments were performed using a different reference compound – rhodamine b dissolved in methanol. Two different pulsed-laser excitation wavelengths: ~820 nm and ~1200 nm was used for this experiment. The ~820 nm excitation beam was obtained using a Kapteyn-Murnane (KM) Lab. Inc. mode-locked Ti:sapphire laser pumped by a Millennia diode laser delivering a pulse width of ~100 fs at a repetition rate of 90 MHz, while the 1200 nm excitation beam was obtained using a Spectra Physics Mai-Tai diode-pumped mode-locked laser delivering ~100 fs pulses at a repetition rate of 80 MHz to a 1.1 – 1.4 μm spec. OPAL optical parametric oscillator (OPO). Beam power from the laser was varied using a neutral density filter and focused unto the sample cell (1 cm path, quartz cuvette) using a lens of 11.5 cm focal length and the resultant fluorescence was collected perpendicular to the excitation beam. Another lens (plano-convex) with focal length of 2.54 cm was used to direct the fluorescence into a monochromator whose output was coupled to a photomultiplier tube. During each scan, the monochromator was set to the maximum emission wavelength of the sample (where max. photons are generated), and the photons are converted into counts by a photon-counting unit.

A logarithmic plot of the fluorescence signal versus the incident power intensity was performed to confirm if the signal to power intensity relationship is indeed quadratic.

6.4.5 Time-Resolved Fluorescence Measurements

To perform time-resolved fluorescence measurements, the ultrafast fluorescence upconversion (UPC) setup was used. The femtosecond UPC spectroscopy technique and setup have been described previously and in good detail.[25,26,36–38] 80 fs pulses at 800 nm wavelength with a repetition rate of 82 MHz generated by a mode-locked Ti:Sapphire laser was made to pass a non-linear β-barium borate crystal. 400 nm excitation pulse was generated, and the residual 800 nm beam was made to pass through a computer controlled motorized optical delay line. The polarization of the excitation beam was controlled by a Berek compensator. The power of the excitation beam varied between 33 to 36 mW. The fluorescence emitted by the sample is collected, and then up-converted by a nonlinear crystal of β-barium borate by using the residual 800 nm beam, which had been delayed by the optical delay line with a gate step of 6.25 fs. By this procedure, the measurement of the fluorescence is enabled and can be measured temporally. The monochromator is used to select the wavelength of the up-converted beam of interest, and the selected beam is detected by a photomultiplier tube. Coumarin 30 dye was used for calibrating the laser at different collection wavelengths. The instrument response function (IRF) has been determined from the Raman scattering of water to have a width of 110 fs. Lifetimes of fluorescence decay were obtained by fitting the fluorescence decay profile to the most accurate fit.

6.4.6 Time-Resolved Absorption Spectroscopic Measurements

In order to investigate the evolution of non-emissive states and dark states of the OPV polymers after the emissive states have been studied, time-resolved absorption measurements were

performed. A known procedure for this setup has been described in the literature.[39–41] Low power, high repetition rate, seed pulses were generated from a Millenia Pro diode – pumped Spectra Physics Tsunami Ti:sapphire oscillator. The seed pulses were fed to an Nd:YLF (Empower) – pumped Spectra Physics Spitfire® Ti:sapphire regenerative amplifier which generated high power (1 mJ), low repetition rate (1kHz), 800 nm pulses with pulse width of ~100 fs i.e. 10 nm band width for a Gaussian pulse. A beam splitter was used to split the beam to a pump beam (85%) and probe beam (15%). The excitation beam (~400 nm) was generated from the pump beam by an optical parametric amplifier (OPA-800C). The probe beam was sent through a computer-controlled optical delay line and then focused into a 2 mm sapphire plate to generate a white continuum. The white light (smaller diameter) is then overlapped with the excitation/pump beam in a 2 mm quartz cuvette containing the sample that is constantly stirred by a rotating magnetic stirrer to minimize sample degradation. The polarization of the pump beam is set at the magic angle (54.7º) with respect to the polarization of the probe. The change in absorbance i.e. the difference between the excited sample and the sample in ground state is collected by an Ocean Optics charge-coupled device (CCD) detector connected to a computer, and data acquisition and analysis is done using a software from Ultrafast Systems Inc.

6.4.7 Quantum Chemical Calculations

Theoretical investigations were conducted to explain the experimental absorption spectra and describe the ground state geometries. The photophysical properties of polymers should not be based on a single repeat unit, due to the significant coupling between repeating units.[42] Therefore, the minimum geometry that can include the coupling – a dimer – was chosen as a model for the photophysical properties of the polymers. The model structures include methyl groups which replace the decyl chains ($C_{10}H_{21}$) and serve as end groups at the dimer termini. In addition, the side

chains attached to the nitrogen atoms in the DPP acceptor moieties (dodecyl and hexylethyl groups) were truncated to propyl and isopropyl groups, respectively. These structural alternations only weakly affect the absorption properties since the low-lying electronic transitions are known to occur within the π backbone. The ground state geometries of each dimer were optimized with density functional theory (DFT), using the ωB97X-D functional and 6-31G* basis sets.[43,44] Single point time-dependent DFT (TD-DFT) calculations were performed to obtain the absorption energy. A system-dependent, non-empirically tuned ωB97X-D which is known to significantly improve the charge delocalization problems in conventional DFT functionals[45] was employed, and the same basis set was applied. The tuned ω value was chosen to minimize the square sum of the difference between HOMO energy and ionization potential (IP), and LUMO energy and electron affinity (EA), $(\epsilon_{HOMO}+IP)^2+(\epsilon_{LUMO}+EA)^2$ of the dimer model. The range-split parameter ω is heavily affected by the environment, and the inclusion of solvent dielectric field induced a reduction in ω value.[46] This process yielded the optimal ω value to be 0.004 for all the studied compounds, where chloroform (dielectric constant is 4.31) was used as the dielectric through a polarizable continuum model.[47,48] Characters of excitations were described with natural transition orbitals (NTOs).[49,50] All simulations were carried out using Q-Chem 4.0.[51]

6.4.8 Device Performance

All experiments were performed at the UMass Centre for Electronic Materials and Devices (Amherst, MA) under inert conditions, unless otherwise stated. Photovoltaic devices were fabricated with a conventional architecture (ITO/PEDOT:PSS/Polymer:PC$_{71}$BM/Ca/Al). ITO-coated glass substrates were cleaned by sonication in detergent (Mucasol^{TM}), deionized water, acetone, and isopropanol, followed by UV-ozone treatment for 15 min. PEDOT:PSS layers (Clevios^{TM} P VP Al 4083) were spin-coated (3500 rpm, for 2 min), and annealed at 150°C for 30

min in air. Polymer:PC$_{71}$BM active layer solutions were prepared in a blend ratio of 1:1 (15 mg/mL

P1-P3, 20 mg/mL P4) from either CF, or *o*-DCB with varying amounts of DIO additive (0 to 4 vol

%), and stirred at 55 °C (CF) or 80 °C (*o*-DCB) for 48 h prior to spin-coating (2000 rpm, for 2

min). Films were annealed at 70 °C for 10 min and placed under vacuum (10^{-7} mbar) for a

minimum of 3 h to remove DIO. Finally, Ca (15 nm) and Al (100 nm) electrodes were deposited

under vacuum (10^{-6} mbar) by thermal evaporation through a shadow mask, to give a device area

of 0.06 cm^2. Current density-voltage (*J-V*) characteristics were measured using a Keithley 2400

source-meter, and simulated AM1.5G illumination (100 mW/cm^2, Newport 91160), calibrated

against a KG5-filtered Si reference cell.

6.5 Results

6.5.1 Synthesis and Characterization

The synthesis for the polymers is shown in **Scheme 6.1**. The composition of the conjugated

monomers was varied to evaluate the impact of heteroatom substitution on the photophysical

properties of the resulting polymers. The length of the side chain on each of the co-monomers was

also varied to improve the solubility and processabillity of the polymers. All of the polymer has

good solubility in organic solvents such as chloroform and THF allowing for characterization using

gel permeation chromatography. The details are summarized in **Table 6.2**.
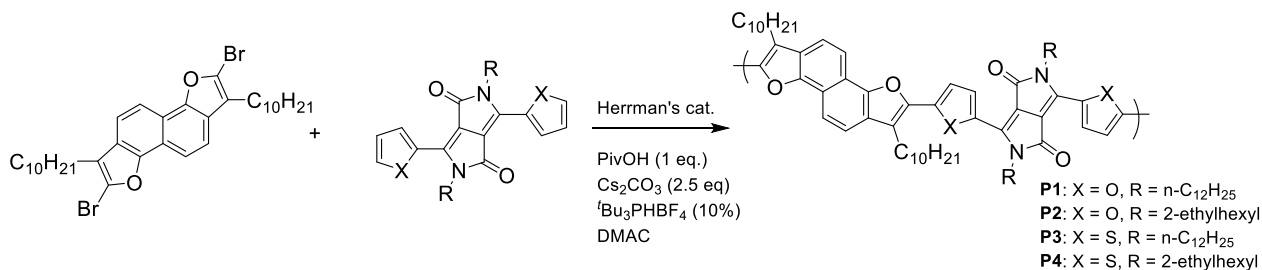
Scheme 6.1 Synthesis of copolymers **P1** – **P4**
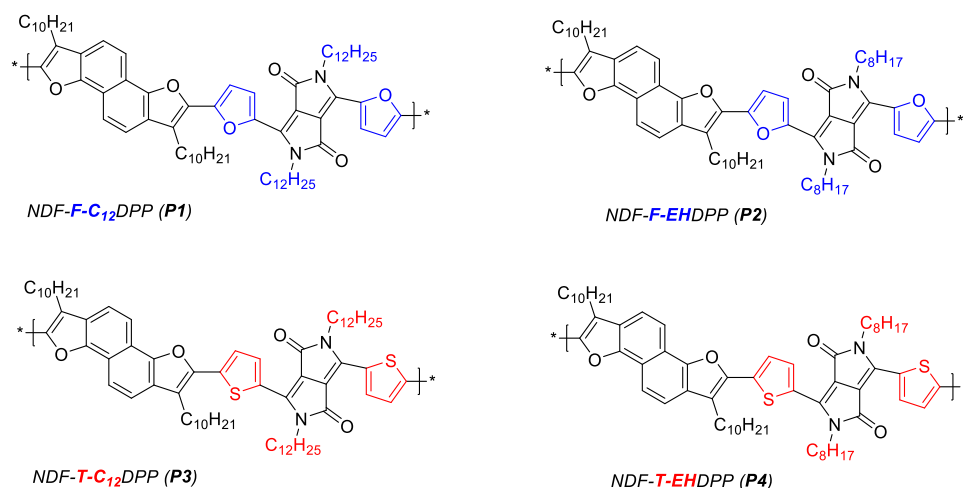
Figure 6.1 Structures of the repeat unit of the investigated polymers.
A common donor moiety naphthodifuran (NDF) is present in all polymers, a furan or thiophene linker serving as a π-bridge between the donor moiety and the acceptor moiety – diketopyrrolopyrrole (DPP). Solubilizing sidechains: 2-ethyl hexyl or dodecyl are attached to the DPP moiety.

6.5.2 Quantum Chemical Calculations

The optimized ground state geometries for **P1-P4** are displayed in **Figure 6.2**. The four structures are nearly planar, with small distortions from planarity occurring at the seven rotatable single bonds (three within each monomer and one between monomers). Previous works have observed the relationship between the molecular planarity and the two-photon absorption cross-section.[26,52]
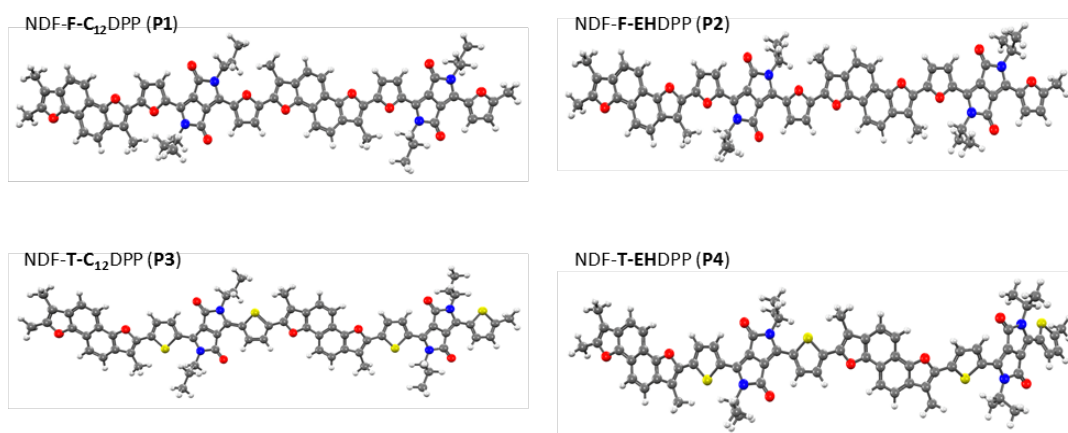
Figure 6.2 Optimized ground state geometries of NDF-**F-C₁₂**DPP (**P1**), NDF-**F-EH**DPP (**P2**), NDF-**T-C₁₂**DPP (**P3**), and NDF-**T-EH**DPP (**P4**).

Color scheme: carbon atom, gray; hydrogen atom, white; oxygen atom, red; nitrogen atom, blue; sulfur atom, yellow.

The planarity was quantified using the following seven dihedral angles (see **Figure 6.8** for graphical description of these dihedral angles and their averages): The angle between the donor NDF unit and the linker (φ_{OCCX}, pink and orange in **Figure 6.3**), between the linker and the acceptor unit (φ_{XCCN}, blue and cyan in **Figure 6.3**), between the acceptor unit and the linker (φ_{NCCX}, green and light green in **Figure 6.3**), and between monomers (φ_{XCCO}, red in **Figure 6.3**); where X is O or S for the compound containing a furan or thiophene linker, respectively. The numerical values for these dihedral angles are tabulated in **Table 6.1** below.
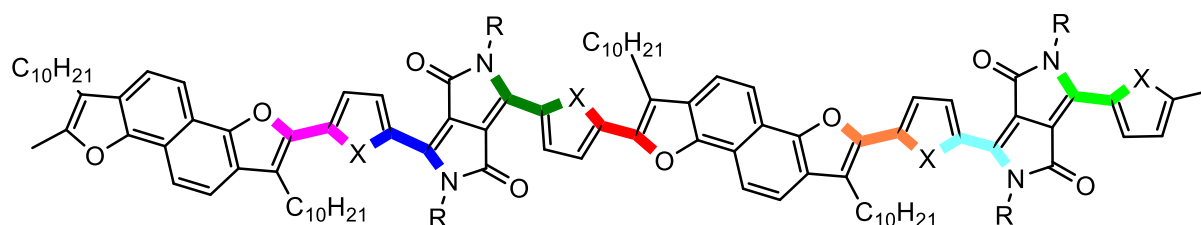
Figure 6.3 Dimer structure used for theoretical simulation showing the seven selected dihedral angles to measure the molecular planarity.
Color scheme for 1st/2nd monomer: pink/orange - $\boldsymbol{\varphi_{OCCX}}$; blue/cyan - $\boldsymbol{\varphi_{XCCN}}$; dark green/light green - $\boldsymbol{\varphi_{NCCX}}$; and connector red - $\boldsymbol{\varphi_{XCCO}}$.

Table 6.1 Monomer-average values of the dihedral angles across the selected three single bonds in the dimer model structures, and the dihedral angle at the junction between monomers.

Polymers	φ_{OCCX}[a]	φ_{XCCN}[a]	φ_{NCCX}[a]	φ_{XCCO}
F-C$_{12}$ (**P1**)	0.3	2.2	2.8	0.8
F-EH (**P2**)	6.1	5.1	6.9	6.4
T-C$_{12}$ (**P3**)	10.2	2.6	4.3	8.6
T-EH (**P4**)	6.4	19.9	25.0	15.0

[a] denotes the average value of two monomers of the dimer model

As expected, the thiophene linkers (T-C$_{12}$ and T-EH) produce more distortion from planarity compared to the furan linkers (F-C$_{12}$ and F-EH) due to the steric hindrance of the larger sulfur atom of the thiophene with the adjacent methyl and carbonyl groups. For the linear (dodecyl) side chain polymers, the furan-linker compound achieves an almost perfectly planar conformation

(φ_{OCCX} is 0.3°), while the thiophene linker compound shows a relatively larger distortion in the backbone, yielding torsional angle (φ_{OCCX}) of 10.2°. For the other two dihedral angles in a single monomer unit, φ_{XCCN} and φ_{NCCX}, the side chain sterics also produce a clear effect on the polymer structure. The bulky, branched alkyl chains of EH significantly interact with their neighboring linkers, resulting in larger deviation from planarity compared to those with the linear chains (n-$C_{12}H_{25}$). In addition, the dihedral angle at the junction between two monomers (φ_{XCCO}) reflects the bulky side chain effect as well as the heteroatom size effect, with molecule T-EH having the largest dihedral angle. The effects of planarity and deviations from planarity on the two-photon absorption cross-section will be discussed later on (Section 6.5.6).

Figure 6.4 shows the electron-hole orbitals for the excited states of **P1-P4** at the ground state geometries, based on NTO analysis (see computational details). In all cases, these orbitals represent >95% of the first excited state transition, and therefore provide the dominant excitonic character for each compound. In all cases, the hole orbitals are delocalized over all repeating units, and electron orbitals show more localization at acceptor unit, DPP. All repeat units feature charge transfer character from the NDF donor unit to the DPP acceptor unit with some contribution from local π-π^* transition in the main chain. This indicates that there exists some form of photo-induced electron transfer from the conjugated backbone to the DPP unit when the polymers are photo-excited.
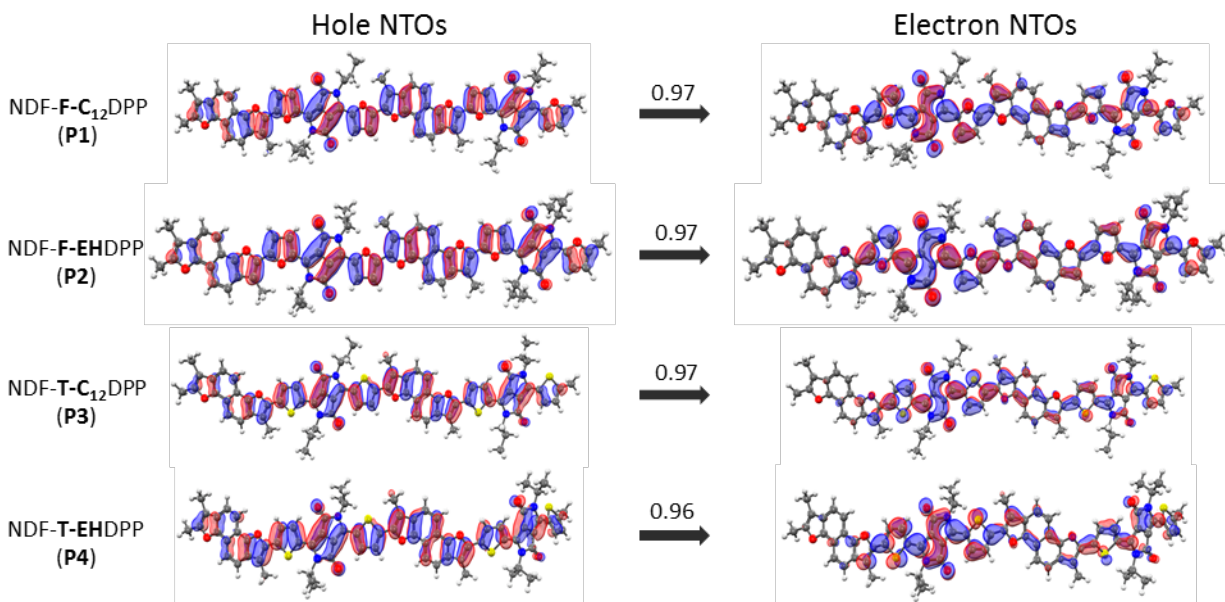
Figure 6.4 Natural transition orbitals of NDF-**F-C$_{12}$**DPP (**P1**), NDF-**F-EH**DPP (**P2**), NDF-**T-C$_{12}$**DPP (**P3**), and NDF-**T-EH**DPP (**P4**) for the S$_1$ vertical exciton at the ground state geometries. *The contribution of each transition is given above the arrow. (Isovalue = 0.05).*

6.5.3 Steady-state Measurements: UV-Vis Absorption

The UV-Vis (steady-state absorption) spectra for the donor-acceptor polymers in dilute chloroform (CHCl$_3$) solution are shown in **Figure 6.5**. The steady-state properties are summarized in **Table 6.2**. All four polymers showed interesting absorption spectra suitable for organic photovoltaics applications. Both kinds of polymers (with either furan or thiophene units) exhibited peaks in the visible region. All four polymers share a common absorption band peak in the UV region between ~346 – 353 nm; this is a clear indication of the common donor moiety (NDF). The band from 320 nm to 450 nm belongs to the π-π* transition of the main chain components, and the lower energy absorption band is attributed to the intramolecular charge transfer between the donor and the acceptor of the polymer backbone[9,12,53] as will be discussed in this study by time-resolved absorption measurement. By comparing the furan-backbone polymer F-EH and the thiophene-backbone polymer T-EH (both have the same solubilizing unit, ethylhexyl), F-EH shows a broader and red-shifted absorption band. A similar trend, to a lesser degree, is observed in comparing F-

C_{12} and $T-C_{12}$. This is due to the less steric, smaller-sized, highly electronegative oxygen atom[9;54] of the furan relative to the sulfur atom of thiophene. One would conclude that the furan-backbone polymer adopts a more planar geometry [as confirmed by the optimized ground state geometry calculations performed]. Measurements of the linear absorption were also carried out in the solid state, by making thin films of the amorphous conjugated polymers. For the polymers with a thiophene-backbone, the solid-state spectra and the chloroform-solution-based spectra were similar in both spectral width and λ_{max}. However, for the furan containing conjugated polymers there was a broader and slightly red-shifted (~10 nm) spectra obtained. This redshift is indicative of more aggregation (or molecular backbone packing) and possibly stronger intramolecular interaction.

Shown in **Figure 6.5a** *inset* is the molar absorptivity per monomer **(ε_{monmr})** done using sample concentration in the range 3E-7 to 3E-6 M. The highest absorptivity per monomer with respect to the individual solubilizing unit is ascribed to the furan-backbone polymers, and this is in accordance with previous studies.[26,28] For the thiophene-backbone polymers, low absorptivity in the visible and near-IR region may be attributed to the poor intramolecular charge transfer between the donor NDF and the acceptor DPP through the thiophene π-linker. This is clearly observed in the case of T-EH where the bulky side chains further prevent adequate π-stacking for charge transfer. In a previous study of similar D-A functional system by Vazquez et al[26] and Kobilka et al[28], the presence of two extra thiophene units with the BDF and DPP moieties induced a higher degree of bathochrochromic shift (~60 nm) in comparison to these polymers with only an additional benzene (i.e. NDF unit). This illustrates that effective conjugation length can be increased by the inclusion of an electron donor moiety like thiophene and at the same time achieving higher electron density, in contrast to the addition of just benzene to enhance conjugation

length. Similar molar extinction coefficient per monomer was obtained ($\sim10^4$ $M^{-1}cm^{-1}$) in both systems with the furan- displaying higher absorptivity in comparison to the thiophene-backbone polymers in both studies. The higher energy band displayed smaller absorptivity values compared to the lower energy band, but this wasn't the case in this study. This could be tied to poor coupling between the NDF and DPP units hence lower probability for effective charge transfer.
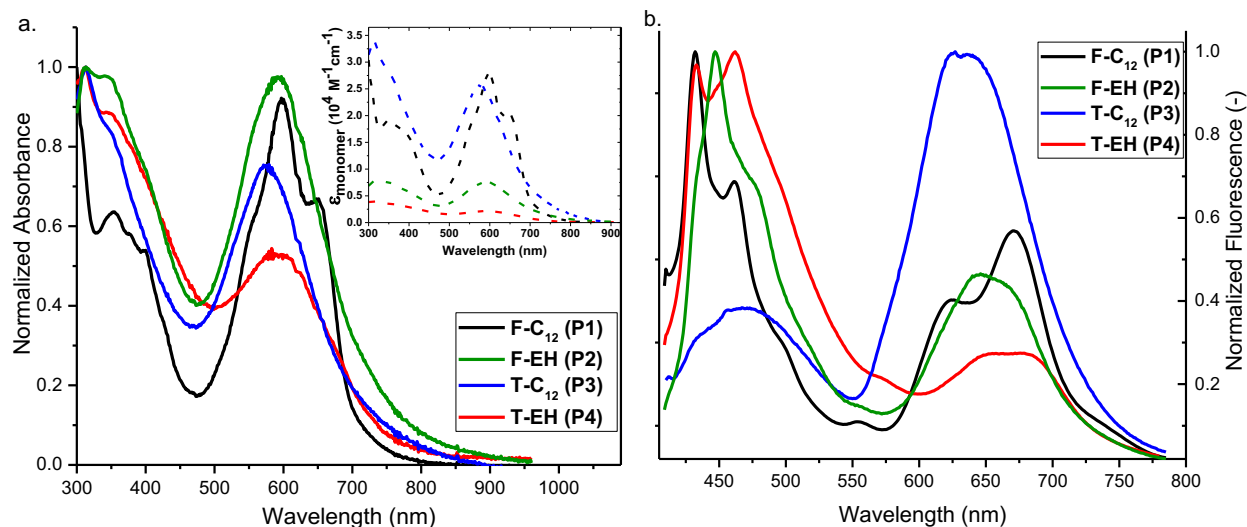
Figure 6.5 Steady state spectra of the polymer molecules in dil. $CHCl_3$ solution at 295K. (a) Absorption, inset is Molar Extinction Coefficient of one monomer unit (b) Normalized Emission spectra excited at 400 nm.

6.5.4 Steady-state Measurement: Fluorescence Emission

The emission spectrum for the four investigated polymers is shown in **Figure 6.5**. These measurements were also carried out in chloroform solutions. The spectra show two core peaks in each polymer obtained after exciting at three different wavelengths: 350, 380, and 400 nm. Each polymer exhibited emission at ~460 nm and ~640 nm when excited at 400 nm. However, one notices that for the case of F-C$_{12}$ there is considerably more structure in the emission spectra with a shoulder in the band in the 620 nm region. This shoulder peak is not resolved in the spectra for the other polymers under similar experimental conditions. Exciting at ~550 nm however yielded only the second emission peak, clearly indicating that only the DPP part of the molecule was

excited, therefore the second emission peak can be allotted to the acceptor part of the molecule. The first emission peak for all polymers can be attributed to the common donor – NDF as all possess strongly emitting 350-500 nm band.[55,56] **Table 6.2** contains all the emissive peaks as observed in the spectra. Stokes shift (E_{stokes}) was lower in the furan-backbone polymers. Owing to weak coupling of the NDF and DPP moieties, the emission primarily stems from both components of the molecule. The fluorescence quantum yield (Φ_F) of the polymers is given in **Table 6.2**. A high Φ_F of 73% was obtained for F-C$_{12}$. A significantly smaller quantum yield was obtained for T-C$_{12}$ for the same side chain group but with different core group. This was surprising that the furan with alky side chains would be more than an order magnitude different in quantum yield. As mentioned previously, one of the attractive characteristics of the furan containing polymers is their relatively good solubility. Also, as discussed previously from molecular weight data, the molecular weight from soluble conjugated polymers was relatively high for the furan containing polymers in comparison to the thiophene systems. Generally, the less soluble higher molecular weight fractions when synthesized have difficulty in obtaining accurate quantum yield results. We do not expect that to be the case here where the polymers solubility and molecular weights were verified. This leaves a considerable effect of the side chain on the actual fluorescence quantum yield of the conjugated polymers studied in this investigation.

Comparing the fluorescence spectra for similar structures like those in this study as obtained by Vazquez et al,[26] only one intense spectra peak is observed for all four BDFTh-X-DPP polymers regardless of the excitation wavelength. The emission spectra they obtained was also independent of the side chain, and the peak emission of the polymer with thiophene-backbone was slightly red-shifted. The Φ_F was greatest in the furan-linked polymer in comparison to the thiophene for the two side chains considered, however the highest PCE was still obtained by the

furan-linked compounds. In this study however, excluding F-C_{12}, polymers with thiophene backbone displayed higher Φ_F. This goes to say that as much as exciton relaxation by fluorescence (high Φ_F) opposes non-radiative relaxation processes in organic photovoltaic compounds, those other non-radiative members such as charge transfer, internal conversion, and conformational changes, need to be quantified to ascertain their contribution to the overall efficiency.

Table 6.2 Summary of the Steady State Optical properties, and Two Photon Absorption cross-section (TPA-δ) of all four polymers at ambient temperature.

Polym.	M_w (kDa)	DP_n	λ_{abs} (nm) soln [a]	λ_{abs} (nm) film	ε_{monmr} ($M^{-1}cm^{-1}$)	λ_{em} (nm) [a]	E_{stokes} (cm^{-1})	Φ_F (-)	δ (GM)
F-C_{12}	45.7	41	600, 651*	608, 670*	27937	461, 624, 675*	641	0.734	25.33
F-EH	47.9	37	600	610	7585	463, 643	1114	0.042	6.30
T-C_{12}	52.4	38	576	578	25721	463, 627	1412	0.085	9.03
T-EH	57.7	44	578	578	2035	462, 650	1916	0.109	5.69

* shoulder peak, [a] the underlined peaks were used to compute the stokes shift.

6.5.5 Electrochemistry

Finally, the electrochemical properties of the four polymers were investigated, and the result of the cyclic voltammetry is summarized in **Figure 6.6**. Similar electrochemical properties were observed for the furan and thiophene-based polymers as earlier reported by Jeffries-El et al.[16,28] The HOMO energy levels ranged between -4.9eV and -5.1eV, and the LUMO levels ranged between -3.4 and -3.5eV; the high lying HOMO level is due to the presence of a much stronger electron donating effect than withdrawing, resulting in a low V_{oc}. The experimentally obtained electrochemical energy band-gap (E_g^{EC}) were compared to the computed optical energy band gap (E_g^{opt}) estimated from the onset absorption edge of the polymers in the thin film, and a slight difference is observed as described in **Figure 6.6**. Effective conjugation was obtained in all four polymers as indicated by the optical band gap of all the polymers within 0.1eV confirming a previous study[28] that the replacement of the thiophene π-bridge with furan (flanking the DPP

monomer) only has a negligible influence on the electrochemical properties, whilst the replacement of sulfur atoms of BDT (in this case NDT) with oxygen atoms to give BDF (in this case NDF) has a slight impact on the electronic properties.
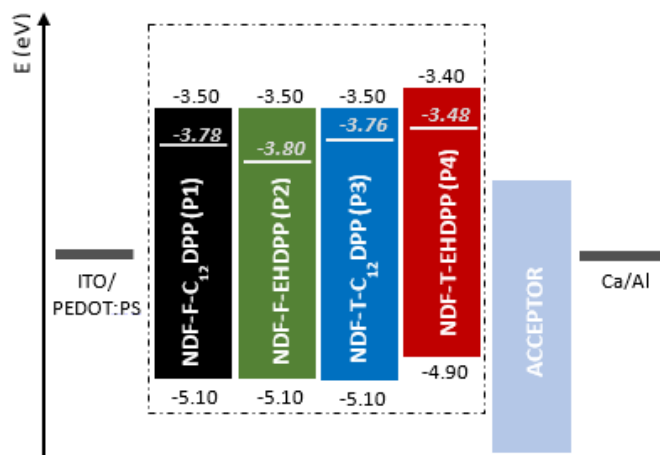
Figure 6.6 HOMO-LUMO electronic (outer) and optical (inner) energy levels of the polymers.

6.5.6 Two Photon Excited Fluorescence (TPEF)

Finally, TPEF measurements were carried out to determine the TPA cross-section (TPA-δ) of the four polymers. TPA cross-section is 'somewhat' like the molar absorptivity of a two-photon excited measurement and is directly correlated to the charge transfer property of the molecule. The TPA-δ of a molecule is strongly dependent on the π-conjugation length of a system (at least until conformational planarity is lost), and hence is dependent on the number of π electrons.[33,57] Two of the four polymers were excited by the 820 nm femtosecond light pulse from the KM laser, but only one-photon absorption was observed, evident from the slope of ~1 obtained by the power scan, indicating that the intensity of the TPEF signal does not increase with the square of the laser intensity (i.e. no quadratic power dependence). This is so because at this wavelength, the probability of a two-photon excitation is quite low relative to the one-photon excitation as clearly observed in the absorption spectrum (**Figure 6.5a**). To this regard, 1200 nm light pulse from a Spectra Physics optical parametric oscillator was used for excitation, TPA was observed

for all four polymer samples as illustrated by the quadratic power dependence shown in **Figure 6.7b**, and the TPA-δ was computed and is presented in **Table 6.2** Similar TPA-δ was obtained when a different experimental reference solution (rhodamine-B) was used validating the accuracy of this approach.
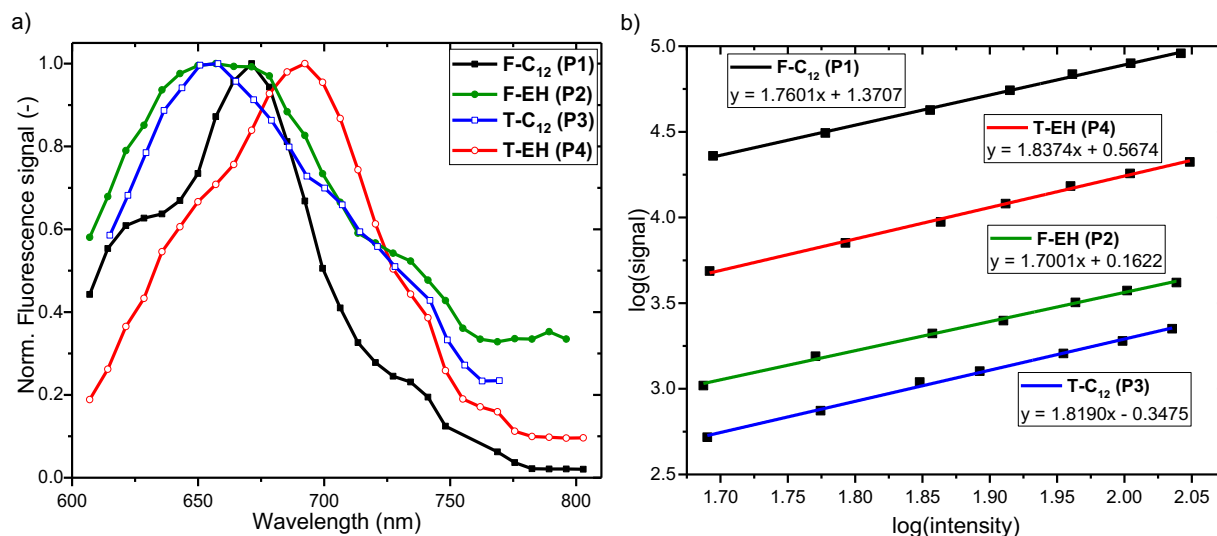
Figure 6.7 a) Two-Photon excited fluorescence spectra, b) Fluorescence signal intensity dependence on average power (pulse intensity), for all four polymers dissolved in chloroform upon 1200 nm pulsed excitation.

The slight deviation from obtaining an exact slope of 2 has been attributed to several processes such as excited state absorption (ESA), stimulated emission, and TPEF saturation.[34,58] It is believed in this study to be as a result of TPEF saturation due to the use of slightly high pulse intensities. Two-photon wave scans were performed within 610-800 nm (**Figure 6.7a**) spectral width using the TPA setup, and an emission spectra similar to that of the one photon 550 nm excitation from the spectrofluorometer was obtained within the same spectral width but with a slight red shift due to the poor sensitivity of the photomultiplier for the TPA setup beyond ~650 nm; this suggests that the achieved singlet S_1 state responsible for the fluorescence is the similar for one-photon and two-photon excitation. The trend in the TPA-δ for the furan and thiophene linkers given in **Table 6.2**, for 1200 nm excitation, is concurrent with that observed in **Figure 6.5a**

inset for the one-photon absorptivity achieved per monomer at 600 nm i.e. F-C$_{12}$ (**P1**) > T-C$_{12}$ (**P3**) and F-EH (**P2**) > T-EH (**P4**). The shorter and bulky solubilizing side chain – EH induces more steric hindrance compared to the longer and less bulky dodecyl side chain. Studies have shown that reducing steric hindrance caused by non-conjugated side chains aids in improving inter-chain π-π stacking,[59] and this can be confirmed in this study with the polymers containing the dodecyl side chains – **P1** and **P3** – as having a higher TPA-δ compared to those with EH side chains – **P2** and **P4**. This is because the inter-chain π-π stacking corresponds to the charge transfer property of organic materials. It is also crucial to note that the polymers with furan-backbone displayed a higher TPA-δ compared to those with a thiophene-backbone of the same side chain i.e. **P3** (thiophene-based) yielded a TPA-δ of 9.03 GM while **P1** (furan-based) yielded a TPA-δ of 25.33 GM which is about three-times the cross-section of **P3**, and **P4** (thiophene-based) yielded a TPA-δ of 5.69 GM while **P2** (furan-based) yielded a TPA-δ of 6.30 GM. This has been attributed to the fact that the presence of furan in a copolymer backbone enhances the coplanarity of the conjugated structure, as confirmed by optimized geometry calculation performed in this study, and this is because the oxygen atom has less diameter than the sulfur atom, is more electronegative and has a larger dipole moment.[7] With a planar structure, promoted π-stacking is encouraged, desirable for higher charge carrier mobility for furan-based relative to thiophene-based copolymers.[8,16,60]

According to a recent study of similar D-A copolymers, DFT calculations showed that polymers with furan as a linker showed lower dihedral angles between the donor and acceptor moiety compared to those with a thiophene linker,[26] and this was then correlated with the TPA-δ to which a linear relationship was obtained. The furan linked copolymers showed higher TPA-δ compared to the thiophene linked copolymers. The same result was obtained in this study in which the furan displayed a higher degree of planarity (**Figure 6.8**), and hence a higher TPA-δ compared

to the thiophene-backbone compound. The BDFTh-X-DPP polymers studied by Vazquez et al[26] generally yielded higher TPA-δ compared to the those studied here. This could be attributed to the extra two thiophenes present in their structure contributing to its increased charge density as well as increased effective conjugation length, and hence higher TPA-δ.
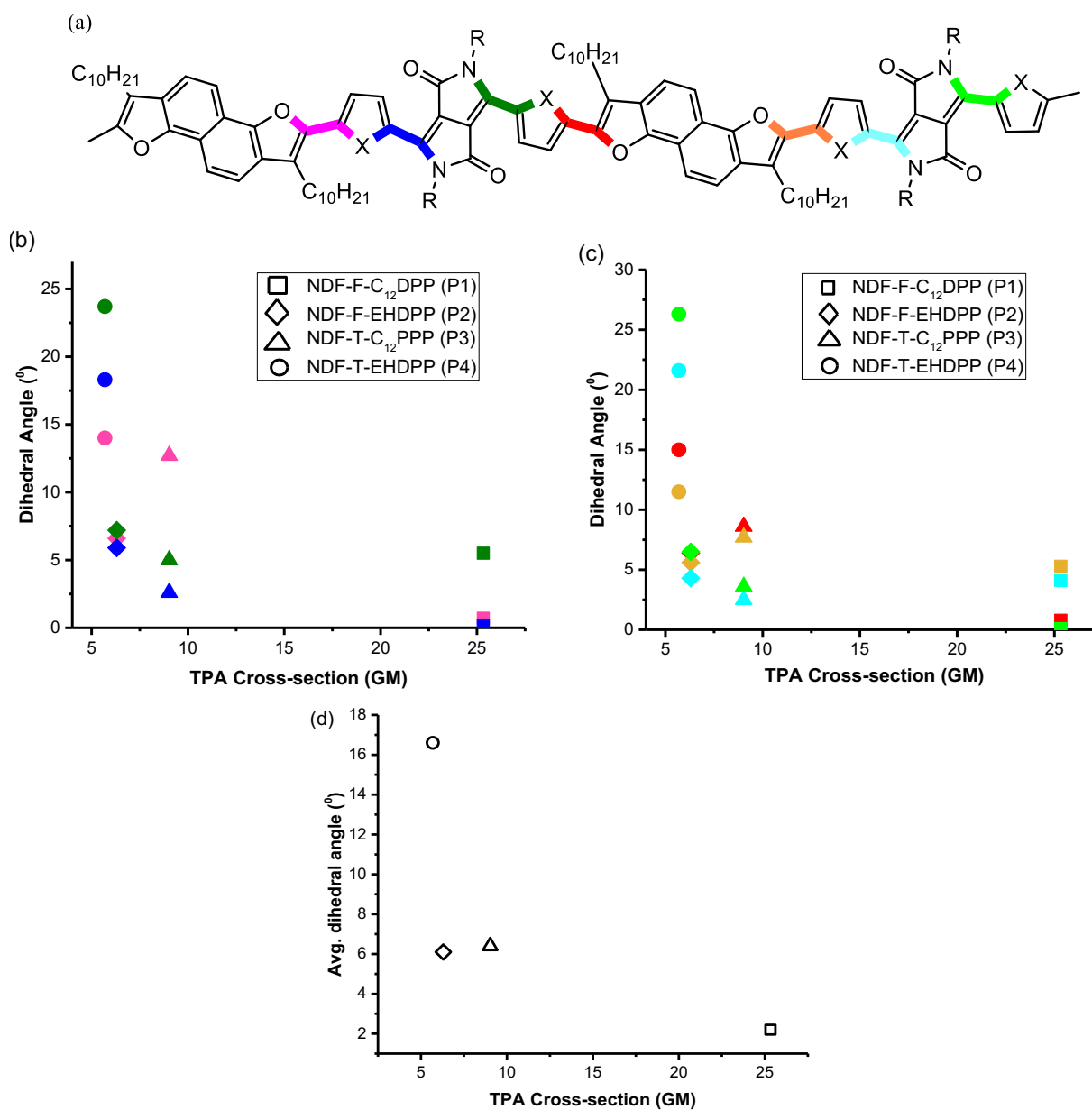
Figure 6.8 Correlation between the TPA cross-section and the individual dihedral angles in (b) 1st monomer (c) 2nd monomer, of the dimer in (a) above as color coded; (d) represents the average dihedral angle of **P1-P4**.
Color scheme for 1st/2nd monomer: pink/orange - φ_{OCCX}; blue/cyan - φ_{XCCN}; dark green/light green - φ_{NCCX}; and connector red - φ_{XCCO}. Respective shapes are represented in the legend.

6.5.7 Time-Resolved Fluorescence Measurements

Ultrafast decay time-resolved fluorescence measurements were performed to determine the fluorescence lifetime of the excitons using an upconversion setup as explained in the experimentation section above. All the polymer samples were excited by a laser beam at 400 nm, and emission detection was carried out in the regions: 460-480 nm and 630-670 nm. For both emission peaks, it was found that there are two emitting components present (the NDF and DPP), hence a bi-exponential fit of the data is performed for both long and very short scans to determine the decay time for both components. The lifetimes for both components (τ_1 and τ_2) are given in **Table 6.3** in the order of picoseconds (ps). **Figure 6.9** shows the decay dynamics of all four polymers in short timescales. A common observable in all four systems is the absence of excited state energy transfer evident from the absence of a rise-time in the decay dynamics. The polymers with the furan-backbone polymer showed a longer lifetime relative to the thiophene-backbone polymer for the long-time component (τ_2). This explains the hypothesis of a long living exciton in the furan-backbone polymer in comparison with the thiophene-backbone polymer. For molecules with the same backbone, polymers with solubilizing component $-C_{12}$ showed a longer lifetime relative to polymers with –EH side chain. This further strengthens the benefits of the longer and less bulky alkyl-side chain molecules having a longer lifetime compared to shorter and more bulky side chain molecules. The fast initial decay component (τ_1) was not affected by the linker/π-bridge component nor the side chain, this is evident from the similar values obtained ~0.2 – 0.5 ps, but the longer decay component was sure dependent on the π-bridge. This may be due to confirmed presence of the same moiety – NDF in all the studied molecules, with the thiophene or furan π–bridges associated with just the DPP moiety in the 3- and 6- position. Very similar experimental finding was obtained in a study by Vasquez et al[26] where the same bridge-acceptor moieties (T-

DPP and F-DPP) were used. They discovered that the copolymers with furan as linker showed longer fluorescence lifetime dynamics relative to the thiophene-linked copolymers. They also discovered that side chain plays a role in determining the fluorescence lifetime of polymers. Two emission peaks were also probed in the study, and the higher energy peak (525 – 560 nm) yielded almost the same lifetime for all the polymers studied regardless of linker or side chain. This could also be attributed to the same donor moiety – BDF they all had in common. The fluorescence lifetimes obtained by Vasquez et al[26] were generally smaller than those obtained here for the same linker and sidechain. This could be attributed to more twists and kinks (thereby serving as fluorescence traps) present in their structures as observed from the DFT calculation. The molecule with a larger dihedral angle (copolymer with thiophene backbone ~ 28°) showed faster decay dynamics, and similar trend is also observed in this study where the mostly planar furan-backbone molecule showed longer lifetime.
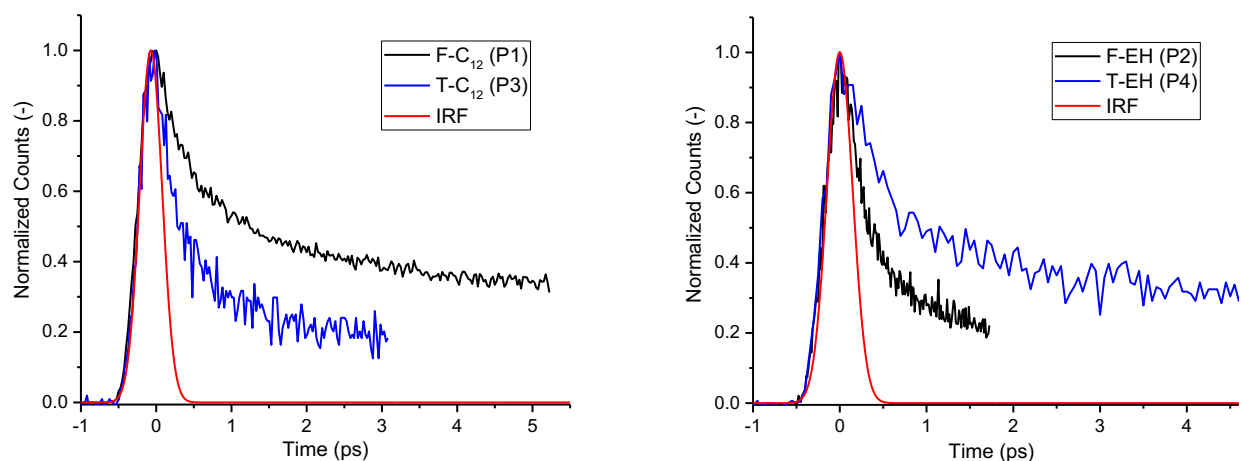
Figure 6.9 Fluorescence upconversion decay data of polymers at 400 nm excitation and 630-670 nm emission.

Table 6.3 Time-Resolved Fluorescence lifetimes of all four polymers with the emission wavelength at which they were monitored.

Polymer	Backbone	Substituent	τ_1 (ps) / λ_{em} (nm)	τ_2 (ps) / λ_{em} (nm)
F-C$_{12}$ **(P1)**	Furan	-C$_{12}$	0.490 / 461	995.79 / 626
F-EH **(P2)**	Furan	-EH	0.226 / 477	828.53 / 654

| T-C$_{12}$ **(P3)** | Thioph | -C$_{12}$ | 0.286 / 463 | 369.21 / 638 |
| T-EH **(P4)** | Thioph | -EH | 0.496 / 461 | 294.75 / 672 |

6.5.8 Time-Resolved Absorption Spectroscopic Measurements

Investigating the fast relaxation of the non-emissive as well as the dark states of the OPV donor polymers, transient absorption pump-probe technique was used. The ~400 nm pump beam (~100 fs width) was used to excite the sample dissolved in chloroform and the probe spanned the range 420-800 nm. The spectral difference in optical density (ΔA) was measured at different time delay between the pump and probe. **Figures 6.10** and **6.11** shows the 3D transient spectra and the time-resolved absorption spectra respectively for all four polymers. All polymers showed both high energy (450-535 nm band) and low energy (660-790 nm band) $S_n \leftarrow S_1$ transitions in the spectral window ~400-800 nm indicative of excited state absorption (ESA). With the exception of T-EH (**P4**), ground-state bleaching in the 510-675 nm region was also observed for all the investigated polymers. The ground-state bleaching exhibited by all the polymers matched the low energy band of their steady state absorption. **P4** interestingly showed a positive ΔA signal, indicative of ESA, for all wavelengths clearly depicting the lower population of the ground state compared to the excited state population of the polymer at all delay time. This can be predicted at a glance from the molar extinction plot of **Figure 6.5a** inset in which **P4** displayed an almost flat spectra indicative of a low ground state population. For F-C$_{12}$ (**P1**), the shoulder peak at 550nm became more pronounced in this measurement unlike in the steady state measurement because of the unique detection and resolution ability of this setup. The ground state bleaching present in all polymers (except **P4**) can be associated with the formation of a charge transfer state as earlier stipulated in the steady state analysis between the NDF and the F-DPP/T-DPP moieties and is clearly represented in **Figures 6.10** and **6.11**. The transient absorption result confirms the

extremely low probability of energy transfer as a non-radiative mechanism for all the analyzed polymers due to the absence of rise time observed for the non-emissive states, and also due to the absence of stimulated emission from their acceptor moiety. For each of the polymer analyzed in this study, for each time delay, no spectra shift was observed indicative of the fact that the polymer's crystallinity is intact and was specifically excited by the ~400 nm beam. It should also be pointed out that the signal overtones in the region between 675 nm and 790 nm are due to the instability of the white light hitting the CCD detector in this setup.

A unique trend in the spectra at various delay time was observed for all four polymers. There was an increase in signal (ΔA becomes more positive for the ESA peak and more negative for the bleaching peak) observed in all the peaks until 1.5 ps, after which the signal decreases reaching a certain level at ca. 1ns – the maximum time limit of the transient set-up. This long lifetime could be indicative of the existence of a triplet state resulting from intersystem crossing[61,62] – owing to the carbonyl group in the DPP unit (El-Sayed rule[63]) – as a recombination pathway. More details can be obtained experimentally by performing near steady-state photoinduced absorption spectroscopy. A common deconvolution technique – single value decomposition (SVD) was used to perform global fit analyses of the transient data, in which linearly independent vectors (scaled by numbers) were employed to separate the various contributions to the data. Global analysis of the collected data for all samples revealed in all cases the presence of two components having two exponential lifetimes – few picoseconds (τ_1) and ~1 nanosecond (τ_2). Data is shown in **Table 6.4**. The longer component can be associated with the excited state dynamics coupled with the fluorescence component of the species, and the shorter component can be associated with the photo-induced charge transfer character of the molecules. At each non-emissive peak wavelength (ESA ~500 nm and ~750nm, bleach ~600 nm), single

wavelength analysis were also performed. Results are shown in **Table 6.5**. At the ESA λ_{max} (i.e. 500nm and 750nm) for all the samples, the fast decay component of the excited state was monitored to obtain an idea about their excited state lifetimes. The furan-backbone structures displayed longer lifetimes compared to the thiophene-backbone compounds at the ~500 nm ESA λ_{max}, and the same trend is observed for the ~750 nm ESA λ_{max} except for compound T-EH (**P4**). This may be due to the absence of ground state bleaching for **P4**, hence an observed population increase in the excited state at 750nm. At the respective bleach λ_{max} of the polymers, the fast relaxation dynamics was also performed to estimate the lifetime of their bleach state. Longer lifetime was also observed by the furan-backbone donor polymers relative to their thiophene counterpart, and longer lifetime was observed for the bulky side-chain donor polymer relative to the linear side-chain compound.

Table 6.4 Global fit lifetimes of all four polymers using the single value decomposition (SVD) technique.

Polymer	Backbone	Side chain	τ_1 (ps)	τ_2 (ps)
F-C$_{12}$ (**P1**)	Furan	-C$_{12}$	10.44 ± 1.89	771.2 ± 34.02
F-EH (**P2**)	Furan	-EH	20.15 ± 1.61	1543.4 ± 216.39
T-C$_{12}$ (**P3**)	Thiophene	-C$_{12}$	5.55 ± 1.03	723.6 ± 162.60
T-EH (**P4**)	Thiophene	-EH	8.87 ± 0.62	1191.6 ± 97.15

Table 6.5 Single wavelength analysis for all four polymers at ESA (~500nm, ~750nm) and Bleach wavelengths (~600nm).

Polymer	ESA1 λ_{max}	τ (ps)	ESA2 λ_{max}	τ (ps)	Bleach λ_{max}	τ (ps)
F-C$_{12}$ (**P1**)	500 nm	45.10 ± 22.41	750 nm	111.06 ± 10.64	600 nm	9.85 ± 2.11
F-EH (**P2**)	500 nm	69.10 ± 20.63	750 nm	26.51 ± 3.16	600 nm	31.36 ± 7.23
T-C$_{12}$ (**P3**)	491 nm	2.42 ± 0.46	758 nm	19.78 ± 0.10	580 nm	7.85 ± 0.59
T-EH (**P4**)	505 nm	15.40 ± 3.87	760 nm	34.14 ± 3.56	-	-
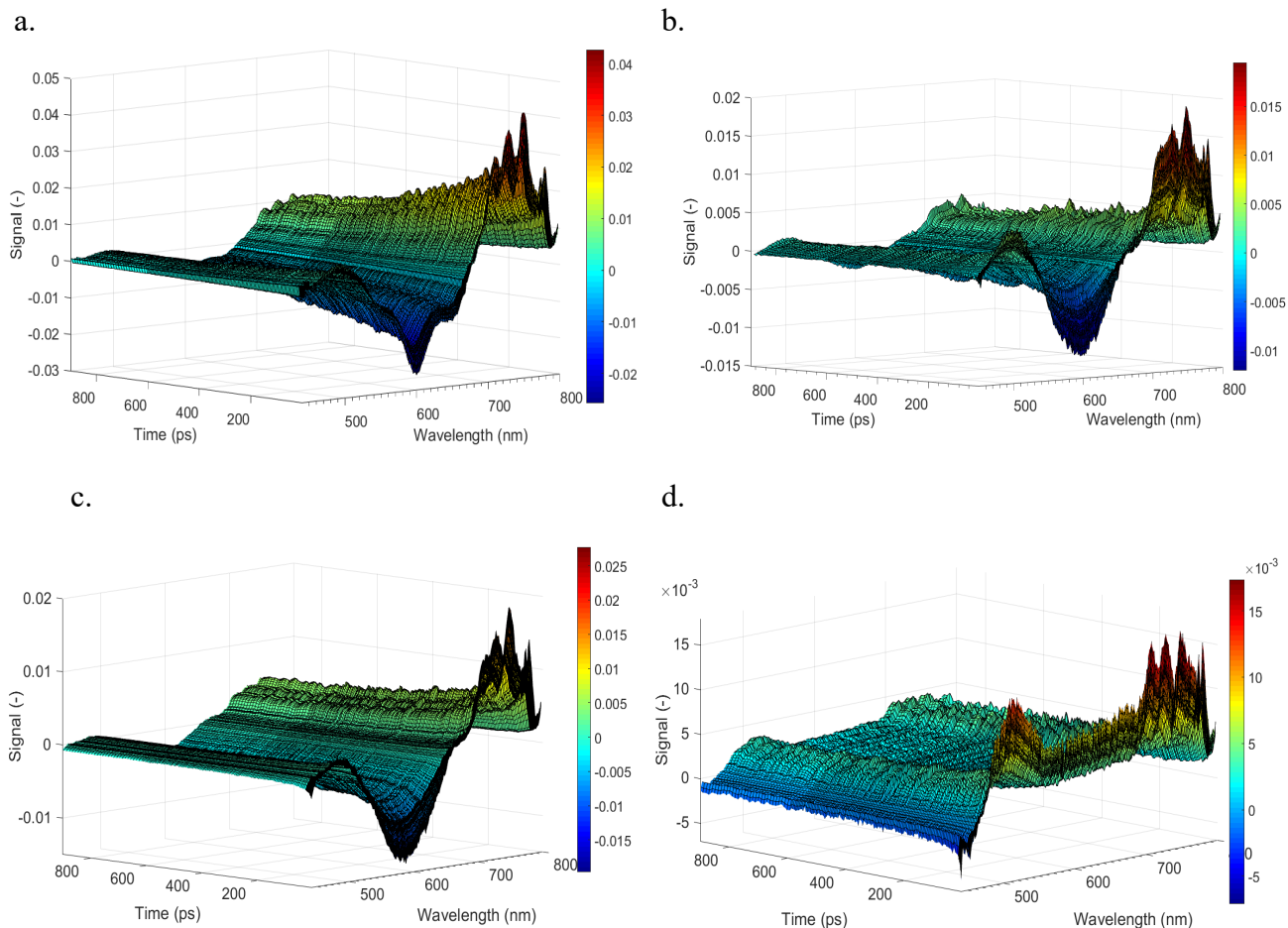
Figure 6.10 3D data of the Transient absorption measurement of **a.** NDF-**F-C$_{12}$**DPP **(P1) b.** NDF-**F-EH**DPP **(P2) c.** NDF-**T-C$_{12}$**DPP **(P3) d.** NDF-**T-EH**DPP **(P4)** clearly showing how the spectra changes over time.
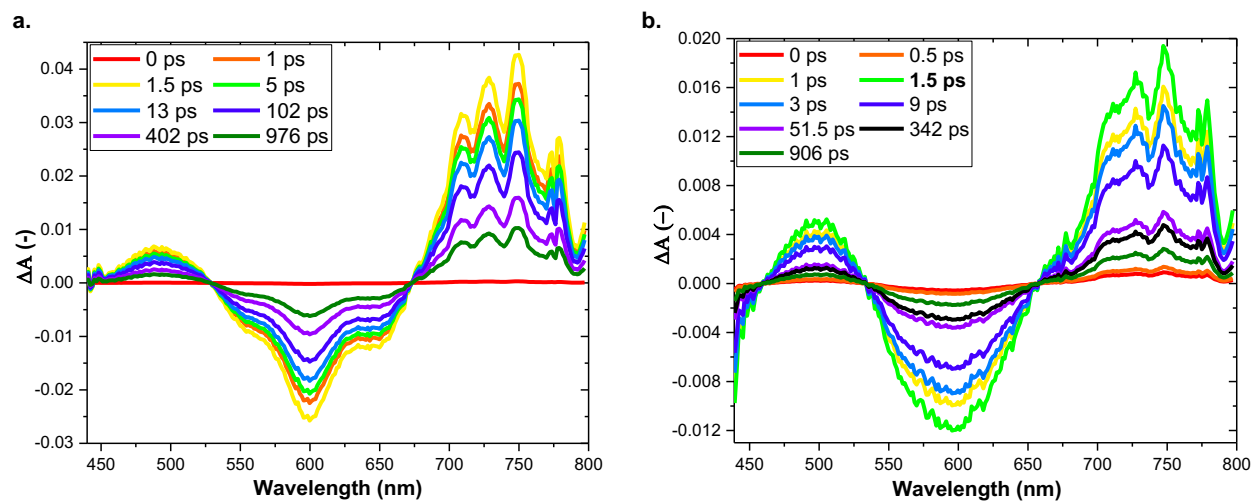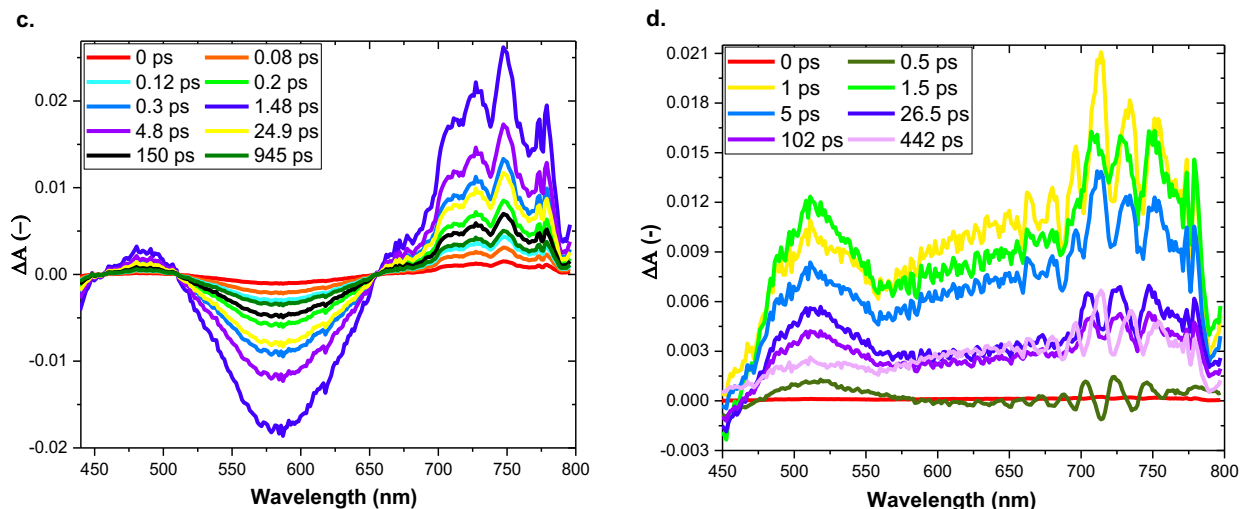
Figure 6.11 Time-Resolved absorption spectra of **a.** NDF-**F-C$_{12}$**DPP (**P1**), b. NDF-**F-EH**DPP (**P2**), c. NDF-**T-C$_{12}$**DPP (**P3**), d. NDF-**T-EH**DPP (**P4**), obtained by femtosecond resolved transient absorption.

6.5.9 Device Performance

The photovoltaic performance of the polymers was investigated in bulk heterojunction OPV devices fabricated in a conventional configuration (ITO/PEDOT:PSS/ Polymer:PC$_{71}$BM/ Ca/Al), and measured under simulated AM1.5G illumination at 100 mW/cm^2. For initial testing, polymer active layers which consisted of a donor:acceptor blend ratio of 1:1 (15 mg/mL P1-P3, 20 mg/mL P4) were spin-coated from either chlorobenzene or *o*-dichlorobenzene, with varying amounts of 1,8-diiodooctane additive (DIO) and annealed at 70 °C for 10 min. All of the polymers had limited solubility in both solvents, which made producing concentrated solutions difficult. Although various conditions were evaluated, we were unable to obtain active layers thicker than 20 nm. In general, thicker layers (~200 nm) are better because they absorb more light. As a result, the performance of the devices was low. The fabrication conditions and key parameters: fill factor (FF), short-circuit current density (J$_{sc}$) and V$_{oc}$ are summarized in **Table 6.6**, and current density-voltage (*J-V*) plots of the best performing devices are shown in **Figure 6.12**. Initially, we focused on devices spun from *o*-DCB, but also tried chloroform without the use of an additive.

Gratifyingly, a slight improvement in power conversion efficiency was observed for all polymers under these conditions. Overall, F-EH (**P2**) exhibited the highest PCE at modest 0.54%. While the performance of these devices is low, this is typical with new systems. We anticipate that the performance can be dramatically improved by optimization of processing parameters, which is currently underway.
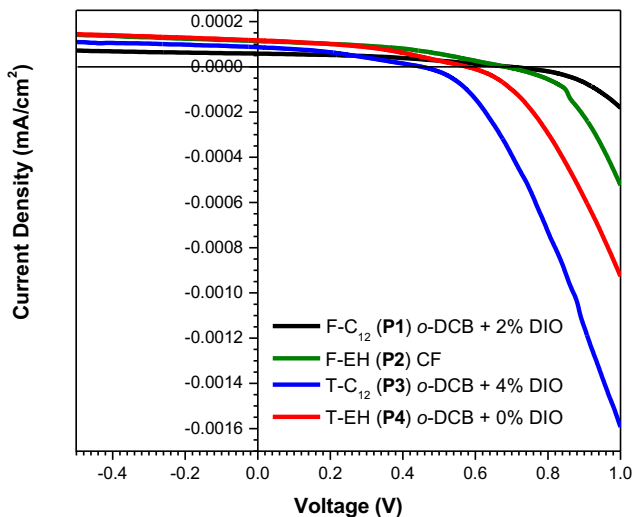
Figure 6.12 J-V curves of the devices under the illumination of AM 1.5G, 100 mWcm^{-2}.

Table 6.6 Peak OPV Device Characteristics.

Polymer	Vol % DIO	J_{sc} [mA/cm^{-2}]	V_{oc} [V]	FF	PCE [%]
F-C$_{12}$ (**P1**)	0	0.72	0.62	0.41	0.18
	0.5	0.75	0.25	0.29	0.05
	2	0.97	0.70	0.39	0.26
	4	0.24	0.12	0.27	0.008
	CHCl$_3$[‡]	n/a	n/a	n/a	n/a
F-EH (**P2**)	0	0.61	0.46	0.39	0.11
	0.5	0.81	0.50	0.37	0.15
	2	0.36	0.26	0.31	0.03
	4	0.36	0.48	0.40	0.07
	CHCl$_3$	**1.90**	**0.68**	**0.42**	**0.54**
T-C$_{12}$ (**P3**)	0[‡]	n/a	n/a	n/a	n/a
	0.5	1.18	0.47	0.39	0.22
	2	0.88	0.42	0.37	0.13
	4	1.45	0.45	0.34	0.22
	CHCl$_3$	1.87	0.47	0.24	0.21

T-EH (**P4**)	0	1.95	0.57	0.40	0.45
	0.5	2.22	0.54	0.32	0.38
	2	1.76	0.47	0.28	0.24
	4[‡]	n/a	n/a	n/a	n/a
	CHCl$_3$	1.80	0.66	0.35	0.42

[†]Conventional devices (ITO/PEDOT:PSS/Polymer:PC$_{70}$BM/Ca/Al). Polymer active layers were spin-coated at 2000 rpm for 2 min, from the respective solution (20 mg/mL) in a blend ratio of 1:1, and annealed at 70 °C for 10 min.
[‡]All devices shorted.

6.6 Discussion

In the study of structure-functional relationship of organic photovoltaic materials, the use of specific heteroatoms (especially chalcogens) to tune the properties of the conjugated polymers has been widely employed.[9,12,17,18,64] Different side chain configurations have also been tried out to evaluate the polymer's processability, if eventually made into films.[7,19,29,64,65] In this study, four new NDF-based donor OPV polymers were synthesized, their photophysical and electronic properties analyzed to determine the functional-effect of a furan/thiophene heterocyclic molecule serving as a π–linker between the donor and acceptor moieties of the compound, as well as the effect of linear vs bulky sidechains on these properties. The polymers with furan backbone displayed higher absorptivity (molar extinction coefficient); extinction coefficient has been shown to be directly related to the absorption efficiency (η_A),[66,67] and the absorption efficiency is proportional to the external quantum efficiency, and hence to the power conversion efficiency (PCE). In making the polymers into thin films, the absorptivity of thiophene-backbone compound was similar as to in chloroform solution, however owing to a higher degree of molecular planarity, the furan backbone compound displayed a broader, slightly red-shifted spectra in thin film than in solution, and this can be associated to increased aggregation and molecular backbone packing. The planarity of a conjugated polymer, which can be achieved by decreasing the steric hindrance between adjacent polymer backbone units, has also been shown to enhance their molecular absorptivity.[10]

The polymers displayed two broad emission peaks. NDF is reported to emit in the 350 – 500 nm region,[23,55] and since this is the common donor moiety present in all four polymers, the first peak has been associated with this moiety. However, weak coupling between the NDF and DPP moiety resulted in this bimodal spectrum, indicative of emission occurring from both components. This could support the absence of energy transfer that was not observed in any of these compounds. The theoretically calculated absorption wavelengths were in close agreement to the experimentally determined wavelengths to the nearest 0.16 eV. The hole NTOs show the delocalization along the entire backbone of the dimer model, while the electron NTOs show localization at the DPP moiety, indicative of the existence of some form of photo-induced electron transfer from the conjugated backbone to the DPP unit when the polymers are photo-excited. For the thiophene-backbone polymers, fluorescence quantum yield was slightly higher for the bulky side chain compound relative to the linear counterpart, and this could be attributed to reduced aggregation when a bulkier side group is used. Comparing the fluorescence quantum yield values for the same EH side chains, the furan backbone compound displayed a lower quantum yield in comparison to the thiophene backbone compound. This can be attributed to lesser intermolecular packing owing to larger sulfur atom size of the thiophene, thereby restricting molecular aggregation.

The nonlinear TPA cross-section was measured at 1200 nm utilizing the TPEF technique. The results show that for the same side chain, the furan-backbone compound displayed a higher TPA cross-section relative to its thiophene counterpart, indicating better charge transfer, and hence better charge separation with an acceptor compound. The results of the theoretical calculations show that the polymers with furan-backbone have lower dihedral angles between the donor moiety and the linker (φ_{OCCX}), and between the linker of one monomer to the donor moiety of another

(φ_{XCCO}) as shown in **Figure 6.8** and **Table 6.1**, thus making them more planar compared to their thiophene analogues. Owing to the enhanced steric hindrances induced by the shorter, bulky side chain – EH thereby leading to poor inter chain π-π stacking, lower TPA cross-section was observed for compounds containing this bulky side group compared to those with the linear dodecyl side group. These results were also supported by the findings from the theoretical calculation which showed that the compounds with EH side chains possessed higher dihedral angles between the linker and the DPP moiety, onto which the side chain is attached (φ_{XCCN}, φ_{NCCX}), compared to its counterparts with linear dodecyl side chains. The low TPA-δ obtained in this study in comparison to that obtained in a previous study of similar structures by our group [26] can be linked to the broader one-photon film absorption band obtained here hence limiting the accessible window for TPEF measurement, and can also be tied unarguably to the poor coupling between the donor and acceptor moieties of the copolymers limiting effective charge transfer. It has been studied and reported that the TPA-δ correlates with: (i) the π-conjugation length of the system,[33,41] (ii) the nature of the π-bridge between a donor and an acceptor moiety, and (iii) the structural conformation.[33] The four polymers analyzed in this study have the same number of π-electrons per monomer (measures the length of a π-system), hence this basis cannot be used to discuss the differences in their TPA-δ. The other two criteria i.e. the nature of the π-bridge (in this case furan or thiophene) and the structural conformation (including the effects of the solubilizing side chain), both play a synchronous role in explaining the TPA-δ obtained herein.

Longer fluorescence lifetime was obtained for the polymers having a furan linker relative to those linked with thiophene for both solubilizing side chains, and this explains the idea of longer living excitons in the furan linker polymers in comparison to the thiophene compounds. For both furan and thiophene-linker compounds, those with the linear solubilizing sidechains showed a

slightly longer lifetime relative to those with bulky sidechains. These results as well as those obtained from a previous study of similar OPV polymers[26] could be interpreted from the standpoint of the lower fluorescence lifetime being observed in compounds with larger torsional angles in between their respective atoms (φ_{OCCX}, φ_{XCCN}, φ_{NCCX}). These torsions serve as exciton traps which inhibit the steady movement of excitons thereby leading to shorter fluorescence lifetimes.

The investigation of the non-emissive states of the polymers revealed interesting trends. All the polymers with an exception of T-EH (**P4**) exhibited both ground-state bleaching (perfectly matching their respective steady-state absorption spectra) and ESA in two regions of the studied spectrum width. The ground state bleaching in the polymers may be attributed to the decrease in excited state population owing to charge transfer to a CT* state. For **P4**, this CT* state is quiescent hence leading to the absence of ground state bleaching, but instead an increased population of the excited states. This may be related to the reason **P4** displayed the lowest TPA-δ as well as the lowest molar extinction coefficient among all the studied polymers. Target analysis to determine the excited state lifetimes at the 500 nm ESA wavelength showed furan backbone compounds having longer decay time; also, at their respective bleach wavelengths, longer decay time was once again associated with the furan-containing compound relative to the thiophene-backbone compound.

6.7 Conclusions

Four novel D-A polymers were designed and synthesized whose structure was based on NDF as the donor moiety and X-DPP as the acceptor, where X (furan or thiophene) serves as the linker between the NDF and DPP moieties, and two different alkyl side chains attached to the DPP unit. The effect of the chalcogenic heteroatom – furan and thiophene, as well as the alkyl solubilizing side chains – ethylhexyl and dodecyl on the optical, electrochemical, and photovoltaic

properties have been investigated. The compound with furan in its backbone exhibited a higher extinction coefficient relative to their thiophene counterpart; and in film showed a broader absorption spectrum. The HOMO and LUMO levels were similar for all the molecules confirming the independence of the heteroatom and side chain on the electrochemistry of polymers. The results of the DFT calculation confirms the higher degree of molecular planarity present in the furan-backbone compound compared to the thiophene-backbone compound owing to the smaller sized oxygen atom, and higher electronegativity. The experimentally obtained TPA-δ is almost linearly correlated to the DFT obtained dihedral angles indicating a direct relationship between molecular planarity and the ability of the molecules to absorb two-photons, and consequently the effective charge transfer property of the material. Time-resolved ultrafast measurements show longer exciton lifetime for furan-containing compounds relative to the thiophene-containing structure attributed once again to the lower dihedral angle, hence the absence of molecular traps and kinks. The larger molar absorptivity by the polymers with furan backbone could lead to the generation more excitons, and consequently the increased density of charge carriers; the longer fluorescence lifetime can be highly resourceful for obtaining longer living excitons over the diffusion length of the material, however furan containing conjugated polymers are still rare in comparison to their thiophene counterpart despite the research attention on furan derivatives. These result in concordance to previous study of similar structures stresses once again the productive impact of replacing thiophene donor-acceptor linkers with furan-linkers on the photophysical properties, and ultimately the PCE of light harvesting conjugated polymers.

References

(1) Wan, Q.; Guo, X.; Wang, Z.; Li, W.; Guo, B.; Ma, W.; Zhang, M.; Li, Y. 10.8% Efficiency Polymer Solar Cells Based on PTB7-Th and PC71BM via Binary Solvent Additives Treatment. *Adv. Funct. Mater.* **2016**, *26* (36), 6635–6640.

(2) Hai, J.; Shi, G.; Yu, J.; Zhu, E.; Bian, L.; Ma, W.; Tang, W. Naphthodifuran Alternating Quinoxaline Copolymers with a Bandgap of [Similar]1.2 EV and Their Photovoltaic Characterization. *New J. Chem.* **2014**, *38*, 4816–4822.

(3) Liu, B.; Chen, X.; He, Y.; Xiao, L.; Li, Y.; Zhou, K.; Fan, L.; Zou, Y. Alkyl Substituted Naphtho[1, 2-b: 5, 6-b[Prime or Minute]]Difuran as a New Building Block towards Efficient Polymer Solar Cells. *Rsc Adv.* **2013**, *3* (16), 5366–5369.

(4) Zhang, W.; Li, Y.; Zhu, L.; Liu, X.; Song, C.; Li, X.; Sun, X.; Fang, J. PTB7-Based Narrow Band-Gap Conjugated Polyelectrolyte as Efficient Cathode Interlayer in PTB7-Based Polymer Solar Cells. *Chem. Commun.* **2017**, *53*, 2005–2008.

(5) Wienk, M. M.; Turbiez, M.; Gilot, J.; Janssen, R. A. J. Narrow-Bandgap Diketo-Pyrrolo-Pyrrole Polymer Solar Cells: The Effect of Processing on the Performance. *Adv. Mater. (Weinheim, Ger.* **2008**, *20* (13), 2556–2560.

(6) Bijleveld, J. C.; Gevaerts, V. S.; Di Nuzzo, D.; Turbiez, M.; Mathijssen, S. C. J.; De Leeuw, D. M.; Wienk, M. M.; Janssen, R. A. J. Efficient Solar Cells Based on an Easily Accessible Diketopyrrolopyrrole Polymer. *Adv. Mater.* **2010**, *22* (35), 242–246.

(7) Du, J.; Fortney, A.; Washington, K. E.; Biewer, M. C.; Kowalewski, T.; Stefan, M. C.; Seferos, D. S.; Tristram-Nagle, S.; Smilgies, D. M.; Lambeth, D. N.; et al. Benzo[1,2-b:4,5-B′]Difuran and Furan Substituted Diketopyrrolopyrrole Alternating Copolymer for Organic Photovoltaics with High Fill Factor. *J. Mater. Chem. A* **2017**, *15*, 1617–1622.

(8) Liu, B.; Chen, X.; Zou, Y.; Xiao, L.; Xu, X.; He, Y.; Li, L.; Li, Y. Benzo[1,2- B :4,5- b ′]Difuran-Based Donor–Acceptor Copolymers for Polymer Solar Cells. *Macromolecules* **2012**, *45* (17), 6898–6905.

(9) Peng, H.; Luan, X.; Qiu, L.; Li, H.; Liu, Y.; Zou, Y. New Naphtho[1,2-b:5,6-B′]Difuran Based Two-Dimensional Conjugated Small Molecules for Photovoltaic Application. *Opt. Mater. (Amst).* **2017**, *72*, 147–155.

(10) Zhang, S.; Ye, L.; Wang, Q.; Li, Z.; Guo, X.; Huo, L.; Fan, H.; Hou, J. Enhanced Photovoltaic Performance of Diketopyrrolopyrrole (DPP) Based Polymer with Extended π -Conjugation. **2013**, 50–52.

(11) Gandini, A. Polymers from Renewable Resources: A Challenge for the Future of Macromolecular Materials. *Macromolecules* **2008**, *41* (24), 9491–9504.

(12) Huang, P.; Du, J.; Gunathilake, S. S.; Rainbolt, E. A.; Murphy, J. W.; Black, K. T.; Barrera, D.; Hsu, J. W. P.; Gnade, B. E.; Stefan, M. C.; et al. Benzodifuran and Benzodithiophene Donor-Acceptor Polymers for Bulk Heterojunction Solar Cells. *J. Mater. Chem. A* **2015**, *3* (13), 6980–6989.

(13) Spanggaard, H.; Krebs, F. C. A Brief History of the Development of Organic and Polymeric Photovoltaics. *Sol. Energy Mater. Sol. Cells* **2004**, *83* (2–3), 125–146.

(14) Woo, C. H.; Beaujuge, P. M.; Holcombe, T. W.; Lee, O. P.; Fréchet, J. M. J. Incorporation of Furan in Low Band Gap Polymers for Efficient Solar Cells. *J. Am. Chem. Soc.* **2010**, *132*, 15547–15549.

(15) Scharber, M. C.; Mühlbacher, D.; Koppe, M.; Denk, P.; Waldauf, C.; Heeger, A. J.; Brabec, C. J. Design Rules for Donors in Bulk-Heterojunction Solar Cells - Towards 10 % Energy-Conversion Efficiency. *Adv. Mater.* **2006**, *18* (6), 789–794.

(16) Jeffries-El, M.; Kobilka, B. M.; Hale, B. J. Optimizing the Performance of Conjugated Polymers in Organic Photovoltaic Cells by Traversing Group 16. *Macromolecules* **2014**, *47* (21).

(17) Bhatta, R. S.; Tsige, M. Understanding the Effect of Heteroatoms on Structural and Electronic Properties of Conjugated Polymers. *Polymer (Guildf).* **2015**, *56*, 293–299.

(18) Liu, J.; Walker, B.; Tamayo, A.; Zhang, Y.; Nguyen, T. Q. Effects of Heteroatom Substitutions on the Crystal Structure, Film Formation, and Optoelectronic Properties of Diketopyrrolopyrrole-Based Materials. *Adv. Funct. Mater.* **2013**, *23* (1), 47–56.

(19) Liang, Y.; Yu, L. A New Class of Semiconducting Polymers for Bulk Heterojunction Solar Cells with Exceptionally High Performance. *Acc. Chem. Res.* **2010**, *43* (9), 1227–1236.

(20) Carsten, B.; Szarko, J. M.; Son, H. J.; Wang, W.; Lu, L.; He, F.; Rolczynski, B. S.; Lou, S. J.; Chen, L. X.; Yu, L. Examining the Effect of the Dipole Moment on Charge Separation in Donor-Acceptor Polymers for Organic Photovoltaic Applications. *J. Am. Chem. Soc.* **2011**, *133* (50), 20468–20475.

(21) Adegoke, O. O.; Jung, I. H.; Orr, M.; Yu, L.; Goodson, T. Effect of Acceptor Strength on Optical and Electronic Properties in Conjugated Polymers for Solar Applications. *J. Am. Chem. Soc.* **2015**, *137* (17), 5759–5769.

(22) Chen, J. De; Cui, C.; Li, Y. Q.; Zhou, L.; Ou, Q. D.; Li, C.; Li, Y.; Tang, J. X. Single-Junction Polymer Solar Cells Exceeding 10% Power Conversion Effi Ciency. *Adv. Mater.* **2015**, *27* (6), 1035–1041.

(23) Mitsui, C.; Soeda, J.; Miwa, K.; Tsuji, H.; Takeya, J.; Nakamura, E. Naphtho[2,1-b:6,5-b']Difuran: A Versatile Motif Available for Solution-Processed Single-Crystal Organic Field-Effect Transistors with High Hole Mobility. *J. Am. Chem. Soc.* **2012**, *134* (12), 5448–5451.

(24) Oniwa, K.; Kanagasekaran, T.; Jin, T.; Akhtaruzzaman, M.; Yamamoto, Y.; Tamura, H.; Hamada, I.; Shimotani, H.; Asao, N.; Ikeda, S.; et al. Single Crystal Biphenyl End-Capped Furan-Incorporated Oligomers: Influence of Unusual Packing Structure on Carrier Mobility and Luminescence. *J. Mater. Chem. C* **2013**, *1* (26), 4163.

(25) Keller, B.; McLean, A.; Kim, B. G.; Chung, K.; Kim, J.; Goodson, T. Ultrafast Spectroscopic Study of Donor-Acceptor Benzodithiophene Light Harvesting Organic

Conjugated Polymers. *J. Phys. Chem. C* **2016**, *120* (17), 9088–9096.

(26)   Vázquez, R. J.; Kim, H.; Kobilka, B. M.; Hale, B. J.; Jeffries-EL, M.; Zimmerman, P.; Goodson, T. Evaluating the Effect of Heteroatoms on the Photophysical Properties of Donor–Acceptor Conjugated Polymers Based on 2,6-Di(Thiophen-2-Yl)Benzo[1,2-b:4,5-B′]Difuran: Two-Photon Cross-Section and Ultrafast Time-Resolved Spectroscopy. *J. Phys. Chem. C* **2017**, *121* (27), 14382–14392.

(27)   Matsidik, R.; Luzio, A.; Askin, Ö.; Fazzi, D.; Sepe, A.; Steiner, U.; Komber, H.; Caironi, M.; Sommer, M. Highly Planarized Naphthalene Diimide-Bifuran Copolymers with Unexpected Charge Transport Performance. *Chem. Mater.* **2017**, *29* (13), 5473–5483.

(28)   Kobilka, B. M.; Hale, B. J.; Ewan, M. D.; Dubrovskiy, A. V; Nelson, T. L.; Duzhko, V.; Jeffries-El, M. Influence of Heteroatoms on Photovoltaic Performance of Donor-Acceptor Copolymers Based on 2,6-Di(Thiophen-2-Yl)Benzo 1,2-b:4,5-b ' Difurans and Diketopyrrolopyrrole. *Polym. Chem.* **2013**, *4* (20), 5329–5336.

(29)   Kirkus, M.; Wang, L.; Mothy, S.; Beljonne, D.; Cornil, J.; Janssen, R. A. J.; Meskers, S. C. J. Optical Properties of Oligothiophene Substituted Diketopyrrolopyrrole Derivatives in the Solid Phase: Joint J- and H-Type Aggregation. *J. Phys. Chem. A* **2012**, *116* (30), 7927–7936.

(30)   Furgal, J. C.; Jung, J. H.; Goodson, T.; Laine, R. M. Analyzing Structure − Photophysical Property Relationships for Isolated T 8 , T 10 , and T 12 Stilbenevinylsilsesquioxanes. *J. Am. Chem. Soc.* **2013**, *135*, 12259–12269.

(31)   Maciejewski, A.; Steer, R. P. Spectral and Photophysical Properties of 9,10-Diphenylanthracene in Perfluoro-n-Hexane: The Influence of Solute-Solvent Interactions. *J. Photochem.* **1986**, *35* (1), 59–69.

(32)   Jobin Yvon. *A Guide to Recording Fluorescence Quantum Yields Introduction:*; 2014; Vol. 15.

(33)   Pawlicki, M.; Collins, H. A.; Denning, R. G.; Anderson, H. L. Two-Photon Absorption and the Design of Two-Photon Dyes. *Angew. Chemie - Int. Ed.* **2009**, *48* (18), 3244–3266.

(34)   Xu, C.; Webb, W. W. Measurement of Two-Photon Excitation Cross Sections of Molecular Fluorophores with Data from 690 to 1050 Nm. *J. Opt. Soc. Am. B* **1996**, *13* (3), 481.

(35)   Makarov, N. S.; Drobizhev, M.; Rebane, A. Two-Photon Absorption Standards in the 550-1600 Nm Excitation Wavelength Range. *Opt. Express* **2008**, *16* (6), 4029–4047.

(36)   Varnavski, O.; Leanov, a.; Liu, L.; Takacs, J.; Goodson, T. Femtosecond Luminescence Dynamics in a Nonlinear Optical Organic Dendrimer. *Phys. Rev. B* **2000**, *61* (19), 12732–12738.

(37)   Varnavski, O.; Goodson, T. Femtosecond Fluorescence Dynamics and Molecular Interactions in a Water-Soluble Nonlinear Optical Polymeric Dye. *Chem. Phys. Lett.* **2000**, *320* (5–6), 688–696.

275

(38) Varnavski, O.; Samuel, I. D. W.; Palsson, L. O.; Beavington, R.; Burn, P. L.; Goodson, T. Investigations of Excitation Energy Transfer and Intramolecular Interactions in a Nitrogen Corded Distrylbenzene Dendrimer System. *J. Chem. Phys.* **2002**, *116* (20), 8893–8903.

(39) Berera, R.; van Grondelle, R.; Kennis, J. T. M. Ultrafast Transient Absorption Spectroscopy: Principles and Application to Photosynthetic Systems. *Photosynth. Res.* **2009**, *101* (2–3), 105–118.

(40) Ramakrishna, G.; Bhaskar, A.; Goodson, T. Ultrafast Excited State Relaxation Dynamics of Branched Donor-??-Acceptor Chromophore: Evidence of a Charge-Delocalized State. *J. Phys. Chem. B* **2006**, *110* (42), 20872–20878.

(41) Bhaskar, A.; Ramakrishna, G.; Lu, Z.; Twieg, R.; M, J.; Hagan, D. J.; Stryland, E. Van; Goodson, T.; Hales, J. M.; Iii, T. G. Investigation of Two-Photon Absorption Properties in Branched Alkene and Alkyne Chromophores Investigation of Two-Photon Absorption Properties in Branched Alkene and Alkyne Chromophores. **2006**, No. 12, 11840–11849.

(42) Larsen, R. E. Simple Extrapolation Method to Predict the Electronic Structure of Conjugated Polymers from Calculations on Oligomers. *J. Phys. Chem. C* **2016**, *120* (18), 9650–9660.

(43) Chai, J.-D.; Head-Gordon, M. Long-Range Corrected Hybrid Density Functionals with Damped Atom–Atom Dispersion Corrections. *Phys. Chem. Chem. Phys.* **2008**, *10* (44), 6615.

(44) Chai, J. Da; Head-Gordon, M. Systematic Optimization of Long-Range Corrected Hybrid Density Functionals. *J. Chem. Phys.* **2008**, *128* (8).

(45) Körzdörfer, T.; Brédas, J. L. Organic Electronic Materials: Recent Advances in the Dft Description of the Ground and Excited States Using Tuned Range-Separated Hybrid Functionals. *Acc. Chem. Res.* **2014**, *47* (11), 3284–3291.

(46) Zheng, Z.; Brédas, J.-L.; Coropceanu, V. Description of the Charge Transfer States at the Pentacene/C $_{60}$ Interface: Combining Range-Separated Hybrid Functionals with the Polarizable Continuum Model. *J. Phys. Chem. Lett.* **2016**, *7* (13), 2616–2621.

(47) Lange, A. W.; Herbert, J. M. Symmetric versus Asymmetric Discretization of the Integral Equations in Polarizable Continuum Solvation Models. *Chem. Phys. Lett.* **2011**, *509* (1–3), 77–87.

(48) Lange, A. W.; Herbert, J. M. Response to Comment on A Smooth, Nonsingular, and Faithful Discretization Scheme for Polarizable Continuum Models: The Switching/Gaussian Approach' [J. Chem. Phys. 134, 117101 (2011)]. *J. Chem. Phys.* **2011**, *134* (11).

(49) Plasser, F.; Wormit, M.; Dreuw, A. New Tools for the Systematic Analysis and Visualization of Electronic Excitations. I. Formalism. *J. Chem. Phys.* **2014**, *141* (2014), 024106.

(50) Plasser, F.; Bäppler, S. A.; Wormit, M.; Dreuw, A. New Tools for the Systematic Analysis

and Visualization of Electronic Excitations. II. Applications. *J. Chem. Phys.* **2014**, *141* (2014), 024107.

(51) Shao, Y.; Gan, Z.; Epifanovsky, E.; Gilbert, A. T. B.; Wormit, M.; Kussmann, J.; Lange, A. W.; Behn, A.; Deng, J.; Feng, X.; et al. Advances in Molecular Quantum Chemistry Contained in the Q-Chem 4 Program Package. *Mol. Phys.* **2015**, *113* (2), 184–215.

(52) Guo, Y.; Ma, Z.; Niu, X.; Zhang, W.; Tao, M.; Guo, Q.; Wang, Z.; Xia, A. Bridge-Mediated Charge Separation in Isomeric N-Annulated Perylene Diimide Dimers. *J. Am. Chem. Soc.* **2019**, *141* (32), 12789–12796.

(53) Beaujuge, P. M.; Amb, C. M.; Reynolds, J. R. Spectral Engineering in π -Conjugated Polymers Interactions. *Acc. Chem. Res.* **2010**, *43* (11), 1396–1407.

(54) Havinga, E. E.; ten Hoeve, W.; Wynberg, H. Alternate Donor-Acceptor Small-Band-Gap Semiconducting Polymers; Polysquaraines and Polycroconaines. *Synth. Met.* **1993**, *55* (1), 299–306.

(55) Chaudhry, A. R.; Ahmed, R.; Irfan, A.; Muhammad, S.; Shaari, a.; Al-Sehemi, A. G. Influence of Push–Pull Configuration on the Electro-Optical and Charge Transport Properties of Novel Naphtho-Difuran Derivatives: A DFT Study. *RSC Adv.* **2014**, *4* (90), 48876–48887.

(56) Mitsui, C.; Tsuji, H.; Sato, Y.; Nakamura, E. Carbazolyl Benzo[1,2-b:4,5-b']Difuran: An Ambipolar Host Material for Full-Color Organic Light-Emitting Diodes. *Chem. - An Asian J.* **2012**, *7* (6), 1443–1450.

(57) Drobizhev, M.; Stepanenko, Y.; Rebane, A.; Wilson, C. J.; Screen, T. E. O.; Anderson, H. L. Strong Cooperative Enhancement of Two-Photon Absorption in Double-Strand Conjugated Porphyrin Ladder Arrays. *J. Am. Chem. Soc.* **2006**, *128* (38), 12432–12433.

(58) Gryczynski, I.; Kuśba, J.; Bogdanov, V.; Lakowicz, J. R. Quenching of Fluorescence by Light: A New Method to Control the Excited State Lifetimes and Orientations of Fluorophores. *Biophys. J.* **1994**, *66* (1), A237.

(59) Hou, J.; Guo, X. Active Layer Materials for Organic Solar Cells. In *Organic Solar Cells, Green Energy and Technology*; Choy, W. C. H., Ed.; Springer-Verlag London Limited, 2013; pp 17–42.

(60) Bunz, U. H. F. Alpha-Oligofurans: Molecules without a Twist. *Angew. Chemie - Int. Ed.* **2010**, *49* (30), 5037–5040.

(61) Karsten, B. P.; Bouwer, R. K. M.; Hummelen, J. C.; Williams, R. M.; Janssen, R. A. J. Charge Separation and (Triplet) Recombination in Diketopyrrolopyrrole–Fullerene Triads. *Photochem. Photobiol. Sci.* **2010**, *9* (7), 1055.

(62) Williams, R. M.; Chen, H.-C.; Di Nuzzo, D.; Meskers, S. C. J.; Janssen, R. A. J. Ultrafast Charge and Triplet State Formation in Diketopyrrolopyrrole Low Band Gap Polymer/Fullerene Blends: Influence of Nanoscale Morphology of Organic Photovoltaic Materials on Charge Recombination to the Triplet State. *J. Spectrosc.* **2017**, *2017*, 1–16.

(63)   El-Sayed, M. A. The Triplet State: Its Radiative and Nonradiative Properties. *Acc. Chem. Res.* **1968**, *1* (1), 8–16.

(64)   Park, Y. S.; Kale, T. S.; Nam, C.-Y.; Choi, D.; Grubbs, R. B. Effects of Heteroatom Substitution in Conjugated Heterocyclic Compounds on Photovoltaic Performance: From Sulfur to Tellurium. *Chem. Commun. (Camb).* **2014**, 7964–7967.

(65)   Piliego, C.; Holcombe, T. W.; Douglas, J. D.; Woo, C. H.; Beaujuge, P. M.; Fre, J. M. J. Synthetic Control of Structural Order in N -Alkylthieno [3 , 4- c] Pyrrole-4 , 6-Dione-Based Polymers for Efficient Solar Cells. **2010**, 7595–7597.

(66)   Peumans, P.; Yakimov, A.; Forrest, S. R. Small Molecular Weight Organic Thin-Film Photodetectors and Solar Cells. *J. Appl. Phys.* **2003**, *93* (7), 3693–3723.

(67)   Forrest, S. R. The Limits to Organic Photovoltaic Cell Efficiency. **2005**, *30* (January), 28–32.

Chapter 7

Optical and Photophysical Studies of Partially- and Fully-Functionalized Silsesquioxanes

7.1 Original Publication Information

The work in this chapter resulted in three (3) publications:

Jin Zhang, Santy Sulaiman, Ifeanyi K. Madu, Richard M. Laine, and Theodore Goodson III. "Ultrafast Excited State Dynamics of Partially and Fully-Functionalized Silsesquioxanes" *J. Phys. Chem. C*, 2019, 123, 8, 5048–5060.

Jun Guan, Kenji Tomobe, Ifeanyi K. Madu, Theodore Goodson III, Krishnandu Makhal, Minh Tuan Trinh, Stephen C. Rand, Nuttapon Yodsin, Siriporn Jungsuttiwong, Richard M. Laine. *Macromolecules*, 2019, 52, 11, 4008–4019. **&** *Macromolecules*, 2019, 52, 19, 7413–7422.

The first project was started by two previous students in the Goodson group – Jin Zhang (graduated 2013) and Santy Sulaiman (graduated 2011). Ifeanyi K. Madu continued with the study and carried out the steady-state, non-linear and time-resolved spectroscopic measurements, and published the results. This will be the focus of this chapter. Modifications were made to the original publication to adapt it to the style of the content of this dissertation. References of the original manuscript are included in this chapter. For the second and third projects, the synthesis, modeling and magnetic studies was done by the Dr. Laine's team at the University of Michigan. Ifeanyi K. Madu carried out the steady-state and non-linear measurements for the second and third project.

7.2 Abstract

A series of dimethylaminostilbene substituted silsesquioxanes (SQs) – $Me_2NStilbeneSi$ $(OSiMe_3)_3$ {Corner}, $[Me_2NStilbeneSi(O)(OSiMe_3)]_4$ {Half} and $[Me_2NStilbeneSiO_{1.5}]_8$ {Cube}, which contain partially, and fully functionalized cages were investigated by ultrafast fluorescence upconversion and femtosecond transient absorption spectroscopy. These nonlinear techniques were used to study the mechanism of excitation energy transport and excited state dynamics of these functionalized SQ structures. A strong fluorescence lifetime dependence was observed in all three systems. Depolarization of the fluorescence in the Half and Cube systems indicates excitation energy delocalization between the chromophores due to strong electronic coupling. The ultrafast rise time obtained from the upconversion experiment clearly depicts the fast transition taking place in the system after photoexcitation. Transient absorption dynamics and two photon absorption (TPA) measurements reveal the presence of ultrafast charge delocalization in the Half and Cube systems. Blue shifts in the excited state absorption (ESA) observed in all three SQ systems correlate with the solvation process and reveal a solvent-stabilized state. The amount of ESA blue shift indicates an increase in the charge-transfer character of the excited state in the case of the Half and Cube systems. This explains their enhanced two-photon cross sections in comparison to that of the Corner SQ system.

7.3 Introduction

From the time of the original thermal rearrangement by Scott[1] in 1946, polyhedral silsesquioxanes (SQs) have shown significant promise for a number of applications with examples such as nanocomposite materials for dentistry,[2,3] reaction catalyst,[4,5] flame retarded coating,[6] nano-imprinting lithography,[7] and biomedical devices.[8] There is a wide degree of interest in these materials. Cubic SQs, $(RSiO_{1.5})_8$, having a three-dimensional structure with a diameter of 0.53nm, provides eight or even more possible sites for functionalization with organic chromophores.[9] Their electronic and photonic properties can be tuned by tailoring the structures of the chromophores. For this reason, SQ materials incorporating a silica cage as the core and with versatile conjugated chromophores as the shell, have drawn extensive attention as candidates for photovoltaic materials.[9–12] Additionally, SQ hybrids offer special features that make them attractive as organic electronic materials. SQ hybrids are exceptional candidates for developing well-defined, molecular nanobuilding blocks with perfect cubic symmetry. They exhibit excellent solubility in various organic solvents such as tetrahydrofuran (THF), toluene, dioxane, dichloromethane (CH_2Cl_2) and chloroform ($CHCl_3$), and therefore they can be easily purified by standard methods.[13] Most importantly, with eight or even more chromophores in a single molecule, potential electronic coupling among the chromophores could possibly enhance the charge transfer (CT) character of the entire SQ system, and therefore have an impact on the overall solar capture efficiency.

In the past few years, several sets of cubic SQ derivatives with different degrees of functionalization have been synthesized by Laine et al.[14–18] The UV-vis absorption, photoluminescence and two-photon absorption properties of these compounds were investigated. The emission spectrum of one of the cage structures – $[NH_2VinylStilbeneSiO_{1.5}]_8$ shows exceptional red-shifts up to 120 nm. Its excellent two-photon absorption cross-section (up to 810

GM) reveals strong interactions between each substituent chromophore, and may suggest that the silica core serves as an electron acceptor in the system.[15] The photophysical properties and two-photon properties of Corner and Half cage systems, were also studied and compared with the full cage. The results suggest that full cages with perfect symmetry offer better nonlinear properties with the largest two-photon cross sections per chromophore.[16]

There have also been extensive computational studies carried out on the electronic structure, electronic spectra, optical properties and reactivity of T_8 octahedral SQs over the past two decades.[19–24] Phillips et al[21] investigated the absorption excitation energy of functionalized octahedral SQs via time-dependent density functional theory. Using the B3LYP and RSH functional, they found that the excitations are mainly localized on the chromophores, except for vinylsilsesquioxane. Zheng et al.[22] reproduced the experimental results of the absorption and emission spectra of stilbene-functionalized octahedral SQ, by combining time-dependent density functional theory and the Tamm-Dancoff approximation with range-separated hybrid functional of Baer-Neuhauser-Livshits. They also reported that their modeling studies suggest that the emissive state of these octahedral SQs is ligand-to-ligand rather than ligand-to-SQ.[22]

Time-resolved fluorescence upconversion and transient absorption are very powerful experimental tools for the purpose of this study. The time-resolved spectroscopic methods have been applied extensively to study the excited state behavior of many kind of materials including organic macromolecules,[25–28] nanoclusters,[29–32] metallacycles.[33–35] Maya et al[36] studied the nonlinear absorption properties of lead phthalocyanines substituted with siloxane chains using picosecond time-resolved transient absorption. The results suggest that CT through the polysiloxane chain was not observed. Cohen et al[37] reported the femtosecond fluorescence dynamics of a proton-transfer chromophore covalently bonded to the inner surface of amorphous

silica nanoparticles. In these studies, it was reported that an excited state intermolecular proton-transfer process occurs from the chromophore to the silica surface, suggesting the development of nanophotonic devices based on mesoporous silica nano materials. Understanding the mechanism of energy transfer and excited-state CT processes in silica-cage materials, as well as the extent of intramolecular interactions among the chromophores, is crucial in order to make significant improvements of the photophysical properties for their application as organic optoelectronic materials.

Although there are many synthesis and theoretical studies on these classes of materials, reports of the excited-state absorption (ESA) and excited state CT processes of chromophore-substituted SQs have been limited. In this paper, we use nonlinear optical and ultrafast spectroscopy to investigate the excited state dynamics of chromophore-functionalized SQs to ascertain if there is interaction between the substituted chromophores and the silica core in the excited state. We also investigate the fluorescence emission dynamics to study the energy transfer process and fluorescence lifetimes of functionalized SQ systems. For this purpose, corner and half cage systems, and full cubic cages are investigated using ultrafast absorption and emission spectroscopic techniques. The structures of these SQ systems are shown in **Figure 7.1**. Investigations have revealed interesting features in relation to the excited-state dynamics with increase in branching, which are very important in elucidating the mechanism behind the observed trends in the to-photon absorption (TPA) cross-sections of the branched systems.
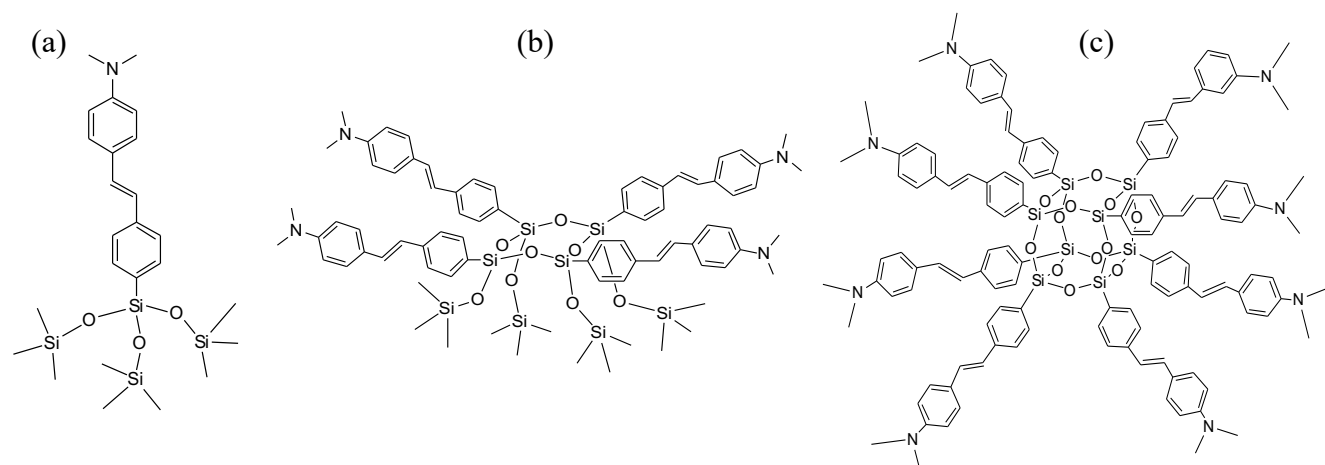
Figure 7.1 Molecular structure of investigated (a) Corner, (b) Half, and (c) Cube SQ systems.

7.4 Experimental Section

To investigate the nonlinear optical and ultrafast spectroscopic properties of these SQs, the fluorescence upconversion and femtosecond transient absorption measurements were carried out. Steady-state absorption and emission measurements, as well as the two-photon absorption cross-section results of these materials have been reported earlier.[16]

7.4.1 Materials

All the investigated compunds were synthesized by Ronchi *et al*,[38,39] and the methods given therein. Tris(trimethylsiloxy)silyldimethylaminostilbene {Corner} and cyclotetra[(trimethyl siloxy)(dimethyl-aminostilbene)]siloxane {Half} were synthesized using the published procedure.[38,39] The synthesis procedure for [Me$_2$NStilbeneSiO$_{1.5}$]$_8$ {Cube} was described previously.[17] All compounds were studied as received without further purification. All the measurements were carried out in THF (Sigma-Aldrich, spectrophotometric grade).

7.4.2 Steady-State Measurements

The absorption spectra were obtained using a Shimadzu UV-1601 absorption spectrophotometer at room temperature. The device was referenced with a spectrophotometric-grade THF, and 1cm quartz cuvettes were used with a concentration range between 10^{-3} and 10^{-4}

M for the samples where the absorption maximum was less than 10%.[16,17] The photoluminescence spectra was obtained using a Fluoromax-2 fluorimeter with the concentration range between 10^{-5} and 10^{-6} M, and the samples were excited at 320 nm. The fluorescence quantum efficiency (Φ_F) of the samples was determined by a comparison method[40,41] using Coumarin 307 [7-Ethylamino-6-methyl-4-trifluoromethylcoumarin] as standard.[16]

7.4.3 Two-Photon Excited Fluorescence (TPEF) Measurements

The two-photon absorption cross-section (TPA-δ) reported in this study was obtained using the two-photon excited fluorescence (TPEF) method as reported in the literature[42,43]. Here, the two-photon excited fluorescence excitation spectra of the samples were compared to that of a reference compound, Coumarin 307 dissolved in methanol, under identical conditions, and at different wavelengths.[16] To confirm the experimental accuracy of this approach, another set of experiments were performed using a different reference compound – rhodamine B dissolved in methanol. The laser used for the study is a Mai Tai diode-pumped mode-locked Ti:sapphire laser. Beam power from the laser was varied using a neutral density filter and focused unto the sample cell (1 cm path, quartz cuvette) using a lens of 11.5 cm focal length and the resultant fluorescence was collected perpendicular to the excitation beam. Another lens (plano-convex) with a focal length of 2.54 cm was used to direct the fluorescence into a monochromator whose output was coupled to a photomultiplier tube (PMT). During each scan, the monochromator was set to the maximum emission wavelength of the sample (where maximum photons are generated), and the photons are converted into counts by a photon-counting unit. A logarithmic plot of the fluorescence signal versus the incident power intensity was performed to confirm if the signal to power intensity relationship is indeed quadratic.

7.4.4 Fluorescence Upconversion Measurements

Time-resolved fluorescence of the Corner, Half, and Cube systems was carried out using femtosecond upconversion spectroscopy. The up-conversion system used in our experiments has been previously described.[27,28,44,45] We have employed a mode-locked Ti-Sapphire laser for the present investigation. The instrument response function (IRF) was obtained from the Raman signal of water and it was found to be around 110fs.[44] The sample cuvette was made with quartz, 1mm thick and held in a rotating holder to avoid possible photo-degradation and other accumulative effects. The gate step size in this system is 6.25 fs. Spectral resolution is achieved by dispersing the up-converted light in a monochromator and detecting the signal using of a PMT (Hamamatsu R1527P). The average excitation power is kept at a level ~ 33 mW. At these excitation intensities, the fluorescence dynamics were found to be independent of the excitation intensity for all investigated solutions. Polarization of the excitation beam for the anisotropy measurements was controlled using a Berek compensator. Horizontally polarized fluorescence emitted from the sample was upconverted in a nonlinear crystal of β-barium borate using the pump beam at 800 nm, which first passed through a variable delay line. Lifetimes were obtained by convoluting the signal with the IRF. Spectral resolution was achieved by using a monochromator and PMT. Under these experimental conditions, the investigated systems are quite stable; no photo-degradation was observed. Anisotropy measurements were obtained from repeating the fluorescence lifetime measurements with parallel excitation and parallel emission ($I_{\parallel}$) and again with perpendicular excitation and parallel emission ($I\perp$). The isotropic (rotation-free) intensity is given by $I(t) = I_{\parallel}(t) + 2I\perp(t)$. Anisotropies as a function of time are then presented as a result of the following relationship, comparing the amplitudes of emission at a given time by $r(t) = \frac{I_{\parallel}(t) - I\perp(t)}{I_{\parallel}(t) + 2I\perp(t)}$ for each sample. Coumarin 30 was used as anisotropy standard and provided a G-factor of 0.95. Data fitting

and deconvolution at less than 10 ps was done using Surface Xplorer software.[26,46] Maximum deconvolution time resolution gives a minimum resolution roughly $1/6^{th}$ of the cross-correlation function, or 30 fs. Data fitting at a longer time scale was performed using Origin 8 software. All emission lifetimes are the result of multiexponential decay fitting. When contributions to total emission are presented for a given relaxation lifetime as a percentage, the percentage is given as a ratio of the separated and deconvoluted integrations for the decay, weighted by the fitted amplitude for each decay and compared to total emission.

7.4.5 Femtosecond Transient Absorption Measurements

Transient absorption measurement was carried out to observe the excited state dynamics of the Corner, Half, and Cube systems. A known procedure for this setup has been described in the literature.[27,28] This system contains 1 mJ, 100 fs pulses at 800 nm with a repetition rate of 1 kHz. The output beam was split to generate pump and probe beam pulses with a beam splitter – 85 and 15% respectively. The pump beam was produced by an optical parametric amplifier (OPA-800C). It was obtained from the fourth harmonic of the signal-idler beams and focused onto a 2 mm quartz cuvette containing the sample. The probe beam was delayed with a computer-controlled motion controller and then focused into a sapphire plate to generate a white light continuum. The white light was then overlapped with the pump beam in the sample cuvette, and the change in absorbance for the signal was collected by a charge-coupled device detector (Ocean Optics). Data acquisition was controlled by specialized software from Ultrafast Systems Inc. The typical power of the probe beam was less than 0.1 μJ, and that of the pump beam was between 0.1 and 0.4 μJ per pulse. Magic angle polarization was maintained between the pump and probe beam using a wave plate. The pulse duration was ~130 fs. The sample was stirred with a rotating magnetic stirrer, and hence no photo degradation of the sample was observed.

7.5 Results and Discussion

7.5.1 Steady State Measurements

According to previous studies,[16,17] steady state absorption and emission spectra of Corner, Half and Cube systems are shown in **Figure 7.2**, and the data are listed in **Table 7.1**. It should be noted that the SQ cage without chromophores has absorption maximum near 224 nm.[47] In comparison, the Cube sample with eight conjugated chromophores attached to the SQ cage, has an absorption maximum at 356 nm. The absorption maximum of the Corner structure (348 nm in THF) is blue shifted with respect to 4-dimethylaminostilbene (DAS) chromophore (365 nm in THF).[48–50] This can be explained by the negative mesomeric effect[51] indicating that there is no lone pair electron available from a saturated Si atom. This steady state absorption result corresponds with the fluorescence decay results discussed below. In the Corner molecule, DAS chromophore is attached with a relatively large group, -Si(OSiMe$_3$)$_3$, through a single bond. The steric hindrance effect reduces the electron mobility through the π-conjugation and therefore the photoisomerization process is retarded. The absorption maxima of the Half and Cube systems are slightly shifted to longer wavelengths in relation to the Corner structure. It may suggest that this shift is due to either mesomeric effect from the half/full cage and/or the dipole-dipole interaction between the DAS chromophores. The emission results of these systems are also listed in **Table 7.1**. The emission maxima of Corner, Half and Cube are at 445, 451 and 459 nm, respectively. The emission spectra of the three systems are dramatically red-shifted with respect to that of single chromophore, 4-DAS (407 nm) due to the loss of energy by non-radiative decay processes.

Studies regarding σ*–π* conjugation between the σ* orbital of the silicon and the π* orbital of the conjugating moiety have been reported.[52–56] On the basis of their ab initio calculations, it has been found that the other substituents on the silicon atom could largely affect the resulting

288

low-lying lowest unoccupied molecular orbital level as well as the highest occupied molecular orbital level not because of perturbation through the σ*–π* conjugation, but by an inductive effect.[52] An increase in electronegativity of substituents on the silicon could induce the bathochromic shift of the absorption maxima to the longer wavelength.[52] According to these previous reports, the red-shift of the Half and Cube systems with respect to the Corner might be an indication that cyclotetrasiloxane (Half SQ) and full Cubic SQ cage have higher electronegativity in comparison to the $Si(OSiMe_3)_3$ group.
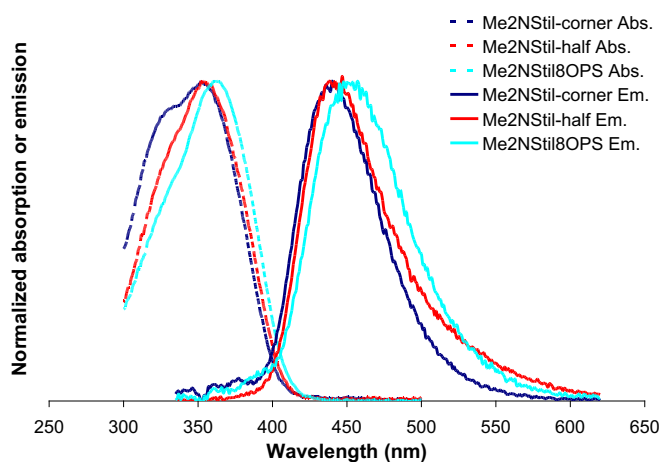
Figure 7.2 Steady-state spectra of the three systems in THF solution.

Table 7.1 Steady state absorption and emission spectra of Corner, Half and Cube SQ systems and single chromophore 4-Dimethylaminostilbene.[16,48]

Sample*	λ_{abs} (nm)	λ_{em} (nm)	E_{stokes} (cm⁻¹)
Corner	348	445	6264
Half	350	451	6398
Cube	356	459	6303
DAS	365	407	2827

*THF is used as solvent.

7.5.2 Two Photon Excited Fluorescence

Two-photon absorption cross-section results, according to previous studies,[16] are listed in **Table 7.2**. With eight chromophores attached, the Cube has the largest two-photon cross section

(211 GM) among these three systems. When considering the two-photon cross section per chromophores, the Cube system also has the largest value (26 GM) among the three. The enhanced two-photon cross section found in the Cube sample suggests a complex interplay between intramolecular interactions and the improvement of CT character. As a result, the SQ cage plays an important role in affecting the overall photophysical properties of attached conjugated chromophores. In order to understand the fundamental process, it would be very interesting to study energy transfer and the excited-state CT processes via time-resolved spectroscopic measurements. In the following sections, we present and discuss the time-resolved fluorescence and excited-state dynamics of the studied systems.

Table 7.2 Two-Photon Cross Section of Corner, Half and Cube SQ systems.[16]

Sample	δ (GM)	δ/chromophore (GM)
Corner	12	12
Half	30	8
Cube	211	26

7.5.3 Fluorescence Upconversion Measurements

The time-resolved fluorescence upconversion technique was applied to measure the fluorescence lifetime of the three systems. The fluorescence up-conversion decay dynamics under 380 nm excitation are shown in **Figure 7.3**. **Figure 7.3a** presents the fluorescence decay curve of the three investigated SQ systems. The fluorescence lifetime fitting was performed on the time-resolved fluorescence curves for the Corner, Half, and Cube SQ systems and their lifetimes (τ) are 146, 73, and 75 ps, respectively; and are shown in **Table 7.3**. Given the quantum yields which are 0.08, 0.09, and 0.03 for Corner, Half, and Cube systems respectively,[16] the radiative and nonradiative rate constants can be calculated, and the results are also shown in **Table 7.3**.
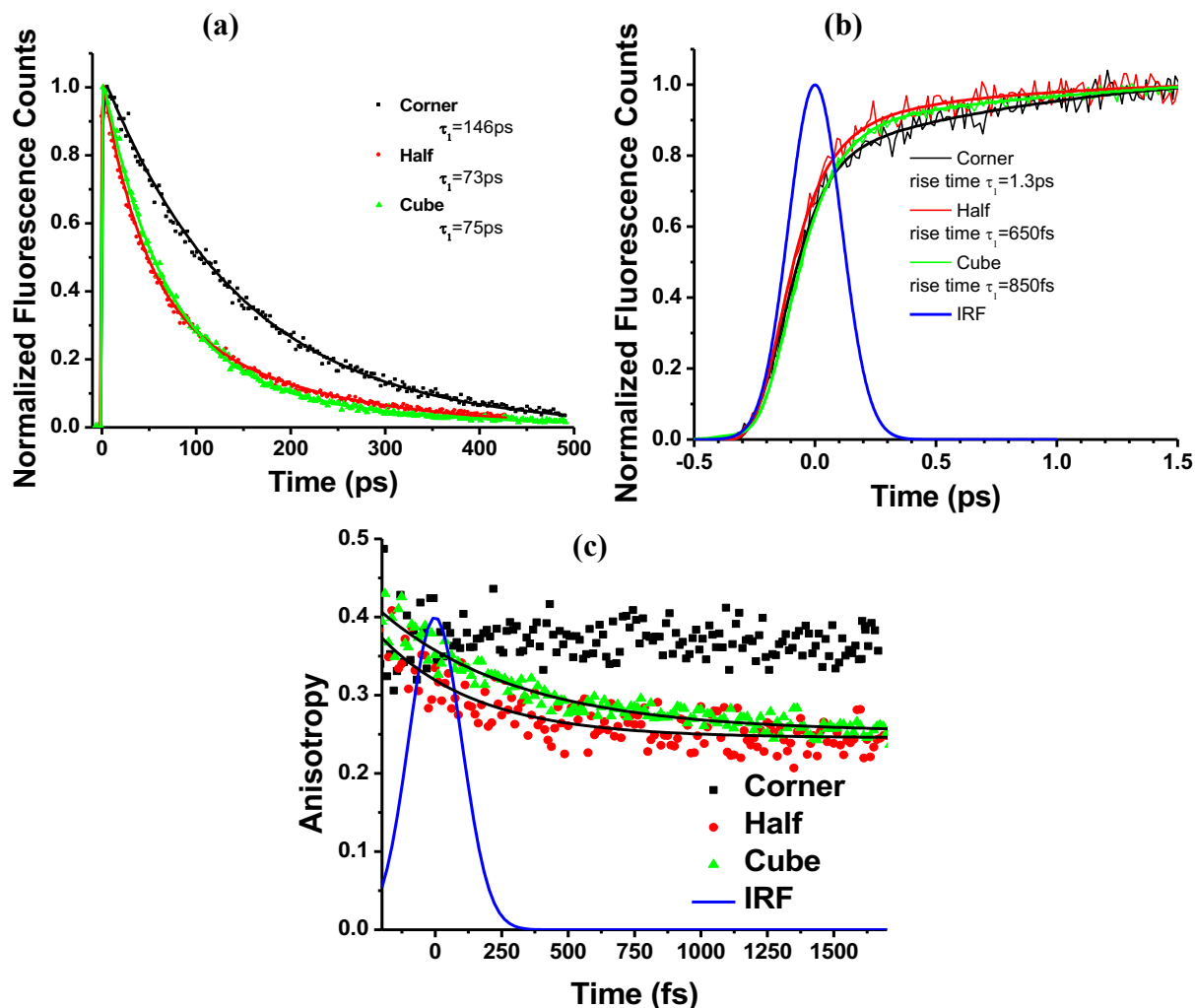
Figure 7.3 Time-resolved femtosecond measurements of Corner (at 445 nm), Half (at 451 nm), and Cube (at 459 nm) SQ systems: (a) fluorescence decay, (b) fluorescence rise time, and (c) fluorescence anisotropy for the investigated systems.

Table 7.3 Quantum Yield (ϕ_F), Fluorescence Lifetimes, Radiative, and Nonradiative Decay Rate Constants of Corner, Half, Cube SQ systems, and trans-Stilbene.

Sample	ϕ_F (-)	rise time/decay time (ps)	k_r (10^7 s^{-1})	k_{nr} (10^8 s^{-1})
Corner	0.08	1.30 / 146	55	63
Half	0.09	0.65 / 73	120	121
Cube	0.03	0.85 / 75	40	129
Trans-stilbene[a]	0.05	- / 108	46	87

[a] Obtained from ref 57

The fluorescence dynamics of the substituted *trans*-Stilbene chromophore itself needs to be taken into consideration. The fluorescence dynamics of *trans*-Stilbene and its derivatives have been studied experimentally and theoretically.[57–66] Similar to donor-acceptor-type *trans*-Stilbene derivatives, possible twisting around single and double bonds is expected as illustrated in **Figure 7.4a**. The main fluorescence state of the donor/acceptor substituted *trans*-Stilbene is the A* state, or a "twisted intramolecular CT" (TICT) state. Here, the phenyl ring twists by $\Phi_s = 90^\circ$ around the single bond starting from a planar geometry.[67] The electronic structure of A* corresponds to a CT state from the donor to the acceptor. The kinetic scheme according to a three-state model[68–70] is presented in **Figure 7.4b**. Here, E* is the primary excited (Franck-Condon) state, and D* is the excited state with a geometry having the phenyl ring twisted by 90° around the double bond that is the double-bond twisted conformation state. There is a competition between the formation of A* and D*. In the trans-planar configuration, an intense intramolecular CT to the S_1 state may result in a significant energy barrier on the S_1 potential energy surface for the trans- to cis-isomerization process.[67] Under these conditions, ultrafast excited state deactivation through the S_1 photochemical funnel is expected. Given that the fluorescence quantum yields of both Corner and *trans*-Stilbene at room temperature are very small, an assumption can be made that $k_{EA} \ll k_{ED}$. Therefore, k_{nr} mainly corresponds to a transition from E*→D*. At room temperature, the typical fluorescence lifetime of *trans*-Stilbene is ~108 ps, involving bond twisting, and the quantum yield is about 0.05.[57,66,71] According to these results, the radiative and non-radiative rate constant of *trans*-Stilbene can be calculated as $k_r = 46 \times 10^7 \, s^{-1}$, and $k_{nr.} = 87 \times 10^8 \, s^{-1}$.

In the case of the Corner SQ molecule, a longer fluorescence lifetime (146 ps) and a slightly slower k_{nr} rate ($63 \times 10^8 \, s^{-1}$) was observed in comparison to the pure *trans*-Stilbene. This is expected if the formation of the principle fluorescence state A* in the Corner is lengthened by

steric hindrance caused by the large substitution (-Si(OSiMe$_3$)$_3$) on the *trans*-Stilbene, as shown in **Figure 7.5**. This result corresponds well with the observed blue shift in the steady-state absorption spectrum of the Corner with respect to the DAS chromophore. In addition, it has been found out that donor/acceptor substitutions with a large dipole moment on *trans*-Stilbene could further stabilize the A* state with respect to D* because the dipole moment of A* is larger than that of D*.[57,66] The difference in the dipole moments expected for A* and D* states is consistent with the observed anomalous solvent polarity dependence of the absorption wavelength maxima.[16,17] In the case of the Corner SQ system, comparing the kinetic rates with *trans*-Stilbene, the slower k$_{nr}$ and similar k$_r$ value suggests that the dipole moment is somewhat in favor of an increasing A* fluorescence state and decreasing D* state. This also corresponds well with quantum yield results of Corner (0.08) and *trans*-Stilbene (0.05). In a previous study, structural equivalence of the Corner and Half systems was investigated as push-pull nonlinear optical chromophores substituted by –NMe$_2$ and [-Si(-O-)$_3$] interacting through a π-conjugated trans stilbene.[39] Ronchi et al found that the –Si(OSiMe$_3$)$_3$ group behaves as an electron-withdrawing group equal to that of a nitro group by a theoretical study. Although –NMe$_2$ is a good electron-donating group, the donor/acceptor substitution pair on the Corner system did not provide a substantial dipole moment. The absorption cross-section ($\sim$2 x 10^{-18} to 10^{-17} cm^2) could also be used in the explanation of the radiative rate constant obtained via the Strickler and Berg model equation. Close agreement between the model results and the radiative rate estimated via time-resolved fluorescence measurements have also been shown for several molecules. Hence, the radiative rate constant obtained in this study via time-resolved measurement and the fluorescence quantum yield, is suitable.

As observed, the fluorescence lifetime of the Half (73 ps) and Cube (75 ps) SQ systems is shorter than that of the Corner system (146 ps). The fluorescence lifetime of the Corner system is much longer than that of *trans*-Stilbene (~108 ps), and this has been explained by the steric hindrance effect caused by the -Si(OSiMe$_3$)$_3$ group. However, because the Half and Cube SQ cages are even bulkier than the -Si(OSiMe$_3$)$_3$ group, twisting around both the single bond (ϕ_S) and double bond (ϕ_D) is considered much more difficult. In addition, for the case of the Half SQ, both k_r and k_{nr} are faster than those of the Corner SQ, which means that the conformational transition to A* and D* states are easier in spite of the steric hindrance effect. It has been found that when a bulky group is substituted on one side of a stilbene chromophore, twisting along its backbone may occur mainly around the single bond which is near the side opposite the bulky group [72] (labelled as ϕ_S in **Figure 7.4a**). Theoretically, in the case of twisting of the N,N-dimethylamino group, the barrier height is as high as about 0.303 eV.[73] Therefore it would be expected to see that both the Half and Cube offer slower radiative and nonradiative rates, as well as longer fluorescence lifetime than those of Corner. However, this argument does not completely correspond with our experimental results. These results might be due the possibility that a stronger dipole moment is formed after excitation to facilitate the twisting processes,[57,66] and the possible $\sigma^*-\pi^*$ conjugation between the Si atom and the DAS chromophore might be stronger in the excited state.[52–56] In the case of the Half and Cube systems, steady state absorption wavelength maxima are shifted to the red in comparison to that of the Corner, and this observation suggests that the electronic transitions are perturbed by the chromophore-chromophore interactions. With more than one chromophore attached to a single macrostructure, the possibility of dipole-dipole coupling between the chromophores increased dramatically. This inter-chromophore interaction and the possible formation of a delocalized/localized state under photo-excitation are discussed below in the

Fluorescence Anisotropy Decay Measurements section. The Cube has a larger number of chromophores attached, and thus allows for a higher probability of excitation energy redistribution. The slower radiative rate observed for the Cube SQ relative to the Half SQ corresponds accurately with the quantum yield (Φ) obtained; the Φ of Cube SQ is one-third that of the Half SQ (same with its radiative rate). On the basis of the fluorescence decay results, it can be concluded that both cyclotetrasiloxane (Half SQ) and full cubic SQ cage exhibit stronger electronegativity in the excited state than in the ground state.

Figure 7.3b presents the initial ultrafast fluorescence rise-time curve for each investigated system within 1.5 ps. Fluorescence rise time data are also listed in Table 7.3. The Corner, Half and Cube SQs display fluorescence rise-times: 1.3 ps, 650 fs and 850 fs respectively, with IRF of 110 fs. The fluorescence rise-time components reveal the initial energy redistribution process to the fluorescence state right after the excitation. It corresponds well to the proposed transition from the primary excited state (E*) to the main fluorescent TICT state (A*) in these three systems.
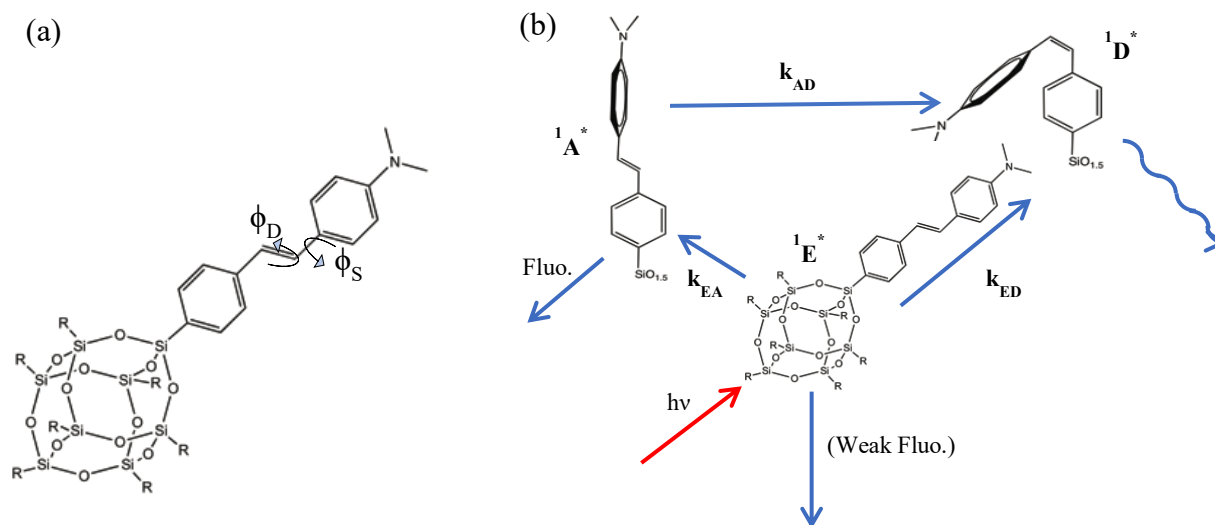
Figure 7.4 (a) Schematic illustration of the twisted single-bond (A*) and twisted double-bond (D*) conformation of the Corner SQ structure (b) three-state kinetic scheme proposed for the interpretation of the photophysical behavior of D-A substituted stilbenes.[68–70]
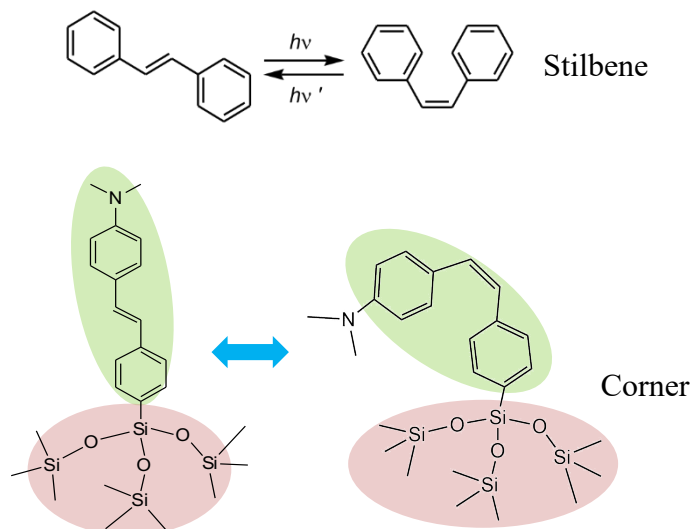
Figure 7.5 Photoisomerization processes in stilbene and the Corner SQ system.

7.5.4 Fluorescence Anisotropy Decay Measurements

The decay of the fluorescence anisotropy is used to characterize the electronic interaction strength and excitation energy transfer (exciton or hopping dynamics) among chromophores, which are mainly reflective of the first few steps of energy transfer.[74–76] Exciton migration via intermolecular excitation transfer in macromolecules with a high degree of symmetry has been studied both experimentally and theoretically.[44,77–80] Kopelman et al[79,80] demonstrated the correlation between the molecular geometry and the electronic properties on a series of dendrimer based on phenylacetylene chromophores. The efficient and unidirectional energy transfer from an initially excited state on a phenylacetylene dendrimer to a trap located at its core has been found. Others have reported the study on excitation energy transfer in different dendritic core branched structures.[44,78] In these systems, both Förster-type hopping and excitonic-type coherent transport mechanism are observed depending on the different architectures. Wynne and Hochstrasser[81] examined the coherent-type energy transfer between identical molecules by the anisotropy associated with degenerate intermediate states. The chromophore-chromophore coupling causes the excitation energy transfer between the two chromophores by the Coulomb interaction of the

electrons of the two molecules. Theoretically, the efficiency can be determined by transition density, orientation, and spatial location of the two chromophores.[82]

The fluorescence anisotropy decay curves are illustrated in **Figure 7.3c**. The initial anisotropy decay profile before rotational diffusion was studied. The decay dynamics of the Half and Cube systems are different than what is observed for the Corner (as monomer). The Corner shows no significant anisotropy decay during this experimental time window. A depolarization of fluorescence in the Half and Cube in comparison to the Corner system indicate that electronic energy transfer takes place between the chromophores within the molecule. The initial dynamics of fluorescence anisotropy of the Half and Cube systems are very fast and compete with the IRF. Therefore, a deconvolution process is performed in order to estimate the fluorescence anisotropy decay time.[83] The anisotropy decay of the Half SQ system can be fitted by a mono-exponential decay with the decay time constant of 420 fs. The anisotropy decay time was found to be 525 fs for the Cube. In the case of the Half and Cube, the fast fluorescence anisotropy decay provides clear evidence of the interactions among the DAS chromophores.[78] This result obtained strongly corresponds to the fast rise time component obtained in the fluorescence upconversion measurements shown in **Table 7.3**. In this excitonic regime, the interaction (J) between the chromophores is much larger than the homogeneous line width (Γ). Under this condition, nonequilibrium initial preparation effects must be applied with inhomogeneous broadening terms.[76] As a result, the weak interaction limit (Föster limit), which was used for interpretation by a small perturbation, could not be applicable for the intramolecular chromophores energy migration.[76,84] Therefore, in our case, the presence of ultra-fast decay time components in both Half (420 fs) and Cube (525 fs) systems suggests the substantial contribution of coherent-type

energy migration.[25,44] The excitation energy transfer process is accompanied by the reorientation of the transition dipole moment.

The residual value of the fluorescence anisotropy before rotational diffusion also contains information of the arrangement of transition dipole moments and gives the molecular geometry information. In general, the initial anisotropy value is 0.4 for a randomly oriented single chromophore. For some symmetrical molecular systems, the initial anisotropy is larger than 0.4.[81,85] The Cube system with perfect symmetry can be considered as a spherical-like structure before excitation with the initial anisotropy value 0.4, which means that molecules are more randomly orientated in the solution. The residual anisotropy for the equilibrated system is another important parameter related to the geometry of the molecular system. The Cube and Half structures make an average angle between absorption and emission transition dipoles of the chromophores that is different from that of the Corner. Hence, it alters the residual value of the fluorescence anisotropy before rotational diffusion.

7.5.5 Time-Resolved Transient Absorption Measurements

Many of the molecular photochemical and photophysical properties depend on the kinetics of excited-state processes that occur after the absorption of a photon. Therefore, femtosecond transient absorption measurements have been carried out under a 330 nm excitation in order to understand the fundamental mechanism of the excitation delocalization, charge localization process and the extent of CT character in these systems. The detection window of our apparatus is from 450 to 750 nm.

Figures 7.6-7.8 show the transient absorption spectra at different time delays for the Corner, Half, and Cube in THF, respectively. The transient absorption features of the Corner, Half, and Cube SQs look similar in the region of 450 to 750 nm with a positive absorption below 650

nm and a maximum around 525 nm. The positive absorption is due to the excited singlet state ($S_n \leftarrow S_1$) absorption. The spectra also show very weak negative absorptions below 475 nm. These samples absorb strongly below 365 nm, and the fluorescence spectrum has a strong emission band with maxima at 445, 451, and 459 nm for Corner, Half, and Cube SQs, respectively. According to the steady state photophysical properties and previous ultrafast pump-probe studies on push-pull stilbene, these negative absorptions can be ascribed to the simulated emission (SE) originated from the S_1 state.[73] Owing to the limitation of our apparatus, only the shoulder of the SE in each spectrum was observed. The spectra of these three systems also show a broad but relatively weak ESA band in the 675 – 750 nm region, as presented in **Figures 7.6b – 7.8b**. Because both the decreasing of the SE band population below 475 nm region and the increasing of ESA band population in the 675-750 nm region are observed, the ESA band with the maximum at ~ 735 nm is assigned to the excited triplet state transition $T_1 \leftarrow S_1$, according to previous reports.[72,73] Another interesting finding from the **Figures 7.6b – 7.8b** is that the maxima of the ESA band in the 470 - 650 nm region shows a blue shift mainly within the first 7 ps delay time. This time dependence of dynamic shift on the maxima of the ESA band suggests the transition between two distinctly different excited states. The resulting state is ascribed to the TICT state, accompanied by the twisting around a σ bond in the *trans*-Stilbene close to either the electron donating or withdrawing substituent, to populate the TICT state.[72,73,86]

The transient dynamics at the ESA peak maxima are plotted in **Figure 7.9**. In order to quantitatively estimate the lifetimes associated with the different relaxation processes, exponential fitting functions were used to fit the kinetic curves at the probe wavelength of 550 nm. The lifetime components are listed in **Table 7.4**. Trifluoroaminostilbene (CF_3stilbeneNH_2) is also measured as a model compound for comparison. The first decay component is 1.4 ps for the Corner, 2.5 ps for

the Half, 1.6 ps for the Cube, and 2 ps for the model compound. This component could be assigned to the vibrational relaxation or the solvent relaxation in a locally excited singlet (S_1) state, which is the LE (S_1) state. The second lifetime component – 166 ps for the Corner, 58 ps for the Half, 75 ps for the Cube, and 32 ps for model compound is ascribed to the conformational relaxation process of stilbene involving the rotation around the single bond and the lifetime of the S_1 state, as suggested by the previous reports.[73,87] In the case of the Corner, the longer lifetime component 166 ps is larger than that of the *trans*-Stilbene ~100 ps,[57,66] and even larger than that of the push-pull stilbene model compound (32 ps). This is due to the retardation of the cis-trans isomerization process caused by the steric hindrance effect of the large substituted group in Corner. It is worth noting that the transient lifetime components are in accordance with the fluorescence lifetime results. As a result, these evidences suggest the conversion from the vibrational relaxed LE (S_1) to another lower energy state which is the TICT state (A* as shown earlier). Similar excited states transitions of push-pull stilbenes have been reported recently.[73] In addition, this transition is also associated with the blue shift of the absorption maxima of the ESA band from 475nm to 650nm.
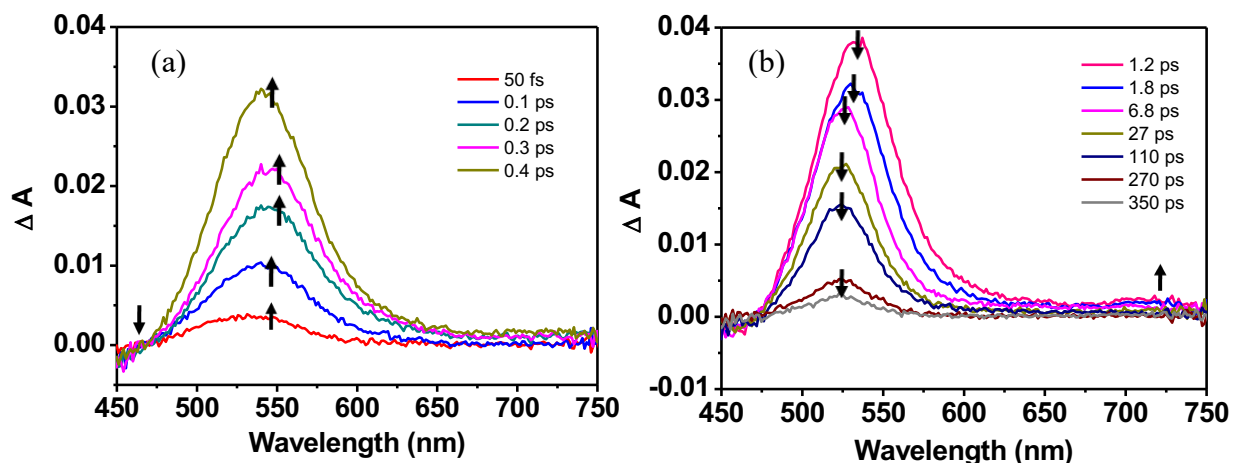
Figure 7.6 Femtosecond Transient absorption spectra of the Corner SQ at (a) time delays before 1.2 ps, and (b) time delays between 1.2 and 350 ps.
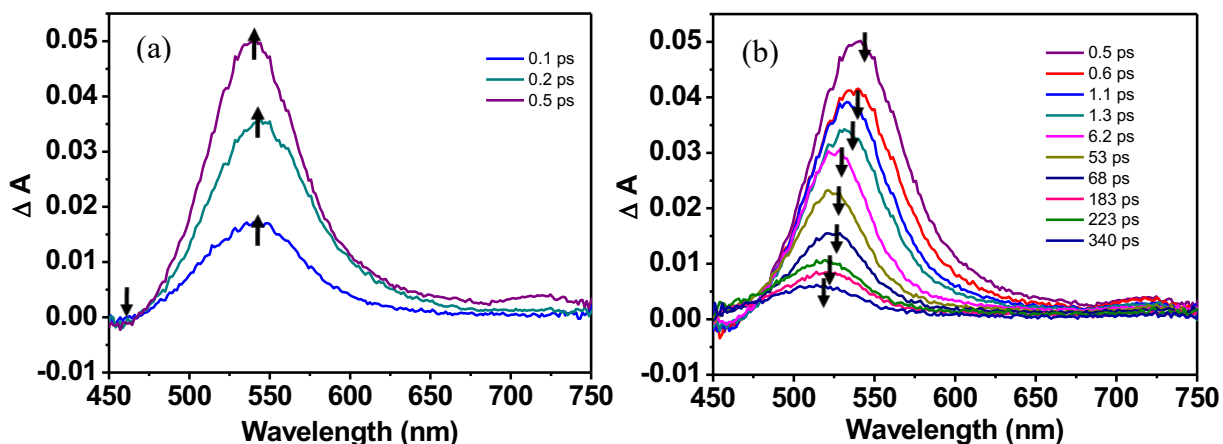
Figure 7.7 Femtosecond transient absorption spectra of the Half SQ at (a) time delays before 0.5 ps, and (b) time delays between 0.5 and 340 ps.
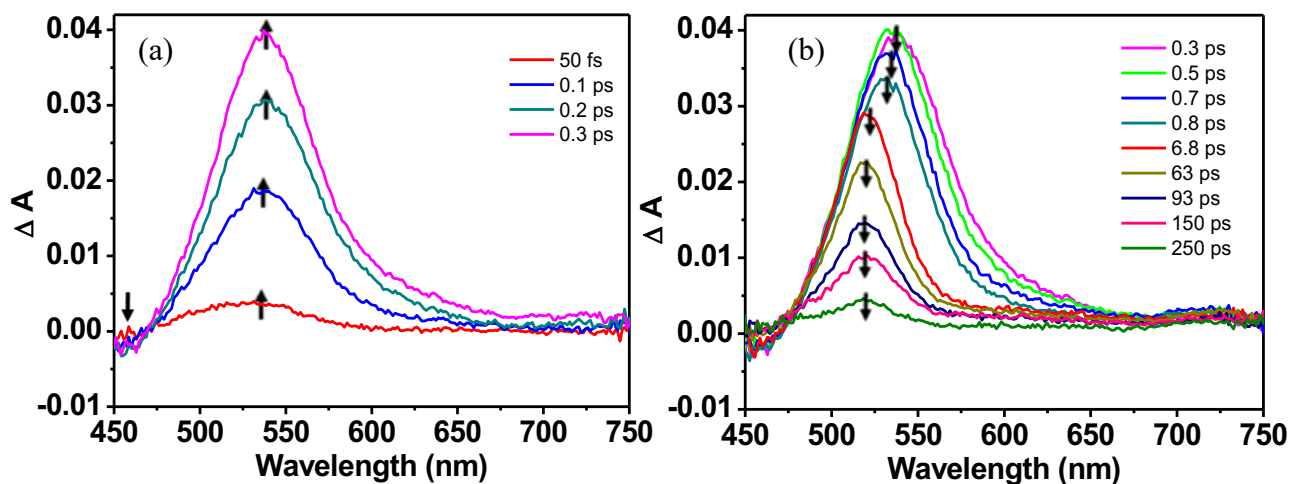
Figure 7.8 Femtosecond transient absorption spectra of the Cube SQ at (a) time delays before 0.3 ps and (b) time delays between 0.3 and 250 ps.
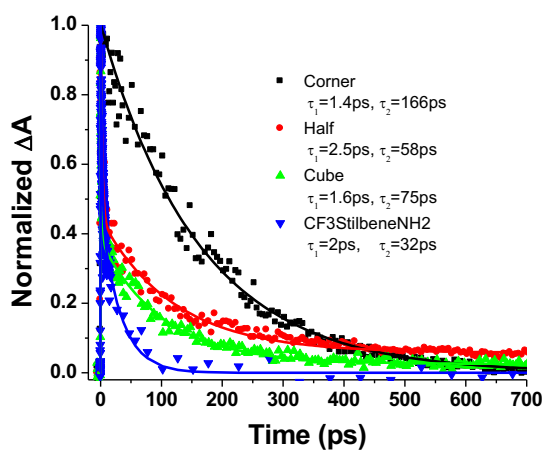
Figure 7.9 Transient absorption kinetics of Corner, Half and Cube and model compound CF$_3$stilbeneNH$_2$ at target wavelength 550 nm.

Further examination on the CT state (TICT) is performed. **Figure 7.10** presents the dynamics providing evidence for the formation of the TICT state of each system. The probe wavelengths are 467 nm for the Corner, 470 nm for the Half, and 469 nm for the Cube, which are at the left shoulder of the ESA band assigned to the $S_n \leftarrow S_1$ transition of the solvent stabilized TICT state of the push-pull stilbene system (TICT′).[72] It is very clear that the excited dynamics of the Corner is under a different mechanism in comparison with the Half and Cube. The fitted lifetime components are listed in **Table 7.4**. In the case of the Corner SQ, the ESA undergoes a decay process with a lifetime of 170 ps after an ultrafast transition within the initial 350 fs. This decay process indicates a nonradiative relaxation process back to the ground state. In contrast to the Corner, a growth in the amplitude is observed after the formation of this TICT′ state in both the Half and Cube, within 16 and 3.5 ps, respectively. It suggests that a solvent stabilized long-lived CT state is favored in the case of Half and Cube. Upon photoexcitation, transient absorption measurements have shown the presence of a CT (TICT) state depending on the number of chromophores. The results point to the ultrafast delocalization of charge in this particular system.

As mentioned earlier, the time dependent dynamic blue shift of the maxima of the ESA band in the 470 - 650nm region was observed within the initial timeframe (several picoseconds). The ESA maxima shifts for each sample at different time delay are listed in **Table 7.5**. It has been reported that in the non-substituted *trans*-Stilbene, the ultrafast transient shifts to the blue within a few picoseconds, and this is interpreted as the formation of an intermediate state before isomerization.[88–90] In addition, a red shift, as a result of the solvation effect, was observed from time-resolved emission spectra of push-pull stilbene derivatives,[50] indicating that the excited state energy level is lowered by vibrational coupling. The shift of maximum wavelength of emission spectra of 15–20 nm is observed within the first few hundred picoseconds delay time after the

excitation. In our case, a spectral blue-shift in transient absorption is more likely a combination of solvation and conformational relaxation along the potential energy surface associated with the CT process. Because the conversion from the LE (S_1) to TICT state upon excitation is extremely fast, there is no significant change in the geometry of the central double bond in the DAS chromophore. In this CT state, the character of the stilbene central double bond acts more like a single bond and facilitates the torsional motion hence resulting in a stronger dipole moment.[91] As a result, this conformation could assist the CT process so as to reinforce the electrostatic interaction. Another process between solvent and chromophores is required to further stabilize the twisting geometry. The interactions between the chromophore(s) and the surrounding solvent molecules are different in each excited electronic state. This change in interaction can originate because of different dipole moments in these two states. A solvent stabilized *relaxed* intramolecular CT state (TICT') is reached after the solvation shell is in thermodynamic equilibrium with the molecule. In order to further study the effects of solvation, femtosecond transient absorption measurements of the Cube SQ in dimethyl sulfoxide (DMSO) – a more polar solvent – was carried out. The transient absorption spectrum of the Cube SQ in DMSO is shown in **Figure 7.11**. The time dependent dynamic blue shift of the ESA maxima is from 540 to 511 nm, which is 7 nm more than the shift obtained using THF as solvent. In addition, a new transient band was observed from 600 to 675 nm. This transient band is assigned to conversion from the vibrational relaxed LE S_1 state to the S_n state.[73] In the transient absorption spectrum of the Cube SQ in THF, this ESA band was overlapped with the ESA band from 450 and 600 nm, as shown in **Figure 7.8b**. These evidences thus support the fact that some observed time-dependent dynamics might be due to solvation. It is also observed from **Figure 7.11** that the SE negative absorption band below 480nm region was vanishing along with the formation of TICT'. It gives the evidence supporting the claim that the

resulting solvent stabilized TICT' state is a non-emissive state. In the theoretical consideration, the solvent-controlled non-adiabatic CT rate is expressed by the following equation:[92]

$$k_{CT} = \frac{4\pi^2}{h} V_{el}^2 \left(\frac{1}{4\pi\lambda k_B T}\right)^{1/2} exp\left(-\frac{\Delta G^*}{k_B T}\right) \qquad \textbf{Equation 7.1}$$

Where, V_{el} is the electronic coupling matrix element, λ is the solvent reorganization and internal reorganization energy (i.e. $\lambda = \lambda_s + \lambda_i$), k_B is the Boltzmann constant, ΔG^* is the barrier to CT, and h is Planck's constant. According to the Born-Hush equation:[94,95]

$$\lambda_s = \frac{e^2}{4\pi\varepsilon_0} \left[\frac{1}{2}\left(\frac{1}{r^+} + \frac{1}{r^-}\right) - \frac{1}{R_{cc}}\right]\left(\frac{1}{\eta^2} - \frac{1}{\varepsilon_r}\right) \qquad \textbf{Equation 7.2}$$

Here, η is the refractive index of the solvent, r^+ and r^- are the ionic-radii of the charged molecules, R_{cc} is the center-to-center distance of the photogenerated charges, and ε_r is the relative dielectric constant of the solvent. According to Marcus theory, the barrier of the CT process, ΔG^* is related to the change in free energy for the CT state via the following expression:[93]

$$\Delta G^* = \frac{(\Delta G_0 + \lambda)^2}{4\lambda} \qquad \textbf{Equation 7.3}$$

Here, ΔG_0 is the energy gap between the reactant and product states. In our case, ΔG_0 is related to the blue shift observed in the transient absorption ESA band. A stronger CT character in the product states could actually decease the energy gap ΔG_0 (more negative), and this leads to a decrease of the activation energy barrier. Therefore, charge transfer rate is optimized when the reorganization energy equals the change of free energy ($\lambda = -\Delta G_0$). According to **Eq. 7.2**, λ_s is dependent on the geometry of the molecule, and the distance between the chromophore and the center core.

It has been well established that photoexcitation drives the linear push-pull stilbene derivatives into the CT state.[73,91] Fully charge separated TICT states have been found in the push-

pull type stilbene derivatives.[94] The formation of the photoinduced CT state of a similar chromophore, 4-dimethylamino,4'-cyanostilbene has been investigated theoretically by the free energy decomposition analysis.[91] Two important factors affecting the stable CT geometry of push-pull stilbenes have been found: (1) the torsional motion of the single bond linkage between the stilbene and its substituted functional groups, and (2) the electrostatic interaction, which is enhanced by twisting geometrically assisted charge separation process.[91] The photoexcitation process of branched multichromophore shell-core systems have been investigated both experimentally and theoretically.[44,95–97] It has been found that the photoexcitation produces a CT state and the excitation is actually localized on one of the chromophores.[44,95–97] In our systems, **Table 7.5** lists the amount of shifts of the ESA peak in wavenumber (Δv) for each system. This value is a strong indication of the extent of the CT character. A greater amount of CT observed in the case of the Cube and Half SQs (720 and 750 cm^{-1} respectively) when compared to the Corner SQ (250 cm^{-1}) suggests that the charge is more in favor of the entire molecule than localized on one arm of the chromophore. This result is in accordance with the dynamics presented in **Figure 7.10**. A similar increase (by more than a factor of 2) of CT character with an increasing number of chromophores has been found in the core-branched systems.[98,99]

Therefore, the strength of the non-emissive TICT′ excited state is increased with the increasing number of the chromophores, which was roughly predicted by the steady-state stokes shift measurements. These results correspond well with the two-photon absorption results; that the TPA cross section is enhanced with an increasing number of chromophores in the Half and Cube systems in comparison with the Corner. In addition, the acceptor strength is also crucial in affecting the population of the CT state. Mattori et al [100] reported computational results on the trapping and the release transition states (TS) of atomic hydrogen in an octasilsesquioxane cage. The stronger

CT state found in the Half and Cube might be an indication that Half and full SQ cages have better electron accepting ability than the Corner as an electron trapper.

Based on the observations above, a simplified energy diagram of our investigated system is drawn in **Figure 7.12**. After photoexcitation, the molecule reaches the main emissive TICT state within subpicoseconds. The fluorescence emission process takes about 146, 73, and 75 ps for Corner, Half, and Cube, respectively. A further solvent stabilized CT TICT' state is reached with a long lifetime for Half and Cube. Intersystem crossing to the dark state is observed after few tens of picoseconds time delay.

Table 7.4 Transient Absorption Lifetime Kinetic Components at Probe Wavelengths 550nm and ca. 470nm

SQs	Lifetime at 550 nm (ps)	Lifetime at ca. 470 nm (ps)
Corner	1.4 / 166	0.35 / 170
Half	2.5 / 58	16.0 / 70, long
Cube	1.6 / 75	3.5 / 70, long
CF$_3$-Stilbene-NH$_2$	2.0 / 32	-
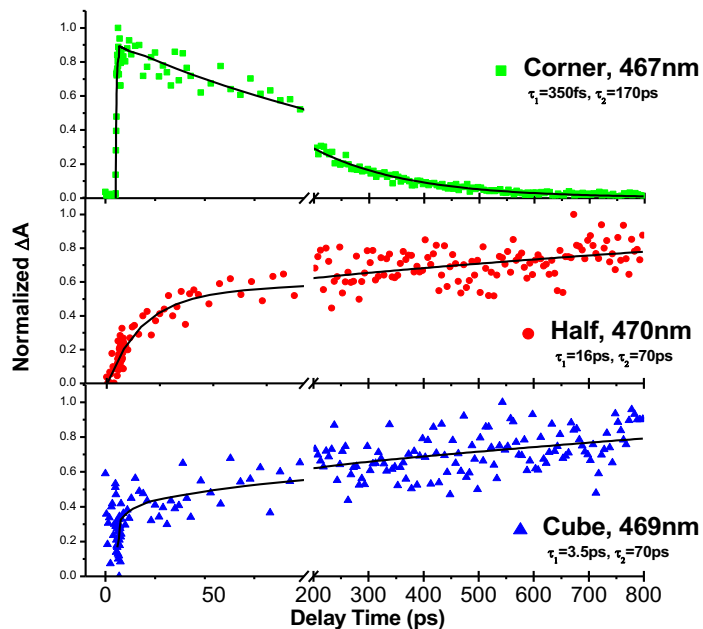
Figure 7.10 Transient absorption kinetics of the Corner SQ at 467nm, the Half at 470nm and Cube at 469nm.

Table 7.5 Details of the Time-Dependent Dynamic ESA Blue shift.[a]

Sample	ESA peak maximum		ESA peak maximum		Shift $\Delta\nu$ (cm^{-1})
	λ (nm)	Delay (ps)	λ (nm)	Delay (ps)	
Corner	532	1.2	525	6.8	250
Half	540	0.5	519	6.2	750
Cube	538	0.3	518	6.8	720

[a]ESA band maxima of Corner, Half and Cube at different delay times in the 470 -650 nm region.
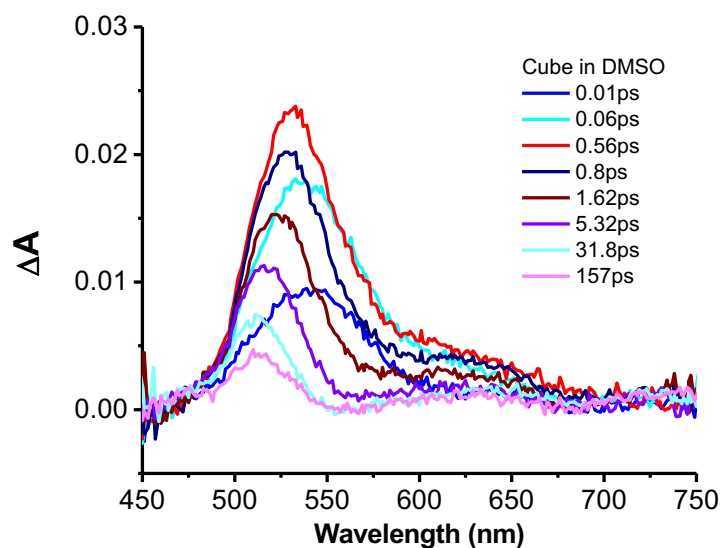
Figure 7.11 Femtosecond transient absorption spectrum of the Cube SQ in DMSO.
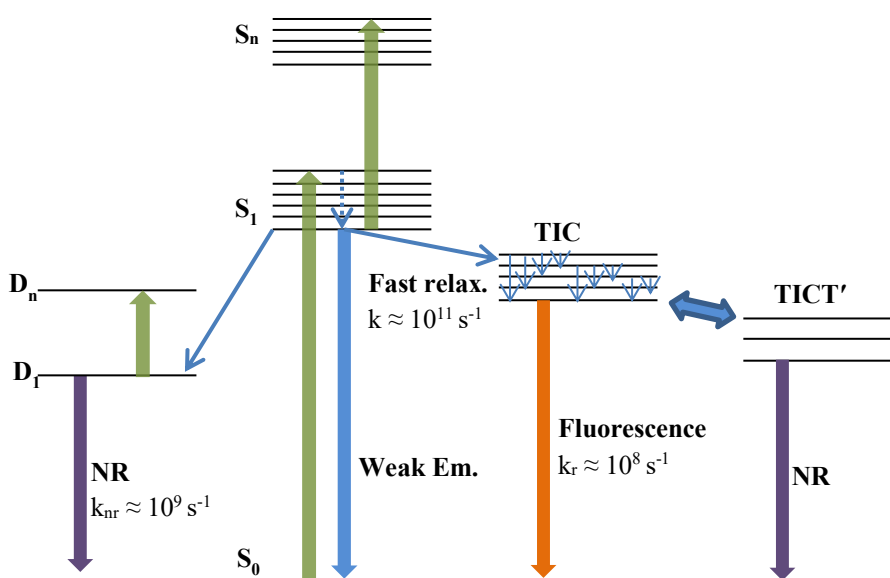
Figure 7.12 Simplified schematic energy diagram of investigated systems.

7.6 Conclusions

In summary, a series of dimethylaminostilbene-substituted SQs with partial and full cages has been investigated by steady-state measurements, time-resolved fluorescence up-conversion and femtosecond transient absorption measurements. Fluorescence upconversion measurements provide an insight into the energy transfer process in these three systems. The kinetics obtained indicate that the twisting around the double bond of the substituted stilbene chromophore is more sensitive to the degree of its dipole moment than the size of its substitutes. The Corner SQ yielded a longer fluorescence lifetime compared to the lifetime of the Half and Cube SQs, by a factor of 2. In the case of the Corner SQ, the twisting is retarded by the steric hindrance effect compared to free stilbene chromophore. In the case of the Half and Cube SQs, strong dipole moments are induced by the substitution which could facilitate the twisting process, overcome the steric hindrance effect and decrease the fluorescence lifetime. The excited state dynamics obtained by the transient absorption measurement show significant differences between the Corner and the Half and Cube SQs. The pump-probe measurements have shown the presence of a TICT state in the ~500 - 600 nm region. The lifetimes of this TICT state corresponds well with fluorescence lifetimes for each system. The transient absorption results also reveal a combination of CT dynamics – mostly due to the conformational twisting of the chromophore – and solvation processes associated with excited-state absorption blue shifts, and a resulting solvent stabilized non-emissive TICT' state. Ultrafast transient measurements have shown an interesting trend with respect to the amount of CT character with increasing number of chromophores. Both Half and Cube SQs show enhanced CT character compared to the Corner SQ. In addition, this explains the enhanced two-photon absorption cross sections found in the Half and Cube systems. Upon photoexcitation, transient absorption measurements have shown the presence of a CT (TICT) state

depending on the number of chromophores, suggesting the ultrafast delocalization of charge in Half and Cube systems. It can be inferred that the increased CT character, observed by the TPA cross section and transient absorption measurement, might be associated with the degree of excited state symmetry breaking observed in the stilbene chromophore (due to enhanced twisting around the single and double bonds). A poor CT character observed in the Corner SQ system might be due to the reduced twisting, hence maintained-symmetry, in the chromophore backbone owing to increased steric hindrance by the tris(trimethylsiloxy)silyl unit.

References

(1)   Scott, D. W. Thermal Rearrangement of Branched-Chain Methylpolysiloxanes. *J. Am. Chem. Soc.* **1946**, *68* (3), 356–358.

(2)   Gao, F.; Tong, Y.; Schricker, S. R.; Culbertson, B. M. Evaluation of Neat Resins Based on Methacryplates Modified with Methacryl-POSS, as Potential Organic-Inorganic Hybrids for Formulating Dental Restoratives. *Polym. Adv. Technol.* **2001**, *12* (6), 355–360.

(3)   Fong, H.; Dickens, S. H.; Flaim, G. M. Evaluation of Dental Restorative Composites Containing Polyhedral Oligomeric Silsesquioxane Methacrylate. *Dent. Mater.* **2005**, *21* (6), 520–529.

(4)   Pescarmona, P. P.; Waal, J. C. Van Der; Maxwell, I. E.; Maschmeyer, T. COMMUNICATIONS A New , Efficient Route to Titanium-Silsesquioxane Epoxidation Catalysts Developed by Using High-Speed Experimentation Techniques. *Communications* **2001**, No. 4, 740–743.

(5)   Carniato, F.; Bisio, C.; Boccaleri, E.; Guidotti, M.; Gavrilova, E.; Marchese, L. Titanosilsesquioxane Anchored on Mesoporous Silicas: A Novel Approach for the Preparation of Heterogeneous Catalysts for Selective Oxidations. *Chem. - A Eur. J.* **2008**, *14* (27), 8098–8101.

(6)   Devaux, E.; Rochery, M.; Bourbigot, S. Polyurethane / Clay and Polyurethane / POSS Nanocom- Posites as Flame Retarded Coating for Polyester and Cotton Fabrics. *Fire Mater.* **2002**, *154* (February), 149–154.

(7)   Ro, H. W.; Popova, V.; Chen, L.; Forster, A. M.; Ding, Y.; Alvine, K. J.; Krug, D. J.; Laine, R. M.; Soles, C. L. Cubic Silsesquioxanes as a Green, High-Performance Mold Material for Nanoimprint Lithography. *Adv. Mater.* **2011**, *23* (3), 414–420.

(8)   Kannan, R. Y.; Salacinski, H. J.; Butler, P. E.; Seifalian, A. M. Polyhedral Oligomeric Silsesquioxane Nanocomposites: The next Generation Material for Biomedical Applications. *Acc. Chem. Res.* **2005**, *38* (11), 879–884.

(9)   Laine, R. M. Nanobuilding Blocks Based on the [OSiO1.5]x (x = 6, 8, 10) Octasilsesquioxanes. *J. Mater. Chem.* **2005**, *15* (35–36), 3725–3744.

(10)   Chan, K. L.; Sonar, P.; Sellinger, A. Cubic Silsesquioxanes for Use in Solution Processable Organic Light Emitting Diodes (OLED). *J. Mater. Chem.* **2009**, *19* (48), 9103–9120.

(11)   Lo, M. Y.; Ueno, K.; Tanabe, H.; Sellinger, A. Silsesquioxane-Based Nanocomposite Dendrimers with Photo-Luminescent and Charge Transport Properties. *Chem. Rec.* **2006**, *6* (3), 157–168.

(12)   Sellinger, A.; Laine, R. M. (12) United States Patent, 2003.

(13)   Brick, C. M.; Tamaki, R.; Kim, S. G.; Asuncion, M. Z.; Roll, M.; Nemoto, T.; Ouchi, Y.; Chujo, Y.; Laine, R. M. Spherical, Polyfunctional Molecules Using Poly(Bromophenylsilsesquioxane)s as Nanoconstruction Sites. *Macromolecules* **2005**, *38*

(11), 4655–4660.

(14)   Asuncion, M. Z.; Laine, R. M. Fluoride Rearrangement Reactions of Polyphenyl- and Polyvinylsilsesquioxanes as a Facile Route to Mixed Functional Phenyl , Vinyl T 10 and T 12 Silsesquioxanes. *J. Am. Chem. Soc.* **2010**, *132*, 3723–3736.

(15)   Hwan Jung, J.; Furgal, J. C.; Goodson, T.; Mizumo, T.; Schwartz, M.; Chou, K.; Vonet, J. F.; Laine, R. M. 3-D Molecular Mixtures of Catalytically Functionalized [VinylSiO1.5]10/[VinylSiO1.5]12. Photophysical Characterization of Second Generation Derivatives. *Chem. Mater.* **2012**, *24* (10), 1883–1895.

(16)   Laine, R. M.; Sulaiman, S.; Brick, C.; Roll, M.; Tamaki, R.; Asuncion, M. Z.; Neurock, M.; Filhol, J. S.; Lee, C. Y.; Zhang, J.; et al. Synthesis and Photophysical Properties of Stilbeneoctasilsesquioxanes. Emission Behavior Coupled with Theoretical Modeling Studies Suggest a 3-D Excited State Involving the Silica Core. *J. Am. Chem. Soc.* **2010**, *132* (11), 3708–3722.

(17)   Sulaiman, S.; Bhaskar, A.; Zhang, J.; Guda, R.; Goodson, T.; Laine, R. M. Molecules with Perfect Cubic Symmetry as Nanobuilding Blocks for 3-D Assemblies. Elaboration of Octavinylsilsesquioxane. Unusual Luminescence Shifts May Indicate Extended Conjugation Involving the Silsesquioxane Core. *Chem. Mater.* **2008**, *20* (17), 5563–5573.

(18)   Sulaiman, S.; Zhang, J.; Goodson, T.; Laine, R. M. Synthesis, Characterization and Photophysical Properties of Polyfunctional Phenylsilsesquioxanes: [O-RPhSiO1.5]8, [2,5-R2PhSiO1.5]8, and [R3PhSiO1.5]8. Compounds with the Highest Number of Functional Units/Unit Volume. *J. Mater. Chem.* **2011**, *21* (30), 11177–11187.

(19)   Lin, T. T.; He, C. B.; Xiao, Y. Theoretical Studies of Monosubstituted and Higher Phenyl-Substituted Octahydrosilsesquioxanes. *J. Phys. Chem. B* **2003**, *107* (50), 13788–13792.

(20)   Xiang, K.-H.; Pandey, R.; Pernisz, U. C.; Freeman, C. Theoretical Study of Structural and Electronic Properties of H-Silsesquioxanes. *J. Phys. Chem. B* **1998**, *102* (44), 8704–8711.

(21)   Phillips, H.; Zheng, S.; Hyla, A.; Laine, R.; Goodson, T.; Geva, E.; Dunietz, B. D. Ab Initio Calculation of the Electronic Absorption of Functionalized Octahedral Silsesquioxanes via Time-Dependent Density Functional Theory with Range-Separated Hybrid Functionals. *J. Phys. Chem. A* **2012**, *116* (4), 1137–1145.

(22)   Zheng, S.; Phillips, H.; Geva, E.; Dunietz, B. D. Ab Initio Study of the Emissive Charge-Transfer States of Solvated Chromophore-Functionalized Silsesquioxanes. *J. Am. Chem. Soc.* **2012**, *134* (16), 6944–6947.

(23)   Zhen, C. G.; Becker, U.; Kieffer, J. Tuning Electronic Properties of Functionalized Polyhedral Oligomeric Silsesquioxanes: A DFT and TDDFT Study. *J. Phys. Chem. A* **2009**, *113* (35), 9707–9714.

(24)   Shen, J.; Cheng, W. D.; Wu, D. S.; Li, X. D.; Lan, Y. Z.; Zhang, H.; Gong, Y. J.; Li, F. F.; Huang, S. P. Modeling of Configurations and Third-Order Nonlinear Optical Properties of Methyl Silsesquioxanes. *J. Chem. Phys.* **2005**, *122* (20).

(25)   Zhang, J.; Fischer, M. K. R.; Bäuerle, P.; Goodson, T. Energy Migration in Dendritic Oligothiophene-Perylene Bisimides. *J. Phys. Chem. B* **2013**, *117* (16), 4204–4215.

(26)   Raymond, J. E.; Casado, J.; Lopez Navarrete, J. T.; Takimiya, K.; Goodson, T. Two-Photon Mediated Three-Photon Fluorescence: Lessons from a Quinoidal Oligothiophene Dimer. *J. Phys. Chem. Lett.* **2011**, *2* (17), 2179–2183.

(27)   Carlotti, B.; Cai, Z.; Kim, H.; Sharapov, V.; Madu, I. K.; Zhao, D.; Chen, W.; Zimmerman, P. M.; Yu, L.; Goodson, T. Charge Transfer and Aggregation E Ff Ects on the Performance of Planar vs Twisted Nonfullerene Acceptor Isomers for Organic Solar Cells. *Chem. Mater.* **2018**, *30*, 4263–4276.

(28)   Madu, I. K.; Muller, E. W.; Kim, H.; Shaw, J.; Burney-Allen, A.; Zimmerman, P. M.; Jeffries-EL, M.; Goodson III, T. Heteroatom and Side Chain Effects on the Optical and Photo-Physical Properties: Ultrafast and Nonlinear Spectroscopy of New Naphtho[1,2-B:5,6-B′]Difuran Donor Polymers. *J. Phys. Chem. C* **2018**, acs.jpcc.8b03914.

(29)   Varnavski, O.; Ramakrishna, G.; Kim, J.; Lee, D.; Iii, T. G. Optically Excited Acoustic Vibrations in Quantum-Sized Monolayer-Protexted Gold Clusters. *ACS Nano* **2010**, *4* (6), 3406–3412.

(30)   Yau, S. H.; Abeyasinghe, N.; Orr, M.; Upton, L.; Varnavski, O.; Werner, J. H.; Yeh, H. C.; Sharma, J.; Shreve, A. P.; Martinez, J. S.; et al. Bright Two-Photon Emission and Ultra-Fast Relaxation Dynamics in a DNA-Templated Nanocluster Investigated by Ultra-Fast Spectroscopy. *Nanoscale* **2012**, *4* (14), 4247–4254.

(31)   Yau, S. H.; Varnavski, O.; Gilbertson, J. D.; Chandler, B.; Ramakrishna, G.; Goodson III, T. Ultrafast Optical Study of Small Gold Monolayer Protected Clusters:\rA Closer Look at Emission. *J. Phys. Chem. C* **2010**, *114*, 15979–15985.

(32)   Devadas, M. S.; Kim, J.; Sinn, E.; Lee, D.; Iii, T. G.; Ramakrishna, G. Unique Ultrafast Visible Luminescence in Monolayer-Protected Au 25 Clusters. *J. Phys. Chem. C* **2010**, *114*, 22417–22423.

(33)   Yoon, Z.; Chan, Y.; Li, S. Ultrafast Time-Resolved Spectroscopy of Self-Assembled Cyclic Fe (II) - Bisterpyridine Complexes. *J. …* **2010**, No. Ii, 11731–11736.

(34)   Flynn, D. C.; Ramakrishna, G.; Yang, H.; Northrop, B. H.; Stang, P. J.; Iii, T. G. With Charge Transfer Properties. *J. Am. Chem. Soc.* **2010**, No. 14, 1348–1358.

(35)   Ramakrishna, G.; Goodson, T.; Joy, E. R. H.; Cooper, T. M.; McLean, D. G.; Urbas, A. Ultrafast Intersystem Crossing: Excited State Dynamics of Platinum Acetylide Complexes. *J. Phys. Chem. C* **2009**, *113* (3), 1060–1066.

(36)   Maya, E. M.; Snow, A. W.; Shirk, J. S.; Pong, R. G. S.; Flom, S. R.; Roberts, G. L. Synthesis, Aggregation Behavior and Nonlinear Absorption Properties of Lead Phthalocyanines Substituted with Siloxane Chains. *J. Mater. Chem.* **2003**, *13* (7), 1603–1613.

(37)   Cohen, B.; Wang, S.; Organero, J. A.; Campo, L. F.; Sanchez, F.; Douhal, A. Femtosecond

Fluorescence Dynamics of a Proton-Transfer Dye Interacting with Silica-Based Nanomaterials. *J. Phys. Chem. C* **2010**, *114* (14), 6281–6289.

(38)   Ronchi, M.; Pizzotti, M.; Orbelli Biroli, A.; Macchi, P.; Lucenti, E.; Zucchi, C. Synthesis and Structural Characterization of Functionalized Cyclotetrasiloxane Rings [4-RC6H4Si(O)OR′]4 (R = Cl, Br, CH{double Bond, Long}CH2, CH2Cl; R′ = Na, SiMe3) as Scaffolds for the Synthesis of Models of a Silica Bound Monolayer of Fluorescent or Se. *J. Organomet. Chem.* **2007**, *692* (9), 1788–1798.

(39)   Ronchi, M.; Pizzotti, M.; Biroli, A. O.; Righetto, S.; Ugo, R.; Mussini, P.; Cavazzini, M.; Lucenti, E.; Salsa, M.; Fantucci, P. Second-Order Nonlinear Optical (NLO) Properties of a Multichromophoric System Based on an Ensemble of Four Organic NLO Chromophores Nanoorganized on a Cyclotetrasiloxane Architecture. *J. Phys. Chem. C* **2009**, *113* (7), 2745–2760.

(40)   Maciejewski, A.; Steer, R. P. Spectral and Photophysical Properties of 9,10-Diphenylanthracene in Perfluoro-n-Hexane: The Influence of Solute-Solvent Interactions. *J. Photochem.* **1986**, *35* (1), 59–69.

(41)   Jobin Yvon. *A Guide to Recording Fluorescence Quantum Yields Introduction:*; 2014; Vol. 15.

(42)   Makarov, N. S.; Drobizhev, M.; Rebane, A. Two-Photon Absorption Standards in the 550-1600 Nm Excitation Wavelength Range. *Opt. Express* **2008**, *16* (6), 4029–4047.

(43)   Xu, C.; Webb, W. W. Measurement of Two-Photon Excitation Cross Sections of Molecular Fluorophores with Data from 690 to 1050 Nm. *J. Opt. Soc. Am. B* **1996**, *13* (3), 481.

(44)   Varnavski, O.; Samuel, I. D. W.; Palsson, L. O.; Beavington, R.; Burn, P. L.; Goodson, T. Investigations of Excitation Energy Transfer and Intramolecular Interactions in a Nitrogen Corded Distrylbenzene Dendrimer System. *J. Chem. Phys.* **2002**, *116* (20), 8893–8903.

(45)   Varnavski, O.; Yan, X.; Mongin, O.; Blanchard-Desce, M.; Goodson, T. Strongly Interacting Organic Conjugated Dendrimers with Enhanced Two-Photon Absorption. *J. Phys. Chem. C* **2007**, *111* (1), 149–162.

(46)   Varnavski, O. P.; Ranasinghe, M.; Yan, X.; Bauer, C. A.; Chung, S. J.; Perry, J. W.; Marder, S. R.; Goodson, T. Ultrafast Energy Migration in Chromophore Shell-Metal Nanoparticle Assemblies. *J. Am. Chem. Soc.* **2006**, *128* (34), 10988–10989.

(47)   Hjung, J. Chapter : 1 Introduction; 2010; pp 1–95.

(48)   Létard, J. F.; Lapouyade, R.; Rettig, W. Structure-Photophysics Correlations in a Series of 4-(Dialkylamino)Stilbenes: Intramolecular Charge Transfer in the Excited State As Related to the Twist around the Single Bonds. *J. Am. Chem. Soc.* **1993**, *115* (6), 2441–2447.

(49)   Lewis, F. D.; Weigel, W. Excited State Properties of Donor−Acceptor Substituted *Trans*-Stilbenes: The *m Eta*-Amino Effect. *J. Phys. Chem. A* **2000**, *104* (34), 8146–8153.

(50)   Yang, J.; Chiou, S.; Liau, K. Fluorescence Enhancement of Trans -4-Aminostilbene by N -Phenyl Substitutions: The "Amino Conjugation Effect." *J. Am. Chem. Soc.* **2002**, *124* (11), 2518–2527.

(51)   Murrell, J. N. The Electronic Spectrum of Aromatic Molecules VI: The Mesomeric Effect. *Proc. Phys. Soc. Sect. A* **1955**, *68* (11), 969–975.

(52)   Yamaguchi, S.; Jin, R. Z.; Tamao, K. Modification of the Electronic Structure of Silole by the Substituents on the Ring Silicon. *J. Organomet. Chem.* **1998**, *559* (1–2), 73–80.

(53)   Tamao, K.; Yamaguchi, S. Silole-Pyrole Co-Oligomers: Their Synthesis, Structure and UV-VIS Absorption Spectra. *Chem. Commun.* **1996**, *2*, 1873–1874.

(54)   Tamao, K.; Yamaguchi, S.; Ito, Y.; Matsuzaki, Y.; Yamabe, T.; Fukushima, M.; Mori, S. Silole-Containing .Pi.-Conjugated Systems. 3.1 A Series of Silole-Thiophene Cooligomers and Copolymers: Synthesis, Properties, and Electronic Structures. *Macromolecules* **1995**, *28* (25), 8668–8675.

(55)   Tamao, K.; Yamaguchi, S. Oligosiloles: First Synthesis Based on a Novel Endo-Endo Mode Intramolecular Reductive Cyclization of Diethynylsilanes. *J. Am. Chem. Soc.* **1994**, *116* (26), 11715–11722.

(56)   Yamaguchi, S.; Tamao, K. Theoretical Study of the Electronic Structure of 2,2′-Bisilole in Comparison with 1,1′-Bi-1,3-Cyclopentadiene: σ*-π* Conjugation and a Low-Lying LUMO as the Origin of the Unusual Optical Properties of 3,3′ ,4,4′-Tetraphenyl-2,2′-Bisilole1. *Bulletin of the Chemical Society of Japan*. 1996, pp 2327–2334.

(57)   Yoshihara, K.; Namiki, A.; Sumitani, M.; Nakashima, N. Picosecond Flash Photolysis of Cis- and Trans-Stilbene. Observation of an Intense Intramolecular Charge-Resonance Transition. *J. Chem. Phys.* **1979**, *71* (7), 2892–2895.

(58)   Todd, D. C.; Jean, J. M.; Rosenthal, S. J.; Ruggiero, A. J.; Yang, D.; Fleming, G. R. Fluorescence Upconversion Study of Cis-Stilbene Isomerization. *J. Chem. Phys.* **1990**, *93* (12), 8658–8668.

(59)   Meier, H. Blue Fluorescent Exciplexes Consisting of Trans-Stilbene and Antibodies. *Angew. Chemie - Int. Ed.* **2001**, *40* (10), 1851–1853.

(60)   Kubicki, A. A. Time-Resolved Emission Spectra of Stilbene Derivatives in Various Solvents. *Chem. Phys. Lett.* **2009**, *483* (4–6), 268–272.

(61)   Lapouyade, R.; Czeschka, K.; Majenz, W.; Rettig, W.; Gilabert, E.; Rulliére, C. Photophysics of Donor-Acceptor Substituted Stilbenes. A Time-Resolved Fluorescence Study Using Selectively Bridged Dimethylamino Cyano Model Compounds. *J. Phys. Chem.* **1992**, *96* (24), 9643–9650.

(62)   Lapouyade, R.; Kuhn, A.; Letard, J. F.; Rettig, W. Multiple Relaxation Pathways in Photoexcited Dimethylaminonitro- and Dimethylaminocyano-Stilbenes. *Chem. Phys. Lett.* **1993**, *208* (1–2), 48–58.

(63)   Letard, J. F.; Lapouyade, R.; Rettig, W. Multidimentional Photochemistry in 4- (N,N-Dimethylamino) Stilbene. *Chem. Phys.* **1994**, *186*, 119–131.

(64)   Létard, J. F.; Lapouyade, R.; Rettig, W. Relaxation Pathways in Photoexcited Electron-Rich Stilbenes (DD Stilbenes) as Compared to DA Stilbenes. *Chem. Phys. Lett.* **1994**, *222* (3), 209–216.

(65)   Gustavsson, T.; Baldacchino, G.; Mialocq, J. C.; Pommeret, S. A Femtosecond Fluorescence Up-Conversion Study of the Dynamic Stokes Shift of the DCM Dye Molecule in Polar and Non-Polar Solvents. *Chem. Phys. Lett.* **1995**, *236* (6), 587–594.

(66)   Sumitani, M.; Nakashima, N.; Yoshihara, K.; Nagakura, S. Temperature Dependence of Fluorescence Lifetimes of Trans-Stilbene. *Chem. Phys. Lett.* **1977**, *51* (1), 183–185.

(67)   Rettig, W.; Majenz, W. COMPETING ADIABATIC PHOTOBEACTION CHANNELS IN STILBENE DERIVATIVES. *Chem. Phys. Lett.* **1989**, *154* (4), 335–341.

(68)   Dekhtyar, M.; Rettig, W. Charge-Transfer Transitions in Twisted Stilbenoids: Interchangeable Features and Generic Distinctions of Single- and Double-Bond Twists. *J. Phys. Chem. A* **2007**, *111* (11), 2035–2039.

(69)   Le Breton, H.; Bennetau, B.; F., L. J.; Lapouyade, R.; Rettig, W. Nonradiative Twisted Intramolecular Charge Transfer State in Polar Stilbenes: Photophysical Study of 4-Pedtuorooctylsulfonyl-4'-N,Ndimethylamino Stilbene and Two Bridged Derivatives. *J. Photochem. Photobiol. A Chem.* **1996**, *95*, 7–20.

(70)   Yang, J. S.; Lin, C. K.; Lahoti, A. M.; Tseng, C. K.; Liu, Y. H.; Lee, G. H.; Peng, S. M. Effect of Ground-State Twisting on the Transcis Photoisomerization and TICT State Formation of Aminostilbenes. *J. Phys. Chem. A* **2009**, *113* (17), 4868–4877.

(71)   Charlton, J. L.; Saltiel, J. An Analysis of Trans-Stilbene Fluorescence Quantum Yields and Lifetimes. *J. Phys. Chem.* **1977**, *81* (20), 1940–1944.

(72)   Fujiwara, T.; Lee, J. K.; Zgierski, M. Z.; Lim, E. C. Intramolecular Charge Transfer in the Excited State of 4-Dimethylaminobenzaldehyde and 4-Dimethylaminoacetophenone. *Chem. Phys. Lett.* **2009**, *481* (1–3), 78–82.

(73)   Singh, C.; Ghosh, R.; Mondal, J. A.; Palit, D. K. Excited State Dynamics of a Push-Pull Stilbene: A Femtosecond Transient Absorption Spectroscopic Study. *J. Photochem. Photobiol. A Chem.* **2013**, *263*, 50–60.

(74)   Savikhin, S.; Buck, D. R.; Struve, W. S. Pump-Probe Anisotropies of Fenna-Matthews-Olson Protein Trimers from Chlorobium Tepidum: A Diagnostic for Exciton Localization? *Biophys. J.* **1997**, *73* (4), 2090–2096.

(75)   Bradforth, S. E.; Jimenez, R.; Van Mourik, F.; Van Grondelle, R.; Fleming, G. R. Excitation Transfer in the Core Light-Harvesting Complex (LH-1) of Rhodobacter Sphaeroides: An Ultrafast Fluorescence Depolarization and Annihilation Study. *J. Phys. Chem.* **1995**, *99* (43), 16179–16191.

(76) Leegwater, J. A. Coherent versus Incoherent Energy Transfer and Trapping in Photosynthetic Antenna Complexes. *J. Phys. Chem.* **1996**, *100* (34), 14403–14409.

(77) Yeh, A. T.; Shank, C. V; Mccusker, J. K. Ultrafast Electron Localization Dynamics Following Photo-Induced Charge Transfer. *Science (80).* **2000**, *289* (AUGUST), 935–938.

(78) Wang, Y.; Ranasinghe, M. I.; Goodson, T. Ultrafast Fluorescence Investigation of Excitation Energy Transfer in Different Dendritic Core Branched Structures. *J. Am. Chem. Soc.* **2003**, *125* (32), 9562–9563.

(79) Kopelman, R.; Shortreed, M.; Shi, Z. Y.; Tan, W.; Xu, Z.; Moore, J. S.; Bar-Haim, A.; Klafter, J. Spectroscopic Evidence for Excitonic Localization in Fractal Antenna Supermolecules. *Phys. Rev. Lett.* **1997**, *78* (7), 1239–1242.

(80) Swallen, S. F.; Zhu, Z. G.; Moore, J. S.; Kopelman, R. Correlated Excimer Formation and Molecular Rotational Dynamics in Phenylacetylene Dendrimers. *J. Phys. Chem. B* **2000**, *104* (16), 3988–3995.

(81) Wynne, K.; Hochstrasser, R. M. Coherence Effects in the Anisotropy of Optical Experiments. *Chem. Phys.* **1993**, *171* (1–2), 179–188.

(82) Renger, T. Theory of Excitation Energy Transfer: From Structure to Function. *Photosynth. Res.* **2009**, *102* (2), 471–485.

(83) Soutar, I.; Swanson, L.; Christensen, R. L.; Drake, R. C.; Phillips, D. Time-Resolved Luminescence Anisotropy Studies of the Relaxation Behavior of Polymers. 1. Intramolecular Segmental Relaxation of Poly(Methyl Methacrylate) and Poly(Methyl Acrylate) in Dilute Solutions in Dichloromethane. *Macromolecules* **1996**, *29* (14), 4931–4936.

(84) Jang, S.; Cheng, Y. C.; Reichman, D. R.; Eaves, J. D. Theory of Coherent Resonance Energy Transfer. *J. Chem. Phys.* **2008**, *129* (10).

(85) Knox, R. S.; Gulen, D. Theory of Polarized Fluorescence from Molecular Pairs: Forster Transfer At Large Electronic Coupling. *Photochem. Photobiol.* **1993**, *57* (1), 40–43.

(86) Schulte-Frohlinde, D.; Gorner, H. CIS-TRANS PHOTOISOMERIZATION OF 4-NITROSTILBENES. *Pure Appl. Chem.* **1979**, *51*, 279–297.

(87) Oberlé, J.; Jonusauskas, G.; Abraham, E.; Lapouyade, R.; Rullière, C. Time-Resolved Charge Transfer in "Push-Pull" Stilbenes. *Bull. Chem. Soc. Jpn.* **2002**, *75* (5), 1041–1047.

(88) Becker, H. C.; Kilså, K. Size- and Solvent-Dependent Kinetics for Cis-Trans Isomerization in Donor-Acceptor Systems. *Spectrochim. Acta - Part A Mol. Biomol. Spectrosc.* **2009**, *72* (5), 1014–1019.

(89) Rice, J. K.; Baronavski, A. P. Ultrafast Studies of Solvent Effects in the Isomerization of Cis-Stilbene. *J. Phys. Chem.* **1992**, *96* (8), 3359–3366.

(90) Doany, F. E.; Hochstrasser, R. M.; Greene, B. I.; Millard, R. R. Femtosecond-Resolved

Ground-State Recovery of Cis-Stilbene in Solution. *Chem. Phys. Lett.* **1985**, *118* (1), 1–5.

(91)   Amatatsu, Y. Skeletal Relaxation Effect on the Charge Transfer State Formation of 4-Dimethylamino,4′-Cyanostilbene. *J. Phys. Chem. A* **2006**, *110* (28), 8736–8743.

(92)   Nagasawa, Y.; Yartsev, A. P.; Tominaga, K.; Johnson, A. E.; Yoshihara, K. Temperature Dependence of Ultrafast Intermolecular Electron Transfer Faster than Solvation Process. *J. Chem. Phys.* **1994**, *101* (7), 5717–5726.

(93)   Marcus, R. A. On the Theory of Oxidation-Reduction Reactions Involving Electron Transfer. I. *J. Chem. Phys.* **1956**, *24* (5), 966–978.

(94)   Zgierski, M. Z.; Lim, E. C. The Role of Πσ* State in Intramolecular Electron-Transfer Dynamics of 4-Dimethylaminobenzonitrile and Related Molecules. *J. Chem. Phys.* **2004**, *121* (6), 2462–2465.

(95)   Katan, C.; Terenziani, F.; Mongin, O.; Werts, M. H. V.; Porrès, L.; Pons, T.; Mertz, J.; Tretiak, S.; Blanchard-Desce, M. Effects of (Multi)Branching of Dipolar Chromophores on Photophysical Properties and Two-Photon Absorption. *J. Phys. Chem. A* **2005**, *109* (13), 3024–3037.

(96)   Rogers, J. E.; Stogie, J. E.; McLean, D. G.; Sutherland, R. L.; Sankaran, B.; Kannan, R.; Tan, L. S.; Fleitz, P. A. Understanding the One-Photon Photophysical Properties of a Two-Photon Absorbing Chromophore. *J. Phys. Chem. A* **2004**, *108* (26), 5514–5520.

(97)   Li, B.; Tong, R.; Zhu, R.; Meng, F.; Tian, H.; Qian, S. The Ultrafast Dynamics and Nonlinear Optical Properties of Tribranched Styryl Derivatives Based on 1,3,5-Triazine. *J. Phys. Chem. B* **2005**, *109* (21), 10705–10710.

(98)   Beljonne, D.; Wenseleers, W.; Zojer, E.; Shuai, Z.; Vogel, H.; Pond, S. J. K.; Perry, J. W.; Marder, S. R.; Brédas, J. L. Role of Dimensionality on the Two-Photon Absorption Response of Conjugated Molecules: The Case of Octupolar Compounds. *Adv. Funct. Mater.* **2002**, *12* (9), 631–641.

(99)   Ramakrishna, G.; Goodson, T. Excited-State Deactivation of Branched Two-Photon Absorbing Chromophores: A Femtosecond Transient Absorption Investigation. *J. Phys. Chem. A* **2007**, *111* (6), 993–1000.

(100)   Mattori, M.; Mogi, K. Studies on the Trapping and Detrapping Transition States of Atomic Hydrogen in Octasilsesquioxane Using the Density Functional Theory B3LYP Method. *J. Phys. Chem. A* **2000**, *104* (46), 10868–10872.

Chapter 8

Thesis Summary and Future Directions

8.1 Thesis Summary

In the ongoing research and development of new efficient materials for organic photovoltaic applications, it is crucial to have an understanding of the core optical and photophysical properties of these organic compounds to advise a more targeted design and synthesis procedure. The active layer of an organic photovoltaic device comprises of an electron donor – mostly an electron-rich D-A polymer, and an electron acceptor – an electron-deficient D-A macromolecule, and a record power conversion efficiency of 18% for single-junction organic photovoltaic devices have been obtained.[1–3] More background details on the components of organic solar cells, are given in Chapter 1. The introduction chapter also provides an overview on the current and future trends for energy production and energy consumption, the historical evolution of solar harvesting, the key principles of solar harvesting devices, benefits of organic over inorganic solar devices, the ideal active layer materials, the fundamental mechanisms (such as charge transfer, triplet production) occurring in these active layer materials, and most importantly the motivations for my research. In summary, this dissertation seeks to provide the fundamental structure-property-performance relationships and correlations that are critical in designing organic and hybrid macromolecules (including polymers) for efficient light harvesting, charge generation and charge transfer. The studies in this work were carried out using highly sophisticated time-resolved, steady-state and non-linear spectroscopic techniques, to point out the underpinning optical processes that make these organic and hybrid materials excellent solar cell

alternatives. The experimental techniques employed were described comprehensively in Chapter 2 alongside their theory, placing more emphasis on transient absorption spectroscopy – the most versatile spectroscopic technique for detecting, tracking and quantifying bright and dark states' species generated following photoexcitation.[4] This thesis places more emphasis on a special class of organic electron acceptor known as perylene diimides (PDIs). They are the most popular in the class of rylene diimide non-fullerene electron acceptor and also the most popular in the general class of non-fullerene acceptors.[5]

Singlet exciton fission (SEF) – the generation of two triplet excitons from one photoexcited singlet exciton by the absorption of a single photon – is an important process which would allow for an increase in the efficiency of photovoltaic cells by up to a factor of 1.5, provided that each triplet injects an electron into the receiving electrode.[6] In Chapter 3, the physical science of intramolecular singlet exciton fission (SEF) was studied in PDI trimer systems. Understanding the structural motif of PDI acceptor compounds that activate *intra*molecular SEF represent a significant step forward in structure–property understanding & device manufacturing. The charge-transfer PDI trimers consist of A-π-D-π-A-π-D-π-A configuration, for which -A- is a PDI monomer with 1-hexylheptyl solubilizing side group on its imide position, -D- is a benzodithiophene donor moiety and -π- represent the *flexible* or *rigid* bridge connector.[7] For one of the PDI trimers, the presence of a flexible π-bridge led to the compound assuming a twisted geometry and for the second PDI trimer, its rigid π-bridge led to the compound assuming a planar geometry. The required energetics for SEF $E(S_1) \geq 2 \cdot E(T_1)$ was satisfied only in the flexible π-bridged PDI trimer. Using steady-state absorption and fluorescence spectroscopy, backed by quantum chemical calculation, I found that the flexible π-bridged PDI trimer displayed weaker electronic coupling (poor electronic communication among PDI chromophores). The femtosecond

transient absorption technique was used to measure the rate of triplet formation, and nanosecond transient absorption was used to evaluate the efficiency of SEF by quantifying the singlet-to-triplet yield (ϕ_T) via triplet sensitization and relative actinometry measurements. I found that the flexible π-bridged PDI trimer displayed a fast triplet formation (340 ps) and $\phi_T \gg 100\%$, thus confirming the unique role the π-bridge structure plays in predicting intramolecular SEF in PDI systems.

Charge transfer and subsequent charge separation are very important processes in organic solar cells. In fact, in the photocurrent generation process of organic solar cells (**Figure 1.11**), the charge transfer step is most often described as the rate-determining step. Hence, a crucial understanding of the charge transfer rate and the charge separation mechanism in active layer materials is required. Chapter 4 discusses the impact of ring-fusion on the optical properties of N-annulated thiophene π-bridged dimer systems. The two dimers studied showed a NPDI–thiophene–NPDI configuration, where the thiophene moiety served as a flexible (unfused) or rigid (fused) π-bridge between the two N-annulated PDI units. Steady-state absorption and emission measurements were used to confirm molecular rigidity in the case of the fused thiophene π-bridged N-annulated dimer, owing to the one order of magnitude smaller Stokes-shift obtained. The two-photon absorption and femtosecond transient absorption measurements confirmed the ultrafast charge separation in the fused dimer. More importantly, using time-resolved spectroscopic techniques, I found that ring-fusion of the N-annulated thiophene π-bridged dimer opened up the triplet excited state deactivation pathway (via the CT state) that was not present in the unfused dimer. In Chapter 5, a charge transfer study on two dimeric PDI positional isomers characterized by acceptor–weak acceptor–acceptor (PDI–core–PDI) structure, was carried out. The weak acceptor or core moiety is a thieno-pyrido-thieno-isoquinoline-dione rigidly connected through cyclization to the lateral PDIs. The two PDI dimers are positional isomers and thus analogous in

structure. Switching the relative position of the alkyl amino and keto groups in the core moeity should induce steric hindrance and thus introduce torsion in the conjugated backbone of one (twisted), which is absent in the other (planar). The twisted and planar isomers were studied using steady-state, non-linear, femtosecond time-resolved spectroscopies and quantum-chemical computations as well as electrochemical, and X-ray scattering techniques. We found from the study that a more efficient charge separation mechanism – symmetry-breaking charge separation, was observed for only the planar PDI isomer. Also, the planar isomer displays an attractive strategy to ultimately achieve charge separation with a donor polymer with much lower driving force, enhanced directionality, and retarded recombination rate. Higher efficiencies were indeed observed in the device made with the planar compound in comparison to the twisted.

Most donor polymers for organic photovoltaic application use thiophene as the heterocyclic π-bridge in their backbone relative to furan – a more sustainable counterpart derived from furfural (a biomass derivative). In Chapter 6, the effect of alternating the heterocyclic π-bridge moiety (thiophene vs furan) on the photophysical and electronic properties of D–π-bridge–A polymers, was investigated. I also investigated the effect of alternating the alkyl group side chain (linear vs bulky), on the photophysical and electronic properties. In the polymeric backbone, the -D- is naphtho difuran (NDF), and the -A- is diketopyrrolo[3,4-c]pyrrole (DPP). Steady-state absorption studies showed that the polymers with the furan π-bridge in the backbone displayed a favorable tendency of capturing more solar photons when used in a photovoltaic device. Owing to their higher degree of molecular planarity (obtained by quantum chemical calculation), the furan π-bridge polymers showed a larger TPA-δ. Also, the linear side chain polymers, with better solution-processability, showed longer fluorescence lifetime and higher TPA-δ. These suggest that the furan π-bridge and the linear side chain polymers will display higher charge transfer (CT)

tendencies in comparison to the thiophene π-bridge and the bulky side chain analogues, respectively. In general, it was concluded that the furan-backbone polymer is a potential substitute, if not a more suitable candidate, and could be used for the efficient harvesting of solar radiation and the conversion of excitons into separated charge carriers.

Chapter 7 investigates the ultrafast excited states dynamics of fully and partially functionalized silsesquioxane cage structures for photovoltaic application. Functionalization of the T8 silsesquioxane (8-corner caged compounds) with several kinds of chromophoric arms have been long studied, alongside their steady-state optical properties.[8–12] This work seeks to study the excited states dynamics of these fully functionalized caged compounds (Cube), alongside the study of its partially-functionalized derivatives – Half and Corner. Attaching a strong donor like dimethyl stilbene on its corners induces strong electronic and charge transfer properties. These properties can be altered by varying the number of chromophoric arms attached owing to inter-chromophore coupling. Ultrafast fluorescence upconversion and femtosecond transient absorption spectroscopy were used to study the mechanism of excitation energy transport and the charge transfer property. The Half and Cube systems showed a faster excitation energy delocalization, and the Cube system showed a stronger intramolecular charge transfer and larger two-photon absorption cross section.

8.2 Set of Molecular Geometry Guidelines for Structure-function Relationships

Strong aggregation effects are most often observed with monomeric systems, which are detrimental to organic solar cell devices. In multichromophoric systems (two or more monomers connected via a π-bridge), aggregation effects are greatly reduced depending on their molecular geometry. For organic solar materials with donor–π-bridge–acceptor configuration, molecular geometry also plays a key role in also predicting their optically-excited properties such as charge

transfer and triplet production via intersystem crossing (ISC) or singlet exciton fission (SEF) pathway. Unfortunately, with polymers, it is difficult to control their chain length which goes on to alter their optically-excited properties. Hence, small multichromophoric molecules are most preferred because they offer much better control.

In the literature, multichromophoric perylene diimides (PDIs) have been said to show better charge stabilization relative to monomeric PDI systems. In these multichromophores, efficient intramolecular charge transfer (CT) and electron delocalization is attributed to *molecular planarity* achieved via either ring-fusion of the donor/acceptor moiety with the π-bridge and/or the absence sterics. This is similar to the observed behavior of fused-ring non-fullerene electron acceptors (e.g. ITIC, IEIC) that have shown the highest power conversion efficiency (PCE) in organic solar cell devices (18%).[1–3] In this dissertation, two-photon absorption and femtosecond transient absorption (fsTA) measurements have been used to confirm the correlation between *molecular planarity* and charge transfer in PDI multichromophores and polymers with donor–π-bridge–acceptor. Ultrafast photoinduced intramolecular CT have been observed with ring-fused systems (planar) relative to their unfused (twisted/flexible) counterpart. In these planar systems, following ultrafast CT, triplet production has also been observed to take place via spin-orbit CT ISC owing to strong electronic coupling within its backbone. With this, it is safe to conclude that *molecular planarity* favors ultrafast photoinduced CT and could lead to the production of long-lived triplet-associated charges.

Twisted or flexible π-bridged systems show weaker electronic coupling. In my study, triplet production via SEF was observed in only the trimer and tetramer systems with more than two PDI units. However, excimer formation owing to overlapping π-π stacking and common in flexible π-bridged systems could impede SEF. Although SEF in PDI multichromophoric systems leads to the production of more charge density, the voltage of these charges could be lower owing

to their low triplet energy achieved by down-conversion. Therefore, it is important to continue the search for novel organic SEF compounds, with higher triplet energies relative to PDIs.

8.3 Future Directions

The measurements in this dissertation were carried out in solution phase. OPV cells are made in thin films. In thin films, the organic molecules are tightly packed and the interaction between the molecules (*inter*molecular) becomes important. It is therefore essential to study the spectroscopic behaviors of the organic materials in thin films. Solid-solid interactions must be considered if the complete picture of the excited state dynamics of OPV materials, following photoexcitation, is desired. It is necessary to carry out characterizations of organic materials in solid state using the steady-state techniques, the two-photon absorption technique, and more importantly the femtosecond and nanosecond transient absorption techniques.

Most of the triplet studies for OPVs are carried out using only one component of the active layer at a time – either only the donor or the acceptor. Given the importance of understanding the triplet production mechanism as it occurs in OPV device, it is therefore essential to carryout triplet studies with the mixture of both donor and acceptor materials. Most of the triplet studies in this thesis were for the acceptor macromolecule – perylene diimide. It will be important to characterize their triplet species in the presence of a donor polymer, just as in the active layer of the OPV device. The new and powerful nanosecond system installed in the Goodson lab provide researchers with the tools needed to be able to carry this out. With the help of the accompanying optical parametric oscillator (OPO), selected sample excitations can be done at any wavelength of your choosing in the far UV, Visible and near-IR – important excitation wavelengths for OPV systems.

In organic photovoltaic (OPV) systems, tracking the decay of triplet species is as important as quantifying the amount of triplets produced from an excited singlet. Charge recombination

leading to the formation of triplet species is an important mechanism in organic solar materials; ae well as singlet exciton fission – the direct production of two triplets from one excited singlet. Two rigorous experiments – triplet sensitization and relative actinometry – combined together are carried out to quantify the singlet-to-triplet yield, each using a reference compound which has a known triplet extinction coefficient and triplet yield. One of the bottlenecks in these measurements is in choosing a suitable reference compound for the triplet energy sensitization measurement. It is essential to have a repository of suitable reference compounds specifically for OPV systems, just as was done by Murov, Carmichael and Hug in the Handbook of Photochemistry.[13] Also, for OPV triplet studies oxygen purging is paramount to the triplet dynamics obtained. Accurately controlling the purging condition is vital. In the future, it will be essential to control the time to flow in N_2 or argon (for purging oxygen) into the sample, the flow position, as well as control the accurate flow rate of N_2 into the sample. These will ensure that for each measurement involving triplet species, more accurate rates, $k_{Triplet}$ (triplet decay rate), k_{rISC} (rate of reverse intersystem crossing), k_{ET} (triplet energy transfer rate from D to A) are obtained.

Quantum theoretical calculations are becoming an essential tool in the development of new materials because of the rapid development in the computational technology over the years. All the studies in this dissertation relied on the results of some theoretical calculation such as density functional theory (DFT), time-dependent DFT, and restricted active space spin-flip (RAS-SF). These computations are limited by the size of the organic molecule; they are mostly suitable for a monomer or dimer, and at most a trimer system. A more rigorous computational approach will be required in the modeling of electronic structure of polymers, like those in Chapter 6 of this thesis where results past dimers are desired.

References

1   Q. Liu, Y. Jiang, K. Jin, J. Qin, J. Xu, W. Li, J. Xiong, J. Liu, Z. Xiao, K. Sun, S. Yang, X. Zhang and L. Ding, *Sci. Bull.*, 2020, **65**, 272–275.

2   Z. Wang, Z. Peng, Z. Xiao, D. Seyitliyev, K. Gundogdu, L. Ding and H. Ade, *Adv. Mater.*, 2020, **2005386**, 2005386.

3   Y. Cui, H. Yao, J. Zhang, K. Xian, T. Zhang, L. Hong, Y. Wang, Y. Xu, K. Ma, C. An, C. He, Z. Wei, F. Gao and J. Hou, *Adv. Mater.*, 2020, **32**, 1–7.

4   R. Berera, R. van Grondelle and J. T. M. Kennis, *Photosynth. Res.*, 2009, **101**, 105–118.

5   C. Yan, S. Barlow, Z. Wang, H. Yan, A. K. Y. Jen, S. R. Marder and X. Zhan, *Nat. Rev. Mater.*, 2018, **3**, 1–19.

6   J. Michl, A. J. Nozik, X. Chen, J. C. Johnson, G. Rana, A. Akdag and A. F. Schwerin, in *Organic Photovoltaics VIII*, 2007, vol. 6656, p. 66560E.

7   B. Carlotti, I. K. Madu, H. Kim, Z. Cai, H. Jiang, A. K. Muthike, L. Yu, P. M. Zimmerman and T. Goodson, *Chem. Sci.*, 2020, **11**, 8757–8770.

8   M. Z. Asuncion and R. M. Laine, *J. Am. Chem. Soc.*, 2010, **132**, 3723–3736.

9   J. Hwan Jung, J. C. Furgal, T. Goodson, T. Mizumo, M. Schwartz, K. Chou, J. F. Vonet and R. M. Laine, *Chem. Mater.*, 2012, **24**, 1883–1895.

10   R. M. Laine, S. Sulaiman, C. Brick, M. Roll, R. Tamaki, M. Z. Asuncion, M. Neurock, J. S. Filhol, C. Y. Lee, J. Zhang, T. Goodson, M. Ronchi, M. Pizzotti, S. C. Rand and Y. Li, *J. Am. Chem. Soc.*, 2010, **132**, 3708–3722.

11   S. Sulaiman, A. Bhaskar, J. Zhang, R. Guda, T. Goodson and R. M. Laine, *Chem. Mater.*, 2008, **20**, 5563–5573.

12   S. Sulaiman, J. Zhang, T. Goodson and R. M. Laine, *J. Mater. Chem.*, 2011, **21**, 11177–11187.

13   S. Murov, I. Carmichael and G. L. Hug, *Handbook of Photochemistry*, Marcel Dekker, Inc., New York, second., 1993.